



Baltica IX

International Conference on Life Management and Maintenance for Power Plants

Baltica IX

International Conference on
Life Management and Maintenance
for Power Plants

Helsinki–Stockholm–Helsinki

11–13 June, 2013

Edited by Pertti Auerkari & Juha Veivo



ISBN 978-951-38-8025-5 (USB flash drive)
ISBN 978-951-38-8026-2 (URL: <http://www.vtt.fi/publications/index.jsp>)

VTT Technology 106

ISSN-L 2242-1211

ISSN 2242-122X (Online)

Copyright © VTT 2013

JULKAISIJA – UTGIVARE – PUBLISHER

VTT

PL 1000 (Tekniikantie 4 A, Espoo)

02044 VTT

Puh. 020 722 111, faksi 020 722 7001

VTT

PB 1000 (Teknikvägen 4 A, Esbo)

FI-02044 VTT

Tfn +358 20 722 111, telefax +358 20 722 7001

VTT Technical Research Centre of Finland

P.O. Box 1000 (Tekniikantie 4 A, Espoo)

FI-02044 VTT, Finland

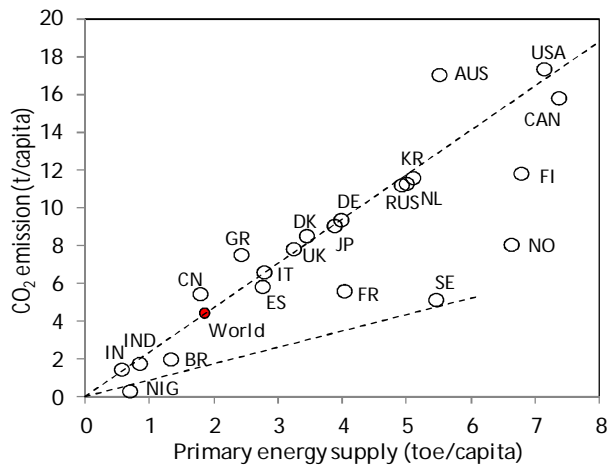
Tel. +358 20 722 111, fax +358 20 722 7001

Cover picture Fortum Oyj

Kopijyvä Oy, Kuopio 2013

Preface

Since 1988, the triannually organised Baltica Conferences have witnessed continuous change in the environment of operating and maintaining power plants, and Baltica IX in 2013 is no exception. The first conference took place two years after the Chernobyl accident, and although new nuclear plants are again under construction even in Europe, the trouble in Fukushima has revealed risks that needed to be addressed. The accelerating use of coal in the fast growing parts of the world, and new availability of fracking gas has resulted in increasing reliance on fossil fuels in spite of simultaneous emphasis on renewables. The rate and direction of change are making it very difficult to reduce the atmospheric CO₂ content from the present to the target level of 450 ppm any time soon. Even if we must prepare for rising seawater, future policies will retain countermeasures. What is needed is better technology to remove or fully recycle millions of tons of CO₂ per TWh produced, or equivalent capability for alternatives not releasing CO₂.



Reliance on fossil fuels is characteristic to most countries

However, the shift towards more renewables like wind and solar power will also mean more fluctuation in the supply, and a challenge of compensating with other capacity and avoiding heavy subsidies. The issues are far from solved by the current technology and policies, and also show much regional variation. At the same time, not unlike in the issues addressed in the previous Baltica Conferences, existing capacity is ageing and may require attention for example with extended operational timescales, or with new materials, fuels, structures or process solutions.

The editors wish to thank all authors, reviewers, organisers and the Board of the Conference for their invaluable help in preparing for the event and the proceedings. Financial and other contributions by the supporting and sponsoring organisations are also gratefully acknowledged.

Pertti Auerkari & Juha Veivo

Contents

Preface.....	3
Session 1 – Introductory keynotes	
Development of future power plants – demand and challenges	8
Risk-Based Inspection (RBI) in fossil-fuel fired power plants: Developing further the EU approach and applying it in the large-scale projects	19
Similitude of residual stresses and the warm pre stress effect.....	50
Session 2 – Nuclear plant	
French Ageing Management Program in connection with IAEA Safety Guides.....	63
Fatigue of stabilised steel in NPP primary piping – discussion on design curves	75
Effect of initial flaw and load assumptions on risk estimate changes	103
NB-3650M fatigue calculation procedure	125
Weld repair simulation for the Mock-up 2 of EU FP7 STYLE Project.....	139
Fracture mechanical characterisation of ferrite-austenite dissimilar metal welds (DMWs) for elevated temperature service in view of metallurgical mis-match	152
General corrosion and SCC tests on ODS steels in supercritical water.....	174
Session 3 – Combustion plant	
Qualification of structural materials for the advanced 700 C fossil fired power plant – experience gained in the GKM field test loops	194
Creep-fatigue properties of nickel-base superalloy 263	204
Fireside corrosion of Ni-based alloys in simulated co-firing combustion environment.....	218
Degradation of single-crystal gas turbine blades	233
Evaluation of creep damage in martensitic 9–10%Cr-steel components ...	251
Influence of boiler operating conditions to component lifetime, case study: pulverized coal burner.....	262

High temperature multiaxial component testing and modelling for the prediction and monitoring of creep-fatigue behaviour	275
Self-heating and autoignition of coal in rock silos	292
Session 4 – Nuclear plant	
Creep properties of Zircaloy-4 for nuclear fuel cladding FEA simulation ..	302
New applications of pneumatically powered testing equipment for extreme environments.....	318
30 years of nuclear structural integrity – Lessons learned and proposals for future directions	337
Forecast reliability of embrittlement trend curves for Swedish nuclear reactor pressure vessel steels	353
Application of Alloy 690 and associated weld metals in PWRs.....	377
Performance of copper overpack for repository canisters.....	378
The effect of sulphide exposure on the mechanical behaviour of OFP copper.....	395
NDE of the disposal canisters	411
Session 5 – Combustion plant	
TÜV NORD concept COOP – A powerful tool to meet the challenges of power plant flexibilization	424
Risk assessment of power station production unit	441
Importance of pressure equipment inspection in power plants: Looking to the future.....	447
Investigations of superheater materials from Nordjyllandsværket coal-fired plant after 100.000 hours service.....	458
Assessment of remaining lifetime of the boiler tube and microstructure analysis.....	477
Long term and pilot study of HAZ creep behaviour of weld repaired low alloyed heat resistant steels.....	484
Corrosion resistance of Kanthal A-1 and Fe-12Cr-2Si alloy coatings in Cl-containing environment.....	500
A material solution against fireside chloride corrosion.....	513

Corrosion and carburization of superheater materials in oxyfuel combustion.....527

Session 6 – Cross-cutting issues: methods of condition assessment

A renaissance in Small Punch testing at Swansea University538

Practical application of impression creep data to power plant553

“On site” X-Ray Diffraction method to observe the creep phenomenon and its propagation at the nano-scale.....567

Differences in defect indications of three artificially produced defects in ultrasonic inspection.....581

Detection of magnetite piles on steam generator tubing with eddy current method603

Model assisted calculations for NDE reliability611

Session 7 – Combustion plant

Experience in integrity assessment of steam turbine casings operated beyond the design lifetime.....619

Evaluation of mechanical properties and microstructure of dissimilar weld joint of COST F and FB2 steels after long term creep test.....630

Determination and solution of power plant furnace problems with pilot-scale studies640

New model for steam oxidation of power plant steels.....647

Coating solutions against high temperature corrosion – performance validation and feasibility at biomass fired boilers656

Life in plant – challenges and solutions671

Development of future power plants – demand and challenges

Rudolph Blum

Retired R&D Director, DONG Energy Thermal
Denmark

Abstract

Worldwide Increasing demand for sustainable energy calls for flexible solutions depending on the local conditions. Even wind power and solar energy capacity are expanding all over the world high efficient fossil fuel power plant will continue to be the basic concept in development countries where the need for new energy is large and coal is cheap. The potentials for improved coal fired plants are revealed. In the western countries especially Europe the massive increase in renewable energy is challenging the future energy system and high degree of flexibility may only be establish in the long run using gas turbines as back up for the intermitting out put from wind and solar generation.

1. Introduction

We are in the middle of an enormous change of the energy system worldwide. Due to increasing concerns about limitations in fossil fuel reserves and the climate changes, all countries have a strong focus on how to organise and develop future sustainable energy systems. The challenges are very much depending on the local circumstances in the countries – rich or poor, high or low energy consumption and level of development. Therefore, the kind of development activities and their intensity reflect to a great deal the local situation. In the new economies, BRIC, and in other developing countries, we see an annual growth rate of more than 10% whereas the western world still assumes increases of 1–2%. Therefore, the world will demand more energy in the coming decades. Renewable energy like hydro, wind, solar and biomass will cover an increasing share of this increase. However, the major part will still be based on fossil fuel – primarily coal and gas and to some extent on nuclear, see Figure 1. Especially those developing countries, which have direct access to coal, will predominately make use of these coals for a long period to cover their energy demand. On this background, the development of new power plants roughly spoken will have to face different challenges to obtain a relatively low emission and efficient development. Both highly efficient fossil fuel power plant as well as flexible generation concepts based on renewable energy will come into play. For countries who choose the fossil fuel for their basic energy production, high efficiency is the most important issue. However, flexibility

has also to be part of the solution as wind and solar power get an increasing importance even in these countries.

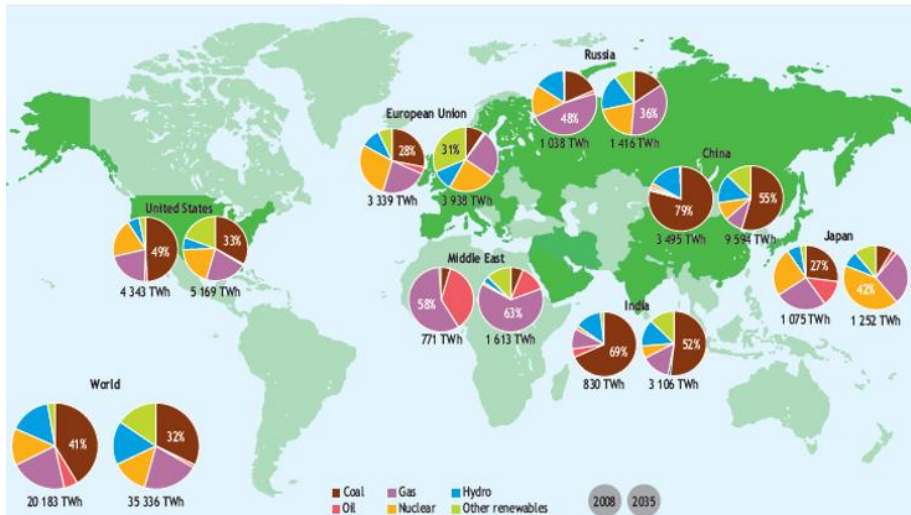


Figure 1. Electricity generation by fuel and region for the period 2008–2035; IEA 2010.

For countries where basic energy policy focuses on the shift to renewable energy, the majority of new plants will be wind power and solar energy. These concepts need a strong flexible backup to cover the demand when the wind is not blowing or the sun not shining. The challenge for such a backup is to have a very high degree of flexibility based on thermal power with biomass as primary fuel. Of course, many countries will choose a development route somewhere in between these two extremes but trying to describe the needs and trends for these two development routes most of the building blocks for any future are covered.

2. High efficient fossil fuel power plants

2.1 USC 600°C

The state of the art for fossil fuel power plants are 500–1000 MW coal or lignite fired units operating with advanced USC (Ultra Super Critical) steam parameters 600°C and 250–300 bar using single or double reheat. The majority of this kind of plants built since the 1990’s in Japan, Europe and China has limited the pressure to 250–260 bar and use single reheat mainly to minimise capital cost. These units demonstrate efficiencies about 43–46% depending on fuel quality – bituminous coal or lignite and on condenser cooling – cooling tower or seawater cooling.

The right choice of materials has been a central question for a successful realisation of these plants. During the 1980's and 1990's, the Japanese steel industry developed the basic pallet of materials for these plants, see Table 1.

Table 1. The Japanese steel development for USC power plants.

Furnace wall tubes	HCM2S
Superheater & reheater tubes	TPH347HFG, SUPER304H, HR3C
Thick section boiler component and steam lines	P92
Turbine rotor materials	TMK1, TMK2

In Europe, within the COST research activities, mainly turbine materials were successfully developed and qualified. Steels E and F for rotor forgings – materials close to the Japanese TMK 1 and 2 were the first COST turbine materials to be used in Europe. Development in the late 1990's and in the 2000's resulted in even stronger turbine materials adding B to the alloys. With the COST materials FB2 and CB2 for forgings and castings, excellent European turbine materials for the construction of USC power plant are available.

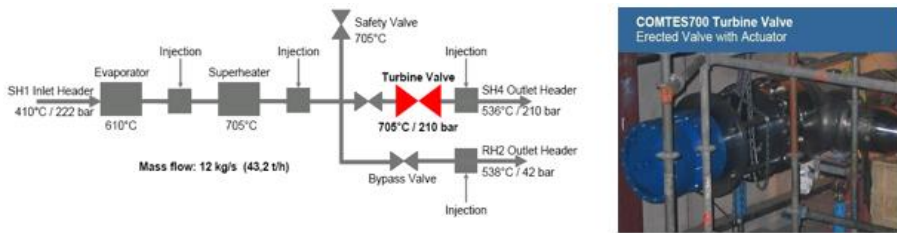
Apart from some preliminary problems mostly related to the increase in temperature and the associated steam oxidation problems the USC concept can only be considered as a success. Today more than 20 GW USC plants are in service in Japan and Europe and the USC plants are the only concept to be considered if new coal fired power plants are going to be built. In China USC is the concept for the future. More than 70% of the new installed capacity in China is 600–1000 MW USC plants and today the total generation capacity is far above 100 GW and still increasing. In USA as well as in India new coal fired plants will be based on the USC concept.

2.2 700°C project

In the late 1990's the struggle for making an even more efficient coal fired plant for reducing the CO₂ emission resulted in the formation of the European AD700°C project. If the efficiency of the Carnot process shall increase, elevated steam parameters – higher steam temperature and pressure must be demonstrated. The USC design was limited to 600°C due to lack of a ferritic material for thick section boiler component and steam lines to operate at temperatures higher than 600°C. The design of a USC plant with temperatures above 600°C had to utilise nickel based materials for these components including the last section of the superheaters and reheaters as well as the hot end of the HP and IP turbines. As nickel based materials are approximately 10 times as expensive as high-alloyed ferritic materials, a construction using nickel based materials had to show efficiencies at its outmost to pay for the additional investment by saving fuel cost.

The AD700°C project aimed for a power plant operating at the highest possible steam parameters combined with an optimised thermodynamic architecture and improved design concept – compact design – combined with the use of nickel based materials with the highest possible strength to be able to minimise the overall costs.

The AD700°C project and the succeeding projects – COMTES700 and ENCIO have been active for 15 years. During these years, it has been possible to identify, develop and qualify all materials needed for such a power plant. Fabrication trials of tubes, pipes, forgings and castings of these advanced materials were successfully done as well as fabrication of the most critical components. Through substantial in-plant testing of full-scale components under real operation condition, lot of experiences were gained, see Figure 2.



COMTES700 In-plant testing of turbine valve

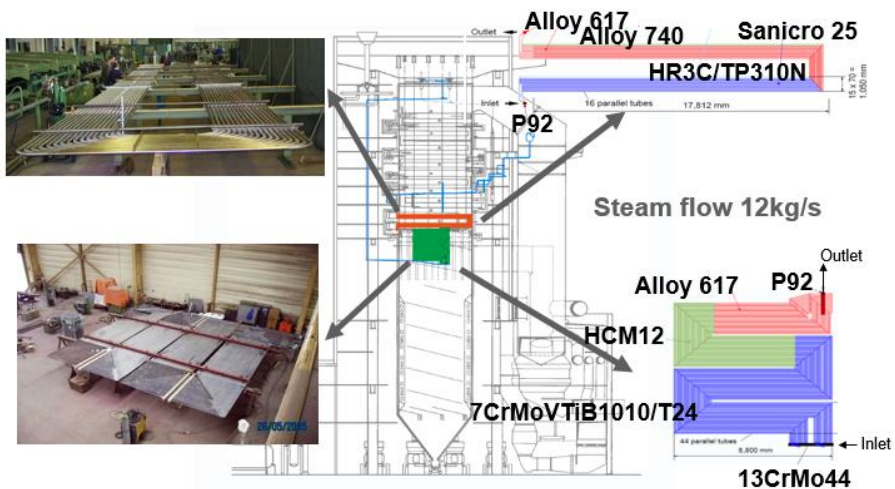


Figure 2. COMTES700 In-plant testing of furnace panels and superheaters in an existing boiler.

Table 2 shows the materials selected for the AD700°C project for boiler and turbine apart from the well known materials used for 600°C USC plants, shown in brackets.

Table 2. Materials selected for development and qualification for a 700°C power plant.

Furnace wall tubes	IN617 (HCM2S, HCM12)
Superheater & reheater tubes	Sanicro25, IN617, Alloy 740 (SUPER304H, HR3C, NF706)
Thick section boiler components and steam lines	IN617, Alloy 263 (P92)
Turbine materials for rotor and casing	IN625, IN617, Waspaloy 105 (FB2, CB2)

In USA and in Japan similar development projects are running. In USA EPRI coordinate the projects which more or less have the same goals and content as the European projects. In Japan their program covers interesting ideas about development of new types of alloys less expensive but heading for the same mechanical strength and oxidation and corrosion resistance.

In spite of significant progress in the development process there is an increasing doubt about the commercial success for a 700°C nickel based coal fired power plant. The estimated plant cost have gone up during the years due to the facts that nickel alloys are expensive and very difficult to handle which increases the total cost further. Only the very best – mechanical strong candidate Alloy 740 with an expected mechanical strength 30–50% higher than the most analysed material IN617 may show major reductions in the tonnage of nickel based materials used for a plant. Combined with the most advanced thermodynamic design heading for efficiencies about 53% the overall plant cost can be reduced to its minimum. Such a concept may be of interest to countries who are continuing massive exploitation of coal based generation. For Europe and most probably for Japan and USA as well the concept may not have any chance due to a mismatch with the expected energy policy. However, there is still a very long way to go and lot of difficulties – handling problems of the bare materials as well as welding problems– need to be solved before a conclusion can be taken.

2.3 Improved USC 600°C

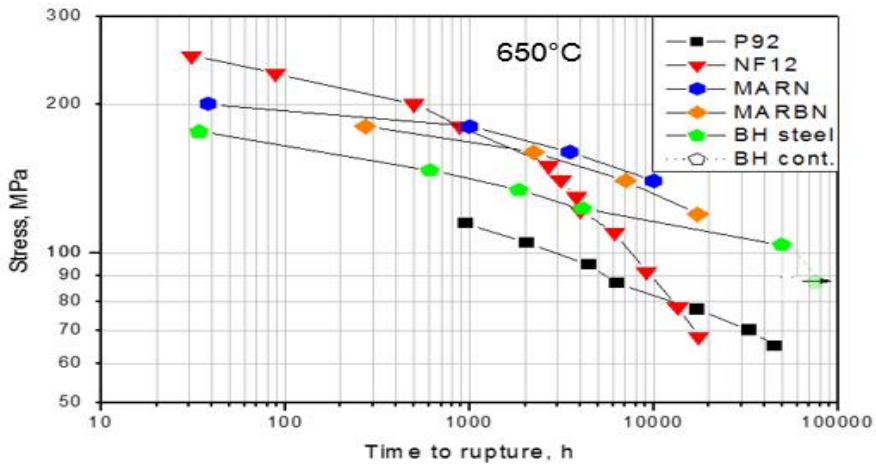
As an easier and cheaper alternative to the 700°C projects, improvements of the efficiency of the existing 600°C USC concepts should be considered. Introducing an upgrade of thermodynamic design realising double reheat with live steam pressure close to 300 bar, improved LP exhaust, serial condenser coupling, boiler cold end optimisation including those improvements demonstrated by the turbine manufacturers during the last decade an efficiency for a seawater cooled 600°C USC plant above 49% can be realised.

Such a plant will cost about 15% more than the standard version of a USC 600°C plant and the choice of materials will be very much the same. The higher live steam pressure will increase the metal temperature in the furnace panel tubes. This calls for improved material qualities like the newly developed T23 or T24. These materials have recently been under dispute due to a large number of reported problems. Mainly T24 but also T23 have demonstrated cracking problems associated to a welding process not using PWHT. Thorough investigations of the problems have shown that the metallurgy of these alloys is much more delicate than first expected. Even smaller deviation from a perfect procedure may cause too high residual stresses and hardness resulting in through wall thickness cracks during commissioning.

As most of the reasons for the problems have been revealed and as some boiler manufacturers seem to handle the fabrication without problems, it should be possible to use these materials for future boilers.

Anyhow, all the advanced ferritic materials used in modern USC boilers have a complicated metallurgy that need to be understood and respected if problems are going to be avoided. All problems reported on premature failures in the advanced martensitic pipe materials P91 and P92 are related to inadequate observance of the given specifications. It covers both specifications related to the fabrication of the pipes – chemical composition and heat treatment as well as specifications related to component fabrication – bending, welding and final heat treatment.

Even if many attempts have failed in the development of a better ferritic material than P92, the dream of a ferritic-based steel for 650°C still exists. Ongoing materials development for an improved 9–12%Cr-steel is still proceeding. In spite of the negative results obtained during the last decades, documenting that all of the proposed 12%Cr-steels failed due to microstructural instability of the MX precipitates caused by the high chromium content, new attempts have shown more positive indications. The development of a 12%Cr-steel based on fine dispersed Z-phase precipitation to stabilise the microstructure instead of the unstable MX precipitates may come up with a solution for a mechanically stronger pipe material to be used at temperatures above 600°C. Such a material will also show the necessary steam oxidation resistance due to the high content of chromium. Recently, Japanese developments of a 9%Cr-steel with high tungsten, boron and nitrogen content have shown excellent creep rupture strength – major improvements compared with P92 – at 650°C up to 75.000 h duration, see Figure 3. If this steel continue to perform stable after more than 100.000 h exposure it might be a candidate for 650°C if a suitable coating can be demonstrated to improve the steam oxidation resistance.



	C	Si	Mn	Cr	Mo	W	Ni	Co	V	Nb	N	B	Norm °C	Temp °C
P92	0.11	0.10	0.45	8.82	0.47	1.87	0.17	-	0.19	0.06	0.047	0.0020	1070	780
BH steel	0.03	0.36	0.49	9.12	0.15	2.40	0.01	1.8	0.20	0.05	0.050	0.0060	1050	780
NF12	0.085	0.25	0.44	11.60	0.14	2.68	0.17	2.48	0.20	0.08	0.045	0.0026	1100	760
MARBN	0.078	0.31	0.49	8.88	-	2.85	-	3.00	0.20	0.051	0.0079	0.0135	1150	770
MARN	0.002	0.29	0.51	9.19	-	2.96	-	3.09	0.20	0.060	0.049	0.0070	1100	800

Figure 3. Promising new development of 9% Cr-steels for + 600°C.

A successful development of a 650°C ferritic pipe material opens the door to a future 650°C power plant with efficiencies above 50% as all the other steel materials are available as well as a thermodynamically optimised Carnot cycle.

2.4 Flexibility of USC plants

As the exploitation of wind and solar energy is increasing worldwide, most of the thermal power plants will be forced into cyclic operation demanding extremely low loads and very steep load gradients in the future. Most USC plants are already able to demonstrate some flexibility. If the demand of flexibility is taken into account during the design phase it is possible to achieve a rather impressive cyclic performance. For existing boilers where there is a need for optimised flexibility, a thorough study of the construction and the assessment of the maximum cyclic stresses that the individual components can accept can often reveal a further potential hidden behind conservative design rules. For the future such features should be addressed especially using vertical furnace tubes to be able to reduce minimum load of the boiler.

3. Flexible generation concepts based on renewable energy

For countries where a general change from black to green energy have been decided, wind and solar power will be exploited to large extent in combination with a thermal power generation backup primarily based on biomass. This backup needs to be flexible in the outmost of the meaning of the word. In some countries the wind and solar power capacity covers about one third of the annual electricity consumption and is even increasing. Such high average figure means that when the wind is blowing and the sun is shining there will be no need for any backup. Wind and solar can produce what is needed or even more. But, when there is no wind or sun, all electricity demand has to be generated by thermal power.

In such a system, even advanced USC plants can operate with satisfying flexibility on coal, coal and biomass or even on biomass only. But in case of only using biomass, precaution is needed to prevent gas side corrosion due to potassium chloride from biomass. But even if such a plant can operate with the demanded flexibility, it will not be economically attractive in the future when the number of equivalent full load hours is cut to a minimum. A top tuned USC plant represents a big investment and calls for a relative high basic operational cost. If the utilisation of such a plant goes down the economy is ruined. Therefore new concepts have to be developed, to replace the classic thermal plant design for a relatively large number of equivalent full load hours with easy production capacity with low investment cost as well as relatively low operational cost.

3.1 Solid biomass fired boilers

Many alternatives are considered today. All kind of biomass fired boilers pulver fired, grate fired or CFB operating with moderate steam parameters and with a relatively small generation capacity ~ 100 MW. The main challenges for such concepts are the overall economy, flexibility and access to adequate materials for the superheater constructions to secure acceptable resistance to high temperature corrosion.

Many development projects are being carried out, trying to understand the basic mechanisms of high temperature corrosion in a biomass fired boilers. Whatever fuel we are considering – straw, wood chips or wood pellets it is the potassium chloride that causes the problems and has to be prevented. An increasing content of chromium improves the resistance towards general corrosion but increases the risk for intergranular corrosion. A minimum of about 18–20% Cr seems to be the optimal solution. But roughly spoken this minimum only allows steam temperatures up to approximately 540°C. At higher steam temperatures the lifetime of the superheaters is reduced dramatically.

Use of additives like sulphur or sulphur containing products, sewage sludge or coal fly ash converts or imbeds the potassium chloride and reduces the corrosion rate remarkably. To secure an unproblematic operation it is unfortunately necessary to use large amount of such additives.

Different coating systems are also being investigated. There are great expectations to find suitable coatings to do the job but the coating has to be easy to apply, secure a 100% sealing and be robust towards mechanical wear. More investigations are needed to achieve a thorough result.

From an economical point of view any solution based on a boiler turbine concept may at the end fail if the number of equivalent full load service hours is reduced too much.

3.2 Gas based generation

An interesting alternative to the solid fired biomass boilers is a solution based on gas and where the gas is produced from biomass. This alternative generates electricity, and if wanted also heating, from a gas turbine, and can to a large extent utilise low quality biomass or biowaste from the agriculture.

The gas turbine solution offers low investment cost compared with the cost for a complicated boiler system. The gas turbines do not necessarily need any operational personnel. It can be remote controlled which reduces the standby cost close to zero. The gas turbine can be installed in an existing gas distribution system and be fed with either natural gas or upgraded biomass based gas. The gas can be produced when it is optimal and stored in caverns for use when needed. This disconnection between gas production and gas consumption is of great importance for the flexibility of the whole energy system.

Gas turbine technology is already at a very advanced stage to secure that the demand for high efficiency, flexibility and size of capacity can be met. The biomass based gas can be produced either by bio gasification or by thermal gasification. An energy system based on large wind power production capacity with gas turbines as backup power is shown in Figure 4.

3.2.1 Bio gasification

This process has been known for long. Lot of plants are in operation. The big challenge for this system is economy and supply of feed stock. Intensive studies are going on to secure both demands.

New biogas systems are under development with the scope to half the investments cost through a reduced process duration. As this development involves IPR further disclosure is not possible. But it can be stated that the first results from these developments appear very interesting and stimulating.

With respect to the feedstock, new ideas abound how the agriculture could optimise their waste suitable for biogas production from normal production. In Denmark such preliminary studies indicate that the potential for more biowaste is large. The future activities will underline these findings further.

3.2.2 Thermal gasification

Thermal gasification of biomass has been under development for many decades. Gasification of wood can be described as a fully proven technology, which is exploited in many concepts ranging from simple energy production to advanced syngas production for liquid fuel syntheses. Most of the concepts are oxygen blown gasifiers using relatively high quality of wood. Investment and operational costs are relatively high and therefore the economy turns quickly into a regime where a valuable output is demanded to balance the business. When major limitations on gasoline are showing up this concept will have major interest and success.

Low temperature gasification allows the gasifier to use low grade biomass – waste and the concept can separate the valuable nutrient species so they can be returned to the agriculture. The relatively nutrient clean gas containing large amount of tar can be burned directly in an existing boiler. At present this concept can be used to enlarge the acceptable feed stock quality to be used on a plant and thereby to optimise the use of a large variety of biomass on a single plant.

All thermal gasification concepts call for intensive knowledge of the interaction between fuel, gas and materials at elevated temperature. The atmosphere is tough and highly corrosion resistant materials are needed.

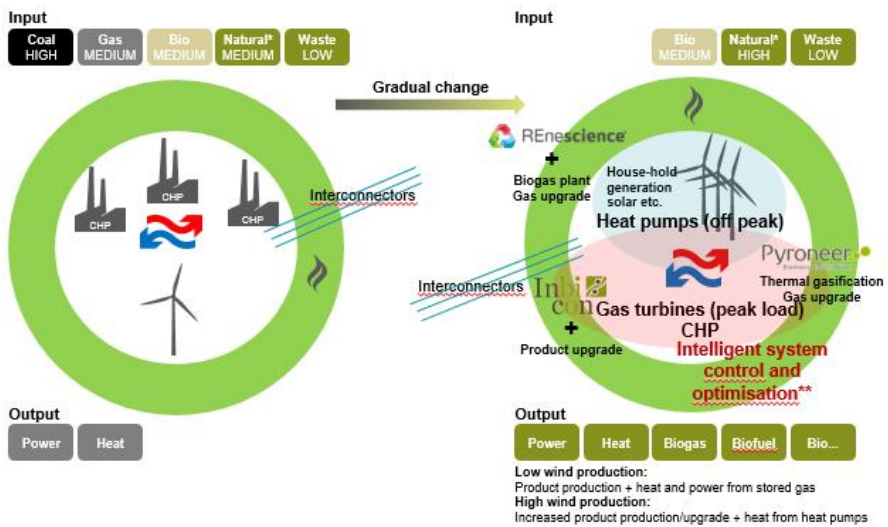


Figure 4. A scenario on the transformation of the Danish energy system from central fossil fuel units in 2010 to input/output flexible non fossil fuel decentralised units in 2050.

4. Conclusion

The future calls for new concepts supported by new materials if the change from black to green energy system shall happen and the demand for increasing energy demand shall be met. The different attitudes to these challenges define a number of development routes depending on in what continents we are focusing. Even if an increasing amount of renewable energy is foreseen, the existing concepts based on fossil fuel mainly coal will cover the major part of the extension of the whole energy system. In spite of a tremendous development of the efficiency of coal fired plants during the last decades there are further improvements to be realised within an economically interesting framework, making the on-going expansion of the coal feed fleet less polluting.

More development on power plant materials is needed in order to enlarge the regime for use of new materials and to increase the basic knowledge of the existing materials to avoid major problems.

Biomass based energy production will be an important part of the green development. Feed stock and concepts for biomass energy plants will call for further development.

Development of materials with better resistance to high temperature corrosion is the main challenge for improving the efficiency of biomass boilers.

Biogas can become an important player if improved gasification systems are developed.

Thermal biomass gasification can be an important part of the solution for future liquid biofuel.

Risk-Based Inspection (RBI) in fossil-fuel fired power plants: Developing further the EU approach and applying it in the large-scale projects

A. Jovanovic¹, J. M. Bareiss^{1,2}, P. Stanojevic^{1,3} & Liu Yan^{1,4}

¹ Steinbeis Advanced Risk Technologies
Stuttgart, Germany

² EnBW, Stuttgart, Germany

³ Ministry of Energy, Serbia, NIS-GazpromNeft, Serbia (formerly)

⁴ BMILP, Beijing, China

Abstract

The paper highlights the practical aspects of further development and practical application of the EU approach set up in CWA 15740:2008 document, with special emphasis on critical components in large fossil-fuel fired power plants. Further development of the concept involves (a) primarily economic analysis and includes aspect related to NPV (net present value) and CAPEX/OPEX (capital/operational expenditure), (b) further development of the concept of CWA 15740:2008 towards a European standard (EN), and (c) embedding the concept in the overall concept of aging management. The first development is implemented within the assessment methodology applied by Steinbeis Advanced Risk Technologies, the second one in a multi-client project involving currently a dozen of industrial parties and coordinated by the Dutch standardization body (NEN), and the third one is part of the EU Coordination project. Overall concept has been practically applied in a number of power plants, among others, is currently being applied in power plants in South Africa.

1. Introduction

The CWA 15740:2008 [1] to [4], provides the essential elements of risk based assessment of industrial assets according to the RIMAP approach which has been developed and demonstrated in and by the European R&D project RIMAP (GIRD-CT-2001-03008 and the corresponding RIMAP Network: "Risk-Based Inspection and Maintenance Procedures for European Industry"). One of the main goals of the project, as well as of this CWA, has been to contribute to the harmonization of the EU national regulatory requirements related to the inspection and maintenance

programs in the industrial plants and make them more cost-efficient while, at the same time, safety, health, and environmental performance is maintained or improved.

The document is intended for the managers and engineers establishing the RBIM (Risk-based Inspection and Maintenance) policies in the companies in power, process, steel and other relevant industries. It is supposed to be used in conjunction with the relevant internationally accepted practices, national regulations and/or company policies. The document is supposed to provide a common reference for formulating the above policies and developing the corresponding inspection and maintenance programs within different industrial sectors, such as oil refineries, chemical and petrochemical plants, steel production and power plants. Each part of this Agreement can be used as a stand-alone document.

The positive impact and transfer of industry practices resulting from the use of this document and from the approach promoted by/in it are expected to be of benefit for the European industry and strengthening of its competitiveness through better inspection and maintenance practices.

The objective of this CEN Workshop Agreement document is to present a set of transparent and accurate framework for applying / implementing risk-based inspection and maintenance (RBIM) and risk-based life management (RBLM) in industrial organizations

The CWA formulates the procedure for risk based approach, thereby supporting optimization of operations and maintenance (O&M) as well as asset management.

The development of the CWA since it has been approved in 2008 has been marked by the following major developments of the methods and the document:

- Creation of the respective VGB Guideline (VGB 506) for German power plants
- Inclusion in to the South African regulation
- Development of the concept involving
 - a) economic analysis and includes aspect related to NPV (net present value) and CAPEX/OPEX (capital/operational expenditure),
 - b) further development of the concept of CWA 15740:2008 towards a European standard (EN), and
 - c) embedding the concept in the overall concept of aging management.

The first development is implemented within the assessment methodology applied by Steinbeis advanced Risk Technologies, the second one if a multi-client project involving currently a dozen of industrial parties and coordinated by the Dutch standardization body (NEN), and the third one is part of the EU Coordination project. Overall concept has been practically applied in a number of power plants, among others, in South Africa.

2. CWA Principles and requirements

The purpose of RBIM is to ensure that clearly defined and accepted levels of risk related to safety, health, environment and business/production/operation are achieved using resource-efficient methods of inspection and maintenance. The methodology for RBIM described here is based on that developed in the European project RIMAP (Risk-based Inspection and Maintenance Procedures for European Industry) [2]. Within the RIMAP project, the RBIM methodology has been developed and validated for chemical, petrochemical, power and steel industries in Application Workbooks [6], [7], but the methodology as such is intended to be industry independent. The methodology addresses the following aspects:

- Inspection and maintenance
- All types of equipment, e.g. pressure containing, rotating, electrical, instruments and safety devices
- Technical and managerial aspects of maintenance and inspection planning
- Asset management related to inspection, maintenance and life assessment for plants, systems and components
- Production and operation

Although RBIM encompasses RBI & RCM, this document focuses primarily onto RBI. The RCM is included only up to the extent to demonstrate the applicability in the overall context of RBIM.

2.1 The Principles

Since the late 1990's the maintenance approaches in industry have been globally moving from prescriptive/time-based towards risk-based inspection decision making. This trend is driven by the clear objective to increase the on-stream production time to reduce unscheduled downtime due to breakdown maintenance or unknown equipment condition which may ultimately cause a shut down.

In general terms, if a company wants to apply a simple prescriptive maintenance/inspection approach then it is necessary to apply strictly conservative criteria for the decision making process.

A risk-based approach on the contrary needs a detailed multi-discipline engineering analysis to ensure that safety issues are not sacrificed by implementing a maintenance/inspection planning process. An appropriate risk-based methodology covers following principles:

- Plan the primary work products of RBIM assessments and management approach in such a way that risks at system and/or equipment level are managed, highlighting risks from both safety/health/environment (HSE) perspective and/or from the economic standpoint

- Define the RBIM methodology in a framework which meets common sense (such as good engineering practices or industrial reference standards) in handling hazardous materials and situations in industrial equipment
- Address a generic work flow and competencies needed to handle projects in an appropriate manner

Define minimum requirements for performing and documenting RBIM assessments in order to comply with legal or normative regulations and guidelines

2.1 General requirements

General requirements of RIMAP as applied to RBIM are:

- a) The objectives and risk criteria should be clearly defined for the assessment.
- b) The assessment and the applied detailed procedure should comply with the locally applicable legal and regulatory framework
- c) The required level of input information should be available for the assessment.
- d) The assessment should be performed in a multidisciplinary team by personnel with the required competence, and using procedures and tools that can provide the required results on the selected level of assessment.
- e) The assessment and the applied procedure should be able to provide results, which are
 - safe
 - conservative
 - representable in risk matrix, auditable and consistent with both the objectives and applied risk criteria
 - supporting RBIM planning and decision making on the target system or component.
- f) RBIM should be based on a team approach
- g) RBIM should reflect the prevailing conditions in the plant, i.e. RBIM needs to reach the “evergreen” status.

2.3 Personnel requirements

Risk based inspection and maintenance management requires experienced personnel at all levels as well as appropriate routines for the execution of the work. Current relevant standards do not set fully comprehensive formal requirements for the qualifications of people that perform inspection and maintenance planning, even if the execution of inspection and maintenance activities is partly regulated

through qualification schemes, such as e.g., ISO standards such as 17020 [8], 17025 [9], and European standard EN 473 requirements [10]. RBIM planning requires a multidisciplinary team with engineering competency within:

Inspection and maintenance

- Specific equipment disciplines (e.g. materials, corrosion, electrical, fixed and rotating equipment)
- Safety and health issues
- Plant operation and process
- Reliability and risk assessment.

Particular cases may require special competencies. In addition, local rules and legislation, and the type of industry may set detailed requirements to competencies involved. Due consideration should be given to the width of background skills and expertise collated in the team. One or more of the skills may be possessed by one person, but it is emphasized that RBIM planning is a team effort.

2.4 Requirements for performing the Probability of Failure (PoF) analysis

Main RIMAP requirements for PoF analysis as given in [11] are:

- a) **General acceptability.** RIMAP describes a methodology for PoF assessment, which can be either used alone, or alternatively combined with established methods. PoF assessment method should be verified / benchmarked against a recognized (established) methodology, which is generally being used, accepted and referred to in the open literature.
- b) **Conservatism** of simplified approaches. The results from the risk screening may be on average conservative compared to the results from a detailed analysis. Available methods for determining Probability of Failure may vary in the level of detail. Method with less detail (e.g. qualitative analysis) can be conservative, in other words it may yield higher or equal average score of probability of failure compared to a more detailed approach.
- c) **Auditability** of results. The results should be auditable to similar experts (peer view); therefore the methodology, the input data, the decision criteria and the results may be documented (the results may be recorded in an approved document).
- d) **Qualification.** The RBIM team may include with written evidence the following areas of expertise: inspection, maintenance, materials technology, process technology, operations and facilitation. For each area of expertise a certain requirement should be defined related to education and experience. The facilitator should have expertise on the methodology and lead the analysis process. Some of the expertise may be combined in one per-

son. An expert should back up the RBIM team on process fluid characteristics and the possible modes for loss of containment.

- e) **Multi-level approaches** (qualitative-quantitative, in depth of plant). Both qualitative and quantitative approaches (ranging from screening to detailed) may be used. The use of descriptive terms, such as “very high” to “very low” or similar can be used only if the meaning (explanation) of these terms is provided. The approach can be multi-level both in terms of “qualitative/quantitative” and in terms of going “in-depth” into plant equipment hierarchy.
- f) **Procedural** character. The PoF assessment shall be structured as a procedure with well defined boundary conditions (e.g. as provided within the RIMAP procedure).
- g) **No averaging**. The PoF rating should be such that the highest rating for one of the individual aspects of different damage mechanisms and trigger events should control the final rating score in order to prevent averaging of the ratings for various aspects. Alternatively, probability tree diagrams can be used to model the causes leading to single PoF’s. In such a case, the probability of each branch in the reliability diagram can be combined (parallel/serial – OR/AND) in order to define the final PoF. The same applies to single PoF’s: they can be combined in the same way to avoid averaging and producing consequent unrealistic values of PoF.

Additional aspects to be considered. PoF analysis shall be done in such a way that the following aspects are covered to screen the operation to identify the active damage mechanisms in order to identify susceptible damage mechanisms, establish realistic (“best estimate”) damage rates, link PoF to the effectiveness of the inspection program in the past as well as in the one planned for the future, determine the confidence level in the damage rate, assess the effect of the inspection program on improving the confidence level in the damage rate, assess the probability that a given level of damage will exceed the damage tolerance of the equipment and result in failure and analyze possible interaction or synergy effects for all damage mechanisms, determine PoF with respect to the planned interval for the next inspection and determine PoF with respect to risk acceptance criteria

2.5 Requirements for performing CoF analysis

RIMAP requirements for CoF analysis address [12]:

- a) **General** requirements for CoF assessment. In order to assess the CoF, at least the aspects Health, Safety and Environment should be included. There are two possible ways to deal with CoF (a) real consequences related and (b) potential consequences related (e.g. the RIMAP CoF). If the RBIM process is used for assuring Health, Safety and Environment rather than a financial optimisation, averaging of individual aspects (Health, Safety and Environment and/or business consequences) is not allowed.

- b) **Safety:** Requirements on $\text{CoF}_{\text{safety}}$. The $\text{CoF}_{\text{safety}}$ assessment shall be documented and approved by the responsible authorities recognized by the national regulations, if necessary. The methods can be based on at least one or more of the following aspects (depending on the type of equipment and fluid): released mass flow rate of fluid; type of release (instantaneous discharge of total contained quantity or by leakage at a specified rate); flammability; toxicity; energy release (pressure or heat); kinetic energy of projectiles.
- c) **Health:** Requirements on $\text{CoF}_{\text{health}}$. The $\text{CoF}_{\text{health}}$ assessment shall be documented and approved by the responsible authorities recognized as per the national regulations, if necessary. The methods can be based on at least one or more of the following aspects (depending on the type of equipment and fluid): properties of the fluid that effect health; released mass of fluid; effect on people in the long term.
- d) **Environment:** Requirements on $\text{CoF}_{\text{environment}}$. The $\text{CoF}_{\text{environment}}$ assessment shall be documented and approved by the responsible authorities recognized as per the national regulations, if necessary. Environmental impact shall include effects on soil, air, surface water and ground water. The methods can be based on at least one or more of the following aspects (depending on the type of equipment and fluid: properties of the fluid that effect the environment; released mass of fluid; direct and indirect effect on flora and fauna; remediation effort.

Requirements on $\text{CoF}_{\text{business}}$. The $\text{CoF}_{\text{business}}$ assessment shall be documented, if necessary.

2.6 Requirements related to Risk Assessment

All requirements specified for personnel, PoF assessment and CoF assessment are also applicable to Risk assessment requirements [13]. In addition, the following requirements shall also be satisfied for conducting risk assessment:

- a) Development of a scenario for each failure mode is a critical step. Even though various techniques are available such as fault tree analysis, event tree cause-effect methods, etc., bow-tie modelling is recommended due to the simplicity of charting different scenarios and the ease with which the result can be understood. When the bow tie model is constructed (the fault and event tree established) different scenarios for the failure modes can be developed by following different paths from root cause/damage mechanism to potential final consequence.
- b) It is not allowed to combine PoF's and CoF's related to different scenarios (e.g. different failure modes) even if they refer to the same equipment.

- c) Efficiency of the risk mitigating activities shall be connected to identified failure modes and the projected risk reduction shall be quantified.

3. Implementation (general)

The development and implementation of a RBIM plan requires resources such as personnel, budget, spare parts and documentation. Management should assess the effectiveness of the RBIM by monitoring performance indicators like reliability, costs and risks. RBIM planning requires a multidisciplinary team with a range of engineering competency. Management should identify and define the objectives related to acceptable levels of risk in inspection and maintenance activities. The objectives should be transparent and support the company's overall objectives, with respect to health, safety, environment, production, quality, etc. The objectives should also be in line with national and other normative requirements, and possible contractual requirements.

The RBIM strategy should ensure that risk mitigating actions are identified and implemented before the health, safety or environmental (HSE) risks associated with an equipment failure become unacceptable. If the HSE risks are 'tolerable'/acceptable, actions to reduce economic and other business risks may still be needed.

RIMAP framework shall be seen as a part of the overall "Working process" consisting of

- Definition of objectives, goals and requirements
- Establishing of inspection and maintenance program
- Plan for tasks and activities in inspection and maintenance
- Execution of the work orders
- Reporting about failures and status
- Evaluation of the technical conditions
- Preparing for the improvement tasks
- Performing of corrective action
- Active management
- Management of change
- Operating procedures
- Safe work practices
- Pre-start-up reviews
- Emergency response and controls
- Investigation of incidents
- Training
- Quality assurance.

4. RIMAP procedure

The RIMAP procedure provides guidance for developing and maintaining a risk-based inspection and maintenance program, preferably embedded into a higher level quality or risk management environment. The procedure is applicable to many industries and to different types of equipment (for example static equipment, rotating equipment, safety systems, and electrical/instrument equipment). The steps in the procedure are the same for all cases, even if the models and tools for assessing probability or consequence of failure may vary from one application to another.

The procedure includes the following main steps:

1. Initial analysis and planning
2. Data collection and validation
3. Multilevel risk analysis
4. Decision making and action planning
5. Execution and reporting
6. Performance review / evergreen phase

For each of the above steps the following elements are defined such as:

7. General description and scope
8. Requirements
9. Input
10. Procedure
11. Output
12. Warnings and applicability limits.

An overview of the RIMAP procedure is shown in Figure 1.

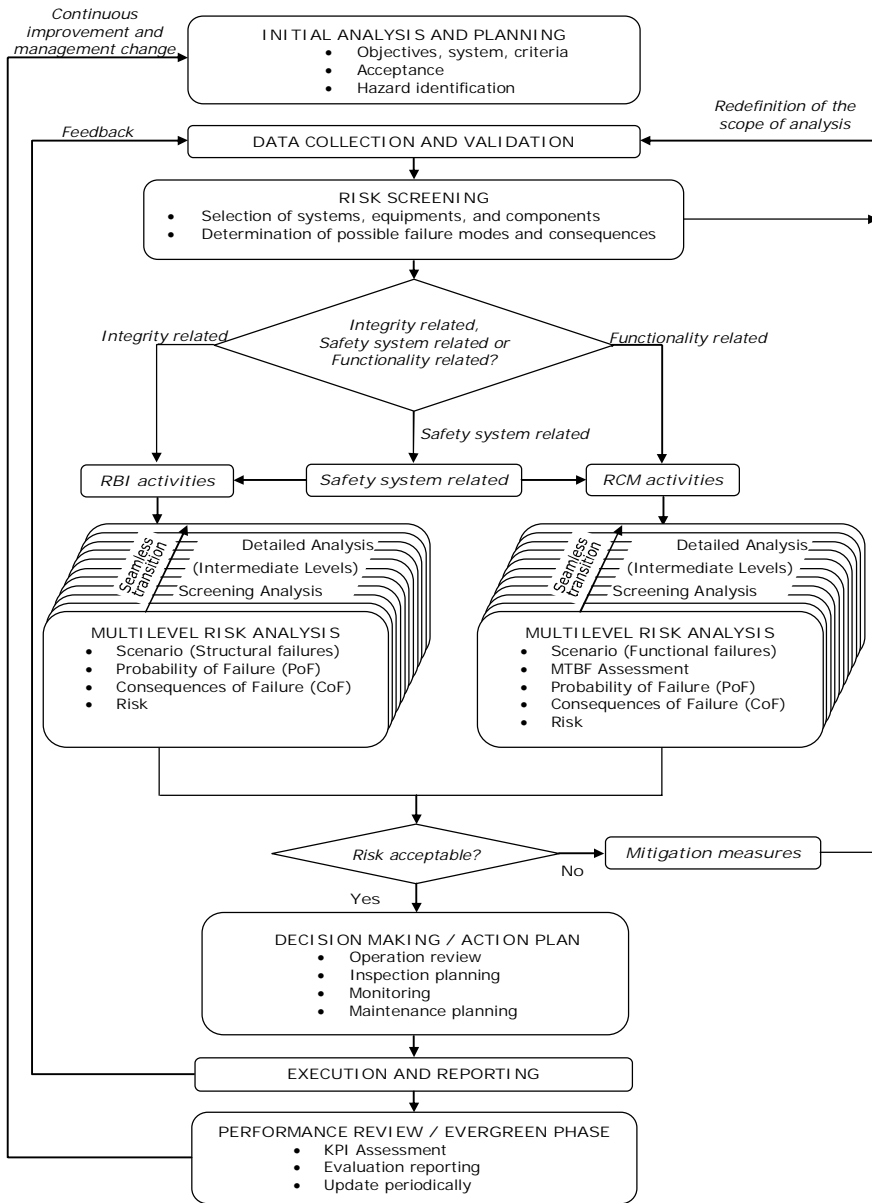


Figure 1. RIMAP procedure.

4.1 Initial analysis and planning

This stage consists of the following steps:

- a) Definition of objectives (e.g.: company Health and Safety objectives, optimize timing and extent of next inspection)
- b) Definition of the systems and components to be considered as well as the respective boundaries (example: preheating system from inlet x to outlet y (P&ID No. xyz) including pressure vessels xyz, heat-exchangers xyz, and pumps xyz)
- c) Definition of the scope of analysis, including operating conditions and exceptional situations to be covered (e.g. disturbances, accidents etc.), as well as the operating period covered.
- d) Definition of data sources available (e.g. design data, equipment history)
- e) Definition of regulatory requirements to be considered
- f) Setup of the multi-disciplinary team
- g) Tools (software) to be used
- h) Assurance of the acceptance of the methodology and objectives with relevant institutions concerned (internal e.g.: management and external e.g. approved bodies and authorities)

The expected output from the preparatory work is the following:

- selection of the applied procedure, competent assessment team and supporting tools
- defined system of interest, system/component hierarchy and boundaries for the assessment
- objectives, scope and methods of the effort, as well as confirmation of stakeholder support for these
- collected regulatory requirements to set boundaries to the assessment and decisions affected by the results
- collected risk assessment criteria from foreseen health, safety, environmental, business and other impacts.

4.2 Data collection and validation

The collection and organisation of relevant data and information are mandatory prerequisites to any form of risk based analysis. Much of this data is probably related to design, operation and failure information. The data are used to assess

both the probability and consequence (and thus the risk) of a failure scenario with analysis method(s) that meet the requirements of the generic RIMAP procedure.

Information for risk-based analysis may be available or obtainable from many sources. However, the quality of the data can be very case-dependent. Where the data are sparse or of poor quality, the uncertainty associated with the risk assessment will be greater.

Before collecting data, the RBIM team should estimate the data that will actually be needed. This is partly to match the data collection with the analysis, and partly to assess the effort needed considering the data and information that are already available and data that require additional work. The collected data are best stored in a well-structured database, which will not only facilitate the assessment process but also updating and auditing the processes that are an essential part of the RIMAP procedure.

The output of the data collection and validation should be an assessment of all relevant and representative data, which are needed for the risk calculation of the components of interest. This data should be collated in an appropriate way, e.g. by storage in a database.

Depending on the availability of data, a change in the system/component boundaries identified during the initial analysis and planning may be needed. Also, insufficient data may require additional effort to produce new data through engineering analysis or by other means. In such a case, data validation and re-assessment is also needed.

The output of data collation and validation mainly consists of raw technical data and information related (or processed) to failure probabilities and consequences. The defined objectives and the system to be assessed can largely dictate the depth and extent of the output of data collection serving these higher purposes.

Support of the management and involvement of the plant personnel are important and will contribute to their acceptance of the outcome of the risk based analysis, and may also positively influence the quality of the data.

4.3 Multilevel risk analysis

Risk analysis consists of the following steps:

- a) Identify hazards
- b) Identify relevant damage mechanisms and failure modes
- c) Determine probability of failure (PoF)
- d) Determine consequence of failure (CoF)
- e) Determine risk and classify equipment.

Multilevel risk analysis defines the risk assessment in terms of (i) complexity of the analysis (e.g. from the simplified/screening analysis to the detailed one), and in terms of (ii) plant hierarchy level (depth). Accordingly, there are two levels of risk analysis, namely risk screening and detailed assessment.

Risk screening shall be relatively fast, simple and cost effective compared to more detailed risk analysis. Risk screening is particularly suited for broadly based problems and limited populations of items to consider. Risk screening divides the systems and groups of equipment into two groups: high-risk items and medium/low risk items. The high-risk items should be analyzed in detail. The medium risk items should be considered additionally in order to decide if minimum surveillance or detailed assessment should be followed. The low risk items should only require minimal surveillance to verify and ensure that the assumptions made during the screening process remain true. This could, for example, amount to verifying the condition of a painting, coating, functional compliance or the correct undistorted position of a structure. If information is missing during the screening so that the risk associated with the equipment cannot be determined, the equipment should be regarded as having a high risk and reassessed using a more detailed assessment.

The detailed assessment differs from screening in the depth of detail required for analysis and hence involves considerably higher work effort for the assessment. Detailed assessment should be applied to the high risk systems and groups of equipment identified in risk screening, and to all equipment within the scope of work if no risk screening has been performed. For each system or group of components, the relevant degradation mechanisms shall be identified and the extent of damage shall be estimated. Furthermore, the most likely damage development shall be determined. Based on this information, the maximum time interval to the next inspection / maintenance activity shall be determined subject to the condition that the health, safety and environmental risks remain acceptable (as defined in the acceptance criteria). This should then be combined with inspection / maintenance cost and inspection / maintenance effectiveness to derive cost optimal maintenance / inspection intervals such that the health, safety, and environmental, risks are acceptable, i.e., the acceptance criteria are satisfied

Typical results from these tasks are:

- a) PoF value or category for the piece of equipment under consideration
- b) CoF value or category for the piece of equipment under consideration
- c) Risk value or category for the piece of equipment under consideration

For the risk screening, risk value or category from screening risk matrix shown in Figure 2.

For the detailed assessment, risk values and/or categories from Figure 3 can be used.

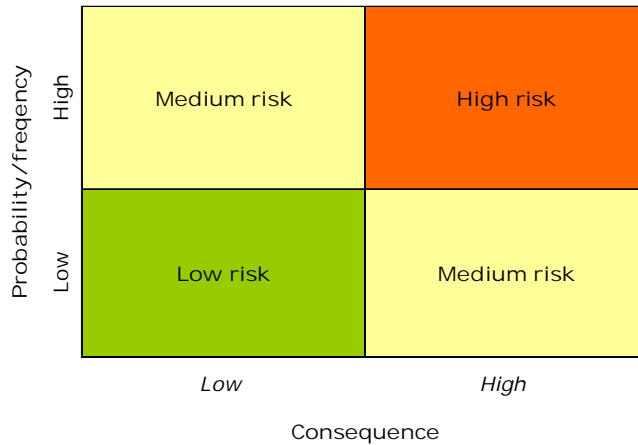


Figure 2. CWA 15740:2008 Screening risk matrix.

Examples of PoF scales	Very probable	< 1 year	$> 1 \times 10^{-1}$	5	PoF category					Very high risk
	Probable	1-5 years	1×10^{-1} to 1×10^{-2}	4					High risk	
	Possible	5-10 years	1×10^{-2} to 1×10^{-3}	3				Medium risk		
	Unlikely	10-50 years	1×10^{-3} to 1×10^{-4}	2			Low risk			
	Very unlikely	>100 years	$< 1 \times 10^{-4}$	1			(Very Low, negligible risk)			
						CoF category				
Discoi phase	MTBF	PoF				A	B	C	D	E
					Health (Long term visibility)	Warning issued No effect	Warning issued Possible impact	Temporary health problems, curable	Limited impact on public health, threat of chronic illness	Serious impact on public health, life threatening illness
					Safety (Instant visibility)	No aid needed Work disruption	First aid needed No work disability	Temporary work disability	Permanent work disability	Fatality(ies)
					Environment	Negligible impact	Impact (e.g. spill) contained	Minor impact (e.g. spill)	On-site damage	Off-site damage Long term effect
					Business (€)	<10k€	10-100 k€	0.1-1 M€	1-10 M€	> 10 M€
					Security	None	On-site (Local)	On-site (General)	Off site	Society threat
					Image Loss	None	Minor	Bad publicity	Company issue	Political issue
					Public disruption	None	Negligible	Minor	Small community	Large community
						Examples of CoF scales				

Figure 3. CWA 15740:2008 Detailed risk matrix.

4.4 Decision making and planning

Conservative inspection and maintenance is an efficient approach when the mitigating actions are cheap compared to developing an optimized inspection and maintenance plan. In order to manage inspection and maintenance on a daily basis, programs with predetermined intervals are established. Based on the deliv-

erables of the project so far, this section describes a proposed decision framework for the determination of an inspection and maintenance strategy.

The need for inspection and maintenance is directly caused by several factors:

- Wear and tear, and unreliability of equipment/machinery
- Unreliability of humans operating, maintaining or inspecting the equipment/machinery
- Legislation and other regulatory requirements
- External factors (earthquakes, harsh weather, etc.)
- Severity of consequence
- The action plan consists in particular,
- Operation review
- Condition monitoring.

Inspection and maintenance programs are established in response to this unreliability and risks as well as to the legal/regulatory requirements. Maintenance induced by human errors and external factors is not considered as a part of the usual inspection and maintenance program.

The termination of the ability of an item to perform a required function is linked with a failure cause, which could originate from circumstances with use, or maintenance. The inspection and maintenance strategy is the maintenance approach chosen in order to prevent physical and environmental damage, injury and loss of life or assets.

In principle, the decision logic gives guidance for establishment of the preferred inspection and maintenance strategy on basis of the criticality assessment, detectability of damage and the failure characteristics. The outcomes defined from the decision logic are:

- Elimination of failure cause
- Regular functional testing/inspection
- Time and condition based maintenance
- Operational maintenance
- Corrective maintenance.

4.5 Execution and reporting

The output of an RBIM plan is the input for the planning and scheduling for all involved departments, disciplines and contractors for the inspection and maintenance work for the facility and its maintainable items. The output of the development of the RBIM plan will be based around a maintainable item and will have a broad variety of strategies such as the elimination of the risk through monitoring, performance testing and improvement of procedures for process, operation and/or

maintenance, inspection, modification, repair, replacement, or operation to failure. Maintenance work can be split into three main categories shown in Table 1.

The output from the maintenance execution work is a plant where the preventive maintenance is based on RBIM analyses, and corrective maintenance is also managed using risk-based principles. As a result, the risk for failure is under control and reduced to an acceptable level. Furthermore, the work is documented and reported so that reports, tools and information for continuous improvement are available.

Table 1. Possible split of the maintenance work into three main categories (example).

Type of maintenance	Typical procedure	By whom
1. On-stream	No plant shutdown required	Operating/own staff/ specialists
2. Short shut-down	Shutdown up to a week to change worn equipment, or changes called by process (catalysts, molecular sieves, etc.)	Own staff / specialists / contracting companies
3. Turnaround	Larger plant stops for major upgrades, repair, inspection, process upgrades	Own staff and contracting companies

4.6 Performance review / evergreen phase

The purpose of the evaluation of the risk-based decision-making process is to assess its effectiveness and impact in establishing the inspection and maintenance programs. This will allow the identification of areas where modifications and improvements are needed. Specifically, evaluation consists of the following tasks:

- Assessment of the effectiveness of the risk-based decision-making process in achieving the intended goals (assessment of effectiveness)
- Updating the risk-based decision-making process by taking into account possible plant changes and available new knowledge (reassessment of the risk). This should be done periodically.

From this step of RIMAP procedure, following outputs are envisaged as a measure of assessment of effectiveness of inspection / maintenance strategy:

- a) Periodical reports from internal reviews
- b) Reports from external audits
- c) List of discrepancies from requirements and expectations
- d) Methodical analysis of discrepancy causes, when applicable
- e) Proposal for improvement actions.

From this step of RIMAP procedure, following outputs are envisaged as a measure of reassessment of risk:

- a) Periodical reports from internal reviews

- b) Reports from external audits
- c) Monitoring and feedback from operation
- d) Feedback from new knowledge
- e) Proposal for improvement actions.

5. Practical application in industry (A case study of a refinery using RIMAP procedure)

5.1 The plant

A case study of a refinery using RIMAP procedure has had the main objective to assess the risk profile of the refinery equipment through the application of the Risk-Based Inspection methodology and to prioritize equipment for inspection. The scope of the RBI study covered all the equipment items and related piping as originally agreed prior to the project and has comprised the following components (also shown in Figure 4):

Component type	Number of items
Pressure vessel	41
Condenser, Shell	17
Heat Exchanger, Shell	13
Column Top	10
Filter	7
Furnace Tubes (general)	6
Other Equipment	5
Heat Exchanger, Tube Side	4

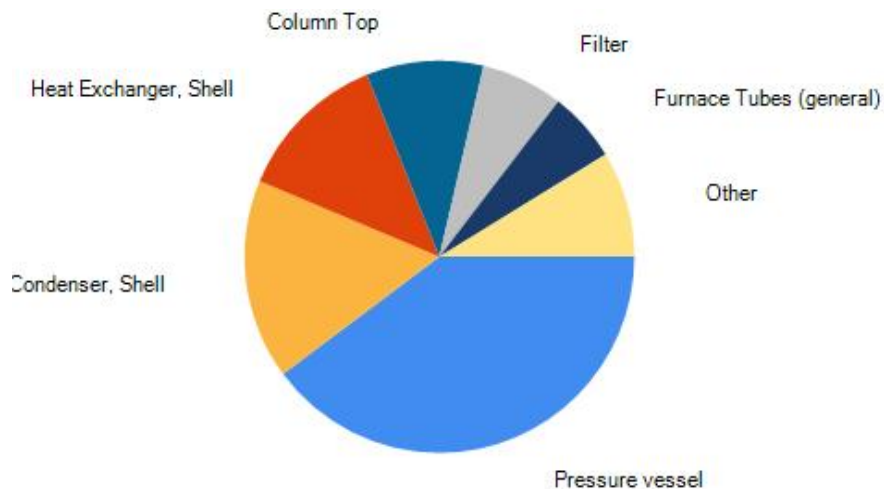


Figure 4. Integration of RBI with other systems in place.

5.2 The work

The scope of work covered the following activities:

1. Understanding the system
This includes activities like HAZOP analysis, review of design assumptions, process flow diagrams, P& IDs, survey of all maintenance, inspection documents (location, nature and criticality of flaws, thickness measurements, corrosion rates etc.), repair and modification records, operating conditions, PSV settings, stream data, materials of fabrication, vessel coating and insulation details. Review of financial data including cost of plant shut down and averages cost of process plant.
2. Preparation of Simplified Process Flow Diagrams (PFDs) with all data essential to the RBI analysis of the equipment items.
3. Development of corrosion circuits and determination of expert corrosion rates.
4. Data entry and analysis using Steinbeis R-Tech iRIS-Petro software.
5. Preparation of documentation of corrosion rates and assessment of damage mechanisms and mode of failure.
6. Review of inspection records.
7. RBI analysis and results checking.
8. Preparation of RBI analysis report.

In order to be able to perform the given analysis, the following activities have taken place:

1. Training in RBI methodology and presentation of qualitative methods during the RBI Training
2. First Certification RBI Training participants
3. Complete implementation of the qualitative assessment tool in a form of Web-based software tool
4. Integration of the software tool in the project web
5. Export facility in the software in order to allow offline completion of the questionnaire
6. Basic demonstration of the methodology and training
7. Data collection and assessment performed by the refinery team, extended with the representatives of the refinery in two sessions.

LIKELIHOOD	5						0 - 0%
	4			1 component		1 component	2 - 2%
	3			4 components	4 components	5 components	14 - 14%
	2		15 components	36 components	31 components	2 components	83 - 84%
	1						0 - 0%
		A	B	C	D	E	
		0 - 0%	15 - 15%	40 - 40%	36 - 36%	8 - 8%	99
		CONSEQUENCES					

Figure 5. Qualitative risk matrix for component level, for year 2009.

5.3 Results

The qualitative analysis has been performed for 99 components, without connecting piping and rotating machinery (Figure 5). Acc. to results of the preliminary (qualitative, screening) analysis detailed quantitative analysis has been made for selected components and these results are shown in Figure 6.

Based on these results it was possible to analyze potential savings in inspection costs overview of financial risk for the whole unit, which are given in Figure 7, Figure 8 and Figure 9.

The figures are showing (Figure 7) that significant savings can be made and that RBI offers a lot of saving potential in the given case. It also provides a better insight into risks and the possibility to prioritize them (e.g. the financial ones as shown in Figure 8).

The extended method of looking at risks in terms of parameters of investment (CAPEX) and operational costs (OPEX) and the change of the net present value (NPV) of the equipment in time, allow to "pick the right components" for the RBI process and ensure that the optimized inspection program will bring maximum safety and minimize costs.

LIKELIHOOD	5						0 - 0%
	4		4 components	10 components	3 components		18 - 72%
	3			1 component			2 - 8%
	2		1 component	1 component	1 component		5 - 20%
	1						0 - 0%
		A	B	C	D	E	
		0 - 0%	5 - 20%	14 - 56%	6 - 24%	0 - 0%	25
		CONSEQUENCES					

Figure 6. Quantitative risk matrix for selected components (after screening).

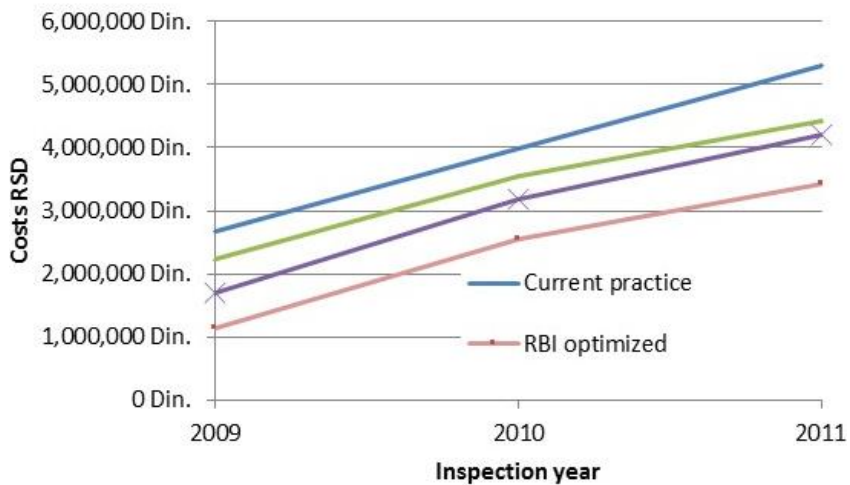


Figure 7. Comparison of different inspection strategies (costs).

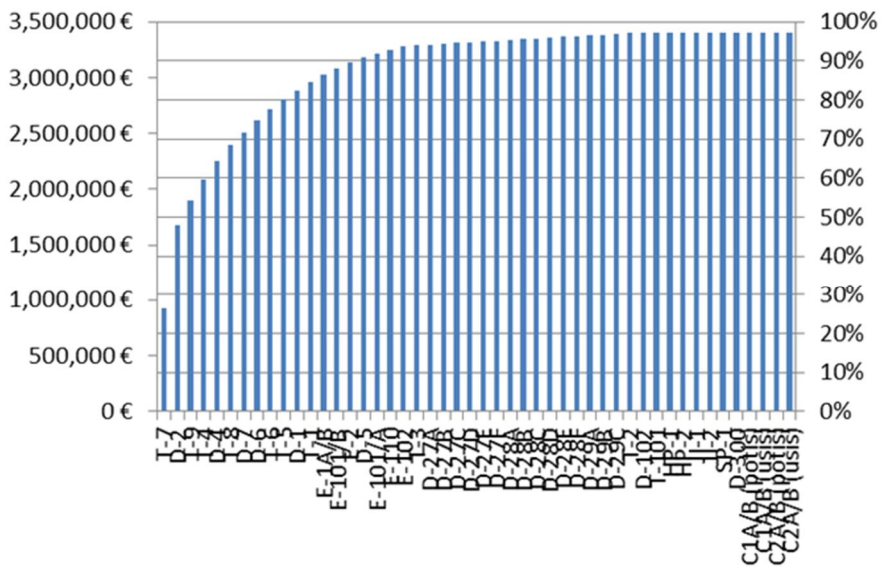


Figure 8. Financial Risk Prioritization.

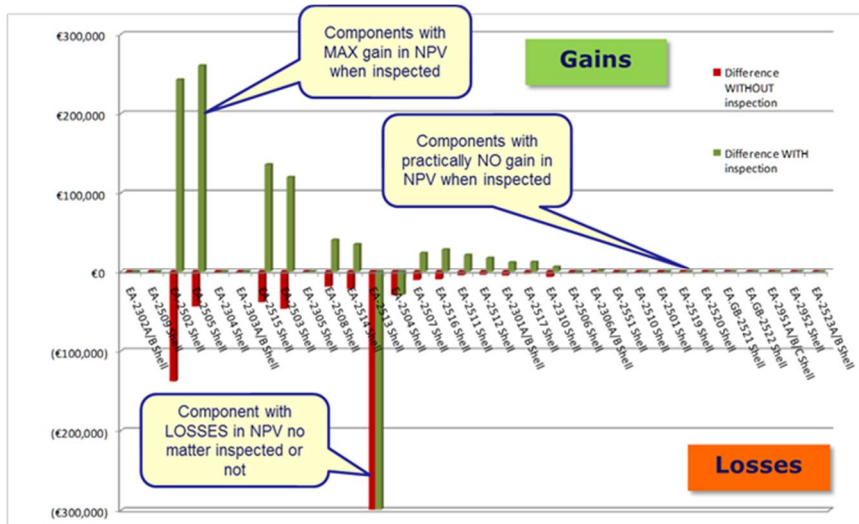


Figure 9. Selecting the components where inspection will bring the most.

6. Extension of the initial methodology

The principles of the methodology applied takes into account:

- Cash flow in a corporation
- Flow of working capital
- Production costs
- Maintenance costs
- Capitalized cost
- Maintenance cost – operational expenditure or capital expenditure
- Net present value
- S-Factor
- Engineering aspects.

It looks to optimize maintenance plan to obtain maximum capital value at any time of the plant life (or given time horizon) and it is used for maintenance of equipment with the degradation over time damage mechanisms. The indicator used in the process is the so-called S-factor, defined on the basis of

- Risk before (probability x consequences)
- Risk after (probability x consequences)
- Estimated costs of action / consequence of action.

The application is shown in principle in Figure 10.

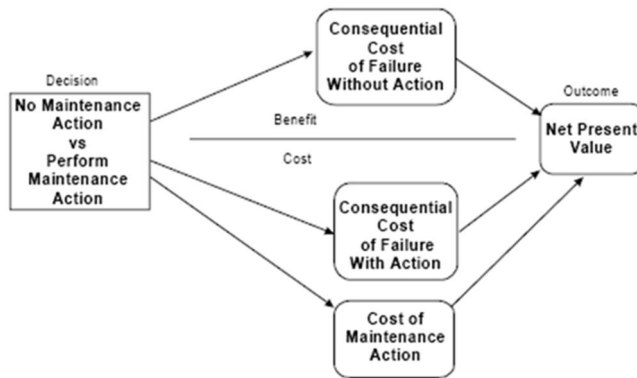
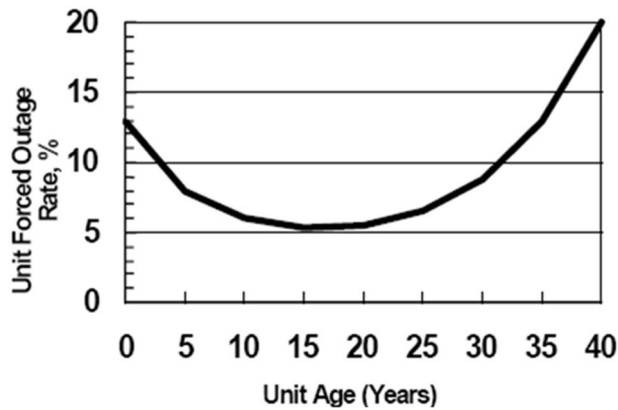


Figure 10. The principle of the applied methodology.

7. Implementation of CWA in a national system

In the case of South Africa, the practical implementation has been made according to the principles shown in Figure 11 and requiring that the RBI processes of an effective RBI system should be integrated into the company's quality- and safety management systems. Although certification is not a specific part of RIMAP CWA, the South African system foresees it (Figure 12). DOL denotes the Department of Labour (government), SANAS is the national accreditation body and the CB is the Certifying Body. The place of the CWA 15740:2008 in the overall system is shown in Figure 13.

The national application in South Africa shows two main further development of the initial RIMAP approach, namely:

- a) Certification aspect and
- b) Consideration to use the approach for nuclear power plants (secondary loop), too.

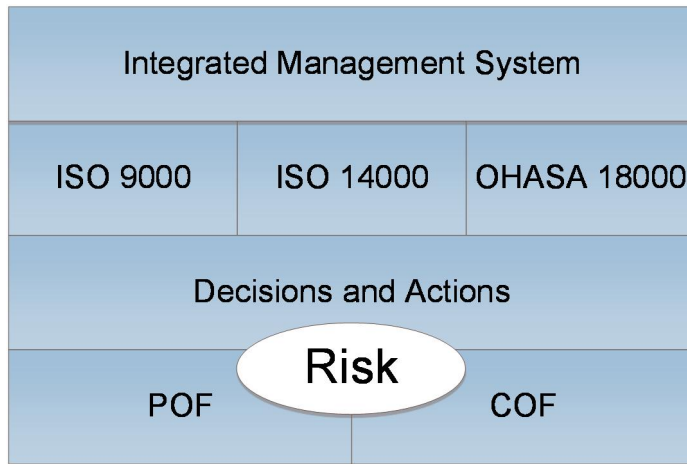


Figure 11. Integration of RBI with other systems in place.

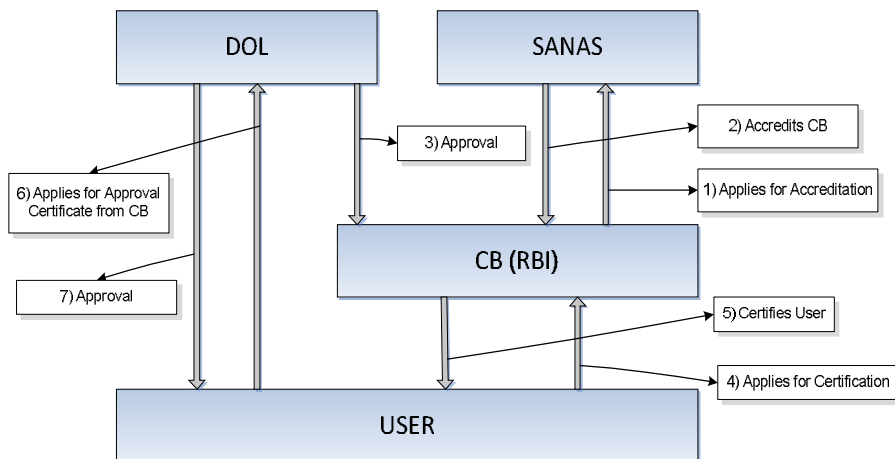


Figure 12. Although certification is not a specific part of CWA, the South African system foresees it [14]

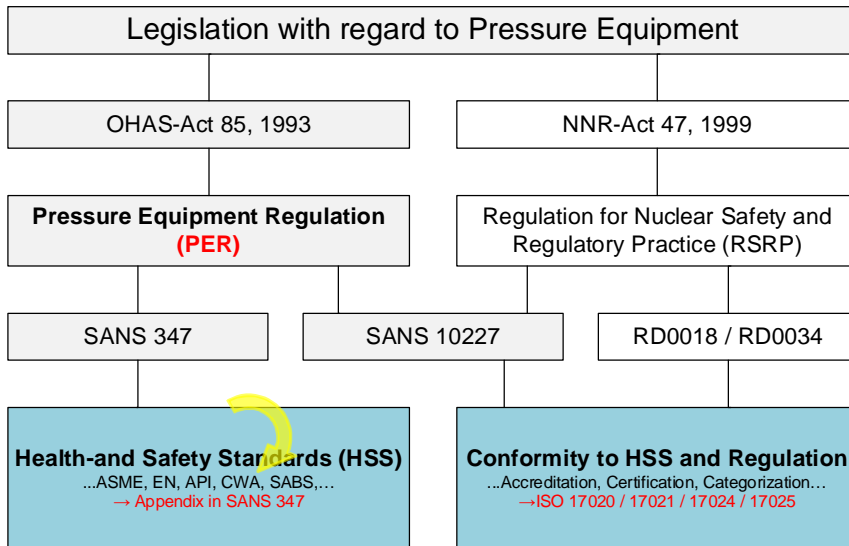


Figure 13. Place of the CWA 15740:2008 in the overall system it is mentioned as “CWA” [14].

8. Further development of the CWA towards an EN, new EU Coordinated Action on Aging

The activity on upgrading CWA document has started since February 2011, in the framework of the meeting held in Munich – "Future of standardization of Risk-Based Inspection and Maintenance in Europe. After the meeting, the stakeholders made a decision to start the process of the development of a European standard (EN) based on the CWA 15740:2008 document. Accordingly, the status of the document has been prolonged in 2011 up to 2014 so the work on standardization will take place within the legal framework.

To promote the progress of Upgrading of the CWA 15740:2008 towards a EN, a kick-off meeting of potential stakeholders was held in Rotterdam and 19 participants coming from 10 European countries attended the meeting and expressed their interest in the involvement of RBI processes as well as readiness to go further in the procedure of upgrading, including the financing of the activities of the national standardization bodies (the secretariat was assigned to the Dutch standardization body NEN).

In spring 2013 the EU has approved the project “Safe-LifeX: Safe Life Extension management of aged infrastructures networks and industrial plants”, as the response to the EU FP7 call **NMP.2013.4.0-6 Safe Life Extension management of aged infrastructures networks and industrial plants**. The call is based on the idea that in Europe, many industrial facilities, such as power production plants and large chemical installations, as well as infrastructure network elements, like

bridges, tunnels and railway systems, are reaching the end of their designed operational life time. New ways to extend the service life of current infrastructure networks and industrial plants without jeopardizing their safety requirements need to be investigated in order to guarantee a decrease of major accidents in the industry and major disruptions of economic activity. Hence, the areas of investigation to be addressed include new **risk-based inspection technologies**, innovative reliability-based solutions, comparison between deterministic and probabilistic approaches, influence of degraded physical state on potential domino effects, and resilience. Methods and technologies vary between industrial sectors and therefore a benchmark study is necessary to understand the practices in the various industries and Member States, and to prepare the deployment of best practice solutions in Europe without compromising on safety and sustainability. In addition to the technical approaches, barriers linked to financing, risk insurance, decision making, public acceptance and regulations need to be addressed. Safety risks have to be identified locally (at element level) and globally (at network level, taking into account the interconnection). The new project Safe-LifeX, is expected to start in Sept. 2013 and run for 3 years.

9. Conclusions

RIMAP framework is applicable to industries other than those directly addressed (petrochemical, chemical, power, and steel), however it is limited to non-nuclear applications. The RBIM framework only applies to systems and equipment in the in-service phase of the operation. For the design or fabrication phase, the relevant legislation and engineering standards shall be followed. If RIMAP principles or procedures are used, it shall be ensured that all measures are in compliance with local and national legislation. While applying RBIM following aspects should be kept in mind

1. An RBIM assessment is only as good as input data provided
2. RBIM is not a replacement for good engineering practices/judgment.

The overall RIMAP approach is in general compatible with most other major risk-based approaches such as those designed by API [15], VGB [16], [17] or ASME and intended broadly for similar purposes. However, while the principles are largely similar, the user is warned against expecting identical results. There are differences in detail that may result in significant differences when using different approaches on the same plant, case or system. For example, unlike most other known approaches, RIMAP was originally designed to be in principle industry independent and providing seamless transfer between different levels of analysis (ranging from screening to detailed).

Acknowledgements

The work presented in the paper has included important inputs from persons (such as Ms Guntrum, Ms Quintero, Mr Abrahams, Mr Balos, Mr Caillard, Mr Eremic, Mr Husta, Mr Orlic – we apologize to others not explicitly mentioned here) and from organizations/companies participating in the development and implementation phases of the respective projects. Their precious contributions in terms of inputs, support on site, development of the software system and, last but not least preparation of this paper are gladly and gratefully mentioned here.

References

1. Jovanovic, A. (2008). EU RBI Guide document CEN CWA 15740:2008, API RBI European Workshop, Milan, Italy (The Equity Engineering Group, Inc., USA), October 27–31, 2008.
2. CEN CWA 15740:2008 Risk-Based Inspection and Maintenance Procedures for European Industry, CEN EU 2008 (Chair A. Jovanovic).
3. Jovanovic, A. (2010) Role of Risk-Based Inspection when dealing with risks related to new technologies in industry. In: Proceedings for the 2nd International Conference on Reliability, Safety and Hazard – Risk based technologies and physics of failure methods. Mumbai, India. 14–16 Dec. 2010.
4. Jovanovic, A. (2010) Globalization aspects of Risk-Based Inspection and Reliability-Centered Maintenance practices world-wide. In: Proceedings for the RBE-5 5th International Workshop on Risk-Based Engineering. Convention Center University of Science & Technology, Beijing, China. Nov 16–18.
5. RIMAP WP2/D2.1 – “Generic RIMAP Procedure”, GROWTH Project GIRD-CT-2001-03008 “RIMAP”, RIMAP RTD Consortium, Version: Rev. 6, (2002).
6. RIMAP WP4/D4.3 – “RIMAP Application Work book for the Chemical Industry”, by Rino van Voren, GROWTH project GIRD-CT-2001-03008 “RIMAP”, RIMAP RTD Consortium, Version: Rev. 0, (2003).
7. RIMAP WP4 – “RIMAP Petrochemical workbook”, by Stefan Winnik, Andrew Herring, Rick Gregory, GROWTH project GIRD-CT-2001-03008 “RIMAP”, RIMAP RTD Consortium, Version: Rev. 1.1, (2003).
8. EN ISO/IEC 17020 (ISO/IEC 17020) – “General criteria for the operation of various types of bodies performing inspection”, European Committee for Standardization (CEN).

9. EN ISO/IEC 17025 (ISO/IEC 17025) – “General requirements for the competence of testing and calibration laboratories”, European Committee for Standardization (CEN).
10. EN473 – “Non destructive testing – Qualification and Certification of NDT personnel – General principles”, European Committee for Standardization (CEN).
11. RIMAP WP3/I3.3 – “Assessment of Probability/ likelihood of failure”, by A.S. Jovanovic, P. Auerkari, R. Giribone, GROWTH project GIRD-CT-2001-03008 “RIMAP”, RIMAP RTD Consortium, Version: Rev. 10, (2004).
12. RIMAP I3.2 – “Assessment of the Consequence of Failure”, by J. Heerings, A. den Herder, M. Johanson, J. Reinders., GROWTH project GIRD-CT-2001-03008 “RIMAP”, RIMAP RTD Consortium, Version: Rev. 1, (2003).
13. RIMAP D3.1 – “Risk assessment methods for use in RBMI”, by S. Angelsen, G. Vaje, M. Johanson, J. Heerings, A. den Herder, GROWTH project GIRD-CT-2001-03008 “RIMAP”, RIMAP RTD Consortium, Version: Rev. 0, (2003).
14. TÜV Rheinland, South Africa – private communication.
15. ANSI/API RP 580 – “Risk-Based Inspection”, American Petroleum Institute (API), (2002); www.api.org/publications/.
16. Empfehlung zur Einführung Risikobasierter Instandhaltung VGB – KRAFTWERKSTECHNIK GmbH, 2004, ArtNr.:M130, existing English version: Recommendation for the introduction of Risk based maintenance ArtNr.:M130e.
17. VGB-Standard Condition Monitoring and Inspection of Components of Steam Boiler Plants, Pressure Vessel Installations and High-Pressure Water and Steam Pipes VGB-Standard- S-506-R-00;2012-03.EN Second edition (published 2012) (Formerly VGB-R 506e), VGB PowerTech e.V.
18. RIMAP WP4, D4 – Application Workbook for Power Plants, A. S. Jovanovic, P. Auerkari, R. Giribone GROWTH project GIRD-CT-2001-03008 “RIMAP”, RIMAP RTD Consortium, Version 2, (2003).
19. SAE JA 1011 – “Evaluation Criteria for Guide to the Reliability Centered Maintenance (RCM) Processes” (1998) – SAE International G-11 Supportability Committee; www.sae.org/technical/standards/JA1011 199908.
20. SAE JA 1012A – “Guide to the Reliability-Centered Maintenance (RCM) Standard” (2002), SAE International G-11 Supportability Committee; www.sae.org/technical/standards/JA1012 200201.

APPENDIX: Plant data (unit and process description)

Purpose of the unit/plant – natural gas refining – separation of the higher fractions of the carbon hydrates from the lighter ones.

Feed: natural gas

Outputs: refined gas, Propane 45 t/day, n-Butane 34 t/day, iso-Butane 38 t/day, Debutanised gasoline 60 t/day, process oil 5 t/day and Gasoline Gt 4,2 t/day

Year of construction: 1963

Re-engineered and re-constructed for operations up to -23°C in 1969.

Design life time- not given in the project documentation, most of the equipment has been designed according to the ASME Section VIII, edition valid at the time of construction. This is equivalent to approx. ASME Section VIII, Division 1 according to the current standard edition. Re-qualification of the equipment to the latest code of construction (ASME) has not been performed. Analysis of the design and qualification to the current regulation of pressure vessels in Serbia has been performed on several occasions, mostly by the local Universities.

Elevation above sea level: 80 m

Seismic zone: 7 (Mercalli), zone 3 according to API 581 classification.

Typical wind direction: NE-SW

Maximum soil load: 16 N/m²

Expected soil deformation: 6–10cm for 1,85 m depth of foundations

Underground water level: 4m below

Depth of soil freezing: 60 cm

Temperature range: 36 in summer to -30°C in winter, corresponding to the -30 to -5 class in API 581

Wind loads (to be considered in strength calculations for equipment):

- structures lower than 10 m: 687 N/m²
- structures from 10–30 m: 803 N/m²
- structures from 30–60m: 1003 N/m²
- structures higher than 60m: 1177 N/m²

Snow weight: 740N/m²

Maximal rainfall in 24 hours: 120mm

Temperature zone: Temperate (rainfall between 500–1000 l/(m² year)

Process stability: from 0–1 unplanned shutdowns per year, from 0–1 planned shutdowns per year. Process is very stable

Detection systems: Process instrumentation – i.e. high level of liquid propane detector, regulation and automation system for operating parameter maintenance, security system AMOT for automatic shutdown of compressors, high concentration of hydrocarbon detectors, 24 hour human supervision of the process parameters with hand logging and hourly walk-around, local detectors, visual detection.

Insulation systems: Most of the insulation systems are manually activated, on the spot. The only exception is the AMOT system for automatic shutdown of the compressors, AMOT, that can automatically shut down the compressor in cases of high number of rotation, high level registered in D-1, increased vibrations, low pressure of the fluid (oil), high temperature of cooling water.

Fire-fighting equipment: Portable fire-fighting equipment S-9, S-250, CO2-10, CO2-30, water cannons with foam

Temporary repairs and signs of deterioration: some signs of deterioration are present, however, they are logical consequence of the overall equipment age. Temporary repairs and repairs with inappropriate materials have been made during the 1990s, mainly due to the fact that it was not possible to obtain better equipment

Modification of the original design:

- Re-design of the input part of the system
- Change of the working fluid – instead of the proprietary oil, refining-generated oil is used

History of incidents:

- Propane leakage on the compressor, and auto-ignition of the fluid. Apart from material damage, there was no other damage to the people or environment mainly due to an early detection of the incident and fast fire extinguishing
- Leakage of propane, butane and gasoline from the underground lines due to the corrosion of the underground lines. Consequences – propane and butane was easily spotted, and quickly fixed. Gasoline leakage was discovered at a relatively late stage, due to the fact that it did not evaporate. Soil remediation has been done by pumping up the gasoline from the soil, the whole operation lasted 2,5 months
- Problems at the furnace firing – the firing process is manual and can in some cases lead to the explosive concentrations inside the furnace and consequent injury of the person performing firing. So far no serious injuries.

Safety and relief valves: the process is inherently clean, there is a potential for some corrosion mainly from the outside. No significant fouling of the RV has been registered, however, in the general process of control, some of the valves have been found not to be functioning.

Fluid information:

Present fluid in the system are:

- Natural and refined gas – 3,8–17,0% vol explosive concentration, Auto ignition temperature 640–645°C, gas with no smell or color, flammable and explosive, in higher concentration might cause suffocation. Danger mark 23, F+, Risk mark R12, information marks S9,S16,S36/37/39
- Propane – 2,1–9,5% vol explosive concentration, Auto ignition temperature 465°C, gas with no smell or color, flammable and explosive, in higher concentration might cause suffocation. Danger mark 23, F+, Risk mark R12, information marks S9,S16,S36/37/39
- Butane – 1,5–8,5% vol explosive concentration, Auto ignition temperature 365°C, gas with no smell or color, flammable and explosive, in higher concentration might cause suffocation. Danger mark 23, F+, Risk mark R12, information marks S9,S16,S36/37/39
- Debutanized gasoline – 1,3–7,6% vol explosive concentration, Auto ignition temperature 257°C, liquid with no color, flammable and polluting for soil and water. Danger mark 33 Xn,F, Risk marks R11,R22/21,R52/53,R58,R65, information marks S36/39,S45,S61,S62
- Heavy gasoline – 1,3–8,0% vol explosive concentration, Auto ignition temperature 205–220°C, liquid with no color, flammable and polluting for soil and water. Danger mark 33 Xn,F, Risk marks R11, R22/21, R52/53, R58, R65, information marks S36/39, S45, S61, S62
- Methyl-alcohol – 7,3–36% vol explosive concentration, Auto ignition temperature 455°C, liquid with no color, flammable and poisonous. Danger mark T,F, Risk marks R11 R11, R23/24,25, information marks S-2,7,16,24
- Water and steam

Similitude of residual stresses and the warm pre stress effect

Kim R. W. Wallin

VTT Technical Research Centre of Finland
P.O. Box 1000, FI-02044 VTT, Finland

Abstract

A material's apparent fracture toughness, at a specific temperature and loading rate, is affected by two factors: residual stresses and the so called Warm Pre Stress (WPS) effect. Residual stresses are global stresses, independent of a pre-existing flaw. They are generally due either to welding or thermal loads, but can also be introduced by plastic deformation. The WPS is due to a local plastic deformation of the material in front of a crack. The residual stresses can be either detrimental or beneficial, whereas WPS is always beneficial. Despite their different nature and origin, they do show a similitude on the apparent fracture toughness response. This similitude is highlighted here.

1. Introduction

Structural integrity assessment requires information regarding the stresses, possible or postulated flaws and the materials fracture toughness. Besides a reliable estimate of the material's fracture toughness, information about its transferability to the assessment of the structure is needed. The transferability is affected by parameters such as: the fracture toughness parameters' validity range, differences in constraint between test specimen and structure, secondary stresses in the structure and load history effects. To complicate matters further, the transferability of ductile and brittle (cleavage) fracture toughness reacts to the various factors differently.

A material's apparent fracture toughness, corresponding to a fixed constraint level at a specific temperature and loading rate, is affected by two factors: residual stresses and the so called Warm Pre Stress (WPS) effect. Residual stresses are global stresses, independent of a pre-existing flaw. They are generally due either to welding or thermal loads, but can also be introduced by plastic deformation. The WPS is a load history effect due to a local plastic deformation of the material in front of a crack. The residual stresses can be either detrimental or beneficial, whereas WPS is always beneficial.

The nature of the residual stresses and WPS are discussed in more detail in the next two chapters.

2. Residual stresses

Residual stresses due either to welding or thermal loads can have a drastic effect on the transferability of fracture toughness values, unless the residual stresses are properly accounted for. Figure 1 show as an example a comparison of wide plate data for a structural steel. The majority of the data corresponds to welded plates, with a few CC(T) specimens of base metal. Below a certain temperature the fracture stress drops close to one fifth of the base plate value. At higher temperatures the failure loads for all specimens appear to coincide. This is due to the fact that, with sufficient plasticity, the residual stresses disappear.

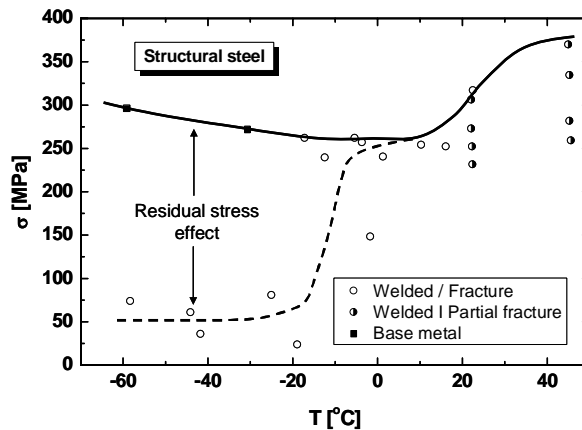


Figure 1. Effect of residual stresses on failure stress for structural steel wide plates [1].

The effect of residual stresses can also be looked at in terms of a shift in ductile to brittle transition. Figure 2 shows two sets of U-profile specimens tested in bending. All WX 420 and part of the WX 700 specimens were welded from three parts. These welds caused “long range” tensile residual stresses at the crack tips (one on each flange). Part of the WX 420 specimens were stress relieved and part of the WX 700 specimens were manufactured by bending from one plate. A significant effect of the residual stresses due to welding can be seen in the figure. The ductile/brittle transition shifts approximately 15°C.

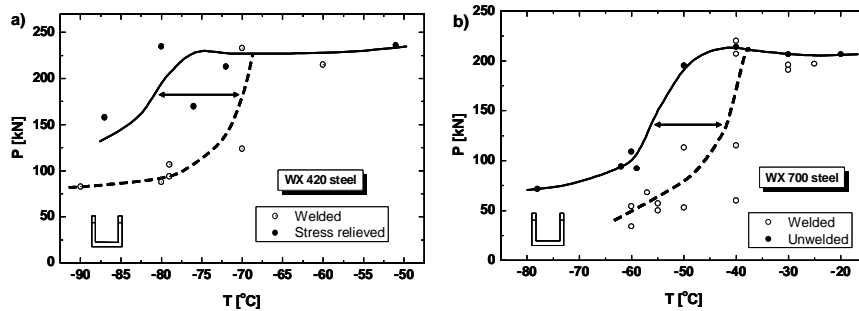


Figure 2. Effect of residual stress on failure load of high strength steel U-profile bend specimens [2].

Residual stresses basically cause, as long as the structure remains predominantly elastic, an offset in the effective fracture toughness. This is highlighted in Figure 3, where two data sets, including residual stresses, have been analysed with distribution comparison, as described in [1]. Both data sets correspond to nuclear pressure vessel steel grade A533B, but the material in Figure 3b has been given an atypical heat treatment. The residual stresses were in both cases introduced by in-plane compression, which results in tensile residual stresses in front of the crack. For the low temperature data, a separate estimate of the residual stress was about $K_{IS} = 42 \dots 46 \text{ MPa}\sqrt{\text{m}}$ and for the room temperature data a value of $25 \text{ MPa}\sqrt{\text{m}}$ was estimated based on FE-analysis. Those values are well in line with the results based on the distribution comparison of the actual test data.

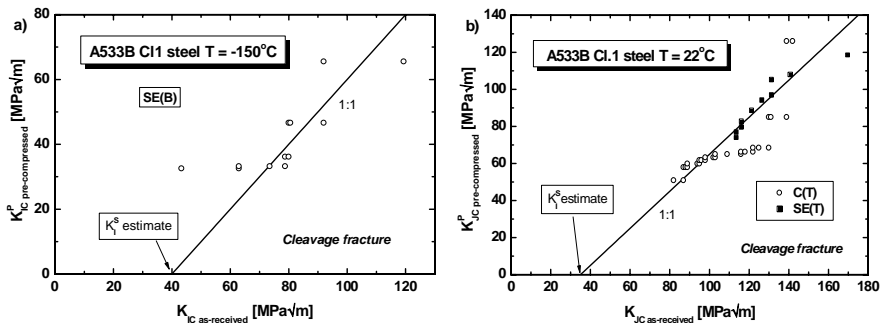


Figure 3. Effect of residual stresses on apparent cleavage fracture toughness. Data taken from [3] and [4].

The effect of residual stresses is not restricted to brittle fracture. As long as the loading remains elastic, ductile fracture is similarly affected. Figure 4 shows two ductile fracture data sets for two aluminium alloys. The material in Figure 4a refers to a brittle aluminium with a limited tearing resistance [1], whereas the more duc-

tile material in Figure 4b shows a full tearing resistance curve. Figure 4a shows a distribution comparison of the measured K_{\max} values, whereas Figure 4b compares tearing resistance curves with varying residual stresses. The residual stresses were in both cases introduced by local out-of-plane compression [5].

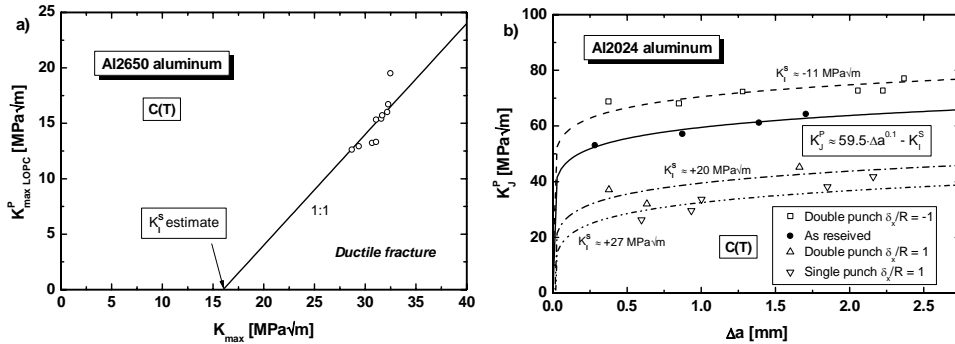


Figure 4. Effect of residual stresses on apparent tearing resistance. Data taken from [5].

By altering the punching procedure, it is possible to introduce both tensile and compressive residual stresses of varying magnitude in front of the crack. This is very interesting, since the same method is widely used with the intent to remove residual stresses for the attainment of a straight pre-fatigue crack. For both materials, the effect of residual stress is simply described by an offset of the fracture toughness or the tearing resistance curve. It is, however, important to note that the specimens in Figure 4 were mainly elastic. Figure 5 shows tearing resistance data for an austenitic steel, where the specimens are loaded into the plastic region. The residual stresses were introduced into the specimens by edge-welding which caused a residual tensile stress in front of the crack. A separate best estimate of the residual stress was about $K_{IS} = 31 \dots 37$ MPa√m. The test results indicate only a residual stress of $K_{IS} = 16$ MPa√m, there seems still to be an effect of the residual stresses also in the elastic-plastic region.

The effect of plasticity is further examined in Figure 6, which contains a compilation of the above residual stress estimates based on test results and stress analysis. The data is plotted as a function of the ratio between the elastic stress intensity value corresponding to limit load estimated using the materials yield strength and the average fracture toughness in the different data sets. Up to limit load there appears to be mainly random scatter, due to the uncertainty in the residual stress estimate; beyond this, the actual residual stress begins to drop and finally disappears altogether.

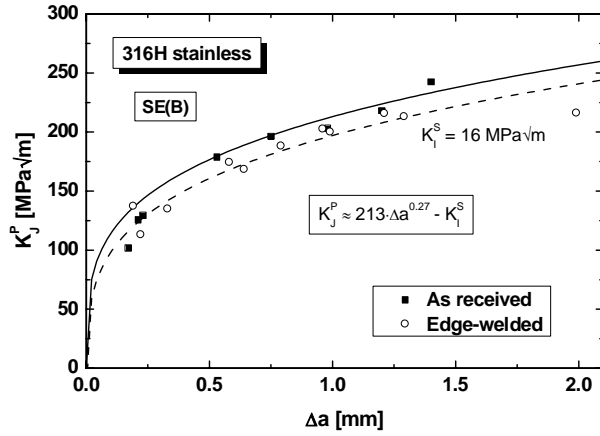


Figure 5. Effect of residual stresses on apparent tearing resistance. Data taken from [6].

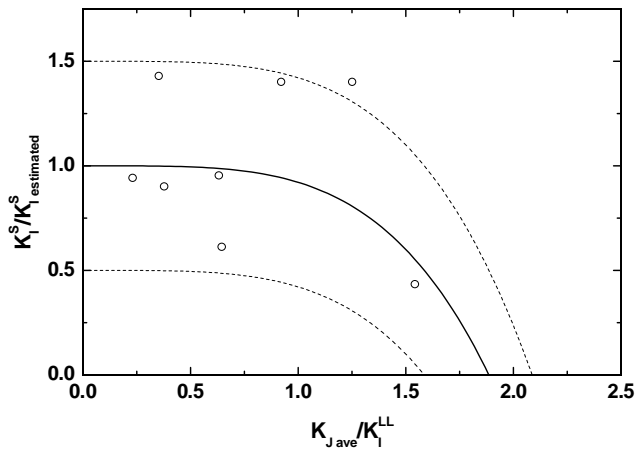


Figure 6. Effect of load level on residual stress [1].

3. Warm Pre Stress (WPS)

The Warm Pre Stress (WPS) effect describes the effect of a prior loading on the subsequent effective fracture toughness. When a crack is loaded to some crack driving force parameter value (K , J or $CTOD$) that is lower than the fracture toughness at the temperature in question, the effect will be an effective increase in fracture toughness if the specimen is re-loaded at a lower temperature at which the prior loading exceeds the fracture toughness (Figure 7). The WPS does not affect the material's fracture toughness directly. It alters the stress field around the

crack and this way produces an apparent increase of toughness. The WPS effect can be connected to a variety of possible transients, some of which are depicted in Figure 7.

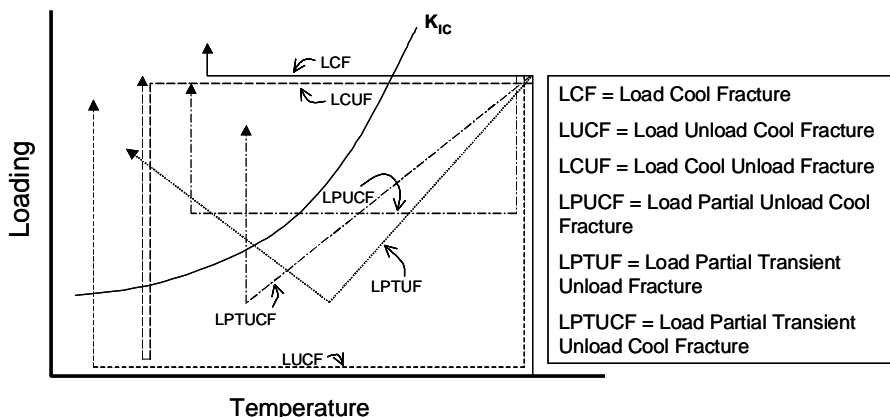


Figure 7. The principle and some possible transients of the WPS effect [7].

Experimental investigations have focussed on LCF (Load Cool Fracture), LUCF (Load Unload Cool Fracture) and LPUCF (Load Partial Unload Cool Fracture) transients. A considerable amount of research, verifying the effect, has been performed during the last 30 years [7]. The existence of the WPS effect is unquestionable if the result is not affected by time dependent processes like strain aging. Several investigations have shown that strain aging decreases, or even removes, the WPS effect [7]. The WPS effect is thus not to be recommended for life extension purposes, but in a structural integrity analysis, involving a prior overload or thermal transient, the effect can well be taken into account. The most accurate description of the WPS effect was introduced by Chell [8]. Figure 8 shows a graphical summary of the Chell model. Chell proposed a failure criterion that describes fracture when plastic and residual stress zones occur. The criterion uses the J-integral (J_e) accounting only for the elastic components. This criterion was used, together with a model for strip yielding, to determine the conditions for onset of failure for different loading paths. The only problem with the Chell model is that its use is somewhat complicated. The model contains several different criteria affecting the outcome and it requires numerical methods to solve the equations.

Usually, investigations have compared the WPS affected result with the mean "baseline" fracture toughness value. As an example, Figure 9 shows the outcome of the Chell model when used with the average fracture toughness. This is appropriate for determination of the mean behaviour, but makes interpretation and use with respect to scatter difficult. The Chell model is seen to provide nearly a 1 to 1 prediction, but the scatter is of the order of 25%. This scatter is mainly due to the scatter in fracture toughness. It is not due to the WPS effect itself. In structural

integrity assessment, where a lower bound type fracture toughness estimate (like the 5% or 1% MC) is used, it is imperative to know that the WPS affected value corresponds to an equivalent lower bound. This requires a simple reliable WPS correction.

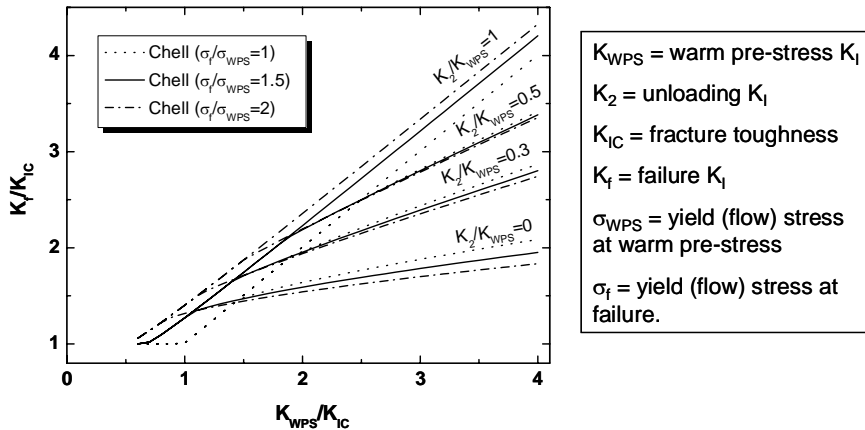


Figure 8. WPS model by Chell [8].

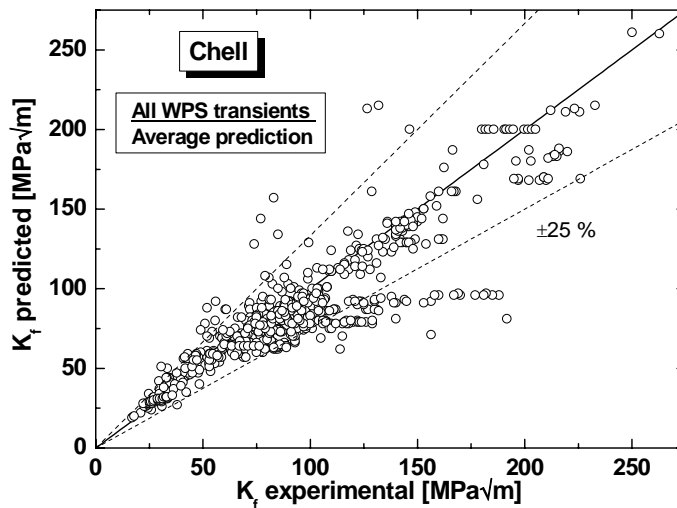


Figure 9. Predictive capability of the Chell WPS correction for 751 results representing varying WPS transients using average fracture toughness as input [7].

The WPS effect has two extreme transients. The LCF transient produces the maximum effect and reduces scatter the most. The LUCF transient produces the minimum effect and reduces scatter the least. All other transients fall in their effects between these two leading transients.

Since LCF shows the least scatter, let us examine this first. Figure 10 contains all the LCF data where K_{WPS} and K_f have been normalized with the median baseline fracture toughness. It can be seen that, for WPS levels exceeding the fracture toughness, there is a very clear dependence between the parameters. This leads to a best estimate definition, which is valid for LCF transients, equation (1).

$$K_f \approx 0.25 \cdot K_{IC} + K_{WPS} \quad (1)$$

Theoretically, the LCF transient behaviour is due to the requirement of a constant stressed volume increase equivalent to the volume corresponding to K_{IC} . This can be expressed in the form of equation 2, where the constant 1.25 accounts for the yield stress and strain hardening differences between the WPS and failure temperatures.

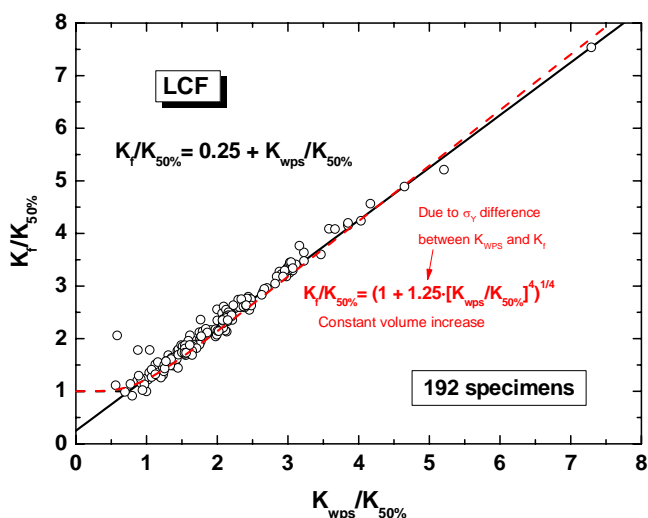


Figure 10. Relation between baseline fracture toughness ($K_{50\%}$), WPS level (K_{WPS}) and apparent fracture toughness (K_f), for the LCF transient. Data taken from [7].

$$K_f \approx K_{IC} \cdot \left(1 + 1.25 \cdot \left[K_{WPS}/K_{IC}\right]^4\right)^{1/4} \quad (2)$$

The other extreme transient (LUCF) is analysed in Figure 11, in a similar way as in Figure 10 for LCF. For WPS levels exceeding the fracture toughness there is a clear dependence (even though less clear than for LCF) between the parameters. This leads to a best estimate simple correction, which is valid for LUCF transients, in the form of equation (3). The use of the simple square root expression makes the correction a slightly conservative for high K_{WPS} values, but this is not a major problem.

$$K_f \approx 0.25 \cdot K_{IC} + \sqrt{K_{IC} \cdot K_{WPS}} \quad (3)$$

The WPS effect can be treated as affecting the Master Curve in two ways. First, it increases the value of the lower limiting fracture toughness K_{min} . Second, it increases the value of the 63.2% failure probability toughness K_0 . The comparatively large scatter in LUCF data comes from the smaller effect of the transient on the lower limiting fracture toughness K_{min} than for the LCF transient. Since K_{min} is further away from K_0 than for LCF, also the scatter will be larger than for the LCF transient.

A general formulation is required to handle all possible WPS transients. This is achieved by combining equations (1) and (3) so that a smooth transition between the extreme transients LCF and LUCF is obtained. For consistency with the Chell model, the combined correction has been modified by changing the constant 0.25 to 0.15. The result is given by equation (4) [7].

$$\begin{aligned}
 K_f &= 0.15 \cdot K_{IC} + \sqrt{K_{IC} \cdot (K_{WPS} - K_2)} + K_2 \\
 \text{if } K_2 &\geq K_{WPS} - K_{IC} \Rightarrow K_2 = K_{WPS} \\
 \text{if } K_f &\leq K_{IC} \Rightarrow K_f = K_{IC}
 \end{aligned} \tag{4}$$

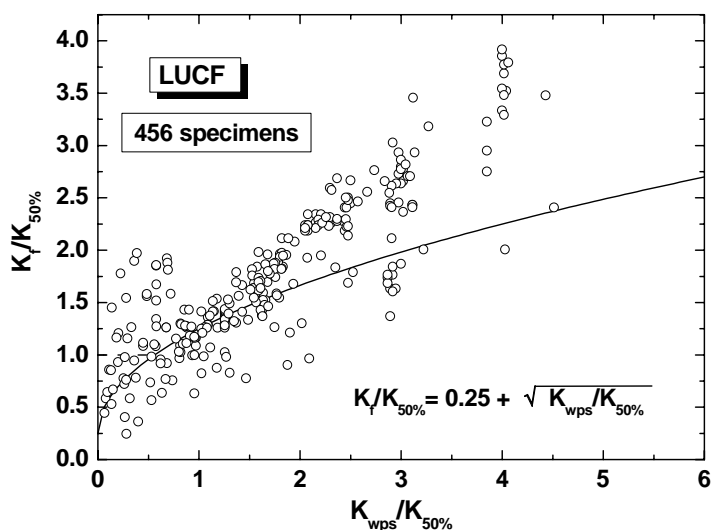


Figure 11. Relation between baseline fracture toughness ($K_{50\%}$), WPS level (K_{WPS}) and apparent fracture toughness (K_f), for the LUCF transient [7].

Equation 4 intends to be a best estimate prediction (with a small built-in conservatism) and it requires the knowledge of K_{IC} . An even simpler, generally more conservative French WPS correction has been proposed in [9], where knowledge of K_{IC} is not required. The correction has the form of equation (5) [9].

$$\begin{aligned}
 K_f &= K_{WPS} / 2 + K_2 \\
 \text{if } K_2 &\geq K_{WPS} / 2 \Rightarrow K_f = K_{WPS}
 \end{aligned} \tag{5}$$

Even though equation (5) does not contain K_{IC} , it implicitly assumes some K_{IC}/K_{WPS} ratio. Equation (5) is generally conservative with respect to Equation (4), but in the region $K_2/K_{WPS} = 0.3 - 0.6$, equation (6) assumes implicitly a K_{IC}/K_{WPS} ratio > 0.3 (Figure 12). This means that as long as the WPS transient is not higher than approximately three times the materials fracture toughness at the failure temperature, equation (5) provides a conservative description of the WPS effect.

4. Similarity between residual stress and WPS

Even though residual stresses due to welding or thermal loads, are in nature more global than the residual stresses caused by WPS. There is a clear similarity in their behaviour. Figure 13 shows a set of LUCF data plotted in a MC failure probability diagram coordinate system. The WPS LUCF transient has the effect of raising both the K_{min} value as well as K_0 by a similar amount. This means that the LUCF transient mainly only cause an offset to the real material fracture toughness similar to what was seen to occur for normal residual stresses. This is highlighted even more in Figure 14, where the data in Figure 13 have been analysed with distribution comparison, as described in [1]. The LUCF transient introduces a compressive local residual stress that enhances the apparent fracture toughness by a constant amount. The main difference between WPS and normal residual stresses is that the WPS causes always a compressive residual stress, leading to an enhanced apparent fracture toughness, whereas normal residual stresses may be compressive or tensile thus either enhancing or decreasing the apparent fracture toughness.

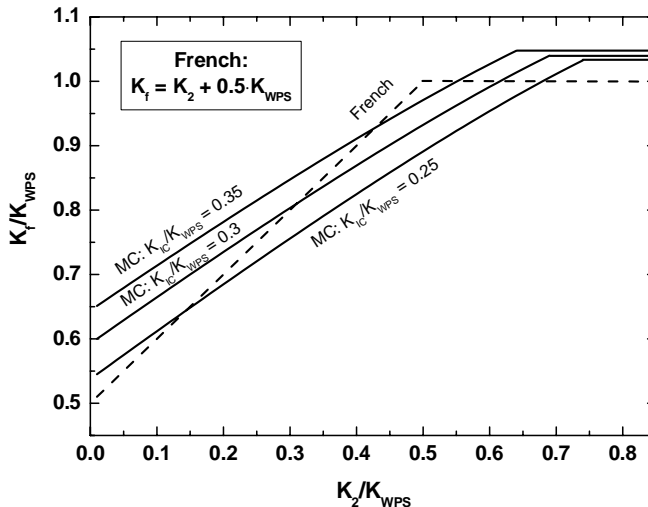


Figure 12. Comparison of “Best estimate” (MC) and “Simple” (French) WPS corrections.

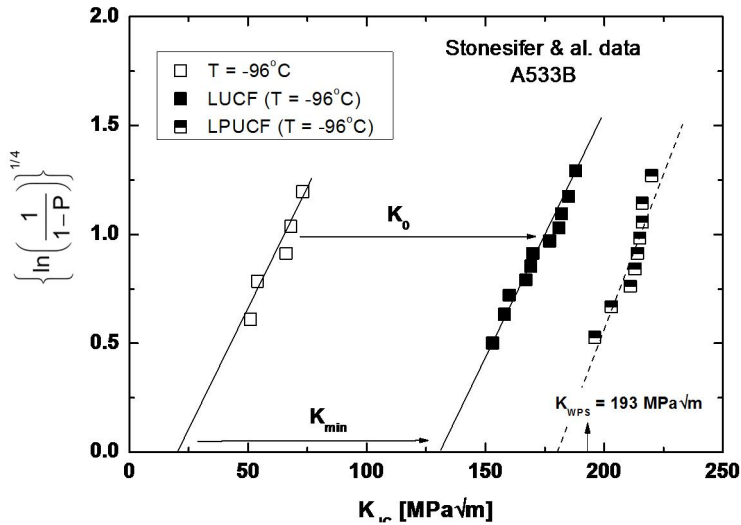


Figure 13. The effect of a LUCF transient is to raise both K_{\min} and K_0 by a similar amount [10].

5. Conclusions

The similitude of residual stresses and the warm pre stress effect have been examined. It can be concluded that in both cases the main effect is to introduce an apparent offset of the materials true fracture toughness. The WPS causes always a compressive residual stress, leading to an enhanced apparent fracture toughness, whereas normal residual stresses may be compressive or tensile thus either enhancing or decreasing the apparent fracture toughness.

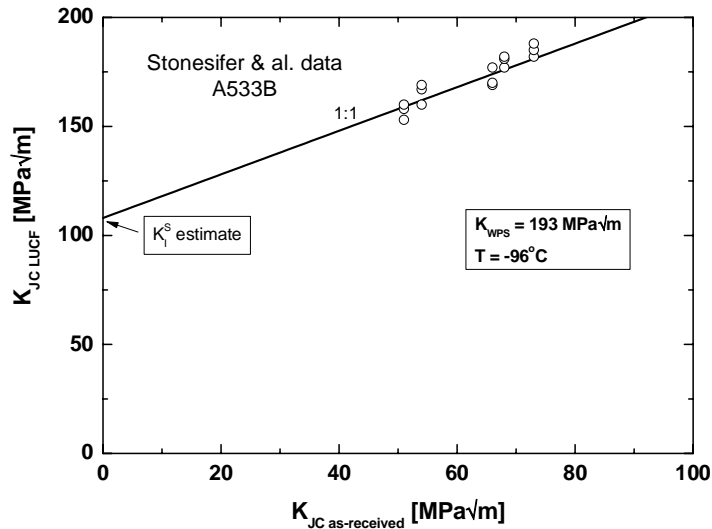


Figure 14. The effect of a LUCF transient on apparent cleavage fracture toughness based on the data from Figure 13.

Acknowledgements

The present work is part of the FAR project belonging to the SAFIR 2014 research program funded by VTT and by the State Nuclear Waste Management Fund (VYR), as well as other key organizations.

References

1. Wallin K. Fracture Toughness of Engineering Materials – estimation and application. Warrington UK, EMAS Publishing 2011.
2. Wallin K. Methodology for Selecting Charpy Toughness Criteria for Thin High Strength Steels. Part III: Verification. Jernkontoret, Stockholm, 1994. Jernkontorets Forskning D 735.
3. Mirzaee-Sisan A., Truman C. E., Smith D. J. and Smith M. C. Interaction of Residual Stress with Mechanical Loading in a Ferritic Steel. Engng. Frac. Mech., Vol. 74, 2007, pp. 2864–2880.
4. Lee K. S., Goldthorpe M. R., Birkett R. P. and Sherry A. H. Residual Stress and Constraint Effects on Cleavage Fracture in the Transition Temperature Regime. Fatigue Fract. Engng. Mater. Struct., Vol. 32, 2009, pp. 752–768.

5. Mahmoudi A. H., Truman C. E. and Smith D. J. Using Local Out-of-Plane Compression (LOPC) to Study the Effects of Residual Stress on Apparent Fracture Toughness. *Engng. Frac. Mech.*, Vol. 75, 2008, pp. 1516–1534.
6. Mirzaee-Sisan A., Truman C. E., Smith D. J. and Smith M. C. Interaction of Residual Stress with Mechanical Loading in an Austenitic Steel. *Fatigue Fract. Engng. Mater. Struct.*, Vol. 31, 2008, pp. 223–233.
7. Wallin K. Master Curve Implementation of the Warm Pre-Stress (WPS) Effect. *Engng. Frac. Mech.*, Vol. 70, 2003, pp. 2587–2602.
8. Chell G. G. Some Fracture Mechanics Applications of Warm Pre-Stressing to Pressure Vessels. 4th Int. Conf. on Pressure Vessel Technology. *Inst. Mech. Eng. Paper C22*, 1980, pp. 117–124.
9. Chapuliot S., Izard J.-P., Moinereau D. and Marie S. WPS Criterion Proposition Based on Experimental Data Base Interpretation. Fontevraud 7 – Contribution of Materials Investigations to Improve the Safety and Performance of LWRs, Avignon 2010, Paper A141 T01.
10. Stonesifer R. B., Rybicki E. F. and McCabe D. E. Warm Prestress Modeling: Comparison of Models and Experimental Results. NUREG/CR-5208, 1989.

French Ageing Management Program in connection with IAEA Safety Guides

C. Faidy

Consultant
Claude.faidy@gmail.com
Lyon, France

Abstract

During the past 15 years many works have been done on Ageing Management Program (AMP) of Safety classed components in EDF.

The paper will describe all the different aspects concerning these programs, and in particular the EDF step by step procedure and the major results.

To-day, EDF is starting the 3rd ten-year shutdown of all these 3-loop plants (34 plants). During the associated Safety Review, a specific task is devoted to ageing effects and control of all the safety concerned components. A large list of components has been reviewed: mechanical, civil engineering, instrumentation and control, cables, non metallic components. Few non safety but important in term of availability components are considered, like turbine or some balance of plant components. A general review of results and difficulties for 40 and 60 years are presented in the paper.

The second part is devoted to a short review of our procedure with IAEA guidelines.

The third part will shortly describe the associated R&D program for metallic components and knowledge management associated to AMP.

The major conclusions are clearly supporting the needs of international basic procedure and harmonization on the major topics.

1. Introduction

Managing ageing and remaining lifetime of an industrial facility is a concern that must be taken in account as part of daily activities. Bad practices may be detrimental in the short as well as the long term and the capital assets are of considerable value.

Ageing management of Nuclear Power Plants is an essential issue for utilities, in term of safety and availability and corresponding economical consequences.

Practically all nuclear countries have developed a systematic program to deal with ageing of components on their plants.

EDF recognized since the beginning of plant operation the importance of that need for its nuclear facilities: 58 PWR (Pressurized Water Reactor) units built on 20 sites are producing more than 75 % of electricity used in France (Table 1).

Keeping these facilities in good operating conditions as long as possible is economically important for EDF, before a progressive replacement of these existing plants by new reactors.

For nuclear power plants, "good operating conditions" undoubtedly means safety and cost-effectiveness.

In parallel, in 2001, USNRC (United State Nuclear Regulatory Commission) produced a specific document to be used for US utility license renewal: "Generic Ageing Lesson Learn" (GALL report) [2]. Different other countries are on the way to develop their own Ageing Management Program and the corresponding Safety Requirements, like: Japan, Netherlands, Hungary, Czech Republic...

2. EDF procedure for ageing management

For EDF French PWR plants, the lifetime management policy of the nuclear power plants is based on four principles [3]:

- daily operation and maintenance activities, with an effective experience feedback organization taking advantage of the high level of standardization of the units,
- "Exceptional Maintenance Program" is charged to identify possible future problems, to estimate potential consequences and to propose appropriate measures to be taken. Of course, consequences of the "anticipation / no anticipation" choice must be integrated on the whole plant lifetime.
- every ten years, a complete safety review of each group of similar plants, including ageing evaluation of systems, structures and components (SSC)
- a Life Management Program, at corporate level, which permanently scrutinizes operation and maintenance activities to identify decisions which could impair plant lifetime and which surveys research and development programs related to ageing phenomenon understanding.

2.1 Ageing management program review

The major objectives of these past 15-years are to justify that all the safety important systems, structures and components (SSC), concerned by an ageing mechanism, remain in the design and safety criteria, including all feedbacks from the field.

This ageing occurs along normal operation, including periodic tests and routine maintenance activities.

This ageing of SSC's is considered under control through different actions:

- prediction and detection, early in the SSC life, of degradations that can affect design rules (integrity of barriers) or safety function of the plant (final safety analysis report),

- definition of mitigation and corrective actions (including repair, replacement) to assure the safety level of the plant and the economic competitiveness of the final decision on anticipation process bases.

This ageing management program review is formed of 3 steps:

- selection of structures and components,
- specific report to continue operation of the more sensitive components and structures
- synthesis report.

All these reports have to be prepared in accordance with the French regulation, as the decree for surveillance of primary and secondary system, the different French Codes & Standards, as RCC-M Code for Design and Construction of French PWRs and RSE-M Code for Surveillance in operation of French PWRs and the corresponding plant Final Safety Analysis Report (FSAR).

2.2 French procedure for AMP review

2.2.1 Structure and component selection

The selection is based on the FSAR that defines rules for safety importance of components and structures:

- mechanical components: class 1-2-3
- electrical components: class 1E
- civil engineering structures: connected to safety

Around 15000 components are concerned by plant. The selection is based on the different ageing degradation mechanism that can affect a part of each components and structures.

In order to do that systematically and with a minimum of references that support the decisions, we proposed a specific table with one line per component, structures, or element for each potential degradation mechanism. In the same time different other information are collected through the columns:

- is the degradation mechanism potential or encountered in French or International similar plant?
- did we encounter difficulties that can have affected a safety function?
- is the degradation mechanism analyzed in the design report? If yes, what is the expected life in this report?
- is the present maintenance program adapted, easy to adapt or unadapted for this degradation mechanism?

- is the repair easy or difficult for this degradation mechanism and this location?
- is the replacement of the component easy or difficult? Do we have any risk of obsolescence of the components (no vendor available or no manufacturer of this type of components)?
- After the completion of a matrix (location versus potential degradation mechanism), each component or group of components (with similar function or similar degradation or similar design...) is affected in 3 categories: 0-1-2:
 - 0: no complementary studies
 - 1: intermediate level to be moved to 0 or 2 shortly
 - 2: prepare a specific justification report to confirm the continuation of operation, a Detailed Ageing Analysis Report (DAAR), similar to Time Limiting Ageing Analysis (similar to TLAA)

A specific data sheet is attached to each line of the matrix in order to collect all the references used to complete the matrix.

2.2.2 Report to justify continuation of operation

For the category 2 components or structures, a report has to be produced to justify on what basis continuation of operation can be permitted.

This report has to collect and identify references and present it as follows:

- introduction
- description: design, materials, fabrication process, water chemistry
- design basis: regulation, codes & standards, specification and guidelines
- operating experience and ageing mechanism
- assessment methods of corresponding ageing mechanisms
- inspection, monitoring, leak detection
- mitigation, repair, replacement
- synthesis of ageing management program recommendations.

2.2.3 Synthesis report

This synthesis report has to collect the major information of the 2 previous steps: selection and report to justify continuation of operation. A comparison is done with existing maintenance practices for all components and structures. A set of recommendations for maintenance improvements is done to the Utility service in charge of "maintenance and ISI" program definition. All the recommendations are analyzed, including the economical aspect of the changes in order to update all the ISI and maintenance documents. All these reports and synthesis are transferred to each plant, in order to identify any particular aspect of each of them and to assure that all the recommendations will be implemented.

2.3 Major results of EDF AMP

The corresponding analyses have been done for EDF 3-loop plants (34 similar plants, oldest in operation since 1977). We considered more than 1500 safety class systems, structures and components (SSCs), we obtained around 500 lines in the cross table (1 line = 1 potential degradation in 1 location of an SCC) and we developed 12 DAARs: reactor pressure vessel and internals, pressurizer, main coolant pump, main coolant loop and auxiliary class 1 piping steam generator, containment, containment electrical penetration, nuclear civil engineering structures, cables, Instrumentation & Control (I&C).

The corresponding reports have been reviewed by French Safety Authority and after different meetings we have received a general agreement to move from 30 years to 40 years of operation. This agreement received in July 2009 has been associated to particular requirements:

- update of the cross table and associated Ageing Sheet every year, including any national or international field experience,
- update the DAAR every 5 years,
- develop a specific review of generic studies at each plant level to develop any specificity of the plant concerning AMP one year before the periodic shutdown,
- develop a concluding report in the 6-months following the plant back in operation to analyze consequences of all the information collected during the shutdown in term of AMP.

Same procedure is under application for EDF 4-loop PWR plants (oldest has 25 years of operation).

3. Comparison with IAEA Safety Guide

A comparison of IAEA NS G 2-12 Safety Guide [1] has been done with EDF procedure [3 to 11] on Ageing Management. Different aspects are considered: design, operation, long term operation, obsolescence, decommissioning for passive and active safety classified components and structures.

The first index of this report is more focused on mechanical components; future indices will check if improvement or particular comments have to be added for Civil Engineering Structures, Cables, Electrical and Instrumentation & Control components.

3.1 Objective of the IAEA Safety Guide

The objective of this Safety Guide is to provide recommendations for managing ageing of SSCs important to safety in nuclear power plants, including recommendations on key elements of effective ageing management.

The Safety Guide is intended for use by operators in establishing, implementing and improving systematic ageing management programme for nuclear power plants. The Safety Guide may be used by regulators in preparing regulatory standards and guides, and in verifying that ageing in nuclear power plants is being effectively managed.

3.2 Scope of the Safety Guide

This Safety Guide deals with the establishment, implementation and improvement of ageing management programme for SSCs important to safety in nuclear power plants.

The Safety Guide mainly focuses on managing the physical ageing of SSCs (Systems, Structures and Components) important to safety. It also provides recommendations on safety aspects of managing obsolescence and on the application of ageing management for long term operation.

Issues relating to staff ageing and knowledge management are outside the scope of this Safety Guide.

3.3 Major conclusions of the comparison

All the major objectives of the IAEA Safety Guide are covered by EDF procedure.

The requirements of the IAEA guide are not associated with the safety importance of the component (class 1-2-3); in EDF procedure some simplifications are used for class 2 and 3 components (larger group of similar components, no needs of Detailed Ageing Analysis Report...)

Few differences are identified in the comparison:

- at the design level, appropriate arrangements to facilitate decommissioning activities is not yet covered by EDF on EPR for example
- the recommendation of IAEA guide to develop indicators in order to evaluate Ageing Management Program efficiency; these indicators have not been considered as efficient and reliable tools to measure efficiency of EDF-AMP
- ageing effects on qualification of active components ("qualified life") is slightly different
- no peer review process used for the moment in EDF; WANO or OSART are doing similar audit to EDF and include Long Term Operation

- very limited use of Risk-Informed, for example no Risk-Informed In-Service Inspection in EDF-AMP.

Some other differences are partial EDF answers or EDF answers through alternative methodologies:

- the documentation is slightly different: screening cross table, Ageing Analysis Sheet, Detailed Ageing Analysis instead of one synthetic document by component
- level of detail information concerning Ageing Management in the initial Safety Analysis Report (SAR) and periodic updated SAR during the 10-Year PSR
- synthesis of ageing effects, monitoring results, ISI results component by component through a summary sheet; partially done in EDF AMP
- the 9 attributes of AMP for each degradation mechanism are partially developed
- obsolescence of knowledge and consequences of Regulation and Codes & Standards revision [12,13]: not so formal in EDF-AMP
- multi-competence of actors is replaced by different people working in an EDF team with different competences
- the PLAN-DO-CHECK-ACT loop principle (table 2) proposed on a continuous basis in the Safety Guide leads to continuous review of all parts of the AMP, partially done in EDF AMP.

4. Research and development to support EDF AMP

Many actions are going on in different direction to cover AMP and degradation understanding and modeling to perform some prediction and develop fitness for long term operation of SSCs.

In this presentation only R&D activities for metallic components is covered, nevertheless similar programs exist for Civil Engineering Structures, I&C components, cables...

3 directions for these R&D activities:

- the material degradation and associated material properties,
- the ageing mechanism models and the major parameter evaluation,
- the safety margins.

The different mechanisms concerned are:

- corruptions
- fatigue
- corrosion-erosion
- thermal ageing

- radiation embrittlement

with possible degradation interactions.

4.1 Material degradation and associated material properties

Different topics are covered:

- High irradiation level of RPV beltlines for 60 years of operation,
- Corresponding toughness of the cladding,
- Thermal ageing of low alloy steels and welds,
- Consequences of heterogeneities in the underclad areas,
- Irradiated Assisted Stress Corrosion cracking, creep under irradiation, swelling, fatigue, loss of ductility of materials of RPV internals,
- Wear of stellite guide parts in RPV internals
- Air fatigue curve of stainless steel material, plus environmental effects
- Thermal ageing of cast duplex stainless steels and different welds, including dissimilar metal welds
- Fatigue crack initiation curves and crack growth curves for stainless steels and welds
- Stress corrosion cracking of cold work stainless steel
- Stress corrosion cracking of Nickel based alloys (600 and 690): initiation and crack growth rates for penetration base metal and welds and steam generator plates
- High cycle fatigue of main coolant pump internals and shaft
- Erosion-Cavitation of pump wheel
- Strain ageing and thermal ageing of carbon steels
- Flaw accelerated corrosion: thinning rates
- Fatigue environmental effects for carbon steels and welds

4.2 Ageing mechanism models and the major parameter evaluation

These different degradation mechanisms can lead to local thinning, cracks or loss of material properties. The degradation rate is generally expressed in thinning rate or crack initiation/crack growth. For the loss of material properties it's more the flaw tolerance of the component that can be strongly reduced.

The mechanical parameters used are generally the fracture mechanic parameters (K or J). The French RSEM Code [12] is extremely detailed and does not need any further development.

The remaining questions are:

- the plastic limit load for plastic instability of normal, thinned or cracked components,
- the toughness transferability from CT specimen to the real structure
- mismatch and dissimilar metal welds
- for brittle fracture: the warm pre-stress effect, the crack arrest, the effect of local brittle zone in low alloy steel
- the residual stress level and their effects on crack growth (corrosions), rupture in brittle regime or in ductile regime for low toughness materials
- the large ductile crack growth (on 10 mm or more)
- the rupture criteria of high toughness materials, like stainless steels or nickel based alloys.

4.3 Safety margins

It's a very important issue to understand how the different uncertainties, in data or in models, can affect the ageing effect and the acceptable degradation.

For simple degradation mechanisms, using a limited number of data it's not a real concern. But for more complex situation moving from safety scenario, transient definition, flaw evaluation the final conclusion with all the models and parameters in the safety side it's impossible to reach a reasonable conclusion.

2 ways are under analysis in our R&D work:

- the partial safety factors
- the probabilistic evaluation of margins.

The bridge between deterministic and probabilistic approaches is a key issue for safety margin evaluation.

5. Conclusion

EDF has developed a general procedure for Ageing Management of safety class components. This program is applied to the 3-loop plants and regularly reviewed by French Safety Authorities. This procedure is globally in accordance with IAEA Safety Guide recommendations.

In addition, an important R&D program is on going to understand and quantify the major degradation mechanisms and their consequences.

The major conclusions are clearly supporting the needs of international basic procedure and harmonization on the major topics.

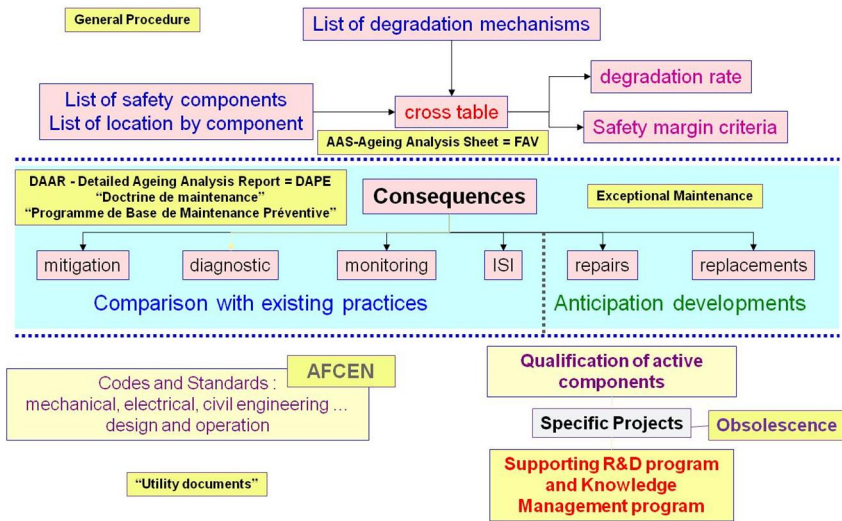


Table 1. General overview of EDF AMP.

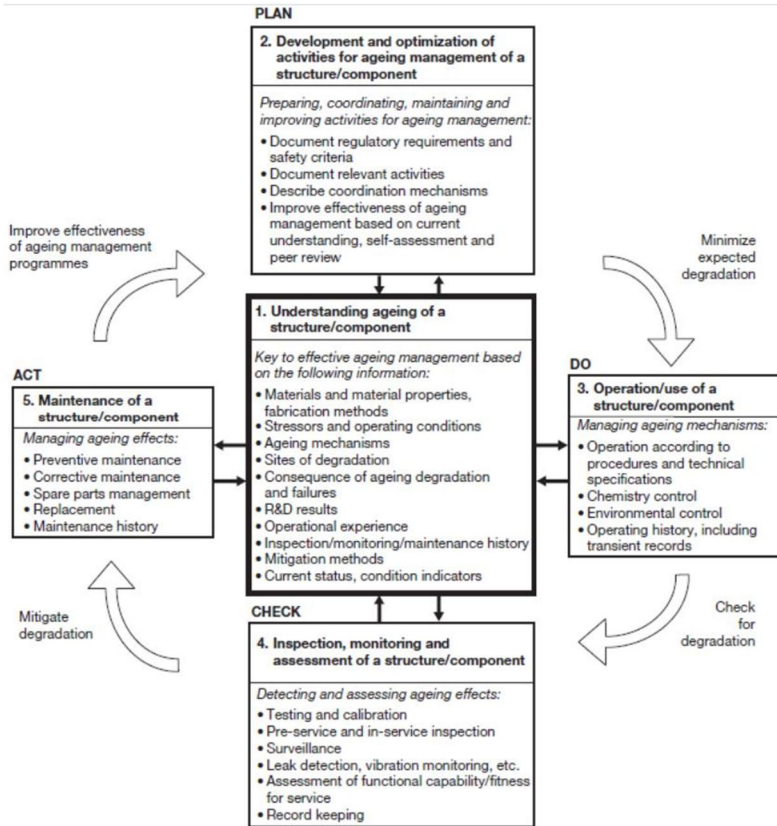


Table 2. The IAEA PLAN-DO-CHECK-ACT diagram for AMP.

References

1. IAEA Safety Standards- Ageing Management for Nuclear Power Plants- Safety Guide NS-G-2.12
2. USNRC, "Generic Aging Lessons Learned (GALL) Report", NUREG-1801, rev.2, December 2010.
3. C. Faidy, " French Procedure for Ageing management program of safety components", ASME Pressure Vessel & Piping Conference, Cleveland OHIO, USA, July 2003
4. C. Faidy, "Ageing Management Program: Comparisons between EDF methodology and US GALL report", ASME Pressure Vessel & Piping Conference, San Diego, CA, USA, July 2004.

5. C. Faigy, " Overview of EDF Ageing Management Program of Safety Class Components", International Conference on Ageing Issue in Nuclear Power Plants - NuPEER 2005 – Dijon France, June 22-24, 2005
6. C. Faigy, F. Hedin, " EDF lifetime management of nuclear components : a safety and economical issue", "PLIM-PLEX 2006", Paris, France, April 10–11, 2006.
7. C. Faigy, "Aging management of EDF NPP : from the design phase up to end of life", 2nd international Symposium on NPP Life Management, Shanghai, China, 15–18 October 2007.
8. D. Dallery, JJ Nicolay, " Ageing Management, In-Service Inspection and Exceptional Maintenance", 2nd international Symposium on NPP Life Management, Shanghai, China, 15–18 October 2007.
9. C. Faigy, " Degradation Mechanisms – Overview in Connection with AMP", Pressure Vessel and Piping Conference , paper PVP2007-26349, July 22–26, 2007, San Antonio, TX, USA.
10. C. Faigy, "EDF Ageing Management and International Cooperation", 2009 ASME Pressure Vessels and Piping Conference, paper PVP2009-78024, July 26–30, 2009, Prague, Czech Republic.
11. C. Faigy, " Ageing Management Program: A key Issue for Operating plants and New Design", 20th International Conference on Structural Mechanics in Reactor Technology, SMiRT 20, Espoo, Finland, August 9–14, 2009.
12. RSE-M Code, "Rules for In-Service Inspection of PWR Nuclear Power Plant Components", Appendix 5, 2012 Edition, AFCEN, Paris.
13. RCC-M Code, "Design and Construction Rules for Mechanical Components of PWR Nuclear Islands", 2012 edition, AFCEN, Paris.

Fatigue of stabilised steel in NPP primary piping – discussion on design curves

Jussi Solin

VTT Technical Research Centre of Finland
Kemistintie 3, Espoo, Finland

Abstract

The ASME Code Section III fatigue design methodology is based on local strain approach and transferability of material performance measured using small scale laboratory samples. Strain controlled tests data shall be transferred to fatigue assessment in a compatible way to provide relevant prediction and follow-up of fatigue usage. Transferability to real components is secured by appropriate margins and full scale testing. Transferability can be studied and improved through better simulation of component operation conditions such as loading mode and sequence, temperature and environment. But the design curves shall be based only on standard tests compatible with the design procedure.

A new design curve for stainless steels has been adopted into the ASME Code Section III. However, it is suspected that derivation of the curve is not fully compatible with the design procedure. Variable temperature data has been mixed inappropriately. Furthermore, the code curve is not applicable to all grades of stainless steel. This paper reports contradictory data for stabilised austenitic stainless steels extending up to 10 million cycles. Niobium and titanium stabilised stainless steel specimens were sampled from 100% relevant material batches fabricated to be used in NPP primary piping.

Fatigue tests periodically interrupted for holds indicated time and temperature dependent hardening during holds at 25°C to 325°C. Notable extension of fatigue life was measured when loading patterns consist of cyclic deformation in lower temperatures than hold annealing. Many NPP piping thermal transients separated by normal operation belong to this category and fatigue assessment based on standard fatigue data seems to underestimate fatigue endurance.

1. Introduction

The book “Criteria of the ASME Boiler and Pressure Vessel Code for design by analysis in sections III and VIII division 2” [1] is a central reference document for revisiting the basic assumptions and design philosophy behind the ASME III code. Also the European codes, the French RCC-M and German KTA are based on the same principles.

The original ASME Code “*design by analysis*” philosophy assumes that the “designer” is able to take responsibility of managing complex material perfor-

mance. Today, the “designer” probably means a multidisciplinary team, which hopefully co-operates and communicates ensuring that the materials laboratory and stress analysis office know each other’s challenges and solutions.

1.1 Design based on local strains

The ASME code was primarily aimed to prevent catastrophic fractures of pressure vessels. Therefore, the fatigue assessment was focusing on severe but rare thermal transients that can cause notable low cycle fatigue damage in heavy equipment. The committee pointed out that the code was developed for pressure equipment, for which “the number of cycles seldom exceeds 10 000” [1]. In other words, the ASME III code was not originally intended for high cycle fatigue. It is only later, when high cycle thermal fatigue has been considered as a potentially important ageing mechanism, in particular for small bore pipes. Another important point is that the loading typically originates from thermal expansion and the mechanical loading is limited to prevent general yielding. Thus, local yielding in stress concentrations sets limits for the local stresses.

High cycle fatigue is often described by stress amplitude versus life relationship, which is measured in load controlled tests using components, more or less realistic samples (e.g. welded specimens) or with smooth bars. But low cycle fatigue – and spectrum fatigue including cycles in low cycle regime – is better described in terms of local strain. Cycles to create a growing crack correlate with the strain history.

Figure 1 shows the rationale for adopting a version of local strain approach for ASME III design. Similar shape of fatigue curves makes strain controlled data better transferable to components than stress controlled smooth specimen data. Fatigue endurance depends on the local strain and material at a stress concentration experiences strain control also when the component is loaded under load control.

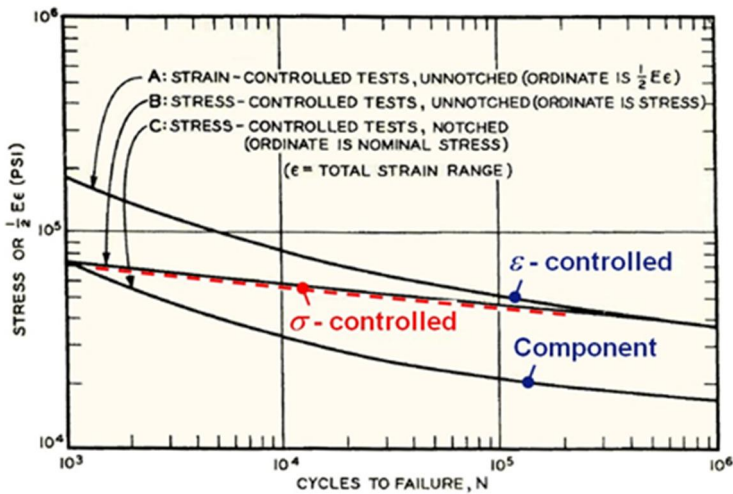


FIG. 4. TYPICAL RELATIONSHIP BETWEEN STRESS, STRAIN, AND CYCLES-TO-FAILURE.

Figure 1. Transferability of strain or stress controlled data to component behaviour. [1]

Automotive industry normally uses strain controlled endurance data in form of strain – life curves, but for the ASME code, the vertical axis units are translated to quasi-elastic stress units. A *temperature dependent elastic modulus is applied to total strain (including also plastic strain)*. This yields to very high values of stress intensity amplitudes allowable for short lives. In laboratory test measured stress amplitudes are not comparable to the design curve. Stainless steels experience nonlinear strain even at endurance limit. This has created a need for strain controlled tests to high numbers of cycles. Only strain based data is valid for design assessment according to ASME III design by analysis procedure.

2. Design curve

For fatigue design according to ASME III [2], the allowable loading is given in form of design curves, which are based on *strain controlled low cycle fatigue tests in room temperature*. Similar curves are applied also in the German KTA and French RCC-M.

2.1 Designers responsibility on selecting the curve

Generalized design curves have been included in the codes to reduce need for material testing, but applicability of the design curve for the particular application remains a responsibility of the designer. The designer may prefer an appropriately determined and more relevant experimental curve, if available. This is often forgot-

ten, though clearly stated in the Criteria Document for the ASME III design by analysis procedure and formally recommended at least by the Finnish and US regulators [1,3,4].

This is clearly demonstrated in guidance on environmental effects. Replacing the “air curve” with curves for water environments has been discussed for a long time. Very complex approaches even correlating the curves with specified operational parameters have been proposed, e.g. [5]. The code itself does not give specific instructions for accounting influence of reactor coolant in fatigue calculation. Moderate environmental effects were accounted for through the design curve definition, but the responsibility for considering applicability of the “air curve” or eventually more severe effects was left to the designer.

The Criteria Document summarised the case as follows: “protection against environmental conditions such as corrosion and radiation effects are the responsibility of the designer” [1]. The Finnish YVL guide 3.5 (2002) for ensuring strength of NPP pressure devices underlined this request by stating that justification is needed if code curve is used because “fatigue assessment shall be based on S-N - curves applicable to each material and conditions” [3]. Instead of environment and operational parameter dependent design curves, use of a F_{en} factor was requested in the US NRC Regulatory Guide 1.207 (2007). But by the same, the US NRC endorsed a new air design curve for stainless steels and made it clear that it should be used instead of the ASME III code curve, when analysing new designs. [4]¹

2.2 Design curve for stainless steels

The design curves proposed by the ASME Code are often discussed as if they were the only alternatives. This may partially be due to the fact that the design curves are introduced in a “mandatory appendix”. The current code curve for stainless steels with the appendix title is shown in Figure 2.

2.3 Reference curves for stainless steels

A reference curve is needed first to derive a design curve. It represents the mean life curve of smooth specimen laboratory data. Transferability to real components is obtained with certain design margins and these margins were originally verified e.g. through full scale vessel testing.

¹ Use of new design curves given NUREG 6909 for carbon and low alloy steels were also proposed, but not requested in the NRC Regulatory Guide.

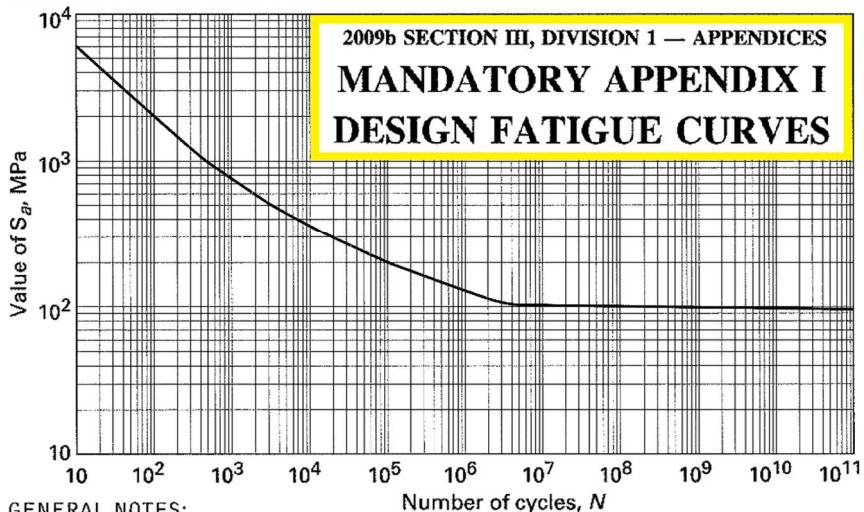
2.3.1 The Langer Curve

An equation for fitting the reference mean curves was proposed by Langer [1] :

$$S_a = \frac{E}{4 \cdot \sqrt{N}} \cdot \ln\left(\frac{100}{100-A}\right) + B \quad (1)$$

where E is the elastic modulus, N is the number of cycles to failure, A and B are constants. Constant A in eq. 1 could be estimated as the percentage reduction of area in a tensile test and it defines the position of the curve in the low cycle region. Constant B scales off the curve in high cycle region and it represents a fatigue limit of the material.

FIG. I-9.2M DESIGN FATIGUE CURVES FOR AUSTENITIC STEELS, NICKEL-CHROMIUM-IRON ALLOY, NICKEL-IRON-CHROMIUM ALLOY, AND NICKEL-COPPER ALLOY FOR TEMPERATURES NOT EXCEEDING 425°C



GENERAL NOTES:
(a) $E = 195 \times 10^3$ MPa

Figure 2. “Mandatory” design curve for stainless steels by ASME III. [2]

The Langer reference curves were applied as a basis for deriving the ASME design curves. Arbitrary margins, 20 against life and 2 against strain, were considered appropriate to ensure transferability of the laboratory data to plant components. These margins were not aimed to provide specified safety margins and it is not to be expected that a vessel will actually operate safely for twenty times its specified life. [1] Detailed justifications for the margins were not formally published, but are based on three sub factors: [6]

- 2.0 scatter of data
- 2.5 size effect

4.0 surface finish, environment.

It should be noted that, in spite the Langer reference curve is given in stress scales, it actually is a strain life curve. It can also be presented in the following form:

$$\ln(N) = 6.954 - 2 \cdot \ln(\epsilon_a - 0.167) \quad (2)$$

2.3.2 Alternative reference curves

In 1998 Chopra summarized the available experimental data for austenitic stainless steels and provided the following reference curves for room temperature air: [7]

$$\ln(N) = 6.703 - 2.030 \cdot \ln(\epsilon_a - 0.126) \quad (3)$$

$$\ln(N) = 7.422 - 1.671 \cdot \ln(\epsilon_a - 0.126), \quad (4)$$

where eq. 3 applies for alloys 304 and 316, and eq. 4 applies for alloy 316 NG. But in 2007 Chopra and Shack gave a common reference curve for non-stabilized alloys 304, 304 L, 316, 316 L, 316 NG: [6]

$$\ln(N) = 6.891 - 1.920 \cdot \ln(\epsilon_a - 0.112) \quad (5)$$

Japanese data for non-stabilised steels was also included in the previous equations, but the JSME code reference curve for stainless steels in room temperature air is slightly different: [8]

$$\epsilon_a = 23.0 \cdot (N)^{-0.457} + 0.11 \quad (6)$$

The reference curves according to eqs. 2–6 are shown in Figure 3. In the low cycle fatigue (LCF) regime all air data for austenitic stainless steels lie practically within a common scatter band and the later proposed curves do not much differ from the Langer curve. The difference grows in the high cycle fatigue (HCF) regime ($N_f > 10^5$ cycles), where the new curves become more conservative.

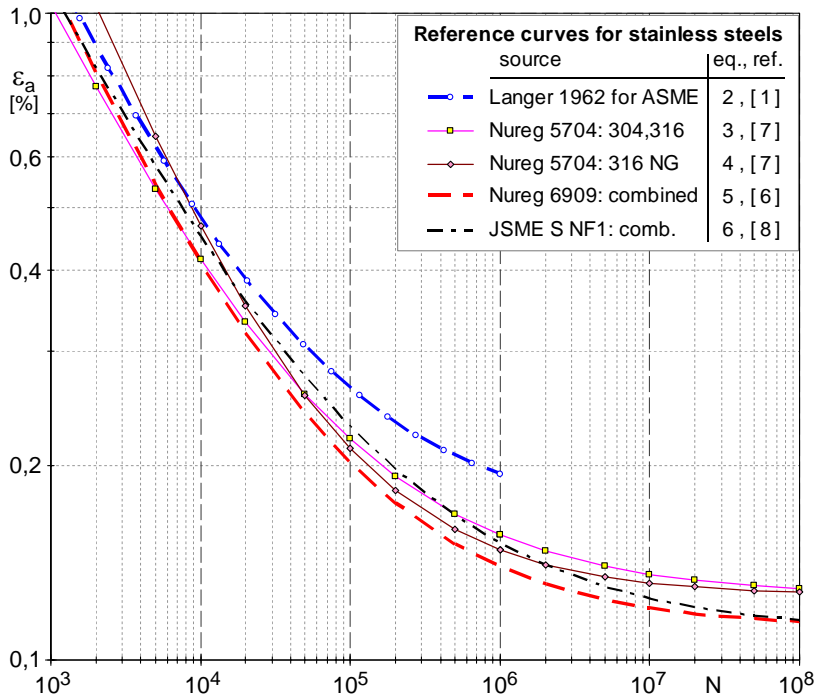


Figure 3. Reference curves for stainless steels. [1, 6–8]

2.3.3 New reference curve entering to ASME III

The NUREG 6909 report and Eq. 5 above [6] are of special interest, because they made a great impact. The report was summarising extensive work aiming to update fatigue design criteria by proposing guidance for accounting environmental effects. This part will be discussed later on, but the “air curve issue” was addressed by the same. Eq. 5 was considered as a more relevant reference curve for modern non-stabilised stainless steels, which were assumed the main options for primary piping in new reactor designs in USA.

Chopra and Shack performed a comprehensive analysis of the available data and reconsidered also the curve margin in the LCF region based on a statistical analysis. As a result eq. 5 modified by margins of 12 in life and 2 in strain was proposed as a generally conservative design curve [6]. That design curve was endorsed by the US NRC as part of a Regulatory Guide 1.207 [4] *for new designs in the USA*.

Though NRC pointed out that the design basis for the present reactors was considered sufficient and the Regulatory Guide with the new curve was aimed only for new designs, only two years later in 2009 the curve appeared in the ASME Code Section III as design curve for austenitic stainless steels, Figure 2. Eq. 5 can

thus be considered as a reference curve also for the latest ASME Code Section III design curve. [2]

2.3.4 ASME Code Section III design curve for austenitic stainless steels

As pointed before and to be discussed below, the design curve provided in the code should not be considered as the only alternative and not applicable to all fatigue assessments. However, after an overnight change in 2009, the Mandatory Appendix 1 contains the curve shown in Figure 2. As laboratory data is not directly comparable to the design curve, the “Chopra model” proposed in NUREG 6909 (eq. 5) will be used below as a main reference. Even though the curve is based only on data for non-stabilized grades, it will be used for comparison also with our data for stabilised stainless steels.

3. Experiments

Stabilized stainless steel grades are used in many European nuclear power plants. Because of different approach for avoiding sensitising for stress corrosion cracking and strengthening, stabilized stainless steel grades can be assumed to have different fatigue performance compared to the non-stabilised grades considered for eq. 5. However, no restrictions on applicability of the new design curve are given and it is entitled for “stainless steels” and nickel based alloys [2]. This created a challenge for German utilities, because stabilized stainless steels are used in German NPP primary piping.

3.1 Research on fatigue performance of niobium stabilized stainless steel

Together with E.ON Kernkraft GmbH VTT has performed and still continues to perform experimental research on fatigue performance of niobium stabilized stainless steel (X6CrNiNb1810 mod) aiming to fill the gap of missing reference curve for stabilized stainless steels and to improve transferability of the laboratory data to plant conditions.

3.1.1 Summary of previous reports

Results of the experimental research have already been reported in PVP 2009, 2011 and 2012 [9–12]. The dissemination continues in PVP 2013 and in SMiRT 22. Strain controlled constant amplitude tests demonstrated good long life performance in room temperature at air environment [9]. Different kinds of non-standard tests showed that cycles just below the ($N_f > 10^7$) endurance limit were not damaging as normally assumed and indicated that holds between the fatigue cycles may notably increase the number of cycles to failure [10]. Further experimental evidence was provided and it was shown that the hardening caused by hot holds is a

generic phenomenon, effective also for non-stabilised stainless steel grades [12]. The relevance of the ASME Code Section III new design curve concerning the stabilized stainless steels are used in German NPP primary piping was questioned [11, 13]. Soon appearing new contributions will report and discuss effects of temperature and environment in air and in PWR water [14–15]. The current paper will revisit selected experimental results and continue critical discussion on the reference and design curves in the NUREG 6909 report and ASME Code Section III [2, 6].

3.1.2 Test material

Solution annealed niobium stabilized austenitic stainless steel (X6CrNiNb1810 mod) was received as a $\phi 360 \times 32$ mm pipe, which fulfils all German KTA material requirements for primary components in LWR. The grain size in this pipe varies so that the material report classified 50% to ASTM 0–1 and 50% to ASTM 2–3. Variable grain size typical for a full scale pipe in solution annealed condition is shown in Figure 4, which is taken longitudinally from the same depth as the fatigue samples. The chemical composition and strength properties are given in Tables 1–2.

Table 1. Chemical composition of the test niobium stabilised stainless steel (wt %).

C	N	Si	Mn	Cr	Ni	Mo	Nb	P	S
0.031	0.021	0.235	1.885	17.30	10.29	0.405	0.357	0.030	0.004

Table 2. Monotonic strength properties of the test niobium stabilised stainless steel.

data source	E	R _{p0.2}	UTS
minimum of 5 tests	195 GPa	224 MPa	535 MPa
maximum of 5 tests	201 GPa	249 MPa	559 MPa
average of 5 tests	197 GPa	238 MPa	544 MPa
material report / pipe	-	239 MPa	548 MPa
material report / melt	-	251 MPa	544 MPa

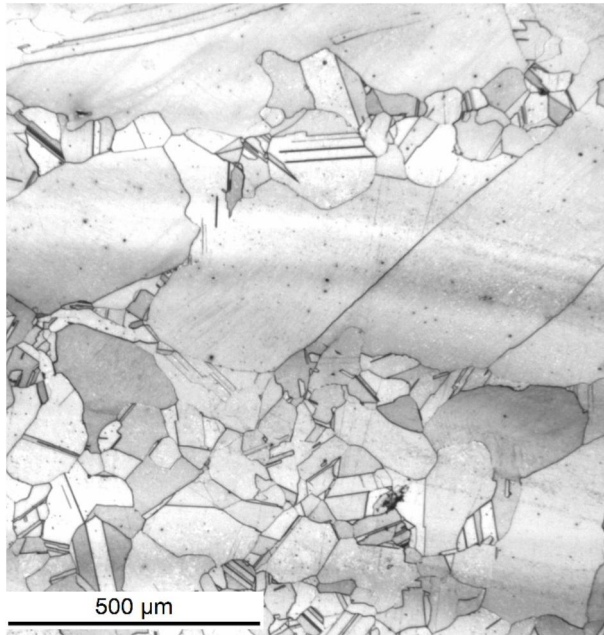


Figure 4. Microstructure of the test material.

Smooth round bar specimens were turned and polished from longitudinal samples of the pipe. The first 200 mm section was cut for 44 standard tensile and low cycle (LCF) specimens. Altogether four such sections have been sampled to feed follow-up test series. The material properties are assumed constant. Similar results with specimens sampled from different sides of the circumference support this assumption. All tensile and fatigue specimens have a gauge section diameter of 8 mm. The LCF specimen geometry is shown in Figure 6.

3.1.3 Test materials for comparative tests

Comparative tests were performed to clarify whether the results are material grade specific, or generally applicable for different material grades. Another kind of stabilised stainless steel was studied as part of the national research programme. Solution annealed titanium stabilised austenitic stainless steel (08X18H12T) was received in form of a $\phi 460 \times 32$ mm pipe, which fulfils all requirements for primary piping in VVER reactors. Fatigue tests for this material were focused to low strain, high life region only. [20]

Additional experiments were performed for non-nuclear material batches. Titanium stabilised alloy 321 and non-stabilised alloys 304 L and 316 L were received as 25 mm thick plates. A very limited number of non-standard experiments were

sufficient to show that the hold hardening effect is not limited to the stabilised grades. Similar trend was measured to all studied grades. [12]

3.1.4 Experimental methods

Tests were performed in MTS 100 kN and 250 kN rigs with precision alignment grips and MTS 653 furnace. Alignment of load train was adjusted with strain gauged specimens according to the ASTM E 1012 procedure [16]. Strain controlled low cycle fatigue tests were performed according to the ASTM E 606 procedure [17]. The basic LCF tests in RT were performed using sinusoidal waveform with an average strain rate of 0.02 1/s for constant amplitude tests (e.g. 1 Hz for $\epsilon_a = 0.5\%$) and 0.01 1/s for determination of cyclic stress strain curves by the spectrum straining. Strain control was consistently applied even for the longest tests up to 10^7 cycles, but after entering to the secondary hardening and decreasing plastic strain phase the frequency was increased to 6 Hz. Later tests to study effects of temperature, strain rate and loading pattern were performed using triangular waveform with constant strain rates of 0.005 1/s and 0.0001 1/s. Strain rate of 0.005 1/s (or slower, when specified) was used for all tests in elevated temperatures.

A simplified definition of failure criterion was adopted to avoid practical problems with variable cyclic softening and hardening behaviour of stainless steels. Fatigue life (N₂₅) was determined as the number of cycles to 25% drop of peak stress from its absolute maximum. However, all final load drop phases were so short that the obtained lives are insensitive to the selected failure criterion.

3.2 Simulation of operational conditions

3.2.1 Typical fatigue transients in NPP operation

The NPP primary piping components spend most of the time in operation temperature between fatigue cycles originating from thermal transients. The average temperature during such transients is always lower than the normal operation temperature and varies between the operational and cold flow or shut down temperatures. A typical form of alternating cold and hot flow transients in a PWR surge line is shown in Figure 5. The rate of loading is variable during the in-surge and out-surge events. Variable strain rate and the time between the cycles challenge transferability of the standard laboratory test results.

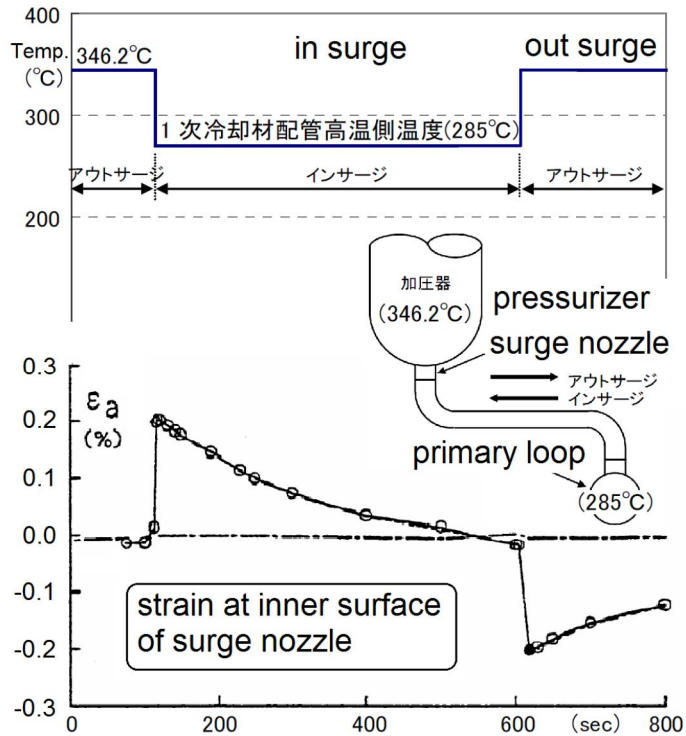


Figure 5. Sample transient in the surge line. Graphs edited from [18].

3.2.2 Tests interrupted for holds in elevated temperature

The case of Figure 5, where NPP primary piping components spend long times in operation temperature between thermal fatigue cycles was roughly simulated by performing fatigue straining in room temperature and periodically interrupting at zero stress during rising ramp for intermediate annealing in elevated temperature as load-free. A short period in higher temperature was selected instead of operation temperature for acceleration. Annealing for 16 hours in 420°C was justified by a simple thermo-dynamical calculation and Arrhenius equation.

Assuming the activation energies for mechanisms involved to be in range of 0.9 eV to 1.4 eV, which are for vacancy migration and diffusion of carbon respectively [19], the annealing would compare with 17 to 100 days at 300°C. The annealing temperature 420°C is within the applicability range ($\leq 425^\circ\text{C}$) of the ASME III design curve, Figure 2. The thermally activated processes could be notably accelerated with such increase of temperature, but it was assumed that the mechanisms remained mainly unchanged. See ref. [10] for experimental details and more results of these tests.

4. Results

4.1 Standard tests for a reference curve

Strain controlled constant amplitude tests demonstrated good long life performance in room temperature, Figure 6. Similar data for titanium stabilised stainless steel [20] also sampled from real NPP piping was added for comparison. Comparison to the reference curve for non-stabilized steels (eq. 5) reveals a *notable difference in long lives*. The trend is the same for both these stabilised steels.

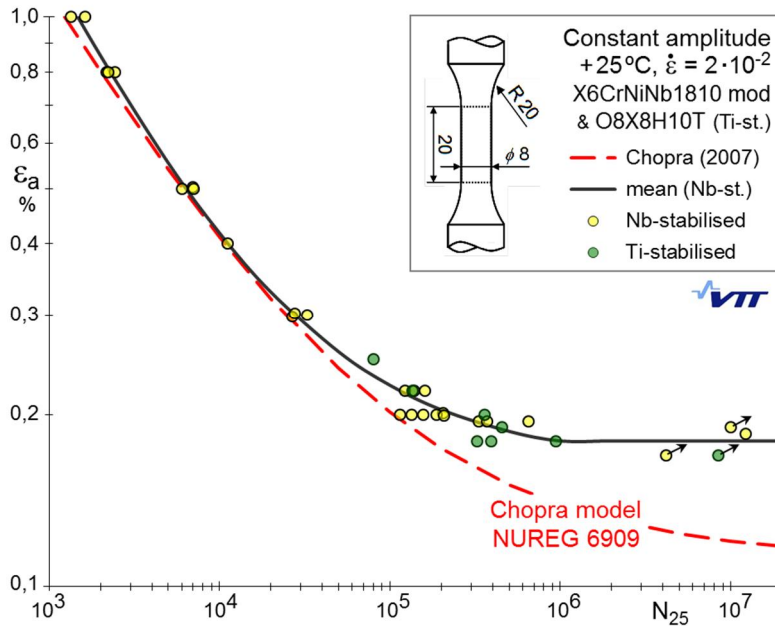


Figure 6. Fatigue data for two stabilised stainless steels. [9, 20]

4.2 Endurance limit behaviour

Both tested stabilised steels exhibit endurance limit behaviour in room temperature. The strain life curve turns horizontal at about one million cycles, Figure 6. This can be attributed to secondary hardening, which becomes effective after about 10^5 cycles at low strain amplitudes. The hardening decreases plastic strain amplitude and reduces fatigue damage for specimens lasting until this secondary hardening becomes effective, Figure 7.

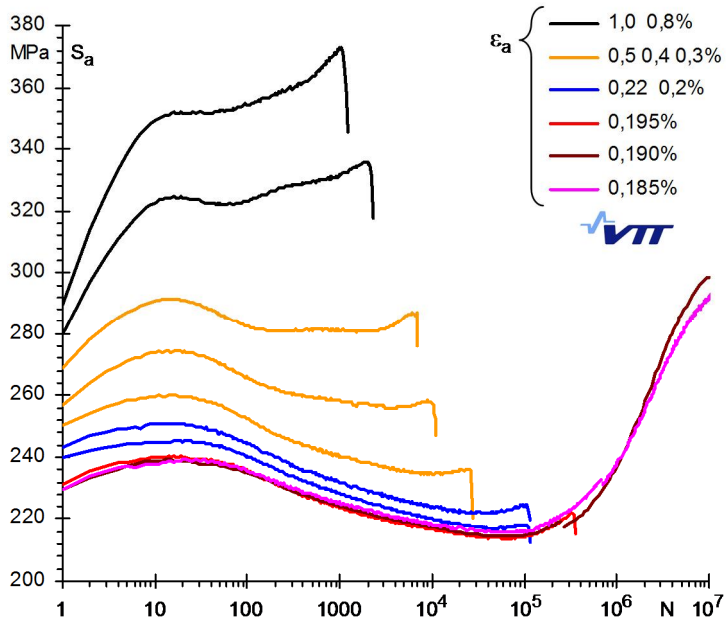


Figure 7. Stress response in constant amplitude straining showing cyclic hardening and softening during strain controlled tests for niobium stabilised stainless steel. [9]

Additional non-standard tests confirmed the effectiveness of the endurance limit behaviour. A strain spectrum ($0.17\% \leq \varepsilon_a \leq 0.25\%$) was designed to investigate damage accumulation just below and above the endurance limit. Such test was continued to a total of 3.4 million cycles without fatigue failure. The long life together with hardening stress response gave evidence that the *endurance limit can be effective also for variable amplitude straining* [10]. This result is completely opposite, what would normally be expected in variable amplitude fatigue.

Further evidence was obtained through “re-cycling” specimens after run-out at low strain amplitudes. At the second level these specimens endured longer than virgin specimens. This all suggests that hardening, which is effective also below the endurance limit, improves fatigue resistance of this steel, when tested in room temperature [10].

4.3 Effect of operational loading conditions

Experimental results on the effect of temperature and environment in standard tests will be published in ref. [14,15] and discussed later. Here we consider the time and temperature sequences of loading. Fatigue relevant thermal transients

typically begin when cold water flow meets hot piping, cools the surface and creates tensile stress and strain, Figure 5. This leads to complex thermo-mechanical loading, which we have simplified and simulated by combinations of cyclic straining and static holds in constant temperatures.

4.3.1 Interrupted straining – effect of hot holds

Rough simulations of the case, where NPP primary piping components spend long times in operation temperature between thermal fatigue cycles were reported in ref. [10,12]. Severe acceleration is necessary. The total amount of hold hours cannot be realistic and number of tests is also limited. But it will be shown below that an effect can be measured and that fatigue endurance may be notably extended in certain realistic loading conditions, Figs. 8–9.

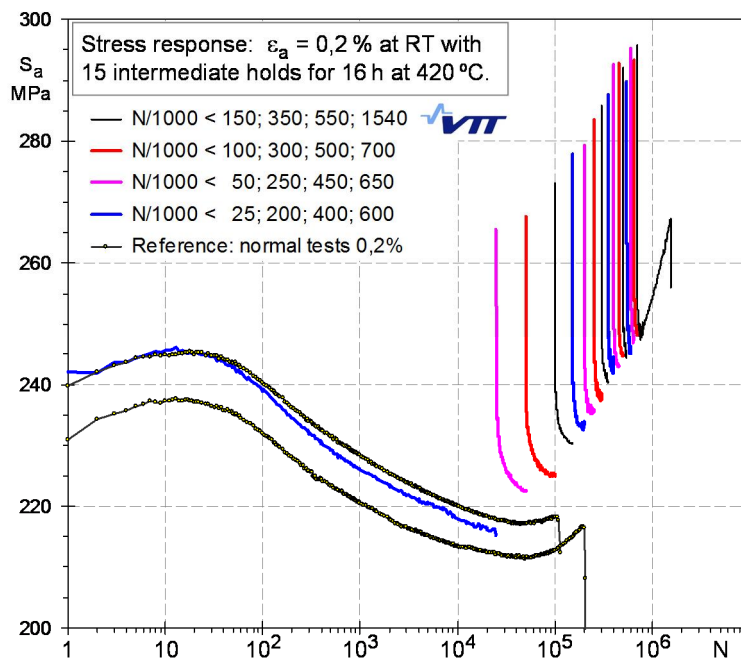


Figure 8. Stress response in constant amplitude room temperature straining interrupted with stress free annealing in elevated temperature. [10]

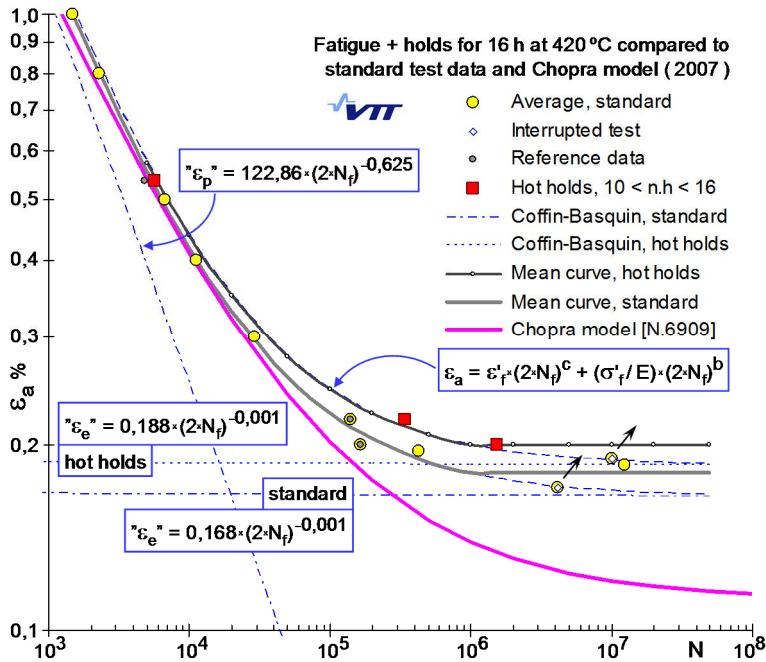


Figure 9. S-N curve model for the niobium stabilised stainless steel with and without holds. [10]

When interrupting fatigue cycling for intermediate annealing in elevated temperature, notable hardening during the holds was observed in all tested cases. At strain amplitudes above 0.5% this had negligible, though positive, effect on fatigue life. But at lower strain amplitudes the hardening was linked to notably improved endurance. The stress response shown in Figure 8 reveals about 20% hardening during the holds followed by subsequent cyclic softening. This procedure was continued until the number of cycles reached about 5 times the life in constant amplitude standard tests. Then the specimen was continuously fatigued with again 5 times the normal number of cycles to failure. A factor of 10 was estimated for the total life extension in this case. It is possible that the specimen had lasted even much more cycles, if we had introduced more holds, but conducting such a test might have required several months to complete or reach 10^7 cycles.

The total number of tests conducted the same way with different amplitudes and cycle block lengths was only 13, but already this set of data hinted that a simple model to describe the effect might be obtained by *increasing the apparent endurance limit* value as illustrated in Figure 9.

4.3.2 Interrupted straining – other loading sequences and grades

After observing the tendency for hardening during holds after cyclic straining for the niobium stabilized stainless steel, it was of interest to clarify, whether this is a grade and loading sequence specific or more generic phenomenon. Small numbers of different types of tests were performed to clarify this.

First it was found that rise of temperature during the holds is not necessary condition for the hardening. Already 16 hours of hold in room temperature (25°C) was sufficient to cause a small, but measurable effect. On the other hand, tests in constant 325°C temperature resulted to faster hardening after severe straining, but build-up of the driving force for hardening is clearly depending on the temperature where cyclic strain occurs, being more effective when straining occurs in lower temperature. Furthermore, tests conducted with holds at different locations within the hysteresis loops showed small differences, if any. Hardening resulted independent of the phase of loading, where the hold was inserted. The results support explanations basing on strain ageing type mechanisms.

Comparative pre-tests for a few samples of different steel grades were also performed to conclude that the hardening was not grade specific phenomenon for the niobium stabilised stainless steel. The resulting stress responses indicate that the *hardening mechanism is relevant to all tested grades*, including non-stabilised alloys 304L and 316 L.

A complex test for alloy 304 L is introduced in Figure 10. The stress response was measured for a specimen tested with constant 0.3% strain amplitude in 325°C temperature. Three durations of holds were varied in five different positions. The results show that hardening occurs in all tested conditions. The influence of hold length can be seen, but differences between the different hold positions were not revealed.

5. Discussion

5.1 New design curve in ASME Code Section III

The “design by analysis” philosophy was considered an essential cornerstone of the ASME Code Section III. Therefore, it is surprising to note that the design curves are provided in a “mandatory appendix”. What does “mandatory” mean in this case?

Even more confusing was the abrupt change of the design curve in 2009 [2]. *Mandatory design curves became also temporary?* New experimental data was available and the US NRC had recommended another curve for new designs. No doubt, there were reasons to add a new curve in the appendix. But couldn't the choice between the old and new design curves have been left for the designer, to be agreed together with the customer?

5.1.1 From limited regulatory guide to generic design code

Based on the proposal by Chopra and Shack [6], the NRC endorsed a new air curve for stainless steels as part of a Regulatory Guide for new designs in USA [4]. But the NRC underlined that the Regulatory Guide was aimed to new designs only and excluded use of the new rules and new curve to existing plant components.

However, the scope became soon generalised, when the same curve was copied to the ASME III as a design curve replacing the original one [2]. This can be criticised from several points of view. A philosophical conflict between an overnight change of the “mandatory” labelled code curve and the designer’s responsibility on the curve selection was discussed above. Engineering points of view will be discussed next.

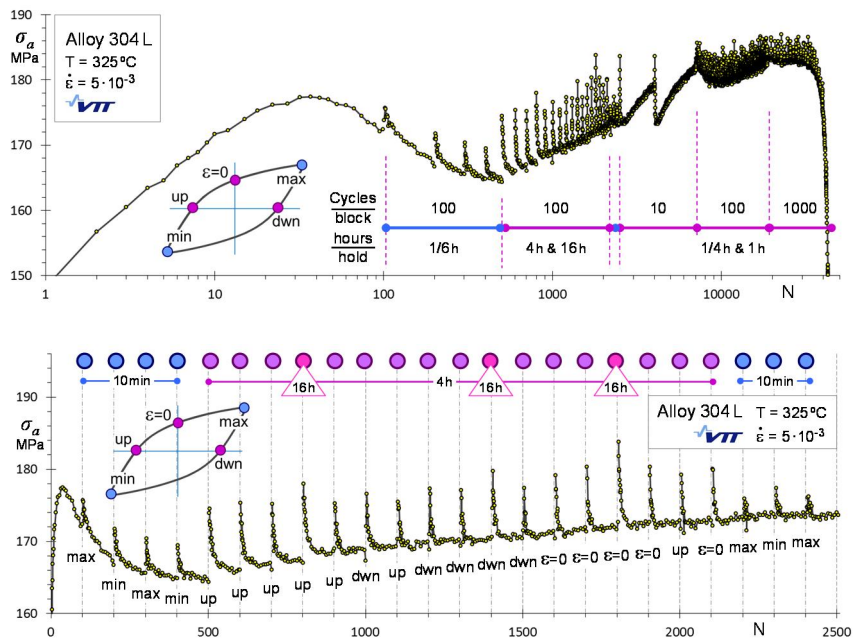


Figure 10. Effect of various types of holds on stress response for alloy 304 L strained at 325°C. [12]

5.1.2 Applicability for stabilised stainless steels

The data sets used to derive the new curve do not cover all grades of stainless steels used in current nuclear power plants. Most strikingly, stabilised stainless steels are completely missing. Experimental data for relevant batches of niobium and titanium stabilised stainless steel grades show better performance in the high

cycle regime and do not support change of the curve for these grades used in many European plants.

The case for stabilised German piping grade is shown in Figure 11. It shall be pointed out that the data shown in Figure 11 is based on extensive testing to long lives up to 10^7 cycles of a fully representative material taken from a pipe manufactured to be used in nuclear reactor primary piping.

In the LCF regime the new data, reference and design curves do not much differ from the old curve, but the difference grows beyond an order of magnitude in life in the HCF regime, where the new design curve becomes more conservative.

5.1.3 Non-stabilised stainless steels in existing plants

Another question mark on relevance of the code curve change arises from the evolution of stainless steels after construction of many reactors. The development of stainless steels to minimise risk of stress corrosion cracking problems has affected also strength and fatigue performance of the steels. It may be speculated that decrease of carbon contents and softening of steels is reflected in the new data. Possibly this hypothesis could – and should – be studied before applying the new design curve to fatigue usage assessment of old plants.

Notable softening due to decrease in carbon content has been partially compensated in nitrogen alloying to some stainless steel grades. A comprehensive fatigue program would be needed to assess effects of the evolution in steelmaking and composition. But until shown, we may question, which of the reference and design curves are more relevant to the piping components in existing plants.

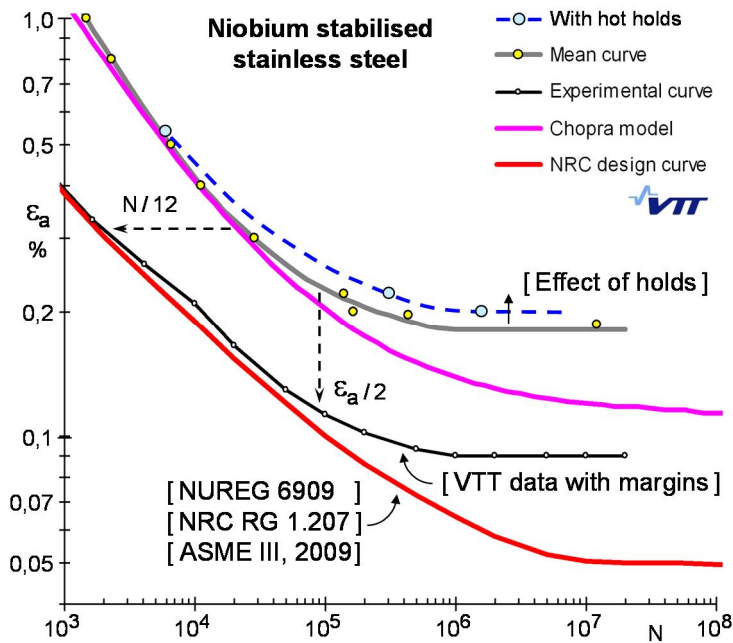


Figure 11. Comparison of the new reference and design curves to an experimental curve for niobium stabilised stainless steel.

5.2 A model of the reference curves – and effects of material strength

It is well known that the slope of strain-life curve depends on the material and its heat treatment. A general tendency is that quenched and tempered high strength steels have lower slopes, while soft and ductile materials have steeper slopes. In other words, change in material strength does not shift the curve, but often turns it round a rotation point, Figure 12.

Applicability of a similar model as in Figure 12 to correlate the S-N-curve with material strength also for stainless steels is not studied, but the current author has experimental data to support such assumption. Austenitic stainless steels usually behave in a ductile manner and they have rather steep slopes in their strain-life curves.

The small carbides in stabilised grades affect dislocation mobility and strengthen the material. The model illustrated in Figure 12 also predicts a better high cycle performance in such case. The above reported difference between the materials tested for the new reference curve and stabilised stainless steels may be explainable in terms of this model.

The model in Figure 12 is in accordance with the effect of hardening as seen in Figure 9. Instead of shifting the curve, *a change in material strength rotates*

the strain-life curve. Applicability of this model to explain also the effects of constant test temperature in strain-life data [15] is an interesting possibility. It seems to correlate, but conclusions on this matter remain a challenge for future studies.

5.2.1 A fixed model of the reference curves

It would be surprising, if the fixed form Langer equation (eq. 1) gave an ideal presentation of all fatigue data for all steel grades. It is obvious that the code committee has been aware of the data fitting problem. Therefore, the curve margins and/or inbuilt conservatism in stress analysis and fatigue assessment was probably aimed to be sufficient to cover also some discrepancy between the laboratory data and reference curve. This possibility has not been considered when proposing modifications to the design curves based on comparison of the original reference curves with later generated laboratory data.

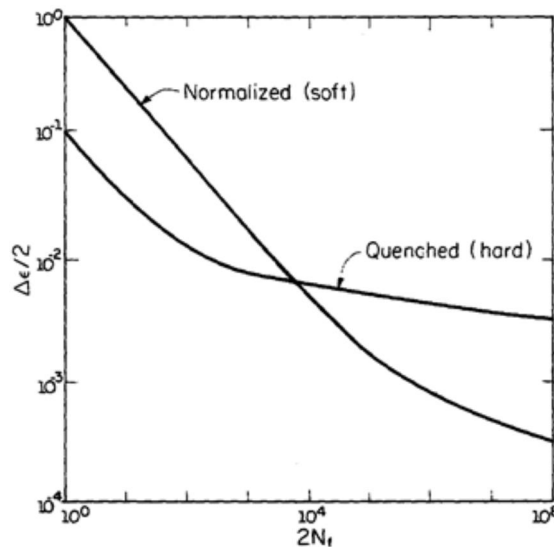


Figure 12. Strain life curves for a medium carbon steel in a quenched and tempered and normalised condition to illustrate the general trend in slopes for hard and soft materials. [21]

5.3 The role of temperature in testing and design

A fundamental question is hidden in the effect of temperature and the way, how it should be accounted for in fatigue testing and component assessment to obtain optimal transfer of laboratory data to real service.

5.3.1 Expected direction of a potential temperature effect

A traditional experience is that the strain life curves are not much sensitive to the test temperature. This assumption may have been partly due to a common practice to look for such parametric effects in form of a (parallel) shift in the curve and temptation to perform comparative tests at convenient regimes of test duration. But this also happens to be the region close to the rotation point in Figure 12, i.e. the region where the test results should be identical also in case of effect, if the effect causes curve rotation instead of shift.

The assumption of ignoring test temperature was adopted also in NUREG 6909, though a closer look in the graphs in the report seems to reveal temperature dependent variability in the strain-life data [6].

Again referring to Figure 12 and assuming that rise of temperature causes softening of the material, we might expect little effect at strain amplitudes close to the rotation point, but a change in the slope should be seen as reduction of life in high cycle and increase of life in very low cycle regions. This is exactly what we recently measured for the niobium stabilised stainless steel [15].

5.3.2 Accounting of temperature in fatigue assessment

The ASME III design curve is defined for room temperature. The design temperature is accounted for by multiplying the stress intensity value by a ratio of elastic modulus in room and design temperatures:

$$S_{a,\text{design}} = E_{RT} / E_{T,\text{design}} \cdot S_a \quad (7)$$

In addition to the change in elastic modulus relevant to the elastic strain, the correction factor is applied also to the plastic strain. Alternative way of presenting the same effect would be definition of the design curve as function of modulus, i.e., temperature. In any case, for a given strain amplitude, a shorter life is predicted in higher temperature. When comparing laboratory data obtained in different temperatures in a common plot to the design or reference curve, a temperature dependent factor should be applied.

Use of eq. 7 as part of the fatigue assessment means that *the design curve and data used to determine it shall represent the material behaviour in room temperature only*, even though design temperatures vary case by case.

5.3.3 Role of test temperature in NUREG/CR-6909

A closer view to NUREG/CR-6909 raises questions on the selection of the data for deriving the reference curve. It is not explicitly specified in the report [6], whether data for elevated temperatures is excluded or not, but the fatigue life model is introduced being applicable to "temperatures up to 400°C". The related strain life curves (figures 30 and 32) indicate some variation with temperatures, but a state-

ment is given: “The model assumes that the fatigue life in air is independent of temperature and strain rate.”

We are tempted to assume that the reference curve proposed in NUREG/CR-6909 is indeed based on average data for variable temperatures. It should not.

The concern can be released, if it turns out that the description on accounting for temperature given in NUREG/CR-6909 is just misleading. But if the concern is true, the original data should be reanalysed to quantify the *eventual bias in the reference curve*. This is needed not only because of the temperature effect alone, but also to update the proposed factors for environmental effects, as needed.

5.3.4 The role of temperature in environmental effects

For two reasons it is important to separate the temperature and rate effects with and without water environment separately. Firstly, understanding and modelling of environmental effects will require it in future. Secondly, transferability of laboratory data will be improved with this separation. The latter concern will be discussed now.

When assessing fatigue according to the ASME III design code, the *environmental and temperature effects are considered in different phases of the analysis*. Moderate environmental effects were already included in the design curve margin and a factor for environmental effects is proposed to more pronounced effects [6]. In other words, the environment affects the allowable number of cycles.

But the temperature is accounted through eq. 7 within the stress analysis phase. We might caricature the difference as follows: “the environmental effects should arrive from the materials report and the temperature effects from the stress analysis”. But these two factors are also combined in one single F_{en} factor:

$$F_{en} = N_{f(RT,air)} / N_{f(T,environment)} \quad (8)$$

The definition of F_{en} as proposed by Higuchi and Iida [22] assumes direct comparison between the reference curve for room temperature air and data for high temperature, slow rate in water. The definition of environmental factor (eq. 8) again points out that fatigue assessment shall be based on room temperature data only, when environmental effects are considered. But the effects of temperature and water environment could also be separated as follows:

$$F_{en} = F_{en,T} \cdot F_{en,water} = \frac{N_{RT,air}}{N_{T,air}} \cdot \frac{N_{T,air}}{N_{T,water}} \quad (9)$$

The effect of temperature on fatigue performance may differ case by case, but this issue can have notable practical implications. Experimental results indicating that the effect of hot water was over predicted and notable parts of the measured F_{en} factors were actually due to temperature instead of water will be soon published in [14].

A simple way to consider the design temperature is already included in the fatigue assessment procedure. When considering environmental effects, the *de-*

signer is supposed to take the design temperature into account twice. Once when calculating the stresses (eq. 7), and again when calculating the F_{en} to account for effects of environment and temperature (eq. 9). Is this right?

I propose that we discuss to find consensus in answering to the following questions:

- If a temperature effect is already assumed in the stress analysis, should this effect be included again in the F_{en} value or be extracted from F_{en} ?
- Or would it be better if the material testing laboratory measuring the environmental effects provided the material data and factors in a form directly compatible with the design code and fatigue assessment approach ?
- Is there a strategy selected for this matter in NUREG/CR-6909 ?
- If yes, what is it ?

5.4 Effect of interrupted straining and holds

Cold worked austenitic stainless steels are known to exhibit strain ageing. It can increase yield strength without reducing ductility in terms of elongation. The exact mechanisms are not known, but ordering and interaction of interstitial atoms and vacancies with dislocations are probably involved [19].

Strain ageing occurring in the cyclic strained material during hot holds (annealing) provides a plausible explanation to the hardening and modified shape of the hysteresis loops immediately after the annealing. We can actually see pronounced yield point behaviour for the few first increasing ramps after holds.

However, the simplest strain hardening models of dislocation pinning by interstitial atoms are probably not sufficient, because the *hardening effect can remain active for thousands of cycles*. Further studies are needed for comprehensive understanding of the mechanisms involved. However, we have demonstrated an improvement of fatigue endurance together with hardening. Reduction of plastic strain due to hardening is one plausible explanation for the life extension.

6. Conclusions

The new stainless steel air curve endorsed in NRC RG 1.207 for new US designs was adopted into ASME Code Section III (2009b) without restrictions on applicability. But generic applicability of the reference curve proposed in NUREG/CR-6909 has been found questionable to component evaluation. This leads us to the following conclusions:

The reference curve is not fully compatible with the ASME III design procedure, because data in various temperatures was mixed in deriving the curve. This question extends also to the current code curve, because it is based on this questionable reference curve.

Furthermore, applicability of the current ASME III code curve to components in existing NPP's is questionable, because evolution in alloy compositions and strength properties since manufacture of piping may have influenced the fatigue performance of material batches tested for the new curve. The old curve may be more relevant for old designs. This should have been studied before change of the code curve.

Only non-stabilised grades were considered for the new reference curve. VTT data for relevant material batches of two austenitic stainless steel grades differ from the new reference curve. The old ASME design curve is probably more relevant for stabilised stainless steels. This should be taken into account when risk informed inspection and plant life management programmes are applied in NPP's, where stabilised stainless steels are used.

6.1 Recommendations

The original ASME Code "design by analysis" philosophy assumes that the designer is able to take responsibility of managing material performance. This together with the facts that the revised curve cannot be considered universally applicable and compatible with the design procedure leads us to the following recommendations:

1. The design curves provided in the ASME III code should not be entitled "mandatory".
2. The applicability limits of the ASME Code Section III (2009b) new design curve for stainless steels should be considered. Until ready, a wording similar to the one in NRC regulatory guide 1.207 is proposed: "for new designs in USA only".
3. The new design curve is not recommended for fatigue assessment of components fabricated of X6CrNiNb1810 mod or other stabilised stainless steel grades without proper consideration.
4. Particular care should be taken in selecting design curve to avoid bias in risk informed inspection and plant life management programmes.
5. When transferability of laboratory data to NPP components is to be improved by considering effects of operational conditions such as water environment, also the effects of steady state operation between fatigue transients should be evaluated.
6. Fatigue data in different temperatures shall not be used without appropriate correction to derive or compare design curves aimed for fatigue analysis compatible with ASME Code Section III.

Acknowledgements

This paper is based on work in the Technical Programme of E.ON Case on Thermal Transients funded by E.ON Kernkraft GmbH. However, the experiments on titanium stabilized steel were a part of the Finnish Research Programme on Nuclear Plant Safety 2007–2010. All experiments were carried out at VTT, mainly by the author, Mr. Jouni Alhainen and Mr. Esko Arilahti.

References

1. Criteria of the ASME Boiler and Pressure Vessel Code for design by analysis in sections III and VIII division 2. Pressure Vessels and Piping: Design and Analysis, A Decade of Progress, Vol. One ASME 1972, pp. 61–83.
2. ASME, 2009. ASME Code, Section III, Division 1, Appendices, Mandatory Appendix 1 Design Fatigue Curves. Addendum 2009b.
3. STUK, 2002. YVL-guide 3.5, Ensuring the strength of nuclear power plant pressure devices, issue 5.4.2002. (in Finnish, translations exist).
4. U.S. Nuclear Regulatory Commission Regulatory Guide 1.207, 2007. Guidelines for evaluating fatigue analyses incorporating the life reduction of metal components due to the effects of the light-water reactor environment for new reactors. 7 p.
5. O'Donnel, W. J., O'Donnel, W. J. & O'Donnel, T. P. 2009. Proposed new fatigue design curves for carbon and low-alloy steels in high temperature water. *Journal of Pressure Vessel Technology*, ASME, April 2009, vol. 131 / 024003. 10 p.
6. Chopra, O. & Shack, W. 2007. Effect of LWR Coolant Environments on the Fatigue Life of Reactor Materials, Final Report. NUREG/CR-6909, ANL-06/08, Argonne National Laboratory. 118 p.
7. Nureg, Chopra, O. K. 1999. Effects of LWR coolant environments on fatigue design curves of austenitic stain-less steels, NUREG/CR-5704, ANL-98/31 for U.S. Nuclear Regulatory Commission, Washington DC, 42 p.
8. JSME, 2009. Codes for Nuclear Power Generation Facilities, "Environmental Fatigue Evaluation Method for Nuclear Power Plants," JSME S NF1-2009, The Japan Society of Mechanical Engineers, Tokyo, Japan, 2009. (comprehensive revision of the 2006 issue)

9. Solin, J., Nagel, G. & Mayinger, W. 2009. Cyclic behavior and fatigue of stainless surge line material (PVP2009-78138). Proceedings of ASME Pressure Vessel and Piping Division Conference, Prague, Czech Republic, July 26–30, 2009. 9 p.
10. Solin, J., Reese, S. & Mayinger, W. 2011. Long life fatigue performance of stainless steel Discussion on fatigue design curves for stainless steels (PVP2011-57942). Proceedings of ASME Pressure Vessel and Piping Division Conference, Baltimore, Maryland, USA, July 17–21, 2011. 9 p.
11. Solin, J., Reese, S. & Mayinger, W. 2011. Discussion on fatigue design curves for stainless steels (PVP2011-57943). Proceedings of ASME Pressure Vessel and Piping Division Conference, Baltimore, Maryland, USA, July 17–21, 2011. 6 p.
12. Solin, J., Reese, S. & Mayinger, W. 2012. Fatigue performance of stainless steel in NPP service conditions (PVP2012-78721). Proceedings of ASME Pressure Vessel and Piping Division Conference, Toronto, Ontario, Canada, July 15–19, 2012. 9 p.
13. Solin, J. 2010. Low cycle fatigue of stainless steel. Baltica VIII. Life Management and Maintenance for Power Plants, Vol. 1. Auerkari, Pertti & Veivo, Juha (eds.). VTT Symposium 264. Espoo, VTT Technical Research Centre of Finland, pp. 77–94.
14. Solin, J., Reese, S., Karabaki, H.E. & Mayinger, W. 2013. Environmental fatigue factors (NUREG/CR-6909) and strain controlled data for stabilized austenitic stainless steel (PVP2013-97500). Proceedings of ASME Pressure Vessel and Piping Division Conference, Paris, France, July 14-18, 2013. 7 p.
15. Solin, J., Reese, S., Karabaki, H.E., Mayinger, W., 2013. Fatigue performance of stabilized austenitic stainless steels – experimental investigations respecting operational relevant conditions like temperature and hold time effects (PVP2013-97502). ASME Pressure Vessel and Piping Conf., Paris, France, July 14–18, 2013. 7 p.
16. ASTM E1012 – 12e1, “Standard Practice for Verification of Testing Frame and Specimen Alignment Under Tensile and Compressive Axial Force Application”, ASTM International, West Conshohocken, PA, 2012, 18 p. DOI: 10.1520/E1012-12E01.

17. ASTM Standard E-606M-12, "Standard Test Method for Strain-Controlled Fatigue Testing", ASTM International, West Conshohocken, PA, 2012, 16p. DOI: 10.1520/E0606_E0606M-12.
18. Japan Nuclear Energy Safety Organization, 2005. Fatigue reliability of nuclear facilities and materials performance in the environment. Annual report on Demonstration Project in 2004. 303 p. (in Japanese)
19. Juuti, T., 2008. Static Strain Ageing in FCC-structured Austenitic Stainless Steels. Master's Thesis, University of Oulu. 129 p. (in Finnish)
20. Solin, J. et al. (9 authors), Fatigue of Primary Circuit Components (FATE), SAFIR2010, The Finnish Research Programme on Nuclear Power Plant Safety 2007–2010, Final Report. VTT Research Notes 2571, pp. 368–380. [<http://www.vtt.fi/inf/pdf/tiedotteet/2011/T2571.pdf>]
21. Bannantine, J. A., Comer, J. J. & Handrock, J. L. 1990. Fundamentals of metal fatigue analysis. Prentice Hall, ISBN 0-13-340191-X. 273 p.
22. Higuchi, M. & Iida, K. 1991. Fatigue strength correction factors for carbon and low-alloy steels in Oxygen-containing high-temperature water. Nucl. Eng. Des. 129, pp. 293–306.

Effect of initial flaw and load assumptions on risk estimate changes

Otso Cronvall

VTT Technical Research Centre of Finland
Kemistintie 3, 02150 Espoo, Finland

Abstract

This study concerns the effect of initial flaw and load assumptions on nuclear power plant (NPP) piping component failure probability and risk estimate changes. As the main criterion for the acceptance of a risk informed in-service inspection (RI-ISI) program is that the overall risk shall not increase when moving from the earlier ISI program to the risk informed one, means for robust quantification of the change in risk are needed. Worldwide, several assumptions and recommendations have been published both for NPP pipe weld initial flaw distributions and welding process induced residual stresses (WRSs), the latter being often the dominant load component for welds. Failure potential and risk analyses were performed with probabilistic fracture mechanics code VTTBESIT and Markov process application for three representative NPP piping welds, covering a wide range of initial flaw and load assumptions. The considered degradation mechanism is stress corrosion cracking (SCC). In the light of the analysis results, it can be concluded that both the size distributions of the initial cracks and WRSs have a remarkable impact on the risk values. The larger the initial cracks and higher on the tensile side the WRSs, the higher the resulting risk values, and vice versa.

1. Introduction

This study is part of the SAFIR2014 research program project RAIPSYS. The overall objective of this project is to support the implementation of risk informed in-service inspection (RI-ISI) at Finnish NPPs by studying and further developing relevant issues related to RI-ISI. The acronym name of the project stands for RI-ISI Analyses and Inspection Reliability of Piping Systems. This study is mainly based on the recent VTT research report [1].

This study concerns the effect of initial flaw and load assumptions on probability of failure (POF) and risk estimate changes for NPP piping components. The results concern POF and risk values computed with probabilistic VTTBESIT code [4, 5, 6, 7, 8] and Markov process based application [1] for three representative NPP piping welds, covering a wide range of initial flaw and load assumptions.

The probabilistic VTTBESIT [4, 5, 6, 7, 8] has been developed both by Fraunhofer-Institut für Werkstoffmechanik (IWM, Germany) and by VTT. The probabilistic features of VTTBESIT have been developed by VTT, whereas the contribution

by IWM concerns the computation of mode I stress intensity factor, K_I , values along the front of a growing crack.

Concerning NPP piping component welds, initial flaw and load assumptions arguably have a major impact on both POF and risk results. Worldwide, several initial flaw distribution assumptions for NPP pipe welds have been published. The main load component concerning welds is most often the WRSs, and also for them several recommendations have been published. Of the degradation mechanisms encountered in the NPP environments, the WRSs affect especially SCC.

Concerning the initial flaw and load assumptions it needs to be clarified:

- what quantitative impact these assumptions have on NPP piping component POF and risk assessment results,
- which assumptions appear unrealistic/overly conservative,
- which assumptions could be recommendable to be applied.

The considered initial flaw assumptions are described next. This concerns probabilistic density functions for their sizes. The considered WRS recommendations are described then. For NPP piping components, cracks most often initiate and grow in welds, where the WRSs are clearly the major load component. The probabilistic piping component degradation potential analyses and their results are described after that. The article ends with a summary and conclusions.

2. Initial flaw assumptions

To be able to carry out quantitative NPP piping component degradation potential analyses, part of the necessary input data are estimates of the initial crack sizes. As the data in the NPP component degradation databases concern only grown cracks, the sizes of the initial cracks have to be assessed recursively. This is not a straightforward task, and thus there are not many estimates for initial crack sizes available. Some selected probabilistic distributions for sizes of initial cracks in NPP pipe components are presented in the following. Among those are a new set of probabilistic density functions for depth and length of SCC induced initial cracks developed within the VTT research study [1].

According to Simonen and Khaleel [9], inputs for crack distributions are the greatest source of uncertainty in calculations of failure probabilities. However, the failure probability assessment accuracy requirements in RI-ISI do not necessitate the exact physical modelling of the involved degradation phenomena, instead it suffices to achieve a reasonable accuracy scale, e.g. one decade in the failure probability exponent.

2.1 Depth and length of existing fabrication induced cracks

The distributions for fabrication induced cracks in stainless steel piping developed by Khaleel and Simonen [10] are presented in the following. An expert system

model [11] was applied in the development of these distributions. The log-normal distribution equation used in defining depth probabilities, $f_x(x)$, for existing fabrication induced cracks in stainless steel piping is:

$$f_x(x) = \frac{1}{\sqrt{2 \cdot \pi \cdot \sigma_y \cdot x}} \cdot \exp\left[-\frac{(\ln x - \mu_y)^2}{2 \cdot \sigma_y^2}\right] \quad (1)$$

and:

$$\mu_y = \ln \tilde{X} \quad (2)$$

where x [mm] is the variable whose probability is computed, σ_y [-] is shape parameter, μ_y [mm] is scale parameter and \tilde{X} [mm] is the median of x . Tabulated values for these three parameters are given pipe wall thickness dependently in ref. [10]. The median depth of fabrication induced cracks varies between approximately 1.0 to 2.5 mm, as depending on the wall thickness. The probability distribution for lengths of existing fabrication induced cracks in stainless steel piping is defined using crack aspect ratio, which is given here as $\beta = b/a$ [-], where b [mm] is half of crack length and a [mm] is the crack depth, as:

$$f_0(\beta) = \begin{cases} 0, & \beta < 1 \\ \frac{C_\beta}{\lambda \cdot \beta \cdot (2 \cdot \pi)^{1/2}} \cdot \exp\left[-\frac{1}{2 \cdot \lambda^2} \cdot \left(\frac{\ln \beta}{\beta_m}\right)^2\right], & \beta \geq 1 \end{cases} \quad (3)$$

where the values for these dimensionless parameters are: $\lambda = 0.5382$, $C_\beta = 1.419$ and $\beta_m = 1.136$. This aspect ratio distribution is assumed to be independent of the flaw depth.

2.2 Depth and length of SCC induced initial cracks according to NURBIT

The depth and length of SCC induced initial circumferential cracks according to analysis code NURBIT [2, 3] are presented in the following. The depth of the initiated cracks is taken to be 1.0 mm. The probability density function for initial crack length, $f_{al}(b)$, was estimated from a total of 98 intergranular SCC cases in Swedish stainless steel girth welds in straight pipes, as collected from nine boiling water reactor (BWR) units. The probability density function for initial crack length is:

$$f_{al} = \frac{\lambda}{2\pi R_i} \exp\left(-\frac{\lambda l_0}{2\pi R_i}\right) (1 - e^{-\lambda})^{-1} H(2\pi R_i - l_0) \quad (4)$$

where b [mm] is initial crack length, R_i [mm] is inner radius of pipe cross-section and H is the Heaviside step function. The parameter λ [-] was chosen with λ_0 equal to 9.380 so that the mean values of the observed and fitted distributions coincided. This corresponds to a mean value for $1/\lambda_0$ of 10.66% of the inner pipe circumference.

2.3 Depth and length estimates of SCC induced initial cracks developed by VTT

The assessment of depth and length of SCC induced initial circumferential cracks developed by VTT [1] is presented in the following. This treatment is based on the same flaw data as was used for the assessment of the corresponding initial cracks included in the NURBIT code.

A recursive method based on fracture mechanics and statistical curve fitting was used to assess the probabilistic distributions for depth and length of cracks initiating due to SCC during plant operation. The first step in the applied approach is to convert the size data concerning detected grown SCC induced cracks to dimensionless form in relation to pipe wall thickness and inner circumference. Then, with recursive fracture mechanics based analyses, the thus obtained data is matched with the assumed initial size criteria, corresponding here to respective mode I stress intensity factor threshold values, $K_{I,threshold}$, for SCC initiated cracks. Finally, the thus obtained data is converted to probabilistic form and suitable reliability distribution functions are fitted to them.

The fitted linear probabilistic density function for estimated initial depths, $f(a_0)$, of SCC induced circumferential cracks is:

$$f(a_0) = 0.00004a_{0\%} + 0.0125 \quad (5)$$

where the unit of the initial crack depth $a_{0\%}$ is %, and in terms of actual dimensions a_0 is limited to region from 0.2 mm to 0.76 mm. For instance, the actual depth of an initial crack with depth of 50% is: $a_0 = (50/100) \cdot (0.76 - 0.2) + 0.2 = 0.48$ mm. This being the median depth for SCC induced initial circumferential cracks developed by VTT.

The fitted linear probabilistic density function for estimated initial lengths, $f(l_0)$, of SCC induced circumferential cracks is:

$$f(l_0) = 0.103 \exp(-0.103l_0) \quad (6)$$

where the unit of the initial crack length l_0 is %, in relation to the inner circumference of pipe component.

3. Weld residual stresses

The load component the effect of which to NPP piping component failure probability and risk values is examined is WRSs. The process of welding causes locally confined and relatively severe stresses to NPP component welds. The WRSs are mechanical stresses that exist in a component without any external applied mechanical or thermal loads, thus all internal forces and moments resulting from the WRSs of a system are in mechanical equilibrium. Of the degradation mechanisms encountered in the NPP environments, the WRSs affect especially SCC.

Manufacturing of welded structures in NPPs is carried out with traditional methods for which there are considerable welding experience. The methods are shielded metal arc welding (SMAW), tungsten inert gas welding (TIG) and submerged arc welding (SAW). However, metal inert gas welding (MIG) is generally not used due to a higher risk for lack of fusion. The resulting WRS state in a welded component is determined by welding related parameters and geometrical constraints. The former issue refers to the local shrinkage, quench and phase transformations resulting from the localised thermal cycle. The latter issue deals with the unbalance in material properties of dissimilar metal welds (DMWs) and the constraining effect of the surrounding structure.

The published experimental WRS data have a substantial scatter. It is also possible to simulate the welding process with finite element method (FEM) applications. The WRS distributions given in the structural integrity assessment guidelines and fitness-for-service procedures have mostly been developed as tensile upper bound solutions based on the experimental and simulated data. The WRS distributions used in the computational study are from the following guidelines and standards:

- as-welded state WRSs from the ASME recommendations [12, 13],
- as-welded state WRSs from the R6 Method, Revision 4 [14], and
- as-welded state WRSs from the SSM handbook [15].

The perpendicular to weld WRSs according to the above mentioned three recommendations are shown for three NPP piping weld thicknesses in Figures 1 to 3.

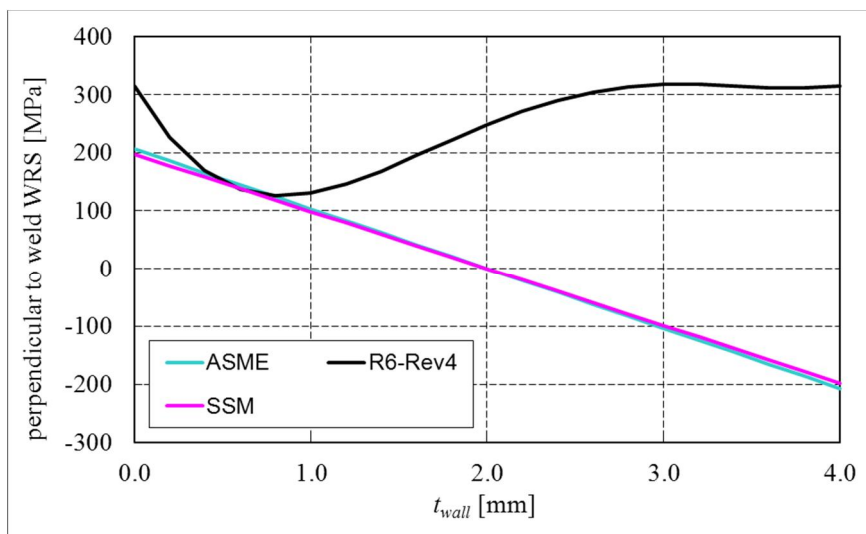


Figure 1. As-welded state WRSs through weld centre-line, wall thickness is 4.0 mm and the coordinate system origin is in the inner surface.

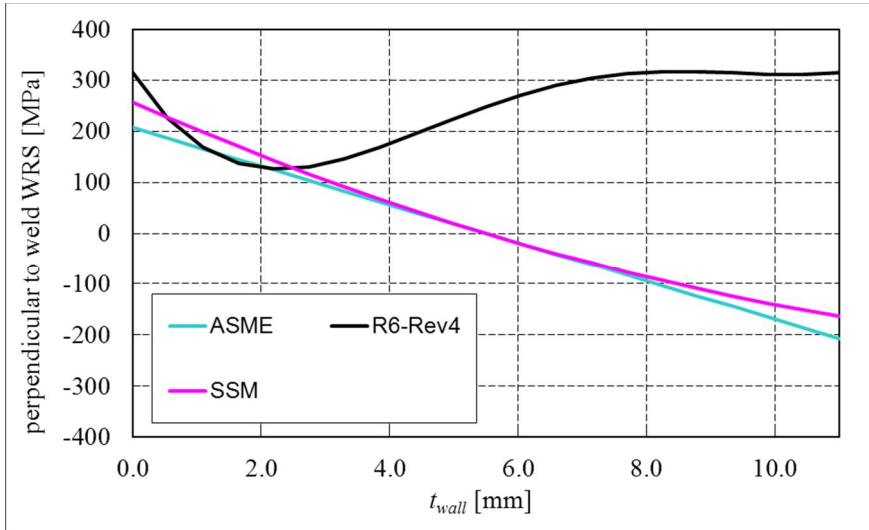


Figure 2. As-welded state WRSs through weld centre-line, wall thickness is 11.0 mm and the coordinate system origin is in the inner surface.

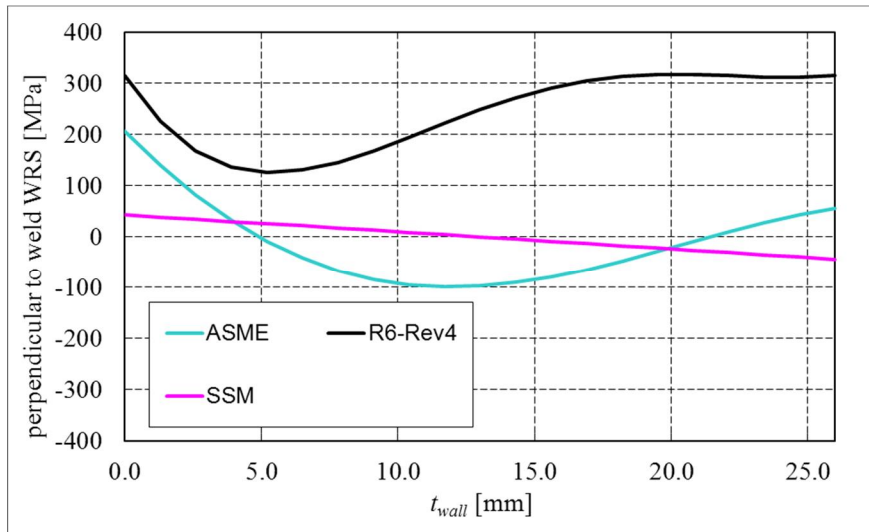


Figure 3. As-welded state WRSs through weld centre-line, wall thickness is 26.0 mm and the coordinate system origin is in the inner surface.

As can be seen from Figures 1 to 3, the as-welded state WRS distributions through wall and perpendicular to weld differ considerably from each other. The most severe WRS recommendations are provided by the R6 Method, Rev. 4 [14],

as the WRS values stay through wall on the tensile side. Whereas the WRS distributions according to ASME recommendations [12, 13] and SSM handbook [15] appear to be much less severe, and also match well in most cases. Within the scope of the present study, only these latter two WRS recommendations give realistic self-balancing perpendicular to weld WRS distributions through wall. As more than 90 % of the detected NPP piping cracks are oriented circumferentially, see e.g. ref. [2], the perpendicular to weld WRSs play a prominent role in piping component crack growth considerations.

4. Probabilistic NPP piping component analyses

4.1 Analysis input data

The performed degradation potential and risk analyses concern a representative selection of NPP piping welds, initial flaw distributions and WRS recommendations. The scope of this study covers:

- three representative BWR pipe weld cross-section sizes, see Table 1,
- material properties of the weld material similar to austenitic stainless steel SS 2353, which corresponds to steel TP 316L according to U.S. standards, see Table 2,
- SCC as the considered degradation mechanism, see equation 7,
- considered flaw postulate is a semi-elliptic circumferentially oriented crack opening to inner surface,
- operational BWR conditions as the considered process loads, with pressure of 70 bar and temperature of 286°C [16], see Table 1 for the corresponding axial stress loads, σ_{BWR} ,
- three sets of probability density distributions for sizes of initial cracks, see Chapter 2,
- three distributions for WRSs as well as the case of no WRSs, see Chapter 3,
- assumed conditional core damage probability (CCDP) value is 0.00001,
- assumed time in operation is 60 years.

Table 1. Geometry and load data used in degradation potential and risk analyses [1].

Pipe size	Outer diameter [mm]	Wall thickness [mm]
Small	60	4.0
Medium	170	11.0
Large	310	26.0
Pipe size	Axial σ_{BWR} [MPa]	Axial total stresses [MPa]
Small	22.8	$\sigma_{BWR} + WRSs$
Medium	23.5	$\sigma_{BWR} + WRSs$
Large	30.8	$\sigma_{BWR} + WRSs$

Table 2. Material property data for austenitic stainless steel SS 2353 for two temperatures [17].

Temperature [°C]	Young's modulus [GPa]	Yield strength [MPa]	Tensile strength [MPa]
20	198	210	515
286	176	125	412
Temperature [°C]	Coefficient of thermal expansion [$10^{-6}/K$]	Thermal conductivity [W/mK]	Specific heat [J/kgK]
20	16.5	13.5	440.0
286	18.0	17.4	537.2

4.2 Conduct of probabilistic analyses with VTTBESIT and Markov application

VTTBESIT uses in the probabilistic analyses the following fracture mechanics based crack growth equation, which depicts the sub-critical intermediate (stage 2) SCC as the derivative of crack depth, a , to time, t , as [18, 19]:

$$\frac{da}{dt} = C_{SCC} \cdot K_I^{n_{SCC}} \quad (7)$$

where the values of material, environment and temperature range specific parameters C_{SCC} and n_{SCC} are given in Table 3. The dimensions used in equation (7) are: $[da/dt] = \text{mm/year}$, $[K_I] = \text{MPa}\sqrt{\text{m}}$.

Table 3. Values for parameters C_{SCC} and n_{SCC} used in the SCC equation for steel SS 2353 [15].

C_{SCC} [[da/dt]/[K_I]]	n_{SCC} [-]	K_I [MPa $\sqrt{\text{m}}$]	Environment
4.60·1.0E-05	3.00	< 55.5	water
$da/dt = 7.884 \text{ mm/year}$		≥ 55.5	

In BWR environment, e.g. certain piping materials are deemed to be susceptible to SCC. For SCC to occur, three conditions have to be fulfilled simultaneously, which are: particular material and environment as well as high enough load induced stresses.

The analysis flow of the probabilistic VTTBESIT is as follows [1]:

1. Reading of the deterministic input data.
2. Random picking of certain input data parameters from the specified distributions; 1) SCC; probability distributions for initial crack depth and length, 2) fatigue induced crack growth; probability distributions for initial crack depth, length, and frequency of load cycles.
3. Crack growth analysis; the magnitude of crack growth in each time step is calculated from the respective crack growth equation \Rightarrow the ending criterion of the analysis is that crack depth reaches the opposite pipe surface.
4. For each analysed circumferential piping weld, at least 5000 separate simulations with Latin hypercube simulation (LHS) procedure are computed.
5. The degradation state to which the crack has grown is computed for each year of the assumed time in operation and for each simulation \Rightarrow these results are used in the ensuing probabilistic Markov process based degradation potential and risk analyses.

The applied discrete time Markov procedure for degradation potential and risk analyses is summarised by the following four steps [20]:

1. Crack growth simulations with probabilistic VTTBESIT.
2. Construction of degradation matrix transition probabilities from VTTBESIT simulation results and database analysis of crack initiation frequencies.
3. Model for inspection quality, as based on applicable probability of detection (POD) functions, which are in turn used to construct inspection matrix transition probabilities.
4. Markov model to calculate pipe leak/break probabilities and risks for chosen inspection programs, including the case of no inspections.

The Markov model uses either 8 or 10 degradation states, as depending on the wall thickness of a NPP piping component. This enables the simulation of all possible inspection programs, including the possibility of detecting a flaw and not repairing it. The degradation states are defined according to crack depth through wall so, that the first state is no crack, as corresponding to intact state, and the last state is for the event of a crack having just reached the opposite wall, as corresponding to pipe break, while the intermediate states correspond to various stages of sub-critical crack growth. Thus, this system covers for NPP piping components all possible states of degradation from intact to break. For NPP pipes with wall

thickness equal to or less than 10 mm the number of degradation states is 8, while for wall thicknesses exceeding 10 mm this number is 10 [1].

The pipe component specific computations with discrete time Markov model divide into two phases. Namely, the degradation potential and risk values from start of operation to the assumed current time are computed according to actual inspection history, whereas those from the assumed current time to the end of planned operational lifetime are computed for optional future inspection programs. For a more detailed description on the Markov process model, see ref. [1].

4.3 Probabilistic analysis results

The pipe break probability analysis results for the considered three pipe component welds are presented in the following. The main characteristics of all 36 analysis cases are presented in Table 4. Besides the cases with fabrication induced initial cracks, each weld is assumed to be at a flawless state in the analyses when the operation of the NPP is started, corresponding to year zero in this study.

The risk results have been computed quantitatively as the product of break probability and CCDP value. As the same constant CCDP value was used for all computations, the resulting risk curves as a function of time are otherwise identical to the corresponding break probability curves but they are offset in the vertical direction by the magnitude of the CCDP. As the risk results only thus repeat the corresponding break probability results, they are excluded here from the presentation of the results.

Table 4. The list of all analysis cases together with their main characteristics. The effect of inspections is excluded from the analysis scope.

Case No.	Pipe	Initial cracks	WRSs
1	Small	Fabrication cracks	ASME recommendations
2	Small	NURBIT	ASME recommendations
3	Small	VTT 2011	ASME recommendations
4	Small	Fabrication cracks	R6 Method, Rev. 4
5	Small	NURBIT	R6 Method, Rev. 4
6	Small	VTT 2011	R6 Method, Rev. 4
7	Small	Fabrication cracks	SSM Handbook
8	Small	NURBIT	SSM Handbook
9	Small	VTT 2011	SSM Handbook
10	Small	Fabrication cracks	No WRSs
11	Small	NURBIT	No WRSs
12	Small	VTT 2011	No WRSs
13	Medium	Fabrication cracks	ASME recommendations
14	Medium	NURBIT	ASME recommendations
15	Medium	VTT 2011	ASME recommendations
16	Medium	Fabrication cracks	R6 Method, Rev. 4

17	Medium	NURBIT	R6 Method, Rev. 4
18	Medium	VTT 2011	R6 Method, Rev. 4
19	Medium	Fabrication cracks	SSM Handbook
20	Medium	NURBIT	SSM Handbook
21	Medium	VTT 2011	SSM Handbook
22	Medium	Fabrication cracks	No WRSs
23	Medium	NURBIT	No WRSs
24	Medium	VTT 2011	No WRSs
25	Large	Fabrication cracks	ASME recommendations
26	Large	NURBIT	ASME recommendations
27	Large	VTT 2011	ASME recommendations
28	Large	Fabrication cracks	R6 Method, Rev. 4
29	Large	NURBIT	R6 Method, Rev. 4
30	Large	VTT 2011	R6 Method, Rev. 4
31	Large	Fabrication cracks	SSM Handbook
32	Large	NURBIT	SSM Handbook
33	Large	VTT 2011	SSM Handbook
34	Large	Fabrication cracks	No WRSs
35	Large	NURBIT	No WRSs
36	Large	VTT 2011	No WRSs

The pipe break probability results obtained with VTTBESIT and Markov application for the considered three pipe component weld sizes are presented in Figures 4 to 9. The results divide into two parts: break probabilities after 1, 5, 20 and 60 years in operation as pipe component weld size specifically, and some representative break probability results as a function of time. In the legends of the result figures, the following abbreviations are used:

- "1 y" is 1 year, "5 y" is 5 years, "20 y" is 20 years, and "60 y" is 60 years,
- "S" is Small pipe, "M" is Medium pipe, and "L" is Large pipe,
- "FC" is fabrication cracks, "NUR" is initial SCC induced cracks according to NURBIT code, and "VTT" is initial SCC induced cracks developed by VTT,
- "ASME" is WRSs according to ASME recommendations, "R6" is WRSs according to R6 Method, Rev. 4, and "SSM" is WRSs according to SSM Handbook.

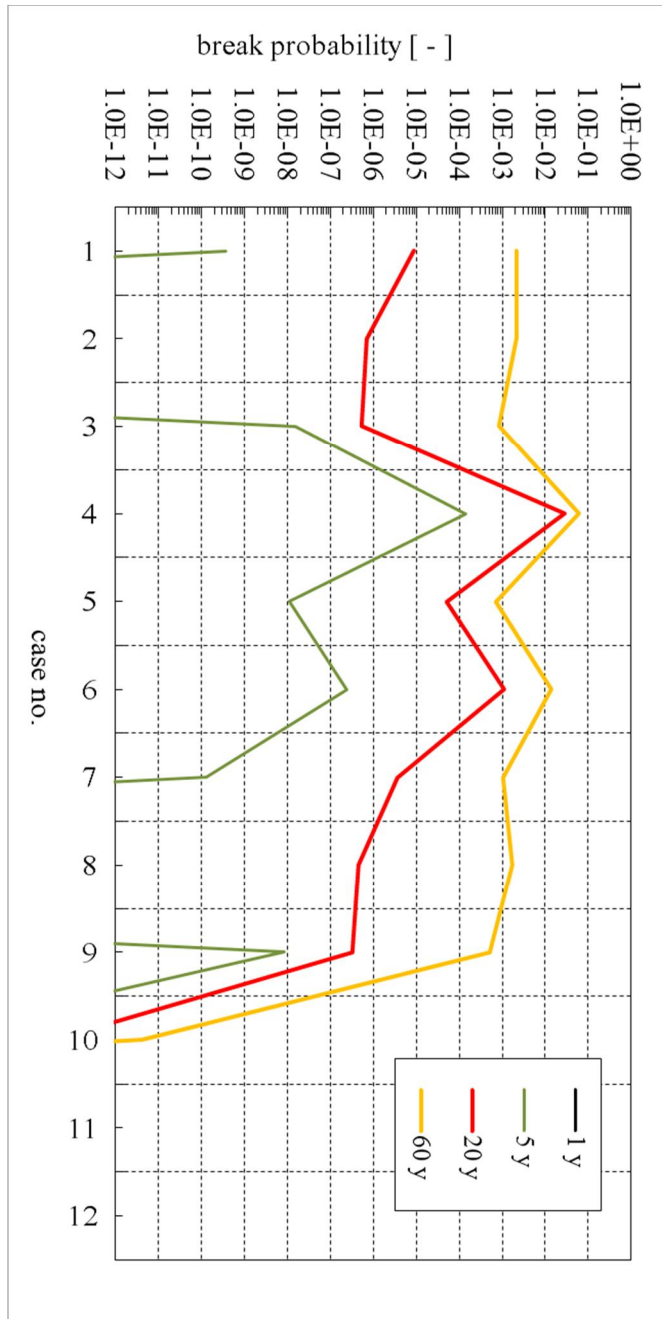


Figure 4. Pipe break probabilities after 1, 5, 20 and 60 years in operation for Small pipe component weld size. The curve corner points correspond to result values. For two cases the failure probabilities are extremely low or zero.

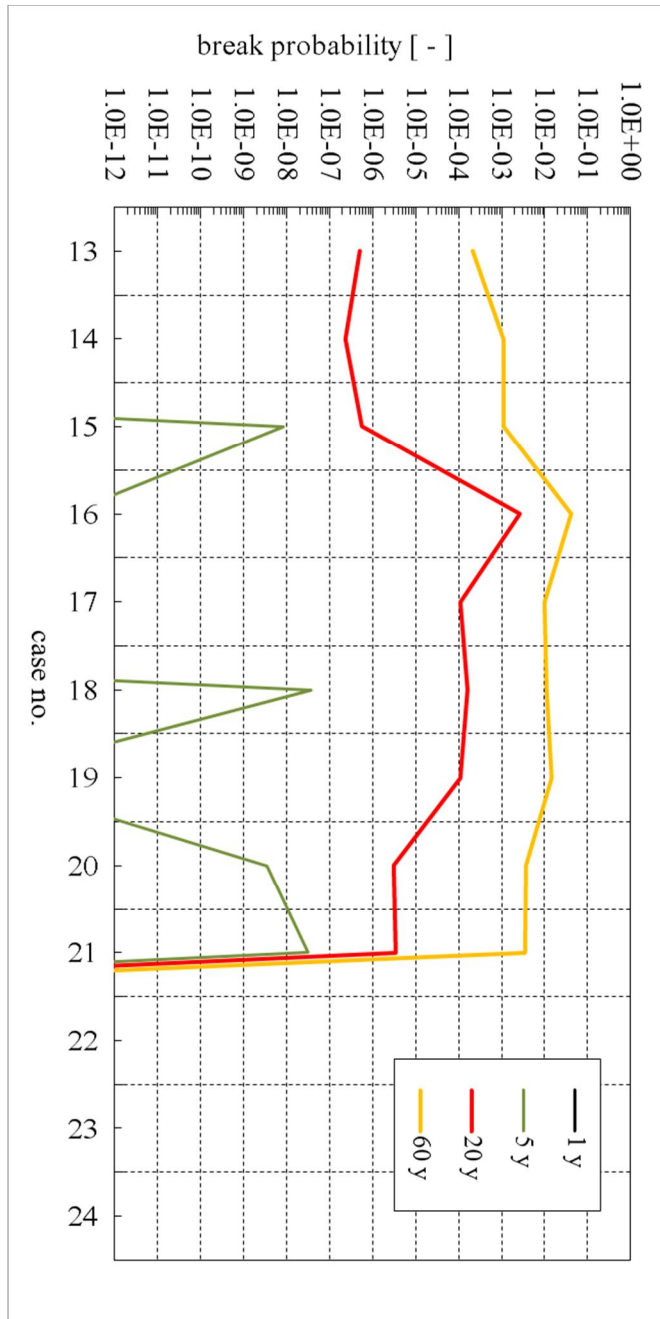


Figure 5. Pipe break probabilities after 1, 5, 20 and 60 years in operation for Medium pipe component weld size. The curve corner points correspond to result values. For three cases the failure probabilities are extremely low or zero.

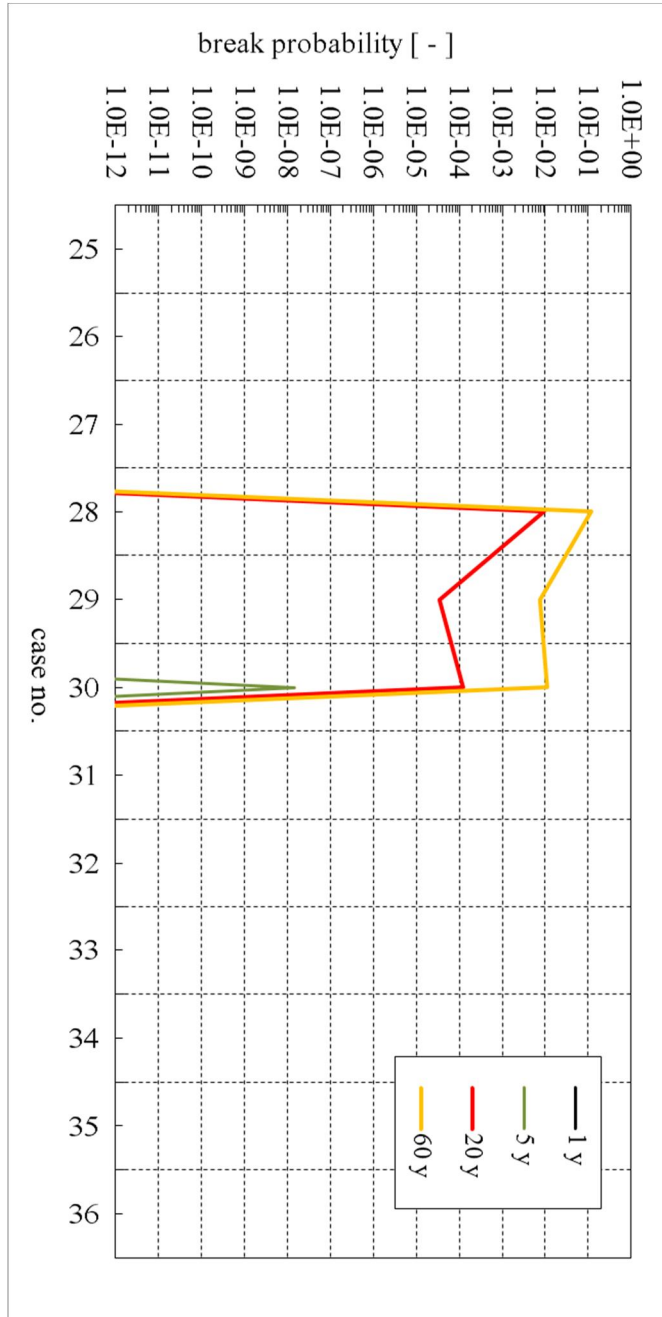


Figure 6. Pipe break probabilities after 1, 5, 20 and 60 years in operation for Large pipe component weld size. The curve corner points correspond to result values. For nine cases the failure probabilities are extremely low or zero.

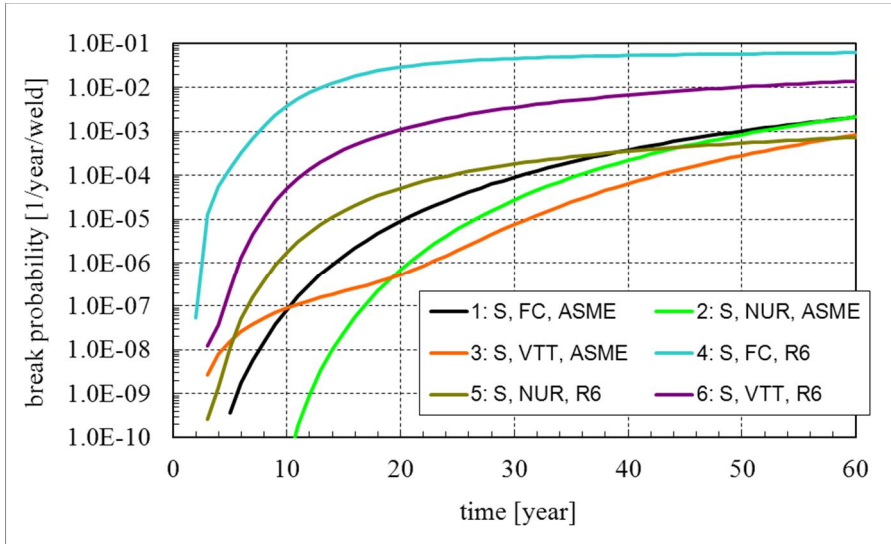


Figure 7. Set of break probability analysis results as a function of time for Small pipe component weld.

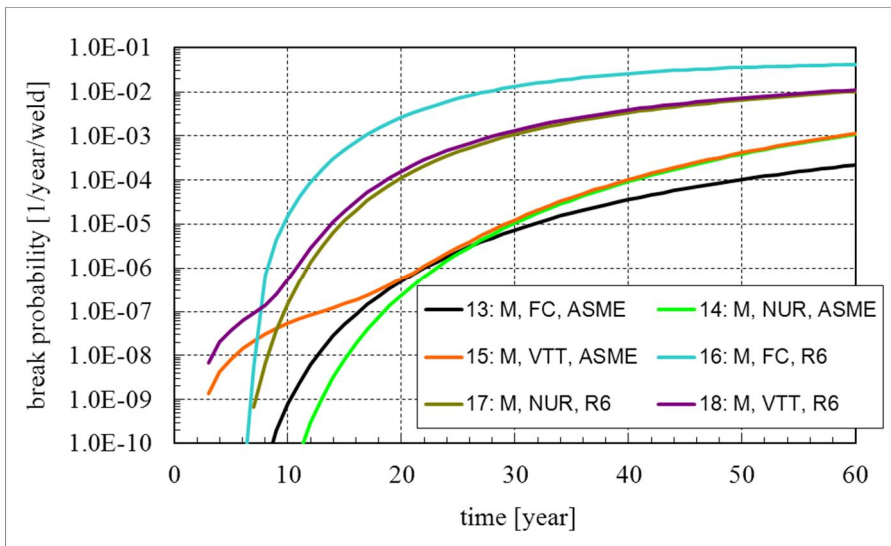


Figure 8. Set of break probability analysis results as a function of time for Medium pipe component weld.

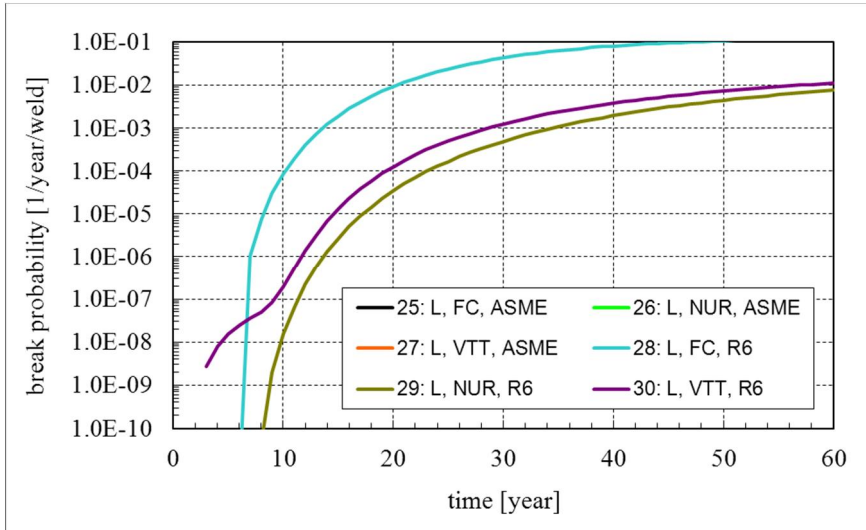


Figure 9. Set of break probability analysis results as a function of time for Large pipe component weld. For cases 25, 26 and 27 the failure probabilities are extremely low or zero.

5. Summary and conclusions

5.1 Summary

All varied input data parameters, namely initial flaw and load assumptions as well as weld cross-section size, have a remarkable effect on the resulting break probabilities and risk results. The discussion on the results here is limited to concern pipe break probabilities, thus risk results are not considered. This is because the risk result curves only repeat with an offset those concerning break probability, due to having used the same CCDP value in all risk computations. The number of analysis cases computed with VTTBESIT and Markov application is 36.

The pipe weld cross-section size clearly has an effect on the resulting break probabilities. For Small weld cross-section with 4.0 mm thick wall, the maximum break probabilities after 5 years in operation are generally from 3 to 10 decades higher than for the other two weld cross-section sizes. The maximum break probabilities after 5 years in operation for the Medium weld cross-section with 11.0 mm thick wall and Large weld cross-section with 26.0 mm thick wall are of the same scale. The maximum break probability values after 20 and 60 years in operation are almost matching for all three considered pipe weld cross-sections, being of the scale of 1.0E-01. However, in general the break probability values after 20 and 60 years are much lower for Medium and Large cross-sections than for Small cross-

section. Especially, for Large cross-section in more than half of the cases the failure probabilities remain extremely low or zero.

The assumptions concerning initial flaw sizes have a considerable effect on the failure probability results. The break probabilities after 5 years in operation are in most cases highest for the cases with SCC induced initial cracks developed by VTT, whereas these probabilities are from 1 to 2 decades lower for the cases with the SCC induced initial cracks from the NURBIT code and fabrication induced cracks. The effect of the initial flaw sizes to break probabilities is most pronounced in the early phase of the time in operation. As for the maximum break probability values after 20 and 60 years in operation, they are of the same scale for all three used assumptions for initial crack sizes, thus reflecting their decreased effect. However, it is now the cases with fabrication induced cracks which most often result with the highest break probabilities.

The magnitude of the loading has the biggest effect on the break probability results. The loading is clearly governed by the WRSs. Of the considered three sets of recommendations for WRSs, those given in the R6 Method, Rev. 4 [14] are by far the most severe. This is strongly reflected in the analysis results, as for the cases with the R6 Method, Rev. 4 [14] WRSs, the break probabilities after 5 years are from 2 to 9 decades higher than for all other cases with WRSs, whereas for break probabilities after 20 and 60 years this difference varies from 1 to 6 decades. For all cases with no WRSs, the resulting break probability values are extremely low or zero.

5.2 Conclusions

Concerning the effect of initial flaw and load assumptions to the degradation potential and risk analysis results for NPP piping components, the purpose of this study is to clarify:

- what quantitative impact these assumptions have on NPP piping component POF and risk assessment results,
- which assumptions appear unrealistic/overly conservative,
- which assumptions could be recommendable to be applied.

Of the used initial crack sizes, fabrication cracks are on average to some extent larger than those induced by SCC. This appears convincing, as there are no strict limitations to the sizes the fabrication cracks can have, whereas cracks induced by SCC during NPP operation are typically nucleated from remarkably small initiation sites, such as inclusions, impurity particles and small pores, and can remain small for several years, as the nucleation and early growth phase of SCC cracks are mainly driven by electro-chemical phenomena. The sizes of the fabrication cracks are based mainly on measurements, see ref. [10], whereas those for SCC induced initial cracks are based on recursive estimation/computation by using data on detected grown SCC induced cracks as a starting point, see refs. [1, 2, 3]. For the

sizes of fabrication induced cracks, it is recommended to use the definitions developed by Khaleel and Simonen [10], as to the knowledge of the author no other applicable definitions for these cracks in the NPP piping component welds are available for the time being. As for the estimates for sizes of SCC induced initial cracks, those provided by VTT [1] and those in the NURBIT code [2, 3] have been developed using the same recursive approach. Of them, those provided by VTT give a wider scope of probabilistic variation than those in the NURBIT code, as in the former case the probabilistic density functions are provided both for the initial crack depth and length, whereas according to the NURBIT code the depth of the initial cracks is fixed to 1.0 mm and a probabilistic density function is given only for the length of initial cracks. This fixed value for the crack depth can be considered as unnecessary conservatism. The median depth for the SCC induced initial cracks provided by VTT [1] is 0.48 mm, being in relative terms much less than the fixed crack depth in the NURBIT code [2, 3]. Thus, it is recommended that for the sizes of SCC induced initial cracks in the NPP piping welds, those developed by VTT [1] are used. Another option would be to use the sizes for SCC induced initial cracks in the WinPRAISE code [21], which are described in detail in the VTT research report [1]. However, the depth of these initial cracks is fixed to 0.0254 mm, which is a considerably small value. Using a fracture mechanics based crack growth rate equation, as is the case for both the VTTBESIT and NURBIT codes, it would take an unrealistically long time for that small cracks to grow to more macroscopic dimensions, i.e. to fracture mechanics scale, which starts from the range of 0.1 to 0.2 mm. In case of the WinPRAISE code [21], it has a separate crack growth rate equation for the small size phase of the cracks, which is a correlation as calibrated to laboratory results. After the crack growth has reached a specific threshold, the WinPRAISE code switches to using a fracture mechanics based crack growth rate equation. Thus, even though the sizes for SCC induced initial cracks in the WinPRAISE code [21] could be used when computing with other pipe leak/break probability analysis codes, it would necessitate the use of the specific correlation equation for the phase when cracks are very small.

One drawback concerning the used version of the Markov application is that in case of SCC induced initial cracks nucleating during operation it assumes that there are no fabrication induced cracks in welds to begin with, while obviously all NPP piping welds contain fabrication induced crack as a starting point, as according to some density. The exclusion of fabrication induced cracks from the analyses concerning SCC induced initial cracks is thus an unrealistic and unsafe assumption, leading to too low pipe break probabilities. However, in the more recent version of the Markov process based application, as developed by VTT, this drawback has been removed, see the VTT research report [22].

According to the analysis results, the magnitude of the loading has the biggest effect on the NPP pipe component break probability and risk results. The loading is clearly governed by the WRSs, which provide the largest part of the total stresses, in particular in and near the inner surface of the weld wall. For the cases with the R6 Method, Rev. 4 [14] WRSs, the break probabilities after 20 and 60 years are from 1 to 3 decades higher than for all other cases with WRSs. For all cases

with no WRSs, i.e. those taking into account only the stresses induced by operational pressure and temperature, the resulting break probability and risk values are extremely low or zero. The WRSs should be self-balancing, meaning that when other loads are removed and WRSs act alone, they should balance themselves across the cross-section in the axial pipe component direction. The R6 Method, Revision 4 [14] axial WRSs for welds joining NPP pipes of austenitic stainless steel remain on the tensile side through the wall, thus being not self-balancing, which is unrealistic. Due to that, and because the magnitude of these WRSs is of the scale of material ultimate strength for almost half of the wall thickness and considerably higher than yield strength elsewhere, they are deemed as overly conservative, and thus it is not recommendable to use them. On the other hand, the ASME recommendations [12, 13] and SSM handbook [15] do provide self-balancing axial WRSs across the wall and cross-section for welds joining NPP pipes of austenitic stainless steel, exceeding the yield strength only at and near the inner surface, and being in no point near the ultimate strength. Of the WRS recommendations, those which are published more recently are also backed by more experimental data and more accurate finite element (FE) simulation results. The ASME recommendations [12, 13] have been published 30 years ago, whereas the WRSs given in the SSM handbook [15] have originally been published 17 years ago, see ref. [23]. The ASME recommendations [12, 13] provide one of the very first published sets of WRS recommendations, but due to relatively small amount of associated background data the presented WRS distributions are in some cases very simple and probably not very accurate. However, the WRS recommendations in the SSM handbook [15] are based on much greater amount of both experimental data and FE simulation results. Thus, the SSM handbook [14] WRSs for welds joining NPP pipes of austenitic stainless steel are recommended to be used. Another more recently published collection of WRS distributions, namely that in the SINTAP procedure [24, 25], is recommended to be used too, application examples concerning these WRSs are presented in the VTT research report [1]. The SINTAP WRS recommendations are backed by more experimental data and FE simulation results than those in the SSM handbook [15], and they are also self-balancing in the axial direction for welds joining NPP pipes of austenitic stainless steel. As for the other recently published WRS recommendations, those in the FITNET procedure [26] are identical to those in the earlier published R6 Method, Revision 4 [14], and are thus not recommended to be used, and neither are those in API 579 procedure [27], as they are not self-balancing through wall in the axial direction for welds joining NPP pipes of austenitic stainless steel, see the VTT research report [1] for an application example.

References

1. Cronvall, O., Männistö, I. & Alhainen, J. First phase of a study – Effect of initial flaw and load assumptions on risk estimate changes, Rev. 1. Espoo, VTT Technical Research Centre of Finland, November 2012. Research Report VTT-R-08024-12. 50 p.
2. Brickstad, B. The Use of Risk Based Methods for Establishing ISI-Priorities for Piping Components at Oskarshamn 1 Nuclear Power Station. SAQ/FoU-Report 99/5, SAQ Control AB, Sweden, 1999. 83 p.
3. Brickstad, B. Appendix D1, A Short Description of the NURBIT Piping Reliability Program for Stress Corrosion Cracking Analyses. NURBIM Project, WP-4, Review and benchmarking of SRMs and associated software, May 2004. 17 p.
4. Varfolomeyev, I. et al. BESIF 1.0: Stress Intensity Factors for Surface Cracks under 2D Stress Gradients. IWM-Report T 14/96, Fraunhofer-Institut für Werkstoffmechanik (IWM), July 1996. 42 p.
5. Busch, M. et al. KI-Factors and Polynomial Influence Functions for Axial and Circumferential Surface Cracks in Cylinders. Fraunhofer-Institut für Werkstoffmechanik (IWM), October 1994. IWM-Report T 18/94. 41 p.
6. Busch, M. et al. Polynomial Influence Functions for Surface Cracks in Pressure Vessel Components. Fraunhofer-Institut für Werkstoffmechanik (IWM), January 1995. IWM-Report Z 11/95. 88 p.
7. Vepsä, A. Verification of the stress intensity factors calculated with the VTTBESIT software. Espoo, VTT Technical Research Centre of Finland. Research Report TUO72-044578. 40 p. + 2 p.
8. Männistö, I. & Cronvall, O. Combining discrete-time Markov processes and probabilistic fracture mechanics in RI-ISI risk estimates. *International Journal of Pressure Vessels and Piping* 86 (2009) 732–737.
9. Simonen, F.A. & Khaleel, M. A. Uncertainty analyses of probabilistic fracture mechanics calculations of piping failure probabilities. Proceedings of the 4th International Conference on Probabilistic Safety Assessment and Management. New York, 13–18 September 1998. Probabilistic Safety Assessments and Management PSAM 4, Vol. 3, pp. 2040–2045.

10. Khaleel, M. A. & Simonen, F. A. Effects of alternative inspection strategies on piping reliability. *Nuclear Engineering and Design* 197 (2000) 115–140.
11. Chapman, V. Reliability and risk in pressure vessels and piping, Proceedings of the Simulation of Defects in Weld Construction. Pressure Vessel and Piping Conference, American Society of Mechanical Engineers, New York, PVP-251, 1993, pp. 81–89.
12. Section XI Task Group for Piping Flaw Evaluation, ASME Code. Evaluation of Flaws in Austenitic Steel Piping. *Journal of Pressure Vessel Technology*, Vol. 108, 1986. Pp. 352–366.
13. Shack, W. J. et al. Environmentally Assisted Cracking in Light Water Reactors: Annual Report, October 1981 – September 1982. NUREG/CR-3292, Washington D.C. U.S. Nuclear Regulatory Commission, June 1983.
14. R6 Method; Assessment of the Integrity of Structures containing Defects, Revision 4. 2004 update of 2001 edition. British Energy (BE).
15. Dillström, P. et al. A Combined Deterministic and Probabilistic Procedure for Safety Assessment of Components with Cracks – Handbook. SSM Research Report 2008:01, Swedish Radiation Safety Authority (Strålsäkerhetsmyndigheten, SSM). Stockholm, Sweden, 2008. 27 p. +196 p.
16. Nuclear power plant units Olkiluoto 1 and Olkiluoto 2. Teollisuuden Voima Oy, Helsinki, Finland, 2009. 51 p.
17. ABB ATOM Materialhandboken – Normer och datablad för metalliska material. ABB Atom AB, 1999.
18. Hazelton, W. S. & Koo, W. H. Technical Report on Material Selection and Processing Guidelines for BWR Coolant Pressure Boundary Piping. Springfield. U.S. Nuclear Regulatory Commission (NRC), Office of Nuclear Reactor Regulation, NUREG-0313-Rev2-F, Final Report. U.S., Jan. 1988. 25 p.
19. Congleton, J. & Craig, I. H. "Corrosion Fatigue" in Corrosion Processes, Parkins, R., N., Ed., Applied Science Publishers, 1982.
20. Cronvall, O., Männistö, I. & Simola, K. Development and testing of VTT approach to risk-informed in-service inspection methodology. Espoo, VTT Technical Research Centre of Finland, 2007. Research Notes 2382. 43 p.

21. Khaleel, M. A. & Simonen, F. A. Evaluations of Structural Failure Probabilities and Candidate Inservice Inspection Programs. Report NUREG/CR-6986, U.S. Nuclear Regulatory Committee (USNRC), March 2009. 194 p.
22. Cronvall, O., Männistö, I. & Alhainen, J. Second phase of a study – Effect of initial flaw and load assumptions on risk estimate changes. Espoo, VTT Technical Research Centre of Finland, 2013. Research Report VTT-R-08805-12. 60 p.
23. Andersson, P., Bergman, M., Brickstad, B., Dahlberg, L., Nilsson, F. & Sattari-Far, I. A Procedure for SWafety Assessment of Components with Cracks – Handbook. 3rd revised edition. Report SAQ/FoU-Report 96/08. SAQ Kontroll AB. Stockholm, Sweden, 1996. 104 p.
24. SINTAP – Structural Integrity Assessment Procedures for European Industry; Final Procedure: November 1999. Project funded by the European Union (EU) under the Brite-Euram Programme: Project No. BE95-1426, Contract No. BRPR-CT95-0024.
25. Barthelemy, J.Y. & Janosch, J.J. Structural Integrity Assessment Procedures for European Industry. SINTAP, Task 4, Compendium of Residual Stress Profiles; Final Report: 18.5.1999. Project funded by the European Union (EU) under the Brite-Euram Programme: Project No. BE95-1426, Contract No. BRPR-CT95-0024. 40 p. + 18 pages.
26. FITNET Fitness-for-Service PROCEDURE – FINAL DRAFT MK7, Revision MK8. Koçak, M. et al. (Eds). European Fitness-for-Service Thematic Network – FITNET, Germany, January 2008.
27. API Recommended Practice 579 – Fitness For Service. American Petroleum Institute (API), Washington DC, 2000.

NB-3650M fatigue calculation procedure

Paul Smeekes¹, Eero Torkkeli², Márten Perklén² and Otso Cronvall³

¹Teollisuuden Voima Oyj
Olkiluoto, Finland

²Insinööritoimisto FEMdata Oy
Espoo, Finland

³VTT Technical Research Centre of Finland
Espoo, Finland

Abstract

Fatigue is considered a significant long-term degradation mechanism for safety significant pressure equipment in nuclear power plants. The ASME Section III [1] procedure aims to prevent formation of fatigue cracks during the specified service period. Practical experience gathered during tens of years with hundreds of reactors has shown that the ASME methodology functions very well or is even conservative. Several studies performed in the USA and Japan indicated significant environmental effects on the fatigue as compared to fatigue without environmental effects. This has yielded a methodology as described in the NUREG/CR-6909 [2] and the JSME S NF1-2006 [17]. This methodology should obviously be applied on a best estimate fatigue analysis with reasonable safety factors. Due to the fact that such an analysis is not available and as the ASME methodology functions well this methodology is applied in conjunction with the ASME methodology. Obviously this is conservative, possibly even far overconservative.

From an analytical point of view the NB3600 (engineering approach) and NB3200 (detailed 3D analysis) fatigue analysis methodology and the one in the NUREG/CR-6909 (full time history) are not compatible. In the work presented here a methodology was developed to combine these methods.

1. Introduction

The main reasons for the ASME NB-3650M (modified) procedure development are:

- The original design-lifetime is running out and will be extended (to 60 years). Also the way the plant is run has gradually changed and this induces changes in the thermal transients. As reanalysis has to be done anyhow this was a good moment to look into the analysis methodology and include the influence of the environmental effects.

- As well for the RI-ISI procedure that is presently in use as for the coming probabilistic RI-ISI procedure it is necessary to determine the cumulative fatigue usage in such a way that cumulative usage factors are commensurate. The new fatigue analysis method is by far more commensurate as the present one.
- In the classic ASME NB-3600 procedure only scalar stress differences are used and the actual time and location of the stress in the pipe cross section is lost. To study the influence of the coolant on fatigue a procedure was developed and documented in the NUREG CR/6909. This procedure uses the change of strain over the time and is thus not compatible with the classic procedure. To enable the best possible application of this procedure it was necessary to develop a strain based transient fatigue analysis procedure where the time is all the time taken into account.
- As the operational record of the present plants in the world shows that low-cycle fatigue is not actually a problem the increase of conservatism due to the application of the NUREG CR/6909 procedure has to be partly covered by a reduction of the intrinsic conservatism in the classic NB3600 fatigue analysis procedure. To reach this goal application of a best estimate procedure is necessary. The new method is a large step into that direction.

The development, testing and validation was organized as follows:

- Method development was done by FEMdata and TVO with some involvement of VTT and FORTUM.
- Programming was done by FEMdata [7] and [8] and tested by FEMdata, TVO and VTT. For the testing the feedwater system of the Olkiluoto plants was used [10] and [11].
- A comparison was made with an Inspecta analysis [16], the latter being more simplified.
- In a Master's Thesis the method was even applied with a full 3-D volume model [12].
- The new full transient stress analysis as well as the ASME NB-3650M procedure and the results for both have been validated by VTT [3], [4] and [5].
- In order to learn more about the new methodology a mutual project was initiated between TVO and VTT to study the influence of different parameters and compare previous and present analysis results. This is reported in [18]

2. Methodology description for analysis of one cross section

The main means to achieve the goal are described below:

1. Determine the full stress/strain time history at distinct locations around the circumference and both at the inside and outside of the pipe, see Figure 1 and 2.
2. Determine the local temperatures, stresses and strains in all directions at all significant time instants. The time instants are determined based on the linearity of the parameters.
3. The tests on which the NUREG CR/6909 procedure is based were 1-D axial monotonic tests in constant temperature water. Obviously application is not straightforward as most of the stress cycles in the plant are mainly the result of temperature transients and the significant stress cycles are the results of thermal shock type of loading. These cycles have a random character as the thermal loads differ in amplitude as well as duration. To approach the NUREG test situation in the distinct locations defined above the full environmental fatigue analysis is performed separately for every requested angle φ , see Figure 1.
4. Shear stresses have been fully taken into account in the determination of the true strains. True strain is here defined as the actual deformation of the material in a distinct direction.
5. The sign of tensional and compressive stress and strain components is taken into account at all times and in all equations. In the classic ASME NB-3600 procedure the sign is lost but the sign is necessary for the NUREG CR/6909 procedure.
6. Stress indices are separately defined for all relevant stress directions and types and taken into account for the stress and strain component that is actually affected.
7. True strains are determined with analytical equations.
8. Fatigue strain cycles and associated time periods are determined with an adapted rainflow method.
9. The allowable number of cycles is directly obtained with help of the fatigue strain cycle.

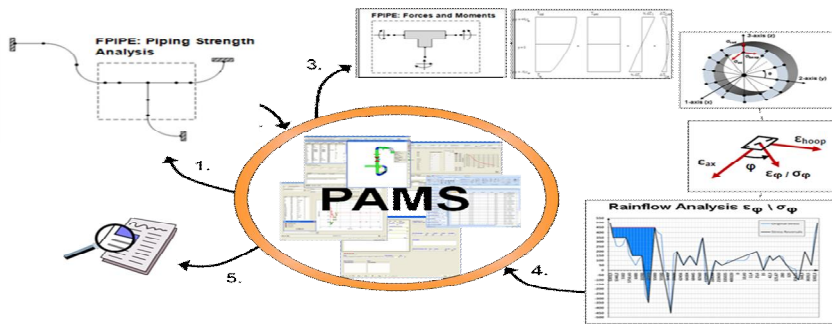


Figure 1. Work flow for the fatigue analysis.

3. Analysis of parameter settings

- In the analysis the following parameters can be set:
- Angle θ defining the number of points to be analyzed around the circumference \rightarrow circumferential output angle $0^\circ \dots 360^\circ$, default step 30° yielding 12 analyses around the circumference, see Figure 2.
- Angle φ defining the directions to be analyzed angles between the angles 0° and 90° alternatively 0° and 180° in case $\tau_{range} > 10$, default step 15° , yielding at least 6 analyses in every location, see Figure 2.
- $\Delta\sigma_{ten}$: thermal stress resolution to save analysis time, as a default no time step may yield a thermal stress change of more than 5 MPa. In case this resolution is taken too small the analysis time will increase.
- IFEN: F_{en} method choice: J1, J2, V1 and V2. These different stress (J) and strain (V) based fatigue analysis methods are later discussed in more detail. One or all methods may be selected. Method V2 is seen as the most adequate method.
- Design fatigue curve selection: ASME, ANL, or user defined (in input data).
- ϵ_{th} : threshold value for strain amplitude, default from [1] (A-8) (A-13) (A-18)
- $\epsilon_{ps_{th+}}$: strain increase to start Fen analysis, default same as for ϵ_{th}
- $\epsilon_{ps_{th-}}$: strain decrease to reset $F_{en,nom}$ to 1, default $\epsilon_{ps_{th-}} = \epsilon_{ps_{th+}}$
- SIGTOL ($\Delta\sigma_{tol}$): stress cycles with range less than $\Delta\sigma_{tol}$ omitted from fatigue analysis, default 10 MPa. In case this resolution is taken too small the analysis time will increase.
- IHIST10: (φ constant over whole analysis, results for “most severe” φ are displayed)

- 0 → the plant history is divided into load cycles and these load cycles calculated individually, usage factors (for the same φ only) are summed
- 1 → calculation over plant history, best estimate for unidirectional fatigue.

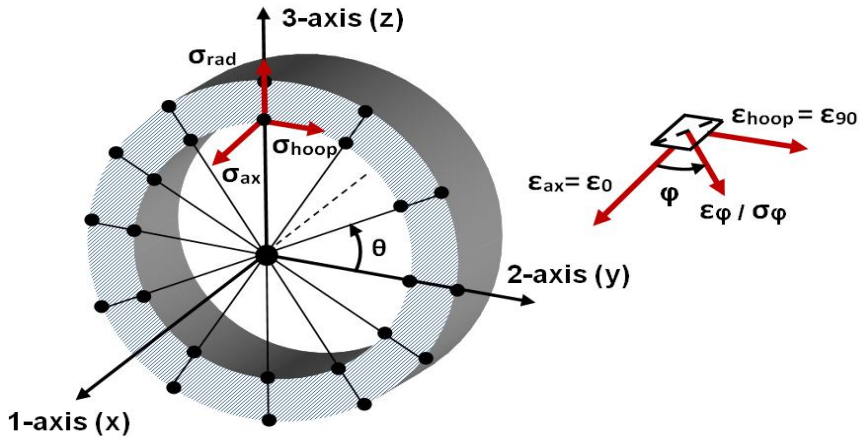


Figure 2. Discrete locations around the circumference of the node and stress/strain directions.

4. Stress analysis

In the fatigue analysis first the nominal transient stresses due to internal pressure, moments and thermal loading are separately determined because even the stress indices are defined separately for internal pressure, moments and thermal loading.

Thermal gradient induced local stresses are determined both in axial and circumferential direction:

- 1-D thermal transient solution using finite difference method.
- The temperature distribution, average temperature $T_{ave}(t)$ and thermal gradients $\Delta T_1(t)$ and $\Delta T_2(t)$ are obtained by numerical integration over the cross-section for each pipe element.

Then these nominal stresses are multiplied by the applicable stress indices in the applicable direction. Separate stress indices were defined for longitudinal and transverse welds and for the load cases internal pressure, moments and thermal loading [6]. These were defined with use of the stress indices from [2] Table NB-3681 (a)-1. For one node more sets of stress indices may be defined:

- For different locations around the circumference different sets of stress indices can be defined, see Figure 2.

- Also for different locations in the axial pipe direction different sets of stress indices can be defined.

Thus the analysis node may still be the same, but stress indices are not combined in an overconservative way. In case for instance the weld does not coincide with a transition of the cross section different analysis can be defined for these cross-sections. An example of the different sets of stress indices for one node is shown in Figure 3 below.

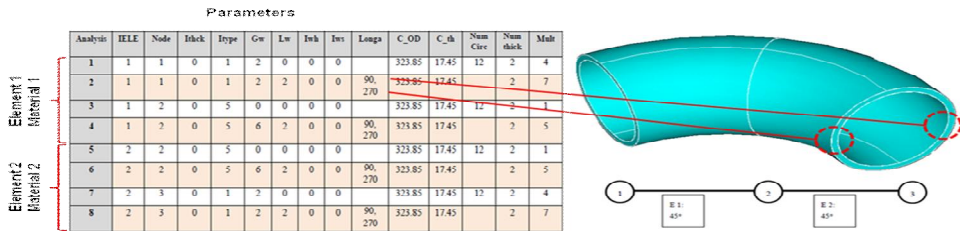


Figure 3. Definition of more than one set of stress intensity factors for one node.

After being multiplied with the stress indices the stresses are used to determine the stress time histories and strain time histories in the locations requested. In these locations the fatigue is separately determined in every direction φ , see Figure 2, with help of the following equations:

$$\varepsilon_{\varphi} = \frac{1}{2} (\varepsilon_{\text{axial}} + \varepsilon_{\text{hoop}}) + \frac{1}{2} (\varepsilon_{\text{axial}} - \varepsilon_{\text{hoop}}) \times \cos(2\varphi) + \frac{1}{2} \gamma \times \sin(2\varphi) \quad (1)$$

$$\sigma_{\varphi} = \frac{1}{2} (\sigma_{\text{axial}} + \sigma_{\text{hoop}}) + \frac{1}{2} (\sigma_{\text{axial}} - \sigma_{\text{hoop}}) \times \cos(2\varphi) + \tau \times \sin(2\varphi) \quad (2)$$

5. Rainflow method G

As a starting point both rainflow methods CEN/TC147/WG2 N23 (ISO) and ASTM E1049-85 were investigated. These methods give the same stress and strain cycles but the time information of the cycle is lost. This is a problem with regard to the application of the NUREG CR/6909 procedure that requires a strain based integration over the time. Therefore, based on the aforementioned methods, an adapted method called method G was developed, see Figure 4 below. This method is specially developed to keep track of the ranges of time that every individual stress cycle has occurred. After application of method G all stress cycles and associated time ranges. Note that one cycle can time wise have consist of more than one time range.

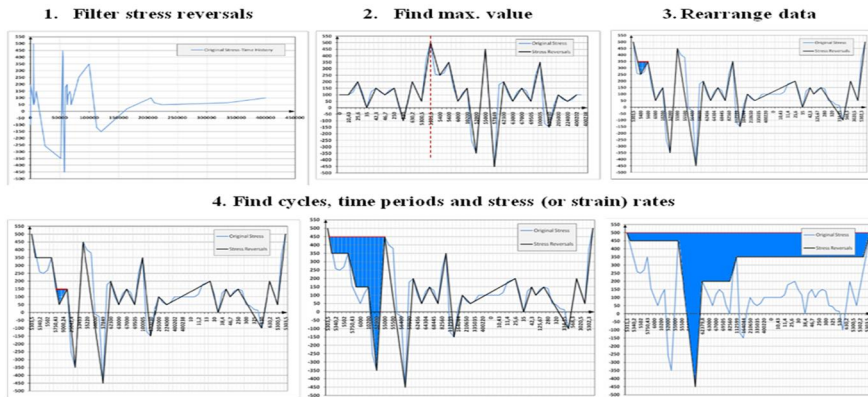


Figure 4. Adapted rainflow analysis method, method G.

6. Stress based methods J0, J1 and J2

Stress cycles are determined with the classic rainflow method CEN/TC149

- **J0:** $F_{en} = 1$, environmental effects are not taken into account.

Stress cycles and associated time steps with rainflow analysis procedure G

- **J1:** F_{en_i} is determined for the whole load cycle i and used for all of its stress cycles m . This is a conservative method.
- **J2:** $F_{en_{i-m}}$ is determined for every stress cycle m based upon the time spans from the rainflow analysis procedure G.

Table 1. Determination of S_{12} , S_{23} and S_{31} for the stress based methods J0, J1 and J2.

Strain / F_{en}	Method J1, J2 Stress intensity	Equations used in the flowchart
ϵ_j	$S_{12} = \sigma_{\varphi}$ (Inner surface and F_{en}) $S_{12} = \sigma_{\varphi} - \sigma_{\varphi+90}$ in case the sign of σ_{φ} and $\sigma_{\varphi+90}$ is different	$S_{12} = \sigma_{\varphi} (\Delta\sigma_{rad} \approx 0)$ $S_{12} = \sigma_{\varphi} - \sigma_{\varphi+90}$
ϵ_{hoop}	$S_{23} = s_{hoop} - s_{radial}$ (Same as $s_{90} - s_{rad}$)	$S_{23} = \sigma_{90} - \sigma_{rad}$
ϵ_{axial}	$S_{31} = s_{radial} - s_{axial}$ (Same as $s_{rad} - s_0$)	$S_{31} = \sigma_{rad} - \sigma_0$

7. Strain based methods V1 and V2

Strain cycles and associated time steps are determined with rainflow analysis procedure G. At present the strain based methods are used for F_{en} -analysis:

- **V1:** $F_{en,i}$ is determined for whole load cycle i and used for all of its strain cycles m . This is a conservative method.
- **V2:** $F_{en,i-m}$ is determined for every strain cycle m based upon the time spans from the rainflow analysis procedure G.

Table 2. Determination of S_{12} , S_{23} and S_{31} for the stress based methods V1 and V2.

Strain / F_{en}	Method V1, V2: Strain intensity, only when F_{en} is computed	Equations used in the flowchart
ε_{axial}	$S_{31} = \varepsilon_{axial} \times E$	$S_{31} = \varepsilon_0 \times E$
ε_{hoop}	$S_{23} = \varepsilon_{hoop} \times E$	$S_{23} = \varepsilon_{90} \times E$
ε_j	$S_{12} = \varepsilon_j \times E (\Delta\varepsilon_{rad} \cong 0)$	$S_{12} = \varepsilon_j \times E (\Delta\varepsilon_{rad} \cong 0)$

8. Determination on the F_{EN}

The following definitions are used:

- $F_{en,k}$ Instantaneous F_{en} factor ($F_{en,nom}$ in [1])
- $F_{en,r}$ F_{en} factor for strain rise r
- F_{en,φ_m} F_{en} factor for stress cycle m
- F_{en,φ_i} F_{en} factor for load cycle i .

The main steps of the F_{en} computations for the considered strain history are computation of $F_{en,k}$ values, computation of $F_{en,r}$ values and finally computation of final F_{en} values F_{en,φ_m} or F_{en,φ_i} . The instantaneous $F_{en,k}$ value for a time step k and time interval $t_1 \dots t_2$ is calculated with the NUREG/CR-6909 Appendix A Equations (A.2) ... (A.18), where:

Strain increase	$\Delta\varepsilon_k = \varepsilon_2 - \varepsilon_1$
Strain rate	$\dot{\varepsilon}_k = \Delta\varepsilon_k / (t_2 - t_1) > 0$
Inner surface temp.	$T_k = \max[T_1, T_2]$
Dissolved oxygen level	$O_k = \max[O_1, O_2]$
Sulfur content	S
For austenitic stainless steels:	$F_{en,k} = \exp(0.734 - T' O' \varepsilon')$

F_{en} for one strain rise, $F_{en,r}$ is determined from Eq. (30) [1]:

$$F_{en,r} = \sum_{k=1}^n F_{en,k}(\epsilon_k, T_k) \frac{\Delta \epsilon_k}{\epsilon_{max} - (\epsilon_{min} + \epsilon_{th})} \quad (3)$$

According to [17] the F_{en} factor for one stress cycle or for the whole load history, $F_{en,\phi}$ is calculated as:

$$F_{en,\phi,m} \text{ or } F_{en,\phi,i} = \frac{\sum (F_{en,r} \times (\epsilon_{max,r} - (\epsilon_{min,r} + \epsilon_{th})))}{\sum (\epsilon_{max,r} - (\epsilon_{min,r} + \epsilon_{th}))} \quad (4)$$

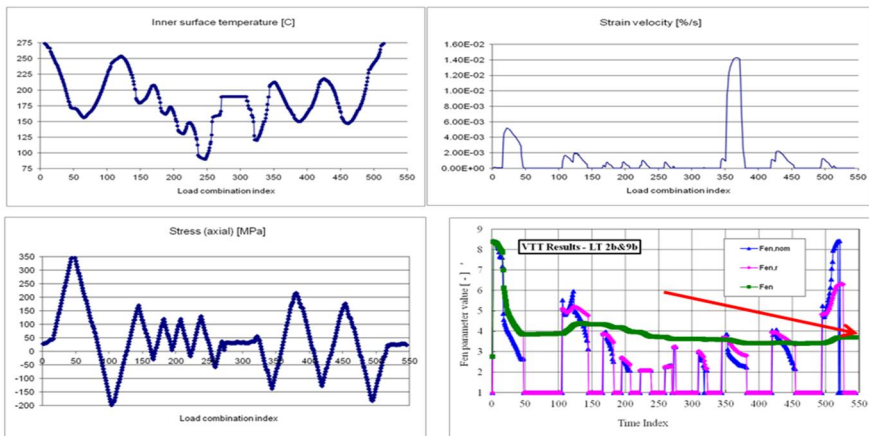


Figure 5. Determination of the F_{en} factor for method V2.

9. Fatigue curves

For the actual fatigue analysis it is possible to apply different design fatigue curves. The ASME and ANL curve, see Figure 6 below, are incorporated in the program but even a user defined fatigue curve can be entered through the indata.

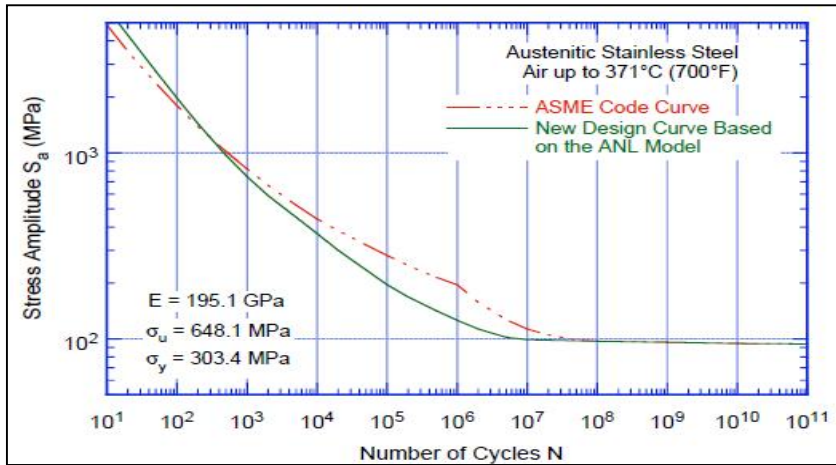


Figure 6. Examples of user selectable design fatigue curves.

10. Result presentation

Below some results are summarized for the ASME NB-3650M cumulative usage factor analysis for Node ID 69 (Weld1.312-3 9B) and for Method V2. Cumulative usage factor is calculated for each circumferential angle θ , at inside/outside surface and for direction angle φ :

```

POINT 5 MEMBER 1 NODE 2
SUMMARY OF LOCAL USAGE FACTORS ALONG CIRCUMFERENCE:
  ANGLE SURFACE USAGE FACTOR TOTAL NUMBER OF MAX RANGE FOR STRESS
  ANGLE [deg.] STRESS CYCLES [MPa] DIFFERENCE
  [deg]
    0.00 IN 0.305261 12279 994.06 S12 0
    0.00 IN 0.273361 12274 977.28 S12 15
.....
    150.00 IN 0.383262 12879 1049.90 S12 0
    150.00 IN 0.341927 12809 1031.94 S12 15
    150.00 IN 0.282664 12656 968.60 S12 30
.....
    150.00 OUT 0.067697 12266 638.44 S12 0
    150.00 OUT 0.054845 12266 606.19 S12 15
.....
LOCATION WITH MAX. USAGE FACTOR:
    150.00 IN .383262 12879 1049.90 S12 0
*** NB-3650M TOTAL USAGE FACTOR 0.383262 = Uen = U * Fen= 0.155090 * 2.47

```

```

POINT 5 MEMBER 1 NODE 2 ANGLE 150. deg., INSIDE, RADIUS 146.25 mm
LOCATION WITH MAX. USAGE FACTOR:FATIGUE FACTOR Fen CALCULATIONS V2 FOR STEEL TYPE
MCUR=12:AUSTENITIC STAINLESS NUREG/CR-6909 IDENTIFICATION OF STRESS INTENSITY S12
CYCLES BY HYSTERESIS COUNTING (RAINFLOW)Ke = ELASTIC-PLASTIC FACTOR USED WHEN RANGE
EXCEEDS 3*Sm
  LOAD SET PAIR STRESS STRESS CYCLES ALLOWABLE Ke Fen USAGE FACTORS
  INDEX INDEX RANGE CYCLES W/O FEN FEN INCREMENT CUMULATIVE
  FEN INCLUDED
    344 7346 14.68 290 99999999 1.00 1.00 0.000000 0.000000
    50 84 41.62 290 99999999 1.00 1.00 0.000000 0.000000
    307 328 96.44 290 99999999 1.00 1.00 0.000000 0.000000
.....
    5121 5160 364.62 280 143095 1.00 9.58 0.001957 0.144635
    4692 5028 1049.90 280 3045 1.00 2.59 0.091954 0.382880
    5840 5941 526.22 5 33618 1.00 1.00 0.000149 0.383028
    6629 6705 384.45 25 112363 1.00 1.00 0.000222 0.383251
    7003 7052 200.69 100 9130375 1.00 1.00 0.000011 0.383262
END OF TABLE
*** NB-3650M TOTAL USAGE FACTOR 0.383262 = Uen = U * Fen= 0.155090 * 2.47

```

Below a more detailed result listing for the ASME NB-3650M total usage factor calculation for Node ID 69 (Weld1.312-3 9B) and for Method V2: Circumferential angle $\theta = 150^\circ$, Inside surface, Stress Intensity S12, Direction angle $\phi = 0^\circ$ is presented.

The actual documentation will be made directly from the PAMS database system with a postprocessor program that is designed to fill a template report with tables, figures and pieces of text while taking care of the index and source reference lists [13], [14] and [15].

11. Future development

In the future the following items will be studied:

1. Simplify and improve the consistency in the determination of the stress intensities, as well with regard to the procedure used as to the type of fatigue testing behind the procedure.
2. Investigate the influence of the temperature used in the different parts of the different analysis steps to make the use of the temperature as consistent as possible, see Table 3 below.

3. EPRI Report [9] presents an improved approach to perform simplified elastic-plastic fatigue analysis by analytical equations. This could be incorporated into ASME NB-3650M fatigue analysis method.

Table 3. Influence of the temperature used in the different parts of the different analysis steps.

Calculation Step	Classic ASME NB-3600	ASME NB-3650M
FPIPE forces and moments	$E = E_h$: Max. T_{ave} for the transient α : T_{ave} for load case at current time	Same
1-D Thermal shock analysis (in FPIPE and ASME NB)	λ : T_{ave} C_p : T_{ave}	Same
Stress components from thermal gradients	E : At room temperature ($T_{room} = 20$ °C) α : At room temperature ($T_{room} = 20$ °C)	E : $(T_{in} + T_{out}) / 2$ α : $T_{integ_location}$ or $(T_{in} + T_{out}) / 2$
K_e factor	S_m : Max. T_{ave} for the loadset pair	Same
Design fatigue curve correction factor (E_{design} / E_c)	E_{design} : For design fatigue curve E_c : At cold state ($T_c = ?$)	Same
Stress Ratchet check	S_y : average T_{in}	Same
Discontinuity stress	E : At room temperature ($T_{room} = 20$ °C) α : At room temperature ($T_{room} = 20$ °C)	E_a : T_{ave_a} and E_b : T_{ave_b} ν_a : T_{ave_a} and ν_b : T_{ave_b} α_a : T_{ave_a} and α_b : T_{ave_b}
Fen,k	-	$T^* : \text{Max.}\{T_{in_time_1}, T_{in_time_2}\}$
Strain ϕ	-	E : $(T_{in} + T_{out}) / 2$ ν : $(T_{in} + T_{out}) / 2$
Stress Intensities	-	E : $(T_{in} + T_{out}) / 2$

12. Conclusions

The system is now taken into use and compared with elder analyses without Fen. The increase of the cumulative usage is moderate but is very much depending on the chosen analysis method. The best method is method V2. This is a consistent strain based method that determines the Fen for every separate strain cycle. Comparison between the classic method and the V2 method showed that increase appears only in a few locations. The number of performed analyses is however not yet large enough to draw any general conclusions. It seems that the extra over-conservatism induced by the NUREG/CR-6909 is mostly compensated by the more accurate and less overconservative analysis by the new methodology. When looking at the low cycle fatigue induced crack records in the nuclear world this is a good thing.

References

1. Chopra, O. K. & Shack, W. J. Effect of LWR Coolant Environments on the Fatigue Life of Reactor Materials. NUREG/CR-6909, Final Report. U.S. Nuclear Regulatory Commission (NRC), February 2007.
2. ASME Boiler and Pressure Vessel Code Section III, Division 1, Article NB-3600. 2004 Edition.
3. Cronvall, O. Validation of Fatigue Analysis Procedure NB-3650M. Espoo, VTT, 2010. VTT-R-06000-10, Rev. 0, 28.12.2010.
4. Cronvall, O. Validation of Fatigue Analysis Procedure NB-3650M. Espoo, VTT, 2012. VTT-CR-00467-12, Rev.1, 16.1.2012.
5. Cronvall, O. OL1 and OL2 – Piping Component Analyses: Stress Analysis Procedure and Input Data Treatment. Espoo, VTT, 2011. VTT-R-03375-11, Rev. 2, 6.5.2011.
6. Komulainen, E. OL1/OL2, Evaluation of stress indices for class 1 piping analyses. SWECO Industry Oy, 2013. OL1-TVO-ASME-STRESS-INDICES, Rev. 3, 15.4.2013.
7. GS-FDT-TVO-ASMENB-110927, FEMdata Oy, FPIPE ASME Postprocessor, Reference Manual.
8. GS-FDT-TVO-ASMENB-110505, FEMdata Oy, FPIPE ASME Postprocessor, User Manual.
9. Carter, R. An Improved Approach for Performing Simplified Elastic-Plastic Fatigue Analysis. EPRI, October 1998. EPRI-TR-107533.
10. Transient analysis report for the 312/327/321 system.
11. Fatigue analysis report for the 312/327/321 system.
12. Lemettinen, P. Automatic Detailed 3-D Fatigue Analysis of Structural Parts in a Piping System. TVO, 2011. RP-TVO-TVO-T0360-110224, Rev. 1, 2.9.2011.
13. Valo, J. Engineering thesis, BA-TVO-VALO-PAMS-100901, Rev. 0, 1.9.2010, TVO, Dokumentaatioautomaatti.
14. Santamaa, S. Engineering thesis, BA-TVO-SANT-PAMS-111006, Document maker.

15. Santamaa, S. TVO. Document maker user manual.
16. Strömbro, J. Evaluation of the Technical Basis for New Proposals of Fatigue Design of Nuclear Components. Stockholm, Sweden, Strålsäkerhetsmyndigheten, 2011. SSM 2011:4.
17. JSME S NF1-2006, Rev. 0, 1.3.2006, The Japan Society of Mechanical Engineers, Codes for Nuclear Power Generation Facilities – Environmental Fatigue Evaluation Method for Nuclear Power Plants.
18. Chauhan, M. Computational sensitivity analysis on environmental fatigue. Espoo, VTT, 2013. VTT-R-00618-13, 27.1.2013.

Weld repair simulation for the Mock-up 2 of EU FP7 STYLE Project

Heikki Keinänen

VTT Technical Research Centre of Finland
Espoo, Finland

Abstract

The Mock-up under study is fabricated of austenitic stainless steel with additions of vanadium and niobium to increase its high temperature strength. The Mock-up comprises two pipes welded together to produce a pipe section of 600 mm overall length. After completion of the girth weld, deep weld repair was inserted into the girth weld.

Abaqus finite element code was utilised in the welding simulation. Part of the input data was generated with in-house codes. Sequential thermal and mechanical analyses were performed with small strain and displacement formulation. In the mechanical analysis, mixed hardening material model and an anneal temperature of 1100°C was assumed. Symmetry conditions were utilised to reduce the size of the model.

The comparison of computed and measured temperatures and stresses shows good agreement. The computed hoop stress at the repair mid-length was higher than axial stress. Both stresses were tensile through the wall thickness. Confidence in the results was also gained as the results were compared to those presented in literature for a repair welding case.

1. Introduction

This work belongs to the computation round robin exercise as part of the EU FP7 STYLE project, which concentrates on predicting the start of life stress state after weld repair. The overall objective of STYLE is to assess, optimize and develop the use of advanced tools for the structural integrity assessment of reactor coolant pressure boundary (RCPB) components relevant to ageing and life time management of nuclear power plants and to integrate the knowledge created in the project into mainstream nuclear industry assessment codes.

The range of assessment tools considered will include those for assessment of component failure by advanced fracture mechanics analyses validated on small and large scale experiments, quantification of weld residual stresses by numerical analysis and by measurements, stress corrosion crack initiation/growth effects and assessment of RCPB components (excluding the reactor pressure vessel) under dynamic and seismic loading.

Based on theoretical and experimental results, performance assessment and further development of simplified engineering assessment methods will be carried out considering both deterministic and probabilistic approaches. Integrity assessment case studies and large scale demonstration experiments will be performed on Mock-ups of safety-relevant components. These will include a repair weld in an aged butt-welded austenitic pipe, a dissimilar metal narrow gap TIG weld (following the EPR design) and a clad ferritic pipe. Moreover experiments on specimens and feature test pieces will be carried out to support the large scale Mock-up analyses.

The Mock-up 2 being studied in this paper is fabricated of austenitic stainless steel (Esshete 1250). The initial data and details are given in [2]. The Mock-up represent a part of the heat exchanger of advanced gas cooled (AGR) reactor although the dimensions of the Mock-up are less than in the real component.

The Mock-up comprises two equal lengths of pipe with an outer diameter of 180 mm and a wall thickness of 35 mm. The pipes are joined by a manual-metal-arc (MMA) butt weld using Esshete 1250 consumables, to produce a pipe section of 600 mm of overall length. After completion of the girth weld, the weld cap is dressed smooth and a short, deep weld repair is inserted into the girth weld again using MMA techniques. The repair weld cap is then dressed. The completed Mock-up 2 is shown in Figure 1 [2].

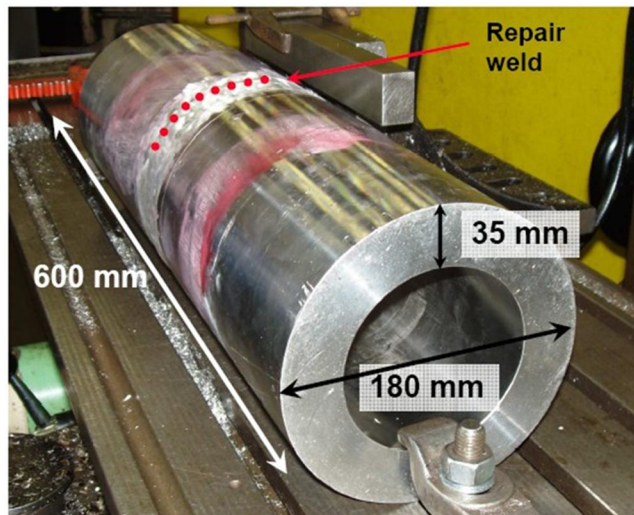


Figure 1. The overall geometry of the examined Mock-up 2 [2].

The girth welds were made using manual tungsten-inert-gas-arc welding (TIG) for the root and first fill passes, and MMA for the remaining passes. A total of 23 passes were deposited for the examined Mock-up, including 3 capping passes. The basic weld parameters and girth welding sequence are presented in [2]. The

repair weld was made using MMA welding for all passes. During the in-fill welding, a large number of short weld length runs were deposited in order to maintain a constant weld layer height.

2. Description of the analysis procedure and the models

Abaqus 6.11-1 general purpose FE code [1] was utilised in the computation. Sequential thermal and mechanical analyses were performed with small strains and displacements assumed. In the mechanical analysis, mixed hardening material model of Abaqus including both isotropic and kinematic hardening with an anneal temperature of 1100°C [2] was used. The input data for Abaqus were generated with in-house codes, see the flowchart Figure 2.

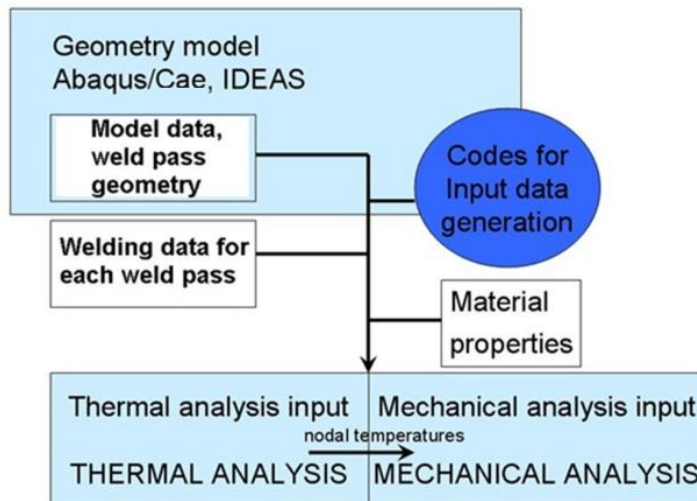


Figure 2. Flowchart of the applied analysis procedure.

Although the real component is not exactly symmetric (repair welding is not located exactly at the centre of the girth weld), symmetry conditions were assumed to reduce the size of the model. Half of both the length and circumference of the structure was modelled with appropriate symmetry boundary conditions. The 8-node brick elements with reduced integration (Abaqus [1] element type C3D8R in mechanical analysis, element type DC3D8 in thermal analysis) were utilised. Additional dummy elements were doubled upon the structural elements used in the weld area. These dummy elements were modelled with low elastic modulus and material strength properties. The dummy elements were needed to track the accumulated deformation of the nodes, which are not yet active in the model. Otherwise the computed deformed shape would be highly distorted. The dummy elements were not present in thermal analysis.

Figure 3 shows the geometry of the repair weld. The geometry is based on the information given in [2]. Finite element model of the repair welding is shown in Figure 4 with boundary conditions. The model parts having incompatible meshes were joined together with the tie option available in Abaqus [1]. The tied surfaces were considered to be sufficiently far away from the areas of interest to prevent the tie from influencing the results.

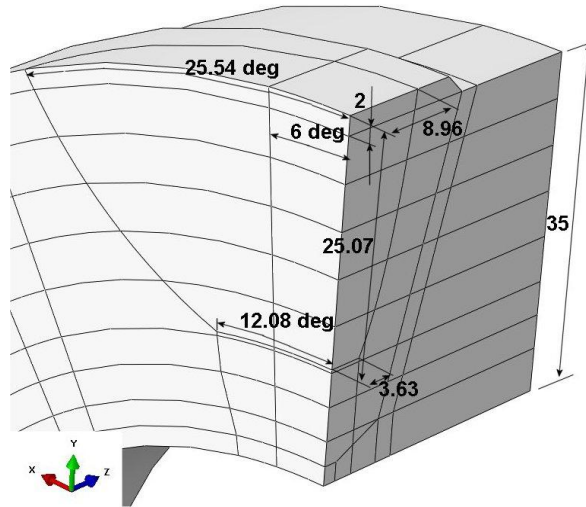


Figure 3. The geometry of the weld repair, dimensions in mm.

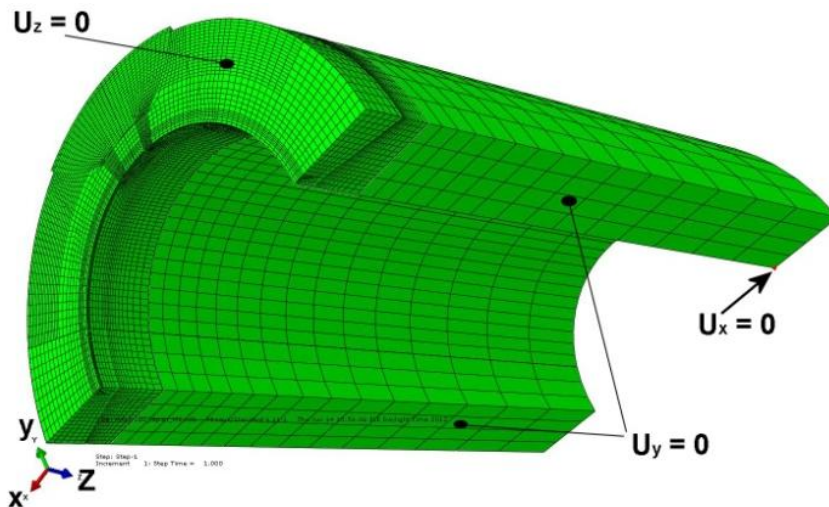


Figure 4. FE model of the repair welding with boundary conditions.

The analysis started from the girth welding stage, thus the quenching performed prior to welding was not modelled. The analysis sequence is presented as follows:

- Thermal analysis of girth welding. Model change option of Abaqus [1] was utilised to add the weld elements to the model as the welding torch proceeds. Thus moving weld torch was modelled (this is not a block dumping procedure);
- Mechanical analysis of girth welding. Temperatures were read from the thermal analysis results and used with structural elements to measure the mechanical response to the changing temperature. The model change option of Abaqus was utilised to add the weld elements to the model as the welding torch proceeds similarly to the thermal analysis. Additional double (soft) elements were used in the weld area to track the deformations;
- Restart of the mechanical analysis. Weld cap dressing was performed by removing the cap elements.
- Thermal analysis of repair welding. Model change option of Abaqus [1] was utilised to add the weld elements to the model as the welding torch proceeds;
- Mechanical analysis of repair welding.

The final stress state from the girth welding was incorporated to the repair weld model using the map solution option of Abaqus. The map solution option was utilised to transfer the girth welding results to the new repair weld mesh. If the repair geometry would have been included already in the mesh related to the girth welding, the mesh would have been highly distorted. The results before and after mapping were compared to estimate the validity of the stress results after mapping.

In the thermal analysis the welding data provided in [2] was utilized. Pass lumping was performed between the first passes. A trapezoidal idealisation of each weld bead was adopted to minimise the model size and simplify the construction of the FE mesh. Figure 5 shows the modelled repair welding process sequence.

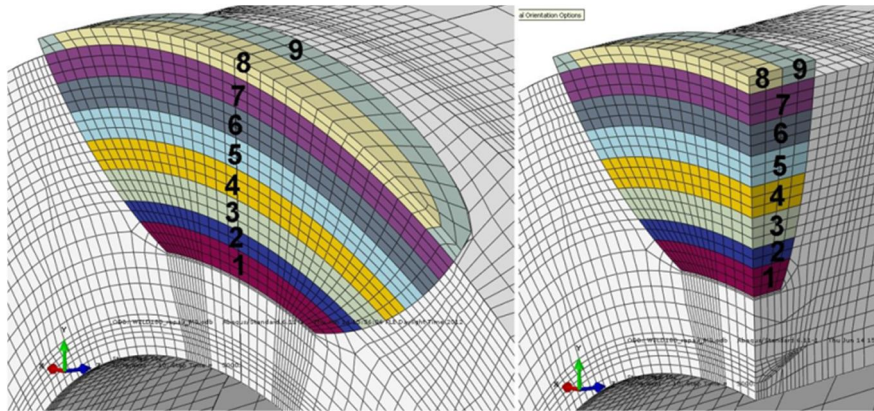


Figure 5. The welding process sequence in the FE analysis of the repair welding.

In the thermal analysis the heat input was modelled using uniform internal heat generation and an exponential time function. The length of the time function was approximately chosen so, that the length of the heat input area was approximately 12–15 mm. In addition, the initial temperature of 1400°C of the weld material was assumed.

Concerning surface heat losses, convection was modelled using the coefficient value of 100 W/m²K. The ambient temperature was 20°C. No heat losses from weld pool were modelled. Radiation was not modelled. The analysis was carried out in such a way, that the given interpass temperatures were obtained. This required some iterative analyses.

The mechanical analysis starts at the ambient temperature of 20°C, which is also assumed to be the stress-free temperature.

3. Results

The computed fusion zone is shown in Figure 6 for the repair welding. The predicted areas of melted parent/weld substrate and fusion zone shapes were judged to be consistent with expected fusion boundaries for the weld pass heat inputs, despite the somewhat crudely layered trapezoidal weld bead idealisation in the FE model. A more quantitative assessment of the weld simulation heat input model will be performed once the test component has been destructively examined and a cross-section of the weld etched to reveal the fusion zone patterns.

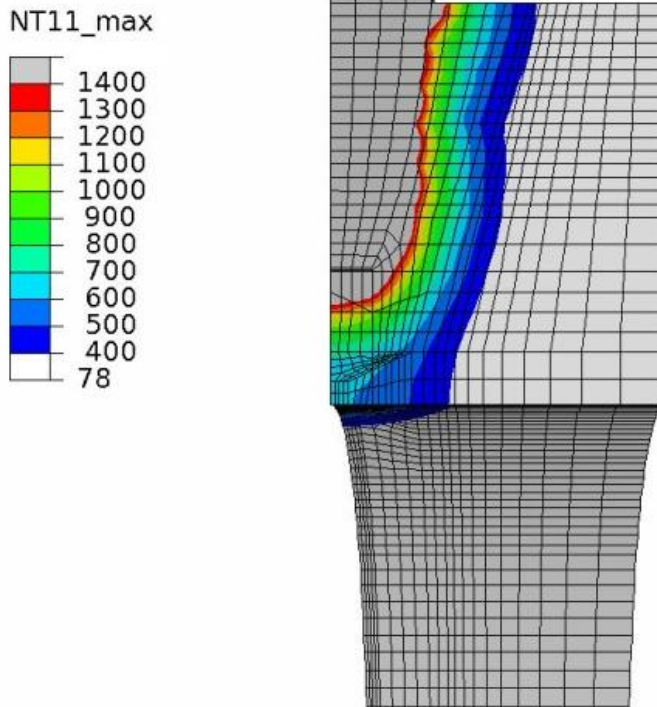


Figure 6. The computed fusion zone after the repair welding at the middle of model circumference.

The computed length of the molten pool was approximately 16–20 mm. Comparison of the computed and measured [2] temperatures is shown in Figure 7. The results are shown for the weld pass 18. The comparison shows good agreement between the computed and measured temperatures. Figure 8 shows computed temperature distribution during repair welding.

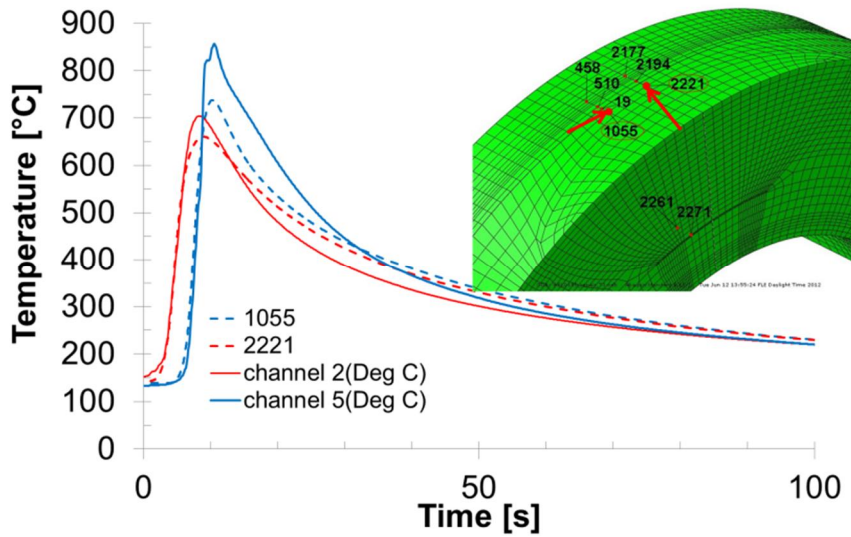


Figure 7. The computed and measured [2] temperatures at two locations during girth welding (pass 18).

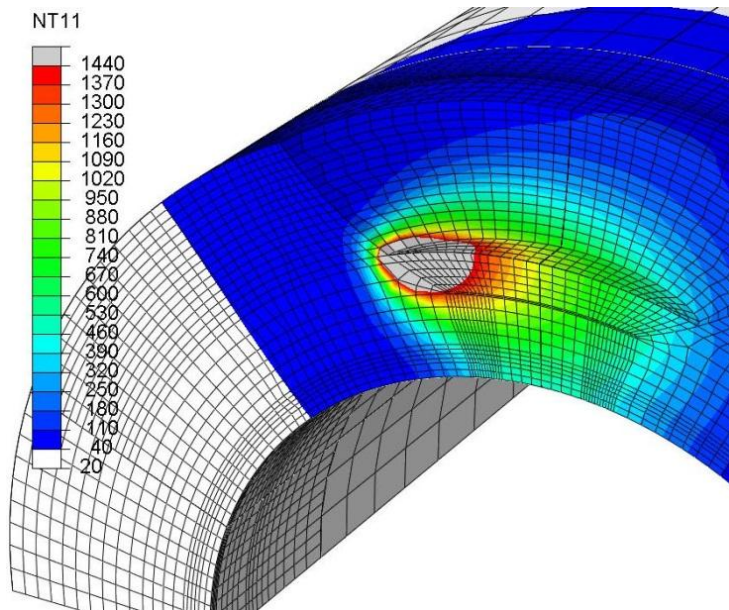


Figure 8. The computed temperature distribution (°C) during repair welding.

Figure 9 shows the computed through wall stress components after the girth welding at the middle of the model circumference at the symmetry plane (middle of the weld).

The computed through wall stress components after the repair welding at the middle of the model circumference at the symmetry plane (middle of the weld) are shown in Figure 10. The highest stresses occur in the circumferential (hoop) direction.

Figure 11 shows the computed circumferential stress distribution after the repair welding. The computed circumferential stresses along the shown trough-wall lines are presented in Figure 12. Figure 13 shows comparison of computed and measured residual stresses in the middle of the repair weld.

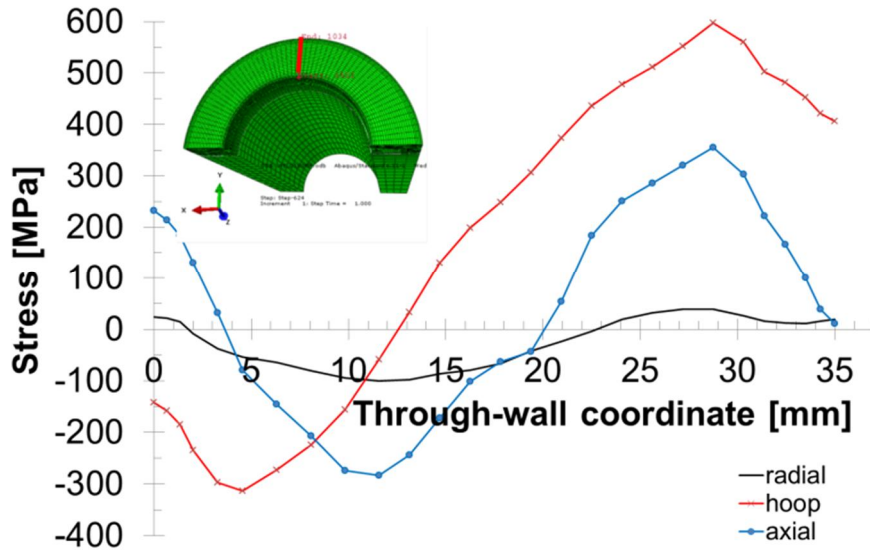


Figure 9. The computed through wall stress components after the girth welding at the middle of the model circumference at the symmetry plane. The origin is at the inner surface.

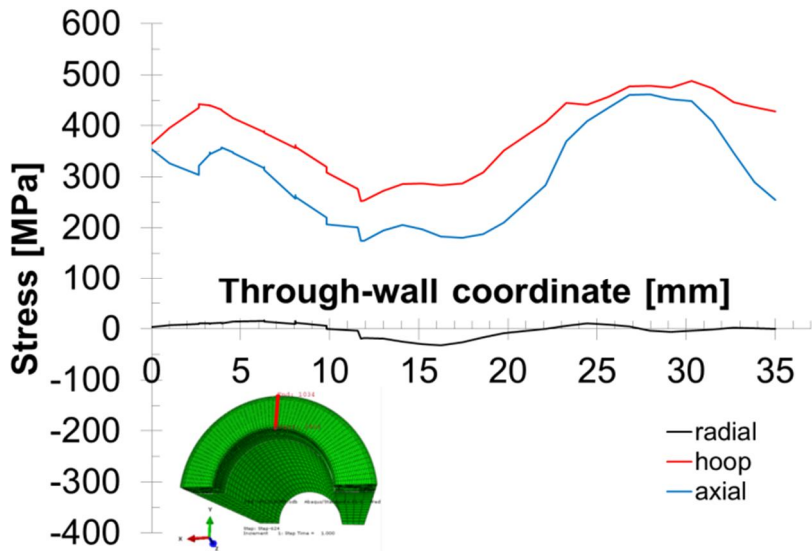


Figure 10. The computed through wall stress components after the repair welding at the middle of the model circumference at the symmetry plane (middle of the weld). The origin is at the inner surface.

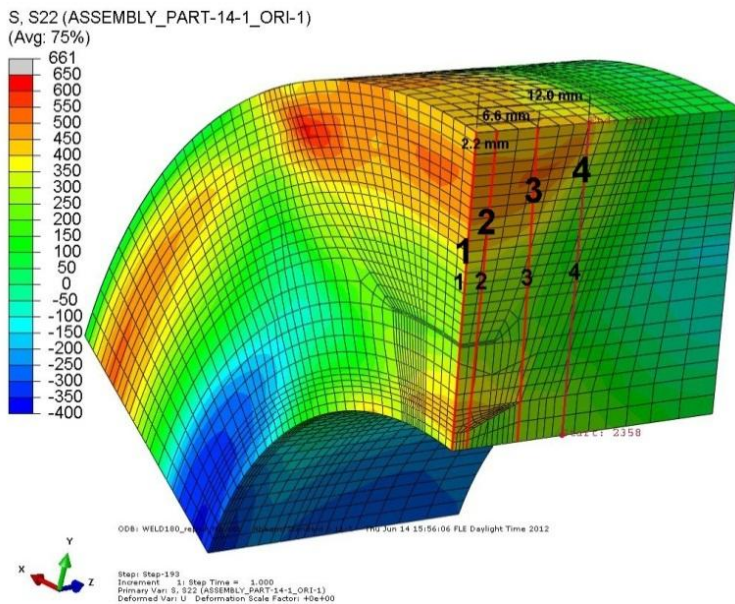


Figure 11. The computed circumferential (hoop) stress after the repair welding distribution [MPa]. The trough-wall lines for results presentation are shown. The origin of the stress presentation lines is at the inner surface.

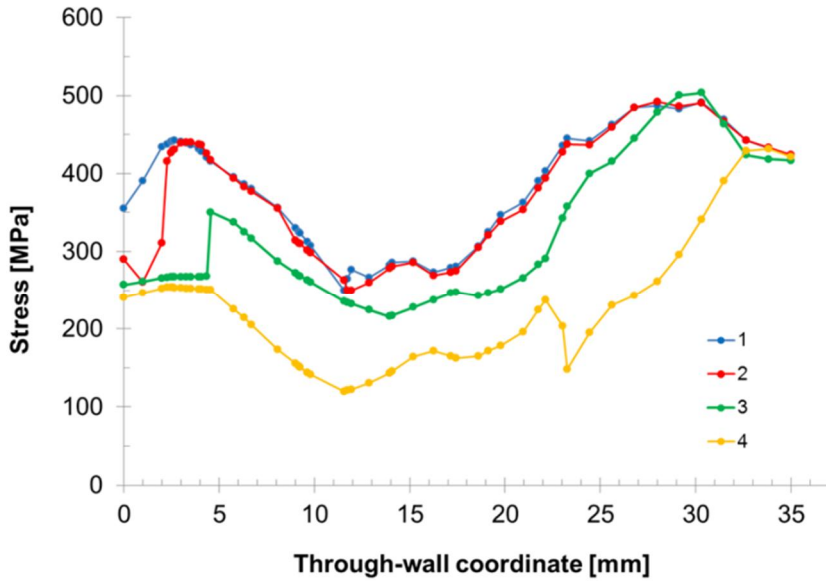


Figure 12. The computed circumferential (hoop) stresses along the through-wall lines shown in Figure 11, with origin at the inner surface.

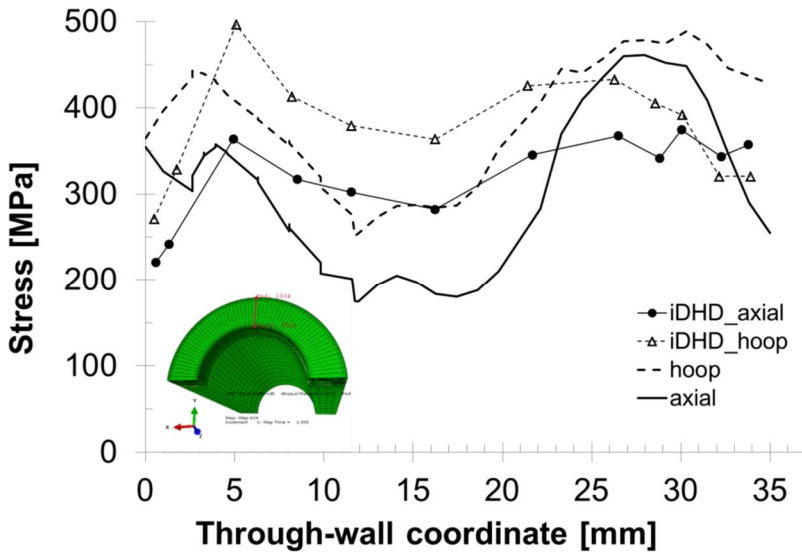


Figure 13. The computed and measured (incremental deep hole drilling, iDHD) [4] through-wall stresses after repair welding in the middle of the weld. Origin is at the inner surface.

4. Discussion

Preliminary computations were performed with a model having a 135 degree of the circumference of the Mock-up component. On the basis of the results, the repair welding cavity and the repair welding changed the stress state at the model boundaries. Thus, a model with a 180 degree circumference was constructed and utilized in the actual computation.

In the present computation, symmetry was assumed with respect to the girth weld centreline. This was also assumed to be the repair weld centreline. On the basis of preliminary comparison between computed and measured stresses these assumptions seem to be reasonable.

In [3] a three dimensionally computed repair welding simulation is presented. In this case the cylinder outer diameter was 432 mm (180 mm in the STYLE case) and wall thickness 19.6 mm (35 mm in the current case). The girth welding phase was ignored and block dumping method was utilized in the welding analysis. There was a rather large difference between the computed and the measured stresses in the case of the longer repair, which is comparable to the current case. The results demonstrated that, experimentally, the tensile hoop stress at the repair mid-length was higher than axial stress. The computational results of the current case presented in this paper show a similar behaviour.

5. Conclusions

The primary objective of the WP2.2 simulation round robin of the STYLE project is to provide accurate predictions of weld residual stresses concerning Mock-up 2, and to compare the predictions with residual stress measurements made using the deep hole drilling and high energy X-ray diffraction within STYLE work package 1.

This work, belonging to the computation round robin, concentrates on predicting the start of life stress state after weld repair.

The Mock-up 2 under study is fabricated of austenitic stainless steel (Esshete 1250) with additions of vanadium and niobium to increase its high temperature strength. The Mock-up comprises two equal lengths of pipe with an outer diameter of 180 mm and wall a thickness of 35 mm, which were welded together to produce a pipe section with 600 mm of overall length. After the completion of the girth weld deep weld repair is inserted into the girth weld. Abaqus 6.11-1 general purpose FE code [1] was utilised in the simulation of the welding. Part of the input data for Abaqus was generated with in-house codes.

The computed fusion zones and comparison of the computed and measured temperatures at selected locations are presented. The computed residual stresses after the girth and repair welding are presented and the results were discussed. The comparison between measured and computed temperatures and stresses show good agreement.

Acknowledgments

This work was a part of the EU granted project “Structural integrity for lifetime management – non-RPV components (STYLE)”. In addition to EU this work was also partly funded by VTT. The work was a part of the Work Package 2.2 of the STYLE project. The primary objective of the WP2.2 simulation round robin is to provide accurate predictions of weld residual stresses concerning a Mock-up and to compare the computational and experimental results against each other.

References

1. Abaqus Theory Manual, version 6.11-1. Dassault Systemes, 2011.
2. STYLE Mock-up 2 finite element simulation protocol. Issue 1, 23rd June 2011. Prepared by M. C. Smith. (project internal report).
3. Elcoate, C. D., Dennis, R. J., Bouchard, P. J. and Smith, M. C. (2005). Three dimensional multi-pass repair weld simulations. *International Journal of Pressure Vessels and Piping*, 82(4), pp. 244–257.
4. <http://style.jrc.ec.europa.eu/index.php>, to be published.

Fracture mechanical characterisation of ferrite-austenite dissimilar metal welds (DMWs) for elevated temperature service in view of metallurgical mis-match

Pekka Nevasmaa¹, Petra Holmström³, Päivi Karjalainen-Roikonen¹,
Teemu Sarikka², Matias Ahonen¹, Roman Mouginot², Ulla Ehrnstén¹,
Anssi Brederholm², Pertti Aaltonen¹ & Hannu Hänninen²

¹VTT Technical Research Centre of Finland
Kemistintie 3, 02150 Espoo, Finland

²Aalto University School of Engineering, Department of Engineering Design and
Production
Puumiehenkuja 3, 02150 Espoo, Finland

³Teollisuuden Voima Oyj
Olkiluoto, 27160 Eurajoki, Finland

Abstract

A characteristic feature of dissimilar metal weld (DMW) is the metallurgical and material property *mis-match* resulting from a steep gradient of microstructures with significantly different strength and toughness properties. This *mis-match* inevitably affects the entire failure behaviour of DMWs under external operational loads, not only from crack initiation standpoint, but especially regarding the development of crack driving force accentuating *crack path deviation* and subsequent crack growth. The determination of relevant *fracture toughness properties* for all the different microstructural regions of the DMW is of utmost importance for successful structural integrity and lifetime analyses. This paper deals with experimental material characterisation of two configurations of ferrite (SA508)–austenite (Type 304/316) DMWs made using (i) a beveled V-groove and Alloy 82/182 filler metal with a buttering layer and (ii) a narrow-gap weld and Alloy 52 filler metal without any buttering. Results of hardness surveys and fracture mechanical (J-R curve) tests are presented and analysed. The role of mis-match (i.e. metallurgical constraint) in e.g. promoting sudden crack path deviations is discussed in the light of detailed *post-test sectioning metallography and specimen fractography* identifying the actual crack initiation and propagation path.

1. Introduction

Dissimilar metal welds (DMWs) are widely used in high-temperature operating components, especially nuclear power plants (NPPs) to join the ferritic steel nozzles of reactor pressure vessels, steam generators and pressurizers to the austenitic stainless steel pipes using a safe-end. DMWs have been found susceptible to environment-assisted cracking (EAC) in boiling water reactor (BWR) conditions where their microstructures and prevailing residual stresses/strains affect the EAC susceptibility [1]. DMWs are also used in primary water systems of pressurised water reactors (PWRs) [2] where nickel-base filler metal DMWs have been found to suffer from the stress corrosion cracking susceptibility in primary water conditions (PWSCC) [3–7]. The operating experience of major NPP pressure boundary components has recently shown [3, 4, 7] that DMW joints can markedly affect the plant availability and safety because of increased incidences of EAC and PWSCC of Alloy 600 and corresponding nickel-base weld metals, such as Alloys 182/82. All-weld metals of Alloy 182 and 82 had been found clearly more susceptible to EAC than all-weld metals of Alloy 152 and 52 which hardly show any crack initiation susceptibility in e.g. doped steam conditions [5–7]. The selection of new welding methods and materials relies mainly on laboratory results and short-term service experience. Their long-term behaviour and performance in the plant has still to be demonstrated [7].

A characteristic feature of DMW is the metallurgical and material property *mis-match* resulting from a steep gradient of abruptly changing narrow microstructural zones with significantly different strength and toughness properties across the weld between two physically different materials. This results in substantial *metallurgical mis-match* which inevitably affects the entire failure behaviour of DMWs under external operational loads, not only from the crack initiation standpoint, but especially regarding the development of *crack (growth) driving force*, subsequent *crack growth behaviour* and development of *metallurgical (local plastic) constraint* that can accentuate *crack path deviation* [8–10]. The strength mis-match between different materials and/or microstructural regions produce different local plastic constraints which will further affect the distribution and magnitude of *local stress triaxiality* and *plastic strain* ahead of the crack tip locating at the interface [2]. Irrespective of the existence of the original flaw or defect in a weld, the actual damage formation can therefore occur and escalate in a neighbouring microstructure [8, 9], see Figure 1. This, in turn, tends to manifest itself as *irregular crack front shape* of a propagating crack, which is another characteristic feature of DMWs.

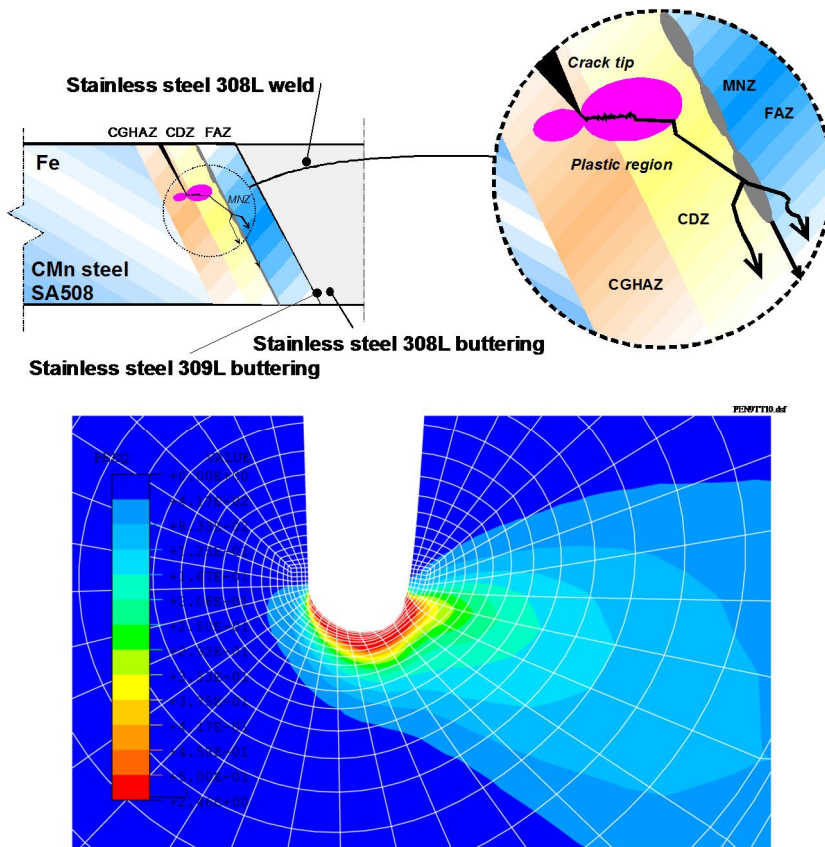


Figure 1. Schematic illustration of microstructures and finite element results for equivalent plastic strain of the failure micromechanism associated with ductile crack growth in a DMW: ferritic SA508 and austenitic 304 base materials, overlaid 309L buttering (1st layer), 308L buttering (rest) and 308L weld metal [9].

Earlier work have shown [8–12] that *unstable crack growth* can occur *after initially ductile initiation* in the fusion boundary/near interface zone (NIZ) of a DMW comprising Ni-enriched buttering and austenitic weld metal. Rather than the presence of a single ‘weak’ region, a combination of several adjacent micro-structures: the *carbon depleted zone (CDZ)* in the ferritic coarse-grained HAZ immediately adjacent to the interface, the *weld interface* with discontinuous *martensitic regions (martensitic narrow zone, MNZ)* and the *fully austenitic region (FAZ)* in the 1st buttering layer, all with mismatching mechanical properties, was found responsible for unstable crack growth [8, 9] cf. Figure 1. In small-scale SE(B) fracture toughness tests, critical conditions were met when a crack located at the interface of two regions, of which one exhibited plastic behaviour while the other still behaved practically linear-elastically. In the case of DMWs, *constraint due to microstructural*

inhomogeneity is thereby argued to play a more essential role in the fracture process than geometry-induced constraint [8, 9, 12]. The combination of (i) *stress triaxiality* (i.e. geometrical constraint) and (ii) un-symmetric *plastic strain* (due to concentration of local deformation into the lower-strength microstructure cf. Figure 1) are considered as the principal (crack) driving force for damage formation and ductile fracture event in DMWs. Thus, the significance of mis-match can be related to the failure behaviour of 'brittle' constituents as an increase in constraint (if linear mismatch is concerned), and the localised deformation experienced by the softer regions and the resulting compatibility requirements set to the harder microstructures (in the case of elastic-plastic mismatch). A notch (or crack-like defect) at the interface of two materials, of which one exhibits plastic behaviour that affects crack tip plasticity development, while the other still behaves practically linear-elastically was hence concluded to represent the worst mismatch scenario in terms of structural integrity [8, 9, 12].

Regarding metallurgical design and fabrication welding, there are certain recent development trends that need to be taken into account in view of structural design and integrity assessment of NPP multi-metal components. New high-chromium ($\approx 30\%$) nickel-base filler metals such as Alloys 52, 152 and 52M with high PWSCC resistance are extensively used to replace former Alloy 82 and 182 in fabrication of new PWRs, as well as for repair and replacement of the affected thick-section components in existing NPPs [2]. Simultaneously, advanced welding processes such as narrow-gap (narrow groove) methods (NGW) have been introduced as gas-tungsten arc welding (GTAW) of thick section components including DMWs for safe-ends made without any buttering layer. All these changes inevitably require mastery of the existing correlations and known relationships between the mixing (dilution) of the base material, the compositional gradients of alloying elements, the resulting microstructures and damage and failure phenomena in DMWs. The distribution of alloying elements, characteristics and widths of microstructural zones and the gradient of mechanical properties in the near interface zone (NIZ) of a narrow-gap Alloy 52/152 weld without any buttering can therefore be expected to differ to some extent from a conventional V-groove Alloy 82/182 weld with a buttering layer.

The determination of relevant *fracture toughness properties* for the various microstructural zones of DMW requires accurate positioning of the pre-fatigued crack in order to sample and hit the desired microstructure. This can be very difficult because of the curvature of the fusion boundary, as well as of the tendency for sudden crack path deflection towards another microstructural region after an inherently ductile initiation event. Obtaining relevant zone-specific strength and toughness based material properties experimentally hence requires the use of *miniature or small-size specimen techniques*. Earlier work have shown [8–12] that even in the case of essentially ductile fracture behaviour, the recorded fracture resistance curve can vary a lot depending on the true position of the pre-fatigued crack and the subsequent crack growth path within the DMW. Among the different weld regions, the fusion boundary/NIZ tends to exhibit the lowest toughness in terms of ductile initiation and tearing resistance. Careful and detailed *post-test*

sectioning metallography and specimen fractography are hence an absolute necessity to identify the actual crack initiation site and propagation path in order to relate the obtained fracture toughness value to the correct weld microstructural zone.

For the moment, no standards are available to assess the structural integrity of DMW components. Moreover, there are no standards for materials testing of DMWs either. Ensuring safe service of a DMW component therefore requires complete strength and fracture toughness based information from all microstructural zones of a DMW. Their true stress-strain behaviour and local fracture resistance and crack growth behaviour should be experimentally investigated and underlying characteristics understood. This paper deals with experimental material characterisation of two configurations of ferrite (SA508)–austenite (Type 316) DMWs made using (i) a beveled V-groove and Alloy 82/182 filler metal with a buttering layer (denoted as BWR type) and (ii) a narrow-gap weld (NGW) and Alloy 52 filler metal without any buttering (denoted as PWR type).

2. Materials and experiments

BWR type – A weld mock-up representing the DMW in the safe-end nozzle of BWR reactor pressure vessel (RPV) was manufactured for the experimental determination of the narrow local strength variations in the DMW. The weld consisted of SA508 pressure vessel steel with Type 309L/308L cladding and Type 304 piping steel, an Alloy 182 buttering layer welded perpendicular to the base material surface, and Alloy 82 and 182 weld metals. The dimensions and materials of the weld are presented in Figure 2.

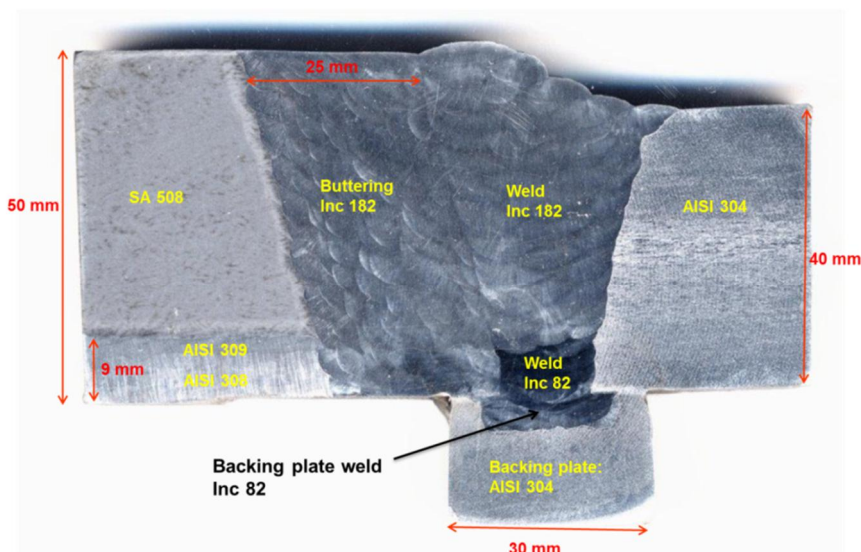


Figure 2. Cross-section macrograph of the finished BWR type DMW weld [1].

The experimental program is described in more detail in Ref. [1]. The strength mismatch state was determined with tensile tests using both miniature and standard size tensile specimens allowing also measurement of the local tensile properties of the narrow zones of the DMW. Special attention was paid to the fusion boundary/interface between SA508 steel and Alloy 182 buttering; this area was characterized using micro- and nanohardness testing. The microhardness profiles of the as-welded (AW) state DMW were made in three lines from the buttering across the interface and the HAZ into the ferritic steel. The distance between the indentations was 0.5 mm and the indentation weight was 300 g (HV0.3). In addition, nano-indentation measurements for the AW state sample, sample aged at 605°C for 6 h and at 605°C for 24 h (denoted as PWHT), were performed at a distance of 0.35 mm. Fracture mechanical tests were performed on two different size SE(B) specimens in the PWHT condition. Miniature size, 5 x 10 x 55 mm, specimens were extracted with the initial crack at the fusion boundary/interface (FL) and at the FL+1 mm into the ferritic steel HAZ. Large size specimens, 10 x 20 x 100 mm, were extracted with the initial crack located in the middle of the buttering, at the FL and FL+2 mm into the ferritic steel HAZ. Tests were performed at room temperature and the fracture resistance (J-R) curves were determined for the different weld zones to examine the effect of local strength mismatch on the fracture behaviour.

PWR type – The welded mock-up represents new design for RPV nozzle/safe-end weld in modern PWR design. The weld was made using a narrow-gap configuration between the ferritic SA508 and austenitic Type 304 steels (the former clad with over alloyed Type 309L filler for the 1st layer and the 2nd layer using Type 308L) and without any buttering layer. The applied welding technique was narrow-gap (NG) GTAW using Alloy 52 as a filler metal and mixture of 70% He + 30% Ar as shielding gas. The dimensions and configuration of the NG-GTAW weld (NG-DMW) are presented in Figure 3.

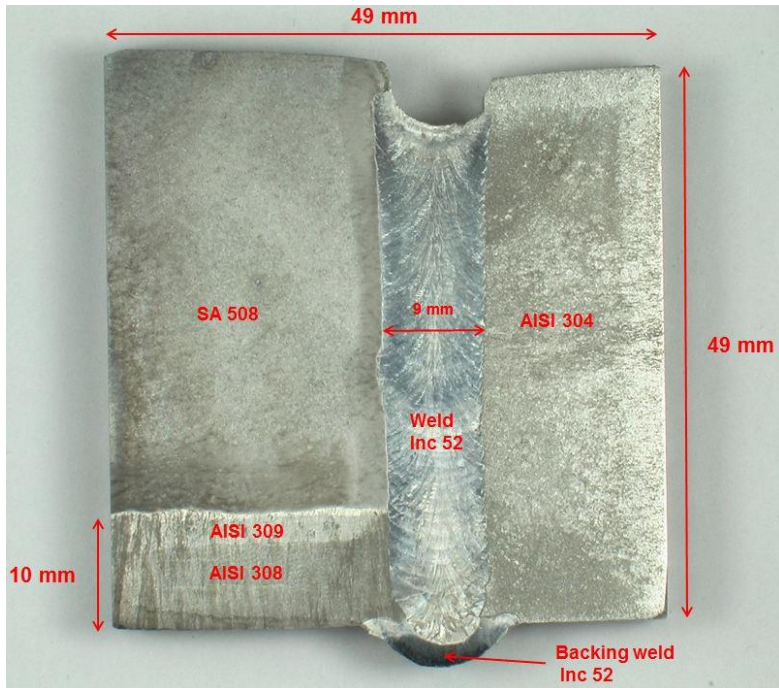


Figure 3. Cross-section macrograph of the narrow-gap GTAW DMW weld (NG-DMW): weld metal Alloy 52, ferritic steel SA508 (with cladding Type 309 + 308), austenitic stainless steel Type 304.

The experimental program is described in more detail in Ref. [13]. Cross-sections were extracted from the NG-DMW. The first section from the weld was not subjected to heat treatment and is denoted “As-welded” (AW), whereas the remaining samples were heat-treated (denoted as PWHT) at 550°C for 20 h, then increasing shortly the temperature to 610°C for 10 h. For both the AW and PWHT cross-sections, five samples were then cut using electrical discharge machining (EDM).

Microhardness and nanohardness testing were carried out to characterise the fusion boundary/ interface between SA508 steel and Alloy 52 weld. Microhardness measurements were made using two indentation weights corresponding to HV0.5 and HV0.1. Fracture mechanical tests were performed according to ASTM E 1820 using two different sized SE(B) specimens representing the AW and PWHT conditions: miniature size, 5 x 10 x 55 mm, and large-size, 10 x 20 x 100 mm, specimens. For both cases, the initial pre-fatigued crack was located at the fusion boundary/ interface (FL), FL–1 mm (i.e. into the weld metal) and at the FL+1 mm into the ferritic steel HAZ. Tests were performed at room temperature and the fracture resistance (J-R) curves were determined for these different weld zones to determine their fracture resistance and to examine the effect of local strength mismatch on the fracture behaviour. Examples of fractured specimens were also

subjected to detailed fractographic investigation using optical 3D profilometry in order to determine the topography of the fracture surface (i.e. topographic fractography).

3. Results and discussion

The microhardness profiles for the BWR type DMW in the as-welded (AW) and PWHT conditions are presented in Figures 4 and 5, respectively. The results are discussed in more detail in Ref. [1].

For the AW condition, the results show a steep increase in the hardness with a maximum value of 381 HV_{0.3} at the ferritic steel side adjacent to the weld interface (FL), the location corresponding to the coarse-grained HAZ (CGHAZ) that consists mainly of bainite [1]. The average hardness of the outer HAZ (at the distance of 1.5–7 mm from the interface) of the SA508 steel and the Alloy 182 buttering (within the distance of –6 mm to –1 mm), respectively, were around 212 ± 12 HV_{0.3} and 226 ± 13 HV_{0.3} [1], see Figure 4.

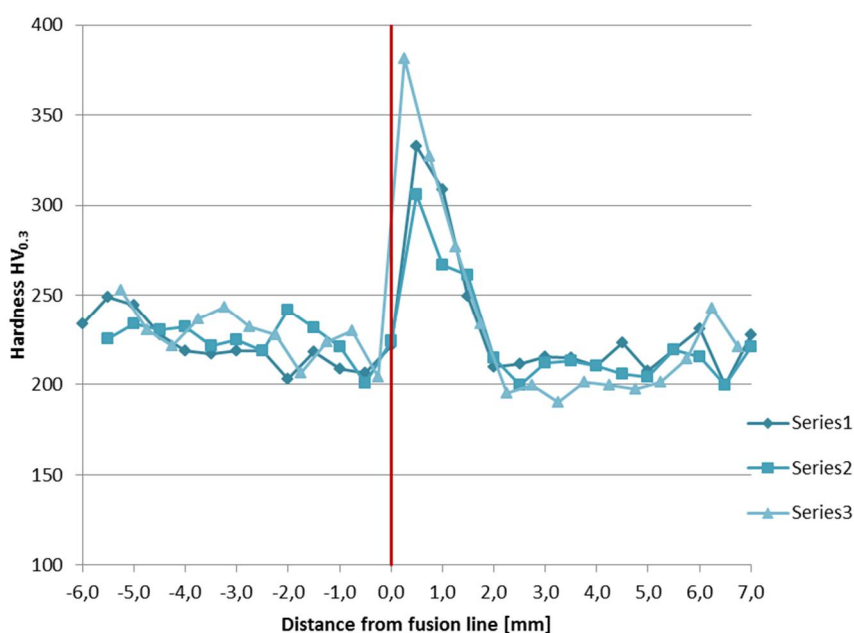


Figure 4. Microhardness profiles across the SA508–Alloy 182 DMW interface in the AW condition [1].

The hardness profiles measured across the SA508 – Alloy 182 buttering interface of the DMW samples post-weld heat treated at 605°C for 6 h and 24 h are presented in Figure 5.

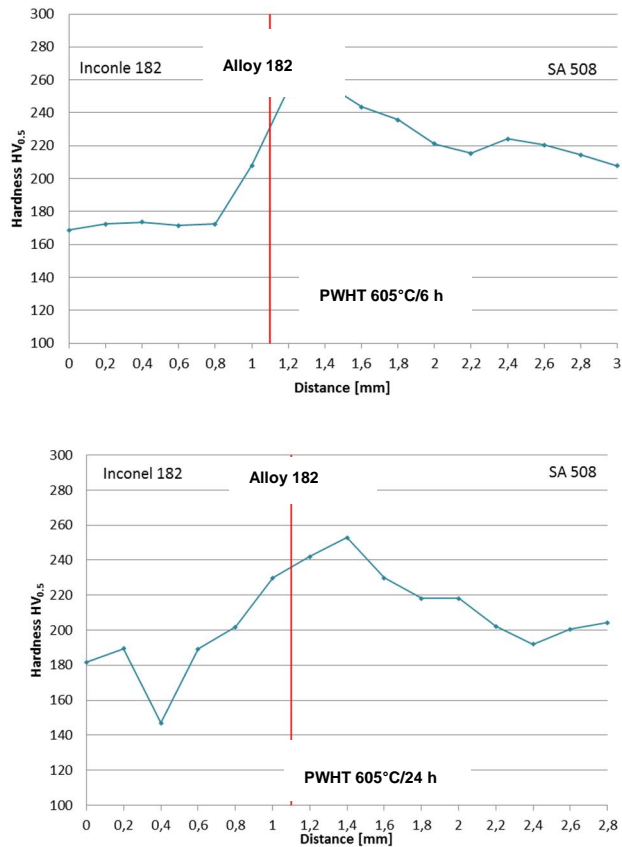


Figure 5. Microhardness profiles across the SA508–Alloy 182 interface of the DMW samples in the PWHT conditions (605°C for 6 h and 24 h, respectively) [1].

The PWHT samples show a substantial reduction in the hardness peak of the SA508 steel CGHAZ of about 120 HV units from that in the as-welded sample. For both 6 h and 24 h holding times, the maximum hardness lies around 260 HV_{0.3}, see Figure 5. This decrease in hardness is presumably a result of the tempering of bainite. There is no detectable difference in the peak hardness values between the two different holding times. Neither is there any significant difference in the shapes of the two profiles that could be attributed to holding time. The hardness profiles of the PWHT samples, however, are seen to be less sharp compared to the hardness profile of the AW sample, which implies that the strength variation across the FL in the PWHT samples is more moderate [1].

The results of the nano-indentations from the AW and PWHT samples were found [1] to be in line with the microhardness results in Figures 4 and 5. The AW sample, again, showed a significant increase in the FL hardness of about 200 HV units from that of the Alloy 182 buttering and SA508 base material; the highest

individual hardness value was 440 HV [1]. The miniature size flat-bar tensile test specimens were found [1] to provide valid results. The highest tensile values were measured for the specimens extracted from the ferritic steel HAZ of the AW sample. As expected, the tensile results of the heat-treated samples were lower compared with the as-welded samples. These results are in compliance with the hardness profiles [1].

With respect to strength mis-match in the BWR type DMW, the weld metal and the buttering layer were found [1] to be under-matched in comparison to the SA508 base material by 10% and 17%, respectively. According to the Mis-Match Option in the SINTAP and Fitnet procedures, over- or under-matching can be considered minimal and hence insignificant if it is less than 10% and needs to be taken into account only with mis-match states exceeding 10%. The highest state of mismatch, 61%, was found [1] at the weld interface (FL) between the ferritic steel HAZ and the Alloy 182 buttering layer in the AW samples, whereas the PWHT lowered the mismatch to a range of 42–48% [1].

The microhardness profiles for the PWR type NG-DMW in the as-welded (AW) and PWHT conditions are shown in Figures 6–7 and 8, respectively. The results are presented and discussed in more detail in Ref. [13].

Similarly to the BWR type DMW albeit not so pronouncedly, the results for the PWR type NG-DMW in the AW condition show a clear increase in hardness with a maximum value of $\approx 280 \text{ HV}_{0.5}$ at the ferritic steel side of the weld interface (FL), the location again corresponding to the coarse-grained HAZ (CGHAZ), see Figure 6. More detailed hardness measurements using $\text{HV}_{0.1}$ and focusing on the immediate vicinity of the interface reveal indications of the presence of the carbon-depleted zone (CDZ) that manifests itself as a continuous decrease in the hardness of the CGHAZ when approaching the interface, see Figure 7. That such a CDZ might exist in the NG-DMW in the AW state is certainly interesting, since no such CDZ was recognized in the case of the BWR type DMW even in the PWHT condition. Nevertheless, this suggests that some diffusion-dependent migration of alloying elements, like carbon (C), might have occurred across the interface – presumably driven by the presence of high-Cr Alloy 52 weld metal on the other side of the FL and accentuated by the narrowness of the different microstructural zones in the NG-DMW. Ongoing metallographic investigations will further illuminate the microstructural characteristics of the discovered low-hardness region.

According to Figure 8, subjecting the PWR type NG-DMW to the PWHT results in dramatic changes in the microhardness profile in the immediate vicinity of the weld interface. Whilst the hardness in the ferritic steel CGHAZ next to the interface (and most likely corresponding to the CDZ) continues to decrease down to 190–200 $\text{HV}_{0.1}$, a simultaneous abrupt increase of the hardness up to about 320–340 $\text{HV}_{0.1}$ is recognized in the Alloy 52 weld metal in the opposite side next to the interface. Whatever the underlying microstructural phenomena might be, it is obvious that the PWHT will change the mis-match state in the NG-DMW in such a manner that was not observed in the case of the BWR type DMW. Thus, whilst the PWHT reduced the state of mis-match in the BWR type DMW [1], the opposite

seems to be true for the PWR type NG-DMW, that is, the mis-match state is in fact raised significantly as a result of the PWHT, as shown in Figure 8.

Ongoing metallographic investigations and awaited miniature specimen tensile tests are expected to provide further illumination on the characteristics of the discovered hardness profile changes and their underlying mechanisms in the NG-DMW; for instance, whether the steep increase in hardness in the Alloy 52 weld metal side can be attributed to precipitation of carbides or other metallic phases during complex stages of the PWHT.

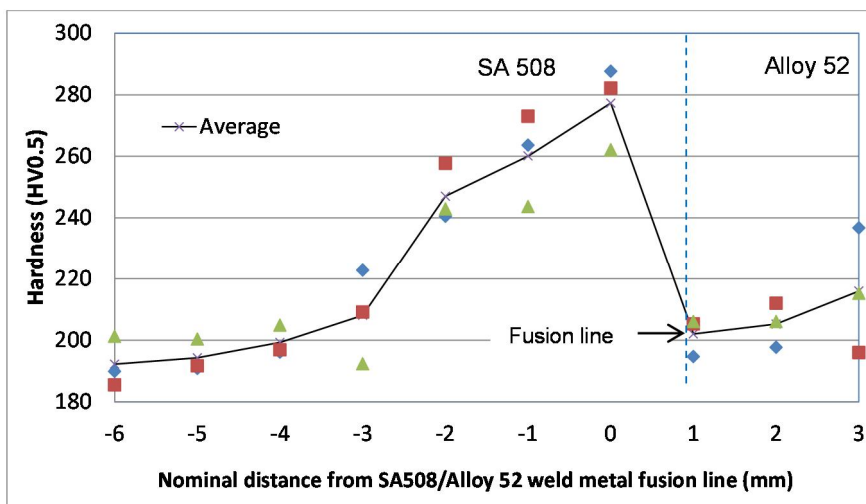


Figure 6. Microhardness profiles (HV0.5) across the SA508 – Alloy 52 interface of the NG-DMW in the AW condition [13].

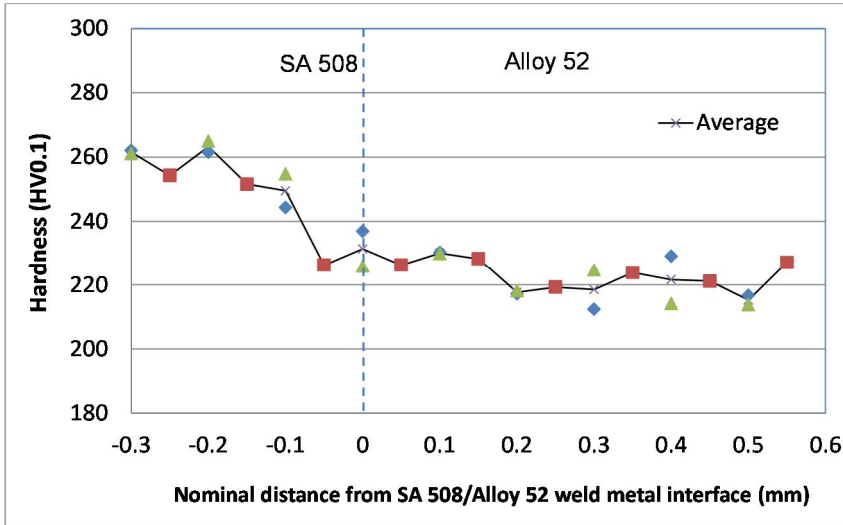


Figure 7. Microhardness profiles (HV0.1) across the SA508 – Alloy 52 interface of the NG-DMW in the AW condition focusing on the NIZ in the immediate vicinity of the FL [13]. Note that these measurements were made in a slightly different location of the weld interface compared to Figure 6.

Results of the fracture mechanical tests for the different weld zones of the AW state and PWHT treated PWR type NG-DMW samples using the large size, 10 x 20 x 100 mm, SE(B) specimens are collated and presented as fracture resistance (J-R) curves in Figure 9. Overall, it can be seen that in terms of absolute values the fracture resistance of all the examined weld zones is comparatively high and characterised by ductile fracture initiation and growth. Among the different weld zones, the lowest fracture resistance was recorded for the fusion boundary/near interface zone (NIZ). This is consistent with the earlier findings on the fracture behaviour of ferritic-austenitic DMWs [1, 2, 8, 9, 11, 12, 14].

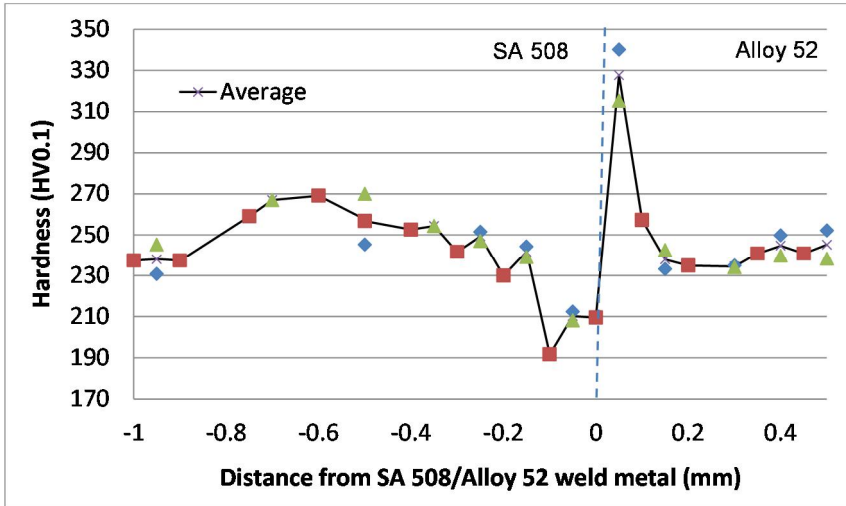


Figure 8. Microhardness profiles (HV0.1) across the SA508 – Alloy 52 interface of the NG-DMW in the PWHT condition focusing on the NIZ in the immediate vicinity of the FL [13].

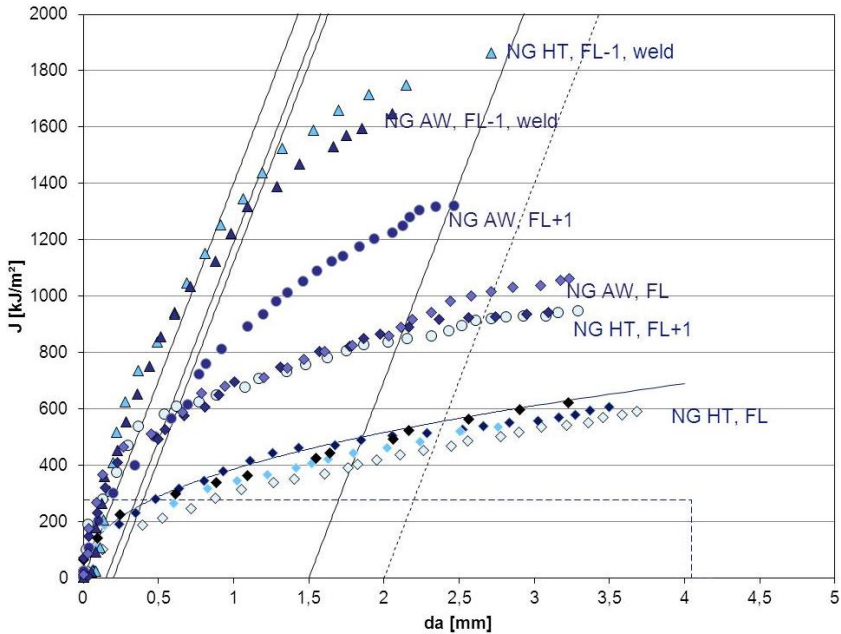


Figure 9. Fracture resistance (J-R) curves for the different weld zones (i.e. FL–1mm, FL, FL+1 mm) of the NG-DMW in the AW and PWHT conditions – large size (10 x 20 x 100 mm) specimen data.

Figure 9, however, reveals striking differences in the fracture resistance of the NIZ between the AW and the PWHT conditions: the PWHT appears to lead into a significant decrease in the fracture resistance, in relation to the AW state. This is the case for both the FL and FL+1 mm specimens. The effect of PWHT in lowering the fracture resistance seems to be particularly pronounced when it comes to the crack growth stage (i.e. propagation part of the J-R curve) after inherently ductile initiation, see Figure 9. Regarding the Alloy 52 weld metal, PWHT had no influence on its fracture resistance. That the effect of the PWHT on the fracture toughness of the NIZ in the PWR type NG-DMW is contrary to that anticipated previously, suggests that the increased strength mis-match state caused by the PWHT as shown in Figure 8, might be responsible for the lowered fracture resistance in the NIZ of the NG-DMW (as this was not encountered in the case of the BWR type DMW). Whether the loss of fracture resistance in the PWHT condition is due to increased crack (growth) driving force accentuated by the elevated mis-match state cf. Figure 8 or increased inherent local inhomogeneity of the NIZ, or both in the combination, cannot be satisfactorily explained yet.

Anyway, further evidence on increased local inhomogeneity as a result of the PWHT can be gained when comparing the outcome of the fracture toughness tests using miniature size, 5 x 10 x 55 mm, specimens for the FL/NIZ in the PWHT and AW conditions, respectively, in Figures 10 and 11. Even if the fracture resistance values in Figures 10 and 11 might not be absolutely accurate (since the individual crack lengths of the specimens were not yet measured), this is thought not to violate any overall comparisons between these two datasets. Later on, also the actual location of the pre-fatigued crack tip in each specimen, being nominally identical, will be determined.

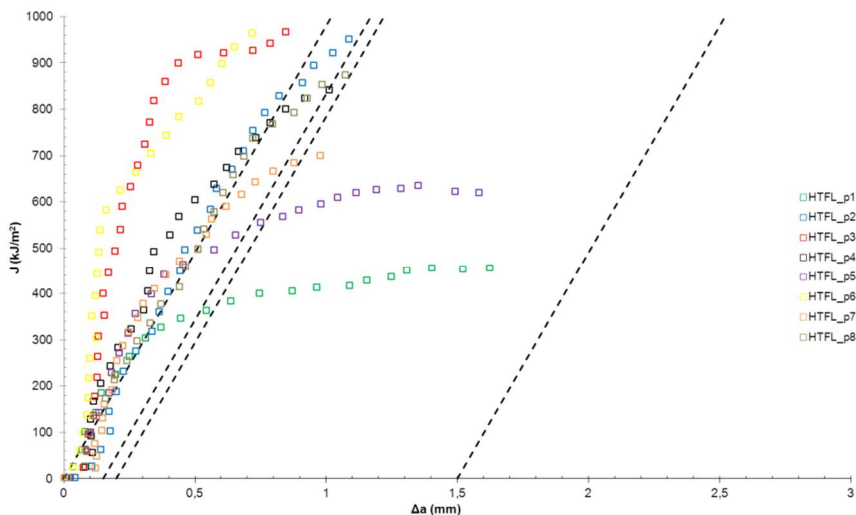


Figure 10. Fracture resistance (J-R) curves for the FL/NIZ of the NG-DMW in the PWHT condition – mini-ature size (5 x 10 x 55 mm) specimen data (the individual crack lengths of the specimens not measured yet).

It can be seen that the overall scatter in the fracture resistance results for the FL/NIZ, especially regarding the propagation part of the J-R curves, is in the PWHT condition remarkably greater than in the AW state. This difference is particularly evident in the case of the lowest individual J-R curves in the two datasets, compare Figures 10 and 11. Larger scatter in the PWHT dataset may thereby be an indication of increased local inherent inhomogeneity of the NIZ owing to its microstructural features in the PWHT condition, albeit without detailed post-test metallography it cannot be solely confirmed that all the parallel specimens in these two J-R datasets had truly accurately hit and successfully sampled the desired FL/NIZ microstructure. Further confirmation is awaited after the ongoing metallographic investigations and individual crack length measurements have been completed.

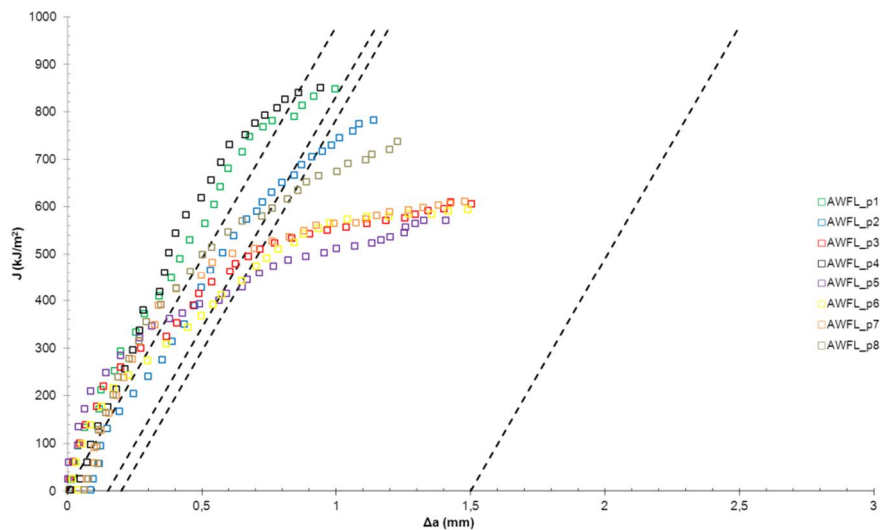


Figure 11. Fracture resistance (J-R) curves for the FL/NIZ of the NG-DMW in the AW condition – miniature size (5 x 10 x 55 mm) specimen data (the individual crack lengths of the specimens not measured yet).

Results of the detailed fractographic examination of the halves of broken SE(B) specimens performed using optical 3D profilometry seem to elucidate the frequently discovered crack growth path deflection behaviour associated with DMWs and its dependence on the mis-match state that, in turn, is influenced, among other factors, by the PWHT. Figures 12–15 present examples of this ‘topographic fractography’ carried out for the NIZ (FL+1 mm) of the NG-DMW in the AW and PWHT conditions. It can be seen that the direction of the path deviation of the propagating crack is totally opposite within the very same nominal NIZ region (i.e. FL+1 mm), depending on whether the specimen was in the AW or PWHT condition. Comparing the 3D profiles in Figures 12 and 13 it can be seen that whilst the crack path in the AW state had, soon after inherently ductile initiation, deviated

from the FL+1 mm zone towards the ferritic steel HAZ (i.e. upwards in Figure 12), the reverse is true for the PWHT condition where the crack path had deviated from the FL+1 mm zone towards the fusion boundary/interface (FL) of the NG-DMW (i.e. downwards in Figure 13). The detailed topographic fractography of the equivalent specimens clearly illustrates the aforementioned differences in the crack growth path deviation behaviour between the specimens representing the AW and PWHT conditions, respectively, compare Figures 14 and 15.

According to the recent experimental and numerical investigations on crack growth path deflection and fracture resistance in similar nickel-base NG-DMWs [2, 14], the crack, soon after ductile initiation, shall always deviate to the material with lower strength. Consequently, the deviation process will be driven by the strength mis-match, rather than toughness mis-match. The results of the present work in Figures 6–9 and 12–15 seem to be in line with that observation. Applying the PWHT clearly yields an increase in the mis-match state (i.e. by softening the CDZ and elevating the hardness in the Alloy 52 weld metal next to the interface cf. Figure 8), which obviously had directed a crack initiated in the FL+1 mm zone to grow towards the lower-strength zone (CDZ) in the immediate vicinity of the interface, whilst the higher strength zone (with a hardness peak as shown in Figure 8) had acted as a barrier against further propagation into the Alloy 52 weld metal side. In the case of the AW state, however, this accentuated mis-match state is missing (see Figure 7); consequently, the crack had deviated towards the ferritic steel HAZ with decreasing strength (shown as continuously decreasing hardness in Figure 6).

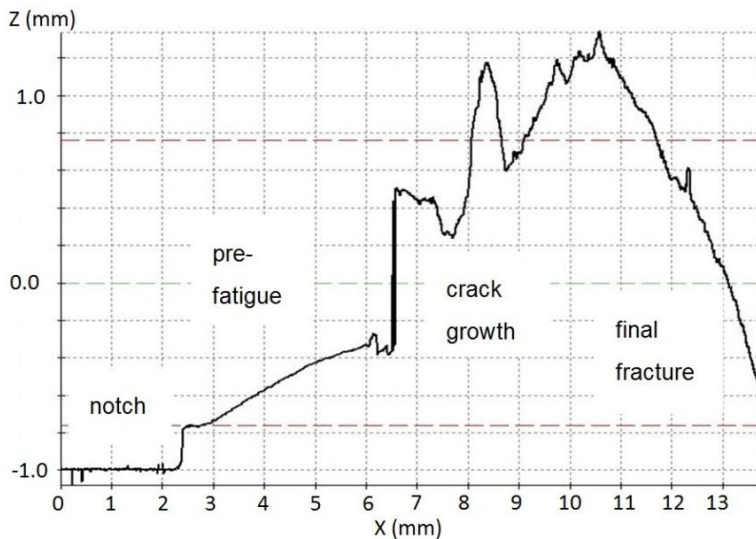


Figure 12. Surface 3D profile of a specimen with the pre-fatigued crack in the FL+1 mm zone – the AW condition: crack growth path deviation towards the ferritic steel HAZ.

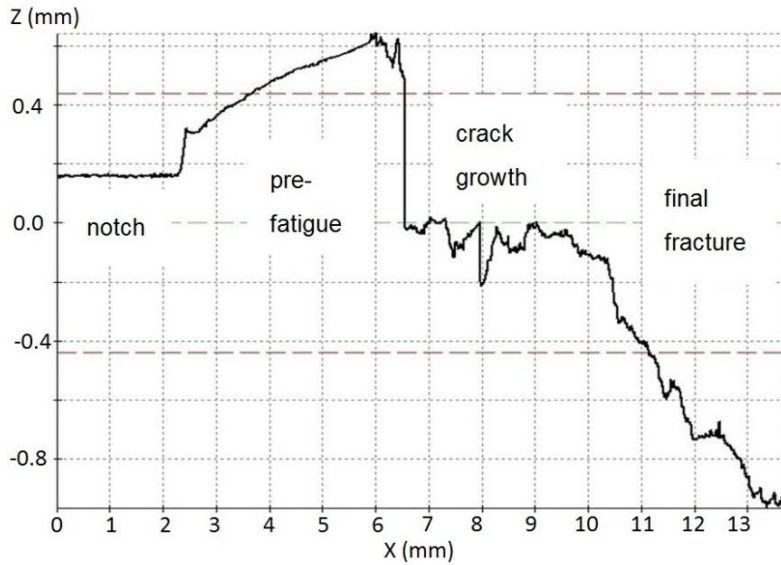


Figure 13. Surface 3D profile of a specimen with the pre-fatigued crack in the FL+1 mm zone – the PWHT condition: crack growth path deviation towards the interface/fusion line (FL).

Overall, the results thereby demonstrate that topographic characterisation of the fracture surface of a SE(B) specimen using optical 3D profilometry can successfully reveal sudden crack path deviations and illustratively describe the fractographic details of the surface. This technique is therefore considered as a potential tool for characterising the surface profile and the true fracture path area in a fracture toughness test specimen extracted from DMWs, especially in cases where abrupt crack deflection will lead to tortuous crack path and complex topographic surface shapes. Moreover, this offers an attractive possibility to apply the optical 3D profilometry as an aid for an attempt to determine representative J values corresponding to the true measured fracture path area in a specimen and perhaps this way, take a step closer to realistic J-integral determination in the case of DMWs.

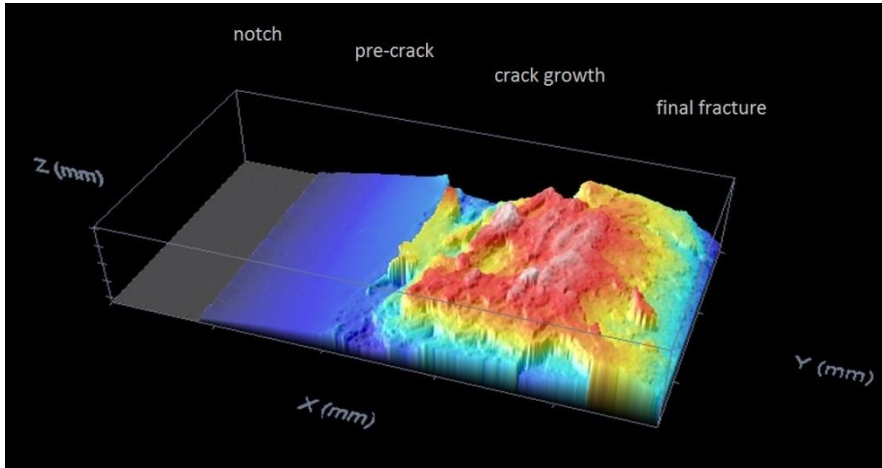


Figure 14. Topographic view of the fracture surface of a specimen with the pre-fatigued crack in the FL+1 mm zone – the AW condition: crack growth path deviation towards the ferritic steel HAZ. The dimensions of the topographic image area are $x = 13.8$ mm, $y = 7.6$ mm and $z = 2.6$ mm.

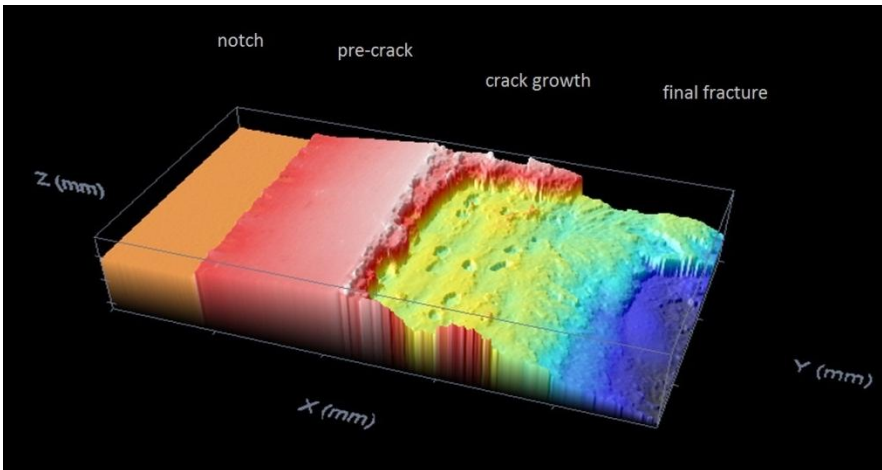


Figure 15. Topographic view of the fracture surface of a specimen with the pre-fatigued crack in the FL+1 mm zone – the PWHT condition: crack growth path deviation towards the interface/fusion line (FL). The dimensions of the shown topographic image area are $x = 13.8$ mm, $y = 7.6$ mm and $z = 1.9$ mm.

Although the present knowledge [2, 14] leans on the view that crack deviation in DMWs is driven predominantly by the strength mis-match, it would be worth investigating whether there exists a critical toughness limit for an individual (low tough-

ness) weld zone below which the local fracture resistance is already so low that it starts to dominate the failure behaviour (i.e. at least crack initiation and possibly even further growth) instead of the low strength. It may well be that such a low toughness is never encountered in practice DMWs behaving, after all, in a ductile manner. A parametric study with either true or postulated local strength and toughness properties across the entire DMW is thought to elucidate these complex stress-strain – fracture toughness interactions.

4. Conclusions

This paper deals with experimental material characterisation of two configurations of ferrite (SA508) – aus-tenite (Type 316) dissimilar-metal weldments (DMWs): (i) BWR type DMW made using Alloy 82/182 filler metal and employing a beveled V-groove with a buttering layer, and (ii) PWR type narrow-gap DMW made using Alloy 52 filler metal without any buttering. On the basis of the results, the following conclusions can be drawn:

1. In absolute J values, the fracture resistance of both DMW configurations is comparatively high and characterised by ductile fracture initiation and growth.
2. Among the different weldment zones, the lowest fracture resistance was recorded for the fusion boundary/near interface zone (FL/NIZ). This is consistent with the earlier findings on fracture behaviour of ferrite-austenite DMWs.
3. The BWR type DMW and the PWR type NG-DMW were found to exhibit different mismatch characteristics. This is obviously due to differences in the (i) filler metal alloying concepts, (ii) applied groove geometries and (iii) widths of the various weldment zones, which all are likely to result in different compositional and mechanical property gradients.
4. Micro- and nanohardness measurements were able to successfully characterise the strength mis-match of the investigated DMWs. Where available (i.e. for the BWR type DMW), the results of miniature flat-bar tensile specimens were consistent to the hardness data in view of describing the state of strength mis-match.
5. The fracture mechanical test results demonstrated that DMWs are prone to abrupt crack path deviations from the original crack initiation position (i.e. the location of the pre-fatigued crack tip) into the neighbouring microstructures. The results show that this deflection tendency is affected by the strength mis-match state.
6. The applied post-weld heat treatments (PWHT) induced different effects on the strength mis-match and fracture behaviour of the BWR type and PWR type DMWs. In the former case, the PWHT was shown to reduce the

strength mis-match in comparison to the as-welded (AW) state, whereas the opposite occurred in the latter case: it was found that carrying out the PWHT in fact accentuated the strength mis-match state and resulted in inferior fracture resistance, compared to the AW state.

7. The miniature size SE(B) specimen results imply, the PWHT increases local inhomogeneity in the FL/NIZ of the PWR type NG-DMW, in relation the AW state. This manifests itself as widened scatter in the corresponding J-R curves between parallel specimens. These findings are in line with the microhardness measurements that demonstrated accentuated strength mis-match state in the NG-DMW when subjected to the PWHT. Furthermore, the findings are in harmony with the large size SE(B) specimen results that exhibited inferior fracture resistance for the FL/NIZ in the PWHT condition, compared to the AW state.
8. The miniature size SE(B) specimens are likely to capture the local inhomogeneous regions more effectively than the large size specimens; thus they can provide indication of the extent of inherent inhomogeneity of the narrow zones within a DMW. On the other hand, in the case of predominantly ductile fracture, the miniature size SE(B) specimens are likely to undergo loss of constraint, in which case their measuring capacity will be exceeded and the results may therefore not describe the actual fracture toughness as accurately as the results of the large size specimens.
9. Topographic characterisation of SE(B) specimen fracture surfaces using optical 3D profilometry was shown capable of revealing sudden crack path deviations and illustratively describe the details of the fractured surface. This technique is hence considered as a potential tool for characterising the surface profile and the true fracture path area in a fracture toughness test specimen in cases where abrupt crack deflection will lead to complex topographic surface shapes.

References

1. Holmström, P., Sarikka, T., Brederholm, A., Karjalainen-Roikonen, P., Saukkonen, T., Nevasmaa, P. & Hänninen, H. Effect of strength mismatch and microstructure on mechanical properties of BWR dissimilar metal safe-end welds. Proc. Conf. 16th Int. Conf. on Environmental Degradation of Materials in Nuclear Systems – Water Reactors. Asheville, NC, USA, August 2013. 13 p. (to be published).
2. Wang, H. T., Wang, G. Z., Xuan, F. Z. & Tu, S. T. Materials and Design 2013, 44, pp. 179–189.

3. Hänninen, H., Toivonen, A., Brederholm, A., Saukkonen, T., Ehrnstén, U. & Aaltonen, P. Environment-assisted cracking and hot cracking of Ni-base alloy dissimilar metal welds. Proc. Conf. 13th Int. Conf. on Environmental Degradation of Materials in Nuclear Systems – Water Reactors. Whistler, British Columbia, Canada, 19–23 August, 2007 (CD-ROM). 19 p.
4. Hänninen, H., Brederholm, A., Saukkonen, S., Gripenberg, H., Toivonen, A., Ehrnstén, U. & Aaltonen, P. Hot cracking and environment-assisted cracking susceptibility of dissimilar metal welds. Espoo: VTT Technical Research Centre of Finland, 2008. VTT Research Notes 2399. 177 p.
5. Karlsen, W. & Pakarinen, J. TEM investigation of cracks in dissimilar metal weld Inconel 182 following doped steam testing. Espoo: VTT Technical Research Centre of Finland, 2009. Research Report VTT-R-05722-09. 29 p.
6. Hänninen, H., Toivonen, A., Saukkonen, T., Brederholm, A., Aaltonen, P. & Ehrnstén, U. EAC crack initiation in nickel-based dissimilar metal welds using doped steam test. Proc. Conf. 14th Int. Conf. on Environmental Degradation of Materials in Nuclear Systems – Water Reactors. Hilton Virginia Beach, Virginia Beach, VA, USA, 23–27 August 2009 (CD-ROM). Pp. 333–343.
7. Hänninen, H., Brederholm, A., Saukkonen, T., Ivanchenko, M., Toivonen, A., Karlsen, W., Ehrnstén, U. & Aaltonen, P. Environment-assisted cracking and hot cracking susceptibility of nickel-base alloy weld metal. Espoo: VTT Technical Research Centre of Finland, 2011. VTT Research Notes 2582. 155 p.
8. Nevasmaa, P., Laukkanen, A. & Ehrnstén, U. Structural Integrity of Bi-Metallic Components (BIMET) – TG2: Material Characterisation of Dissimilar Ferrite-Austenite Welds. Espoo: VTT Manufacturing Technology, 1999. Research Report VAL C 517. 73 p.
9. Nevasmaa, P., Laukkanen, A. & Ehrnstén, U. Fracture Resistance and Failure Characteristics of AISI 304/SA508 Bimetallic Weld in Ductile Regime. Proc. Conf. 13th Eur. Conf. on Fracture – Fracture Mech.: Applications and Challenges (ECF 13). San Sebastian, Spain, 6–9 September 2000. ESIS / Eng. Mat. Advisory Services Ltd., 2000. Paper No. 1N.49 (CD-ROM). 8 p.
10. Faigy, C., Martin, G., Taylor, N., Youtsos, A., Katsareas, D., Keinänen, H., Laukkanen, A., Wintle, J., Sherry, A., Lidbury, D., Safa, N., Cipiere, M. F., Gilles, P., Chapuliot, S., Kaiser, Y. & Lenkey, G. Assessment of Aged

Piping Dissimilar Metal Weld Integrity. ADIMEW Synthesis report. Contract FIKS-CT-2000-00047. European Commission, January 2004. 45 p.

11. Keinänen, H., Laukkanen, A. & Nevasmaa, P. Fracture and Tensile Testing of the 'AD01' Mock-Up' (ADIMEW – Work Package 2: Material Characterization). Espoo: VTT Industrial Systems, 2003. Research Report TUO72-033337. 41 p.
12. Laukkanen, A., Nevasmaa, P., Ehrnstén, U. & Rintamaa, R. Mapping of Characteristic Features of Bimetallic Welds from the Standpoint of Engineering Critical Analysis. Proc. Conf. 16th Int. Conf. on Structural Mechanics in Reactor Technology (SMiRT-16); Div. G, Fracture Mech. Washington DC, 12–17 August 2001. Eds. Vernon C. Matzen and C.C. David Tung. International Association for Structural Mechanics in Reactor Technology (IASMiRT), USA. 2001. Paper #1566 (CD-ROM). 8 p.
13. Mouginot, R. & Hänninen, H. Microstructures of nickel-base alloy dissimilar metal welds. Aalto University publ. series SCIENCE + TECHNOLOGY 5/2013. 178 p. ISBN 978-952-60-5065-2.
14. Wang, H. T., Wang, G. Z., Xuan, F. Z. & Tu, S. T. Eng. Failure Analysis 2013, 28, pp. 134–148.

General corrosion and SCC tests on ODS steels in supercritical water

Aki Toivonen & Sami Penttilä

VTT Technical Research Centre of Finland
P. O. Box 1000, FI-02044 VTT, Finland

Abstract

General corrosion tests and slow strain rate tensile tests (SSRT) were done on 9–20% Cr oxide dispersion strengthened (ODS) steels in supercritical water at 550 and 650°C with 100–150 ppb dissolved oxygen. Based on the results, Al-alloyed high Cr ODS steels PM2000 and MA956 have superior corrosion resistance when compared to 9–14% Cr ODS steels. In SCW at 550°C and above, it is considered that the minimum Cr-content for thin walled components should be higher than 14%. The results indicate that the ODS steels are less susceptible to stress corrosion cracking (SCC) than austenitic stainless steels or Ni-base alloys in supercritical water. However, more extensive studies with different water chemistries and strain rates should be made.

1. Introduction

ODS steels are one of the long term candidate material groups for in-reactor applications such as fuel cladding material in Supercritical Water Reactor (SCWR). Austenitic stainless steels would be very attractive for these applications due to their long and successful history in nuclear power generation. However, results available from the previous EU FP 6 & 7 projects so far, e.g. HPLWR Phase2, have shown that ~15 - 18% Cr / 8 - 15% Ni austenitic stainless steels are prone to high oxidation rates at 650°C which is close to the estimated peak temperature of the fuel cladding in normal operation conditions. When higher alloying is applied in order to improve general corrosion resistance, creep resistance decreases or Ni content becomes too high for reactor core neutronics. Thus ferritic/martensitic (F/M) ODS steels have become more attractive option for future reactor concepts (GenIV systems) as a structural material facing severe environment. The main in-service degradation mechanisms in an SCWR are irradiation damage, general corrosion, stress corrosion cracking (SCC) and creep. Within Europe, many of these issues have been addressed by various research projects funded by European Commission. A large scale project, EU FP7 project GETMAT (GenIV and Transmutation materials), was launched in 2008 in order to address cross-cutting materials issues common to all or part of the GenIV and transmutation systems. One of the GETMAT sub-tasks was to study SCC and general corrosion resistance of ODS steels in supercritical water (SCW).

GETMAT project goals were, partially, to manufacture and characterise ferritic-martensitic ODS steels with different Cr contents. ODS steels are one of the candidate materials group for applications in SCW environment but their commercial production was either stopped (e.g. MA956, MA957 and PM2000) or their development is still under way. These ODS alloys were produced earlier by Dour Metal (Belgium), Special Metals and Plansee [1]. In recent years, ODS steels have been supplied by Dour Metal Sro. (Slovak Republic) and Kobe Steel Ltd but the amounts of produced materials have been very small. ODS versions of Eurofer 97 (9% Cr F/M steel) is the only ODS steel licensed for application in nuclear industry at the moment (i.e., for international thermonuclear experimental reactor, ITER) but the Cr content is not sufficient in order to form corrosion resistant oxide film in SCW conditions [2]. Within GETMAT, tests in SCW were done on five different ODS steels with different chromium contents. The tests were general corrosion tests and SSRT tests.

2. Experimental details

2.1 Test materials

The tests were done on previously commercially available ODS steels and on ODS steels produced specifically for the GETMAT project either by participant organisations or Kobe Steel Ltd. The materials are shown in Table 1. Ferritic-martensitic P92 steel was tested as a reference material.

Table 1. Chemical compositions of the tested alloys (W-%). Fe = balance.

GETMAT Alloys	Cr	Ni	W	Mn	Ti	Al	Si	Other
P92	8,9	0,02	2,1	0,42	<0,01	<0,01	0,09	0,49Mo
9Cr ODS	9,0			0,43			0,68	1,86Mo/ 0,34Y
12Cr ODS	12		2		0,25			0,2Y
14Cr ODS	14	0,15	1	0,3			0,3	0,3Y
PM2000	20	0,03		0,0,08	0,43	5,5	0,02	0,5Y
MA956	20				0,5	4,5		0,5Y

2.2 Test equipment and environment

The tests were done in SCW at two temperatures, 550°C and 650°C. The dissolved oxygen content in the feed water was between 100 and 150 ppb and conductivity was <0.1 µS/cm. The specimens were exposed to SCW at the pressure of 25 MPa in supercritical autoclave connected to a recirculation water loop, Figure 1. The environmental control and monitoring in VTT SCW testing system in-

clude temperature, pressure, inlet and outlet water conductivity, inlet water dissolved oxygen content, and flow rate.

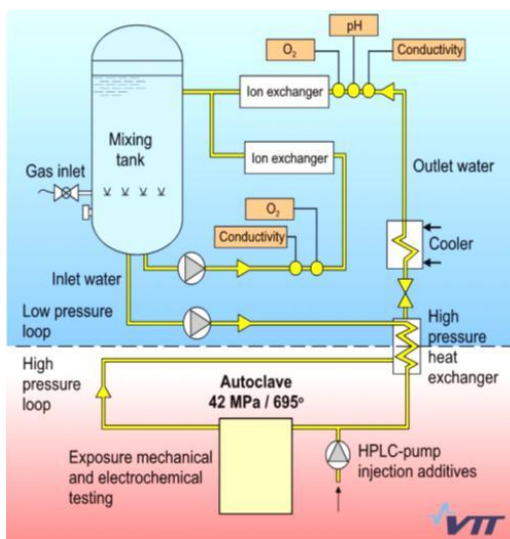


Figure 1. A schematic figure of the SCW testing system.

2.3 Test methods

General corrosion test specimens were electric discharge machined or plane milled to the dimensions of 30 x 10 x 2 mm, 15 x 10 x 2 mm or 25 x 15 x 5 mm and, usually, polished with #1200 grit emery paper. PM2000 and P92 specimens prepared for tests at 550°C were not polished but left in plane milled condition following ASTM G1-03 procedure. A typical specimen geometry is shown in Figure 2.

For exposure to SCW, the specimens were placed on a specimen holder using ZrO₂ washers as electric insulation. The specimen holder was also insulated from the autoclave body using ZrO₂ washers. The samples were weighed before and after exposure using Mettler AT261 scale with a measuring uncertainty of ± 0.002%. The mass change per unit area was calculated using coupon dimensions measured before testing. Metallographic cross sections were prepared after the tests and they were studied using a scanning electron microscope (SEM) and energy dispersive spectroscopy (EDS) and, in some cases, glow discharge optical emission spectroscopy (GDOES).

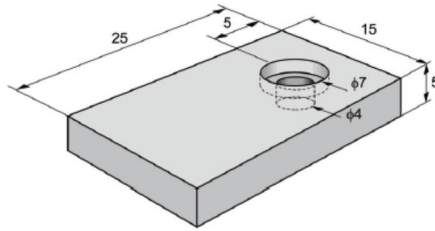


Figure 2. Geometry and dimensions of the general corrosion test coupon.

Stress corrosion susceptibility was studied using slow strain rate tensile (SSRT) tests carried out according to ASTM G129. Specimens were electric discharge machined into 30 mm long plate type tensile specimens with a 2.0 by 1.5 mm gauge section. Plate type specimens have been used previously in order to study the SCC resistance of thin walled fuel claddings from which cylindrical specimens can not be made. The same specimen geometry was used in this test series in order to get comparable results. Specimen geometry and dimensions are shown in Figure 3. Before tests, the gauge sections were polished mechanically with #600 emery paper in axial direction.

The specimens were loaded with a strain rate of 3×10^{-7} 1/s with the exception of tests at 550°C on PM2000 which were done with the strain rate of 1×10^{-7} 1/s (SSRT tests on PM2000 were done in the frame of EU FP6 project HPLWR Phase 2 and FP7 project SCWR-FQT).

The SSRT tests were done simultaneously with the general corrosion tests in the same autoclave, i.e., the environment was the same. After the tests, the specimens were examined using SEM in order to clarify the cracking mode on the fracture and gauge surfaces.

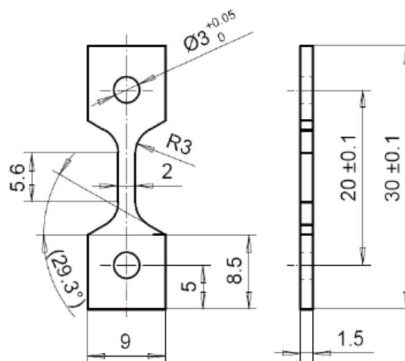


Figure 3. Geometry and dimensions (in mm) of the SSRT specimens.

The test matrix is shown in Table 2. All planned tests on all of the materials were not realised due to test material shortage.

Table 2. Test matrix.

	General corrosion tests, i.e. weight gain tests								SSRT	
	650°C			550°C					650°C	550°C
	600h	1000h	2000h	612h	1008h	1374h	1450h	3010h		
P92	NA	NA	NA	X	NA	X	NA	NA	NA	NA
9% Cr	NA	NA	NA	X	NA	X	NA	NA	NA	NA
12% Cr	X	X	X	NA	X	NA	X	X	X	X
14% Cr	X	X	X	NA	X	NA	X	X	X	X
20% Cr MA956	X	X	X	NA	NA	NA	NA	NA	NA	NA
20% Cr PM2000	X	X	X	NA	X	NA	X	NA	X	X

x = done, NA = not available (not done)

3. Results and discussion

3.1 General corrosion tests

The results of the general corrosion tests are summarised in Figure 4. The mass change (weight gain in Figure 4) at 550°C is shown in the upper plot and at 650°C in the lower plot. All low Cr ODS steels (9% Cr, 12% Cr and 14% Cr) exhibited considerable oxidation at 550°C. At 650°C, the oxidation rates of the tested 12Cr and 14Cr ODS steels remained very similar as at 550°C. At both temperatures the mass increase decreases with increasing Cr content. However, the role of Al-alloying in PM2000 and MA956 steels can not be distinguished from the results. Also, the oxidation resistance of the ODS steels seems to be better than that of the conventional 9Cr F/M steel P92.

SEM photographs of the cross sections of P92 and 9Cr ODS specimens after 1374 h exposure at 550°C are shown in Figure 5 and 12Cr and 14Cr ODS steels after 3010 h exposure in Figure 6, respectively. Three different layers within the oxide can be seen in the photographs. The outmost oxide layer on 9Cr ODS steel exhibit a large number of small pores whereas the outer layer on P92 steel is more compact. Some pores exist also in the outer oxide layer of 12Cr and 14Cr ODS steels. The oxide layer on the 14Cr ODS steel is thinner compared to the lower Cr steels because the thin continuous Cr-rich innermost layer acts as a diffusion barrier for further inward diffusion of oxygen and outward diffusion of cations.

EDS analysis of the 14Cr ODS steel after 3010 h exposure is shown in Figure 7. The EDS analysis shows that the main constituents in the outer layer are iron and oxygen. It suggests that the outer layer forms by outward diffusion of iron ions. The layers beneath the outer oxide are Cr-rich with less Fe than in the bulk metal. The EDS analysis of the other steels tested at 550°C showed very similar element profiles. When the EDS analysis of the 14Cr ODS steel is compared to

the SEM photograph, the following estimation can be made: the outmost layer in Figures 6 and 7 (marked as 1 in Figure 7) is the high Fe / low Cr layer, the middle layer (2) is a transition layer from the high Fe / low Cr layer to the high Cr / low Fe layer (3). Although the element profiles of the other steels were similar, no clear transition layer was observed that could be attributed to the middle layer seen in the SEM photographs.

For some reason the oxide growth was faster on the 12Cr ODS steel than on the 9Cr ODS steel. One possible explanation for the differences between the outlooks and thicknesses of the oxide layers is in the underlying metal matrix: different types of particles (Y-, Cr-rich) at grain boundaries are reported to act as a barrier for cation diffusion in ODS alloys [3]. Another competing process is the diffusion along the grain boundaries per se: the smaller the grains the higher the density of the grain boundaries at the metal surface and the faster the diffusion is.

Based on the results, it can be considered that 14% Cr content in the ODS steel is close to the lower limit to suppress the oxidation rate in SCW enough for thin walled applications. It should be noted that the tested 14Cr ODS steel does not contain Al which typically contributes to the corrosion resistance. Kimura et al. [3] showed that the Cr and Al concentrations adequate for the ODS steels in SCW are: 14–16 w-% Cr and 3.5–4.5 w-% Al. On Al-free 16Cr ODS steel, the oxide (< 1 μm) is reported to be mainly a monolayer of Cr_2O_3 or $(\text{Cr,Fe})_2\text{O}_3$ that forms by an oxidation process with limited inward oxygen diffusion after exposure at 550°C (8 ppm DO_2) [5].

On PM2000 which is Al alloyed, the maximum oxide thickness was around 10 μm after 1008 and 1450h exposure at 550°C. On the other hand, the weight gain between 1008 and 1450h is unexpectedly high indicating that the oxide thickness should be considerably higher after the latter exposure time. The weight gain behaviour of the longer exposed PM2000 coupon very likely results from a large crack in the middle of the sample. Cracking took place during manufacturing process of the test coupon. The crack obviously increases the total surface area of the longer exposed PM2000 sample. An SEM photograph of the cross-section of PM2000 after 1450h exposure time at 550°C is shown in Figure 8. The thin oxide layer cracked and exfoliated during the sample preparation and only two layers can be identified. The maximum and average oxide thicknesses of the samples tested at 550°C are collected into Table 3. All materials were not exposed exactly the same times, but when the average oxide thicknesses are compared after 1374–1450 h exposure times, the oxidation resistances can be put in the following order: PM2000 (3 μm) > 14Cr ODS (10 μm) > 9Cr ODS (30 μm) > 12Cr ODS (65 μm) > P92 (68 μm).

Based on the EDS analyses after exposure to SCW at 650°C, the oxide layers were similar as after exposure at 550°C on the 12Cr and 14Cr ODS steels. Only two different oxide layers could be seen in SEM. The tests at 650°C were performed before the tests at 550°C. Between the tests, a new higher resolution SEM was obtained. The same layers probably exist after the exposure at 650°C as after 550°C, but the two inner layers could not be distinguished with the lower resolution SEM. The cross sections of the 12Cr and 14Cr ODS steels after 2000 h exposure

at 650°C are shown in Figure 9 and the EDS analysis across the oxide layer of the 14Cr ODS steel in Figure 10. An SEM photograph of the cross section of PM2000 is shown in Figure 11.

After 2000h exposure at 650°C the average oxide thicknesses on the 12Cr and 14Cr ODS steels were 32 and 10 µm, respectively, indicating almost the same or even smaller oxide growth rate compared to the results at 550°C. The average oxide thickness on PM2000 was 0.8 µm. When comparing results on PM2000 between temperatures of 550°C and 650°C, it should be noticed that the initial surface conditions were different, i.e. polished with #1200 emery paper vs. plane-milled surfaces, respectively. This is expected to be the reason for higher maximum oxide thicknesses at the temperature of 550°C.

The oxide composition of PM2000 was analysed using GDOES instead of EDS. Based on the results, there is an Fe-rich (with some Cr) outer layer and Cr-rich (with some Fe) inner layer. The Fe concentration in the outer layer decreases and the layer thickness increases somewhat along with increasing exposure time (from 600 to 2000h) whereas the Cr concentration remains the same in both layers. After 600h exposure, the Al concentration is higher than in the bulk metal all the way through the oxide layers, but after 2000h the aluminium has dissolved from the oxide, Figure 12. The behaviour of MA956 is similar at 650°C, except the iron concentration of both oxide layers is lower and aluminium concentration higher after 600h than in PM2000, Figure 13.

Alumina has been reported to show a large increase in solubility during cooling from supercritical temperatures to subcritical region. This might be due to the fact that Al₂O₃ can evaporate in high-temperature water environment as follows [6]:



This means that cyclic operation when cooling and heating the autoclave intermittently in order to remove test coupons might enhance alumina solubility substantially. Solubility of the protective oxide film depletes the Al concentration in the oxide film and thus compensation of the Al loss in the outer oxide is essential in order to maintain protection against outward and inward diffusion of oxygen and metal cations, respectively. Further studies are needed in order to confirm the long term protectiveness of the oxide film on Al-alloyed ODS steels in cyclic temperature conditions.

The observed oxide thicknesses of all the steels tested at 650°C are collected in Table 4. Based on the average oxide thicknesses after 2000 h exposure, the oxidation resistances can be put in the following order: PM2000 (0.8 µm) > MA956 (3 µm) > 14Cr ODS (10 µm) > 12Cr ODS (32 µm).

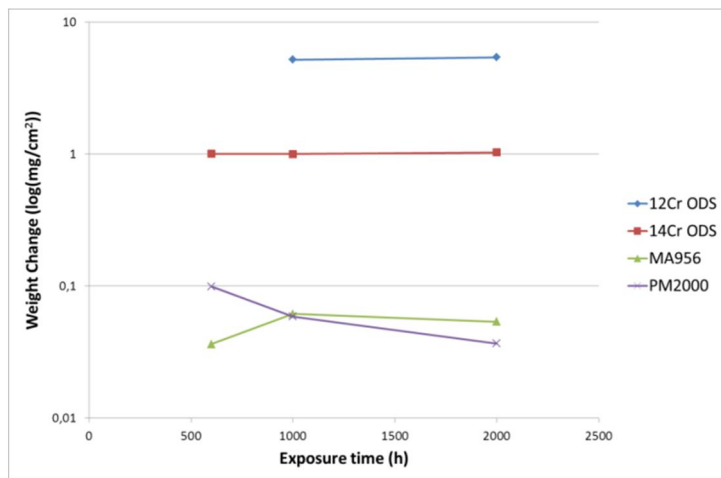
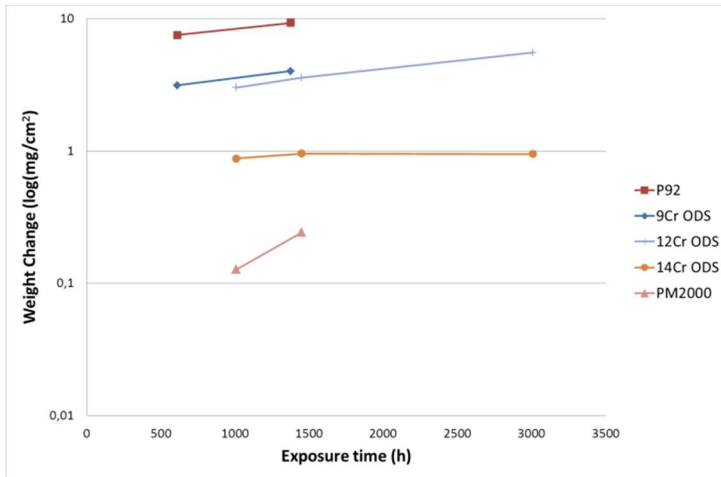


Figure 4. Mass change of tested ODS alloys after exposure to SCW at 550°C (top) and 650°C (bottom).

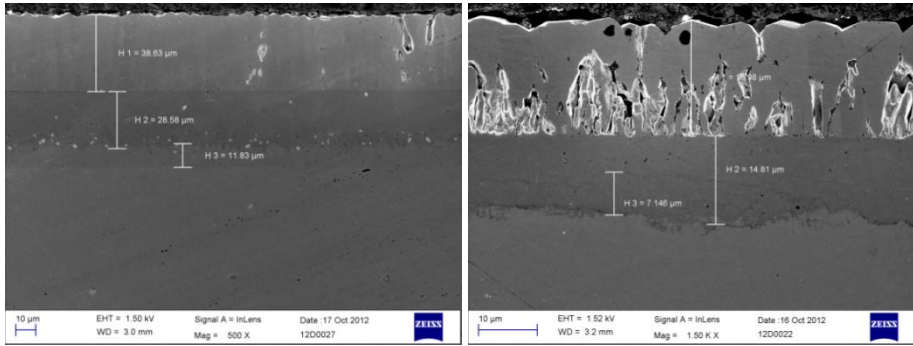


Figure 5. SEM photographs of cross-sections of P92 (left) and 9Cr ODS steels (right) after 1374h exposure to SCW at 550°C. Note different scale.

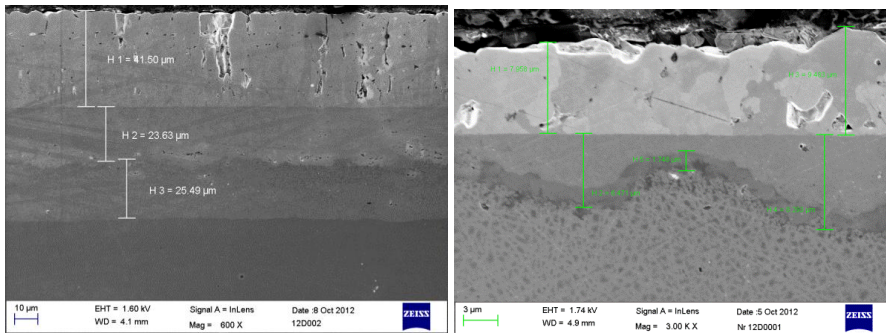


Figure 6. SEM photographs of cross-sections of 12 Cr ODS steel (left) and 14 Cr ODS steel (right) after 3010 h exposure to SCW at 550°C. Note different scale.

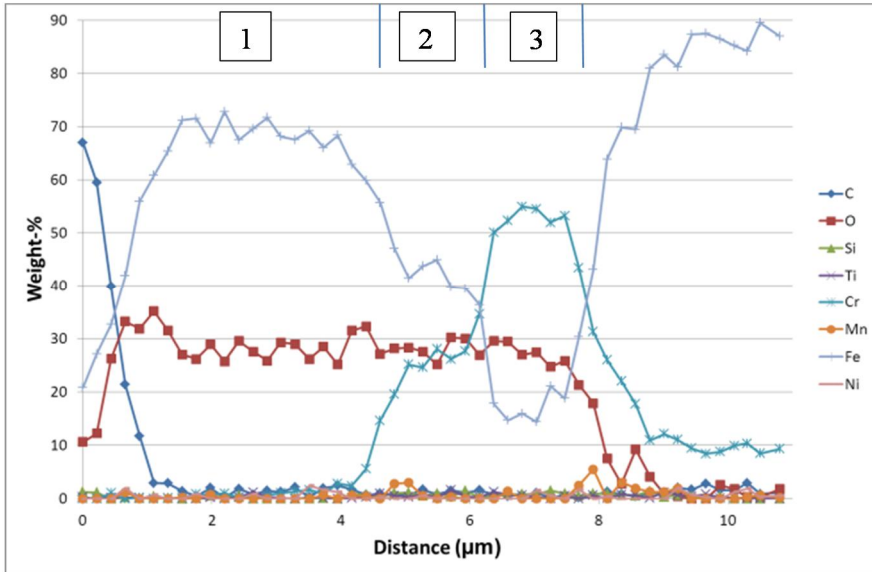


Figure 7. EDS-analysis of 14Cr ODS steel after 3010 h exposure at 550°C in SCW.

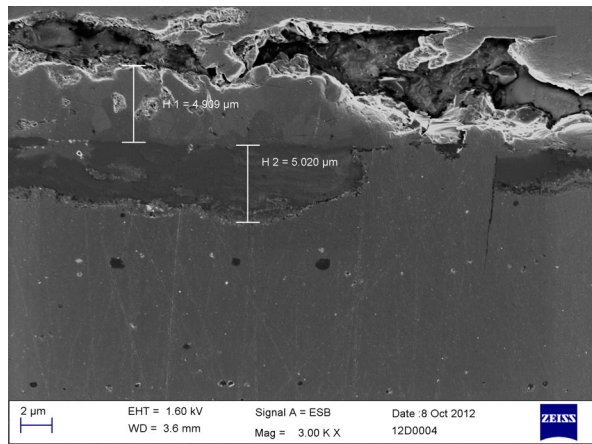


Figure 8. SEM photograph of cross-section of PM2000 after 1450 h exposure to SCW at 550°C.

Table 3. Summary of the results from oxide thickness measurements (SEM) up to 3010 h exposure to SCW at 550°C (n.a. = not available).

Alloy	Exposure time	Max. (μm)	Typical even (μm)
P92	612h	67	65
9Cr ODS	612h	25	23
P92	1374h	80	68
9Cr ODS	1374h	34	30
12Cr ODS	1008h	53	46
14Cr ODS	1008h	18	10
PM2000	1008h	9	3
12Cr ODS	1450h	68	65
14Cr ODS	1450h	15	10
PM2000	1450h	10	3
12Cr ODS	3010h	90	85
14Cr ODS	3010h	18	11
PM2000	3010h	n.a.	n.a.

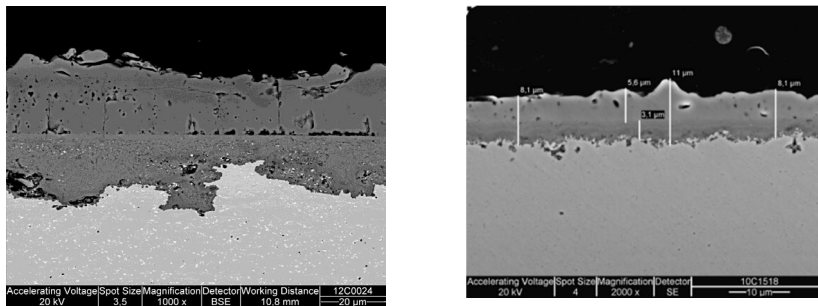


Figure 9. SEM photographs of cross-sections of 12Cr (left) and 14Cr ODS steels (right) after 2000h exposure to SCW at 650°C/25MPa. Note different scaling lines.

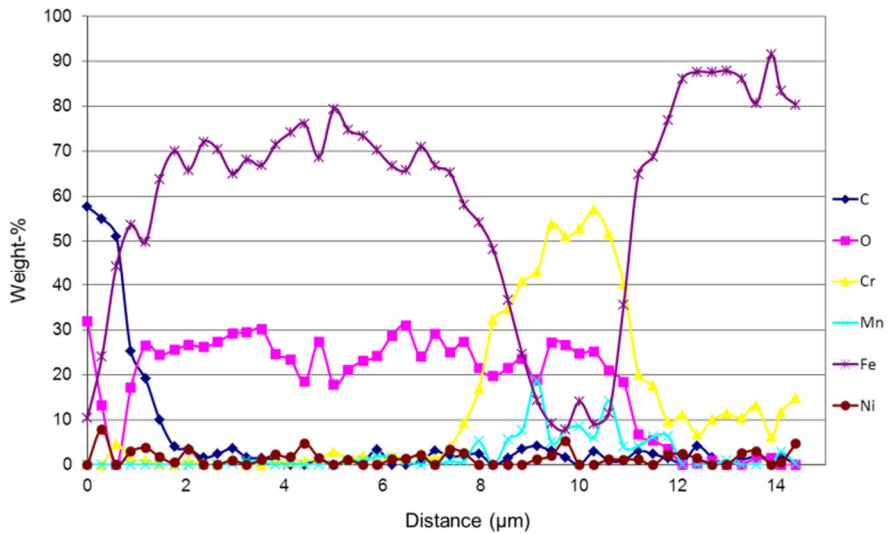


Figure 10. EDS-analysis of 14Cr ODS steel after 2000h exposure to SCW at 650°C.

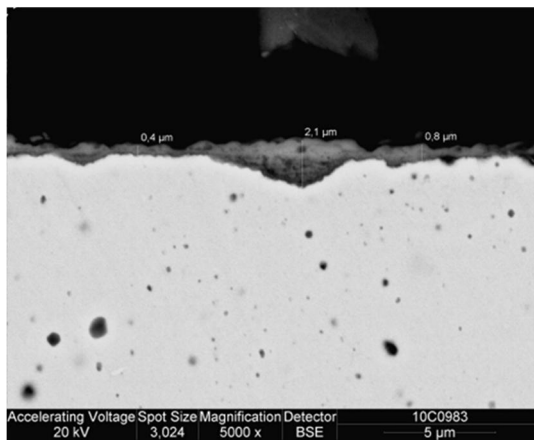


Figure 11. SEM photograph of cross-section of PM2000 after 2000h exposure to SCW at 650°C/25MPa.

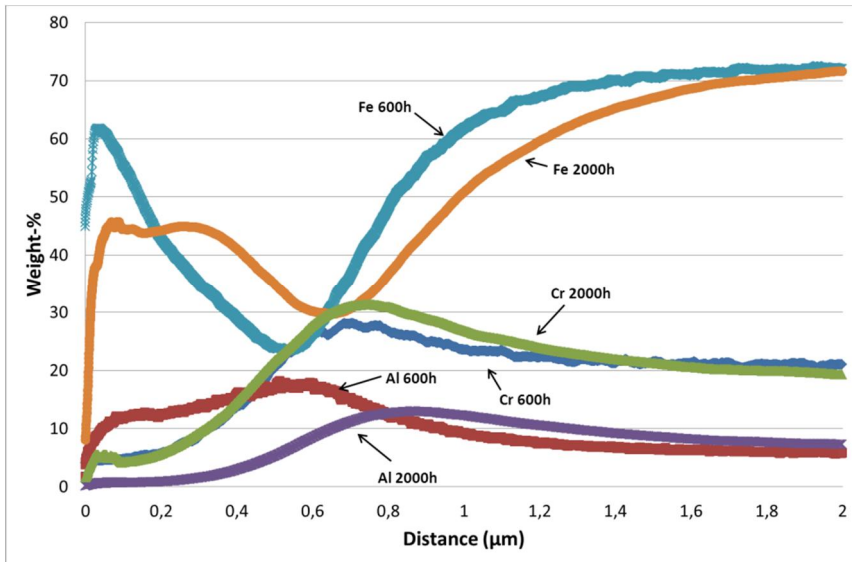


Figure 12. GDOES concentration profiles of Al, Cr and Fe for PM2000 after 600 and 2000h exposures to SCW at 650°C/25MPa.

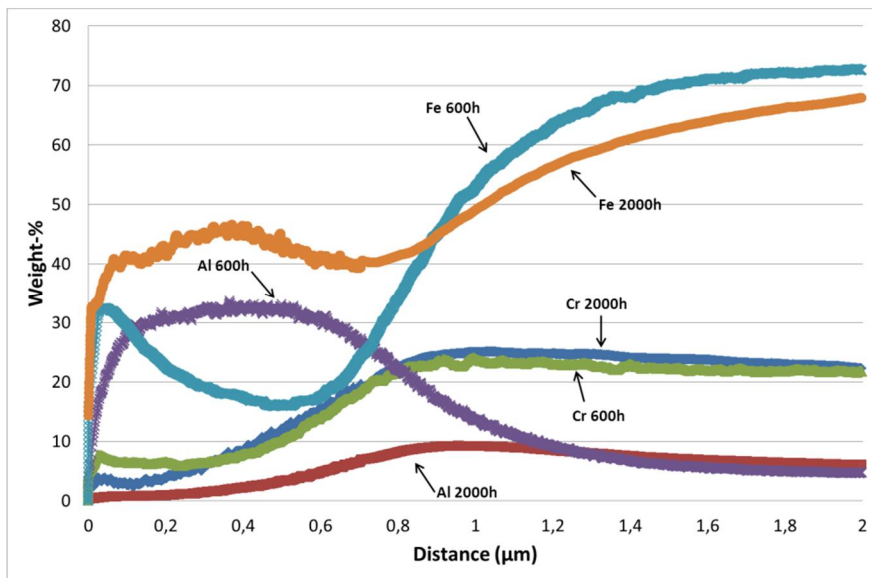


Figure 13. GDOES concentration profiles of Al, Cr and Fe for MA956 after 600 and 2000h exposures to SCW at 650°C/25MPa.

Table 4. Summary of the results from oxide thickness measurements up to 2000h exposure to SCW at 650°C (n.a. = not available).

Alloy	t (h)	Max (μm)	Typical even (μm)
PM2000	600h	1.7	1.2
MA956	600h	2.5	1.7
12Cr ODS	600h	n.a.	n.a.
14Cr ODS	600h	9.5	8.0
PM2000	1000h	6.5	<1.0
MA956	1000h	8.9	3.0
12Cr ODS	1000h	43.2	3.6
14Cr ODS	1000h	10.5	9.0
PM2000	2000h	6.5	0.8
MA956	2000h	12.5	3.0
12Cr ODS	2000h	65.0	32.0
14Cr ODS	2000h	11.0	10.0

3.2 SCC susceptibility

The SSRT stress-strain curves of all tests are shown in Figure 14 and the main results are collected in Table 5. All steels exhibited minimal strain hardening both at 650°C and 550°C. The 12Cr and 14Cr ODS steels showed clearly higher ductility and strength at 550°C than at 650°C. At 550°C the strains to failure were ~12 - 18% and the ultimate tensile strengths ~470–510 MPa. At 650°C, the failure strains were only ~3–4% and the ultimate tensile strengths 320–380 MPa. Due to negligible strain hardening, the yield and ultimate tensile strengths were in the same range. The yield strengths were determined at 1.0% permanent strain instead of the typically used 0.2% due to distinguishing problems related to the low stiffness of the testing machine.

The appearances of the gauge sections and fracture surfaces of the specimens after tests at 550°C are shown in Figures 15 and 16. The fracture surfaces were under thick oxide layers and the microscopic morphology (brittle/ductile, intergranular/transgranular) could not be determined. Overall the appearance of the 12Cr ODS steel fracture surface is very planar without any clear features whereas the appearance of the fracture surface of 14Cr ODS steel reveals the under-laying microstructure of the steel. The fracture surface of the 14Cr ODS steel specimen

resembles intergranular stress corrosion cracking, but that may also result from the microstructure of the material instead of any environmental effect. However, based on the minimal reduction in area and perpendicular fracture surfaces the fractures are assumed to have taken place by a brittle mechanism. The appearances of the fracture surfaces were similar after tests at higher test temperature (650°C), Figure 17.

In the case of the 12Cr ODS steel, the sides of the gauge section were filled with numerous secondary cracks. Similar side cracking has been observed on ferritic-martensitic forged steels after SSRT tests in SCW [7]. The cracking is attributed to the oxide film: brittle failure of the film results in oxidation of the revealed metal and subsequent re-cracking due to stress concentration. On the 14Cr ODS steel, either the mechanical properties and/or smaller thickness of the film prevents this process.

Both 12Cr and 14Cr ODS steels show higher strength compared to the high Cr ODS steel PM2000. The yield and ultimate tensile strengths of PM2000 were in the range of 100–120 MPa at both temperatures in SCW and also in air at 550°C. The strength values are below those given by the original materials supplier [8]. However, the histories of the tested two heats are not known and the low strengths may be a result of recrystallization. No side cracking was observed and the tests, when they were continued till the specimens failed, resulted in ~100% necking without any clear fracture surface.

In general, SCC tests in supercritical water have shown that SCC is a significant problem throughout the SCWR temperature range, i.e. from 290°C to 650°C with austenitic stainless steels and nickel base alloys (< 20% Cr) and, in a lesser degree, with F/M steels [9–14]. However, very little data is available in open literature of the SCC susceptibility of ODS steels in SCW conditions. No clear evidence of SCC was observed in this work, either.

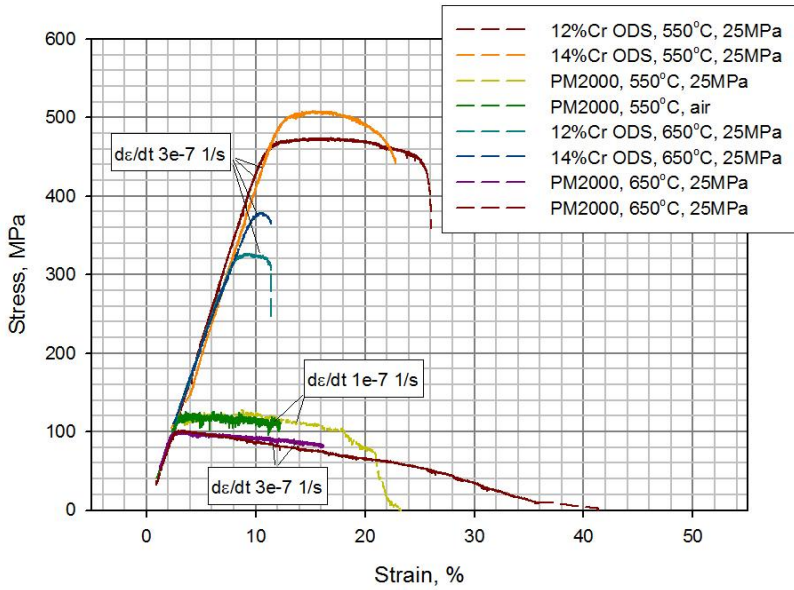


Figure 14. SSRT curves of the tested ODS steels at 550 and 650°C.

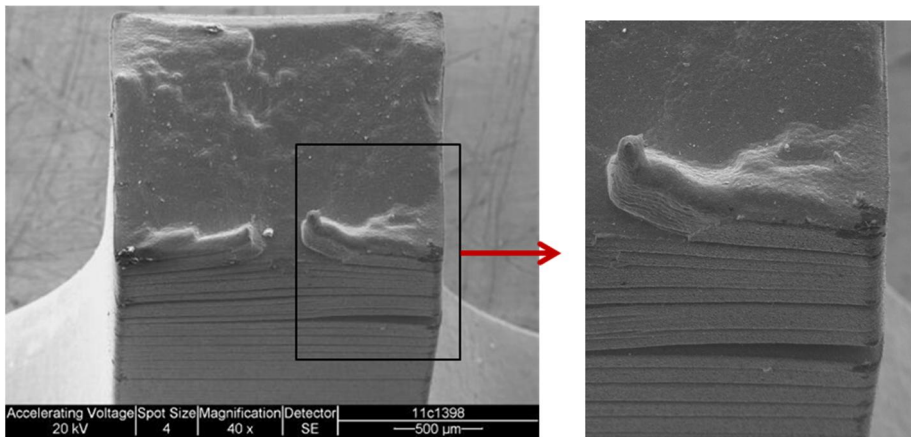


Figure 15. Post-test SEM photograph of the fracture surface of 12Cr ODS steel specimen after test in SCW at 550°C.

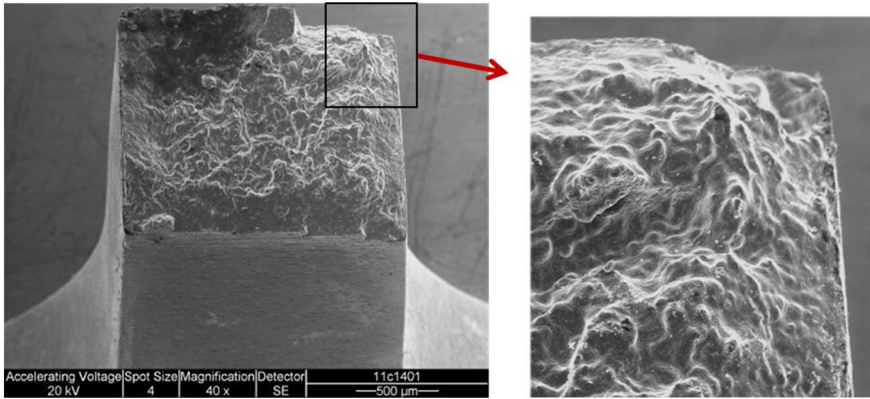


Figure 16. Post-test SEM photograph of the fracture surface of 14Cr ODS steel specimen after test in SCW at 550°C.

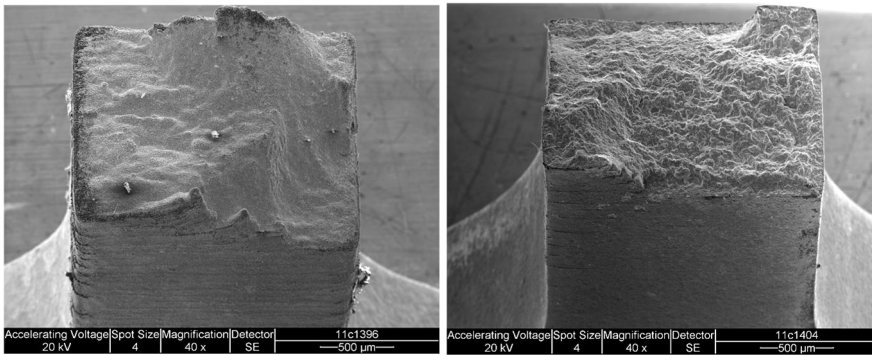


Figure 17. Post-test SEM photograph of the fracture surface of 12Cr ODS (left) and 14Cr ODS steel specimens after test in SCW at 650°C.

Table 5. Summary of SSRT tests of the selected ODS alloys at 550 and 650°C in SCW / air.

Specimen/temperature	Rp _{1.0%}	Max. stress (MPa)	ε (%) at max stress	ε (%) at failure	Fracture mode	Side cracks
12Cr ODS @ 550°C	465	473	4.3	17.8	Brittle*	Oxide cracking**
12Cr ODS @ 650°C	325	327	1.4	4.1	Brittle*	Oxide cracking**
14Cr ODS @ 550°C	502	507	3.9	12.1	Brittle* (macroscopically resembles IGSCC)	No
14Cr ODS @ 650°C	378	379	1.4	2.7	Brittle* (macroscopically resembles IGSCC)	No
PM2000 @ 550°C	118	120	6.1	23.3	Ductile	No
PM2000 @ 550°C in air	119	119	1.3	interrupted at 9.9	-	No
PM2000 @ 650°C	99	99	1.0	interrupted at 14.5	-	No
PM2000 @ 650°C	100	100	1.0	41.3	Ductile	No

*Brittle based on negligible reduction in area. Microscopically could not be determined due to oxidation.

**Side cracks caused by brittle repeatedly cracking oxide film.

4. Conclusions

Based on the weight change tests, Al-alloyed high Cr ODS steels PM2000 and MA956 have superior corrosion resistance when compared to 9–14% Cr ODS steels. The oxidation performance of the high Cr Al-alloyed ODS steels result from the formation of a protective Al–Cr–Fe-rich surface oxide layer. On ODS steels with lower alloying element concentrations, i.e. with no Al, the film is less protective with an iron rich outer and chromium rich inner layers. Based on this work, in SCW conditions at 550°C and above, the Cr-content for thin walled ODS components must be higher than that of the 14Cr ODS steel.

The results indicate that the ODS steels are less susceptible to SCC than austenitic stainless steels or Ni-base alloys. However, ODS steels have been tested very little in SCW and more data is required in order to make any final conclusions.

References

1. Serrano, M., Hernández-Mayoral, M. & García-Junceda, A. Microstructural anisotropy effect on the mechanical properties of a 14Cr ODS steel. *Journal of Nuclear Materials*, 2012, Vol. 428, pp. 103–109.

2. Penttilä, S., Toivonen, A., Heikinheimo, L. & Novotny, R. Corrosion studies of candidate materials for European HPLWR. *Nuclear Technology*, 2010, Vol. 170, pp. 261–271.
3. Chen, Y., Sridharan, K., Ukai, S. & Allen, T. Oxidation of 9Cr oxide dispersion strengthened steel exposed in supercritical water. *Journal of Nuclear Materials*, 2007, Vol. 371, pp. 118–128.
4. Kimura, A. et al. Development of Al added high-Cr ODS steels for fuel cladding of next generation nuclear systems. *Journal of Nuclear Materials*, 2011, Vol. 417, pp. 176–179.
5. Isselin, J., Kasada, R. & Kimura, A. Corrosion behaviour of 16%Cr–4%Al and 16%Cr ODS ferritic steels under different metallurgical conditions in a supercritical water environment. *Corrosion Science*, 2010, Vol. 52, pp. 3266–3270.
6. Zhang, L., Zhu, F. & Tang, R. Corrosion mechanisms of candidate structural materials for supercritical water-cooled reactor. *Front. Energy Power Eng. China*, 2009, 3 (2) pp. 223–240, DOI 10.1007/s11708-009-0024-y.
7. Hwang, S, Lee, B., Kim, J. & Jang, J. SCC and corrosion evaluations of F/M steels for a supercritical reactor. *Journal of Nuclear Materials*, 2008, Vol. 372, pp. 177–182.
8. <http://www.matweb.com/>
9. Was, G. S. & Allen, T. R. Time, temperature, and dissolved oxygen dependence of oxidation in austenitic and ferritic-martensitic alloys in supercritical water. *Proceedings of ICAPP'05*, Seoul, Korea, paper 5690 (2005).
10. Teyseyre, S. & Was, G. Stress corrosion cracking of austenitic alloys in supercritical water. *Corrosion*, 2006, Vol. 62, No. 12, pp. 1100–1116.
11. Was, G. S. et al. Corrosion and stress corrosion cracking in supercritical water. *Journal of Nuclear Materials*, 2007, Vol. 371, pp. 176–201.
12. Penttilä, S., Toivonen, A., Rissanen, L. & Heikinheimo, L. Generation IV Material Issues – Case SCWR. *Journal of Disaster Research*, 2010, Vol. 5, No.4, pp. 469–477.
13. Novotny, R. et al. Stress corrosion cracking susceptibility of austenitic stainless steels in supercritical water conditions. *Journal of Nuclear Materials*, 2011, Vol. 409, Issue 2, pp. 117–123.

14. Zheng, W., Luo, J., Li, M., Guzonas, D. & Cook, W. Stress corrosion cracking of SCWR candidate alloys: A review of published results. The 5th Int. Symp. SCWR (ISSCWR-5) P095, Vancouver, BC, Canada, 13–16 March 2011.

Qualification of structural materials for the advanced 700 C fossil fired power plant – experience gained in the GKM field test loops

Karl Maile¹, Stefan Zickler¹ & Klaus Metzger²

¹Materialprüfungsanstalt Universität Stuttgart
Pfaffenwaldring 32, 70569 Stuttgart, Germany

²Grosskraftwerk Mannheim AG
Marguerrestraße 1, 68199 Mannheim, Germany

Abstract

Components in 700°C power plants which are subjected to highest temperatures and complex loading situations will be made of Ni-based alloys. Two test rigs with high temperature components (tubes, pipes, pipe bends, headers, valves) have been erected in the GKM Power Plant. Aim of the investigation is the qualification of the component fabrication including welding, the basic design and the study of the life time behaviour considering real loading situations. This covers the evaluation of the damage behaviour also. The results gained will be used to adjust life time assessment and inspection strategies on the specific damage evolution in components made of Ni-based alloys.

The paper describes first results gained. Specific emphasis will be put on the appearance of damage in Alloy 617. The conclusions based on this experience considering design, manufacture and inspection will be reported.

1. Introduction

Future power plants will have to operate in a very flexible way in order to compensate the volatile availability of renewable energy sources like wind and solar power. Additional demands come from the need of high efficiency and, for fossil power plants, low emissions.

An increase of efficiency and decrease of emissions is directly connected to an increase of steam parameters, meaning steam temperature and steam pressure. A flexible operation includes a high number of shut-down and start-up cycles with high thermal gradients during the designed lifetime of the power plant.

In the Grosskraftwerk Mannheim two test rigs with thin and thick walled components have been installed to investigate the material and component behaviour of future power plants under future operating conditions. The steam temperature in the test rig is 725°C, the steam pressure 170 bar. By injection of cooling steam and cooling water the stress-strain situation due to shut down and start up cycles

can be reproduced. The material investigations are concentrated on the behaviour of nickel based alloys used for tubes, pipes and valves. Both test rigs are integrated in the steam cycle of unit 6, boiler 17 in the Grosskraftwerk Mannheim.

2. Design of test rigs

Two test rigs have been installed in unit 6 of the Grosskraftwerk Mannheim.

Test Rig HWT 1 is focus on the behaviour of thin walled components, such as the

- Oxidation and corrosive behaviour of superheaters
- Creep and oxidation behaviour of boiler external materials (creep test loops)
- Oxidation behaviour of turbine materials (turbine test loops)
- High-temperature shut-off and control valves

The flow chart of the test rig (HWT 1) is shown in Figure 1.

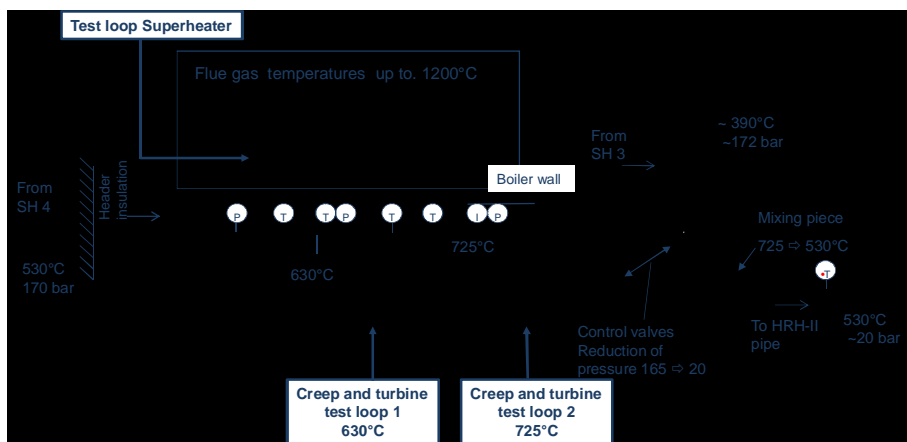


Figure 1. Schematic view of test loop HWT 1 [1].

The steam for the operation of the test rig is taken from superheater-exit 4 with a temperature of 530°C and a pressure of 167 bar. The steam is heated up in a first set of superheater loops to a steam temperature of 630°C. Following this is the first set of boiler-external test loops, the creep test loop and the turbine test loop. After the external test loops the steam runs again into the boiler and is heated up to 725°C and is led through the second set of boiler-external test loops, also a creep test loop and a turbine test loop. Behind the second set of boiler-external test loops are the control valves which operate alternately and control the steam temperature at the boiler exit. In the control valves the steam pressure gets reduced to 20 bar, is cooled down with steam from SH3 to a temperature of 530°C and is recirculated into the GKM steam net.

Test rig HWT 1 operates with the following steam parameters:

- Steam flow: 0.33 kg/s
- Steam conditions at the inlet: 166.5 bar / 530°C
- Steam conditions at the outlet: 156.0 bar / 725°C
- Flue gas temperature: approx. 1260°C
- Tube dimensions: 38 x 8.8 mm
- Tube length (heated): approx. 40 m.

The investigated materials in test rig HWT 1 are martensitic steels, austenitic steels and nickel-based alloys.

After the successful operation of HWT 1 a second test rig was designed and installed in order to extend the scope of investigations towards thick walled components, welds and cyclic behaviour of the materials. This is realized in test rig HWT 2, see also Figure 2.

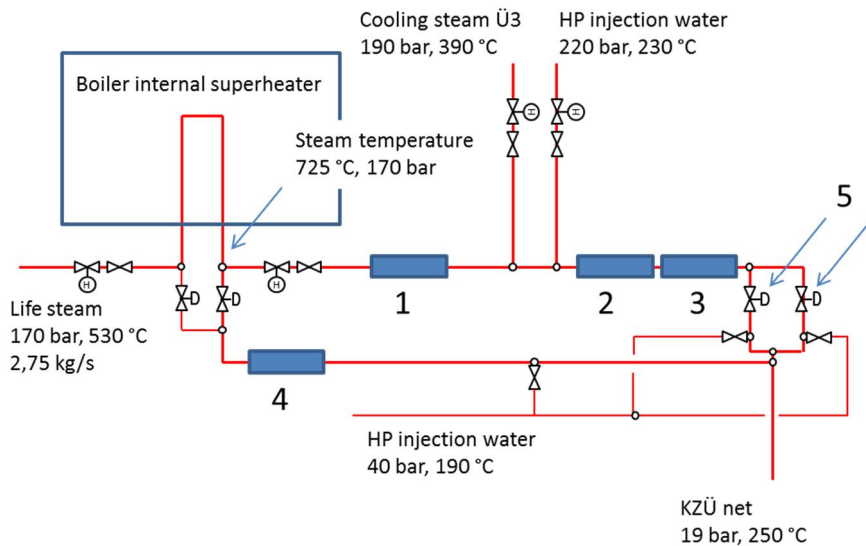


Figure 2. Schematic view of test loop HWT 2 [1].

The focus of test rig HWT 2 lays in the

- component behaviour under primary and additional secondary stresses (1)
- fatigue behaviour with temperature cycles between 400°C and 700°C (2)
- stress-strain situation in headers (3)
- function of HDU bypass valve (4)
- operation of high temperature control and shut off valves (5).

An isometric view of test rig HWT 2 is shown in Figure 3.

Test rig HWT 2 operates with the following steam parameters:

- Steam flow: 4,5 kg/s

- Steam conditions at the inlet: 166.5 bar / 530°C
- Steam conditions at the outlet: 170 bar / 725°C
- Flue gas temperature: approx. 1260°C
- Tube dimensions: 38 x 8.8 mm
- Pipe dimensions: 220 x 50 mm
- Tube length (heated): approx. 400 m.

In test rig HWT 2 the steam is also heated up from a starting temperature of 530°C and 170 bar to 725°C. Following the superheater loops, which are also in the scope of investigations, is the first section of the test path with a static temperature profile. In this section the material behaviour especially regarding a complex loading situation in pipe bends consisting in primary stress due to internal pressure and superimposed secondary stresses. Aim is the investigation of the stress relaxation in this area. Secondary stresses are applied via a cross bar that hinders the thermal expansion of a pipe bend, see also Figure 4.

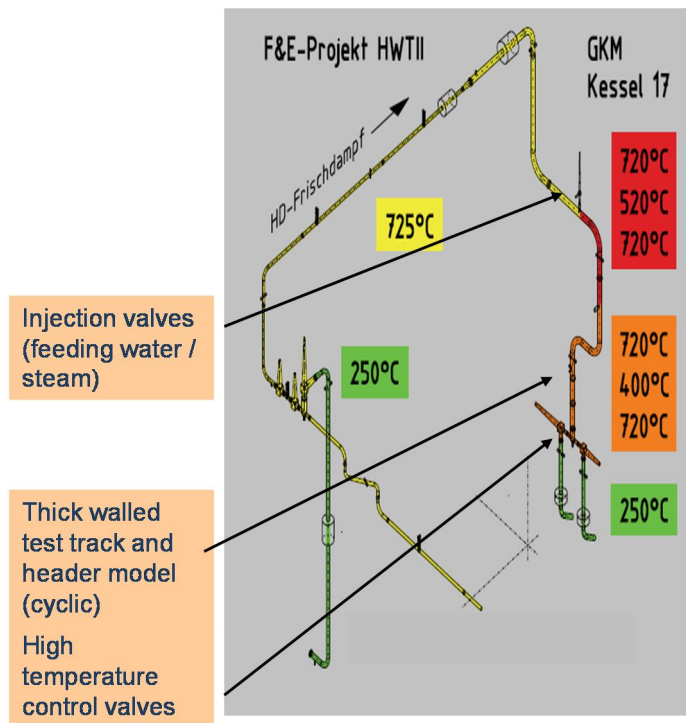


Figure 3. Isometric view of test rig HWT 2.

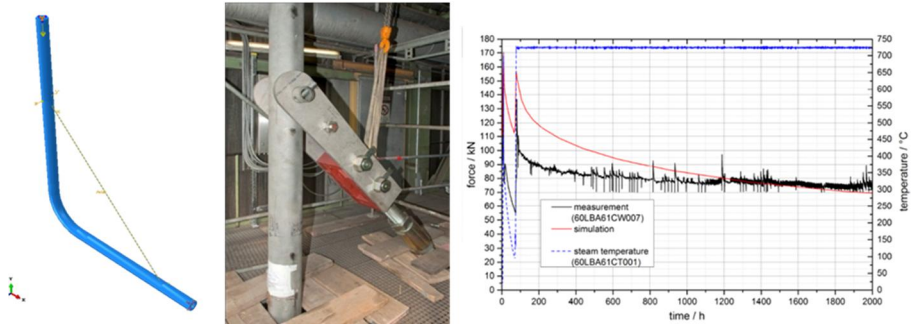


Figure 4. Cross bar for implementation of secondary stresses in pipe bend.

In the second section of the test rig a cyclic operation is realized via injection of cooling steam and cooling water. Within 24 hours of operation 14 load cycles can be achieved, see also Figure 5. The local strains are measured during operation by means of capacitive strain gauges. The measurement is part of the life time surveillance for safe operation of the test rig. They also will be used for the verification of the numerical simulations.

Included in the cyclic area of test rig HWT 2 is specific test piece (header model) in order to reproduce the local stresses and strain in the nozzle area during start up and shut down operation of a future 700°C power plant, see also Figure 6.

Similar to test rig HWT 1 the steam temperature is controlled by two high temperature control valves that are positioned at the end of the test rig. Due to the higher amount of steam in test rig HWT 2 and in order to obtain more operational hours these control valves operate in a parallel way. The pipes are made of Alloy 617 and Alloy 263. Thus similar and dissimilar welds have been implemented. It has to be mentioned that all thick walled parts containing welds have exposed to a stabilization annealing after welding.

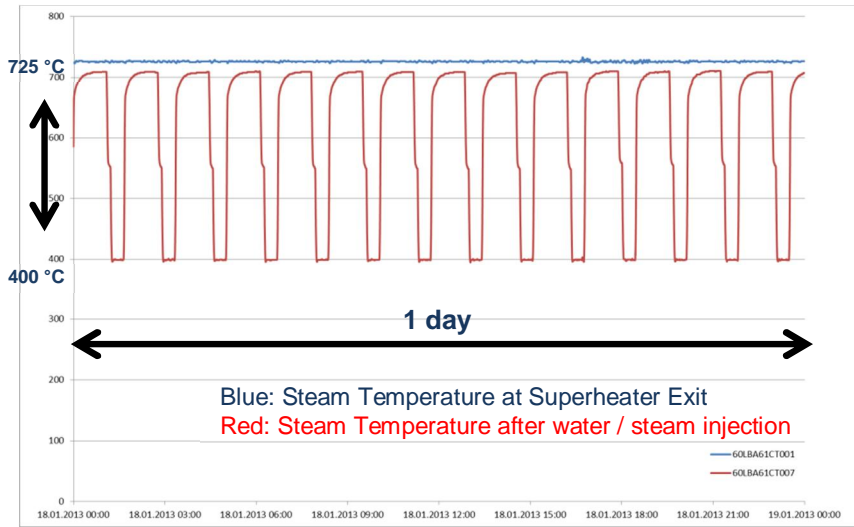


Figure 5. Temperature cycles in test rig HWT 2.

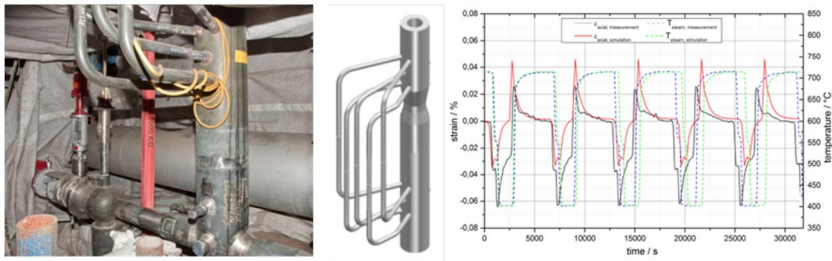


Figure 6. Header test piece in transient section of test rig HWT 2.

3. Material investigations

An overview about the materials investigated is given in Table 1 for the HWT 1 project.

Table 1. Materials used in test rig HWT 1.

Superheater / 635°C			
T92	VM12SHC	SAVE12AD	Sanicro 25
Tempaloy AA1 (SB)	Super 304H (SB)	DMV 304HCu (SB)	HR6W
Post Super 304H	XA704 (SB)	HR3C	HR35
DMV 310N	NF 709	Tempaloy A3	Sumitomo A617
A617 mod.			
Superheater / 725°C			
DMV 310N	HR3C	Sanicro 25	A617 B
HR6W	HR35	HN55	A263
Sumitomo A617	A740	Haynes 230	DMV 141

In HWT II the Alloy 617 and Alloy 263 as pipe material and in addition the Alloy 740 as tube material implemented in the header model is under investigation.

The material qualification programme includes experimental work as creep tests, low cycle fatigue tests with and without holding time at different temperatures, for example Figure 7 and Figure 8, in order to determine the specific material behaviour within the scatter band and to fix the parameters for the constitutive material equations for the Finite Element calculations. Specific emphasis is put on metallographic investigations for the evaluation and quantification of the changes in the microstructure due to mechanical and thermal loading.

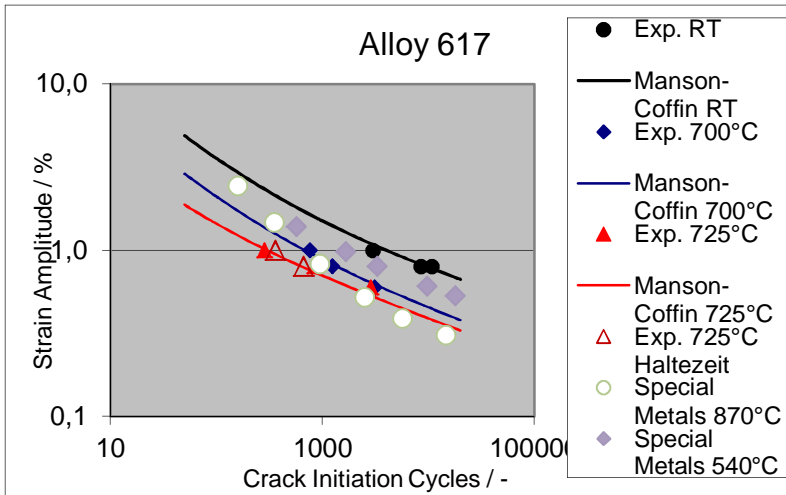


Figure 7. Number of cycles for crack initiation Alloy 617 B [2].

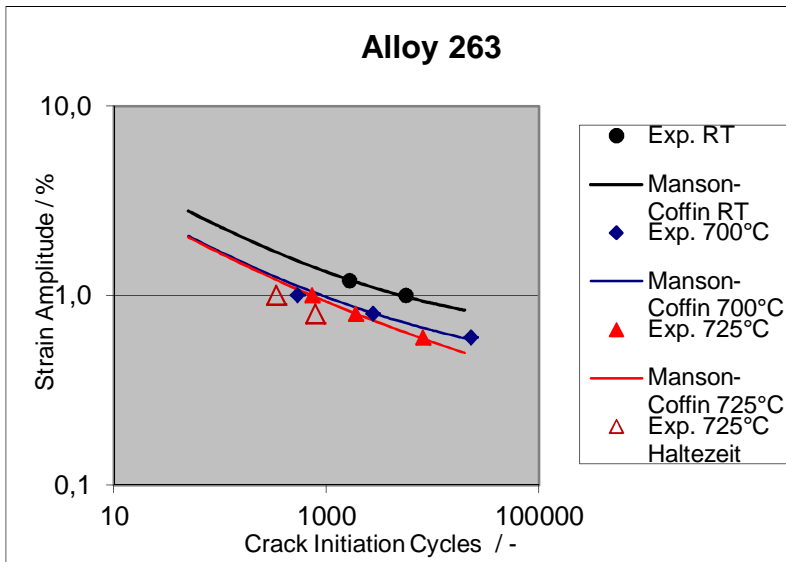


Figure 8. Number of cycles for crack initiation Alloy 263 [2].

4. Numerical calculations

Aim of the inelastic numerical FE- calculation was the determination the local stresses and strains and thus of the allowable cycles and hours of operation in the test rig.

During the operation of the test rigs the local strains and also the changes in temperatures will be measured and compared with results of the FE-calculation. A first comparison between the measured and calculated load in the cross beam of the creep loaded pipe bend is given in Figure 4, demonstrating that the relaxation behaviour of the pipe and cross beam could be described by the numerical calculation.

In Figure 6 the good accordance of the measured and calculated strain cycles is depicted. In Figure 9 the calculation of the von Mises equivalent stress is shown for a T-piece.

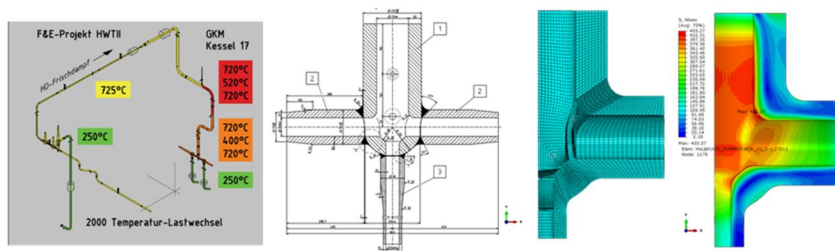


Figure 9. T-piece between temperature control valves HWT 2.

5. Experiences with Test Rig Operation

The HWT I project started in January 2008. The design and erection phase was completed in June 2009. The operation of test rig HWT 1 was started in August 2009. The test rig is still in operation. A total test time at 725°C of 10000 h is achieved (March 2013). Good operational experience has been gained with the superheater test materials. No specific damage reducing the life time as foreseen in the design phase was observed. Especially for the Alloy 617 no significant corrosion attack was observed so far although the tubes were exposed to severe conditions with alternating temperatures up to 725°C and regularly cleaning procedures by means of soot blowers. Cracking was observed in Alloy 617 welds. The reason for that was found in not optimized welding in combination with a missing post weld treatment. The high temperature control valves made of Alloy 617 also showed a very good functionality.

The HWT II project started in January 2011. The design and erection phase was completed in September 2012. The operation of test rig HWT 1 was started in October 2012. The test rig is still in operation. A total test time at 725°C of 3000 h and 700 thermal load cycles is achieved (March 2013). Up to now no dysfunctions with the test rig operation have been identified. The welding of the thick walled pipes (Alloy 617, Alloy 263) and the related post weld treatments caused no significant problems. The effectiveness of the used weld procedures in terms of creep strength and creep ductility was tested in advance by using large scale specimens with original weld dimensions machined out of the pipes.

6. Summary

Within the operation of the two test rigs practical experiences are gained, which will be used for the qualification of components made of Ni-alloys for operation under cyclic loading in the high temperature range up to 700°C.

During the erection phase manufacturing procedures as welding and bending were performed under typical conditions of usual fabrication conditions. A detailed quality engineering strategy was developed in order to meet code requirements under consideration of the specific material behaviours. From qualification, fabrication, operation and the lab test programmes in parallel, a large number of necessary experiences and material data are generated.

The operation phase delivers results and knowledge about the operational and possible damage behaviour of components under real loading conditions. This includes

- Verification of new design methods
- Identification of specific damage mechanisms not to be detected by standard material qualification
- Information about availability and failure risks
- Evaluation of safety margins
- Needs of specific monitoring systems and inspection intervals considering the specific (damage) behaviour of new materials
- Repair and overhaul strategies

Up to now all specified aims have been achieved.

References

1. Zickler, S., Wagner, S., Maile, K., Metzger, K. & Czychon, K.-H. High-temperature-materials-test-rig: materials for future high-efficient power plants. Proceedings of the 38th MPA-Seminar, „Materials Components Behaviour in Energy & Plant Technology“, October 1–2, 2012, University of Stuttgart.
2. Klein, T., Johnson, S., Klenk, A., Straub, S., Knödler, R., Reismann, O., Böhm, D. & Föllmer, B. Untersuchungen zum langzeitigen Betriebsverhalten von Rohren, Guss- und Schmiedeteilen aus Legierungen für zukünftige hocheffiziente Kraftwerke, Abschlussbericht zum Forschungsvorhaben 0327799. Stuttgart, 2012.

Creep-fatigue properties of nickel-base superalloy 263

Rami Pohja, Asta Nurmela, Stefan Holmström & Pekka Moilanen

VTT Technical Research Centre of Finland
Kemistintie 3, Espoo, P.O. Box 1000 FI-02044 VTT, Finland

Abstract

In this paper the creep-fatigue (CF) and low cycle fatigue (LCF) properties of alloy 263 are considered. Both virgin and pre-crept (750°C / 178 MPa / 3000 h) test materials were tested to investigate the impact of creep damage prior to cycling. The tests performed on the high precision pneumatic loading system (HIPS) are in the temperature range of 700–750°C, total strain range of 0.6–1.0% and with hold times in both tension and compression. Curves of peak stress as a function of cycles and curves of stress relaxation are presented for the alloy 263. The creep-fatigue test results are also analysed using methods described in the assessment and design codes of RCC-MR, R5 and ASME NH as well as by the recently developed Φ -model. It is shown that the number of cycles to failure for CF data can be accurately predicted by the simple Φ -model. The practicality in using the life fraction rule for presenting the combined damage is discussed and recommendations are given on alternative approaches.

1. Introduction

Even though the power plant components are subjected to both fatigue damage during the start-ups and shut-downs and to creep damage during the steady state operation, the lifing of power plant components has been traditionally based on creep, prevention of type IV cracking and pipe thinning in bends. The lifing based on creep is no longer considered to be adequate for the advanced ultra supercritical plants. In nuclear codes such as ASME and RCC-MR the creep-fatigue interaction is already accounted for concerning the generation IV technology.

Nickel-base superalloys, like alloy 263, are often used in aircraft engine components such as combustion chamber, casing, exhaust ducting and bearing housings. Ni-based superalloys have excellent creep strength at temperatures above 700°C due to precipitation of γ' . Because of the lower thermal expansion coefficient they are less prone to thermal fatigue damage than the austenitic stainless steels. The nickel-base superalloys are candidate materials for thick section components as well as tubing in advanced ultra super critical power plants.

The creep and tensile properties of the nickel-base superalloys are quite well characterized over a wide temperature range. However, studies of creep-fatigue

interaction for the nickel-base superalloy 263 are scarce in open literature [1, 2]. This paper describes a study for the creep-fatigue interaction of nickel-base superalloy 263.

2. Materials and experimental procedure

2.1 Tested material

The experiments were carried out on a NIMONIC alloy 263 supplied by Special Metals Wiggin Limited. The alloy 263 billet was solution heat treated for 2 hours at 1150°C with a water quench. Additionally, an ageing heat treatment of 4 hours at 800°C was carried out for the billet. The chemical composition of the alloy is shown in Table 1.

Table 1. The chemical composition of NIMONIC alloy 263.

Position	Chemical Composition (Weight % except where stated ppm)																
	C	Si	Mn	S	Ag (ppm)	Al	B (ppm)	Bi (ppm)	Co	Cr	Cu	Fe	Mo	Ni	Pb (ppm)	Ti	Ti+Al
Max	0.08	0.40	0.60	0.007	5	0.60	50	1	21.0	21.0	0.2	0.7	6.1	Bal	20	2.4	2.8
Min	0.04					0.30			19.0	19.0			5.6			1.9	2.4

Alloy 263 is a polycrystalline Ni-base superalloy that exhibits face-centered cubic crystal structure. The initial microstructure for alloy 263 before testing is shown in Figure 1. Twin boundaries inside the grains can clearly be seen. Some grains contained precipitates that were probably titanium carbides. The grain boundaries were found to locally show heavy etching and they probably included $M_{23}C_6$ carbides. The standard heat treatment (8 hours at 800°C) for alloy 263 also produces 10% γ' coupled with precipitate free zones and $M_{23}C_6$ carbide densely distributed at grain boundaries. [3, 4]

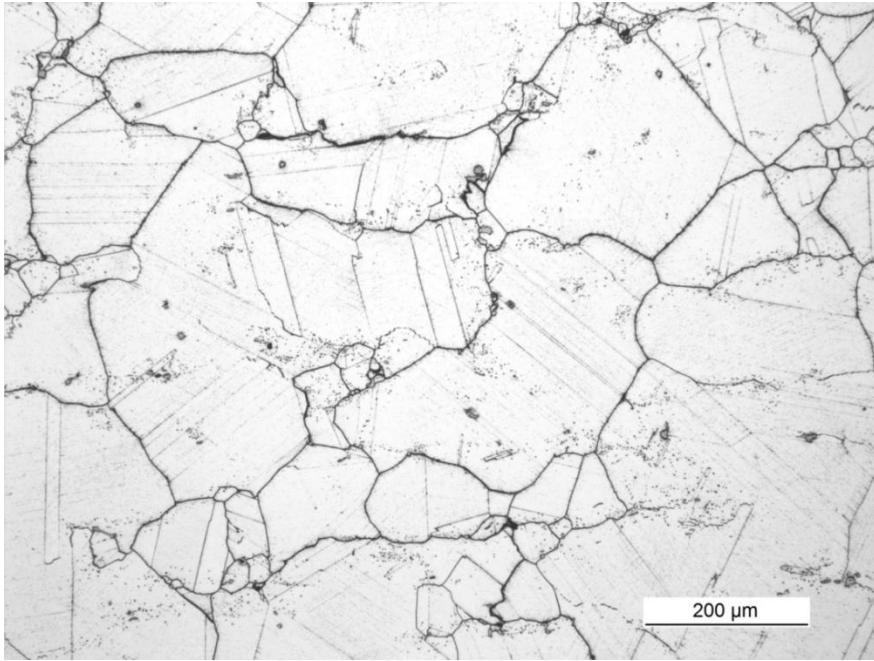


Figure 1. Microstructure of NIMONIC alloy 263 prior to testing.

2.2 Testing parameters

Low cycle fatigue (LCF) tests with fully-reversed ($R=-1$) total axial strain control with and without hold periods were conducted in air atmosphere. The temperature range for testing was between 700 and 750°C. The strain rate was 0.1% / sec and the total strain range was between 0.6% and 1.0% of the gauge length. The LCF tests were performed on material in both virgin state and in pre-crept condition. The pre-crept test specimens had been creep tested at 178 MPa / 750°C for 3000 h hours. The accumulated strain was roughly 0.7%. The pre-crept tests were conducted to investigate the impact of prior creep damage to creep fatigue life. The strain waveform for LCF testing without hold periods and with hold periods, respectively, are shown in Figure 2.

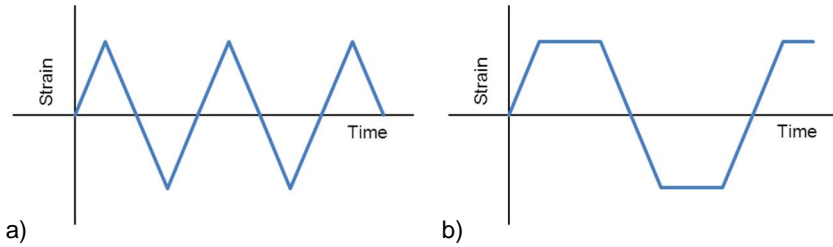


Figure 2. The strain waveforms for LCF testing without hold periods in a) and with hold periods in b).

2.3 Testing facility

Tests were conducted using high precision pneumatic loading system (HIPS) for creep-fatigue testing. Although the tests were conducted at air atmosphere, the pneumatic servo-controlled loading system is capable of operating in a range of extreme conditions such as at high temperature, pressurised water or steam, supercritical water (SCW) and irradiation environments. The main benefit of the pneumatic loading system is that there is no moving parts (loading lead-throughs) required for loading a specimen inside a pressure vessel or otherwise demanding containment (water, gas, radioactive), only pressure lines and electrical feedback connections together with the pneumatic loading unit, bellows, are required [5, 6]. More detailed description of high precision pneumatic loading system and its capabilities is given in reference 5 and 6. A schematic illustration of HIPS creep-fatigue testing equipment is presented in Figure 3.

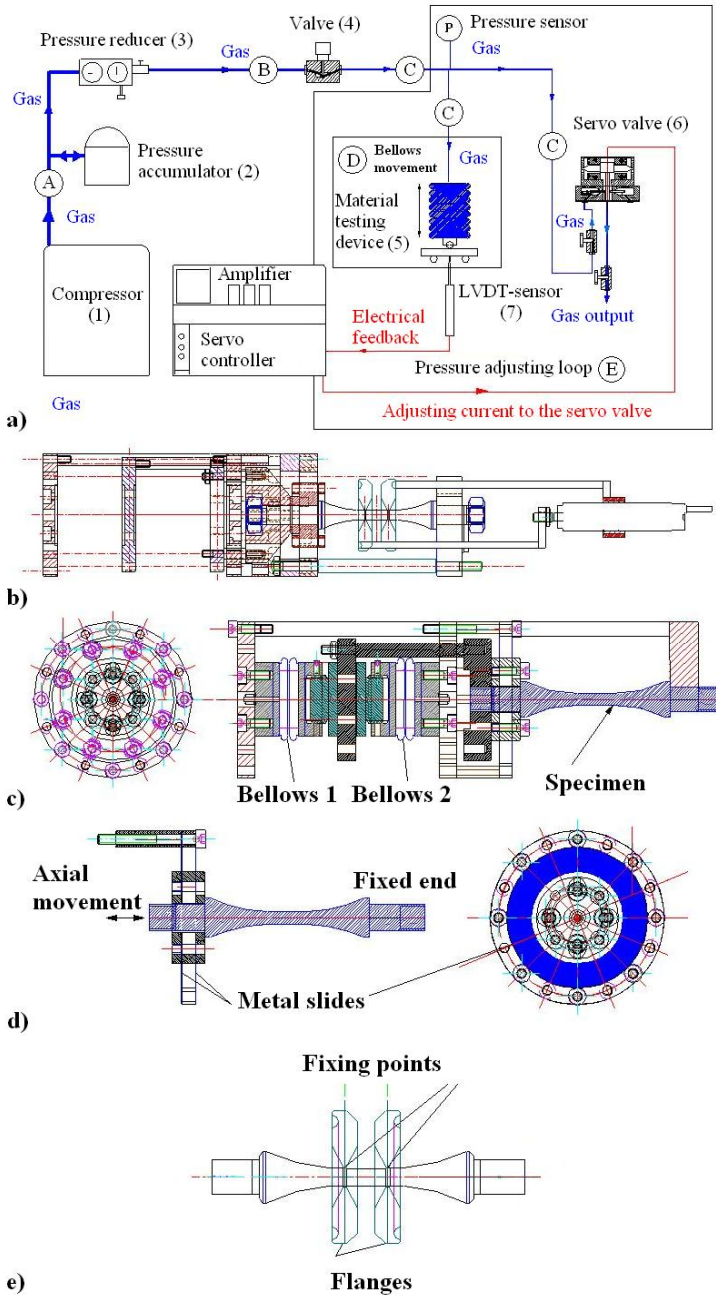


Figure 3. The main components of the HIPS system in a), the main parts of the displacement measurement system in b), the loading frame in c), the specimen fixing parts in d) and LVDT fixing flanges in e).

3. Results

3.1 Cycles to failure

In this study the number of cycles to failure used in the assessment is defined as the number of cycles to 5% load drop. Peak stresses divided by the ultimate tensile strength as a function of cycles for specimens tested at 750°C are shown in Figure 4. The number of cycles is normalized by the number of cycles to failure of the longest test. As expected, the peak stress increased when the total strain range was increased and the number of cycles to failure decreased when the total strain range and the length of the hold periods were increased. However, about the same amount of cycles to failure was achieved with specimens tested with 0.6% and 1.0% total strain range both having 6 minutes hold periods in tension and compression, but the results fit well within the scatter band usually observed in creep-fatigue testing. The largest number of cycles to failure was achieved with a test having the total strain range of 0.6% without hold periods. The smallest number of cycles to failure was achieved with a pre-crept specimen. The total strain range for this specimen was 1.0% and the hold period was 1h both in tension and compression.

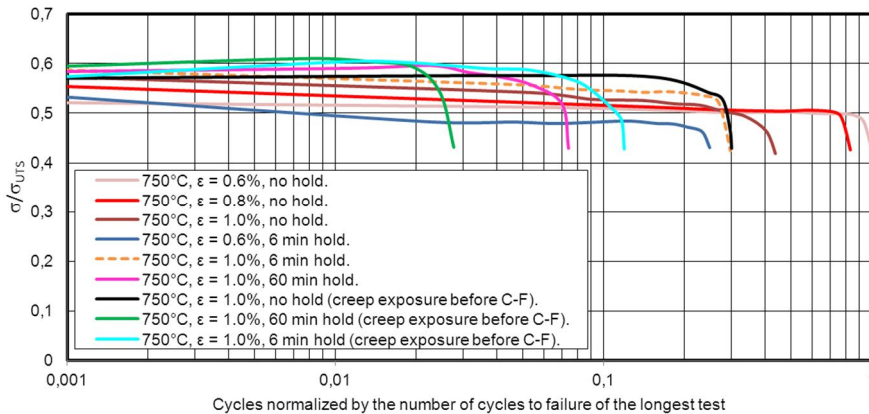


Figure 4. Peak stresses as a function of cycles for creep-fatigue specimens tested at 750°C.

3.2 Relaxation

For NIMONIC 263 pre-crept specimens showed larger relaxation in the strain controlled creep-fatigue tests compared to the specimens in the virgin state. Based on the NIMONIC 263 available creep test data, creep at 0.7% strain can be at tertiary stage of the creep curve and thus expected to include a fair amount of

accumulated creep damage. Furthermore, exposure at 750°C for 3000 h may cause the dissolution of the $M_{23}C_6$ carbides which also increases the creep and relaxation rates. For both the pre-crept and the virgin material specimens a major part of the relaxation occurred during the first 6 minutes in the tests having 1.0% total strain range. Between 6 and 60 minutes the relaxation curves for both sets of specimens became nearly horizontal. However, increasing the hold period from 6 to 60 minutes reduced the total number of cycles to failure approximately by a factor of 3 for both the pre-crept and virgin material specimens. The measured and modelled relaxation curves on the tension side for 6 min and 60 min hold periods at $N_f/2$ cycles for both sets of specimens are shown in Figure 5a and ratio between the peak stresses at the beginning of the hold periods and relaxed stresses at the end of hold periods are shown in Figure 5b.

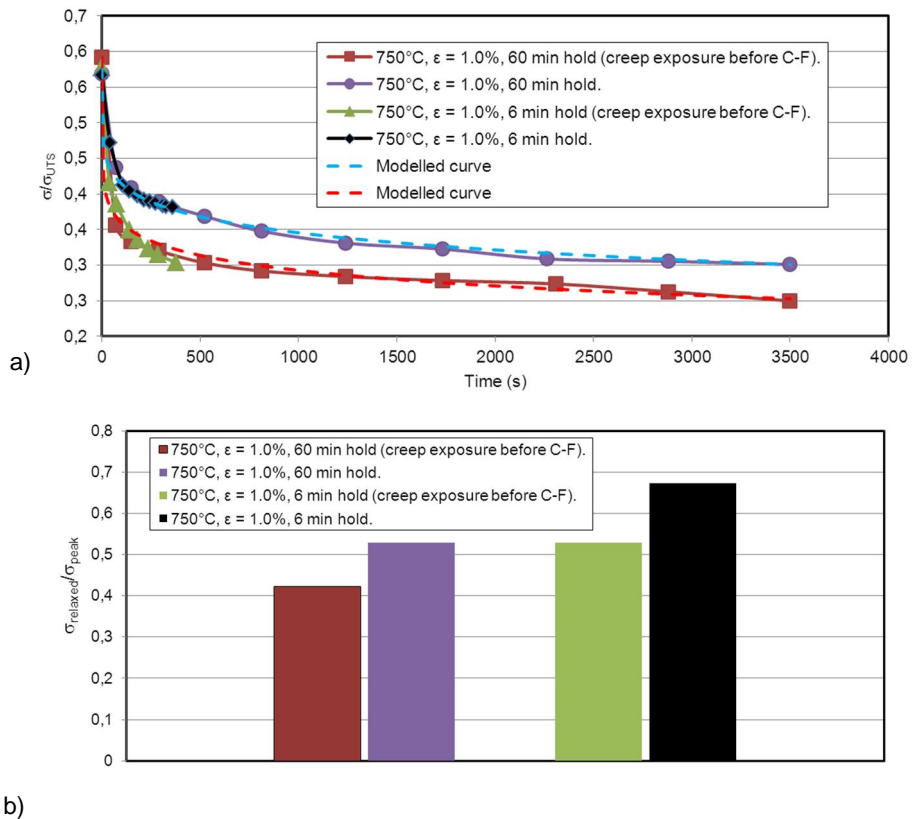


Figure 5. The measured and modelled relaxation curves on the tension side for 6 min and 60 min hold periods at $N_f/2$ cycles in a) and ratio between the peak stresses at the beginning of the hold periods and relaxed stresses at the end of hold periods are shown in b).

The relaxation curves for creep exposed and virgin material specimens at $N_f/2$ cycles were modelled with the following Equation [1]:

$$\sigma = \sigma_{max}/e^{\alpha t^\beta} \quad (1)$$

where σ_{max} is the peak stress at the beginning of the hold period, t is time during the hold period, α and β are material constants. As can be seen in Figure 5a, the measured data correlates well with the modelled curve. The effective stress level of the hold period presented in Figure 6b can be calculated by integrating the Equation (1) for creep damage per cycle (dc) over the hold time t :

$$dc = \int_0^{t_h} dt/tr[\sigma(t)] \quad (2)$$

where $\sigma(t)$ is the relaxation curve. This is considered to be one method to estimate the creep damage of a single cycle of a creep-fatigue test. As shown in Figure 6a, using the method described in ASME nuclear code the creep damage per one cycle is calculated as a summation of damage corresponding from peak stress to the relaxation strength associated with S_{LB} , and damage corresponding to the stress level of S_{LB} [7]. Nuclear code RCC-MR uses different approach in determining the relaxation behaviour and creep damage. in RCC-MR the stress relaxation behaviour is estimated by the creep strain law and the strain hardening rule.

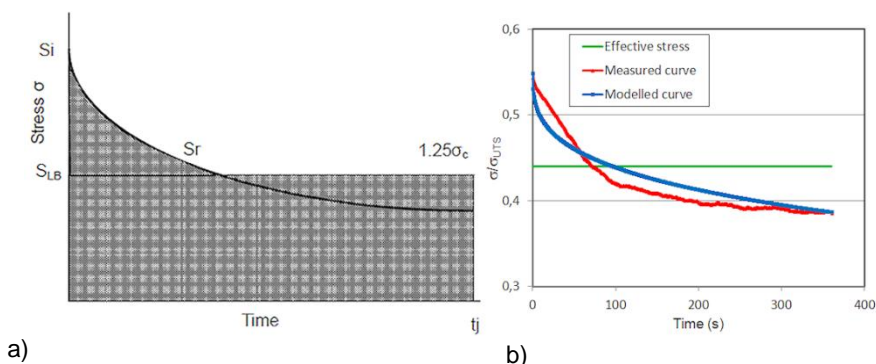


Figure 6. ASME nuclear code method for determining the relaxed stress level in a) [7], measured and modelled relaxation curves and effective stress level calculated by Equations (1) and (2) in b).

3.3 Life fraction rule

The linear damage rule or life fraction rule has been used extensively in the evaluation of creep-fatigue interaction. It is based on the simple assumption that fatigue damage can be expressed as summed cycle fractions and that creep damage can be expressed as summed time fractions. It is also assumed that these quantities can be added linearly to represent damage accumulation. Failure should occur when this summation reaches a certain value, so that:

$$\sum_j \left(\frac{t}{t_r}\right)_j + \sum_k \left(\frac{n}{N_f}\right)_k \leq D \quad (3)$$

Where n is the number of cycles of exposure at a given strain range, N_f is the cycles to failure at the same strain range, t is the time of exposure at the same stress-temperature combination and t_r is the time to rupture at the same stress-temperature combination. In some cases, D is assumed to be unity, because cycle ratio summation should be unity when no creep damage is present. [8] In nuclear codes such as RCC-MR and ASME, the interaction envelope whose intersection point is (0.3, 0.3) is used for nuclear grades 304 and 316 for design purposes. This means that from design point of view the combined fatigue and creep damage that a component experiences should not at any circumstances exceed the (0.3, 0.3) line, otherwise a failure may occur. Furthermore, fatigue and creep damage are calculated with safety margins for design purposes.

The creep-fatigue test results with hold periods were evaluated with the life fraction rule method as shown in Figure 7. The creep component (dc) for one cycle was obtained by comparing the reference stress shown in Figure 6b to the corresponding creep to rupture data at equal stress level and temperature at the $N_f/2$ cycle. The total creep damage was obtained by multiplying the dc (Eq. 2) obtained from the $N_f/2$ cycle with the total number of cycles to failure. This approach (calculating the total creep damage from $N_f/2$ cycle) is similar to the method described in the RCC-MR. In ASME, the creep component for one cycle is calculated from the 1st cycle of the test. The fatigue component was obtained by comparing the total number of cycles to failure of specimens tested with hold periods to those tested without holds. No creep damage is assumed to be present in tests performed without hold periods.

As can be seen in the Figure 7, the test results with 1.0% total strain range and 6 minute hold periods lie near the 0.3, 0.3 line in the life fraction rule plot, and the rest of the test results are near the 0.1, 0.1 line. All test results are below the unity line. As expected, the specimens that were pre-crept have larger creep component in the life fraction rule plot due to the creep exposure.

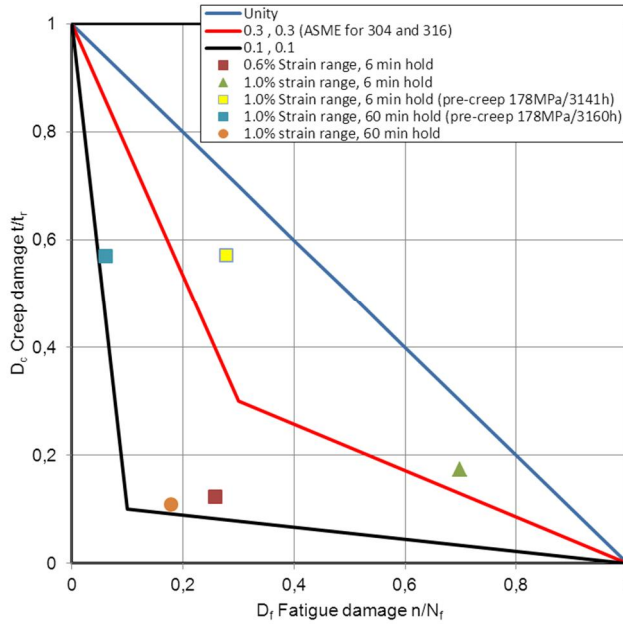


Figure 7. The life fraction rule plot with test results.

3.4 The Φ -model

The Φ -model predicts the expected life under tensile-compressive loading cycles with or without hold periods. The effective creep-fatigue lifetime (t_{CF}) and corresponding number of cycles to failure (N_{CF}) are predicted utilising the creep rupture properties of the material [9]. When using a creep model for assessing creep-fatigue data, the selected model should have good predictive capability both in short and long term range, which is not usually the case for models optimised for best performance for long term predicted life. If the creep rupture model of choice is that of Wilshire, then the measured value of the normalised reference stress Φ_m for each CF data point can be calculated from:

$$\Phi_m = \exp\{-k[t_{CF} \cdot \exp(-\frac{Q}{R \cdot T})]^u\} \quad (4)$$

where k and u are material constants from Wilshire model, Q is the apparent activation energy, T is temperature and R is the gas constant [10]. The required constants for the normalized reference stress as a function of strain range, hold time and temperature are acquired from fitting the multi-linear regression:

$$\Phi_{CF} = c_1 + \frac{c_2}{\Delta \varepsilon} + c_3 \cdot \log(t_h) + c_4 \cdot T \quad (5)$$

where c_1 – c_4 are fitting constants. For alloy 263 test data set it was observed that for LCF tests an effective hold period for t_h can be calculated from:

$$t_h = \frac{\Delta\varepsilon}{\alpha\dot{\varepsilon}} \cdot T \quad (6)$$

where $\Delta\varepsilon$ is total strain range, $\dot{\varepsilon}$ is strain rate, α is a material constant (in Kelvin units) and T is temperature. Combining Eq. (4–6) t_{CF} can be calculated:

$$t_{CF} = -\left(\frac{\ln(\Phi_{CF})}{k}\right)^{\frac{1}{u}} \cdot e^{\left(\frac{Q}{RT}\right)} \quad (7)$$

The total number of cycles to end criterion is:

$$N_{CF} = \frac{t_{CF}}{t_h} \quad (8)$$

The VTT creep-fatigue test results for virgin material specimens and public domain data were predicted using the Φ -model. A comparison of the predicted versus measured creep-fatigue life in terms of total number of cycles to end criterion in logarithmic scale is shown in Figure 8. The Φ -model predicts accurately both LCF and CF cycles to failure up to 10 000 cycles and conservatively when approaching the fatigue limits.

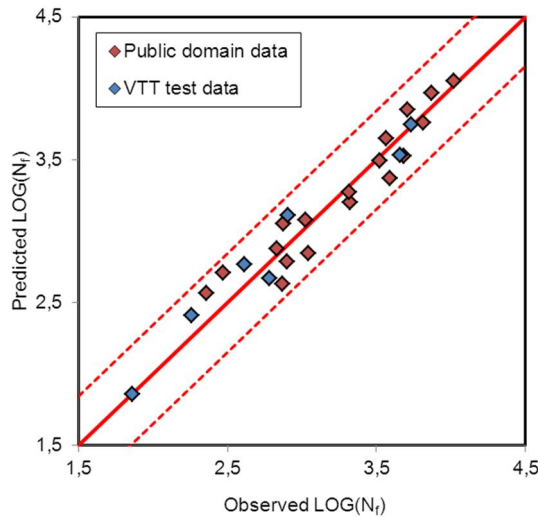


Figure 8. Predicted versus measured creep-fatigue life in terms of cycles to failure in logarithmic scale modelled with Φ -model [1, 11, 12, 13].

4. Discussion

As expected, the test results demonstrated that increasing the total strain range and the length of the hold period decrease the total number of cycles to failure. Furthermore, the test results demonstrated that relaxation is accelerated if the

specimens had been pre-crept to 0.7% strain at 750°C. In the near future, tests with 10 h hold period will be carried out for pre-crept and virgin material specimens and tests with cross-weld specimens will be carried out with the total strain range of 0.6–1.0% and hold periods of 6 min – 10 h.

Although the life fraction rule is widely used in creep-fatigue damage assessment, there are issues to be considered concerning the practicality of the method. Safety margins included in the nuclear codes such as ASME and RCC-MR may lead to very conservative results where single test plots are a thousand times above the unity line in the diagram when assessing creep-fatigue test results. In some cases the evaluation is not even possible. When hold periods are included the determination of the relaxed stress level, which is not straightforward in some cases, has a strong impact on the creep component. The ASME procedure, where the creep component for one cycle is calculated from the 1st cycle of the test, tends to overestimate the stress level used for creep component calculation. Especially with materials such as P91 which exhibit continuous cyclic softening the impact to dc can be considerable. When used for design purposes, the conservatism of the ASME and RCC-MR life fraction procedure may lead to solutions, which are not economically reasonable.

A significant advantage of the Φ -model to predict creep-fatigue life is that at least for a given isothermal test type, it is not necessary to consider further details of individual creep-fatigue cycles, such as features of relaxation, peak stress, softening or hardening behaviour. The extrapolation in hold time may be possible in a similar way as for creep (longest time x 3), but this has still to be validated with culled data sets or by data with longer hold times. Assuming that the Wilshire creep rupture model is used, and the temperature dependence of UTS is described by a 3rd degree polynomial, the total number of fitting constants is four for UTS + three for the Wilshire model + four for Φ model equalling 11 constants. This is a very small number considering that the constants for UTS and Wilshire creep model can be determined separately from relatively simple standard tests. The number of constants may be further reduced if UTS has been tested for the same material batches and isotherms that have been used for creep testing.

The Φ -method has been shown in earlier work to predict well the observed creep-fatigue life of austenitic stainless steel 316FR, ferritic steel P91 and nickel alloy A230 subjected to isothermal strain controlled cycles with tensile hold periods [6, 14]. For alloy 263 (VTT and public domain data) the maximum expected error in prediction is within a factor of 3 with the 99% confidence limit. It is a future objective to find adjustment factors for the Φ model to also predict pre-crept tests in LCF and CF.

The Φ -method also allows a simple definition of creep-fatigue damage $D_{CF} = N/N_{CF} = \Sigma t_h/t_{CF}$ where N is the consumed amount of cycles and Σt_h is the corresponding time in hold. For this damage parameter there is no need to separate creep and fatigue damage or life fractions. The Φ -method hence allows for more straightforward damage assessment for both design and later life assessment than the common methods using summed life (or strain) fractions. It is expected that the approach is applicable for many creep-fatigue cases in power generation,

where strain rates and cycling frequencies are low and even lower (more creep dominated) than in creep-fatigue testing in the laboratory.

5. Conclusions

Creep-fatigue properties of Nimonic 263 have been investigated and creep-fatigue interaction has been evaluated and compared with the linear life fraction rule and the newer Φ -model. The following conclusions were drawn from the test results and evaluation:

- (1) The peak stress increased with increasing total strain range, and the number of cycles to failure decreased with increasing total strain range and length of the hold periods. Increasing the hold period from 6 to 60 minutes reduced the total number of cycles to failure approximately by a factor of 3.
- (2) The pre-crept specimens (750°C / 178 MPa / 3000 h) showed larger relaxation than the virgin material specimens.
- (3) All experimental combinations of creep and fatigue damage resided below the unity line in life fraction rule plot. A major part of the creep life fraction consisted of pre-test exposure of the pre-crept specimens.
- (4) The Φ -model predicted the creep-fatigue life to within a factor of 3 at 99% confidence for the virgin specimens of alloy 263.

Acknowledgements

The authors wish to express their gratitude to the participants of the NextGen-Power project (Project no: ENER/FP7EN/249745/"NEXTGEN-POWER") and to the European Commission for financial support.

References

1. Kubushiro, K., Yoshizawa, H., Itou, T. & Nakagawa, H. Creep-fatigue properties of the candidate materials of 700°C-USC boiler. Proceedings of CREEP8, 8th International Conference on Creep and Fatigue at Elevated Temperatures. San Antonio, Texas, USA, 22–26 July 2007.
2. Zhang, Y. & Knowles D. Isothermal and thermomechanical fatigue of superalloy C263. Superalloys 2000. Edited by Pollock, T., Kissinger, R., Bowman, R., Green, K., McLean, M., Olson, S. and Schirra, J. TMS The Minerals, Metals & Materials Society, 2000.

3. Semba, H., Okada, H., Yonemura, M. & Igarashi, M. Creep strength and microstructure in 23Cr–45Ni–7W alloy (HR6W) and Ni-base superalloys for advanced USC boilers. In: Proc. 34th MPA-seminar, 2008.
4. Wang, W., Hong, H., Kim, I., Choi, B., Jeong, H., Kim, M. & Jo, C. Influence of γ' and grain boundary carbide on tensile fracture behaviors of Nimonic 263. *Materials Science and Engineering A*, 2009, Vol. 523, pp. 242–245.
5. Moilanen, P. Pneumatic servo-controlled material testing device capable of operating at high temperature water and irradiation conditions. Espoo, VTT, 2004. VTT Publications 532. ISBN 951-38-6384-0.
6. Pohja, R., Nurmela, A., Moilanen, P. & Holmström, S. Multifunctional High Precision Pneumatic Loading System (HIPS) for Creep Fatigue Testing. The 6th International Conference on Creep, Fatigue and Creep-Fatigue Interaction, (CF-6). Mamallapuram, India, 22–25 January 2012.
7. Riou, B. Improvement of ASME NH for grade 91 negligible creep and creep fatigue. ASME Standards Technology, LCC, Three Park Avenue, New York, NY 10016-5990, 2008. ISBN 978-0-7918-3165-6.
8. Conway, J. Creep-Fatigue Interaction. In: ASM Handbook, Vol. 8, Mechanical Testing, ASM International, 1992. ISBN 0-87170-007-7.
9. Holmström, S. & Auerkari, P. A robust model for creep-fatigue life assessment. *Materials Science & Engineering A*, 2013, Vol. 559, pp. 333–335.
10. Wilshire, B., Scharning, P. & Hurst, R. A new approach to creep data assessment. *Materials Science and Engineering A*, 2009, Volumes 510–511, pp. 3–6.
11. NIMONIC[®] alloy 263, Datasheet, www.specialmetals.com, Special Metals Wiggin Limited, Hereford, England.
12. HAYNES[®] 263 alloy, Datasheet, www.haynesintl.com. Haynes International Inc., Indiana, USA.
13. Santella, M. Improving the performance of creep strength enhanced ferritic steels. www.ms.ornl.gov/fossil/pdf/ARM/Santella_Manuscript.pdf.
14. Holmström, S., Pohja, R., Nurmela, A., Moilanen, P. & Auerkari, P. Creep and creep-fatigue of stainless steel 316. 6th International Conference on Creep, Fatigue and Creep-Fatigue Interaction (CF-6), Mamallapuram, India, 22–25 January 2012.

Fireside corrosion of Ni-based alloys in simulated co-firing combustion environment

Tanvir Hussain, Nigel J. Simms & John E. Oakey

Centre for Energy and Resource Technology (CERT)
Cranfield University, UK

Abstract

Conventional fossil fuel fired power plants contribute significantly to the CO₂ emissions and EU has put in place legislation to reduce its emission to 20% below the 1990 levels by 2020. Co-firing low levels of biomass in conventional power plants has proved to be a successful way to introduce *carbon neutral* fuel into the electricity generation market. In addition, CO₂ emissions from the power plants can be reduced by increasing the operating pressures and temperatures (hence efficiency) of their steam systems. These modifications will require high corrosion resistant Ni-based alloys in the superheaters/reheaters. This paper reports the laboratory-based fireside corrosion tests of three candidate Ni-based alloys (263, 617 & 740). The gaseous combustion environment was designed to simulate co-firing of Cereal Co-Product (CCP) with Daw Mill coal (a UK Midland coal). The tests were carried out using the deposit recoat test method and a synthetic screening deposit (Na₂SO₄:K₂SO₄:Fe₂O₃) was used. The alloys were tested at temperatures of 650–800°C to represent the superheater/ reheater temperatures anticipated in future power plants. The samples were examined by SEM/ EDX to characterize the damage and to quantify the metal damage, pre-exposure micro-metre measurements were compared to the post-exposure image analyser measurements on sample cross-sections. In all three alloys, broad front type corrosion attack was observed at 650 and 700°C without any internal damage. The damage mechanisms in all three alloys changed at the higher two temperatures (750 and 800°C) and the alloys suffered from significant internal corrosion damage. Alloy 263, 617 and & 740 all suffered from similar median good metal losses at the lower two temperatures (650 and 700°C); however, at the higher two temperatures (750 and 800°C) alloy 740 outperformed alloy 263 and alloy 617.

1. Introduction

Fossil fuel fired power plants are considered to be significant contributors to the greenhouse effect and global warming due to their significant CO₂ emissions [1, 2]. The global energy demand has been increasing at a rapid rate with increasing pressure on the power generation industry to comply with stringent environmental legislations. The EU targets for 2020 and 2050 require major efficiency improvement of the pulverised fossil fuel power plants. The UK government has an ambi-

tious target of reducing CO₂ emissions to 80% of the 1990 levels by 2050 [2]. Reductions in CO₂ emissions from pulverised coal-fired power plants can be achieved by increasing the operating temperatures (and pressures) of the steam systems (which in turn increases the overall efficiency of the plants) [3], since each 1% increase in absolute efficiency results in as much as a 3% reduction in CO₂ emissions [4]. To meet these ambitious national and EU targets supercritical and ultra-supercritical power plants (~45% efficiency) will need to be introduced to replace the conventional sub-critical power plants (~36% efficiency).

Biomass co-firing in large pulverised fuel power plants is another way of reducing the overall CO₂ generation, since biomass is considered to be a carbon neutral fuel. The pulverised coal fired power plants are much larger in capacity and more efficient than dedicated biomass fired plants, so a few percentages of biomass co-fired with coal will provide more biomass derived renewable energy than a dedicated biomass plant using the same amount of biomass [5–9].

Higher operating temperatures with biomass co-firing may result in very aggressive fireside corrosion damages, which is one of the key reasons for tube failures in pulverised fossil fuel fired power plants. Fireside corrosion can lead to failure of superheaters/ reheaters either by general metal loss or by formation of cracks which can allow failure to occur by creep/ fatigue. Higher operating temperatures and aggressive fuels will make the conventional ferritic/ austenitic-based alloys unsuitable for USC/ A-USC superheaters/ reheaters. A new generation of nickel based alloys will be required for the USC/ A-USC power plants operating at 700/ 750°C. Nickel based alloys have higher creep life and can operate at higher temperatures compared to the conventional ferritic/ austenitic steels. A number of research articles have been published recently to assess the oxidation resistance of the nickel based super alloys in steam or air; however, their performance in combustion gases with complex deposits are still largely unknown.

This paper reports the results of a comprehensive study of candidate Ni-based alloys: alloy 263, alloy 617 and alloy 740 for superheater/ reheaters in simulated air-fired combustion gases at temperatures of 650, 700, 750 & 800°C. The gaseous environment was selected based on co-firing a UK coal with Cereal Co-Product and the alloys were studied with a synthetic deposit using the “deposit-recoat” technique that has been developed for high temperature corrosion. Following the exposures the samples were examined using SEM with EDX analysis. In addition, dimensional metrology has been used at the primary route to quantify the metal damage.

2. Experimental methods

In this study three nickel based super alloys: alloy 263, alloy 617 and alloy 740 were sourced from Doosan Power Systems Limited (Glasgow, UK). The nominal compositions of the three alloys are shown in Table 1. All three alloys were solution heat treated followed by precipitation age hardening heat treatment. Alloy 263 and 740 were sourced as long tubes (i.e., boiler tubes) and alloy 617 was sourced

as thick pipe sections. The materials were cut and machined into cylindrical samples with 10mm in diameter and 10mm in height. The surface of all the samples was prepared to a UK 600 grit surface finish.

Table 1. Nominal composition of Ni alloys used in this study.

	Fe	Ni	Cr	Co	Mo	C	Si	Mn	Al	Ti	Nb	Cu	Others
Nimonic 263	0.7	Bal.	19–21	19–21	5.6–6.1	0.04–0.08	0.4	0.6	0.6	1.9–2.4		0.2	B 0.005, S 0.007, Ag 0.0005, Bi 0.0001, Pb 0.002
Inconel 617	3	Bal.	20–24	10–15	8–10	0.05–0.15	1	1	0.8–1.5	0.6		0.5	B 0.006, S 0.015
Inconel 740	0.7	Bal.	25	20	0.5	0.03	0.5	0.3	0.9	1.8	2		

The gaseous environment for the tests was determined following a detailed investigation of the environment that could be found around superheaters/ reheaters in pulverised fuel power plants [10, 11]. The test environments for the fireside corrosion tests were based on co-firing 80:20 wt.% of a UK Coal (Daw Mill) with Cereal Co-Product. The compositions of these fuels are available in previous publications [12]. The gas compositions have been simplified to their key components for the testing and the nominal compositions are given in Table 2. The alloys were tested at 650, 700, 750 & 800°C with a standard screening deposit (composition given in Table 3). The screening deposit has been widely used in simulated fireside corrosion tests and represents a composition of alkali-iron tri-sulphate that has been identified as being the principle cause of corrosion on superheaters/ reheaters in pulverised coal fired power plants [10, 13–16].

Table 2. Nominal gas compositions used in fireside corrosion exposures.

N ₂ (vol. %)	O ₂ (vol. %)	CO ₂ (vol. %)	H ₂ O (vol. %)	SO ₂ (vppm)	HCl (vppm)
73.8	4	14	8	1300	400

Table 3. Deposit compositions used in fireside corrosion exposures (composition in mole %).

	Na ₂ SO ₄	K ₂ SO ₄	Fe ₂ O ₃
Screening Deposit	37.5	37.5	25

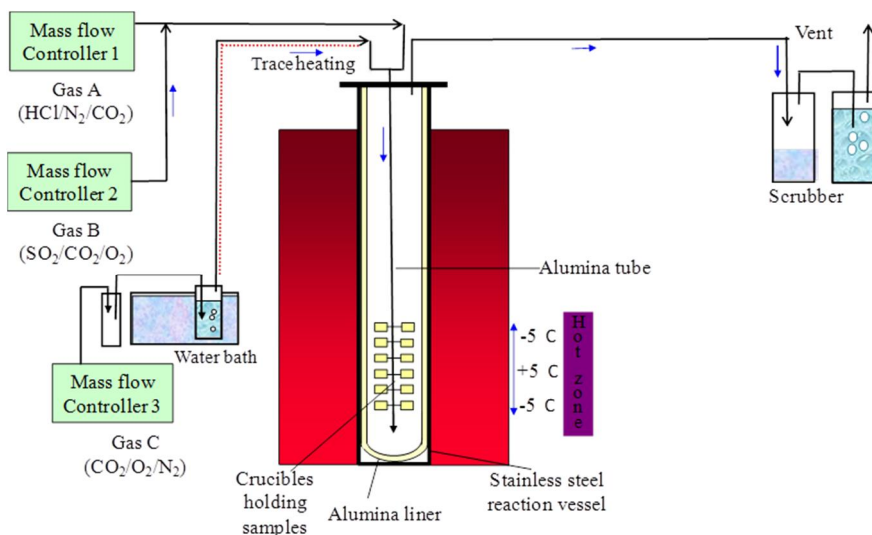


Figure 1. Schematic diagram of a controlled atmosphere furnace setup for fireside corrosion in simulated air-firing combustion gases.

The corrosion tests were carried out in an alumina lined vertical controlled-atmosphere furnace using simulated air fired combustion gases. The setup can accommodate 24 samples in alumina crucibles for each test run. A schematic diagram of the furnace setup is shown in Figure 1. Pre-mixed gases were supplied to the furnace through mass-flow controllers to achieve the desired environment. The gas containing CO₂/N₂/O₂ was passed through a de-ionised water bubbler (kept at 40°C) to add the required amount of moisture to the gas stream. Each test was run for 1000 h using the widely accepted “deposit- recoat” method and cycled every 200 h. The samples were cleaned ultrasonically using isopropyl alcohol before the exposure. The cleaned samples were painted using a paint brush to apply a deposit loading of ~20 mg/cm². The deposit was mixed with IPA to form thick slurries for painting. The samples were weighted every 200 h with and without the crucible as well as before and after applying the deposits (mass change data not reported in this article).

After 1000 h of exposure the samples were vacuum mounted using low shrinkage cold mounting resin filled with ballotini (to reduce shrinkage) in a bespoke jig. The mounted specimens were cross-sectioned and polished to 1 µm diamond grit finish using non-aqueous lubricants. Scanning electron microscope (SEM) with Energy dispersive X-ray (EDX) was used to characterize the scale/ deposits.

The dimensional metrology technique forms a key part of this research. All samples were measured using a digital micrometre to the nearest micron prior to the exposure. Following exposure the samples were analyzed using a bespoke image analyzer connected to an optical microscope with a motorized X-Y coordinate stage to measure the remaining metal thickness with any internal dam-

age. The measured co-ordinates were transferred into spread sheets and compared with the pre-exposure micrometre measurements to determine metal loss data distributions. These distributions were further processed to generate cumulative probability curves. A detailed description of the method is available in previously published papers [12, 17].

3. Results and discussion

3.1 Microstructural investigations

Figure 2 shows the backscattered electron (BSE) images of alloy 263 following exposure at 650, 700, 750 & 800°C for 1000 h in simulated combustion gases with screening deposits. Alloy 263 at 650 and 700°C showed broad front type corrosion attack. The scale/ corrosion product at 650°C was ~100 µm thick and at 700°C was ~ 200 µm thick. Elemental mapping/ EDX area scans (not shown here) detected the presence of Ni, Cr and Co oxides in the scale/ corrosion products. In both 650 and 700°C samples, S was detected in the scale/ corrosion products suggesting sulphidation attack of the alloy. The micrographs of alloy 263 exposed at 750 and 800°C showed different type of corrosion damage. In both cases, significant internal damage to the alloy was observed. In both cases, an inner and an outer scale can be identified. Sulphur was detected in both inner and outer scales and the inner scale was mainly composed of Cr and O. EDX spot analysis performed on the internal damages of the alloy showed the following composition: Al 1%, S 1%, Ti 1.5%, Cr 24%, Co 3.5%, Ni 9% and O- bal.

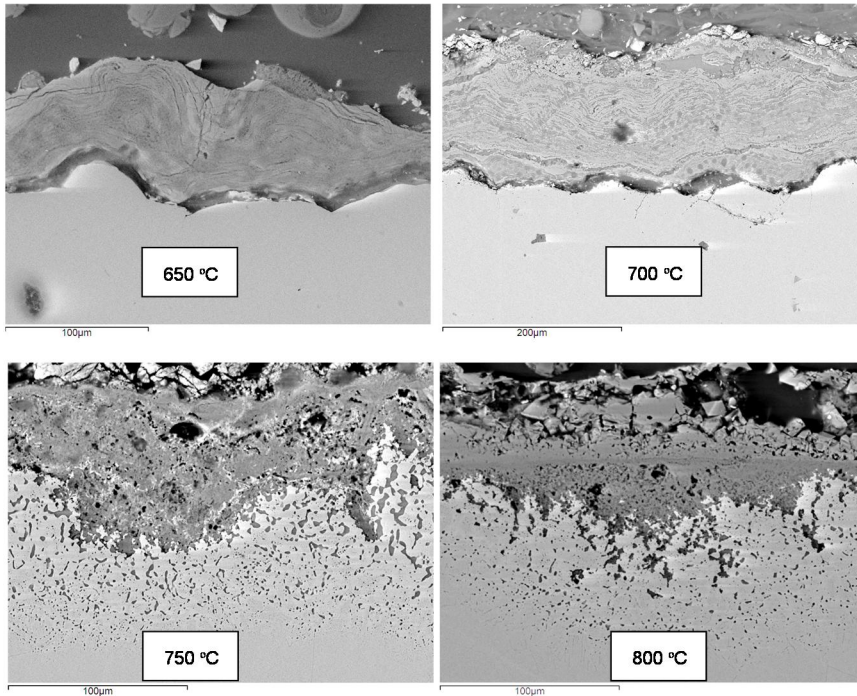


Figure 2. Backscattered electron (BSE) images of alloy 263 following exposures at 650, 700, 750 & 800°C for 1000 h in simulated combustion gases with screening deposits

Figure 3 shows the micrographs of alloy 617 following exposure in the corrosion tests at 650, 700, 750 & 800°C for 1000 h. Similar to alloy 263 a broad front type corrosion attack was seen at 650 and 700°C. The scale/ corrosion product mixture had delaminated from the alloy surface at 750 & 800°C. EDX area scans revealed that the layer at 650°C was mostly composed of O, S and Ni with small amount of Cr, Co and Na. The micrograph of the alloy exposed at 700°C shows two layered structure of scale/corrosion products- both of which detached from the alloy surface either due to thermal cycling or during sample preparation. The outer layer was mainly composed of Ni, S, O with small amount of Co, Na and K and the inner layer was composed of Cr, S and O with small amount of Co, Ni, Na and K.

The micrograph of the alloy 617 exposed at 750°C shows internal attack along the grain boundaries. The grain boundaries were depleted in Cr and showed internal oxidation of Al. Sulphur was also detected at the grain boundaries. The darker contrast spots inside the alloys (internal corrosion) were enriched in Cr and S. A thin band of S was also detected underneath the Cr rich scale. Internal damage to the alloy 617 was also seen at 800°C, but to a lesser extent. The attack resulted in pits on the metal surface which propagated later along the grain boundaries.

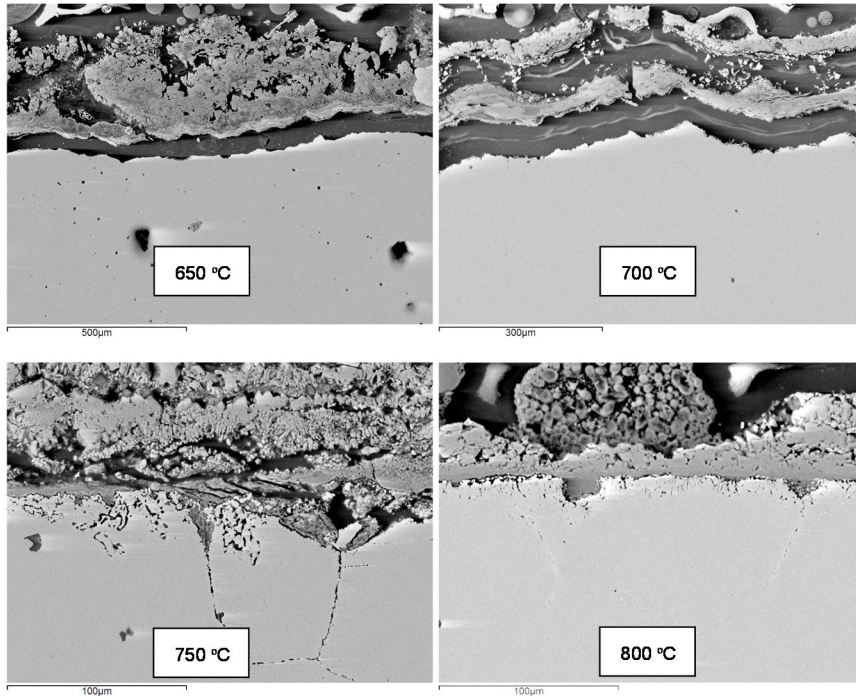


Figure 3. BSE images of alloy 617 following exposures at 650, 700, 750 & 800°C for 1000 h with screening deposits.

Figure 4 shows the BSE micrographs of alloy 740 following exposures in the fire-side corrosion tests. The sample exposed at 650°C shows more than 500 µm of mixed scale/corrosion products layer with cracks along the radial direction of the sample. It should be noted that the samples were cylindrical in dimensions and the stresses produced in the scale could contribute to such cracks (also along the alloy/ scale interface). EDX elemental mapping of the samples showed that the outside layer was rich in Ni and O with the inside layer was rich in Cr and O. Sulphur was present in the multi-layered scale/ corrosion product. The broad font type corrosion attack also occurred to the alloy 740 at 700°C. The scale had a multi-layered structure, similar to the micrograph of alloy 740 at 650°C. The brighter layers were composed of NiO and the darker layers were composed of mainly Ni, S and O. Cr-rich oxide layer was also detected closer to the alloy surface with S along the scale. Alloy 740, similar to alloy 263 and 617, suffered from significant internal damage at 750 and 800°C. The darker contrast spots in the alloy contained Cr and S.

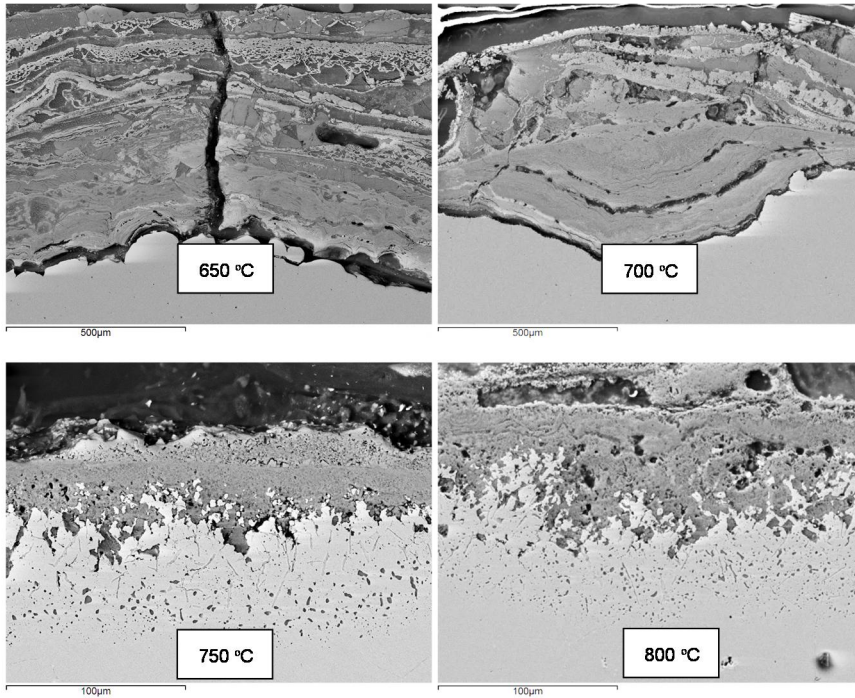


Figure 4. BSE images of alloy 740 following exposures at 650, 700, 750 & 800°C for 1000 h with screening deposits.

3.2 Measurement of metal damage

Dimensional metrology provides the most reliable measurement method of the corrosion damage of alloys, as it produces a distribution of metal damage data for each exposed samples [11, 18–21]. According to the draft standards for high temperature corrosion measurements [18, 19] the results are plotted as metal damage versus cumulative probability. In this paper “Good Metal Damage” has been used to express the damage to the alloys which includes change in metal thickness and internal damage to the alloys. Figure 5 shows the good metal damage versus cumulative probability for alloy 263 following fireside corrosion exposures at 650, 700, 750 & 800°C. The graph shows that alloy 263 exposed at 650°C had the lowest corrosion damage of ~190 μm and the highest corrosion damage of ~390 μm. The gradient of the good metal damage graph implies that the alloy suffered a range of corrosion damages at various places. The median (50% cumulative probability) good metal damage of alloy 263 at 650°C was ~270 μm. The good metal damage distribution of the alloy at 700°C were less than the damages observed at 650°C by ~100 μm. However, the good metal damage distributing of

alloy 263 showed more damage at 750°C compared to the damages seen at 700°C. There was internal corrosion damage at the higher two test temperatures. The worst section of the alloy exposed at 750°C had ~ 570 µm good metal damage. However, the good metal damage distribution of the alloy at 800°C showed significant improvement with maximum damage of ~ 210 µm – only 10% of the sample exposed at 800°C suffered from damages more than 75 µm.

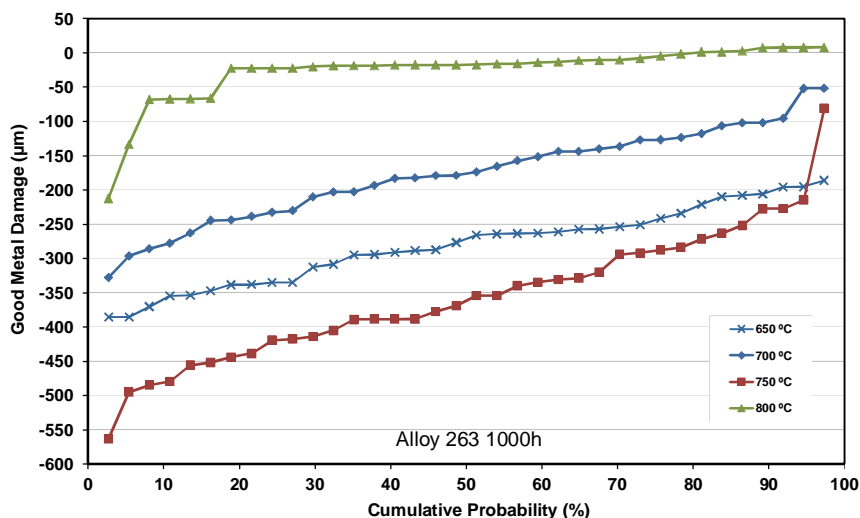


Figure 5. Good metal damage distribution of alloy 263 following exposures at 650, 700, 750 & 800°C for 1000 h with screening deposits.

The good metal distributions of alloy 617 at all four temperatures versus cumulative probabilities are shown in Figure 6. The maximum damage to the alloy was found at 650°C with median good metal damage of ~ 230 µm, which is slightly better than the performance of alloy 263 under similar conditions. Similar to alloy 263 increasing the test temperature from 650°C to 700°C resulted in a reduction in good metal damage distribution. At 750°C, the median metal damage increased again compared to the values seen when the sample was exposed at 700°C. In both alloy 263 and alloy 617 the least damage was seen at the highest test temperature of 800°C. However, both the alloys suffered from significant internal corrosion damage.

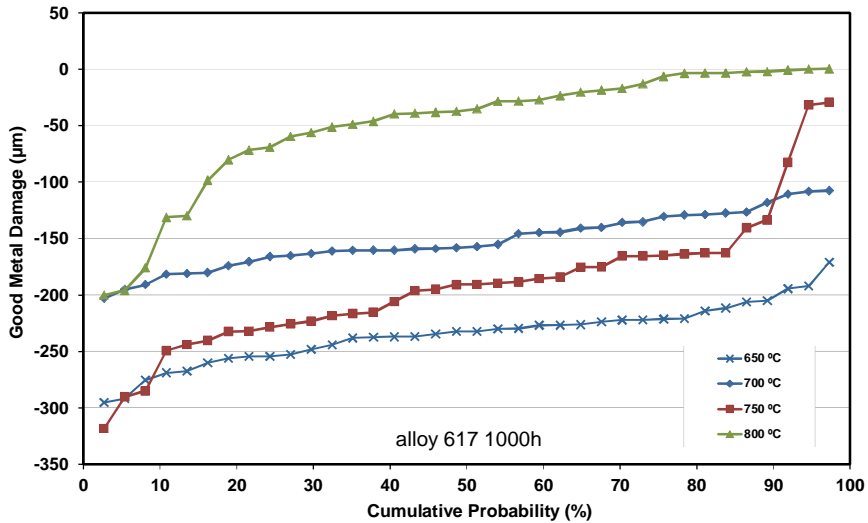


Figure 6. Good metal damage distribution of alloy 617 following exposures at 650, 700, 750 & 800°C for 1000 h with screening deposits.

Figure 7 shows the good metal damage distribution of alloy 740 following corrosion exposures at 650, 700, 750 & 800° C for 1000 h in simulated combustion gases with deposits. The good metal damage distribution at 650°C shows that the median metal damage was ~ 230 µm and only 10% of the sample surface suffered from damages more than ~250 µm. Similar to the other two nickel based alloys, alloy 740 performed better at 700°C compared to at 650°C. Alloy 740 at 750 and 800°C did not show any significant variation in the good metal damage distributions, unlike alloy 263 and alloy 617. At 750°C 25% of the sample surface suffered from metal damages more than ~70 µm and at 800°C 18% of the sample surface suffered from metal damages more than 90 µm.

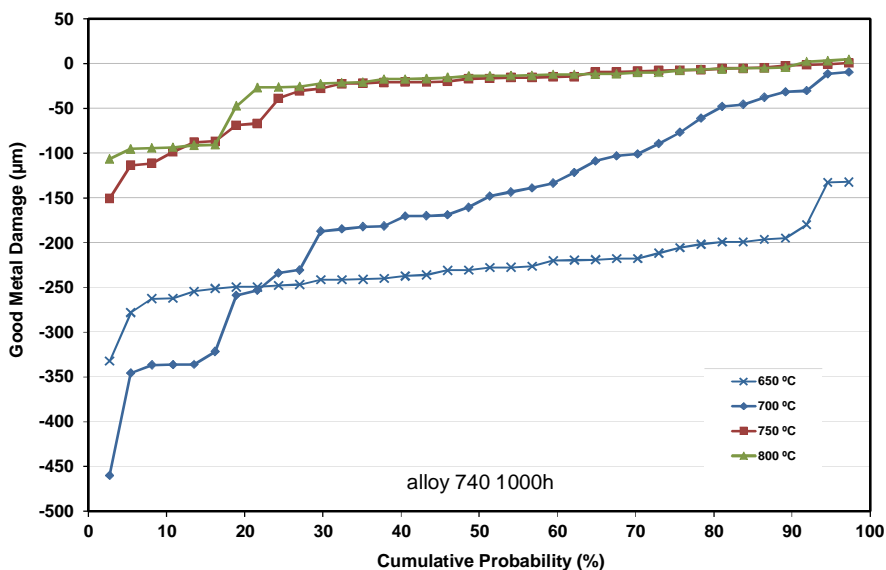


Figure 7. Good metal damage distribution of alloy 740 following exposures at 650, 700, 750 & 800° C for 1000 h with screening deposits.

For ease of comparison, the median metal damage of all three alloys with the maximum and minimum damages as error bars are shown in Figure 8. The median metal damages have been multiplied by “-1” and presented as good metal loss in this figure. It is clear that in all three alloys median metal losses at 700°C were less than the median metal losses at 650°C. In addition, all three alloys showed similar corrosion damages at 650 and 700°C (taking the error bars into consideration). It should be mentioned that the screening deposits used in this study is very aggressive in nature and with this deposit the alloys do not show significant incubation times, when the alloy surface can still be protected by selection oxidation of active elements [8]. The deposit is formulated to produce alkali-iron tri-sulphate, which has been found to be the key corrosive compound of superheater/ reheaters in pulverised fuel power plants. In all three alloys the lowest corrosion damage was seen when the alloys were tested at 800°C. Although there were no significant differences of the performance of the alloys at lower temperatures (650 and 700°C), at higher temperatures (750 and 800°C) alloy 740 outperformed the other two alloys. It is not clear at this stage what contributed to this enhanced performance at higher temperatures, but it should be noted that alloy 740 had the highest amount of Cr in the alloy (also contains Nb which helps scale adhesion).

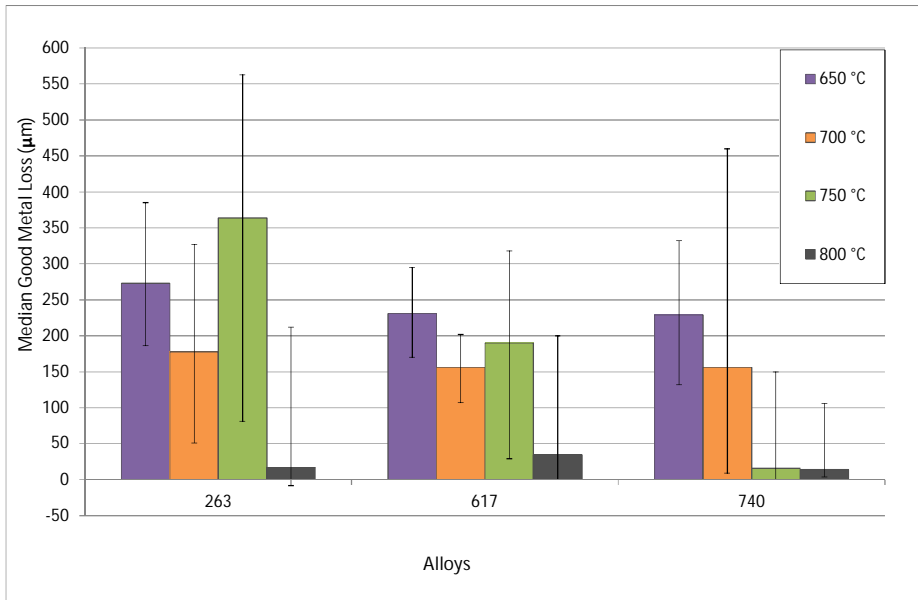


Figure 8. Median good metal loss of alloy 263, 617 and 740 at four different temperatures (650, 700, 750 & 800°C) with minimum and maximum metal loss values as error bars.

Typically with any alloy the corrosion rate increases with increasing temperature. However, in all three cases the alloys showed a decrease in metal loss from 650 to 700°C. It was previously found in the same test conditions (with the same gases and deposits) that austenitic stainless steels showed “peak corrosion damage” (peak of the characteristic *bell-shaped* fireside corrosion curves) at 650°C and the corrosion rate decreased from 650°C to 700°C [6, 7]. The “bell-shaped” behaviour is due to formation and de-stabilization of molten complex alkali-iron tri-sulphates with increasing temperature. Alkali-iron tri-sulphates melt at a much lower temperature than alkali- sulphates, with a minimum melting point of ~550°C compared to 832°C [11, 22–25]. Alkali-iron tri-sulphates need to be stabilized by SO₃. The alkali-iron tri-sulphates formed from the deposit in the gaseous environment will have been molten at the exposure temperature ranges. The rate of corrosion increases with increasing temperature in the presence of molten deposits. However, the corrosion rate decreases as the deposit becomes unstable due to a shift in the balance of SO₂/ SO₃ towards SO₂ at higher temperatures. It is believed that the broad front type attacks seen at 650 and 700°C belong to this corrosion mechanism. However, when the temperature was further increased to 750°C all three nickel based alloys showed significant internal attack (also along grain boundaries). The damage mechanism seen at 800°C was similar to the mechanism seen at 750°C, which suggests a different mode of corrosion attack for these alloys at higher temperatures.

4. Conclusions

In this study, three candidate Ni based alloys (alloy 263, alloy 617 and alloy 740) for superheaters/ reheaters in ultra-supercritical power plants/ advanced ultra-supercritical power plants were exposed in simulated air-fired combustion gases with screening deposits. The samples were tested for 1000 h in controlled atmosphere furnaces at 650, 700, 750 and 800°C. The tests were conducted according to the well-established deposit-recoat test method for high temperature corrosion and dimensional metrology formed a critical part of this study.

In all three alloys, broad front type corrosion attack was observed at 650 and 700°C without any internal damage to the alloys. The median good metal damage decreased from 650°C to 700°C, which is consistent with the characteristic bell-shaped curves for fireside corrosion (where peak damages were found at 650°C). Sulphur was detected underneath the chromium rich scale in all cases, which suggest sulphidation attack. The damage mechanism in all three alloys changed at 750°C – the alloys suffered from significant internal corrosion damage. Sulphur was detected at the locations where internal corrosion damage was seen and also internal oxidation of aluminium took place. In general, all three alloys suffered from similar corrosion damages at the lower two temperatures of 650 and 700°C; however, at the higher two temperatures of 750 and 800°C alloy 740 outperformed alloy 263 and alloy 617.

References

1. Bordenet, B., Influence of novel cycle concepts on the high-temperature corrosion of power plants. *Materials and Corrosion*, 2008. 59(5), pp. 361–366.
2. Skea, J. and P. Ekins, Making the transition to a secure and low-carbon energy system., in UKERC energy 2050 project; S3097:302009.
3. Natesan, K. and J.H. Park, Fireside and steamside corrosion of alloys for USC plants. *International Journal of Hydrogen Energy*, 2007. 32(16), pp. 3689–3697.
4. Henry, J., G. Zhou, and T. Ward, Lessons from the past: materials-related issues in an ultra-supercritical boiler at Eddystone plant. *Materials at High Temperatures*, 2007. 24(4), pp. 249–258.
5. Simms, N.J., et al., Fireside Issues in Advanced Power Generation Systems. *Materials Science and Technology*, In Press, pp. 1–9.
6. Hussain, T., A.U. Syed, and N.J. Simms, Trends in fireside corrosion damage to superheaters in air and oxy-firing of coal/biomass. *FUEL*, In Press.

7. Hussain, T., A. Syed, and N. Simms, Fireside Corrosion of Superheater Materials in Coal/Biomass Co-fired Advanced Power Plants. *Oxidation of Metals*, 2013, pp. 1–12.
8. Hussain, T., N.J. Simms, and J.R. Nicholls, Modelling Fireside Corrosion of Thermal Sprayed Coatings in Co-firing of Coal/ Biomass. *Materials and Corrosion*, 2013. 64, pp. 1–9.
9. Hussain, T., et al., Fireside Corrosion Behavior of HVOF and Plasma-Sprayed Coatings in Advanced Coal/Biomass Co-Fired Power Plants. *Journal of Thermal Spray Technology*, 2013, pp. 1–11.
10. Simms, N.J., P.J. Kilgallon, and J.E. Oakey, Fireside issues in advanced power generation systems. *Energy Materials: Materials Science and Engineering for Energy Systems*, 2007. 2(3), pp. 154–160.
11. Simms, N.J. and A.T. Fry. Modelling Fireside Corrosion of Heat Exchangers in Co-fired Pulverised Fuel Power Systems. in *Materials for Advanced Power Engineering*. 2010. Forschungszentrum, Julich
12. Syed, A.U., N.J. Simms, and J.E. Oakey, Fireside corrosion of superheaters: Effects of air and oxy-firing of coal and biomass. *Fuel*, 2012. 101(0), pp. 62–73.
13. Stringer, J. and I.G. Wright, Current limitations of high-temperature alloys in practical applications. *Oxidation of Metals*, 1995. 44(1), pp. 265–308.
14. Raask, E., *Mineral Impurities in Coal Combustion 1985*: Hemisphere Publishing Corporation.
15. Natesan, K., A. Purohit, and D.L. Rink, Coal-ash corrosion of alloys for combustion power plants in US Department of Energy Fossil Energy Conference 2003.
16. Simms, N.J., *Environmental Degradation of Boiler Components in Power Plant Life Management and Performance Improvement* J.E. Oakey, Editor 2011, Woodhead Publishing pp. 145–179.
17. Nicholls, J.R., N.J. Simms, and A. Encinas-Oropesa, Modelling hot corrosion in industrial gas turbines. *Materials at High Temperatures*, 2007. 24(3), pp. 149–192.

18. Draft Code of Practice for Discontinuous Corrosion Testing in High Temperature Gaseous Atmospheres in EC project SMT3-CT95-2001, TESTCORR. UK: ERA Technology2000.
19. Corrosion of Metals and Alloys- Methods for Metallographic Examination of Samples After Exposure to High Temperature Corrosive Environments, in Draft ISO Standard. ISO/ TC 156 NWI 50920052006.
20. Saunders, S.R.J., Guidelines for Methods of Testing and Research in High Temperature Corrosion H.J. Grabke and D.B. Meadowcroft, Editors. 1995, The Institute of Metals: London. P. 85.
21. Nicholls, J.R. and P. Hancock. Analysis of Oxidation and Hot Corrosion Data – A Statistical Approach. 1983. San Diego, CA, USA: NACE.
22. Hendry, A. and D.J. Lees, Corrosion of austenitic steels in molten sulphate deposits. Corrosion Science, 1980. 20(3), pp. 383–404.
23. Cain, C.J. and W. Nelson, Corrosion of superheaters and reheaters of pulverized-coal-fired boilers. II. Trans. ASME, 1961. 83(4), pp. 468–474.
24. Lindberg, D., R. Backman, and P. Chartrand, Thermodynamic evaluation and optimization of the (NaCl + Na₂SO₄ + Na₂CO₃ + KCl + K₂SO₄ + K₂CO₃) system. Journal of Chemical Thermodynamics, 2007. 39(7), pp. 1001–1021.
25. Syed, A.U., et al., Fireside corrosion of superheater materials in oxy-fired power plants, in Eurocorr2011: Stockholm. pp. 1062–1078.

Degradation of single-crystal gas turbine blades

Petra Jauhiainen, Juhani Rantala, Jorma Salonen, Sanni Yli-Olli & Stefan Holmström

VTT Technical Research Centre of Finland
P. O. Box 1000, FI-02044 VTT, Finland

Abstract

The work presented in this paper aimed to evaluate and classify the microstructural degradation of diffusion coated single-crystal gas turbine blade, so that the characterised features of degradation could be used for assessing the effective in-service material temperatures at the corresponding blade locations.

Two potentially useful indicative measures were evaluated for this purpose: a) gamma prime coarsening and degradation in the substrate microstructure to indicate the condition and temperature in the blade interior and b) combined thickness of the intermediate diffusion zone (IDZ) and topologically close-packed (TCP) precipitate layers to indicate the condition and temperature at the blade coating.

Both applied measures appear to provide meaningful indications of the service temperature, although not with the same level of uncertainty. The thickness of IDZ+TPC layers can indicate the effective temperatures to a relatively good accuracy as long as the IDZ and TPC layers remain sufficiently intact for the assessment. For verification and demonstration purposes, a case example is shown of an ex-service turbine blade.

1. Introduction

Service life of gas turbine blades (buckets) in aircraft engines relies upon the durability of the nickel superalloys that the blades are made of. For good high-temperature strength, the strongest blades are single crystals that avoid the weakening by grain boundaries, and contain a high volume fraction of strengthening small cubic gamma prime (γ') or $\text{Ni}(\text{Al},\text{Ti})_3$ particles that are initially coherent with the gamma (γ) matrix. Coatings are generally necessary to protect the blade from high temperature oxidation and corrosion, and platinum aluminide (PtAl) diffusion coatings are widely used for the purpose. During service both the substrate alloy and the coating show gradual time- and temperature-dependent changes. These changes may in turn reflect and indicate the effective operating temperature, when the service time and the kinetics of the observed change are known to a sufficient accuracy correlated with the associated exposure.

Platinum aluminide coatings can be made by depositing a thin layer of platinum on the superalloy substrate, with a vacuum diffusion heat treatment for improved

adhesion, followed by aluminizing and final heat treatment. The PtAl coatings are typically (Ni,Pt)Al or beta (β) type aluminides, either inward- or outward-grown. The inward-grown coatings generally show three layers: a platinum rich layer on top, then an intermediate beta layer, and a precipitate-rich interdiffusion zone (IDZ) on the inside. An outward-grown coating only has two layers, the outer layer made of single-phase beta and/or ζ -PtAl₂, and the inner layer of IDZ. Platinum improves the oxidation resistance of aluminide coatings primarily by enhancing the protective alumina scale adhesion [1, 2, 3, 4].

Creep resistant superalloys contain refractory alloying additions that promote the formation of topologically close-packed (TCP) phases. The TCP phases can intrude into the substrate to a considerable distance and destroy the γ/γ' microstructure. These often plate-like or needle-like, brittle phases are detrimental to the mechanical properties [4, 5, 6, 7, 8, 9, 10, 11].

In the initial state the small (coherent with γ matrix) cubic γ' particles are surrounded by an elastic stress field which has developed by negative misfit between γ matrix and γ' precipitates. Depending on stress, exposure time and temperature, the microstructure will degrade by gradual coarsening of the γ' , precipitation of secondary phases and finally rafting or transformation of the γ'/γ structure towards platelet-like morphology. [12, 13,14,15,16,17]

Exposure at elevated temperatures accelerates any diffusion-controlled mechanisms and thus also the degradation of the γ' precipitates. The misfit at the γ/γ' interface withstand the degradation of the γ' precipitates at the early stages but when the coherency is lost the γ' began to coarsen.

2. Materials and methods

The base material of the blade was single crystal Ni-based superalloy Rene N4 (Table 1) [18]. The blade was coated with platinum aluminide coating.

Table 1. Nominal composition of the blade material N4 [18].

Element	C	Ni	Cr	Co	Mo	Al	Ti	Ta	W	B	Nb	Hf
wt.%	0.06	62	9.8	7.5	1.5	4.2	3.5	4.8	6.0	0.004	0.5	0.15

The microstructural changes in the base material and coating were simulated in laboratory conditions in ageing tests by heat treating small blade samples in a furnace. The aging was done at five different temperatures (950°C, 1000°C, 1050°C, 1100°C and 1150°C) for different durations varying from 7h to 2000h. The longest ageing time is comparable to the allowable EOT of the actual turbine blades in service.

The samples for the ageing tests were cut from the step blades with a diamond cutting wheel. To simulate a crack extending to the substrate alloy, a relatively narrow notch was spark eroded to all samples, using a wire diameter of 0.1 mm.

The samples were cleaned with ethanol in an ultrasonic bath before the aging treatment. For ageing, the samples were heated up with the furnace, and air cooled to room temperature by taking them out of the furnace after the designated time of exposure. In some cases this rapid cooling led to minor laminar cracking of the coating. In few exceptional cases the samples were cooled down more slowly with the furnace.

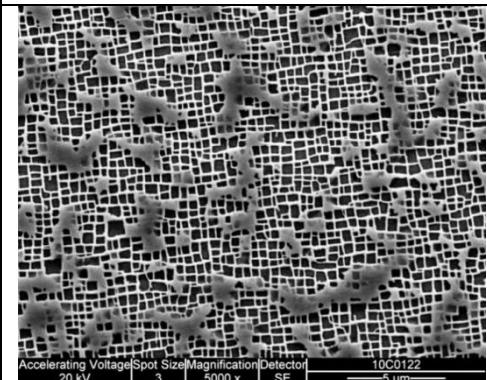
After ageing treatment, polished and etched metallographic cross sections were prepared of all samples to visualise the gamma-gamma prime structure and other phases and layers of the substrate alloy and the coating. Every sample was examined by light optical microscopy (LOM) and scanning electron microscopy (SEM).

3. Results

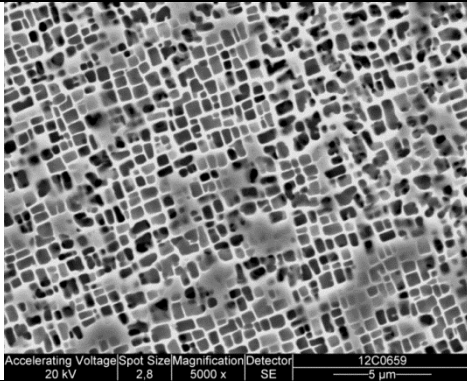
3.1 Microstructural degradation of the substrate material

During the isothermal ageing treatment the microstructure of the blade material will exhibit degradation, or time and temperature dependent change. The degradation of the gamma prime and gamma structure is mainly evaluated from inside the dendrites, from regions with the initial microstructures (grade 1) as shown in Table 2. The grade of degradation is visually evaluated, using classification to five main grades (1 to 5), and allowing for one intermediate level between each main grade.

Table 2. Classification of microstructural degradation.

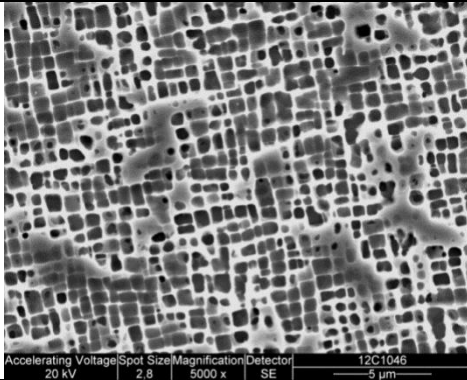
Grade 1	
	<p>In this grade the gamma prime precipitates are clearly cubic (not rounded) in form, and uniform in size. This grade corresponds mostly to as-new or fully rejuvenated microstructures.</p>

Grade 1.5



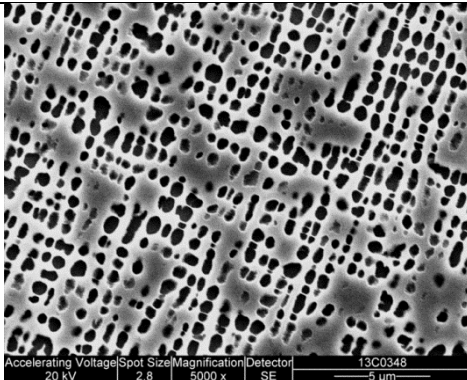
The overall appearance is similar to grade 1, but with slightly rounded corners and very few cases of coalesced gamma prime particles.

Grade 2



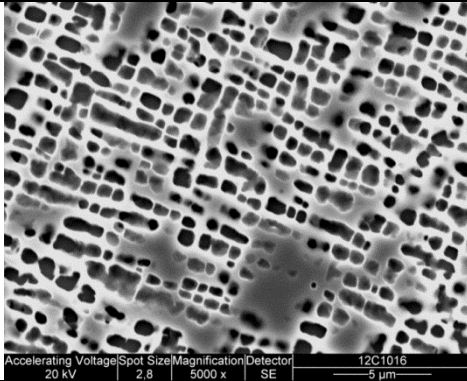
In this structure the rounding and coarsening of gamma prime precipitates has proceeded to include nearly no signs of coalescence.

Grade 2.5



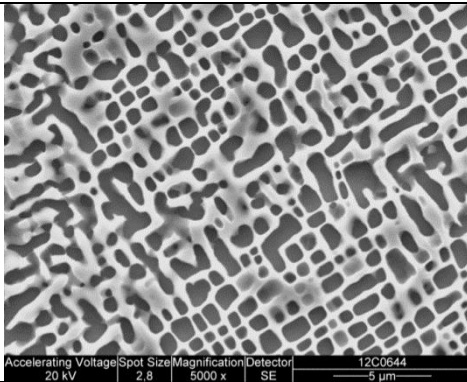
The gamma prime precipitates have further rounded compared to grade 2 but still show little signs of coalescence. The thickness of the gamma matrix between gamma prime precipitates has clearly grown compared to grade 2.

Grade 3



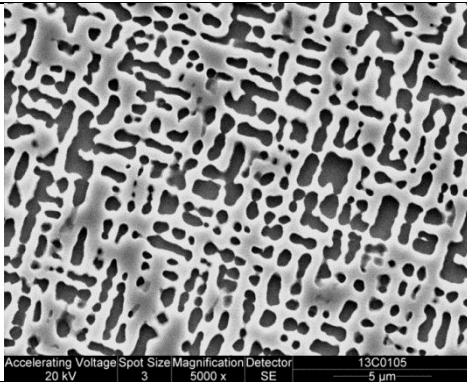
Most gamma prime precipitates are well rounded but fair amount of them have coalesced to elongated shape. The thickness of the gamma matrix between gamma prime precipitates has clearly grown compared to grade 2.

Grade 3.5

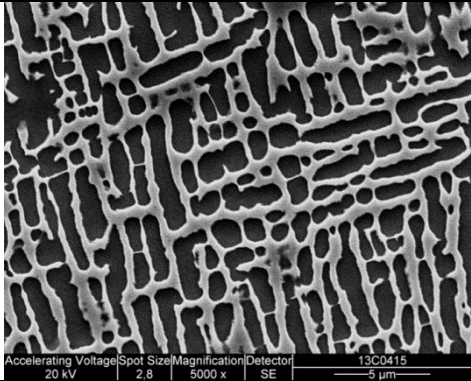
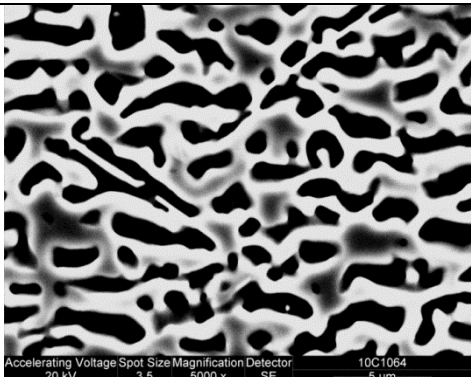


Separate round gamma prime precipitates can still be found (less than 50%). Compared to grade 3, more coalesced gamma prime precipitates, also sideways.

Grade 4



Small amount of separate gamma prime precipitates can be still seen (about 10–30%). The gamma prime precipitates have often coalesced also in transverse direction. The gamma matrix still appears as a grid, without extensive coalescence.

Grade 4.5	
 <p>Accelerating Voltage 20 kV Spot Size 2.8 Magnification 5000 x Detector SE 13C0415 5 μm</p>	<p>Only little signs of original separate gamma prime precipitates, largely coalesced but the appearance of gamma matrix is still a grid.</p>
Grade 5	
 <p>Accelerating Voltage 20 kV Spot Size 3.5 Magnification 5000 x Detector SE 10C1064 5 μm</p>	<p>The gamma prime particles have heavily coarsened and coalesced, and the structure shows little or no traces of the original gamma prime precipitates. The gamma matrix also shows coarsening, coalescence and loss of grid appearance.</p>

3.2 Degradation of the coating

The coating consists of a beta (β) layer on top and an interdiffusion zone (IDZ). During aging a topologically closed packed (TCP) layer is formed. These layers are shown in Figure 1. The initial thickness of the β -layer was 75 μm and that of the IDZ 24 μm . Practically no change is observed in the outer beta layer after 7 h exposure at 950°C, and the TCP zone of needle- or plate-like phases is very small in the substrate under IDZ (Figure 2 and Figure 3). The TCP zone is more prominent after 70 h at 950°C (Figure 4) and becomes similar in thickness with IDZ after 1300 h at 950°C (Figure 5), as well as after 2000 h at 950°C (Figure 6). The beta layer remains almost unchanged after 2000 h at 950°C, without significant microstructural change in the beta phase.

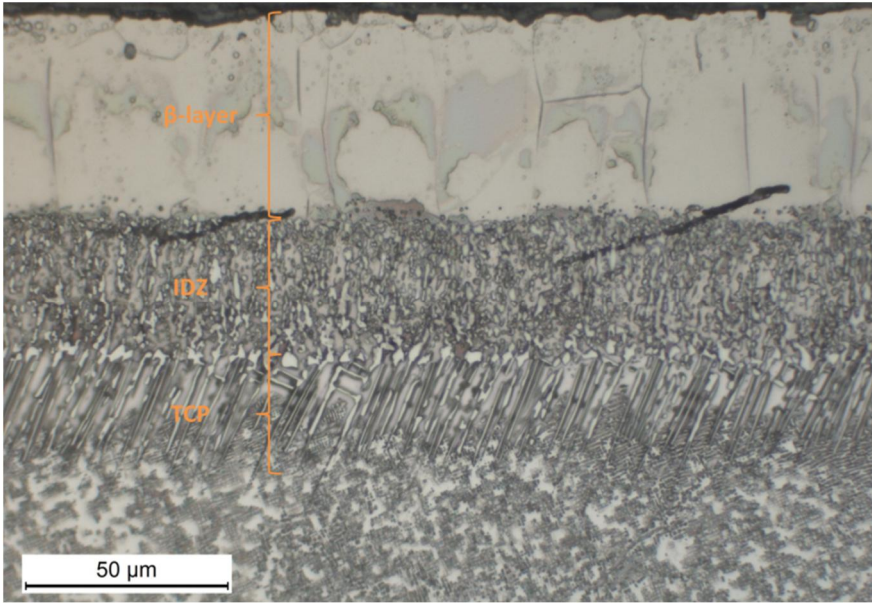


Figure 1. Positions of the surface layers of the coated blade.

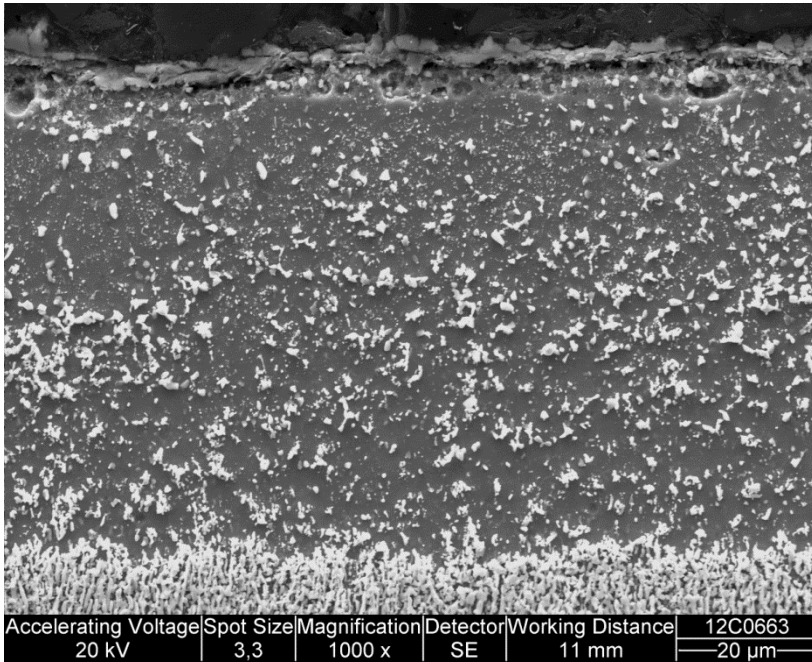


Figure 2. Outer beta layer of the coating after 7 h at 950°C (SEM image).

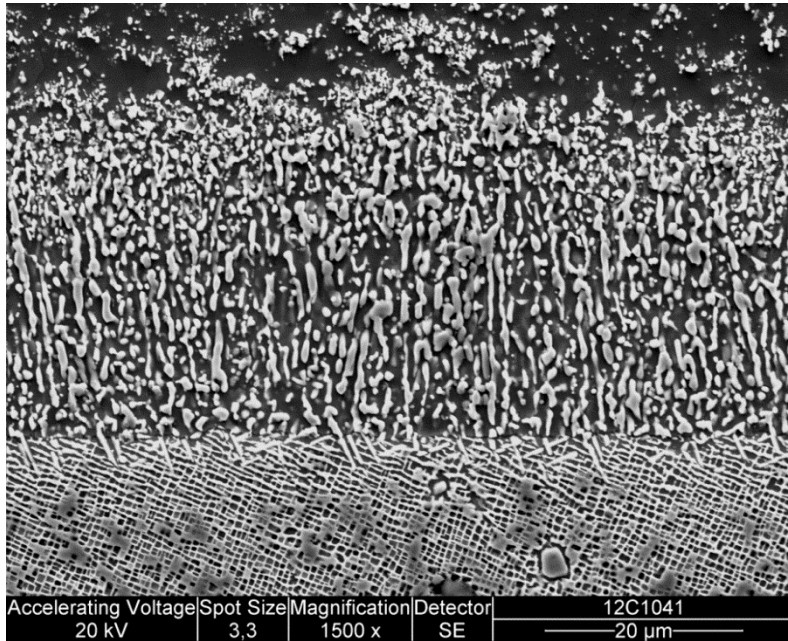


Figure 3. IDZ and TCP layers of the coating after 7 h at 950°C (SEM image).

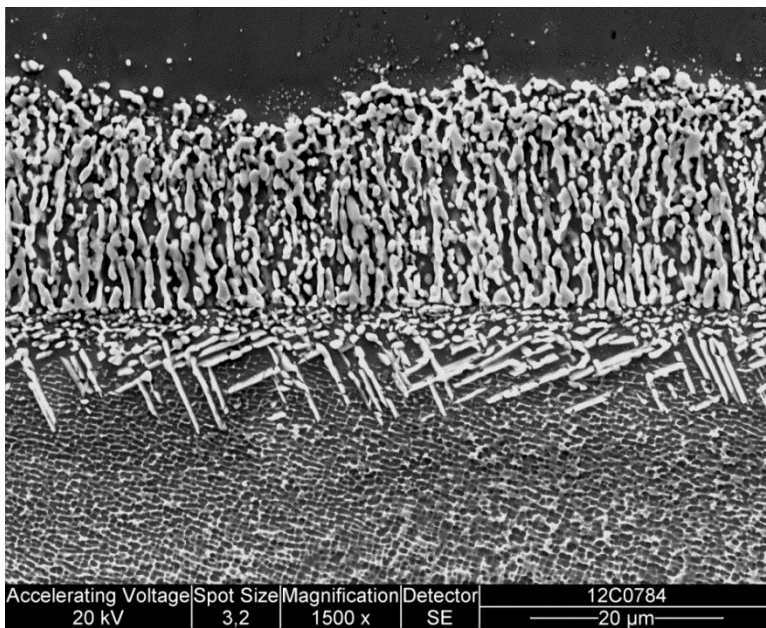


Figure 4. IDZ and TPC layers after 70 h at 950°C (SEM image).

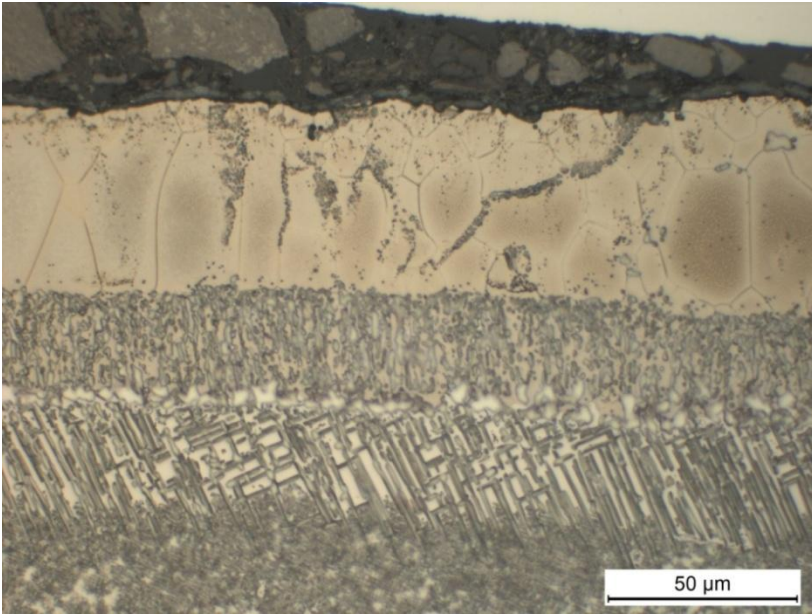


Figure 5. Coating after 1300 h at 950°C (LOM image).

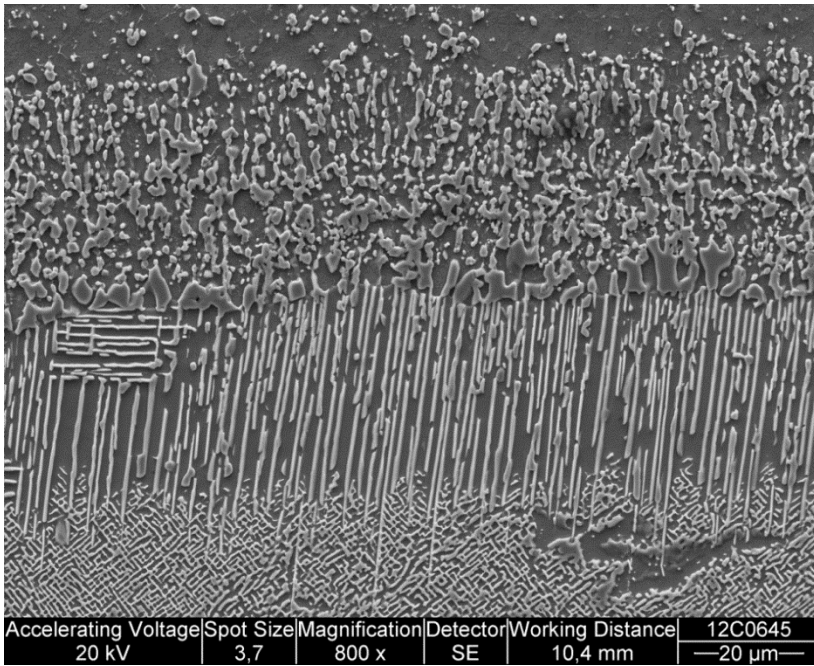


Figure 6. IDZ and TCP layers after 2000 h at 950°C (SEM image).

After 2000 h at 950°C no significant changes in β -phase of the coating layer was observed but some fragments of the β -phase had altered to γ' after 2000 h exposure at 1000°C. The IDZ zone is also more coarsened and thicker than in 950°C (Figure 7). As the temperature increases the changing of the β -phase to the γ' -phase begins earlier and after 2000 h exposure in 1100°C the β -phase has totally disappeared (Figure 8).

A broad TCP zone is distinguished after 2000 h exposure in 1000°C (Figure 7) but after 2000 h exposure in 1050°C a continuous uniform TCP zone under IDZ zone no longer exists, instead individual needle-like TCP-phases are observed in the substrate (Figure 9).

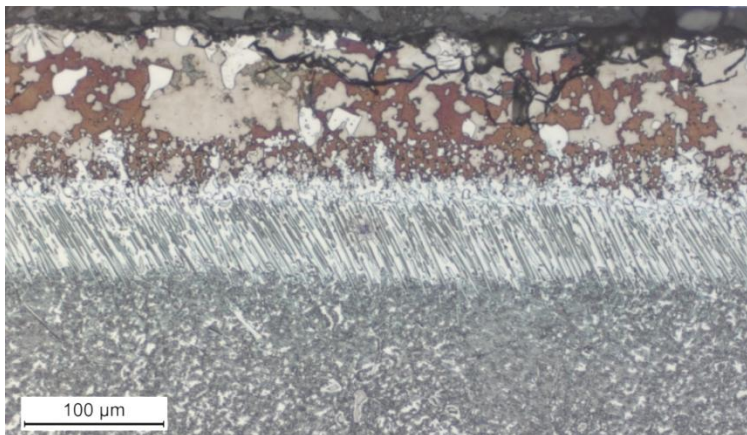


Figure 7. The coating after 2000 h at 1000°C (LOM image) .

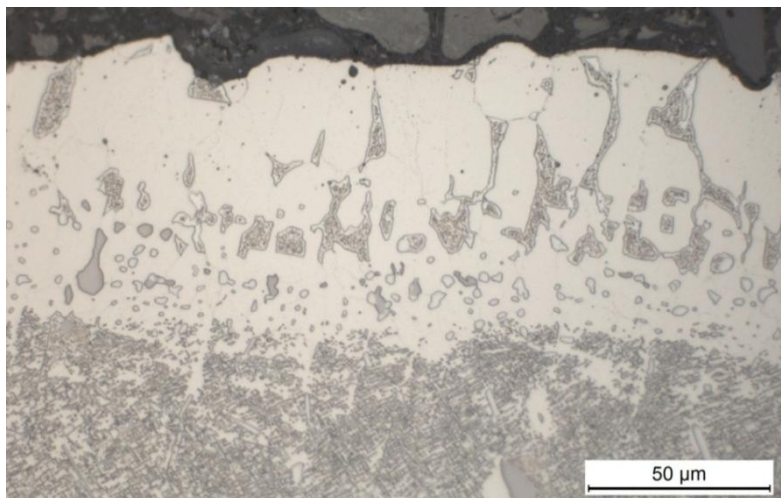


Figure 8. Coating after 2000 h at 1100°C (LOM image).

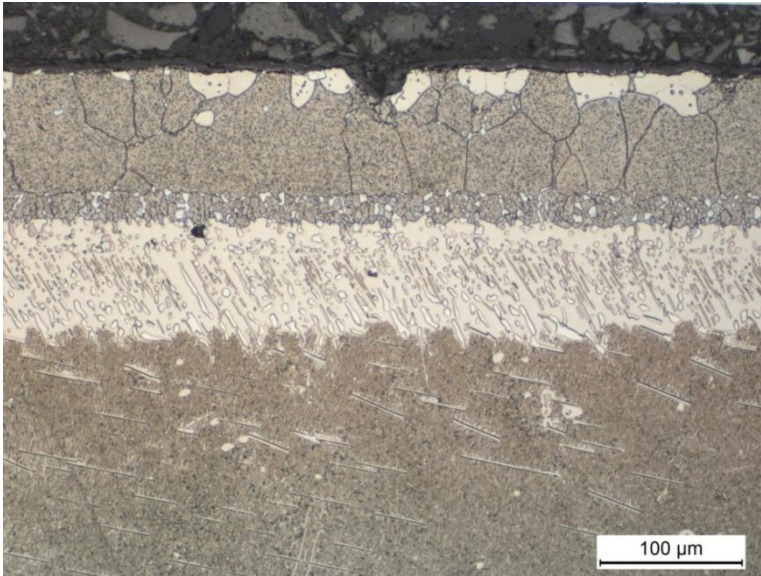


Figure 9. The outer layers of the coating after 2000 h at 1050°C (LOM image).

3.3 Assessment of the measures of degradation

Using the observed measures like microstructural degradation grade and thickness of surface layers of the coating, expressions were developed to correlate the observed quantities with the time and temperature of exposure. In the case of the coating, the measured layers included the inter diffusion zone (IDZ) and the topologically closed packed (TCP) layer next to the substrate.

3.3.1 Assessment of service temperature from blade microstructure

The microstructural classification after ageing is presented in Table 3. These values are fitted to a Larson-Miller type expression (1) [19] to describe the kinetics of the degradation of the gamma prime, so that for temperature T (K) after exposure time t (h)

$$x = A + k \cdot PLM \quad (1)$$

where x is the gamma prime grade number and $PLM = (\log t + C) \cdot T(K) / 1000$ [1]. Hence the predicted temperature (in K) as a function of gamma prime grade is

$$T(K) = 1000 \cdot \frac{x - A}{k \cdot [\log(t) + 10]} \quad (2)$$

When the gamma prime grade number is <2 the slope parameter k is 0.374 and the intercept A is -3.604, for a grade number >2, k is 0.968 and A is -12.50. The fitting results are shown in Figure 10.

Table 3. Classification of microstructural degradation after ageing treatments.

Time/Temperature	950°C	1000°C	1050°C	1100°C	1150°C
7 h	1.5	1.5	2		2.5
20 h	1.5	2	2	3	3
70 h	2	2	2		3.5
200 h	2	2	3	3.5	3.5
700 h	3	3.5	4		
1300 h	3.5	4	4		
2000 h	3.5	4	4	4.5	

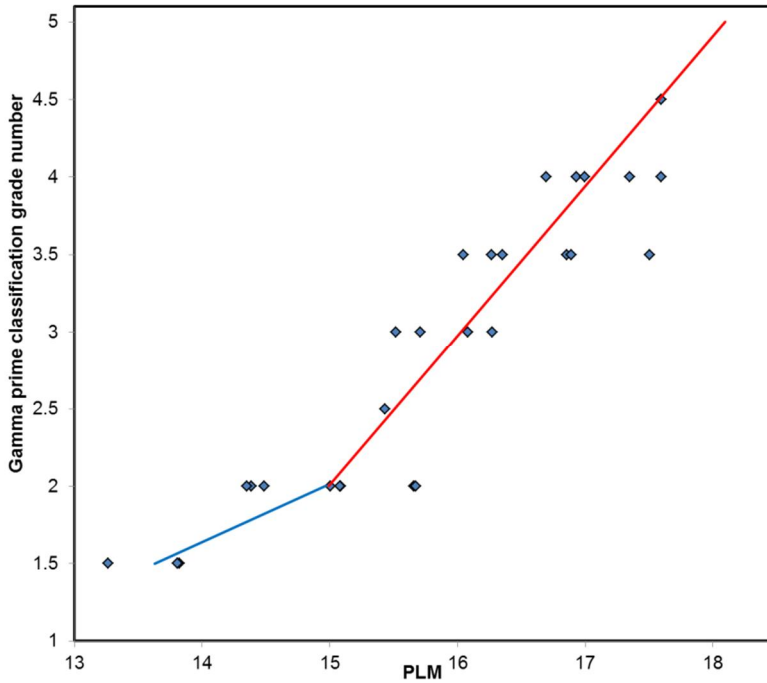


Figure 10. Bi-linear fit of gamma prime classification grade as function of PLM.

3.3.2 Thickness evolution of the coating surface layers

The combined thickness x (μm) of the IDZ+TCP layers (Figure 1) from all aged samples is fitted to a Larson-Miller type (PLM) expression (3) [19] to describe the kinetics of the layer formation, so that for a temperature T (K) after an exposure time t (h)

$$\log(x) = 1.615 \cdot 10^{-4} \cdot T(\log(t) + 10) - 0.7759 = 1.615 \cdot 10^{-4} \cdot PLM - 0.7759 \quad (3)$$

The correlation is fairly good for temperatures from 950°C to 1050°C, but at higher temperatures the kinetics apparently change and therefore the expression (3) does not work for temperatures over 1050°C, as can be seen from Figure 11.

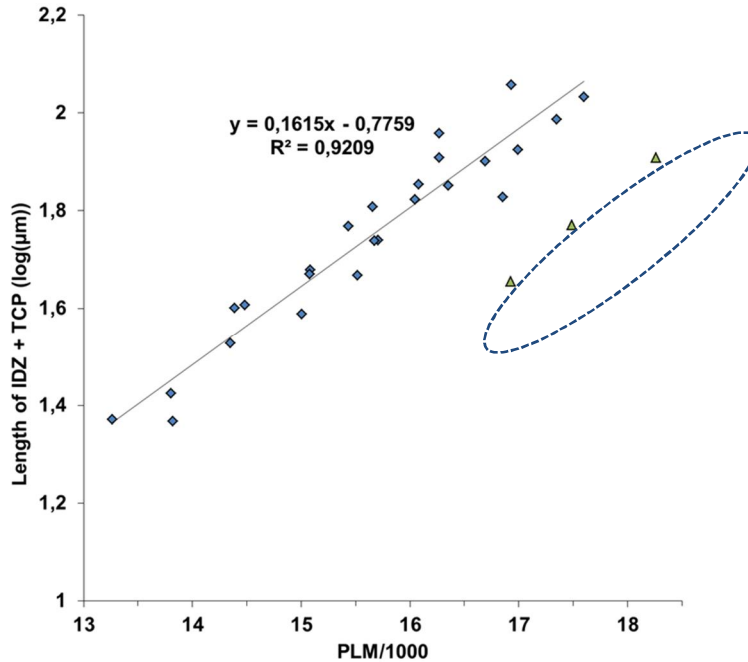


Figure 11. Combined thickness of IDZ and TCP layers as a function of PLM.

3.4 Application of the methodology

The described methodology was applied to an overheated turbine blade that had a locally oxidised region on the pressure side airfoil after 2417 h of effective operating time. With the new methods temperature was estimated using Eqs. 1 and 2 (microstructure) through the blade (Figure 12), and using the TCP+IDZ thickness at the cooling channel (Figure 13).

The results of the temperature evaluation are presented in Figure 14. The microstructure near the surface extended beyond the grading scale, and therefore the surface temperatures were linearly extrapolated from the temperatures obtained from inner structure, Figure 14. The results suggest a surface temperature exceeding locally 1200°C.

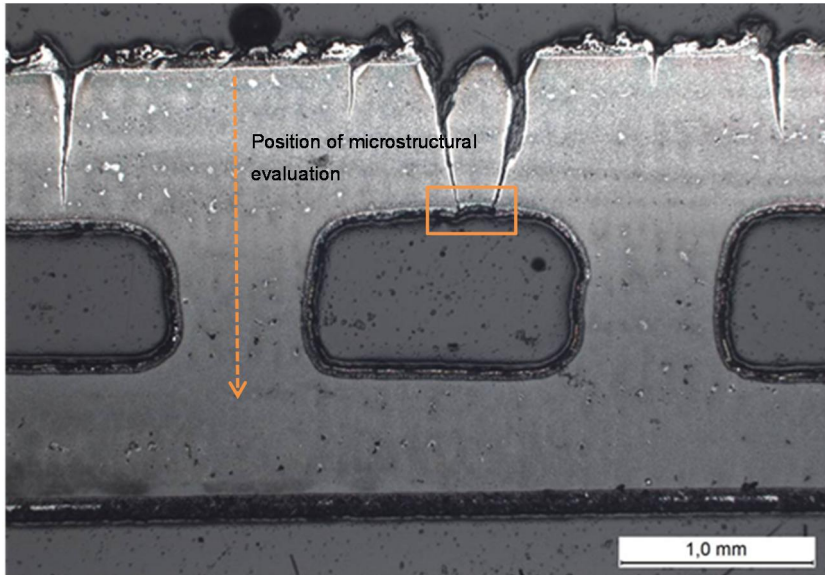


Figure 12. Overheated HTP blade, position of the microstructural temperature evaluation.

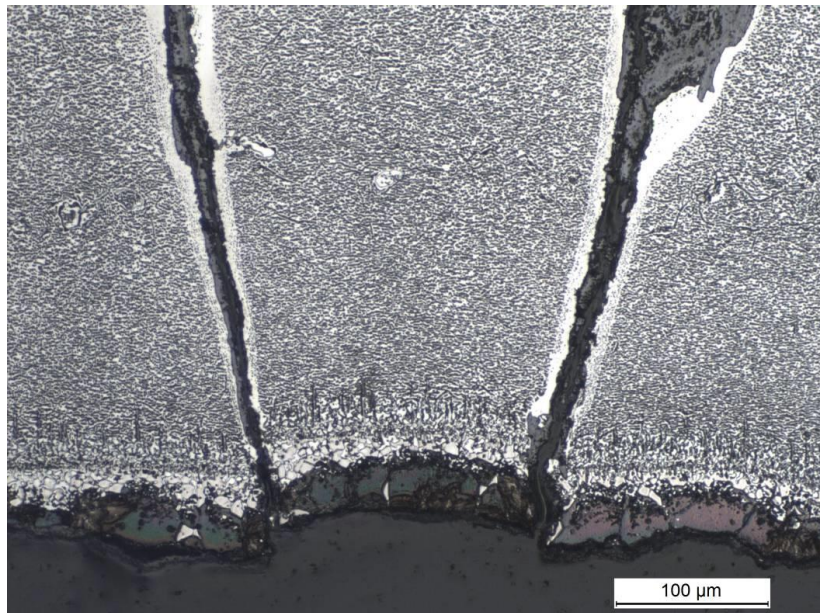


Figure 13. Cracks on the overheated blade (Figure 12), location of the TCP+IDZ temperature evaluation.

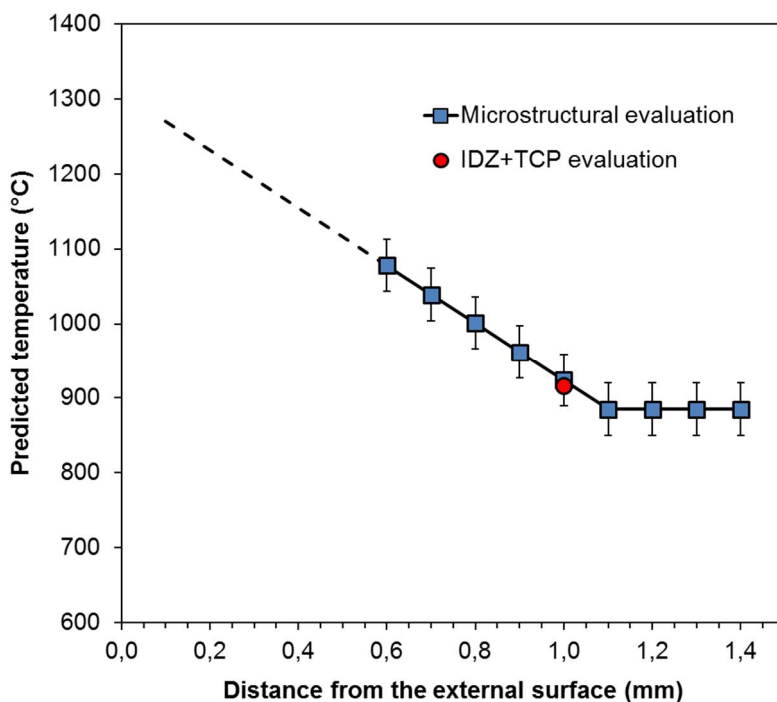


Figure 14. Predicted temperature distribution of the overheated blade.

4. Discussions

In comparison to many other comparable applications, the evaluation of the kinetics of thermal damage in the gas turbine materials of aircraft engines is unusually amenable to testing in the laboratory. Partly this is because testing and treatments can be often done in air, as the real service environment – with some important exceptions – is also largely oxidising due to the air excess provided by the compressor. Perhaps even more importantly, the expected service life of few thousand hours is not beyond the range accessible for experiments within a time frame of few months to a year. Consequently, the resulting conclusions do not need to rely on extrapolation in time, and one can avoid the associated uncertainty.

The composition and fabrication of the blade alloy (substrate) and the details of the diffusion coating process including the heat treatments will influence the initial microstructures and their evolution by thermal exposure during service. Therefore, the ex-service appearance of the substrate alloy (single crystal N4) and its PtAl diffusion coating are specific to the applied alloy, coating and their combination. The temperature gradient by internal cooling will result in a range of the alloy microstructures in the through-thickness direction, particularly towards the specified blade life and at local hot spots of the blade surface.

Note that while exposure to elevated temperature will accelerate any diffusion-controlled mechanisms, diffusion can also be promoted by mechanical stress. Therefore when the microstructural grading is based on unstressed thermal exposure, applying it on real stressed blades will result in somewhat conservative temperature assessment.

The coarsening and degradation of gamma prime in the microstructure of alloy N4 appears to include some nonlinearity. In particular, the appearance from grade 1 to 2 is resilient to change before much more substantial gamma prime coarsening and coalescence at the later stages.

At temperatures below 1050°C a clear dependence was observed between thermal exposure and the growth of the IDZ and TCP phases. Above 1050°C the TCP phase is thermodynamically less stable, and therefore no longer follows the same dependence. The combined thickness of IDZ and TCP layers seems to reflect the thermal exposure at the external surface with reasonable accuracy, suggesting that this measure and the corresponding fitted expression are useful for temperature estimates as long as the layers remain sufficiently intact. The natural disadvantage is the same as with the substrate microstructure, i.e. the need for destructive sampling.

Other observed changes include emergence of gamma prime on the surface of the aluminide coating (beta layer), and loss of gamma prime at crack surfaces after sufficient aluminium loss by oxidation. Such layers were not showing as consistent trends in thickness as the selected IDZ and TCP layers.

The described methodology was applied to an example case of a locally overheated turbine blade. The case example suggests the two temperature estimation methods are well correlated and that the methods can be used to evaluate the local metal temperature with fair confidence.

5. Conclusions

This work aimed to evaluate and classify the microstructural degradation of diffusion coated single-crystal gas turbine blades, so that the characterised features of degradation could be used for assessing the effective in-service material temperatures at the corresponding blade locations.

Two potentially useful indicative measures were evaluated for this purpose: a) gamma prime coarsening and degradation in the microstructure of the blade material (N4) to indicate the condition and temperature in the blade interior, b) combined thickness of the intermediate diffusion zone (IDZ) and topologically close-packed (TCP) precipitate layer of the PtAl diffusion coating to indicate the condition and temperature at the blade surface, as long as these layers remain sufficiently intact for the assessment.

The described methodology was applied to an example case of a locally overheated turbine blade. The case example suggests the two temperature estimation methods are well correlated and that the methods can be used to evaluate the local metal temperature with fair confidence.

References

1. D.K. Das, Microstructure and high temperature oxidation behaviour of Pt-modified aluminide bond coats on Ni-base superalloys. *Progress in Materials Science*, 58, 151–182, 2013.
2. N. Vialas, D. Monceau, Effect of Pt and Al content on the long-term, high temperature oxidation behaviour and interdiffusion of a Pt-modified aluminide coating deposited on Ni-base superalloys. *Surface & Coatings Technology*, 201, 3846–3851, 2006.
3. H. Svensson, J. Angenete, K. Stiller, Microstructure of oxide scales on aluminide diffusion coatings after short time oxidation at 1050°C. *Surface & Coatings Technology*, 177–178, 152–157, 2004.
4. J. Angenete, K. Stiller, E. Bakchinova, Microstructural and microchemical development of simple and Pt-modified aluminide diffusion coating during long term oxidation at 1050°C. *Surface & Coatings Technology*, 176, 272–283, 2004.
5. R.C. Reed, *The Superalloys: Fundamentals and Applications*. Cambridge University Press, Cambridge, 2006.
6. J.H. Chen, J.A. Little, Degradation of the platinum aluminide coating on CMSX4 at 1100°C. *Surface & Coatings Technology*, 92, 69–77, 1997.
7. C.M.F Rae, R.C. Reed. The precipitation of topologically close-packed phases in rhenium-containing superalloys. *Acta Materialia*, 49, 4113–4125, 2001.
8. C.M.F Rae, M.S. Hook, R.C. Reed. The effect of TCP morphology on the development of aluminide coated superalloys. *Materials Science and Engineering A*, 396, 231–239, 2005.
9. Dipak K. Das, Kenneth S. Murphy, Shuwei Ma, Tresa M. Pollock, Formation of secondary reaction zones in diffusion aluminide-coated Ni-base single-crystal superalloys containing ruthenium. *Metallurgical and Materials Transactions A*, Volume 39A, 1647–1657, 2008.
10. J.Y. Chen, Q. Feng, Z.Q. Sun, Topologically close-packed phase promotion in a Ru-containing single crystal superalloy. *Scripta Materialia*, 63, 795–798, 2010.

11. R.C. Reed, T. Tao, N. Warnken, Alloys-By-Design: Application to nickel-based single crystal superalloys. *Acta Materialia*, 57, 5898–5913, 2009.
12. T.M. Pollock, A.S. Argon, Directional coarsening in nickel-base single crystals with high volume fractions of coherent precipitates. *Acta Metallurgica et Materialia* 42, 1859–1874, 1994.
13. N. Matan, D.C. Cox, C.M.F. Rae, R.C. Reed, On the kinetics of rafting in CMSX-4 superalloy single crystals. *Acta Materialia* 47, 2031–2045, 1999.
14. T. Murakumo, Y. Koizumi, K. Kobayashi, H. Harada, Creep strength of Ni-base single-crystal superalloys on the γ/γ' tie-line. *Superalloys 2004*, TMS, 2004.
15. Yu Jinjiang, Sun Xiaofeng, Jin Tao, Zhao Nairen, Guan Hengrong, Hu Zhuangqi, Effect of Re on deformation and slip systems of a Ni base single-crystal superalloy. *Material Science and Engineering A*, 458, 39–43, 2007.
16. N. Ratel, B. Demé, P. Bastie, P. Caron, In situ SANS investigation of the kinetics of rafting of γ' precipitates in a fourth-generation single-crystal nickel-based superalloy. *Scripta Materialia*, 59, 1167–1170, 2008.
17. T. Tinga, W.A.M. Brekelmans, M.G.D. Geers, Directional coarsening in nickel-base superalloys and its effect on the mechanical properties. *Computational Materials Science*, 47, 471–481, 2009.
18. *Metals Handbook Desk Edition*. ASM International, Materials Park, OH, 1999.
19. R. Viswanathan, *Damage mechanisms and life assessment of high-temperature components*, ISBN: 0-87170-358-0. ASM International 1989, p. 497.

Evaluation of creep damage in martensitic 9–10%Cr-steel components

Stefan Zickler & Karl Maile

Materialprüfungsanstalt Universität Stuttgart
Pfaffenwaldring 32, 70569 Stuttgart, Germany

Abstract

Martensitic heat resistant 9–12% chromium steels are widely used for the majority of the components subjected to temperatures up to 620°C maximum in coal fired power plants. There have been numerous investigations on the long-term creep strength behaviour by using uniaxial and multiaxial loaded specimens. As a result it was found that with respect to the damage development, the multiaxiality of the stress state has to be considered. Metallographic investigations showed the influence of material, temperature and state of multiaxiality on the formation of creep cavities as a specific feature of martensitic 9–10% Cr-steels. Based on the results gained, it is obvious that the evaluation of damage could not be done on the same basis used for standard low alloy creep resistant steels.

In the paper the differences in damage development will be reported and new approaches for evaluating the creep damage in high-pressure piping and boiler components made of 9%Cr-steels will be shown.

1. Introduction

The efficiency of power plants using steam turbines for electricity generation is directly connected to the steam temperature and steam pressure. An increase in efficiency demands an increase of steam parameters. Modern coal fired power plants achieve an overall efficiency of 45% and more, the materials within the steam cycle are subjected to a maximum temperature up to 650°C and a steam pressure of about 250 bar.

The materials within the steam cycle need to provide a sufficient creep and oxidation resistance according to their respective temperature range. Martensitic heat resistant 9–12% chromium steels are widely used for components in a temperature range up to 650°C. These materials show different damage behaviour compared to low alloyed heat resistant steels. The microstructure is more complex and the materials show a reduced formation of creep pores with advancing creep damage. Also the number of creep pores varies with the multiaxiality of the stress state.

The evaluation of creep damage normally will be done by means of NDT methods. However the early stage of creep damage at components can only be detected using the replica technique. The demands for the preparation of replicas are very high and additional information about the microstructure in order to evaluate

the damage degree of the investigated component is needed. Magnetic properties of metallic materials are directly connected to their microstructure. Another approach to determine the damage degree therefore is the investigation of the microstructure using non-destructive test methods such as Barkhausen noise amplitude measurements.

2. Creep tests

Creep tests with different levels of stress and multiaxiality have been performed. In order to implement multiaxial stress states hollow cylinder samples, see Figure 1, under inner pressure and axial loads have been tested.

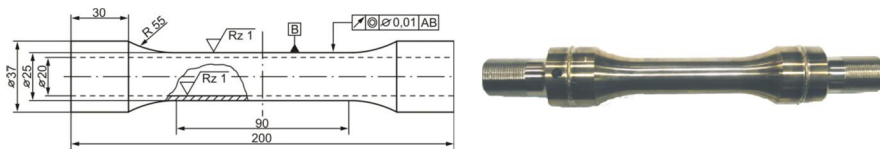


Figure 1. Hollow cylinder with inner pressure and axial load.

The material for the creep specimen is the martensitic steel X11CrMoWVNb9-1-1 (E911) [1]. The chemical composition of the used heat of E911 is listed in Table 1.

Table 1. Chemical composition of E911 creep samples.

	C	Si	Mn	P	S	Al	Cr	Ni	Mo	V	W	Nb
Steel E911	0,11	0,18	0,46	0,015	0,003	0,013	8,61	0,21	0,92	0,19	0,995	0,089

3. Creep damage appearance

Modern martensitic 9–12% chromium steels show, compared to low alloyed heat resistant steels, high creep rupture deformation for long-term rupture times > 50 kh. The number of creep cavities at high levels of creep damage is significantly lower compared to low alloyed heat resistant steels, see also Figure 2.

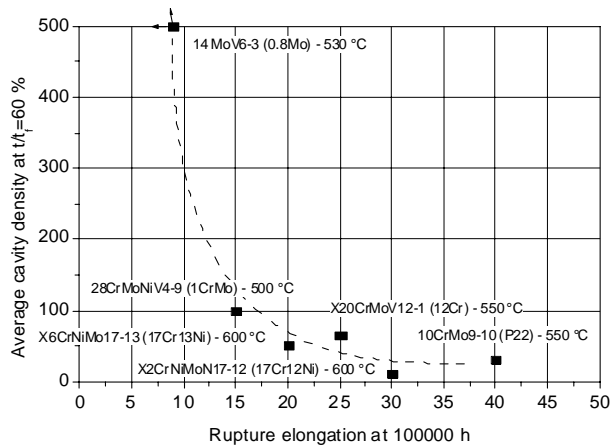


Figure 2. Relation of creep cavity density and fracture strain in creep tests 0.

The difference in creep pore formation between low alloyed heat resistant steels and 9–12% chromium steels is also shown in Figure 3.

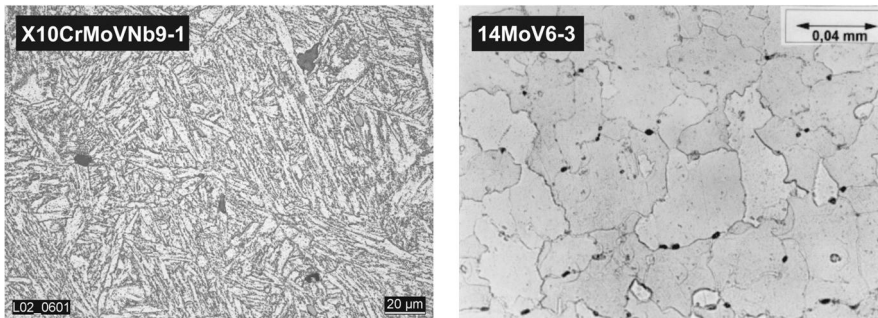


Figure 3. Creep pores in P91 rating class 2a according to 0, left side, and creep pores in 14MoV6-3 rating class 2b according to 0, right side.

Both samples have a similar damage degree, however, the amount of creep pores in the ferritic steel 14MoV6-3 is significantly lower compared to the martensitic P91 steel.

Another influencing factor on the formation of creep pores is the quotient of multiaxiality h , defined as

$$h = \frac{\sigma_{hyd}}{\sigma_v} \quad (1)$$

with

$$\sigma_{hyd} = \frac{1}{3}(\sigma_x + \sigma_y + \sigma_z) \quad (2)$$

and

$$\sigma_v = \frac{1}{\sqrt{2}} \sqrt{(\sigma_x - \sigma_y)^2 + (\sigma_y - \sigma_z)^2 + (\sigma_z - \sigma_x)^2 + 6(\tau_{xy}^2 + \tau_{yz}^2 + \tau_{zx}^2)}. \quad (3)$$

With increasing multiaxiality and therefore reduced creep strain the number of cavities is increasing, see also Figure 4.

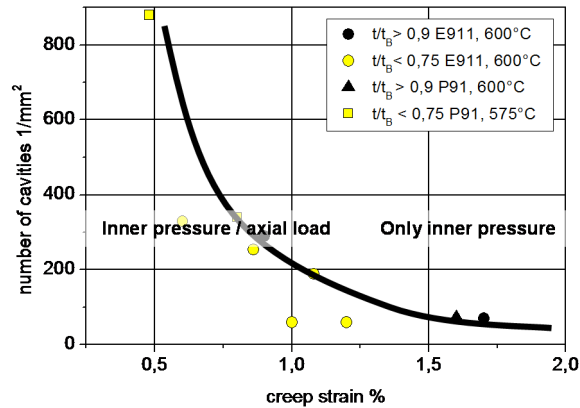


Figure 4. Influence of multiaxiality of stress state on number of cavities.

3.1 Investigation by optical microscope

In order to determine the damage degree of service exposed materials generally a classification of the microstructure according to VGB rating charts 0 is performed. Usually a component will be replaced if the microstructure is rated as class 2b to 3b2, meaning numerous creep cavities, randomly oriented up to chains of creep cavities with specific orientation can be observed. For 9–12% chromium steels some crucial differences compared to low alloyed ferritic steels have to be considered:

- The number of creep cavities in martensitic 9–12% chromium steels is significantly lower
- Neither an orientation of creep cavities nor the formation of cavity chains and grain boundary separations were observed until the formation of macro cracks.

The propagation of damage degree along with creep pore formation is shown in Figure 5, Figure 6 and Figure 7.

² Depending on the criticality of the component.

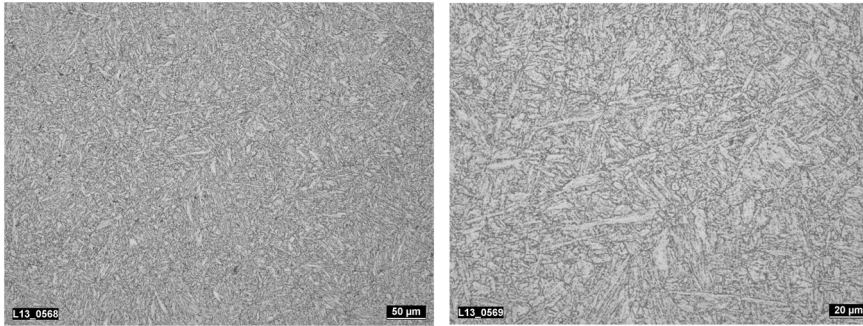


Figure 5. Microstructure of E911 creep sample in initial state.

In comparison with the microstructure of the initial state in Figure 5 the microstructure after an exposure time of 19597 h, sample E6 and a calculated lifetime usage of 78% is shown in Figure 6.

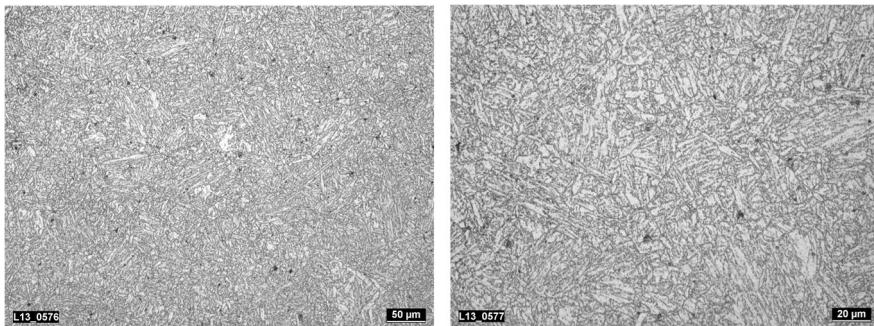


Figure 6. Microstructure of E911 sample E6 after load exposure of 19597 h and damage degree of 78%.

With further progress of damage degree due to a higher load, see Figure 7, the number of creep pores increases.

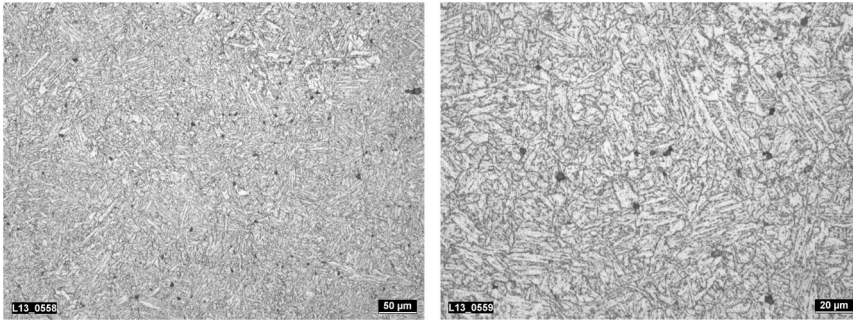


Figure 7. Microstructure of E911 sample E3 after load exposure of 18619 h and damage degree of 98%.

As can be seen, even with a highly progressed damage degree the total amount of creep pores is low. Considering the difficulties in the separation between precipitates and creep pores the absolute determination of damage degree by light optical methods is error-prone.

The evolution of creep pores over advancing damage degree according to Table 3 is shown in Figure 8.

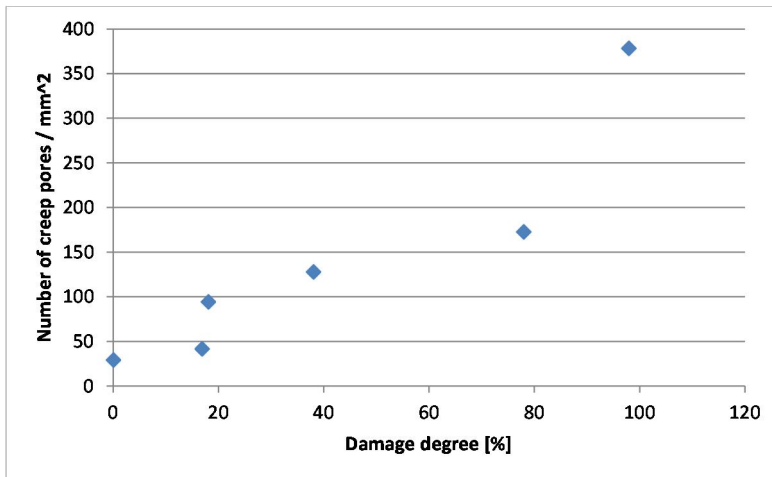


Figure 8. Evolution of creep pores with advancing damage degree.

The evaluation of creep pores has been performed using 50 visual fields with a magnification of 500:1. Sample E0 is used as a reference sample without creep exposure. The amount of creep pores > 0 results from uncertainties in the differentiation between precipitates and creep pores, see also Figure 5. As can be seen,

to overall amount of creep pores is relatively low, a significant increase of creep pores can only be observed after a damage degree of about 80%.

3.2 Characterization via TEM

During creep and temperature exposure changes in the microstructure of the exposed material occur. In order to determine the microstructural changes TEM investigations of different samples with different creep time and damage degree have been performed. The different samples are listed in Table 2.

Table 2. Creep samples for TEM characterizations.

Sample	Creep time [h]	Creep temp. [°C]	Inner pressure [bar]	Axial load [N]	Multi-axiality coefficient	Damage degree [%]
EH15	48000	600	140	6834	0,45	19
EH6	4840	600	340	0	0,33	68
EH6 Head *)	4840	600	0	10	0,33	0
EH7	40000	600	177	8640	0,45	40
EH7 Head *)	40000	600	0	8640	0,33	0
EH9	24410	600	270	0	0,33	100
EH9 Head *)	24410	600	0	0	0,33	0

Within the TEM investigations the particle size, subgrain size and dislocation density have been analysed. Figure 9 shows the appearance of the grain structure in sample EH6 after a load exposure time of 4840 h and a damage degree of 68%.

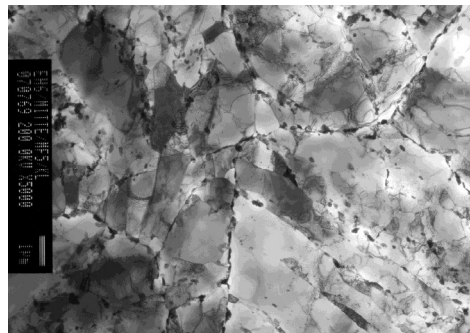


Figure 9. Appearance of grains in creep sample EH6, scale 5000:1.

Figure 10 shows the development of subgrain size and dislocation density with advancing damage degree.

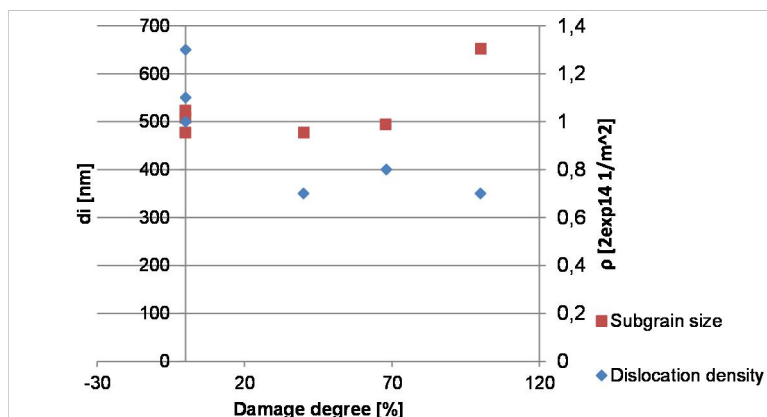


Figure 10. Subgrain size and dislocation density.

With increasing damage degree the subgrain size increases, the dislocation density decreases.

The number and size of precipitations in connection with the development of damage degree is shown in Figure 11.

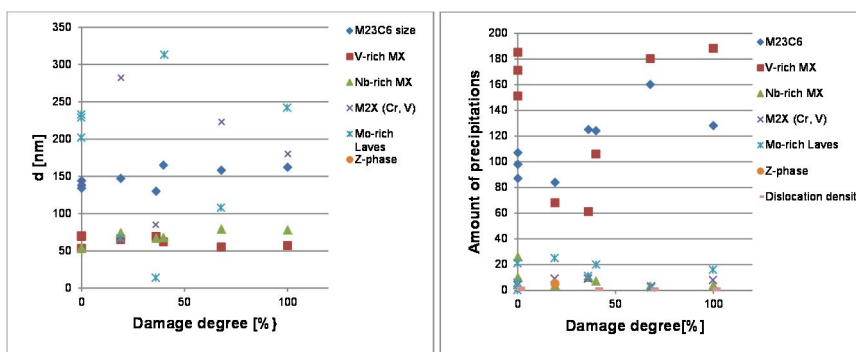


Figure 11. Particle size (left) and number (right) of precipitations versus damage degree.

A correlation between progressing damage degree and particle size or amount of particles cannot be observed. However a correlation between subgrain size, dislocation density and progressing damage degree can be observed.

3.3 Non-destructive damage evaluation with Barkhausen Noise Measurements

Non-destructive testing methods are a possible method in order to support the outcome of the microstructure evaluation via replica. Magnetic material properties show a very sensitive reaction towards microstructural changes. On the creep samples as listed in Table 3 Barkhausen noise measurements and coercive field measurements have been performed.

The NDT measurements have been performed on creep samples with creep temperatures of 575°C and 600°C, see also Table 3.

Table 3. Test conditions for the different creep specimen.

Sample	Creep time [h]	Creep temp. [°C]	Inner pressure [bar]	Axial load [N]	Multi-axiality coefficient	Damage degree [%]	Creep pores / mm ²
E0	0	0	0	0	0	0	29,1
E2	25476	575	175	8543	0,45	17	41,5
E3	18619	575	305	7100	0,42	98	378,2
E6	19597	575	236	9300	0,46	78	172,4
EH2	6643	600	235	11775	0,45	0,33	-
EH8	37669	600	177	8640	0,45	38	127,6
EH10	50217	600	140	6834	0,45	25	-
EH11	45190	600	130	6577	0,45	18	94,1

During power plant operation the exact determination of the material temperature is not always possible. Uncertainties in the determination of the temperature are for example caused by a limited amount of thermocouples, differences between steam temperature und material temperature, thermal gradients and inaccuracies of the thermocouples themselves. Therefore NDT-methods should to be able to determine the damage degree with certain insensitivity towards the exact material temperature.

Figure 12 shows the Barkhausen noise amplitude and the coercive field strength versus damage degree.

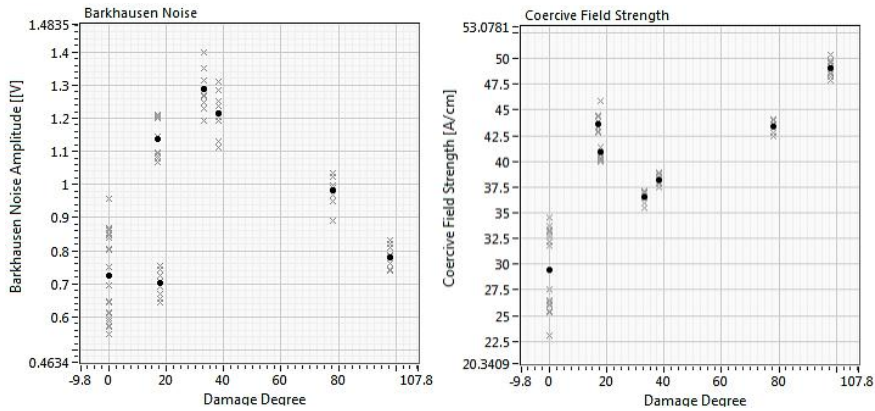


Figure 12. Barkhausen noise amplitude and coercive field strength versus damage degree.

Both measurements show a clear sensitivity towards the damage degree of the sample, independent from the creep temperature of the respective sample. A clear assessment of damage degree with magnetic measurements seems difficult due to the ambiguous progression of the measurement curves. However, in case of repeated measurements during the operation of creep exposed material an identification of the damage progress seems to be possible.

4. Summary and conclusion

Compared to low alloy ferritic steels modern martensitic 9–12% chromium steels show a significantly different damage behaviour:

- The number of cavities is low compared to that of conventional steels
- The formation of creep pores occurs at higher levels of life-time consumption
- An orientation of creep pores and micro cracks are not mandatory at high damage degrees
- Critical damage degrees can be reached while only a few cavities can be observed without orientation towards the maximum principal stress.

The identification of cavities requires a precise preparation technology. NDT measurements such as Barkhausen noise measurements seem to be a possible method in order to support the evaluation of damage degree. However, a clear correlation between magnetic properties and damage degree seems to be difficult.

References

1. Maile, K., Rauch, M., Seliger, P. & Reuter, A. Charakterisierung der Schädigungsentwicklung zur Lebensdauerbewertung von Rohrleitungskomponenten aus den neuen 9%-Chromstählen, Abschlussbericht zum AVIF-Forschungsvorhaben Nr. A152, MPA Stuttgart, SPG Dresden, 2004
2. Richtreihen zur Bewertung der Gefügeausbildung und Zeitstandschädigung warmfester Stähle für Hochdruckrohrleitungen und Kesselbauteile. VGB – TW 507. 2. Ausgabe 2005. VGB-Power Tech Service GmbH Essen.
3. Maile, K., Zies, G., Scheck, R., Kuppler, D., Ruoff, Hr., Rauch, M., Klenk, A. & Scheu, C. Beurteilung der Kriechfestigkeit moderner martensitischer Chromstähle durch die Charakterisierung des Mikrogefüges
4. Lenk, P. & Bühner, S. Gefügeänderung und Schädigungsentwicklung bei Langzeitbeanspruchung. Abschlussbericht zum AiF-Forschungsvorhaben Nr. 234 DI/II, MPA Stuttgart und Tu Chemnitz-Zwickau, 1992
5. Maile, K. & Klenk, A. Creep damage evolution in martensitic 9%Cr-steels. 12th International Conference on Creep and Fracture of Engineering Materials and Structures (Creep 2012). Kyoto, Japan 2012.

Influence of boiler operating conditions to component lifetime, case study: pulverized coal burner

Jukka Meskanen

Fortum Power & Heat
Keilaniementie 1, 02150 Espoo, Finland

Abstract

In coal fired power plants the most common method of burning coal is in pulverized form. The fuel is fed into the furnace via coal pipelines and burners which are the pipelines last components next to the fireside. The burners main purpose is to optimise the fuel flow for staged combustion. The fireside ends of the burners are exposed to temperatures above 1000°C and temperature gradients making the burners susceptible to damage through creep-fatigue. In addition to creep-fatigue the fuel flow wears the component surfaces through abrasion and erosion. In general, power plants emphasize operational reliability and therefore material selection and mechanical construction are essential in burner design. Thermal and thermo-mechanical stresses combined with fireside corrosion degrade component lifetimes. This work presents and assesses temperature records from power plants and their influence on component lifetime. The case study component was analyzed by Finite Element modeling. The thermal loads for calculations were defined from temperature records. The results of the analyses show that the primary factor degrading component lifetime are thermal shocks induced from altering boiler operating conditions. The lifetime of the components can be improved by optimizing the material selection and the mechanical construction of the components. As a result of the work suggestions for component material selection and mechanical construction are presented.

1. Introduction

The pulverized coal contains always some amounts of hard quartz. Quartz has a hardness of 900...1280 HV and is the main element causing wear of components through abrasion and erosion. In burner regions where operation temperatures are low the wear through abrasion and erosion are the primary damage mechanisms.

Operation temperatures increase closer to the furnace. The process design requires the flame to be lit directly at the furnace end of the burner. When full boiler power is not required and burner level is shut the burner end is susceptible to radiation heat flux from the furnace. In these regions the burner components are exposed to high temperatures and temperature gradients from altering boiler con-

ditions. The temperature fields for a single component are uneven inducing thermal stresses within the component. Depending on the construction thermo-mechanical stresses are also induced. When stresses are induced and operation temperatures are above 600°C the components are susceptible to damage through creep. Altering boiler conditions expose the components to thermal cycles and the components are susceptible to damage through low cycle fatigue. As a combination the damage through creep-fatigue has to be analysed.

The coal burner directs the pulverized coal and primary air into the furnace. The burner aligns the fuel stream to a horizontal direction and optimises the flow speeds. A coal burner cross section is presented in Figure 1.

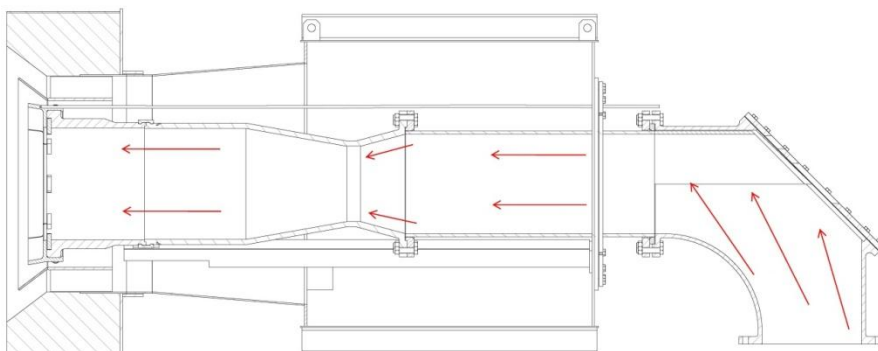


Figure 1. A coal burner cross section.

The fuel and primary air are transported in the coal pipes and enters the burners through the elbow which redirects the stream to horizontal direction. The fuel distribution and flow speeds are optimised by shaping the flow channel cross section. Redirection of the fuel flow alters the burner components to abrasive and erosive wear.

Modernised boilers utilise staged combustion. At lower levels of the boiler the fuel is burnt in a reducing atmosphere to prevent the formation of nitrogen oxides (N_{Ox}). The burn is completed in the upper levels with auxiliary air. At the burner levels the atmosphere is reductive consisting mainly of carbon oxides (CO and CO_2) and sulphur dioxide (SO_2) depending on the sulphur content of the fuel.

The operating conditions of the boiler can alter constantly inducing high temperatures and thermal cycles to the burner components. The highest temperatures and the most severe thermal shocks occur at the furnace end of the burner. Temperatures up to 1134°C and thermal gradients of -45°C/min are recorded from these components.

The burner components are divided in to categories depending on the dominating life-time degrading phenomenon explained above. Near the furnace the component life-times are degraded by high operating temperatures and thermal cycles. Here the selected material should have an adequate creep strength and resist thermal cycles. Mechanical construction should also be optimised to lower the thermal and thermo-mechanical stresses.

2. Field measurements

The component temperatures were measured using a thermocouple temperature sensor and logged with a Grant SQ2020 logging device. The logging interval of measurements was 90 seconds. The measurements were recorded from the burner stabiliser segments from a 23 day operating period. The thermocouple locations are shown in Figure 2.

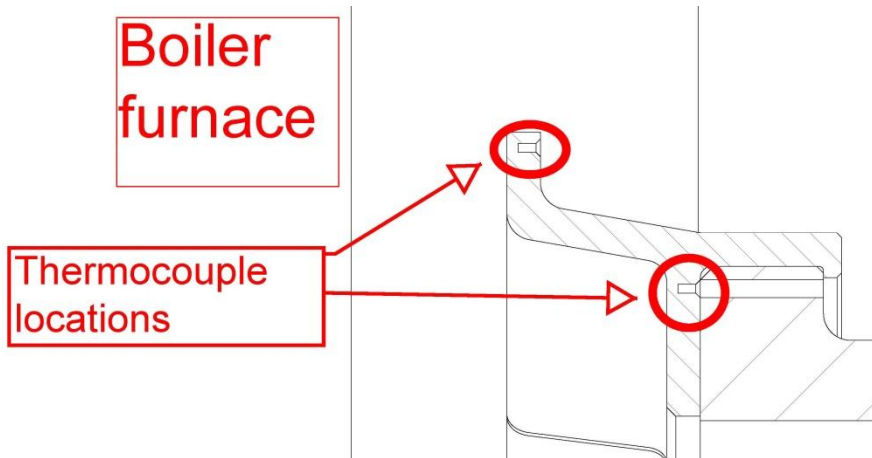


Figure 2. Thermocouple locations.

Ten thermocouples were installed in five clock-face positions when looked from the furnace side. Each clock-face position had two thermocouples. The upper thermocouple is in the stabiliser segment tip and the other in the base as shown in Figure 2. The angular offset between clock-face positions was 72° . During the measurement period the highest recorded temperature was 1070°C at measure point 5 at the stabilizer segment tip. The whole recorded data from measurement points 1 to 5 are presented in Figure 3.

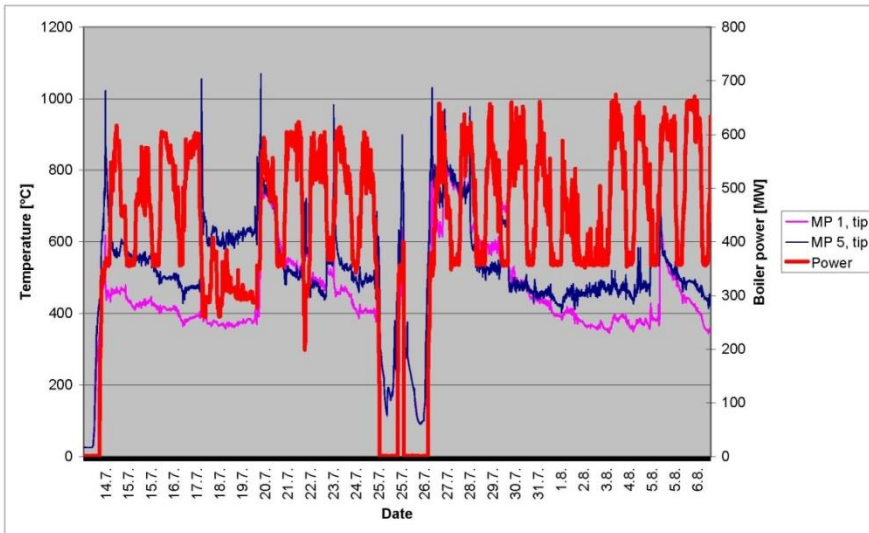


Figure 3. Recorded temperatures, burner stabilizer segment.

During the recorded period the temperatures remain mostly between 400–700°C and the temperature peaks occur during boiler power changes. A detailed example of a measured temperature peak is shown in Figure 4.

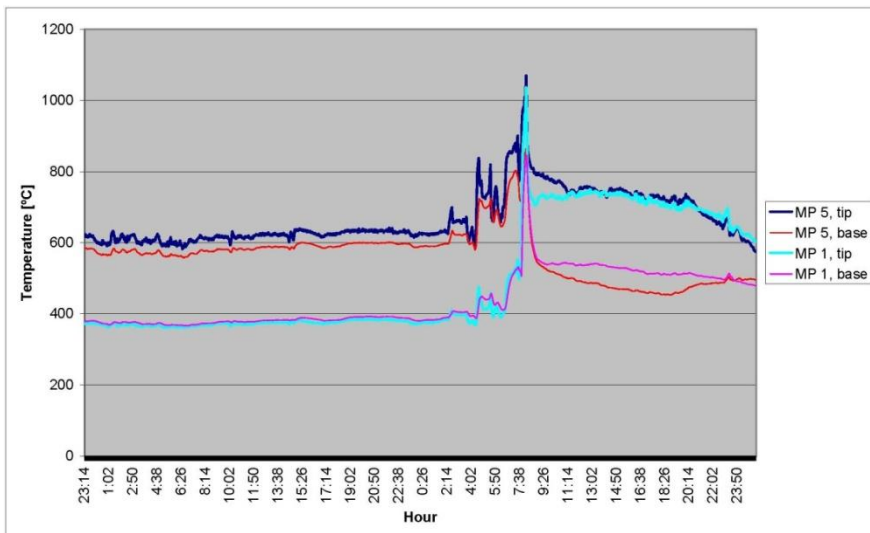


Figure 4. Recorded temperature gradient.

The temperature records from two adjacent measurement points are shown in Figure 4. The records show that the stabiliser segment's temperature field is une-

ven and there is approximately 200°C temperature difference between the measurement points. During the thermal shock the temperature at measurement point 1 increase from 533°C to 1037°C in 21 minutes.

3. Materials

The stabiliser segment was manufactured from austenitic cast steel. The material standard used was SFS-EN 10295 heat resistant cast steels. From the standard, alloy specification G-X40CrNiSi25-20 with reduced carbon content was used. The selected compositions main alloying elements are 25%Cr and 20%Ni. The standards guideline for maximum operational temperature is 1100°C in air [1].

Heat resistant cast steel are used in temperatures above 650°C. Generally these steels are alloyed with 0,3–0,6%C to increase high temperature creep strength which increases with carbon content. The creep strength of these compositions is due to precipitation of secondary carbides at high temperatures which lower the creep rate. The correlation between the carbon content and the alloys creep properties is presented in Table 1 [2].

Table 1. HK40 cast steel creep properties [2].

Carbon content [%]	σ_r 1000h [MPa]		
	760°C	871°C	982°C
0,1	38	17	8
0,2	60	30	14
0,3	74	37	19
0,4	87	43	21
0,5	92	46	23
0,6	90	45	23

HK40 is an ASTM cast steel composition similar to G-X40CrNiSi25-20 which was used. The main alloying elements of HK40 are 25%Cr and 20%Ni.

4. Creep-fatigue damage calculation

The objective of analysis was to evaluate the stabilizer segment's creep-fatigue damage utilising ASME Boiler & Pressure Vessel Code's damage summation equation:

$$\sum \frac{n}{N_d} + \sum \frac{\Delta t}{T_d} \leq D \quad (1)$$

where $\sum \frac{n}{N_d}$ is the fatigue damage

$\sum \frac{\Delta t}{T_d}$ is the creep damage

D is the total creep-fatigue damage.

The allowed damage sum is material dependent. The code presents the allowed damage sum's graphically shown in Figure 5 [3].

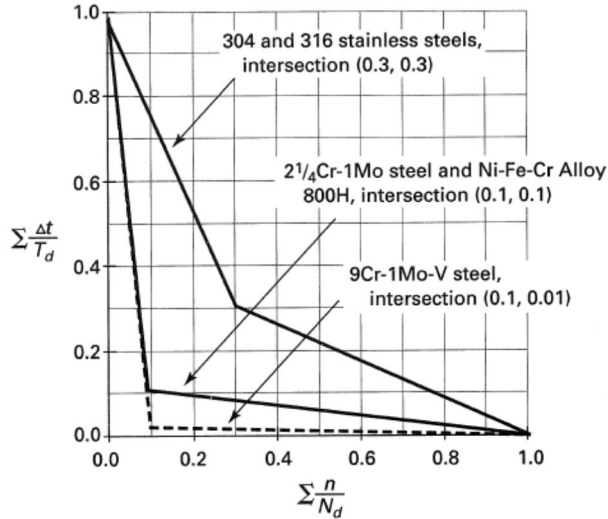


Figure 5. Creep-fatigue damage summation, ASME 2010 [3].

The code's equation for a total fatigue strain range in a thermal cycle is:

$$\varepsilon_t = K_v \Delta \varepsilon_{\text{mod}} + K \Delta \varepsilon_c \quad (2)$$

where ε_t is the total strain range in a cycle

- K_v is the multiaxial plasticity factor
- $\Delta \varepsilon_{\text{mod}}$ is the modified maximum strain equivalent range
- K is the local geometric concentration factor
- $\Delta \varepsilon_c$ is the creep strain increment.

The allowed number of cycles for the total strain range ε_t is determined from Figure 6. The diagrams are material specific and diagram for stainless steel 316 is presented in Figure 6.

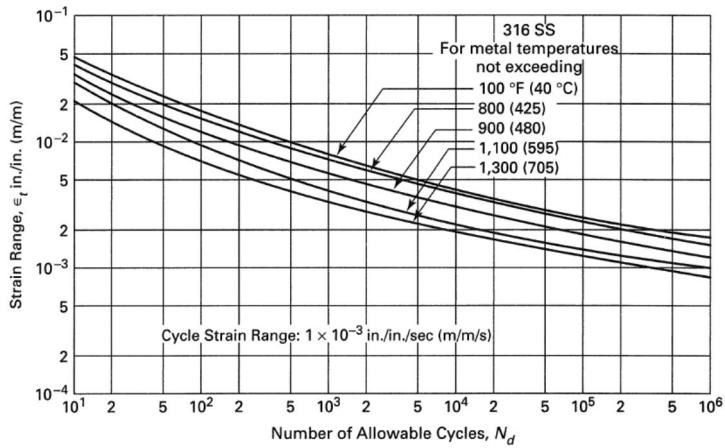


Figure 6. 316 Stainless steel ϵ -N diagram, ASME 2010. [3]

For creep damage evaluation for stainless steel 316 ASME 2010 presents the diagram shown in Figure 7.

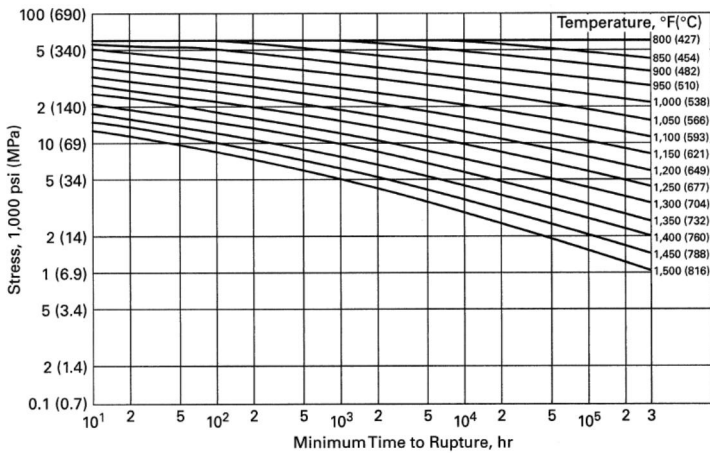


Figure 7. 316 Stainless steel minimum time to rupture, ASME 2010 [3].

To establish the creep-fatigue damage the components creep stress and cyclic total strain must be calculated. From stress and strain levels the damage factors are established and plotted to Figure 5 for evaluation [3].

5. Finite Element Analysis

The analysis was calculated using Abaqus 6.11-1 FE-program using a linear-elastic material model. The temperature boundary conditions were defined from measurement data presented in Figure 4. The recorded temperatures were set to the stabiliser segment corners and linearly interpolated to a temperature field shown in Figure 8. The interpolated temperature boundary condition and consequent stress field are base load profiles for creep damage calculation.

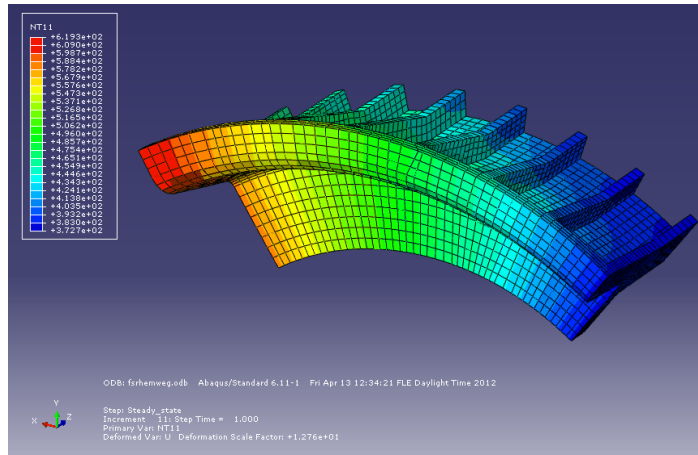


Figure 8. Temperature field of the stabiliser segment.

This temperature field induces a base load of 40 MPa tensile creep stress to the segment's tip area shown in Figure 9.

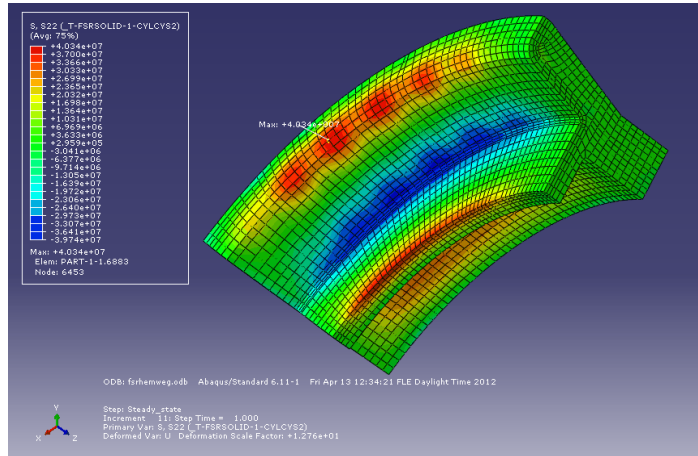


Figure 9. Tensile creep stress of the stabiliser segment.

To establish the total strain range in a thermal shock a transient was modelled based on the recorded temperatures. The total strain range was used for fatigue damage calculation only and calculation assumes no additional creep damage from thermal shocks. The modelled thermal shock and recorded temperatures are shown in Figure 10.

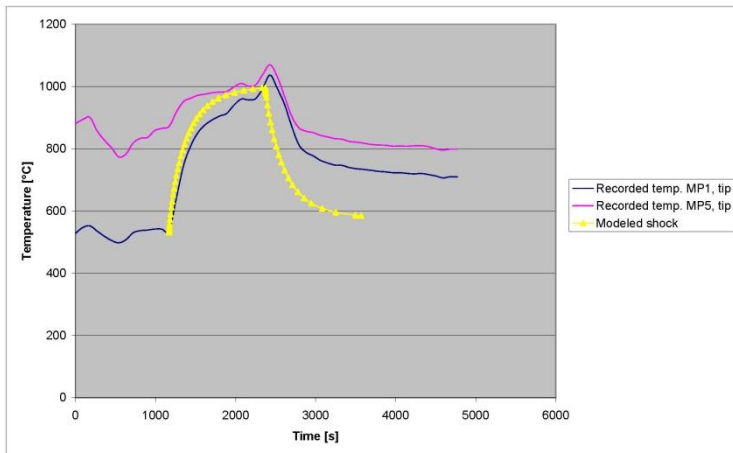


Figure 10. Modelled thermal shock for the stabiliser segment.

The recorded temperature from measurement point 1 increases from 533°C to 1037°C in 21 minutes at the average speed of 24°C/min. The computational total strain range was established utilising the achieved strain variables from the FE-model.

6. Results

The case study assumes a 40 000 hour lifetime for the stabiliser segment. This is equivalent to a 5 years boiler operation with approximately 8 000 hour annual operation. Based on the recorded temperature history an estimate of the total number of thermal cycles for the component can be calculated. Extrapolating the recorded period to component lifetime results into 480 expected thermal shocks for the stabiliser ring.

From the FE-model a tensile creep stress of 40 MPa at 600°C was achieved. The diagram in Figure 7 shows for this stress and temperature the minimum time to rupture of $3 \cdot 10^5$ hours. Utilising equation 1 a creep damage of 0.133 was established. From the modelled thermal shock the model strain variables were recorded. Utilising equation 2 a total strain range of 0.00626 was achieved. Plotting the achieved total strain range to the ϵ -N diagram in Figure 6 results to 172 allowed similar thermal cycles. Utilising equation 1 a fatigue damage of 2.791 was established. In Figure 5 the maximum value for fatigue damage is 1. The achieved numerical value for fatigue damage is greater than the maximum value in the diagram thus making final result plotting impractical.

6.1 Material selection

Alloying carbon to steel stabilises austenitic structure which is desired for high temperature use. As the carbon content is reduced the possibility of ferrite in the material matrix increases. At the stabiliser segment's operation temperatures ferrite is not desired for its brittleness. The influence of reducing the carbon content to 0,1% to the material structure can be seen from the Schaeffler diagram presented in Figure 11 [4].

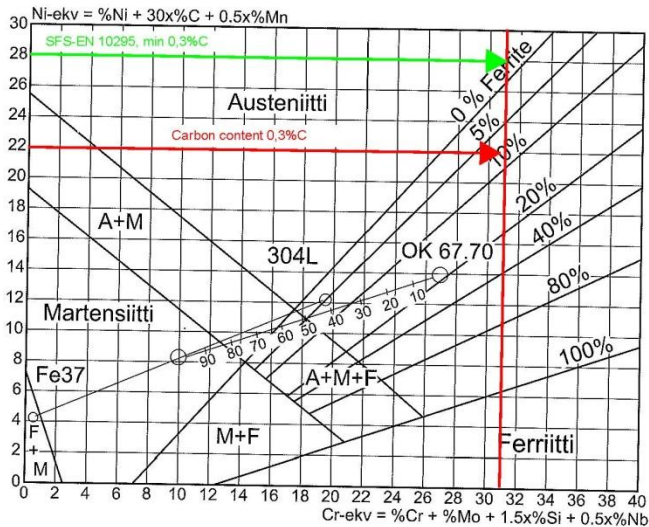


Figure 11. Schaeffler diagram [4].

The material matrix contains ferrite with the reduced carbon content. To achieve a fully austenitic material structure the carbon content should be increased to the material standards specification. This also results to improved creep properties due to secondary carbide precipitation. Service experiences indicate improved high temperature fatigue life with increased nickel alloying. ASTM compositions HT and HU with 33–41%Ni have performed particularly when carburization is involved [2].

Based on the temperature records the operating temperature of the stabiliser segment is between 400–800°C. During thermal shocks the temperature increases above 1000°C. In the normal operation temperature the formation of chromium oxide to the components surface prevents the progression of corrosion into the material. The risk of volatile chromium oxide formation increases if the components normal operation temperature increases to 1000°C. Then the material is susceptible to high temperature corrosion and other alloying elements are needed. Aluminium- and silicon oxides may form a protective oxide layer to the surface in temperatures up to 1200°C. Alloying aluminium to the material could decrease the materials creep-fatigue properties which have to be considered. At temperatures above 1200°C other alternatives such as refractory ceramics have to be utilised [5].

6.2 Mechanical construction

Depending on the implementation the stabiliser ring has been constructed of 5 segments. This construction results to 72° wide segments. The mechanical attachment to connecting part has been with 3 bolts. The temperature records show

the uneven temperature field at the component surface. This combined with multiple attachment points induce thermal and thermo-mechanical stresses to the component.

By modifying the construction to narrow segments the temperature field within one piece is more even. This results to decreased thermal stresses within one segment. The thermo-mechanical stresses can be reduced by allowing the required thermal expansion. Combining the narrow segment design with single point attachment both thermal and thermo-mechanical stresses are reduced.

7. Discussion and conclusions

The furnace end of the coal burner is exposed to high temperatures and thermal shocks due to altering boiler conditions. Locally high temperature erosion and corrosion are active. User experience shows the formation of radial cracks to the stabiliser segments as the most common reason for component failure. The formation of cracks indicates tangential tensile stresses in the stabiliser ring segment.

An FE-model of the stabiliser ring segment was created for analysis. Temperature loads for analysis were defined from service temperature records. The analysis results show that the thermal loads and construction boundary conditions induce tensile stress to the stabiliser segments tip area. The service failures of the components support the analysis results.

The creep-fatigue damage of the component was established utilising the stress and strain variables achieved from the FE-model. Analysis indicates low cycle fatigue as the dominant failure mechanism. Although a result was achieved, the use of ASME codes equation for creep-fatigue damage is not entirely applicable to the analysed case. The code imposes restrictions and limitations for its use which all are not fulfilled by the case study. The ϵ -N diagram in figure 6 gives allowed cycles for a given total strain range at defined temperatures. The highest temperature of the diagram is 700°C and the case study's temperatures are higher. The ASME code provides 3 alternatives for establishing the modified equivalent strain range, a factor in equation 2. The numerical outcome of the total strain range is highly dependent of this factor and thus the achieved numerical value for the fatigue damage is questionable.

To achieve more accurate analysis of the components creep-fatigue damage more alloy specific material test programs are needed. The creep-fatigue behaviour of G-X40CrNiSi25-20 cast steel at high temperatures is not evident and the case study's calculated creep-fatigue damage is questionable. Although the calculated result needs more consideration, the component service failures support the analysis results. The radial cracks form due to cyclic tangential tensile stresses. The lifetime of the component can be increased by optimising the construction and material selection. Narrow segment design enables more even temperature field reducing thermal stresses. Allowing thermal expansion by reducing the constructional attachment points of the component results to decreased thermo-mechanical stresses.

References

1. SFS-EN 10295. Heat resistant steel castings. Helsinki: Finnish Standards Association, 2003. 28 p.
2. Blair, M. & Stevens T. L. Steel Castings Handbook. ASM International, 1995. 472 p. ISBN 0-87170-556-7.
3. 2010 ASME Boiler & Pressure Vessel Code. Rules for construction of nuclear facility components, Division 1 – Subsection NH, Class 1, Components in elevated temperature service. The American Society of Mechanical Engineers, 2011. 192 p.
4. Kyröläinen A. & Lukkari J. Ruostumattomat teräkset ja niiden hitsaus. Metalliteollisuuden keskusliitto, 1999. 514 p. ISBN 951-817-695-7 (In Finnish).
5. Khanna, A. S. Introduction to high temperature oxidation and corrosion. ASM International, 2002. 324 p. ISBN 0-87170-762-4.

High temperature multiaxial component testing and modelling for the prediction and monitoring of creep-fatigue behaviour

Ansgar Kranz¹, Catrin Davies², Joseph Corcoran², Paul Hooper², John Dear²
& Peter Cawley²

¹TÜV Rheinland Werkstoffprüfung GmbH
Am Grauen Stein, Cologne, Germany

²Imperial College London
Department of Mechanical Engineering, South Kensington Campus, London, UK

Abstract

In response to the dynamic electricity market requirements and accommodating the fluctuating availability of energy from renewables, flexible operation of coal fired power plants is required. In addition, maximising operating temperatures is a key requirement to exploit energy efficiency of power plants. For continuous plant operation, creep is a dominant failure mechanism in high temperature components. However for flexible plant operation, which implies fast start-ups, load changes and shutdowns, failure by a complex cyclic stress/strain behaviour can be expected. Therefore, there is a clear need for a deeper understanding of multi-axial high temperature material deformation and damage behaviour in power plant components and validated models are required to predict component failure.

As part of a collaborative European R&D-project denoted MACPLUS, a feature component test of P91 steel is being performed which is being subjected to creep/fatigue conditions by heating and pressurizing the component and simulating shutdown and start-up cycles by employing cooling techniques. A combination of metallurgical material evaluation methods and non-destruct in-service monitoring systems provide valuable tools to assess the condition of plant components and estimate their remaining lifetimes. This paper describes the range of deformation and material damage monitoring tools deployed onto this component and preliminary results from finite element models used to predict the test components elastic-plastic-creep response and damaging behaviour that have been used for the component's design.

1. Introduction

Increasing the efficiency in existing and new build pulverized coal power plant (which can be achieved by increasing operating temperatures) and flexible operation (which implies fast start-ups, load changes and shutdowns) requires intelligent

and cost effective designs, especially for the integration of CCS technologies in coal fired power plants. Increasing efficiency is the sum of many, complex and prolonged improvements on materials, components and thermodynamic design optimisation of power plants for the given steam parameters. For this reason, only an integrated design and engineering approach to the problem may result in a cost-effective, affordable and long lasting solution, that is suitable for industrial scaling-up [1].

A collaborative European R&D-project 'Material-Component Performance-driven solutions for Long-Term Efficiency Increase in Ultra Supercritical Power Plants' (MACPLUS) aims to increase the net efficiency of coal fired plants by increasing the performance and reliability of some critical components, which are identified as follow:

- Refractory materials of the combustion chamber (especially for oxy-combustion application)
- Headers and pipeworks (avoidance of weld Type IV cracking phenomena, working temperature increase)
- Super heaters (optimised creep performance in high temperature oxidation/hot corrosion environments)
- Coated pipes and boiler components able to withstand co-combustion conditions (high temperature oxidation/hot corrosion, erosion-adhesion and wear)
- High and Intermediate Pressure (HP and IP) steam turbine rotor components and turbine casing operating at very high temperatures.

Detailed investigations in MACPLUS are described in six work packages (WP). For each critical component, a full-scale prototype will be developed and installed into an industrial plant and/or test loop(s) at known temperature, pressure and atmosphere conditions. The choice of testing system (loop or plant) is related to actual availability and the optimisation of sensor/monitoring systems.

This paper deals with investigations in work package six (WP 6) which aims to support the design, operation and maintenance of high efficiency ultra super critical (USC) plant. The project partners in WP 6 are E.ON, RWE Technology, Imperial College London, TUV Rheinland, IWM Freiburg, MPA Stuttgart, VTT, Foster Wheeler, Loughborough University, NPL, Doosan Babcock, CSM, UNICAS, Technical University of Graz. High temperature and flexible plant operation relies on the availability of durable materials which can be inspected, component designs that allow for inspection/monitoring, and materials that fail in a predictable manner which are also repairable. Key themes that run through the WP 6 are the development of:

- guidelines/tools to aid plant designers and operators to minimise the occurrence of unplanned outages
- advanced computational models to develop and validate experimental tests (laboratory and full scale) and design/assessment codes

- innovative condition monitoring tools/strategies that provide key information and validation of experimental tests and numerical modelling, and providing confidence in component condition assessments (risk assessment).

The main materials being investigated in WP 6 are P91 (9Cr-1MoVNb) which is a widely used 9% Cr Ferritic steel, P92 (9Cr-0.5Mo-1.8WVNb) which is currently the most advanced 9% Cr Ferritic steel and the nickel based alloy A617 (54%Ni-22%Cr-8.5%Mo-12%Co-AlMnSi) which is a candidate material for use at over 700°C in USC plant. WP 6 has been divided into eleven sub tasks, as illustrated in Figure 1. Condition monitoring of these materials is a key consideration, thus WP 6.4 is highlighted in Figure 1. Hence, to demonstrate the capability and accuracy of the range of condition monitoring techniques, materials deformation and failure models developed by WP 6, a feature pipe component test of P91 steel is being performed onto which a range of sensors are deployed and condition monitoring techniques are applied. This pipe is being subjected to creep/fatigue conditions by heating and pressurizing the component and simulating start-up and shutdown cycles by employing cooling techniques (WP 6.10). This component test is being conducted at the laboratory of StandZeit GmbH (which is a subcontractor of RWE).

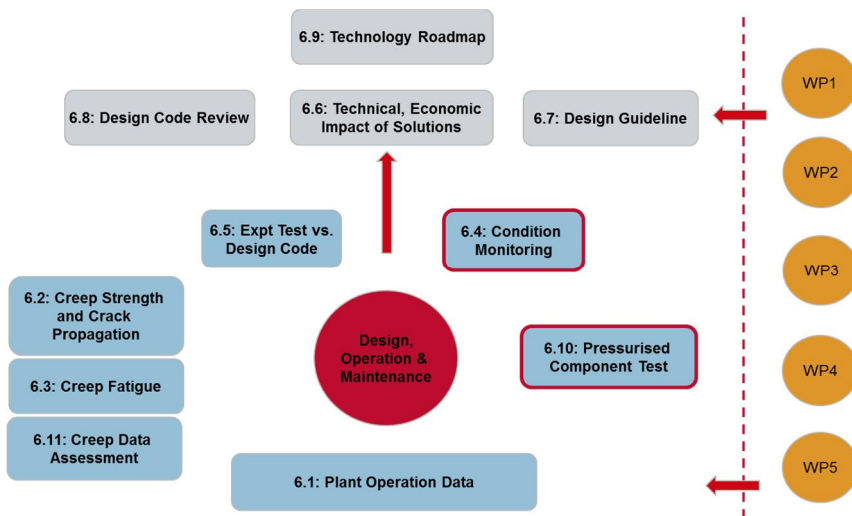


Figure 1. Working structure of Work Package 6 (WP 6).

2. Design and engineering of the pressurized component test (WP 6.10)

The aim of the pressurized component test is to get reliable results under variable loading conditions (both static and cyclic loading).

The subtasks of WP 6.10 has been defined as followed:

- Design and manufacture of a pressurised steam loop to simulate a main steam pipe section
- Deploy instrumentation to monitor the steam loop, temperature, pressure, strain (> WP 6.4)
- Cyclic operation of component and data collection
- Computational model development
- Review and compile findings from experimental data and model, and compare to the design code.

A pipe segment of P91 material (Outer diameter = 450 mm, wall thickness = 50 mm) was provided by project partner RWE for the design and engineering of a component test. Due to limitations of manufacturing (drilling) and thermal conditions of the test stand, a total length of 600 mm was chosen.

The following factors were determined:

- Operating temperature is 600°C
- Operation time approximately 25,000 h (~3 years) to correspond to project duration, which has implications for the extrapolation of results to component lifetimes
- 1–2% creep strain in operation time due to the limitations of some strain sensors (WP 6.4), thus no large deformations can take place
- One thermal cycle each day (crack initiation at around 1000 cycles, within project duration).

The engineering design of the component test specimen is therefore influenced by creep deformation in the thinner walled section, resulting from high temperature loading under pressure, in addition to fatigue behaviour resulting from thermal cycling (simulation of start-up and shutdown scenarios).

To combine these aspects, an optimization strategy has been established which combines the numerical calculation of these material aspects until failure and the engineering aspects for machining and heating/cooling techniques (Figure 2). It is clear that the design leads to thinning the wall in a certain section to reduce the maximum pressure needed for significant creep deformation and to achieve sufficient bending stresses from the change in stiffness during cyclic operation. Initial calculations showed that a minimum wall thickness of 15 mm and radii of “R5” and “R5+120° bevel” are applicable for both purposes. The position of radius “R5” is the assumed region for crack initiation while the position “R5+120° bevel” is applicable to measure through wall thermal behaviour and the dynamic elastic strain. Although during shutdowns, NDE methods like replica examination and ultrasonic testing maybe applicable at the 120° bevel.

The following tasks arose from this geometry:

Figure 3 (b) shows the relaxation of the Mises stress and the creep curve for 100,000 h loading time at a temperature of 600°C and a pressure of 120 bar. The contour plot at 15,000 h time shows the equivalent strain distribution of the component with maximum values of 0.9% in the thin-walled area. The creep curve for this area gives a maximum value of ~1,2% equivalent creep strain for the expected operation time of 25,000 h.

These results led to the final geometry with 15 mm wall-thickness, as shown in Figure 2. In addition a pressure of 120 bar seems reasonable for an appropriate creep behaviour with respect to the design.

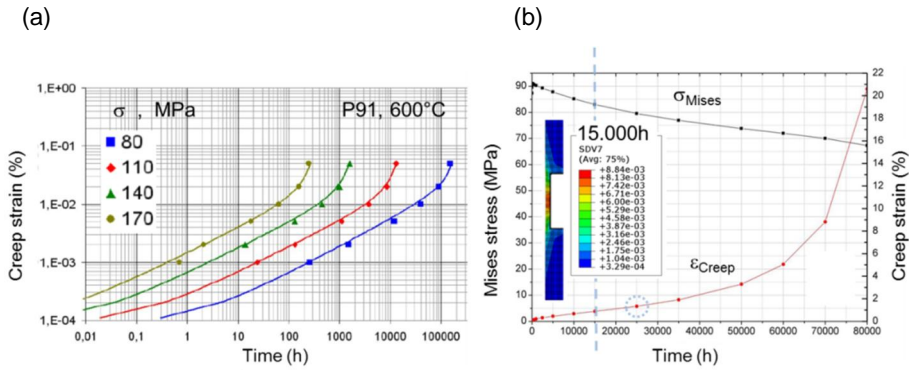


Figure 3. (a) Uniaxial creep tests on P91 at 600°C and (b) Creep modelling of the component at 600°C and 120 bar for 100,000h (results from MPA Stuttgart).

For the interaction of creep behaviour and thermo-mechanical fatigue, mechanistically based models have been proposed [4] [5] which allow prediction of the instantaneous damage levels in the material. Thermo-mechanical fatigue damage can be described by fracture-mechanics models combined with models for cyclic visco-plasticity. Project partner IWM Freiburg carried out intensive FE analysis using the following models:

$$\dot{\varepsilon}^{vp} = \dot{p} \operatorname{sgn}(\sigma - \alpha) \quad \text{where } \dot{p} = \left\langle \frac{|\sigma - \alpha| - \sigma_Y}{K} \right\rangle^n$$

$$\text{and lifetime } N_A = \frac{A}{D_{TMF}^B} \quad (2)$$

to calculate the crack initiation at the radii positions. In Eq. (2) $\dot{\varepsilon}^{vp}$ is the viscoplastic strain rate, α is the backstress K and n are temperature dependent model parameters, σ_Y is the yield strength, N_A is the number of cycles to failure, D_{TMF} is the damage parameter developed by Riedel for non-isothermal cycles and A, B are adjusted to the measurements. For the case of thermal cycling, it is

essential to define the thermo-physical boundaries leading to a dynamic temperature distribution to calculate crack initiation. Therefore, various cases with different (i) isolation techniques on the pipe's interior, (ii) cooling mediums, and (iii) cooling paths, have been modelled and evaluated. Figure 4 (a) illustrates load case "C" – heating the thick-walled component from the outside and cooling the thin-walled region and the FE model's results are given in Figure 4 (b) where the distribution of cycles to failure in the component are shown (see also Figure 5). The critical location is at the "R5" position.

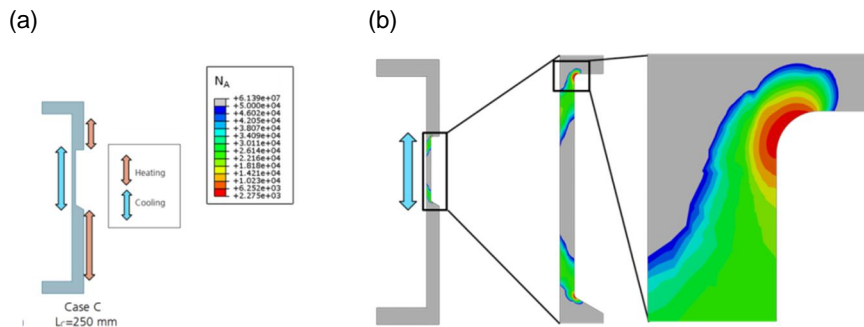


Figure 4. (a) Schematic illustration of thermal distribution in the pipe and (b) FE analysis of crack initiation due to thermal cycling in the R5 radius (results from IWM Freiburg).

For the case of cooling with water, a total number of cycles $N_A \sim 2,000$ can be expected. These results have been evaluated in cooling tests on the component, measuring the temperature distribution on the inside and outside during the cooling procedure. The different cooling techniques used in these preliminary investigations are shown in Figure 5. Further optimization of the cooling technique was performed to reduce the number of cycles until failure.

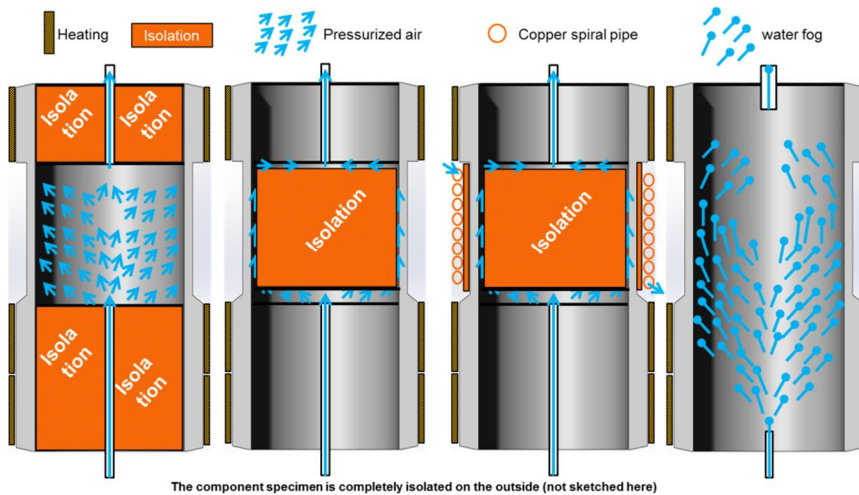


Figure 5. Different cooling techniques used in preliminary investigations (results from RWE/StandZeit).

3. Condition monitoring (WP 6.4)

The aim of WP 6.4 is to assess existing and new condition monitoring systems for use on future high temperature power plant components. To complement the instrumented components test, the monitoring techniques are also being implemented on laboratory test specimens. A sketch of the component is shown in Figure 6 which indicates the locations where the strain, temperature, pressure and crack measurement sensors are placed, according to the defined sections (I–VI) of the component.

As previously noted, creep strain will mainly occur in the thin-walled area. Hence, creep strain measurements are focussed in section (IV). Capacitive creep sensors and optical insets (by TUV), ARCMAC & Potential Drop Strain Sensors (by Imperial) are therefore located in section (IV). DCPD probes for crack detection are installed in the critical sections V = “R5” radius and III = “R5+120° bevel” (see Figure 6). In addition, a high temperature strain gauge is installed on the 120° bevel. Supervision of the component is planned using acoustic emissions sensors connected with wave guides to the component caps. The heated thick-walled sections I,II,VI comprise a large amount of controlled heating elements and therefore thermocouples to ensure temperature stability, especially in the creep section IV, the temperature distribution in which will also be verified using thermocouples.

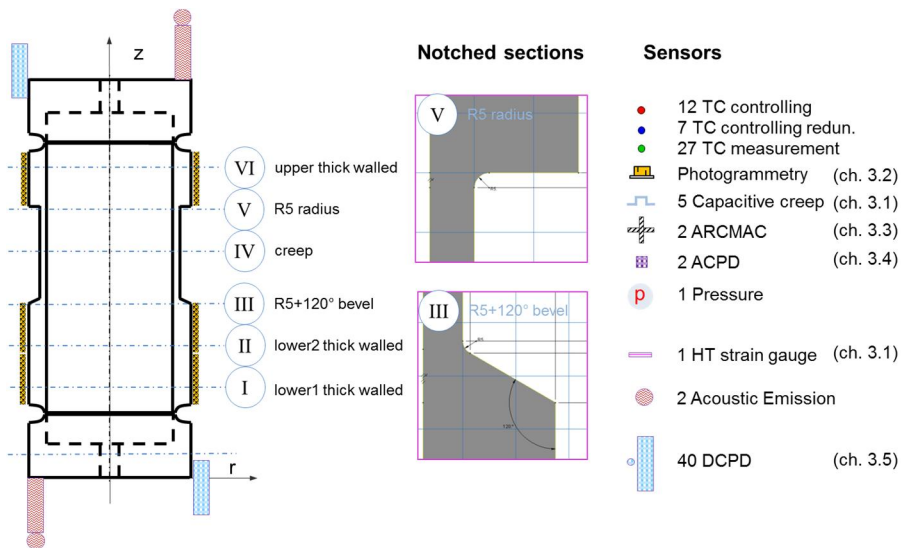


Figure 6. Section definition for condition monitoring techniques (sensors).

The total test duration will be approximately 25,000 hours and every year (at approx. 8,000 hours of testing time) a maintenance procedure will be performed with NDT examination (ultrasonic testing for crack determination and growth and replica examination for microstructure development). All strain and thermo-physical data (i.e. pressure and temperature) will be stored with a dynamic monitoring system provided by TUV. In addition TUV and Imperial have established an online data transmission system for examining the process remotely. The main condition monitoring techniques are next described.

3.1 High temperature strain gauge and capacitive strain sensors (TUV)

Two types of electrical strain gauges at high temperature are employed. One type is based on electrical resistance change through deformation and the other is based on electrical capacitance change through elongation. These are both suitable for high temperature strain measurements during low-cycle-fatigue (LCF). For short term investigations (e.g. for dynamic or quasi-static behaviour in start-up or shutdown) high temperature strain gauges achieve a high strain range ($\pm 6\%$) with excellent resolution ($1 \mu\epsilon$) however drift can be a problem. For long term investigations (e.g. with temperatures above 450°C for creep investigations on power plant components), electrical capacitive transducers that have a very high resolution and low drift are employed, however vibration effects can be a problem for the measurements [6]. Both types of devices are being employed by TUV on the component test. Figure 7 (a) shows a high temperature electrical resistance strain gauge installed in the longitudinal direction on the “R5+120° bevel” position and

Figure 7 (b) shows a capacitive strain gauge and the non-linear calibration curve on P91 steel material. A total number of 5 capacitive sensors, two in longitudinal direction (180° shift) and two in circumferential direction (180° shift), in addition to one dummy sensor for indication of sensor drift are employed on the pressurized P91 steel component.

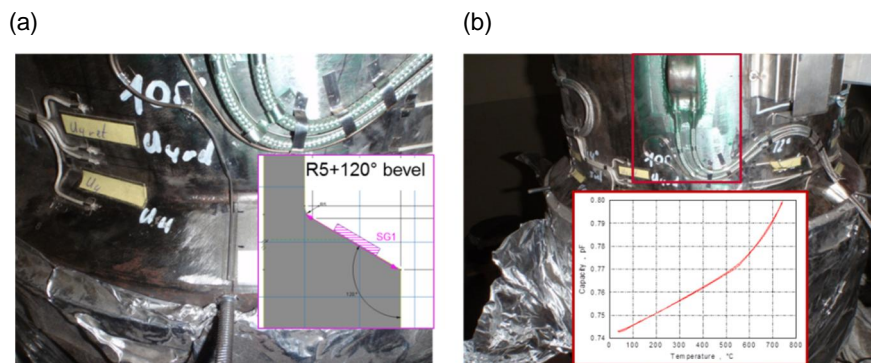


Figure 7. (a) High temperature electrical resistance sensor installed in longitudinal direction on the “R5+120° bevel” (b) Capacitive strain sensor with high temperature cables and thermal calibration curve for P91.

3.2 Photogrammetry (TUV)

Optical indentions like body ceramic inlays are inserted and peened into place on the outside of a high temperature steam pipe. These can be verified using capacitive strain gauges and can measure up to an accuracy of 5 μm in the laboratory and 30 μm on plant. Ceramic inlays are set ca. 5 mm deep into steam pipes or spot-welded on to the surface according to specification and expected total strain. If need be, smaller ceramic inlays can be used e.g. for the P91 steel component test. The ceramic inlay sensors are employed in sets to give diametric and axial strain, using photogrammetric techniques. It is also planned to use optical indentions in laboratory trials. Figure 8 shows the application of the ceramic inlays in a first TUV/RWE validation test, performed as a slow high temperature tensile test on P91 at 650°C with more than 1% plastic strain. A capacitive sensor was attached to the opposite face of the flat specimen for comparison with the optical strain results.

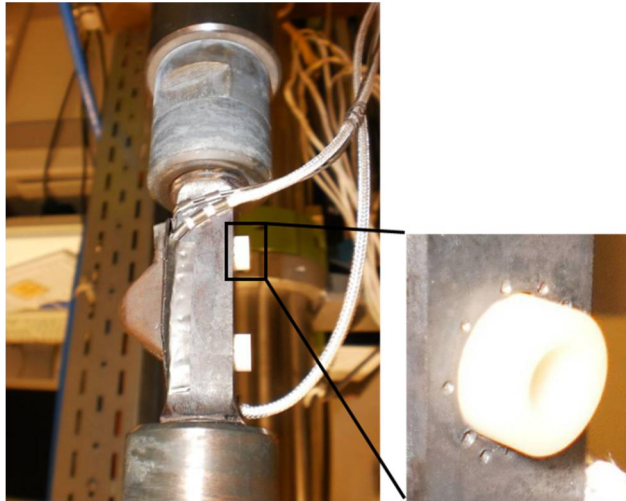


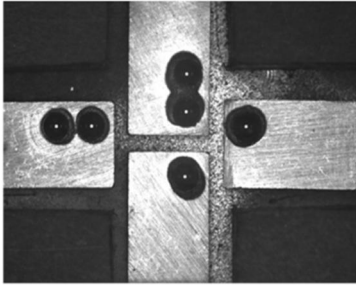
Figure 8. Laboratory validation test of ceramic inlays on a flat specimen with a capacitive sensor attached.

3.3 ARMAC (Imperial)

Alongside high temperature electrical resistance/capacitive strain gauges and the new ceramic inlays, Imperial will employ the Auto-Reference Creep Management and Control (ARCMAC) optical strain measurement technique (visits will be made once a year by Imperial staff to take measurements at shut down). The ARCMAC system uses optics to make a point-to-point measurement of strain.

Each gauge has two Inconel plates studs welded onto the component material. One plate has two Silicon Nitride (SiNi) spheres brazed onto its upper surface, presenting a reference measurement, whilst the other has a single SiNi sphere. The camera system is made up of a CCD camera and collimated light source. The camera unit is placed over the biaxial ARCMAC gauge and the light source illuminates the spheres which appear as three white spots in each orthogonal direction as shown in Figure 9 (a) for a biaxial gauge. As the component accumulates strain, the pair of gauge plates separate and analysis software tracks the movement of the spots of light to give biaxial strain data.

(a)



(b)

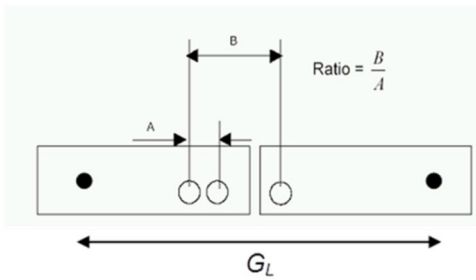


Figure 9. (a) Image captured by ARCMAC camera system showing biaxial ARCMAC gauge on a steam pipe, (b) Key features evaluated during ARCMAC image analysis.

The strain accumulated from time 'n' to 'n + 1' is simply obtained by taking appropriate measurements from the gauge pair (see Figure 9b) and employing the following equation

$$\varepsilon = \left(\frac{B_{t=n}}{A} - \frac{B_{t=n+1}}{A} \right) \bigg/ \frac{G_L}{A} \quad (3)$$

where B is the separation of the two gauge halves over the operating period between selected images, A is the gauge reference distance, G_L is the gauge length, which is controlled by the installation tool, to provide the strain, ε , accumulated over the operating period. The system can be calibrated using a highly sensitive extensometer calibration rig, with additional static calibration blocks used for pre-measurement checks on site. Further details of the ARCMAC gauge are given in [7–9]. The ARCMAC gauge has been installed on the MACPLUS P91 component test, as shown in Figure 10.

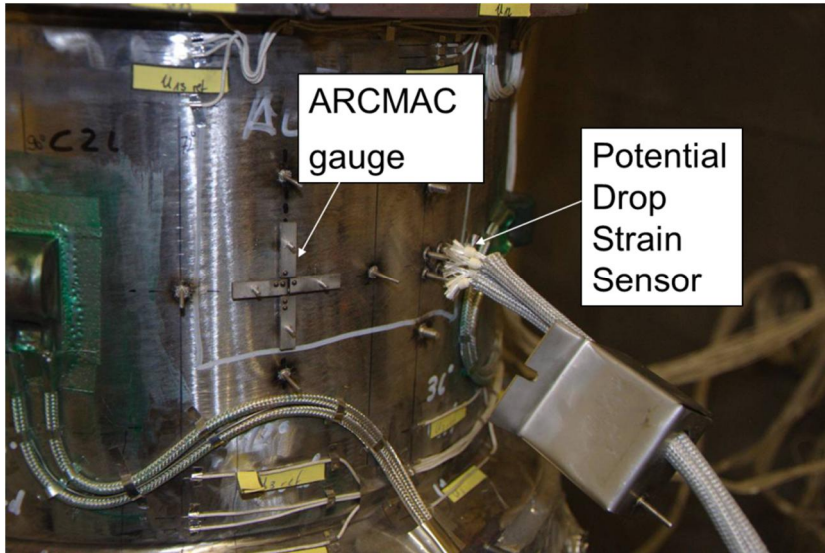


Figure 10. ARCMAC gauge installed next to a potential drop strain sensor on the P91 component test.

3.4 Potential drop strain sensor – ACPD system (Imperial)

The potential drop strain monitoring technique has been developed by Peter B. Nagy at the University of Cincinnati. This functions by using changes in electrode separation to monitor strain through the measured electrical resistance. It is based on a square array, directional electrode configuration, as illustrated in Figure 11. Each electrode consists of a stud welded to the test specimen's surface with appropriate wires leading to the processing electronics. Two orthogonal resistance measurements are obtained, firstly (Figure 11a) by injecting a known current I_1 into electrodes A_1 and A_2 , and measuring the in-phase potential drop across electrodes C_1 and C_2 to find the resistance R_1 . Similarly, as shown in Figure 11 (b), the resistance R_2 is obtained by injecting the current I_2 into electrodes A_1 and C_1 , and measuring the in-phase potential drop across electrodes A_2 and C_2 . The phase detection possible by this AC system provides lower noise levels compared to that of a DC system allowing for the use of smaller currents; 10mA in this case. A low inspection frequency (2 Hz) and small electrode separation, a , is employed thus minimising any influence of permeability and the 'skin' effect. The influence of creep deformation on the specimen can be monitored by examining the variation in the resistance ratio R_1/R_2 . The isotropic temperature dependence is suppressed by use of the resistance ratio. The resistance ratio can be calibrated, based on models [10], to provide strain measurements. An example of the results are shown in Figure 11(c), where the Potential Drop strain sensor has been used

together with an LVDT to measure creep strains on a rectangular cross section specimen of P22 steel (details can be found in [11]).

Excellent agreement between the LVDT and Potential Drop strain measurement were found up to the point of strain localisation where necking begins to occur. The LVDT measurements are external to the furnace and provide an average strain measurement over the length of the sample. However the potential drop technique is within the gauge region and measures the strain local to the necking area. Therefore, beyond the point of strain localisation the potential drop technique measures higher strains than the LVDT.

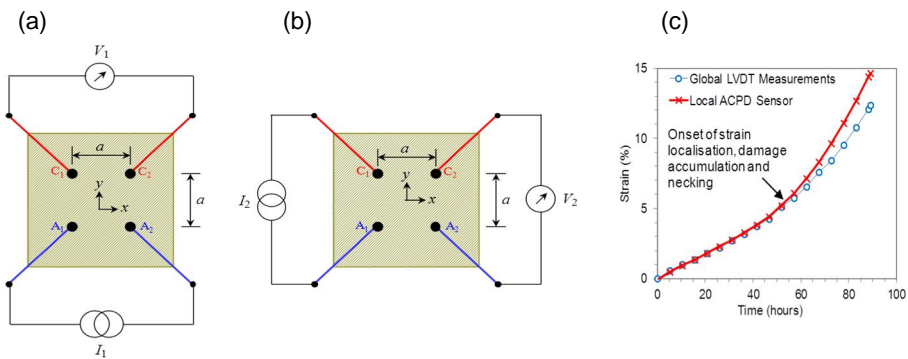


Figure 11. Schematic illustration of a potential drop strain sensor in (a) horizontal and (b) vertical measurement configuration, (c) example results of creep strain measurements from the potential drop strain sensing technique on a uniaxial specimen.

3.5 Potential Drop Crack Detection – DCPD system (TUV)

The DC Potential Drop (DCPD) method is a non-destructive technique for crack length measurements in fracture mechanics laboratory specimens and is suitable for detection of crack propagation in a volume of material (even at the inside of a pressurized component). The DCPD has been developed by TUV (utility patent specification) and qualified for nuclear applications (up to 320°C). Five long term online-applications of critical components in four nuclear power plants have been carried out in the following [12]. In recent years, two applications in coal-fired power plants at temperatures up to 530°C with nearly two year duration [13] have been performed successfully. In WP 6.4 the enhancement of DCPD applications up to 600°C has to be proven. Due to the calculation of crack initiation at the radii sections, as previously described, the DCPD technique is employed in WP 6.10 on the P91 pipe component test in section III and V (according Figure 6), as shown in Figure 12. A constant direct current of around 100–300 amperes is passed through the area to be monitored by means of two or more metal skids. The skids are attached or welded to the surface of the component. A potential field develops

as soon as the current runs through an area and is known to be disturbed once a crack is forming or an existing crack is beginning to grow in the area destined for measurement. Figure 12a) shows the DCPD probes in section III = “R5+120° bevel”. Some parameter studies (“sensitivity analysis”) on the real component geometry using 3D-multi physics simulations showed which sets of parameters (e.g. current, number and position of current sources and potential drop probes) are applicable to ensure that crack initiation will be indicated. A contour plot for a specific electrical measurement setup (Figure 12b) gives the potential field for section V = “R5” radius. A comparison of the technical complexity and the required resolution of potential difference at the probes position resulted in a total number of ten probes at each section, with an angle of 36° between the probes in Figure 12 a). To compensate for electrical noise and temperature effects each probe has a reference probe adjacent to it in the thin-walled region.

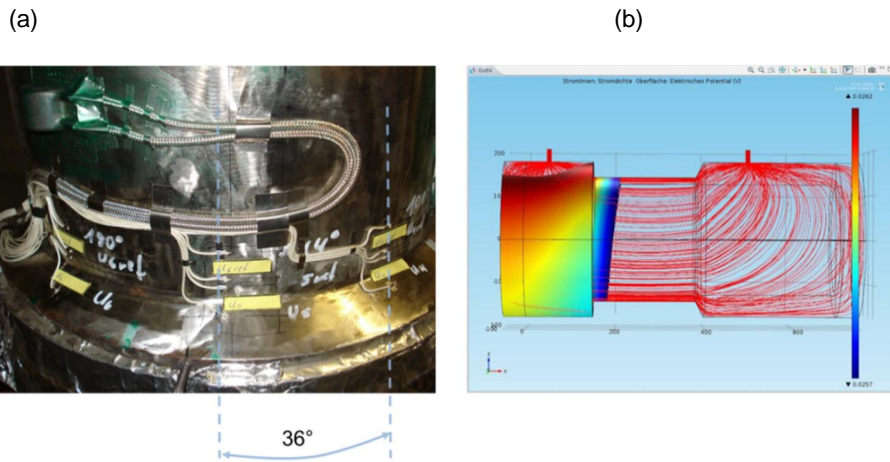


Figure 12. (a) DCPD method – Installation of potential probes on section “R5+120° bevel” on P91 component test, (b) Potential field for section V = “R5” radius using 3D-multi physics simulations on the real component geometry.

4. Conclusions

As part of the collaborative European R&D-project (MACPLUS), a feature test pipe component of P91 steel is being performed. The design considerations have been presented together with an overview of the finite element analyses performed to determine the component geometry required for crack initiation to occur in the projects lifetime. The finite element analyses simulated the thermal and pressure loading cycles that will be experience by the component during operation and calculated the extend of creep strain and combined creep-fatigue damage experiments during the test duration. A novel combination of creep strain transducers, crack growth monitoring techniques and thermocouple probes have been de-

ployed on this component providing experimental validation of the material state during the test duration. These sensors, which will be compared to each other and used to verify and refine the FE model's predictions, have been described. The components critical locations have also been identified and crack growth sensors have therefore been focussed in this region. It has been determined that the test component is to be tested at 600°C/120 bar for creep exposure and additional forced cooling will be employed for thermal cycling to induce fatigue damage.

Acknowledgement

- European Commission for funding the MACPLUS project in FP7 programme
- Imperial College London: Prof Kamran Nikbin
- E.ON UK: Prof Andy Morris
- MPA Stuttgart: Dr Andreas Klenk
- IWM Freiburg: Dr Maria Luiza Ripoll, Heiner Oesterlin, Gerhard Maier
- RWE Technology: Dr Ralf Mohrmann
- StandZeit: Dr Gereon Lüdenbach

References

1. Blum, R. Development of a PF Fired High Efficiency Power Plant (AD700): an important issue for future power.
2. Ringel, M., Klenk, A. & Maile, K. Angepasste Werkstoffmodelle für die Bauteilberechnung bei Kriech und Kriechermüdungsbeanspruchung, 27. Vortragsveranstaltung des VDEh, Düsseldorf, 2004.
3. Klenk, A., Maile, K. & Schmidt, K. Component Lifetime Evaluation based on Longterm Behaviour of Martensitic Steels and Weldments, New High Temperature Materials Seminar, ETD, IOM, London, June 22, 2011.
4. Seifert, T., Riedel, H., Pramhas, G. & Bumberger G. Novel lifetime models for high temperature components, AutoTechnology 7, 2007, pp. 34–38.
5. von Hartrott, P., Holmström, S., Caminada, S. & Pillot, S. Life-time prediction for advanced low alloy steel P23, Materials Science and Engineering: A., 2008.
6. Kranz, A. Condition monitoring and lifetime extension of power plant components using electrical measurement systems, PowerGen2007, June, 2007, Madrid, Spain.

7. Morris, A., Dear, J. P., Kourmpetis, M., Maharaj, C., Puri, A. & Fergusson, A. D. Monitoring Creep Strain in Power Station Engineering Plant Applied Mechanics and Materials, 2007, 7–8. 10.4028/www.scientific.net/AMM.7–8.31.
8. Morris, A., Maharaj, C., Kourmpetis, M., Dear, I., Puri, A. & Dear, J. Optical Strain Measurement Techniques to Assist in Life Monitoring of Power Plant Components, Journal of Pressure Vessel Technology, 2009, 131(2), pp. 024502.
9. Narayanan, A., Morris, A., Davies, C. M. & Dear, J. P. Optical Strain Monitoring Techniques, in ASME 2012 Pressure Vessels & Piping Division Conference, July 15–19, 2012, Toronto, Canada, ASME, PVP2012-78515.
10. Madhi, E. & Nagy, P. B. Sensitivity analysis of a directional potential drop sensor for creep monitoring, NDT & E International, 2011, 44(8), pp. 708–717. <http://dx.doi.org/10.1016/j.ndteint.2011.08.001>.
11. Davies, C. M., Nagy, P. B., Narayanan, A. & Cawley, P. Continuous Creep Damage Monitoring using a Novel Potential Drop Technique, in ASME 2011 Pressure Vessels & Piping Division / K-PVP Conference, July 17–21, 2011, Baltimore, Maryland, USA, ASME, PVP2011-57325.
12. Hofstötter, P. Application of the potential drop method for inservice monitoring of indications for crack initiation or crack propagation – Fundamental principles and practical application, 16th International Conference on Structural Mechanics in Reactor Technologie (SMiRT 16), Washington, DC, USA .
13. Hofstötter, P., Keller, H.P., Hoppe, Th., Protogerakis, E. & Werden, B. Application of the Potential Drop Method for Monitoring an Outside Crack in the Housing of a Quick-acting Valve-Safe Con-tinuation of Operation for Two Years until Removal of the Housing, VGB PowerTech 06/2003 pp. 82–87.

Self-heating and autoignition of coal in rock silos

Juha Sipilä¹, Pertti Auerkari², Stefan Holmström², Jyrki Itkonen¹,
Ulrich Krause³, Iris Vela⁴ & Michael Löscher⁵

¹Helsingin Energia, Helsinki, Finland

²VTT Technical Research Centre of Finland, Espoo, Finland

³Otto-von-Guericke-University, Magdeburg, Germany

⁴BAM, Berlin, Germany

⁵EU-VRi, Stuttgart, Germany

Abstract

Storing solid fuels like coal in large quantity is known to involve a risk of spontaneous combustion. In comparison to conventional open stockpiles, closed storage may in principle decrease this risk by more limited ingress of air, but the risk can also be enhanced for example by reduced access for preventive or mitigating action. The risk of self-heating until ignition is considered here for a unique underground rock storage of a coal-fired power plant. The main adverse consequence of non-functioning storage is interrupted district heating that is more difficult to replace in winter than lost electricity supply. To predict the risk of spontaneous combustion with reasonable confidence, material modelling of coal properties has been applied with verification by comparison to actual field evidence. Fire risk management is discussed in terms of the available early warning indicators and options for cooling, extinguishing and prioritised use of stored fuel.

1. Introduction

With all its poor image and incentives to reduce its use, coal is cheap, plentiful and applied to cover about 40% of electricity production in the world. Since the early days of industrial use, coal is known to be susceptible to exothermic oxidation even at low temperature, so that it can self-heat up to the point of ignition under combined access to sufficient oxygen (air) and insufficient dissipation of the produced heat. Preventive or mitigating procedures are widely applied, but the practices have been mainly developed for open stockpiles and limited scale closed containment in rail and ship transport. More recently, large-scale closed storage facilities have been introduced, with reduced access to intervene at evolving local hot spots, and therefore potentially enhanced risk of spontaneous combustion. Closed storage may also differ from open stockpiles in terms of oxygen limited or

heat transfer limited safety against self-heating. This safety is oxygen limited when oxygen transport is constrained by the containment or effectively lost e.g. in a surface layer of fine reactive coal to retard further reaction deeper in the bed, if the associated heat is sufficiently dissipated. In the heat transfer limited case, storage is typically safer with coarser, less reactive coals [1–8].

The underground coal storage (Figure 1) at the Salmisaari combined heat and power (CHP) plant in Helsinki represents relatively new technology that since 2004 replaces an earlier above-ground open stockpile. The storage consists of four Ø40 m rock silos with a bottom depth of -120 m, each with a capacity of 50 000 t of bituminous hard coal. The most adverse consequence of interrupted fuel flow from the storage is disruption of district heating that is more challenging to replace in winter than lost electricity supply. Although in principle the climate with a mean temperature of 9°C in the surrounding rock could provide an advantage of low initial temperature, self-heating and smouldering fires have been reported [9–11].

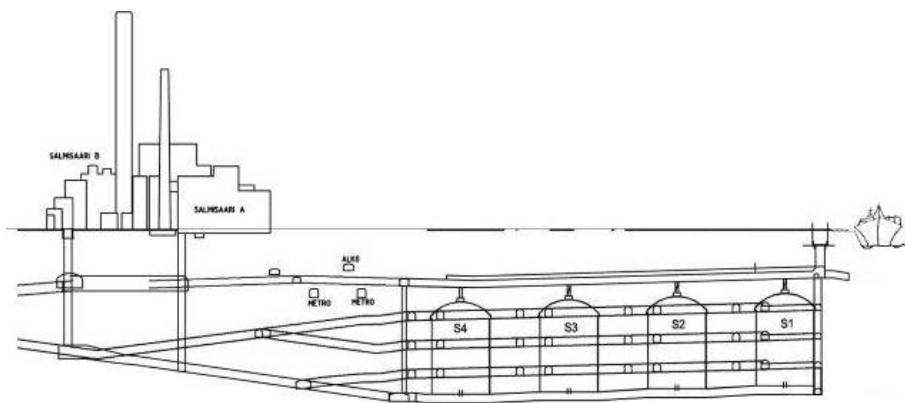


Figure 1. The underground coal storage of Salmisaari (schematic), with the filling and discharge system.

Coal enters to the top of the silos and is also taken out from the top to be dropped to the discharge hoppers (first in last out), so that the oldest stored material remains at the silo bottom. In addition to entering with coal, oxidizing air is in contact with coal on top of the silo and to more limited extent from below through the hoppers. To partially compensate for the hazard of self-heating that tends to increase with storage time, the volume of oldest coal is minimized by keeping the silos nearly empty during the summertime minimum need for district heating. To avoid early self-heating incidents, coal that is warmer than 40°C is rejected from entering the silos. For alarm the system makes use of gas (CO) detectors, thermal cameras, and odour sensing. For extinction, nitrogen filling is available but water hosing is mostly sufficient. To predict the risk of self-heating of coal with reasonable confidence, simple models are thought to be applicable but require verification. In this work the emphasis is in the early stages of self-heating up to about 70°C, thought

to be critical for self-heating and in the same time less complex than the full series of the reaction activity by the numerous flammable components of coal up to the point of ignition. As the initial temperature of coal arriving in winter can be very low and the oxidation rate is a strong function of temperature, there is potential of added induction time from the initial state to the early stages of self-heating, but a heated or otherwise particularly reactive coal batch may wipe out this potential and shorten the induction time. The risk of excessive self-heating of coal in the underground storage is considered below through combined incident modelling and comparison to the available field evidence. Risk management is discussed in terms of a suggested risk matrix and early warning indicators.

2. Materials and methods

Self-heating in a cylindrical silo was numerically modelled using the heat balance of unsteady temperature T at time t , expressed in the one-dimensional form as [12]

$$\frac{\partial T}{\partial t} = \frac{\lambda}{\rho \cdot c_p} \nabla^2 T + \frac{k_0 H_0}{c_p} \cdot \exp\left[-\frac{E}{RT}\right] \quad (1)$$

where k_0 is the pre-exponential or frequency factor (here $3 \cdot 10^5 \text{ s}^{-1}$), ρ is the effective density (here 750 kg/m^3), H_0 is the heating value (heat of reaction), λ the effective thermal conductivity (0.075 W/(mK) for coal), c_p the specific heat capacity (1000 J/(kgK)) and E/R (here 12000 K) is the apparent activation energy normalized by the gas constant. Note that the values of the activation energy and especially the pre-exponential factor may vary widely but much less in combination, as they are not independent. The ambient temperature is taken to be initially $9\text{--}12^\circ\text{C}$ at the silo wall and 40°C in the dome above the coal bed [13–15]. The oxidation process consists in principle of successive contributing reactants at increasing ranges of temperature, with corresponding activation energies and pre-exponential factors in Eq. (1). However, these are strongly constrained by the main interest in the early stages of self-heating up to about 70°C [13]. The numerical modelling of the temperature field evolution was done with methods described in more detail in [16,17], using the FEM code COMSOL Multiphysics v.4.3 in 9000 mesh elements, for simplicity disregarding fuel and oxygen consumption. The properties are those measured from 624 coal batches or shiploads, in total 7.5 million tons, delivered to the utility 2001–2010 from two sources of origin (Poland and Russia) with similar mean ($\pm\text{SD}$) heating value of $28.3(\pm 0.7) \text{ MJ/kg}$. For further comparison, to describe the propensity of all 624 coal batches of the utility to self-heat (low temperature reactivity r), the modified Smith-Glasser index [13–15] was applied:

$$\text{SGI}(m) = \log(r) = 0.89 \cdot m^{0.14} \cdot v^{0.43} \quad (2)$$

where m is moisture content (inherent moisture for original SGI, total moisture for modified SGI here) and v is volatile content. The mean ($\pm\text{SD}$) total moisture content was $8.7 \pm 1.1\%$ for Polish and $10.6 \pm 1.7\%$ for Russian coal, and the mean

volatile content was $30.2 \pm 1.1\%$ for Polish and $35.4 \pm 2.7\%$ for Russian coal. This would suggest that the Russian coal is more reactive, as was also expected [7].

To compare the predicted self-heating behaviour to the actual observations, the history of the coal deliveries to the storage silos was reviewed together with the recorded incidence history for self-heating and spontaneous combustion since the beginning of operation in 2004. In the comparisons the issues of particular interest were the predicted and observed incubation times, the differences in coals in terms of propensity to self-heating, and the characteristics of the observed fire incidences in the underground storage. For the risk associated with spontaneous combustion, a tentative risk matrix was constructed with guidance by the utility personnel.

3. Results

Figure 2 shows the predicted temperature evolution in central core of the silo. The predicted internal peak temperature has risen to about 52°C after one year, shooting rapidly up to likely ignition before one and half years of storage.

The predictions can be compared with the observed incidents of self-heating and spontaneous ignition. The history of the coal deliveries and storage in the silos is quite variable, but the recorded incidence history for self-heating and spontaneous combustion is believed to be particularly clear at the time of starting the storage operation in 2004–2005. In agreement with the prediction, no recorded incident of spontaneous ignition did occur before more than a year had passed from starting the storage operation in 2004.

The first self-heating incident was recorded 13th October 2005 in the bottom part of the silo number 3. This silo contained Russian coal that entered the silo between mid-September and early October 2004, so that the overall time in storage for the particular coal batch was one year and 2–4 weeks. The batches of Polish coal delivered in 2004 and introduced to different silos were also characterized for comparison, however showed no spontaneous combustion in 2005. Thereafter the silos have not been necessarily fully emptied before introducing new coal, and due to variable intermittent filling and discharge it is less certain that the operational records can be reliably used to confirm the time from initial filling to ignition. When the information on origin was clear, like for example in the case of the most extensive reported fire in 2008, the initiation was from batches of Russian coal.

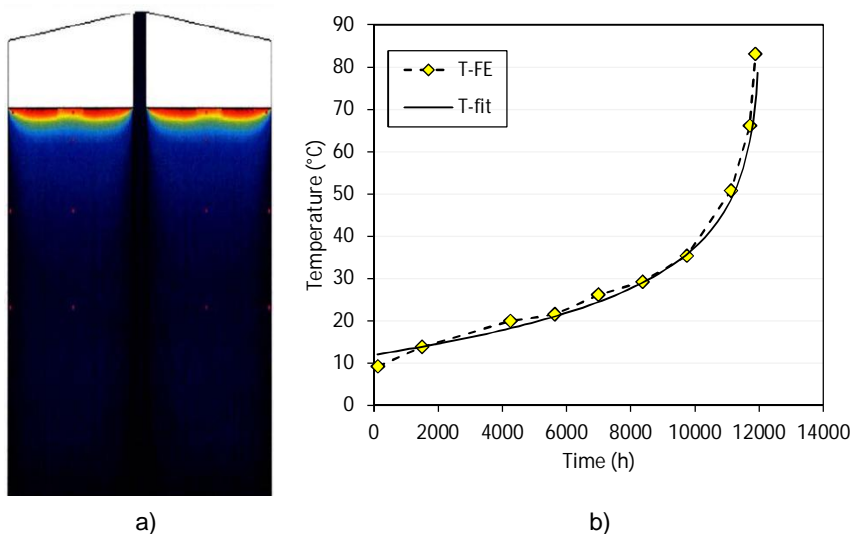


Figure 2. Predicted silo temperature in a) reactive hard coal after 277 days [17]; b) peak temperature.

Although originally intended for dust accumulations, the propensity of the coal batches to self-heat and spontaneously ignite can be experimentally assessed by applying the methods of the standard EN 15188:2007 to provide Arrhenius-type reaction rate data [18], and to support the kind of FE predictions shown above. However, to assess the propensity of coal to self-heat using quantities routinely measured for coal deliveries at the receiving end, the modified Smith-Glasser reaction rate index or SGI(m) [14] appears attractive and clearly differentiates between the mean expected self-heating propensities of Polish and Russian coals (Figure 3a). In particular, the early batches of Russian coal delivered in 2004 and showing self-heating in 2005 after a storage time of slightly more than a year, represented nearly the same (modified) SGI as the average Russian coal batches (Figure 3b), and clearly higher values of SGI than the average or actual Polish batches in the same time frame. As SGI(m) is only a measure of the propensity of the coal batch to self-heat under comparable initial conditions of the process, it does not explain all of the important features and conditions for self-heating and spontaneous combustion in storage [7, 12, 19–23]. In particular, as noted above, additional impact is expected from the time in storage, filling and discharging scheduling and variation in the initial temperatures, even when other factors such as storage and coal bed geometry, oxygen ingress rates and storage management practices remain similar. Low temperature of the entering coal could lengthen the induction time of self-heating, if not compensated by e.g. new warmer batches entering later to the same silo, released moisture absorption heat (especially to dry coal), or freezing trouble from very cold coal [15].

Therefore, although the field observations and the coal data from the storage facility appear to confirm the value of SGI(m) as an indicator of the batch-specific propensity to self-heat, it will need to be complemented by other indicators such as time in storage, particularly if this is not limited to one year or less, and possibly by other features in the history of preventive or mitigating measures. Also shorter term leading indicators will matter. The experience from the facility suggests that rather than using nitrogen inertising to put down smoldering fires, using abundant water to cool and extinguish hot spots is both cheaper and more effective, particularly if it can be started as early as possible. For early action, early detection is necessary, and it appears that often the best sensor is the odour sensor of human nose, although for safety, this needs of course to be complemented with other gas (CO) and thermal sensors.

Efficient fire prevention by denying oxygen ingress requires good air tightness in the storage, as any air leaks will promote self-heating. A case example of a persistent smoldering fire in the storage silo in 2008 resulted in considerable damage of hoppers and silo wall, largely because of an air leak through the seals of a silo bottom maintenance door [9,10]. A proposed tentative risk matrix related to the underground storage fire incidents is outlined in Figure 4.

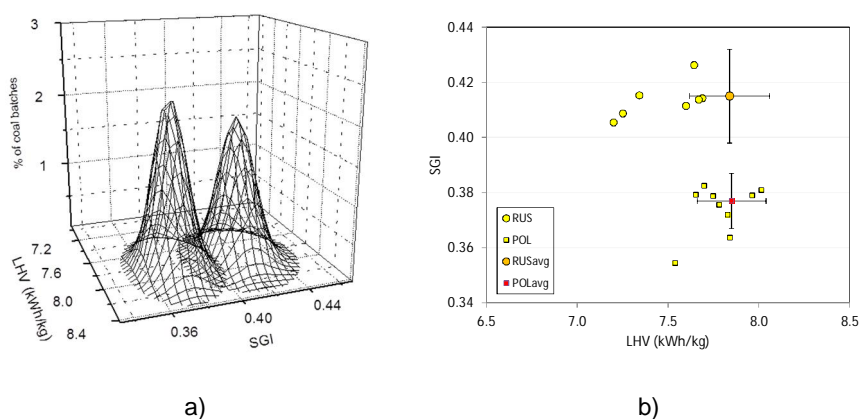


Figure 3. a) SGI(m) as fitted normalized distributions for Polish (left) and Russian (right) coal [21]; b) SGI(m) for the 2004 coal batches of interest with mean values of Russian and Polish coal deliveries as a function of the heating value (LHV).

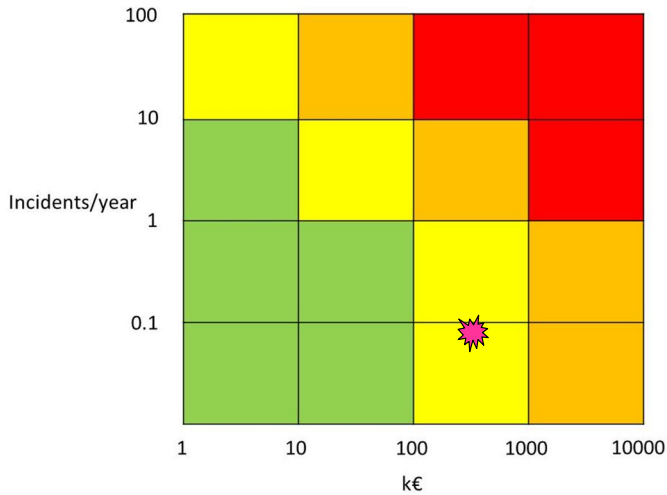


Figure 4. Suggested risk matrix for incidents of spontaneous combustion in the storage; red = immediate action required; orange = action required within defined time; yellow = tolerable; green = minor to negligible risk; marker refers to the 2008 incident.

So far the available evidence suggests that by proper attention to coal rank (properties), handling, timing of silo filling and discharge, adequate response to observed hot spots, and properly maintained capabilities of equipment and personnel, the risk of smouldering and open silo fires is contained at a satisfactory or bearable level and is significantly reduced in comparison to the time of early operation of the storage facility. A part of the success is related to the properly observed leading indicators (see below); however there remains some scope for further improvement.

4. Discussion and conclusions

Although the issue of self-heating and spontaneous combustion of stored coal has been recognized for more than a century [1], there is little published experience on underground coal storage. While this means scarcity of data to compare with the predictions, some features are comparable to more conventional above ground closed storage silos [2,8,20]. Nevertheless, fires in a new type of a closed storage are considered to have introduced new (emerging) risk.

With bituminous coal in the Salmisaari rock silos, the predicted time to significant self-heating was one to one and half years. For verification, the results were compared with the observed incidents of self-heating and spontaneous ignition. In agreement with the prediction, no recorded incident of spontaneous ignition did occur before a year had passed from starting the storage operation in 2004. When ignition was finally observed after slightly more than one year in storage, it was initiated in Russian coal with relatively high SGI(m), i.e. expected propensity to self-heat. In further agreement of the approach, no ignition incident was recorded by

end of 2005 in Polish coal batches with lower SGI(m) or propensity to self-heat. In other known cases the self-heating incidents generally also involved Russian coal.

A set of leading (warning) indicators with suggested quantitative limit criteria are shown in Table 1. Note that the lead time of the indicators varies from actual alarm to about one year. As in the ideal case the silos are emptied before the next heating season, not much more than one year lead time is necessary.

Table 1. Suggested leading or (early) warning indicators of the risk of spontaneous coal combustion in large underground rock storage.

Leading indicator (alarm)	Notes
Storage time > one year	Critical time also depends on coal rank and initial temperature
Odour detection	Practically any indicated level by human detection
Gas level: CO > 10 ppm	High sensitivity needed for early detection
Coal temperature > 40°C	Also for conveyor entry
SGI(m) > 0.42	Provisional for bituminous coal at time of delivery / batch analysis

Compared to coal, renewable solid fuels like wood generally include more volatiles and moisture, depending on the form of preprocessing, with potential to increase the risk of self-heating. This could be further exacerbated by high volumes needed to compensate for the low heating value.

In conclusion, storing large volumes of combustible solids like coal underground has the advantage of keeping the material out of sight but also involves challenges. The Salmisaari coal storage represents new technology with some risk of disrupted wintertime supply of district heating that is less straightforward to replace than lost electricity supply. The hazard of spontaneous combustion appears however tolerably predictable by observing selected leading indicators, and manageable by proper scheduling of filling and discharge, controlling of the coal batches, and when necessary, cooling and eliminating hot spots. It is also important to maintain the necessary preventive and mitigating capabilities of personnel, equipment and procedures against smouldering silo fires. For this purpose, a safe operational season for about one year appears to be validated by comparison of modelling and field experience, provided that the above basic assumptions are fulfilled. In case of unexpected self-heating and ignition due to already heated or unusually reactive coal entering the silos, mitigating routines are in place to reduce the risk of an extensive fire.

Acknowledgements

Technical support by the partnership of the European project iNTeg-Risk, and financing by the 7th Framework Programme (FP7/2007-2013, under grant agreement no. 213345) of the European Union, Helsingin Energia and VTT are gratefully acknowledged.

References

1. H.C. Porter & F.K. Ovitiz. Deterioration and spontaneous heating of coal in storage. *Journal of Industrial and Engineering Chemistry* 4 (1912) 5–8.
2. M. Tuomisaari, D. Baroudi & R. Latva. Extinguishing smouldering fires in silos. Brandforsk project 745–961, VTT Publications 339, Espoo 1998.
3. J. Garcia-Torrent, A. Ramirez-Gomez, E. Querol-Aragon et al. Determination of the risk of self-ignition of coals and biomass materials. *Journal of Hazardous Materials* 213–214 (2012) 230–235.
4. A.M. Carpenter, D. Porter, D.H. Scott et al. Transport, storage and handling of coal. IEA Clean Coal Centre 2003. 139 p.
5. H. Nalbandian. Propensity of coal to self-heat. IEA Clean Coal Centre, Report CCC/172, 2010. 47 p.
6. IMO: International Maritime Solid Bulk Cargoes Code, IMO 2009, London, 337 p + Suppl.
7. H. H. Nijhof. Oxygen access and coal storage. ESI Eurosilos B.V. Report 21.11.2006, The Netherlands. 16 p.
8. C. Rosner & H. Röpell. Experiences with fires in silos for coal storage in the Tiefstack CHP plant (in German). *VGB Powertech* 91 (2011) 84–87.
9. J. Sipilä & P. Auerkari. Fire incidents in underground coal storage. International Conference on Maintenance of Power Plants (Baltica VIII), Helsinki-Stockholm, May 2010.
10. J. Sipilä, P. Auerkari, P. Lerena et al. iNTeg-Risk D1.3.2.1: Package of: Reference solutions for risks related to extreme storage of hazardous materials, EU project iNTeg-Risk, Project Nr. CP-IP 213345-2, Contact: EU-VRI, Stuttgart, Germany.
11. J. Sipilä, P. Auerkari, A-M. Heikkilä et al. Risk and mitigation of self-heating and spontaneous combustion in underground coal storage. *Journal of Loss Prevention in the Process Industries* 25 (2012) 617–622.
12. P. C. Bowes. *Self-heating: evaluating and controlling the hazards*. Elsevier, London, UK. 506 p.

13. M. A. Smith & D. Glasser. Spontaneous combustion of carbonaceous stockpiles. Part II. Factors affecting the rate of the low-temperature oxidation reaction. *Fuel* 84 (2005) 1161–1170.
14. J. Sipilä, P. Auerkari, S. Holmström et al. Observations on the Smith-Glasser index for self-heating of bituminous coal. *Journal of Fire Sciences* 30 (2012) 331–338.
15. P. Auerkari, J. Sipilä, U. Krause et al. iNTeg-Risk T3.6.2, 2012. Self-heating and freezing in large underground storage – validation of simple models to support managing the risk. EU-project iNTeg-Risk, Project Nr. CP-IP 213345-2, Contact: EU-VRi, Stuttgart, Germany.
16. U. Krause, M. Schmidt & F. Ferrero. Investigation of the development of conflagration of solid material via analysis of coupled heat, mass and momentum transport. *Chemical Engineering & Technology* 32 (2009) 292–305.
17. U. Krause, M. Schmidt & C. Lohrer. A numerical model to simulate smouldering fires in bulk materials and dust deposits. *Journal of Loss Prevention in Process Industries* 19 (2006) 218–226.
18. EN 15188:2007. Determination of the spontaneous ignition behaviour of dust accumulations. CEN, Brussels, 21 p.
19. B. B. Beamish, M. A. Barakat & J. D. St George. Spontaneous-combustion propensity of New Zealand coals under adiabatic conditions. *Int J Coal Geology* 45 (2001) 217–224.
20. V. Fierro, J. L. Miranda, C. Romero et al. Model predictions and experimental results on self-heating prevention of stockpiled coal. *Fuel* 80 (2001) 125–134.
21. A.C. Smith & C.P. Lazzara. Spontaneous combustion studies of U.S. coals. RI 9079, Washington DC, U.S. Bureau of Mines, 1987.
22. H. Zhu, Z. Song, B. Tan et al. Numerical investigation and theoretical prediction of self-ignition characteristics of coarse coal stockpiles. *Journal of Loss Prevention in the Process Industries* 26 (2013) 236–244.
23. U. Krause. *Fires in silos: hazards, prevention, and fire fighting*. Wiley-VCH, Weinheim, Germany, 2009.

Creep properties of Zircaloy-4 for nuclear fuel cladding FEA simulation

Stefan Holmström, Tom Andersson, Ville Tulkki & Anssi Laukkanen

VTT Technical Research Centre of Finland
Kemistintie 3, Espoo, P.O. Box 1000, FI-02044 VTT, Finland

Abstract

Zirconium alloys are commonly used as cladding tube material for nuclear water reactors. To improve the understanding of the creep damage accumulation in thin walled fuel cladding tubes made of Zircaloy-4, data collation (tensile, creep strain and rupture) and material modelling has been performed for use in finite element analysis (FEA). In literature there are two distinct areas of creep modelling: creep strain response to short power transients and long term creep strain evolution for storage purposes. In this paper the short term creep strain response is mainly targeted for FEA simulation of fuel-cladding interaction. In addition, the model performance in predicting long term creep strain is verified from the available public domain data. The creep rupture models are optimized for predicting biaxial deformation (hoop strain) of thin walled tubes. The relevant temperature range is selected for postulated system disturbances, i.e. power transients between 300 and 600°C. For the preliminary FEA simulations the material is assumed to be un-irradiated, cold worked and stress relieved. The base material models (constitutive equations) do not at this stage incorporate the effect of anisotropy, however two methods of incorporating irradiation effect are presented. The main models applied for this work are the Wilshire equations (WE) for rupture and the logistic creep strain prediction (LCSP) model for strain.

1. Introduction

Zirconium alloys are commonly used as cladding tube material in nuclear water reactors. Zircaloy-4 (Zr-1.5Sn-0.2Fe-0.1Cr) assessed in this paper is commonly used in pressure water reactors (PWR). Zircaloy-4 has a pseudo-compact hexagonal structure (HPC) with α -phase stable until about 800°C. The material states in the reviewed references for cladding tubes are; cold-worked-stress relieved (SRA), partially (PR) or fully recrystallized (RXA) [1–6]. The recrystallized material tends to be more equiaxed and the SRA material anisotropic with elongated grains in the laminating direction. Typical grain size in the cladding tubes are in the range 2–10 μm . The difference in anisotropy causes the SRA cladding tube to elongate axially during creep under internal pressure but shorten in the RXA case ($\sigma_{\text{hoop}}/\sigma_{\text{axial}}=2$). For the fuel cladding both inward and outward creep is expected during the service life, inward creep is taking place in early service and outward

creep later in life when the fuel burnup causes the pellet to swell. The rod internal pressure might at some point exceed the primary system pressure due to release of fission gas pellet swelling causing outward cladding creep [7]. If the rate of cladding creep exceeds the rate of pellet swelling, the pellet/clad gap will re-open, i.e. lift-off takes place. Lift-off is detrimental for the life of the fuel rod due to the lower thermal conductivity of gaps causing a thermal feedback effect that can potentially lead to fuel failures.

It has been established that irradiation causes strong material hardening, i.e. increase in both yield stress and ultimate tensile strength, and significant decrease of ductility (ϵ_t). Creep irradiated material tend to have longer rupture times and decreased creep ductility (ϵ_{cf}). This is at least true for the short duration test assessed in this work. For the Zircaloy-4 there is a "rule of thumb" for the life limiting creep strain, the cladding life is considered to be exhausted at $\sim 1\%$ [7].

The amount of cold work (CW) from the manufacturing (pilgering) process also has an impact on the creep properties of Zircaloy-4. In this work the CW is the unit less ratio of the area reduction from the final cold working (pilgering) at manufacturing of the cladding tubes. The amount of cold work in the material affects 3 main material parameters, i.e. the dislocation density, the grain shape and the level of anisotropy. For creep with cold worked Zircaloy-4 it generally holds that; the higher the cold work (above $\sim 10\%$), the higher the strain rate, the shorter the rupture time [7].

To improve the understanding of the creep damage accumulation in the thin walled fuel cladding tubes made of Zircaloy-4, material property data and models have been collated from the public domain. The irradiation and CW impact on tensile, creep rupture and creep strain properties have been attempted and models have been created for use in finite element analysis (FEA). The main objective of this paper is to define a robust and more advanced material model for rupture than the classical Larson-Miller approach, furthermore define a strain model more advanced than the Norton minimum strain rate approach. The models selected were the Manson-Brown [8] and the Wilshire equation [9] for rupture and the logistic creep strain prediction (LCSP) model [10] for time to strain or strain rate. Using these approaches the presented models are able (at this stage) to predict primary, secondary and tertiary creep with or without irradiation effect, and level of cold work. The presented FEA simulations are simple verification simulations and do not at this stage take the above mentioned features into account.

To define a model for irradiated Zircaloy-4 two approaches has been used; a reference material methodology [11, 12] and a straightforward Wilshire type model based on the changing yield properties. The approach was selected due to the extensive changes of the material as a function of irradiation dosage. The method is suitable for small data sets, where comparison to a suitable reference material is possible. Naturally in this case the "reference material" is the un-irradiated Zircaloy-4. The changes in Young's modulus, yield stress and tensile strength are substantial and this feature can be utilized by the normalization procedure of the Wilshire model. Since the data on irradiated material is very limited [13] it is clear that the requirements for a full creep model assessment [14] with appropriate

model validation is not possible. The optimal master curves are then used for extrapolation in time and stress to a maximum extent of three times the longest test duration.

3. Materials and methods

The creep rupture (burst) and creep strain properties of the Zr alloy Zircaloy-4 (see Table 1 for nominal chemical composition) are assessed in this work. Zircaloy-4 has a pseudo-compact hexagonal structure with the α -phase stable until about 800°C. The material properties of this alloy, especially for the thin walled tubes used as cladding, are susceptible to cold work and heat treatments. The data compiled (see Table 2) from a number of sources is mainly in the cold worked stress relieved state (SRA), which is the condition of the cladding in the majority of PWRs, or recrystallized (R) state. In this work only SRA material data has been assessed. The recrystallized material tends to be equiaxed and the SRA material anisotropic with elongated grains. An anisotropy factor of +0.05 given by [7] for CWSR material would cause an increase in the axial direction of 0.05% for a hoop strain increase of 1% (with 2/1 ratio of hoop to axial stress). For an isotropic material there is no change in the axial strain with increasing hoop strain. In the preliminary FEA calculations presented in this work the anisotropy is not taken into account.

It has been established that irradiation causes strong material hardening, i.e. increase in both yield stress and ultimate tensile strength, and significant decrease of ductility. This "feature" has been utilized for a new creep rupture model for irradiated materials based on the Wilshire equations where the stress is normalized by tensile strength or yield stress. The time independent models used for normalization of the creep test stress (yield stress and tensile strength) can be found in [15], giving formulations as a function of temperature, cold work and irradiation fluence.

Table 1. Composition of Zircaloy-4 [3] (wt.%).

Sn	Fe	Cr	O	Zr
1.2–1.7	0.18–0.24	0.07–0.13	~0.01	Bal.

Table 2. Type of data, test type (uniaxial/tubular) / models and material state for the references used in this work.

Type of data	Test type	Reference	Material state
Creep rupture non-irradiated also UTS (T)	tubular	[3]	SRA (460°C / 7h)
Creep rupture non-irrad. & irrad.	tubular	[13]	SRA
Creep rupture non-irradiated	tubular	[2, 15, 16]	SRA
Creep rupture non-irradiated	tubular	[4][6]	SRA (450°C / 2.5 h)
Creep strain non-irrad & irrad	tubular	[13]	SRA
Creep strain non-irradiated	tubular	[4]	SRA, PRA & RXA
Young's modulus, yield and tensile strength	tubular, uniaxial & models	[1] [3] [17][18]	varying CW, irradiation and strain rate

3. Models and verification

3.1 Creep rupture modelling

The Wilshire equations [ref] has provided a methodology for direct fitting and prediction of minimum strain rate, time to strain and time to rupture. The method needs additional tensile test data to accompany the constant load tests. The method uses tensile strength normalized (creep) stress and the model curve is fitted to temperature compensated time or strain rate. The model avoids the varying stress exponent n and the creep activation energy is definable in a straight forward way. However, in the case of time to strain the model has so far been used for assessing each strain separately in the same manner as for rupture data, giving at least two fitting parameters for each strain level, i.e. k , u in Eq. 1.

The Wilshire equation [9] for normalized stress (σ/σ_{UTS}) as a function of time to rupture (t_r) is defined as:

$$\ln(\sigma / \sigma_{UTS}) = -k[t_r \exp(-Q_c^* / R \cdot T)]^u \quad (1)$$

or inversely:

$$t_r = \left[-\frac{1}{k} \cdot \ln\left(\frac{\sigma}{\sigma_{UTS}}\right) \right]^{\frac{1}{u}} \cdot \exp\left(\frac{Q_c^*}{R \cdot T}\right) \quad (2)$$

where k and u are fitting constants, Q_c^* is the apparent activation energy, R the gas constant, σ the applied stress and σ_{UTS} the tensile strength at test temperature.

The WE master function for Zircaloy-4 is shown in Figure 1. The function is partitioned at the normalized stress value of 0.8, dividing low temperature / high stress tests and high temperature / lower stress data. Note that the scatter of the WE model is larger than the below described classical model due to normalizing the different data sources by the same nominal UTS function defined from [17] and [3]. The normalization feature is of importance for incorporating the effect of irradiation into the time to rupture and strain predictions.

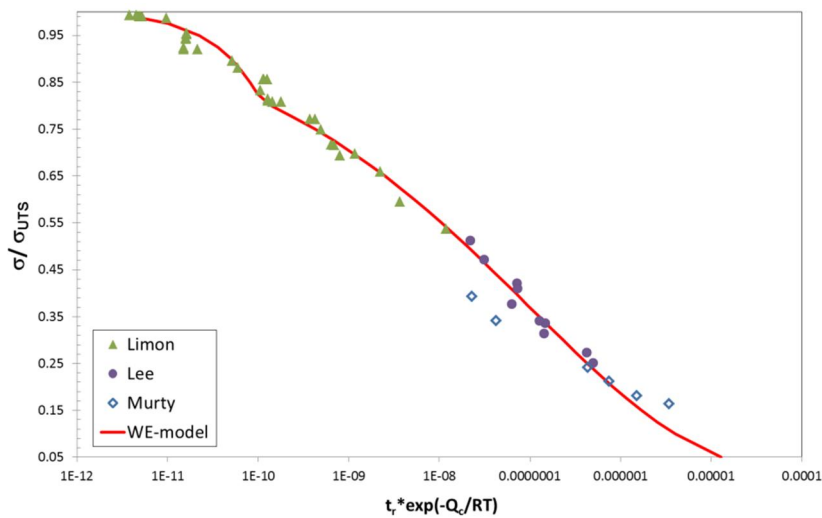


Figure 1. Wilshire (WE) master curve for unirradiated Zircaloy-4.

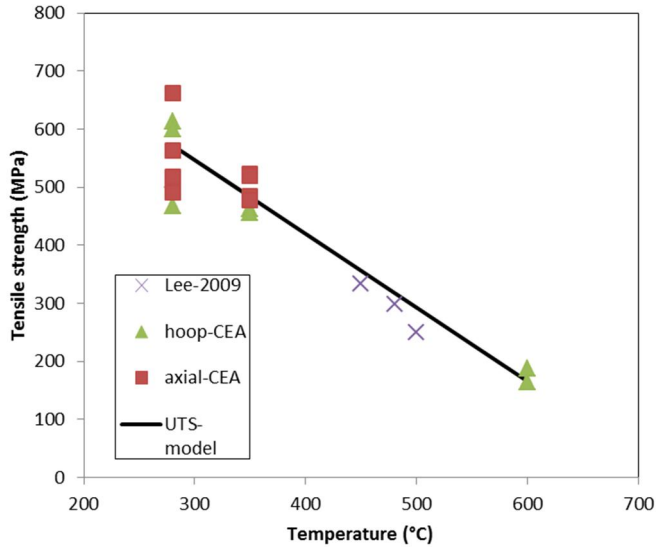


Figure 2. Tensile strength model used for normalization of un-irradiated Zircaloy-4 [17][3]. The measured UTS correspond to a calculated CW level of 36% [19]. UTS (T) = 929.7 - 1.274·T(°C), UTS (600°C) = 165 MPa.

Table 3. WE master curve parameters (Eq.3) for Zircaloy-4. Note that the WE curve is divided into two regions at $\sigma/\sigma_{UTS} = 0.8$.

Parameter	k $\sigma/\sigma_{UTS} > 0.8$	u $\sigma/\sigma_{UTS} > 0.8$	k $\sigma/\sigma_{UTS} \leq 0.8$	u $\sigma/\sigma_{UTS} \leq 0.8$	Q (J/mol)
Value	5.65e+9	1.04	41.86	0.23	130 000

The classical Manson-Brown (MB) model was also fitted to the same data set with the DESA creep assessment tool [20]. The MB master equation is defined as:

$$P_{MB} = \frac{\log(t_r) - \log(t_a)}{\left[\frac{T + 273 - T_a}{1000}\right]^P} = \sum_{i=0}^N B_i \cdot f(\sigma)^i \quad (3)$$

where t_r is the time to rupture, σ the stress and B_i , $\log(t_a)$, T_a and P are fitting parameters as given in Table 4. The MB isotherms and the creep rupture data points are shown in Figure 3.

Table 4. MB master curve parameters (Eq.3) for Zircaloy-4; note that the stress function is $\sigma^{0.5}$.

Parameter	B ₀	B ₁	B ₂	B ₃	B ₄	log(t _a)	T _a	P
Value	56.8974	-45.2342	23.3601	-4.2831	56.8974	-30.51	460	-0.2

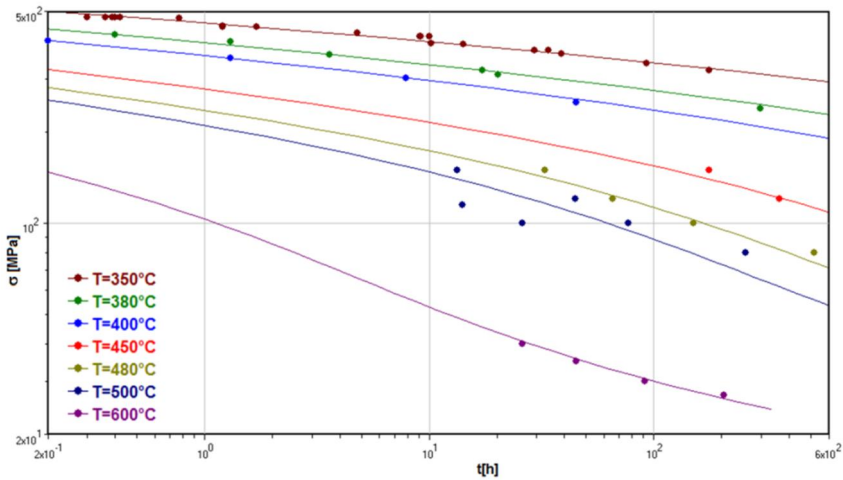


Figure 3. Classical MB model with 3rd degree stress function and isotherms from 350 to 600°C.

Table 5. Calculated creep strength for given times to rupture (MB / WE) for un-irradiated material.

Temp (°C)	1 h	250 h	1000 h
350	459 / 470	300 / 308	300 / 260
375	405 / 418	245 / 257	245 / 208
400	358 / 344	197 / 210	197 / 161
425	315 / 307	154 / 167	154 / 122
450	278 / 269	115 / 130	115 / 89
475	243 / 233	82 / 99	82 / 63
500	210 / 199	57 / 73	57 / 43
525	181 / 166	42 / 52	42 / 28
550	153 / 137	33 / 36	33 / 18
575	127 / 110	27 / 24	27 / 11
600	103 / 85	23 / 15	23 / 6

3.2 Creep strain modelling

The uniaxial creep strain model used in this work is the logistic creep strain prediction (LCSP) model with the creep curve end limits from the time to rupture. The applicable limits of stress and temperature for reliable prediction are naturally set by the available creep rupture and strain data.

The LCSP function is a non-linear asymmetric transition function with a steepness regulated by two variables (p and x_0 , see Eq.4). The transition equation is simple to invert, also giving an algebraic solution for strain as a function of time. Derivation can give the strain rate at a specified time and further derivation and finding the root of the expression gives the minimum creep rate.

$$\log[t(\varepsilon)] = \frac{\log(t_r) + C}{1 + \left(\frac{\log(\varepsilon)}{x_0}\right)^p} - C, \quad (4)$$

For the Zircaloy-4 material the factors x_0 and p are temperature and stress dependent of the form:

$$x_0 = x_1 + x_2 \cdot \sigma / \sigma_{UTS} + x_3 / (T + 273) \quad (5)$$

$$p = p_1 + p_2 \cdot \sigma / \sigma_{UTS} + p_3 / (T + 273), \quad (6)$$

where x_i and p_i (and C) are material constants given in Table 6. It is important to remember that these constants have been optimized on a limited amount of data and it is not recommended to extrapolate them outside of the data range.

Table 6. Shape parameters for Zircaloy-4 as a function of temperature and stress.

x_1	x_2	x_3	p_1	p_2	p_3	C
-0.126	1.14	-1.67E+03	0.824	-3.25	2.07E+03	3

The two data sets assessed for creep strain response refer to a cold pilgered material with two intermediate heat treatments and a final stress relieving (460°C for 7 h) [3] and [6] with a commercial fuel cladding 74% reduction in cross section at last rolling (CW = 74%), stress relieved at 500°C for 2.5 h. The same LCSP shape function parameters used on both data sets gave a good fitting result as seen in Figure 4.

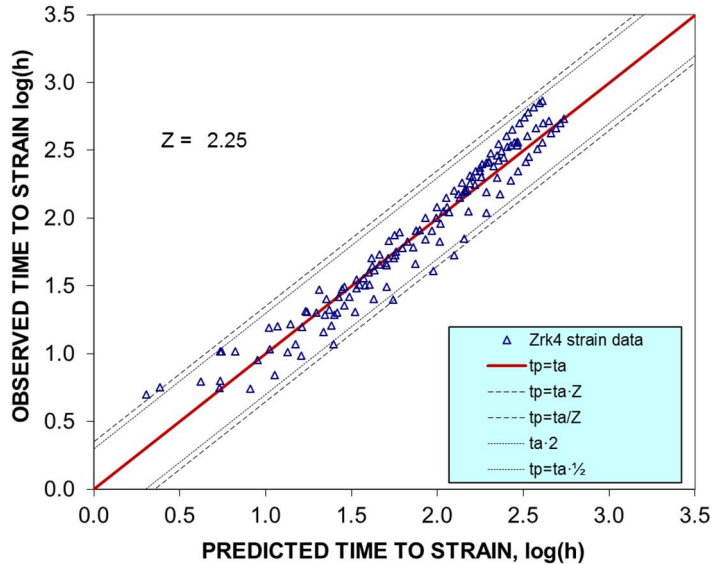


Figure 4. Predicted vs. observed time to specified strain (WE + LCSP model) for given normalized (hoop) stress.

3.2 Creep model including the effect of irradiation

In creep deformation under irradiation conditions (within the creep regime) dislocation movement (climb / glide) and irradiation produced material changes interact. Neutron irradiation causes large quantities of point defects (PDs) such as vacancies and self-interstitial atoms (SIAs). In general creep in reactor consists of two components, i.e. thermal creep (above 300°C) affected by microstructural changes and irradiation creep with weak temperature dependence. The latter is the main contributor to dimensional changes of cladding tubes in normal water-cooled reactor service. Other causes of dimensional changes of Zircaloy-4 are: irradiation growth, pickup of hydrogen and swelling. The initial material state is also of great importance, i.e. the amount of cold work increases both thermal and irradiation growth, the final annealing treatment and the grain size (and shape), the solute alloying content of O / Sn and the stress orientation also has impact on the creep strain rate. Some material properties change as a function of irradiation dose and can be measured through mechanical testing. The common (most reported) ones being: elastic modulus, yield stress and tensile strength [7].

Two different possibilities for building a material model including the effect of irradiation for Zircaloy-4 material are presented. The first is based on utilizing stress correction factors (as a function of fluence) shown in Figure 5. In this methodology the test stress is normalized with the tensile properties of the un-irradiated material.

The irradiated tests are as seen in duration (at the same tests stress as un-irradiated parent material), the more pre-irradiation the longer the creep rupture

time. Also the effect of the irradiation damage seems to decrease as the test durations become longer. The extent of this change towards the properties of the un-irradiated material is not known due to the limited data in the public domain containing mainly very short to short test durations. The impact of this would mainly concern the long term storage at low temperatures for extremely long service times.

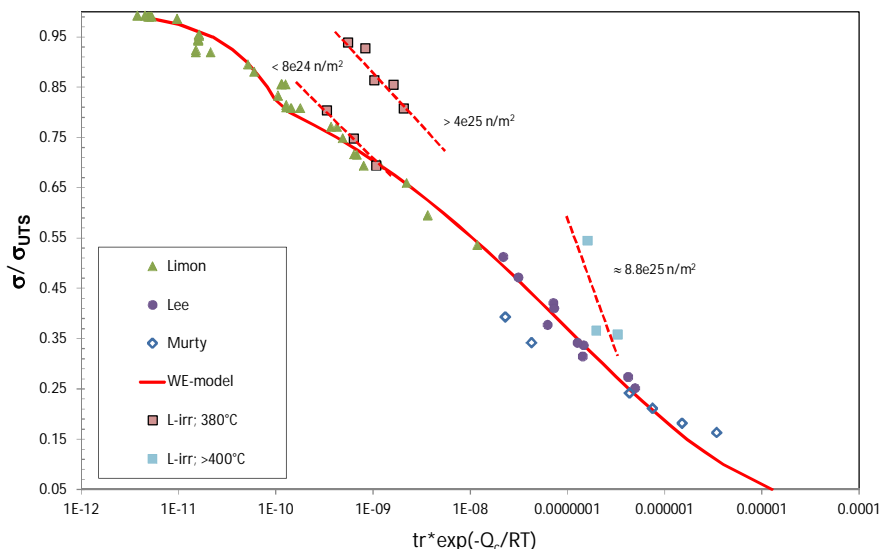


Figure 5. Wilshire (WE) master curve with irradiated creep data normalized by the tensile strength of un-irradiated material. The level of irradiation (fluence) is given next to the irradiated data (L-irr).

The other possibility for the irradiated Zircaloy-4 creep rupture modelling, where the creep stress of the irradiated test is normalized with the irradiated material tensile strength (or yield) as shown in Figure 6. Here the creep results form a WE master curve below the un-irradiated one and the corresponding parameters can be calculated for the irradiated material as given in Table 7. The apparent activation energy 130 kJ/mol (both for irradiated and unirradiated) material is in the range of published values of self-diffusion for α -zirconium (88–143 kJ/mol) [21].

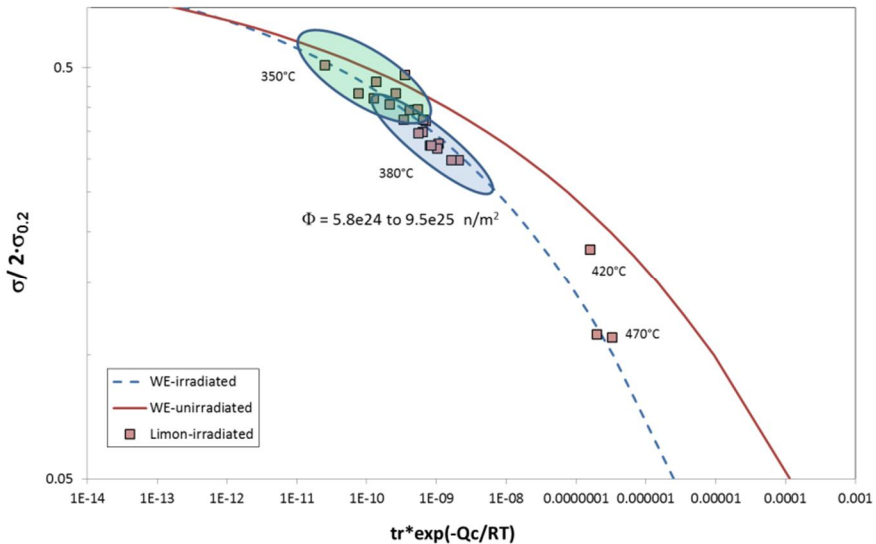


Figure 6. Wilshire (WE) master curve for irradiated material (dashed line). Note that the normalising has been done with two times yield stress instead of UTS. The change in yield as a function of fluence is calculated as in [19].

Table 7. WE master curve parameters (Eq.3) for irradiated Zircaloy-4. Note that the WE curve is not divided into regions as for the unirradiated case and the normalisation is by $\sigma/(2 \cdot \sigma_{0.2})$ instead of UTS.

Parameter	k $\sigma/(2 \cdot \sigma_{0.2})$	u $\sigma/(2 \cdot \sigma_{0.2})$	Q (J/mol)
Value	16.36	0.132	130 000

5. FEA modelling and simulations

The LCSP uniaxial material model is implemented in the Abaqus (version 6.12-3) general purpose finite element software as a user routine by way of the CREEP subroutine interface. This enables the implementation of the model as a function of deviatoric and hydrostatic stress components as well as solution-dependent state variables. The LCSP implementation for the Abaqus translates the uniaxial engineering model to be applied in a multiaxial true-stress, true stress-strain. The subroutine is called for each material point of the FE mesh and it returns the integrated equivalent creep strain increment arising from viscoplastic deformation. Since an accurate value of equivalent stress is required for LCSP analyses, the viscoplastic material model needs to be accompanied by an time-independent

elastic-plastic material model, which in the current work is accomplished by incorporating isotropic linear-elasticity and incremental plasticity with multilinear isotropic hardening utilizing the von Mises yield criterion and flow potential.

The uniaxial model is generalized to a multiaxial form by enforcing normality, i.e. the plastic strain rate is given by

$$\dot{\epsilon}_{pl} = \dot{\epsilon}_{cr} \cdot n, \quad (8)$$

where $\dot{\epsilon}_{cr}$ is the equivalent creep strain rate and n is the gradient of the deviatoric stress potential (e.g. $\partial f / \partial \sigma$), where the yield potential of a von Mises material is utilized resulting in

$$n = \frac{3}{2} \frac{S}{\sigma_e}, \quad (9)$$

where S is the deviatoric stress and σ_e the equivalent stress measure, which in current work is throughout the von Mises stress. The equivalent strain rate is obtained from the uniaxial LCSP model and its evolution equation, i.e. $\dot{\epsilon}_{cr} = h^{cr}(\sigma_e, \epsilon_{cr}, t, T)$, where t is time and T the local temperature. The evolution equation is time-integrated following the chosen means of integration, and the CREEP subroutine provides the creep strain increment for a given time increment. For the simplest explicit integration this means multiplying the rate by time increment size and establishing convergent solutions by specifying criteria for allowable creep strain increments.

The CREEP routine thus requires the creep strain increment and the viscoplastic contribution to terms required for building the material stiffness matrix. The derivation of the Fortran code is performed by computing these terms using Mathematica and writing the user subroutine via a Python (open source code) interface. The subroutine terms are compared to the initial uniaxial LCSP model for verification.

For the preliminary FEA simulation the simplified Zircaloy-4 fuel cladding pipe consisting of 80 linear hexahedral elements of type C3D8R, with the large-displacement formulation. The hexahedral pipe is shown in Figure 7. The first test simulation was done at an internal pressure of 98 bar at a temperature of 500°C. The pipe outer diameter is 9.51 mm and the wall thickness is 0.58 mm. The FEA simulation predicts an initial maximum principal stress of around 91 MPa. Creep strain accumulates rapidly at the free end of the postulated 500 mm tube length, the other end is rigidly constrained as shown in Figure 7. The FEA simulation postulates rupture in about 30 h. The corresponding time to rupture with a nominal stress level of 91 MPa predicts rupture in 90 h for the MB model and 150 h for the WE model.

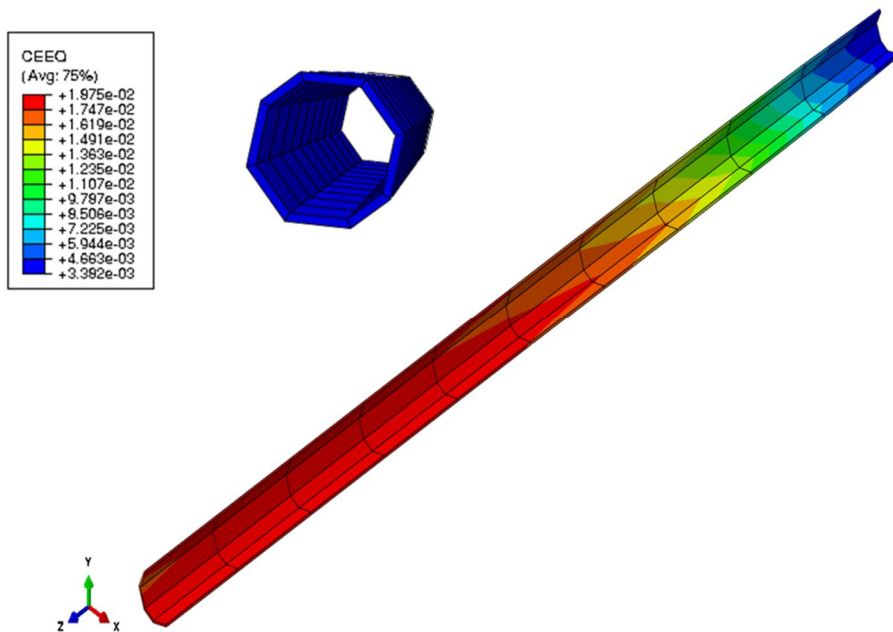


Figure 7. FEA simulated Zircaloy-4 fuel cladding tube 550°C after 3 h of creep at 98 bar internal pressure. Note that the initial simulation is with simple hexahedral mesh only.

6. Discussion and conclusion

Creep models for strain and rupture have been presented for Zircaloy-4, commonly used as cladding tube material for nuclear fuel in water reactors. Public domain creep data from biaxial testing have been assessed and the resulting uniaxial creep strain model has been transferred to multiaxial form and used for initial finite element simulation. The simulation shows that the creep strain evolution under internal pressure can be mimicked. The tetrahedral tube elements do however cause some anomalies such as a somewhat higher stress level than analytically calculated from the cylindrical geometry. The current models have been tuned and fitted to also incorporate the effect of irradiation. This has been done through utilising the changing hot tensile properties of the material as a function of irradiation. The data range and especially the short durations of the available data does not provide tools for long term material prediction but should be sufficient to use as a base for transient modelling. The constitutive equations do not at this stage incorporate the effect of anisotropy and this will be the next target for further development. More extensive tube simulations have also to be done with increased accuracy and mesh density of the cladding tube. It has been shown that the WE model applied for both unirradiated and irradiated Zircaloy-4

creep models together with the logistic creep strain prediction (LCSP) model for strain shows considerable promise in describing the thermal creep of the Zircaloy-4, and has potential benefits in the FEA modelling of complex fuel/cladding interaction.

Acknowledgements

The support of the Academy of Finland, Decision No. 260493 (project IDEA) is gratefully acknowledged.

References

1. Delobelle, P., Robionet, P., Geyer, P. & Bouffioux, P. A model to describe the anisotropic behaviour of Zircaloy-4 tubes. *Journal of Nuclear Materials* 238 (1996), pp. 135–162.
2. Murty, K. L. Deformation Microstructures and creep mechanism in Advanced Zr-based Cladding under Biaxial loading, Final report, DOE-NEER program, grant # DE-FG07- 041D14611 (2008).
3. Lee, S. Y., Kim, K. T. & Hong, S. I. Circumferential creep properties of stress-relieved Zircaloy-4 and Zr-Nb-Sn-Fe cladding tubes, *Journal of Nuclear Materials* 392 (2009), pp. 63–60.
4. Kim, Y. S. Generalized creep model of Zircaloy-4 cladding tubes, *Journal of Nuclear Materials* 250 (1997), pp. 164–170.
5. Mayuzumi, M. & Onchi, T. Creep deformation of an unirradiated Zircaloy nuclear fuel cladding tube under dry storage conditions. *Journal of Nuclear Materials* 171 (1990), pp. 381–388.
6. Mayuzumi, M. & Onchi, T. Creep deformation and rupture properties of unirradiated Zircaloy-4 nuclear fuel cladding tube at temperatures of 727 to 857 K. *Journal of Nuclear Materials* 175 (1990), pp. 135–142.
7. Adamson, R., Garzarolli, F. & Patterson, C. In *Reactor Creep of Zirconium Alloys*, A.N.T International 2009.
8. BS PD 6605. Guidance on methodology for assessment of stress-rupture data. London, UK: British Standard Institution, 1998.
9. Wilshire, B., Scharning, P. J. & Hurst, R. A new methodology for long term creep data generation for power plant components. *Baltica VII Int. Conf.*

on Life Management and Maintenance for Power Plants, Vol. 1. Espoo, VTT Technical Research Centre of Finland, 2007. Pp. 196–207.

10. Holmström, S. & Auerkari, P. Robust prediction of full creep curves from minimal data and time to rupture model. *Energy Materials, Materials Science & Engineering for Energy Systems*, Vol. 1 (2006), pp. 249–255.
11. Holmström, S. & Auerkari, P. Predicting creep life from small sets of test data and reference material characteristics. *Proc. 12th Int. Conf. on Creep and Fracture of Engineering Materials and Structures (JIMIS 11)*. Kyoto, Japan, 2012.
12. Holmström, S. & Auerkari, P. Improved approach for predicting weld creep strength factors of ferritic steels. *Energy Materials, Materials Science and Engineering for Energy Systems* 4 (2009), pp. 23–27.
13. Limon R. & Lehmann, S. A creep rupture criterion for Zircaloy-4 fuel cladding under pressure, *Journal of Nuclear Materials* 335 (2004), pp. 322–334.
14. Holdsworth, S. R. et al. (Eds.). *ECCC Recommendations, Creep data validation and assessment procedures*. ECCC Publication (a) Vol. 1: Overview, (b) Vol. 2: Terms and terminology, (c) Vol. 3: Data acceptability criteria, data generation, (d) Vol. 4: Data exchange and collation, (e) Vol. 5: Data assessment, (f) Vol. 6: Characterisation of microstructure and physical damage for remaining life assessment, (g) Vol. 7: Data assessment – creep crack initiation, (h) Vol. 8: Data assessment – multi-axial, (i) Vol. 9: Component assessment.
15. Murty, K. L. Creep studies for zircaloy life prediction in water reactors. *Journal of Minerals, Metals and Materials (JOM)*, 1999, Vol. 51, Issue 10, pp. 34–38.
16. Murty, K. L. The internal pressurization creep of Zr alloys for spent-fuel dry storage feasibility, *Journal of Minerals, Metals and Materials (JOM)*, 2000, Vol. 52, Issue 9, pp. 34–38.
17. Desquines, J. Release of the PROMETRA V2.5 material data base (Zircaloy-4, ZIRLO, M5), CABRI WATER LOOP IRSN 2007-95, SEMCA-2007-318 (2007).
18. Hagrman, D. T. (Ed). *SCDAP/RELAP5/MOD3.1 Code Manual, Volume IV: MATPRO – A Library of Materials Properties for Light-Water-Reactor Accident*, NUREG/CR-6150, EGG-2720, Vol. IV, 1993.

19. Geelhood, K. J., Beyer, C. E. & Luscher, W. G. PNNL Stress/Strain Correlation for Zircaloy, PNNL-17700, 2008.
20. Fehér, A., Linn, S., Schwienheer, M., Scholz, A. & Berger, C. An interactive approach to creep behavior modeling. *Materials Science and Engineering: A*, 2009, Vol. 510–511, June, pp. 29–34.
21. Hayes, T. A. & Kassner, M. E. Creep of zirconium and zirconium alloys, *Metallurgical and Materials Transactions A*, 2006, Vol. 37, Issue 8, pp. 2389–2396.

New applications of pneumatically powered testing equipment for extreme environments

Pekka Moilanen¹, Stefan Holmström^{1,2}, Radek Novotny², Peter Hähner²
& Karl-Fredrik Nilsson²

¹VTT Technical Research Centre of Finland
Espoo, Finland

²European Commission, JRC-IET, Institute for Energy and Transport
Petten, Netherlands

Abstract

Pneumatically powered loading apparatus designed to allow very accurate and reliable control and measurements of loads and displacements in different environments allow the generation of key mechanical material properties required for the design and life management of nuclear power generation components. This paper describes recent developments and modifications required for new testing applications for challenging environments such as super-critical water, molten lead and hydrogen atmospheres. Also, designs optimized for in-pile material testing are in the conceptual stage. In this paper the basic testing methodology and control systems of the pneumatic loading units are described together with the special features required by the new applications. Test equipment calibration and functionality verification is presented for selected cases together with some unique initial test results. Also, special testing types for future nuclear and hydrogen energy concepts are presented, i.e. liquid metal test loops for lead-cooled fast reactors and test loops for testing in high pressure hydrogen. A set-up for multi-purpose interchangeable specimen types is also presented. The full range of the available testing platforms and environments is briefly reviewed and the future development directions are discussed.

Glossary

Abbr. / Symbol / Object	Definition
Bellows	load producing internally pressurized corrugated chamber
PLA	Bellows-based <u>P</u> neumatic <u>L</u> oading <u>A</u> pparatus
SB / SB-2	<u>S</u> ingle Bellows loading apparatus, pull (SB), push and pull (SB-2)
DB	<u>D</u> ouble Bellows loading apparatus (pressure compensated)
TB	<u>T</u> riple Bellows loading apparatus (enables external loading unit)
DC(T)	Disk shaped Compact Tension specimen for crack propagation tests
LWR / BWR / PWR	Light Water / Boiling Water / Pressurized Water Reactor
SCW	Super-Critical Water ($T > 374^{\circ}\text{C}$, $p > 22 \text{ MPa}$)
CER	Contact Electric Resistance measurements
Gen-IV	Generation IV nuclear energy systems
LFR	Lead-cooled fast reactor
SFR	Sodium-cooled fast reactor
SCWR	Super-critical water-cooled reactor
BR-2	Test reactor (SCK-CEN, Belgium)
OSIRIS	Test reactor (CEA, France)
LLL	Liquid Lead recirculation Loop (JRC-IET)
MELODIE	Loading device for irradiation experiments (CEA, France)
JHR	Jules-Horowitz Research Reactor (Cadarache, France)
CF	Creep-Fatigue
LCF	Low-Cycle Fatigue
SCC	Stress Corrosion Cracking
CCG / CCI	Creep-Crack-Growth / Initiation
CFCG / CFCI	Creep-Fatigue-Crack Growth / Initiation
IASCC	Irradiation Assisted Stress-Corrosion Cracking

1. Introduction

Conventional mechanical material testing systems produce the load on the specimen by using a moving pull rod. This feature, however, is disadvantageous for testing in liquid or pressurized environments since pressure boundary feed-throughs cause problems with leakage and friction forces that are difficult to fully control. With bellows-based Pneumatic Loading Apparatus (PLA) [1–9] it is possible to design test set-ups with no moving parts over the pressure boundary, i.e. a loading unit connected to the control unit via pressure lines and electrical feedback connectors only. The PLA has been designed to operate at temperatures above 600°C for creep-fatigue testing [10, 11]. In this paper some recent test rig applications [12–15] are reviewed together with some new conceptual designs for testing in extreme environments. The different test environments and test types where PLA is used are given in Table 1.

Table 1. PLA test environments, testing types and references.

Environment	Test types	Test specification	Reference
In-pile (BR2 test reactor)	Tensile tests displ. rate 10^{-7} 1/s	2 sample rig, axial loading, stagnant water at 90°C, (SB)	[3]
In-pile (BR-2 test reactor)	Creep Fatigue	2 sample rig, creep fatigue loading (holding 10 and 100 s), stagnant water 90°C (SB-2)	[4]
In-pile (Osiris reactor)	Multiaxial creep internal pressure + tensile/compressive load with diametral strain measurement	Construction finalized, (SB-2)	[5]
Environment	Test types	Test specification	Reference
BWR water chemistry (autoclave)	Stress corrosion cracking (SCC),	6 spec. Autoclaves displ.rate $2 \cdot 10^{-8}$ mm/s, 288°C, 90 bar	[6, 7]
PWR water chemistry (autoclave)	Fatigue	Sinus wave 0.1 Hz, 350°C / 160 bar (SB-2)	[8,9]
High temperature (air)	Creep-Fatigue	Tension and compression LCF and CF tests (SB-2)	[10, 11]
PWR & SCW water chemistry	Crack initiation and growth (K) testing	Miniature autoclave (DB)	[12, 13]
Molten lead or/and lead bismuth environments	Crack growth & cone mandrel tests	Under construction (TB)	[14,15]
Multipurpose test device (air and hot-cell)	Biaxial tube creep, uniaxial creep/fatigue, crack growth (creep, creep-fatigue)	Under construction (TB)	on- going
Hydrogen high pressure environ- ment	Fatigue LCF / HCF	Conceptual stage (TB)	on- going

2. The bellows loading apparatus

There are three main set-ups of the pneumatic bellows loading apparatus. The single bellows (SB, Figure 1), the double bellows (DB, Figure 2) and the triple bellows (TB, Figure 3) system. Note that the TB system had been designated as "double²" bellows in an earlier work [12]. The SB system can be used for one or two directional (push and pull) loading up to 160 bar environmental pressure. The DB system is especially designed for higher environmental pressures (up to 350 bar) by means of a pressure compensation feature. The TB system is designed to

enable direct online load measurement with commercial load cells and can also be used with environmental pressures up to 350 bar.

Commercial load sensors are typically designed for low temperature gas environments. To accurately measure the applied load in high-temperature environments there are two possibilities using PLA: by relying on bellows pressure vs. specimen load relationships, in which case both SB and DB test set-ups can be used or by using the TB configuration and a direct measuring load cell outside the pressure boundary. In the first case accurate and reliable calibration of the pressure/load conversion is of great importance.

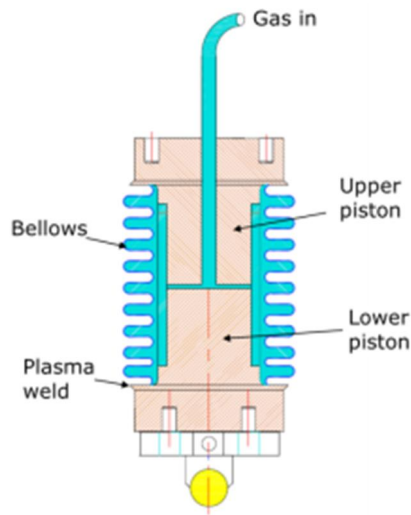


Figure 1. Single Bellows system for crack growth tests.

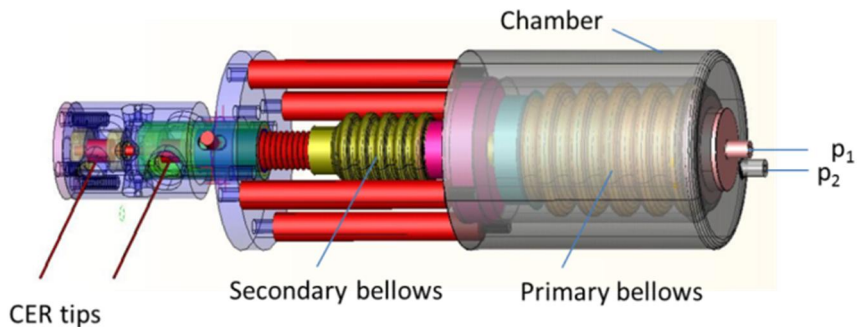


Figure 2. Double Bellows system for CER tests in SCW environment.

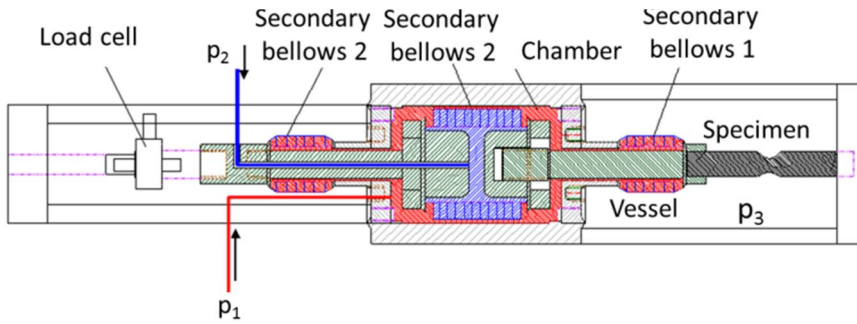


Figure 3. Triple Bellows system for mechanical tests in liquid lead environment.

2.1 Calibration procedure for the SB and DB loading apparatus

For the load calibration of the SB and DB pneumatic loading apparatus the intrinsic bellows stiffness and effective cross-section need to be determined for the calculation of the true load.

The load of a pressurized bellows can be calculated from

$$F = p A_{eff} - F_{\mu} - F_s \quad (1)$$

$$F_s = \frac{c_{\delta} \delta_b}{n_w} \quad (2)$$

where	F	= force [N]
	F_s	= intrinsic bellows stiffness force [N]
	F_{μ}	= friction force [N]
	p	= pressure [MPa]
	A_{eff}	= effective bellows cross-section [m ²]
	c_{δ}	= axial spring constant for the bellows [N/mm]
	δ_b	= axial movement of the bellows [mm]
	n_w	= number of corrugations.

Note that for calibrating the DB load, only the working bellows is pressurized. The stiffness of the bellows decreases as a function of temperature. For example the stiffness of a DB corresponds to 20.6 bar/mm at 23°C and 17.9 bar/mm at 550°C as shown in Figure 4.

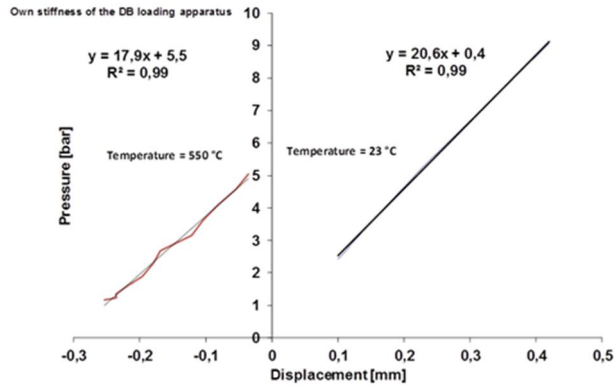


Figure 4. Intrinsic stiffness of the DB loading apparatus at 23°C and 550°C.

For the actual load determination the effective cross-section of the secondary bellows is determined by simultaneously pressurizing the working bellows p_1 and chamber pressure p_2 as depicted in Figure 5.

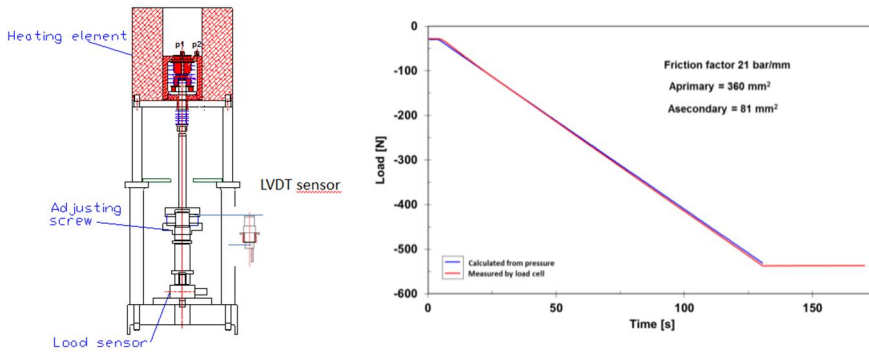


Figure 5. The effective cross-section determination of a DB System: a) High temperature calibration furnace, b) calculated and measured effective cross-section (for the working bellows).

Once the effective cross sections are known, the DB load can be calculated from:

$$F = (dp - Os \cdot \Delta) A_{eff2} - (dp - Os \cdot \Delta) A_{eff1}, \quad (4)$$

where F = measured load level, dp = pressure difference of the working bellows and chamber pressure, Os = Own (intrinsic) stiffness, Δ = displacement of the secondary and primary bellows, A_{eff2} = effective cross-section of the secondary bellows and A_{eff1} = effective cross-section of the working bellows.

One of the main advantages of using the DB loading apparatus is that it can be controlled with relatively low pressure levels of the servo controlled pressure adjusting loops (p_1 and p_2) under high environmental pressure (p_3)

The servo controlled pressure control loop is the main and most delicate part of the load control by the bellows technology. The pressurization of the medium (air or inert gas) is produced by a compressor, or in some cases by high pressure gas tanks, through a pressure accumulator connected to the pressure-adjusting loop. The pressure accumulator ensures the availability of the pressurization medium and reduces the pressure oscillations at the loop inlet. A high pressure reducer and accurate flow valves control the gas flow to the bellows. There is constant gas flow through the servo-valves which, together with the pressure transducers, are the main controlling elements in the load control set-up. A schematic of the pressure/load control loop is given in Figure 6.

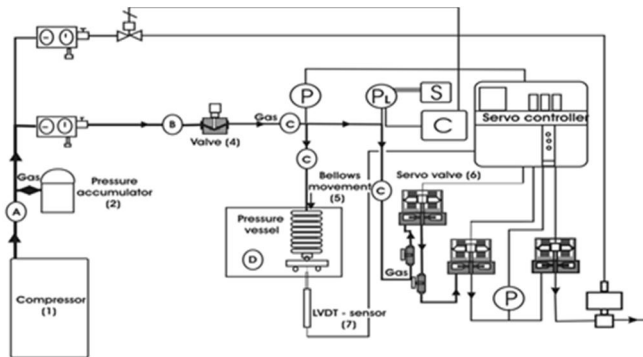


Figure 6. Pressure/load control loop for SCW environment.

The intrinsic stiffnesses and the effective cross sections of the primary and secondary bellows determine the test load together with the pressure differences of the pressure boundaries. To avoid pressure fluctuations in an autoclave, the primary bellows pressure (p_1) and chamber pressure (p_2) must be synchronized with the autoclave pressure (p_3). This can be accomplished through connecting the primary chamber and autoclave pressures using a MAC (Motion Axis Control) program. The pressure synchronization automatically adjusts the primary (p_1) and chamber (p_2) pressures when the autoclave pressure changes and hence compensates for possible pressure fluctuations. This feature is especially helpful in starting up and closing down tests when large pressure differences are expected.

3. New test rig designs and testing environments

The wide applicability of the PLA based testing technology has been demonstrated by several examples in [13]. The technology is suitable for the testing needs for

material qualification and license extensions of GenII and III LWRs. Concepts for future advanced fission concepts of GenIV (incl. SCWR), the thermo-nuclear fusion experimental reactor ITER and demonstrator DEMO are also addressed. Further improvements for PLA applicability at very high temperatures and irradiation in hot-cell and in-pile environments are in the conceptual stage. In order to perform material testing in liquid lead up to 650°C and other demanding environments, the technological development path from SB loading device towards the more demanding DB and TB applications represent technological improvements that will have an impact on testing materials in relevant (service-like or in-situ) environments.

3.1 Miniature testing systems for LWR and SCW test environments

A miniature version of the autoclave testing system together with the DB loading apparatus has been used for AISI 316 material testing in LWR/SCW environment at high temperature. To this end, a small 5 DC(T) specimen was installed to the DB loading frame with potential drop (PD) measurement as illustrated in Figure 7. A non-contact type LVDT sensor was used to measure the load-line displacement (i.e. secondary bellows displacement). Figure 8 shows the heating element and the miniature autoclave with the main feed-through. The PD wires and LVDT sensor wires were placed into the main feed-through with ceramic pliers and graphite box type of the insulators.

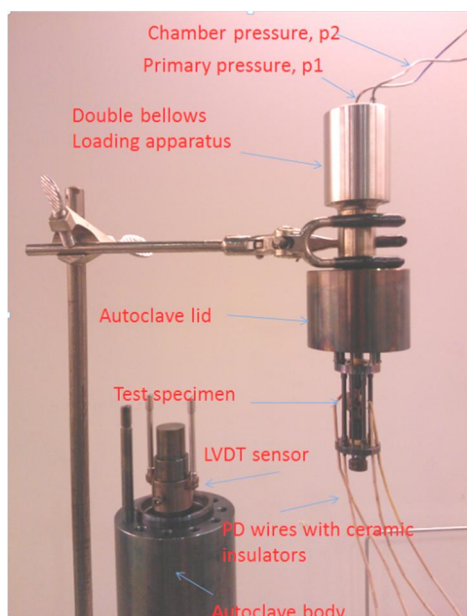


Figure 7. The miniature autoclave material testing system and its main components.

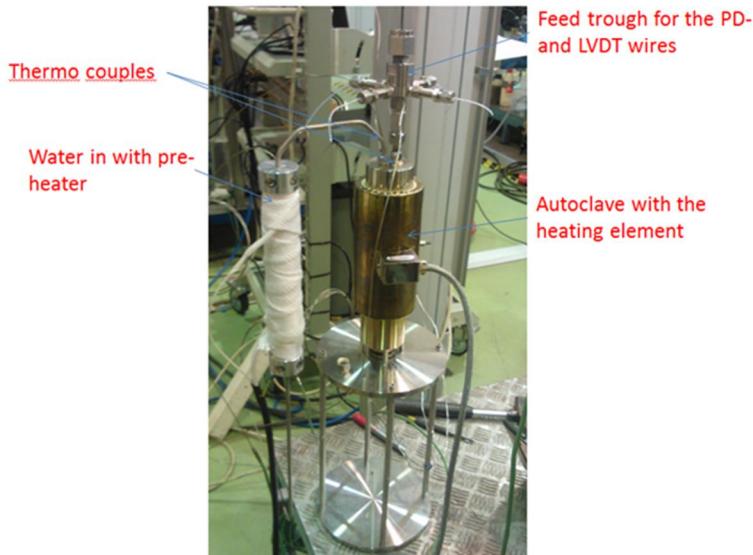


Figure 8. The test set-up for the reference test and LWR test in high temperature environment.

3.2 Molten lead environment

A liquid lead/lead-bismuth eutectic circulation loop (LLL) has been designed for mechanical testing of prospective structural materials to be qualified for future Gen IV fast reactor systems such as LFR or MYRRHA. The experiments to be performed will provide important data for the structural materials, including stress corrosion cracking, corrosion fatigue and fuel-cladding interaction of the demanding environment. The recirculation loop has been developed by a Russian consortium [15] based on their expertise of analogous heavy liquid metal coolant facilities.

The recirculation loop is a closed system (see Figure 9) where the replaceable test sections, in addition to material studies, can also be used to study the processes themselves, e.g. heat and mass transfer, physical chemistry, etc. It consists of magneto hydrodynamic (MHD) pump, a buffer vessel (expansion tank), main electric heaters, test section, two recuperators, cooler, measuring tank, dump tank for lead storage, circuit for filling and discharging, filters, flow rate meters, oxygen sensors, thermocouples, pipelines and fittings. Space for a second test section with high-temperature recuperator and tank for coolant discharge is provided (Figure 9).

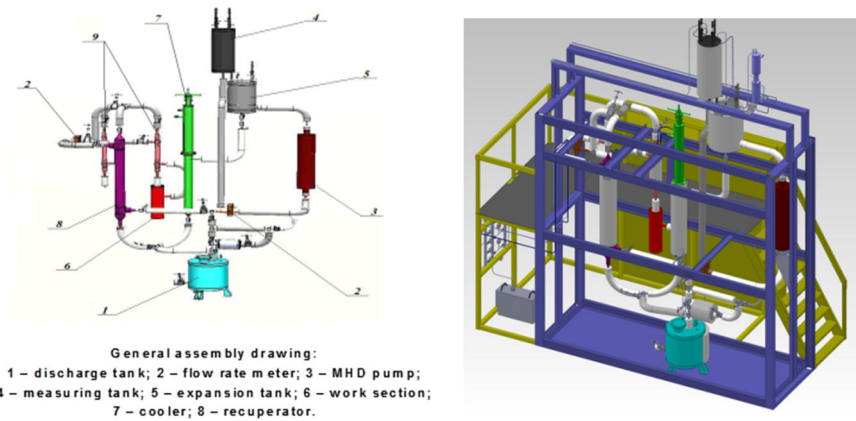


Figure 9. Layout of the liquid lead test loop.

The test sections intended for materials testing in the LLL are based on the miniature autoclave loading devices that have been successfully used in super-critical water environment [2]. The test sections are designed for testing DC(T) specimens (crack growth) and segmented expanding mandrel type test specimens for testing the lead coolant interaction with fuel cladding materials. The tests will be conducted at atmospheric pressure (1 bar) and a maximum temperature of 700°C. The loading frame details are shown in Figure 10 for the 10 DC(T) type of the crack growth specimen. The crack growth measurement system is based on the compliance measurement system on the specimen's load line axis.

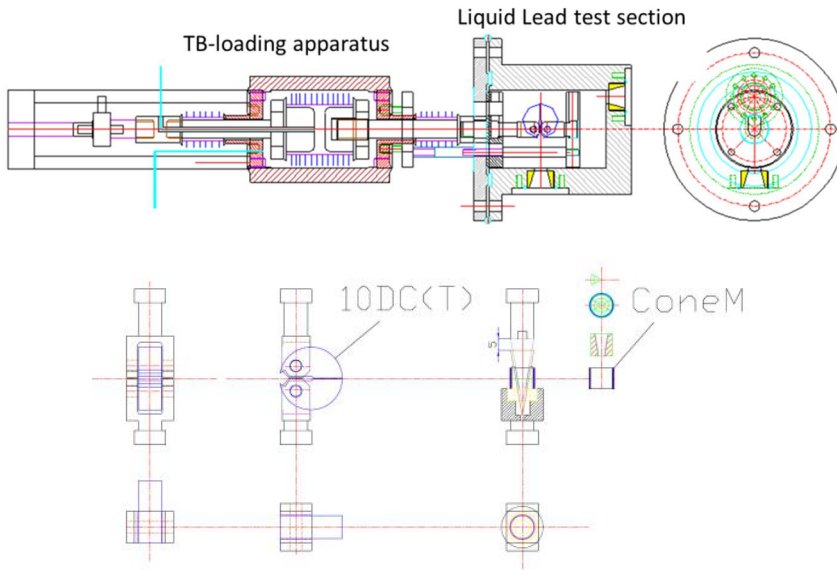


Figure 10. Schematics of the triple bellows loading set-up for DC(T) loading in liquid lead.

For the segmented expanding mandrel tests the same loading device setup (TB) as in Figure 10 can be utilized but then with the DC(T) grips replaced by a cone-mandrel test jig. The cone mandrel test is designed axi-symmetric for material characterization as well as for simulating fuel/pellet cladding interaction. From the tests the stress-strain curves at moderate plastic deformation (and small and known friction coefficients between cone/segment and segment/tube) are derived. The pellet-cladding interaction is simulated by selecting representative friction coefficients and segments to represent cracked fuel. Tests are simple to perform and at the same time only a limited amount of material is needed (typically 10 mm tube length). The tests which can be performed in load or displacement control can be used quantify how defects affect the ductility of thin-walled cladding tubes. The cone-mandrel system is made of NIMONIC 80A Ni-based alloy coated with a high temperature corrosion resistant coating (Mg stabilized ZrO₂). The on-line vertical displacement during the test is recorded (bellows movement) and the change in diameter is measured indirectly by an LVDT displacement gauge.

3.3 Conceptual designs for hydrogen and multi-purpose material testing

Recently, the bellows-based loading technique has been applied for two entirely new testing set-ups: the HYBELLO hydrogen testing device and the MATTER project biaxial creep device. Figure shows the design for the Hybello testing device, while the biaxial creep testing device with its main components is depicted in Figure 12.

Target test:

Specimen: $7 \leq \varnothing \leq 8 \text{ mm}$
Drilled: $100 \leq \varnothing \leq 500 \mu\text{m}$
Nr criterion: Crack $\sim 500 \mu\text{m}$
Instrumentation: $\Delta a / \Delta N$

Target Equipment:

H_2 : $\leq 350 \text{ bar}, \leq 100^\circ\text{C}$
Axial loading: $\pm 30 \text{ kN}$ ($\sim 1\%$)
Internal load train: 2 bellows
Frictionless load: Δp (p123)
Medium: air, He or water
Frequency: LCF \rightarrow HCF

Safety concern:

Vessel volume: ≤ 0.5 liter
 H_2 volume: $\ll 0.5$ liter
Infra: 220V, gas supply \rightarrow find safe place/ H_2 leaks, water pool?

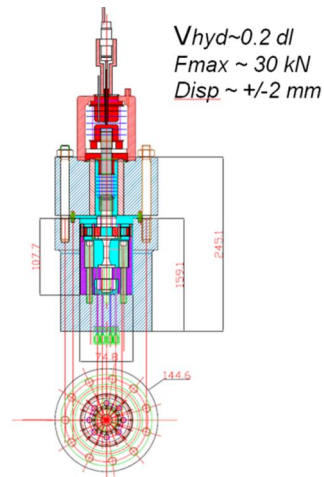


Figure 11. The Hybello Hydrogen testing system.

The biaxial material testing device has new features, in particular, its suitability for hot cell environment, where handling with the manipulators and testing of different types of the specimens with the same loading frame (tubular, bar and compact tension types) are basic requirements. The testing device is also designed for operation with a laser extensometer measurement system. The schematic overview of the whole material testing system is shown in Figure. It is planned to use the equipment for pressurized tube creep tests at MYRRHA cladding relevant conditions both in LBE and in air.

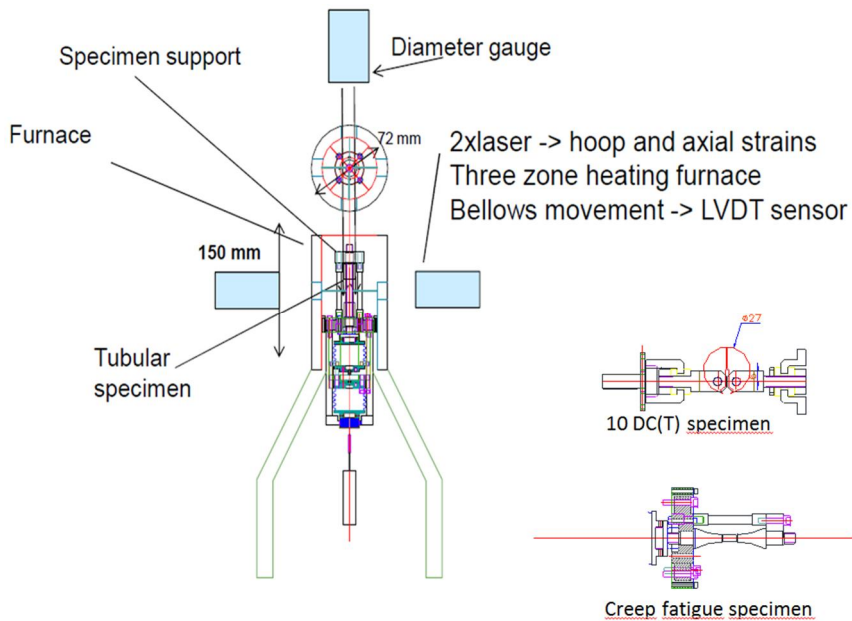


Figure 12. Biaxial creep testing device with its main components.

4. New test results

4.1 Reference test for AISI 316 stainless steel 5 DC(T) specimen

A reference test at 550°C in air was used as a first test for the miniature autoclave testing system together with a pneumatically-powered DB loading apparatus. The specimen used was a pre-cracked 5 DC(T) specimen made from AISI 316 stainless steel. A typical set of raw data from a constant load rate test is shown in Figure 13. The starting point of the specimen loading is easy to determine from the curve, as the load vs. displacement slope is changing when the rising load is applied to the specimen.

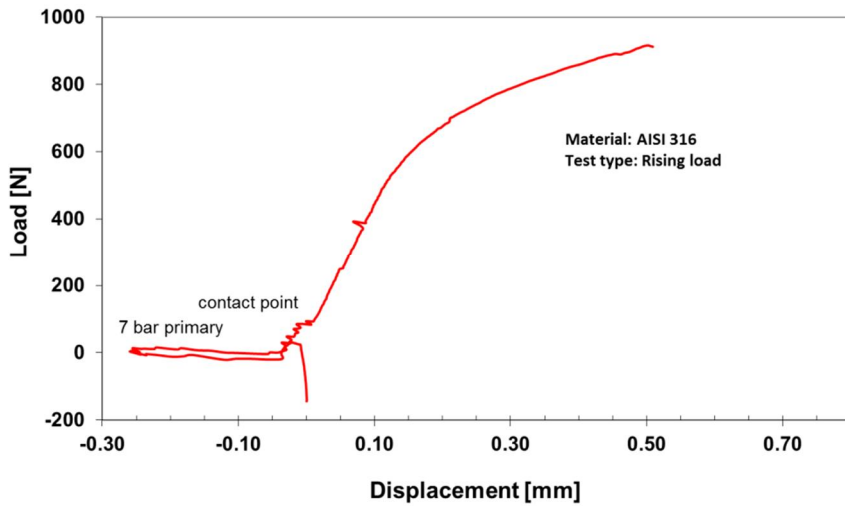


Figure 13. Load as a function of displacement at 550°C.

A second test was run at constant load in LWR environment, at a test temperature of 288°C, an autoclave pressure of 100 bar, and an oxygen level of 7 ppm. The test sequence was as given in Table 2. Figure 14 shows the starting period of the autoclave test.

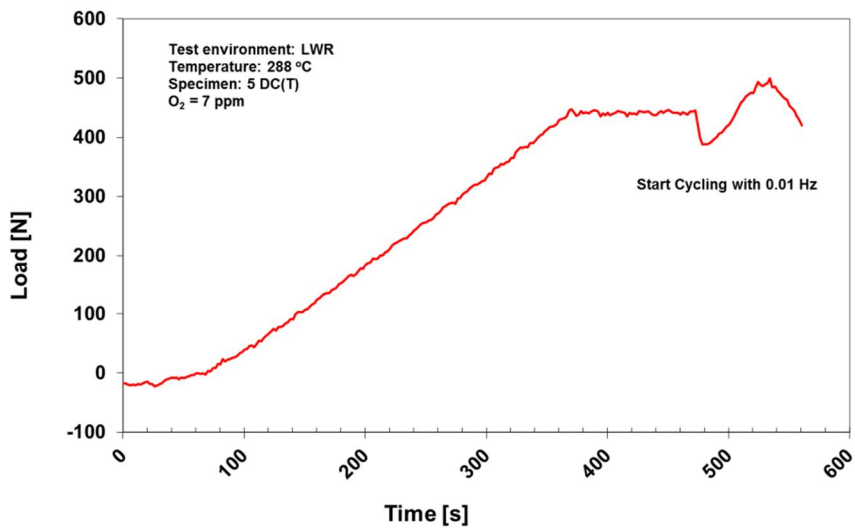


Figure 14. The load as a function of displacement for 5 DC(T) specimen in LWR coolant condition.

If one compares the elastic behaviour of the high temperature test in air and the intermediate temperature test in LWR coolant conditions, the slopes of the load-displacement curves were about the same under both test environments (Figure 15).

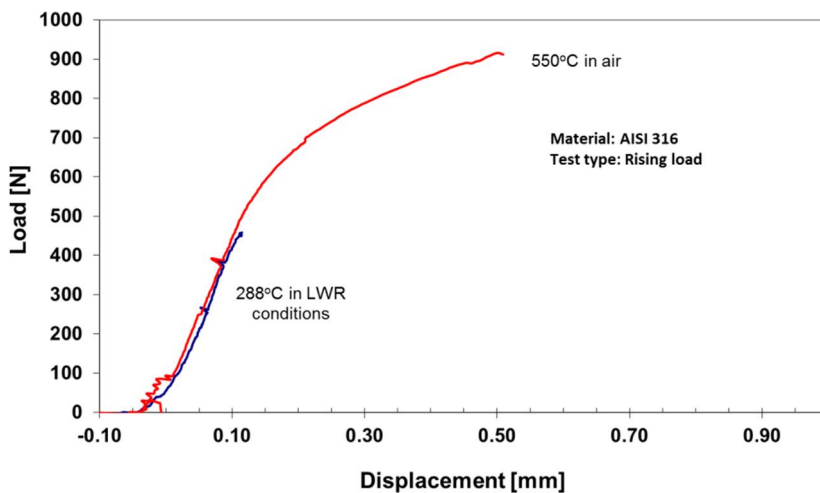


Figure 15. The elastic line for the 5 DC(T) type of the specimen under different testing coolant.

The main purpose for the LWR test was to find the threshold load/fatigue combination for crack growth for the 5 DC(T) specimen. The crack started to grow after about one month testing time at a mean load level of 536 N and a fatigue frequency of 0.1 Hz with an amplitude of 58N (R=0.8).

Table 2. The load variations during the LWR test.

Date	Load [N]	Frequency [Hz]
10.1.2013	360±58N	0.01Hz
15.1.2013	396±58N	0.01Hz
23.1.2013	415±58N	0.01Hz
28.1.2013	483±58N	0.01Hz
29.1.2013	483±58N	0.1Hz
30.1.2013	483±108N	0.1Hz
4.2.2013	536±58N	0.1Hz*Crack growth start
6.2.2013	536±58N	0.01Hz
8.2.2013	536±58N	0.001Hz
11.2.2013	Stop the test	

Figure 16 shows the PD signal response during the test. Crack growth changed as a function of the fatigue frequency as shown in Figure 16. The crack growth was mainly transgranular in nature.

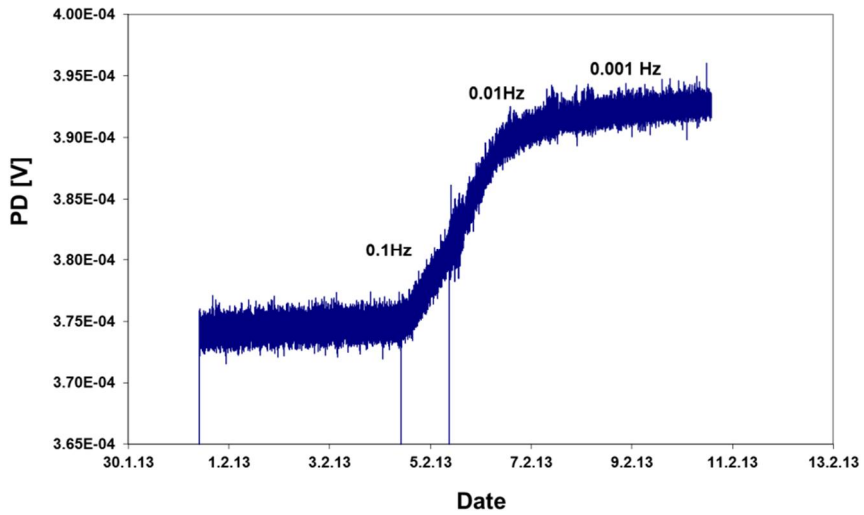


Figure 16. PD signal response as a function of the fatigue frequencies.

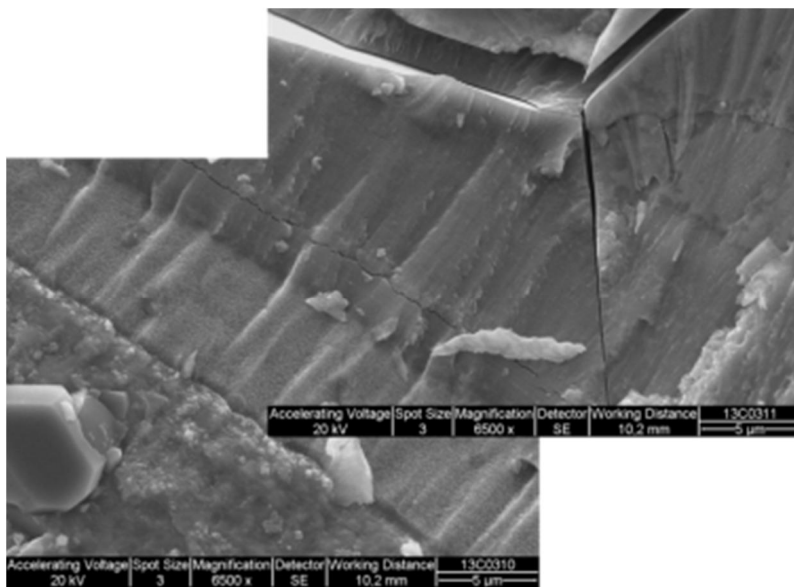


Figure 17. The crack tip of the 5 DC(T) specimen.

5. Discussion and conclusions

The pneumatic loading technology featuring substantial advantages compared to conventional mechanical testing systems in difficult / extreme testing environments has already been successfully applied for many demanding applications. The greatest advantages of the new testing applications are their flexibility in design variants, the increased sensitivity and control and the possibility to make them compact as to serve in miniature testing autoclaves suitable for multiple testing and application in restricted space (such as for in-core testing). Also the total cost for testing with miniature test set-ups decreases without compromising on the requirements on measurement accuracy and stability.

In this paper it has been shown that:

- The miniaturized double bellows (DB) unit is capable of stable operation and accurate testing in LWR and SCW environments.
- The DB calibration methodology was validated and the DB stiffness and pressure/load dependence was acquired.
- The MAC program control of the DB works reliably both at pressurizing (start-up) and testing stage of a test.
- The load threshold for crack initiation of 316 stainless steel has been determined as $538\text{N}\pm 58\text{N}$ ($R=0.8$, 0.1Hz) after around 30 h of cycling with 5DC(T) in LWR coolant (288°C).
- The test equipment for a liquid lead test loop (TB) has been designed for crack initiation and growth testing of DC(T) specimens, and an interchangeable specimen-holder for cone mandrel testing of tubular specimens, up to 700°C .
- The HYBELLO loading frame (TB) for hydrogen atmosphere testing has been designed for small volume autoclave (0.2 dl) and high test pressure (up to 600 bar H_2).
- The multi-purpose MATTER creep device has been designed for interchangeable test specimens, i.e. biaxial tubular specimens, uniaxial creep-fatigue and 10DC(T) crack growth test specimens. The test rig has a semi-vacuum furnace together with laser displacement measurement enabling testing at temperatures up to 1000°C .
- The compactness and versatility of the devices make them particularly suitable for implementation in a hot-cell setting for testing of irradiated materials or for in-pile testing.

References

1. P. Moilanen, Pneumatic servo-controlled material testing device capable of operating at high temperature water and irradiation conditions, Espoo, VTT, VTT Publications 532, 2004.
2. P. Moilanen, S. Holmström, New mechanical testing equipment for testing in real and simulated service environments (HIPS), Baltica VIII Conference on Life Management and Maintenance for Power Plants. Vol. 2. VTT Symposium 265. VTT. Espoo (2010), 209–220
3. Singh. B.N., Tähtinen. S., Moilanen. P., Jacquet. P., Dekeyser. J. "In-reactor uniaxial tensile testing of pure copper at 90°C", Journal of Nuclear Materials (2003). Pp. 12
4. Singh, Bachu Narain; Johansen, Bjorn Sejr; Tähtinen, Seppo; Moilanen, Pekka; Saarela, S.; Jacquet, P.; Dekeyser, J.; Stubbins, J.F. Final report on in-reactor creep-fatigue deformation behaviour of a CuCrZr alloy: COFAT 2 2008. Risø National Laboratory for Sustainable Energy, Roskilde, DK. 41 p. Riso-R-1629
5. Guimbal, Ph.; Auclair, M.; Carassou, S.; Moilanen, Pekka; Tähtinen, Seppo; Villard, J.-F. MELODIE, an advanced device for study of the irradiation creep of LWR cladding with online biaxial control of stress and strain. GORR International Group on Research Reactors, 12th Conference, Beijing, China (2009), 5p.
6. Karjalainen-Roikonen, P., Moilanen, P., Toivonen, A. and Aaltonen, P., "Method development for studies of environmentally assisted cracking (EAC)," RATU2 The Finnish Research Programme on the Structural Integrity of Nuclear Power Plants: Synthesis of Achievements 1995–1998, VTT Symposium 190, J. Solin et al., Eds., Technical Research Centre of Finland, 1998. Pp. 105–123.
7. Toivonen, A., Moilanen P., Pyykkönen M., Tähtinen S., Rintamaa R. and Saario T., "The feasibility of small size specimens for testing of environmentally assisted cracking of irradiated and materials under irradiation in reactor core." Nuclear Engineering and Design 193, 1999, Pp. 309–316.
8. Solin, J., Karjalainen-Roikonen, P., Moilanen, P., Marquis, G., " Fatigue testing in reactor environments for quantitative plant life management.", 2nd International Conference on Fatigue of Reactor Components. Snowbird, UT, 29–31 July 2002. EPRI OECD USNRC (2002), pp.16.

9. Solin, Jussi. Fatigue of stabilized ss and 316 NG alloy in PWR environment, Proc. PVP2006-ICPVT-11. ASME Pressure Vessels and Piping Division conference. July 23–27, 2006, Vancouver, BC, Canada . American Society of Mechanical Engineers, ASME (2006), 11 p.
10. S. Holmström, R. Pohja, A. Nurmela, P. Moilanen, P. Auerkarti, Creep and creep-fatigue of stainless steel 316, *Procedia Engineering*, Vol 55. (2013), p.160–164.
11. R. Pohja, A. Nurmela, P. Moilanen, S. Holmström, Multifunctional high precision pneumatic loading system (HIPS) for creep-fatigue testing, *Procedia Engineering*, Vol 55. (2013), p. 573–577.
12. Novotny, R., Hähner, P., Moilanen P., Piipo J., Ripplinger S., Heftrich T., SCW facilities at JRC Petten – Past, Present and Future, The 5th Int. Sym. SCWR (ISSCWR-5), Vancouver, British Columbia, Canada, March 13–16, 2011.
13. Moilanen, P., Novotny, R., Hähner, P., Holmström, S., Pneumatic Powered Testing for Testing in Real and Simulated Service Environments, 2nd Joint IAEA-EC Topical Meeting on Development of New Materials for Advanced Fission and Fusion Reactor Systems, Book of abstracts, JRC Ispra, 16–20.4.2012, 80
14. 1. V. N. Leonov, Design and safety report – material testing loop with lead coolant, Closed Joint Stock Company, Moscow, 2011 “Resources & Technologies”
15. Nilsson, K-F, Martin O., Chenel-Ramos, C., Mendes, The segmented expanding cone-mandrel test revisited as material characterization and component test for fuel claddings. *J., Nucl. Engng. Design*, 241, (2011), 445–458.

30 years of nuclear structural integrity – Lessons learned and proposals for future directions

C. Faidy

Consultant
Claude.faidy@gmail.com
Lyon, France

Abstract

During the past 30 years, many aspects of technical progress have been accomplished. Nevertheless, different issues of degradation have been discovered on different nuclear plant components. This paper will review shortly both technical improvements and major events in order to propose recommendations in term of Gaps and Needs for future projects.

The key words remain: Anticipation, Competences, Safety Culture and Knowledge transfer.

1. Introduction

Pressure Equipments are extremely important in term of:

- Security of workers and population
- Safety of sensitive installations
- Environment
- Cost consequences

Important Progress have been done in the past 30 years

- Better design and material selection
- Better fabrication procedure and end of fabrication examination
- Better consideration of operating conditions integrated at design level
- Better surveillance in operation
- Better QA

Nevertheless, continuous attention is required and field experience has to be clearly understood. Continuous knowledge acquisition remains necessary to understand the margins.

Pressure Equipments, like Vessels and heat exchangers, including tube bundles, Piping systems, Valves and Safety valves, Some pumps and their supports and their internals are particularly important for safety and security.

Some added information can play a role in the prediction of behaviour: fluids: inside / outside, pressure and temperature (and flow rate) / Volume, External / Internal hazards like seismic/ explosion / flooding / tornados...

Metallic and non-metallic material can be encountered. Civil engineering and electrical components are outside the scope of this paper.

Different failure modes have to be considered, like: gross plasticity, (excessive deformation), burst (plastic instability), rupture (brittle / ductile), buckling (elastic or elastic-plastic instability) or creep rupture.

Different degradation mechanisms have to be considered, like: fatigue (LCF / HCF) and fatigue-ratcheting, corrosions and stress corrosions, thermal ageing and radiation embrittlement, wear...

The general safety objectives are: integrity, operability / functional capability, Leak before break/ Break exclusion / Incredibility of failure.

2. Major technical events in the past 30 years...

- Finite Element Method
- Linear Fracture Mechanic
- Standardized tests for material properties
- Elastic-plastic fracture mechanic
- Local Approach of fracture
- Multi-scale analysis of damages
- Many degradation mechanism analyses / research programs
- Dynamic analysis / Fluid Structure Interaction
- Reliability Analysis
- Field experience collection and analysis
- NDE progress
- Best practice documents / Rules / Codes & Standards
- Quality assurance.

3. Some important Nuclear Industry field experience

- PWR vessel safe fabrication: Marshall report
- Radiation embrittlement of RPV beltline
- Underclad cracks in nozzle and later in vessel shell beltline
- Thermal sleeve release
- Thermal Ageing of cast duplex stainless steel : elbows and valves
- SG tube corrosion
- Pressurizer penetration
- DMW defect / dilution / corrosion
- IASCC of Reactor Vessel Internal baffle bolts
- Leak in RPV head penetration and recently cracks in bottom head
- Nozzle bore vibration
- HRS high cycle fatigue and leak

- Farley, Tihange, Dampierre dead legs: high cycle fatigue
- Stratification in AFWS and Surge Line: fatigue and ratcheting
- PWSCC of Ni-based alloys: SGT, divided plate, penetrations (top-CRDM and bottom-BMI), DMW, radial keys...
- Buckling of vessels
- FAC on FWS
- BWR SCC piping and later internal / BWR: high cycle thermal fatigue in tees
- Large seismic event on aged plant (more than 40 Years of operation...)
- Late discover of hydrogen cracking of RPV forged shells.

4. Piping data bank (OCDE-OPDE)

This databank of piping experience based today on more than 4000 events in the world is a 1st tool to analyse field experience and confirm [Table 1] the extremely limited number of pipe failure, a large number of small bore vibration and a large number of Flaw Accelerated Corrosion events. These 2 degradation mechanism are now under control through surveillance and ISI program, associated with prediction models. The fatigue degradation is limited and thermal fatigue extremely limited.

Table 2 and 3 present the different locations potentially affected respectively to corrosion and to fatigue degradation.

<i>from OPDE-OCDE data bank</i>		Number of Database Records by Failure Type		
Degradation / Damage Mechanism		Non Through Wall Crack / Wall Thinning	Active Leakage	Structural Failure
Corrosion (incl. Crevice corrosion, pitting, galvanic corrosion, microbiologically induced corrosion)		45	272	5
Design, construction & fabrication errors		79	239	9
Erosion-corrosion & flow accelerated corrosion		190	327	50
Stress corrosion cracking (incl. ECSCC, IGSCC, PWSCC, TGSCC)		837	273	0
Thermal fatigue (incl. Thermal stratification, cycling and striping)		62	63	3
Vibration fatigue		60	810	48
Other (incl. Erosion-cavitation, severe overloading/ water hammer, strain induced corrosion cracking (SICC), classification pending)		48	147	44
Total		3611	2131	159
%		37	59	4

Table 1. OPDE synthesis table based on 3600 events.

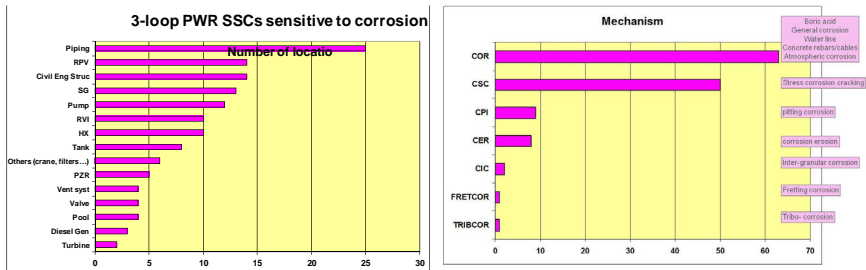


Table 2. Corrosion review of typical PWR plant.

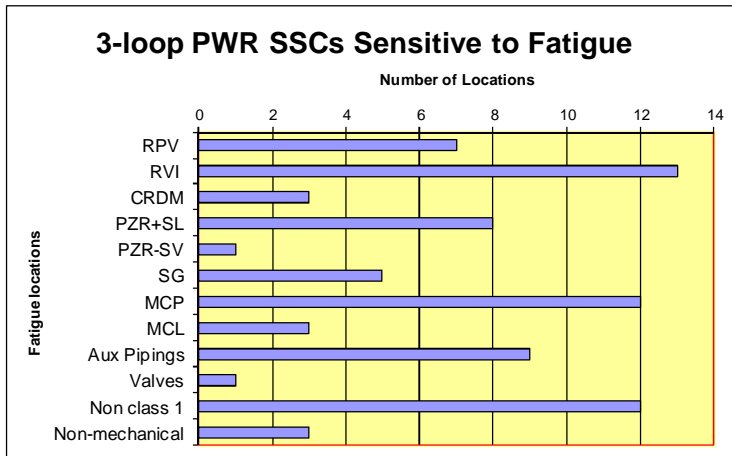


Table 3. Fatigue review of typical PWR plant.

5. Ageing Management Program (AMP)

All plant users develop an Ageing Management Program to assure Safety, Security and Availability of Systems, Structures and Components (SSC). The major aspects of an Ageing management program are presented Table 4.

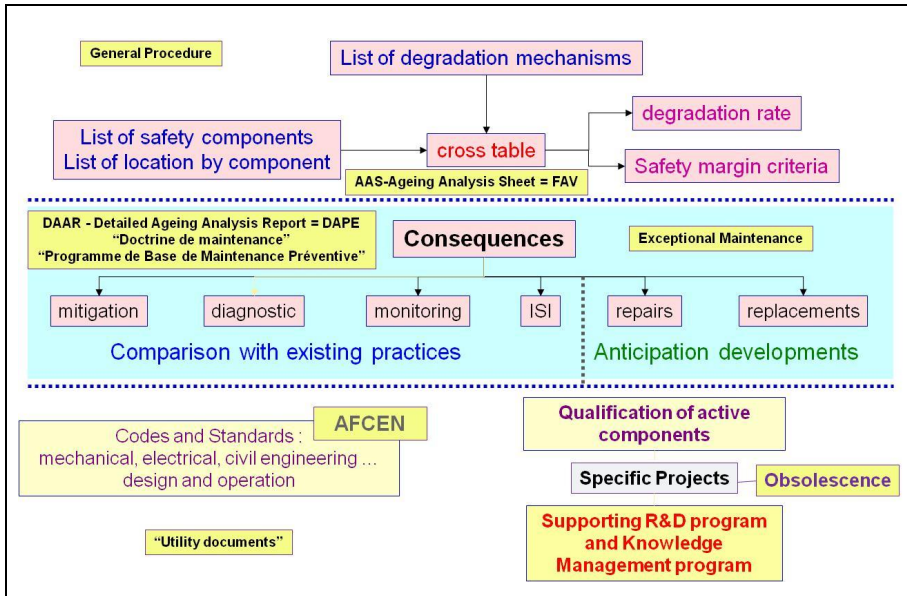


Table 4. General chart of an AMP.

6. Degradation mechanisms

6.1 General considerations

The major task is to list and understand the major degradation mechanisms that reduce the failure mode margins like cracks, thinning, lost of material properties. For each of these degradation mechanisms it's necessary to develop the key parameters, some models associated to the corresponding material properties to make predictions and to define surveillance, monitoring, mitigation and in-service inspection.

Two major degradation mechanisms are considered in PWR: Fatigue and Corrosions.

Two major failure modes are plastic instability and brittle/ductile failure, including EOL material properties affected by radiation embrittlement and thermal ageing.

Models and analytical methods can be strongly affected by Standard material data and transferability to structure.

Uncertainties and safety margins are the last decisions in accordance with knowledge level and safety or security concerns.

A constant review of international state of the art is necessary associated to focused R&D programs in order to increase uncertainty appreciation.

Codes and Standards, associated to Knowledge based data banks: CAPCOV, OPDE, SCAP, CODAP... are important tools to develop prediction and root cause analysis for better future prediction.

Best practice document associated to "Method Verification" and "Validity limits" are also essential tools for support decision process.

sigle	mechanism	domain	sigle	mechanism	domain
ABR01	General abrasion	All materials	FAT01	Fatigue	Ferritic / austenitic steels
CAR01	Carbonatation	Concrete	FAT02	Vibration fatigue	All material
CER01	Erosion-Corrosion (FAC)	Carbon and low alloy steels	FAT03	Fatigue corrosion	Carbon and low alloy steels
CIC01	Intercristallin corrosion secondary w ater	Alloy 600 tubes	FAT04	Environmental fatigue	All steels
CIC02	Intercrystalline corrosion	Austenitic Stainless Steels	FLA01	Buckling	All materials
COR01	Boric acid corrosion	Carbon and low alloy steels	FLU01	Radiation creep	Austenitic Stainless Steels of RV1
COR02	Corrosion concrete rebars	Reinforced concrete	FSI01	Radiation embrittlement	Low alloys RPV steels
COR03	Boric acid corrosion	Stainless steels	FSI02	Radiation embrittlement	Austenitic Stainless Steels of RV1
COR04	Waterline corrosion	All Steels	GOND1	Swelling	Irradiated stainless steels (RV1)
COR05	General corrosion	All materials	HYD01	Hydrolyse	Composite piping
COR06	Atmospheric corrosion	Ferritic/ austenitic DMW interface	INS01	Gross plasticity - Plastic collapse	All steels
CPI01	Pitting corrosion	Carbon and low alloy steels	POL01	Ageing of Polymers	Polymers under nominal env.
CPI02	Pitting corrosion	Stainless steels	POL02	Ageing of Polymers	Sheath and insulator of cables "hot points"
CSQ01	PWR stress corrosion	Ni-based alloys type 600	POL03	Ageing of Neopren	Anti-vibration devices
CSQ03	PWR stress corrosion	Nickel based alloy w elds 82-182	RA G01	Alcali-réaction	Concrete
CSQ04	PWR polluted water stress corrosion	Austenitic Stainless Steels	REL01	Cable pre-stress relaxation	Pre-stressed concrete
CSQ05	PWR stress corrosion	Cold worked Austenitic Stainless Steels	RET01	Shrinkage	Pre-stressed concrete
CSQ06	Nominal PWR water stress corrosion	Carbon and low alloy steels	RUP01	Brittle fracture	Carbon, low alloy and martensitic steels
CSQ07	Nominal PWR water stress corrosion	Austenitic Stainless Steels	RUP02	Brittle fracture	Carbon and low alloy steels
CSQ02	Secondary stress corrosion	Austenitic Stainless Steels	TAS01	Settlement	Ground
CSQ08	PWR stress corrosion	Ni-based alloys type 750	USU01	General wear	All materials
CSQ09	Irradiated Stress Corrosion cracking (IASCC)	Austenitic Stainless Steels of RV1	USU02	Shock and sliding wear	Core instrumentation thimble
DEC01	Ductile tearing	Alloy steels	VIE01	Ageing	I & C
DEC02	Ductile tearing	Cast austenitic duplex stainless steel	VTH01	Thermal Ageing	Carbon and low alloy steels
DEC03	Ductile tearing	Austenitic Stainless Steels of RV1	VTH02	Thermal Ageing	Martensitic stainless steels
DEF01	Plastic Shakedown	All steels	VTH03	Thermal Ageing	Austenoferritic duplex cast stainless steels
ECA01	Erosion Cavitation	all steels	VTH04	Thermal Ageing	DMW - dilution / interface area
ERO01	Erosion	All materials	VTH05	Thermal Ageing	Stainless steel w elds

Table 5. Typical example of list of degradation mechanisms considered on PWR.

6.2 Fatigue

Fatigue due to cyclic loads with or without cracks for different environments is a major issue. The models are based on S-N curves for initiation and $da/dN-\Delta K$ for crack growth. In both domains, due to the number of influencing parameters many open points remain:

- Ke-Kv and material cyclic curves
- key reduction factors of mean curve for fatigue life evaluation
- synergy versus / independency of detrimental effects (surface finish, mean stress, biaxiality, cold work, temperature, environmental, strain history...)
- consequences of low strain rate effects and environmental aspects for vessel/piping/valve (NUREG 6909 developed in USA).

Fatigue crack propagation is also associated to open points:

- residual stresses and mean stress (R ratio), elastic negative K
- rise time and hold
- dynamic loads, like large seismic loads.

Material property needs for all materials (base metal and welds), at different temperature, for different ageing levels: cyclic stress/strain curve, S-N in air mean / design, environmental effects: Fen

The transferability of isothermal triangular signal on small specimen to thermal cycles on structures remains associated to questions, including detrimental effects: surface finish, mean stress/ mean strain...

6.3 Stress corrosion cracking: Ni based alloys and welds (In 600-690; Alloys 82-182; 52-152)

A particular material has been discovered sensitive to PWR water and has developed a lot of degradation on base metal like steam generator tubes or on associated welds like dissimilar welds.

Locations concerned are: SGT, SG divided plate, CRDM penetration, RPV BMI, RPV radial keys and a lot of nickel based alloy DMW (182 weld metal)...

6.4 Loss of material by Flaw Accelerated Corrosions (FAC...)

This is causing major burst events of carbon steel pipe (with no major predictive information just before the burst...). Consequently a large surveillance program is implemented on many plants associated to different prediction models of thinning rate and maximum allowable thinning criteria: selection of potential areas through models and field experience, degradation rate through models and field experience, consequences of the thinning on other degradation mechanism like fatigue. The failure mode is mainly plastic instability, but possible crack rupture or buckling can be encountered.

The major locations concerned are feed-water system, BOP (not safety class).

6.5 Rupture

Different mechanisms can be encountered depending of material, temperature and radiation embrittlement.

6.5.1 Brittle

- Model/method : $K_{cp} < K_{IC}$

- K_{cp} method conservatisms recommendations for direct evaluation by FEM
 - Transferability of K_{IC} : plasticity, crack size and constraint effect
 - Method and criteria for decreasing K and WPS
 - Crack arrest: defense in depth
 - Residual stresses and their evolution in operation
- Material properties
 - $K_{IC} = f(T - RT_{NDT})$ or other correlation ($T - T_0$)
- Uncertainties and validation of KIC curves for different materials, heterogeneity consequences
 - Transferability CT / structures: different mock ups, different thicknesses, different crack length
 - Thermal ageing/ Radiation embrittlement: RT_{NDT} shift
 - BM / HAZ / Weld/ Clad area
- Locations concerned: RPV beltline and nozzle corners, PZR beltline and nozzles.

6.5.2 Ductile

- Model / Methods : $J < J_{0.2mm}$ or $J < J_{Da}$ and $dJ/da_{applied} < dJ/da_{material}$
- J estimation scheme through reference stress for simple/complex geometries
 - Welds, HAZ, DMW
 - Transferability CT to structure
 - Recommendations for J direct evaluation through EP FEM
 - Background to neglect residual stresses and secondary stresses over certain toughness level
- Material properties
 - Today : $J_{0.2mm}$ is a conservative min material property
 - Comparison on tests: toughness of CT with other specimens and structures
 - Thermal ageing effects : over 320°C
- Location concerned: RPV, PZR, RCP, SG, piping welds and DMW, cast material.

6.5.3 High toughness material: Ni based alloys, forged SS ...

When the toughness level is high the component failure mode appears over the plastic collapse limit load; and it's not necessary to develop fracture mechanic analysis. A threshold criterion is needed, for example $J_{IC} > 150 \text{ KJ/m}^2$ for stainless

steel welds. In this case, there are no consequences of "secondary" stresses in the analysis.

To develop this threshold, material properties are needed in term of toughness « valid » test in order to confirm use of plastic collapse load.

6.6 Residual stresses

Residual stresses are frequently associated to different degradation mechanisms, like: corrosion, brittle fracture or mean strain effects in fatigue.

Reduction of residual stresses needs to improve fabrication procedure.

Numerical / Experimental programs on representative components / welds are in progress in different organizations at R&D level and have to be considered more at fabrication level. The consequences of cracks in high residual stress area are an important issue for integrity of different components for long term operation: dissimilar metal welds, alloy 182, cast material, butt welds, penetration welds...

7. Uncertainties and safety margins

Safety factor on loads is a traditional approach for pressure equipments. Is it an optimum idea to use same SF for mechanical, thermal loads and residual stresses? Bending and membrane stresses?

Today in France, with a defect, SF factors are plastic instability SF reduced by 20%: 2.5 → 2 for level A, 2.0 → 1.6 for level C and 1.1 → 1.2 for level D on crack initiation with limited propagation for level D.

Consideration of uncertainties and probabilistic approaches are more and more used, based on statistical analysis of data, characteristic value of parameters and set of partial SF is proposed in RSEM.

Different other projects are based on similar considerations, like: LB-LOCA re-definition, Break Exclusion/IOF (Incredibility Of Failure) of some class 1 components.

8. Codes and standards

8.1 Generalities

A Code is a standard that has been adopted by "governmental bodies" or that is cited in a "contractual agreement" and has the "force of law".

A Standard is a set of technical definitions, requirements and guidelines that have been developed by industry, so corresponding items can be manufactured, operated and evaluated uniformly providing for safety and interchangeability.

Finally C&S: a Set of tools to assure Safety, to optimize Construction and Operation, to assure Life and Replaceability of Components.

C&S are extremely important:

- to contribute to discussion with Safety Authority/Regulator
- to facilitate contractual agreement between owner / vendor – manufacturers
- to harmonize international suppliers.

8.2 Major requests to Codes and Standards

- High safety level through deterministic / probabilistic safety analysis
 - including internal/external hazard considerations
 - including severe accident considerations as design basis
- Large availability factor / Short refueling shutdown :
 - consider potential degradation in operation at design level
 - optimized ISI and maintenance of structures & components
- Low radiation exposure of workers (ALARA)
 - choice of material and fabrication processes
 - ISI and maintenance optimize at design level
- Consideration of new regulation / new standards
 - nuclear = non-nuclear + complementary requirements
 - use of international ISO or EC standards
 - accepted standards in many non-EC countries (China, India, Japan, Korea...)
- Fulfill the present State of the Art in term of
 - design rules and fabrication/ control processes
 - Surveillance, inspection, operation
- Large "open" world market
 - large number of potential manufacturers worldwide
 - harmonization / mutual recognition of rules.

8.3 International harmonization of Codes

7 countries develop "Nuclear Codes & Standards": USA, France, Japan, Korea, Canada, Russia and Germany (China has started an action in this direction). More exchanges and possible harmonization are on-going in different groups:

- OCDE-MDEP project with 10 international regulators
- SDO Convergence Board launch in 2012 to minimize future Code divergence and facilitate areas of convergence
- WNA-CORDEL Codes and Standards Working Groups with all the Nuclear Industry starts 2 pilot projects: non linear analysis at design level and NDT

personal qualification with an objective of international harmonization through detailed review of existing Codes methods, issuance of best practice documents to be included in the different codes, after regulators (MDEP) comments if necessary.

9. Conclusion and proposal

AMP of complex plants is a key safety issue and needs a global approach based on Diagnostic, Mitigation, Monitoring, ISI and Repair/ Replacement capabilities under an anticipation process. It is to be integrated at design level, associated with detailed operating condition description.

An R&D support is needed on mechanisms and key parameters, models and associated material properties, margins through uncertainty management (statistic/probabilistic); from fundamental R&D (multi-scale), to applied R&D (local approach) to practical codified rules (RSEM, R6...). A major open question remains margins in transferability from "standard specimen" to "structure".

Knowledge base databanks with collection of field experience, analysis, lessons learned and consequences on rules (CAPCOV, OPDE, SCAP, CODAP...) and benchmarking associated to detail analysis of results are efficient tools to progress.

Regular update of Codes & Standards / Rules / Best practice documents around harmonization and international cooperation; with easy access to databanks and background documents are required.

The key words to assure Safety, Security and Competitiveness are: Anticipation, Competences, Safety Culture and Knowledge transfer.

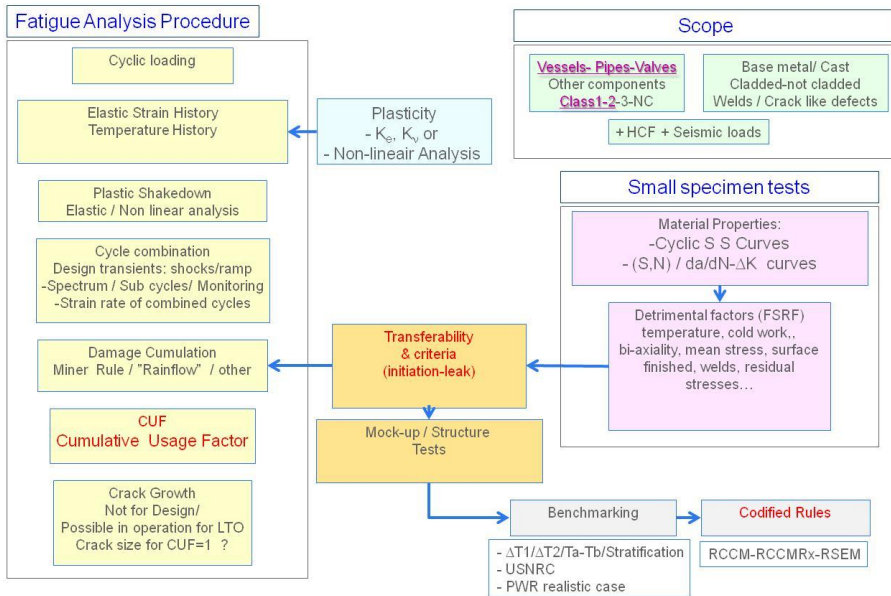


Table 6. General chart for fatigue analysis.

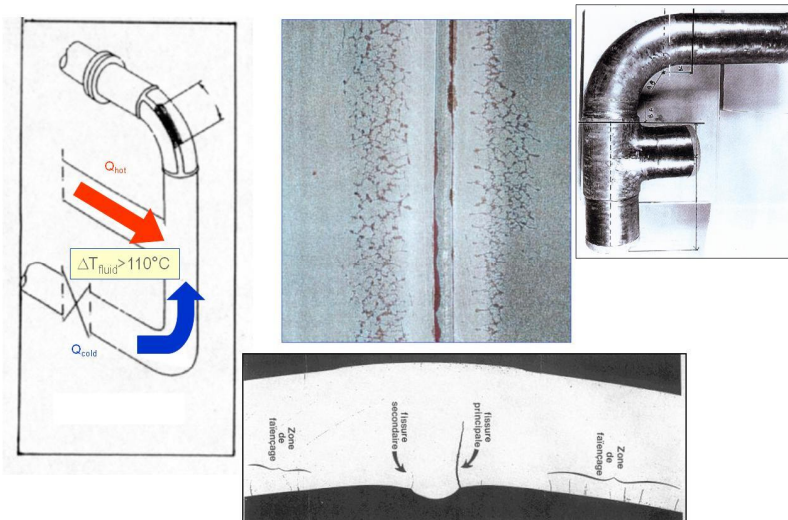


Figure 1. High Cycle Fatigue (HCF) in mixing tees.

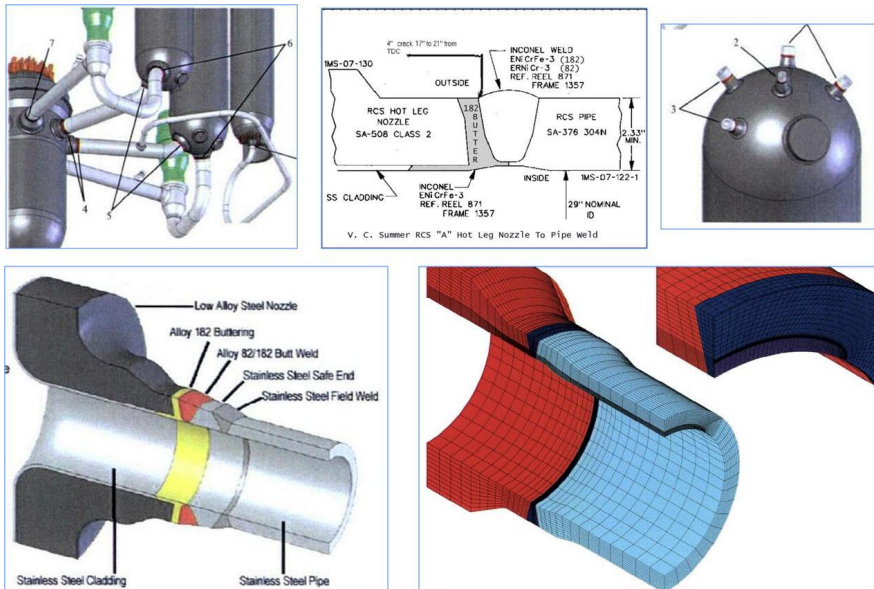


Figure 2. Dissimilar welds.

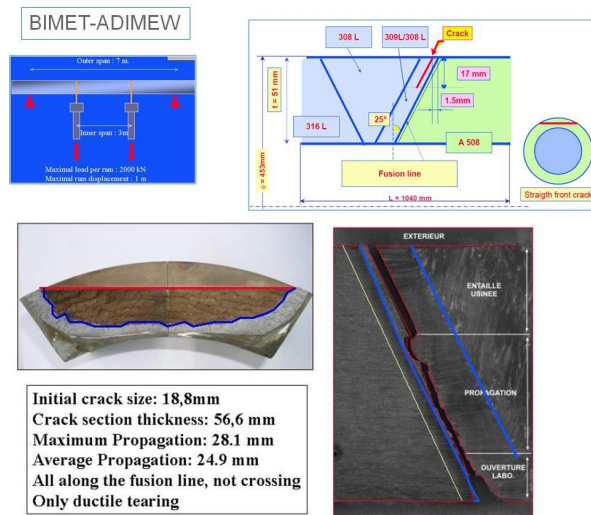


Figure 3. Cracked Dissimilar Metal Weld (DMW) 4-point bending tests.



Figure 4. Vessel buckling.



Figure 5. Davis Besse RPV penetration.



Figure 6. MIHAMA Flow Accelerated Corrosion.

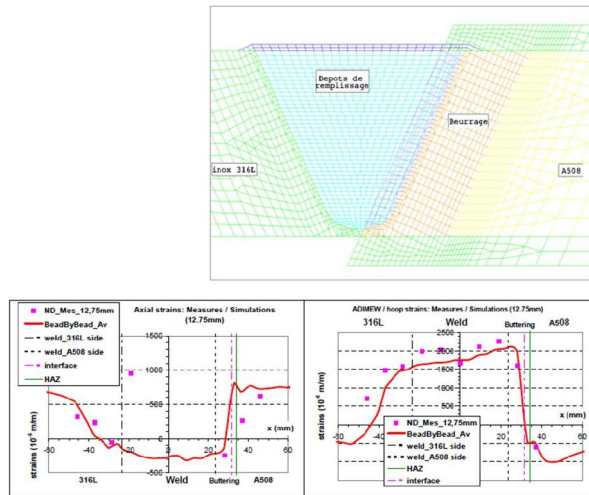
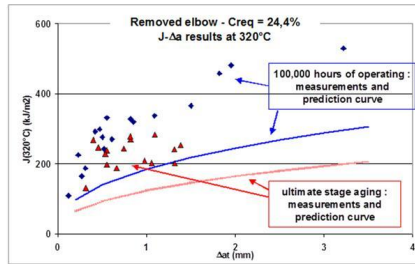
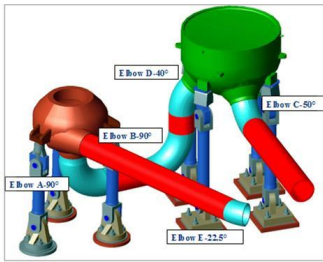


Figure 7. Comparison of strain predictions with ND measurements in the ADIMEW mock-up

Figure 7. Dissimilar weld residual stresses- comparison measurements-computation.



- Diagnostic based on equivalent chromium content $\%Cr_{eq} = \%Cr + \%Si + \%Mo$ max: 23.5%
- Material properties versus time-temperature- $Creq$
- Fracture mechanic analysis of cracked elbows
- Large scale tests
- Sample from real elbows
- Replace one elbow

- Monitoring through TEP ThermoElectricPower
- ISI techniques: RT and many others are tested
- repair : impossible
- Replacement: few elbows for 60 Y of operation

Figure 8. Cast austeno-ferritic elbows.

Forecast reliability of embrittlement trend curves for Swedish nuclear reactor pressure vessel steels

C. Larsson¹, M. Molin² & NE Hannerz³

¹Welding Technology, Royal Institute of Technology
Stockholm, Sweden

²Forsmark Kraftgrupp AB
Östhammar, Sweden

³Welding Technology, Royal Institute of Technology
Stockholm, Sweden

Abstract

Many nuclear reactor pressure vessels world-wide are ageing, which means that for an approval of lifetime extension, their resistance to failure by brittle crack propagation due to irradiated induced material embrittlement must be assessed. There are two ways to make such an assessment, by material testing of irradiated surveillance specimens and by empirical derived models for embrittlement trend prediction. In Sweden the situation concerning ageing nuclear power plants is the same and therefore an evaluation of already established as well as newly developed embrittlement trend curves (ETCs) is performed. From this evaluation it can be concluded that all evaluated ETCs yield global non-conservative transition temperature shift prediction with respect to base and weld metals. Locally, the embrittlement predictability of base metal is generally superior to weld metal and where four ETC models yield satisfactory base metal prediction. The embrittlement predictability can however be improved by applying a fitness-for-purpose approach using actual surveillance data for ETC modelling. For that purpose one established model is applied and in addition two new models of similar kind have been developed to improve the forecast reliability of the embrittlement trend for Swedish nuclear reactor pressure vessel steels.

1. Introduction

Today the lifetimes of many nuclear reactors world-wide are getting closer to their operating license limits and for that reason some nuclear power plants are considering applying for exemption of lifetime extension. This fact makes it important to assess whether the reactor pressure vessels (RPVs) are robust enough to withstand irradiation in a neutron fluence range covering long term operation ranges of

50 to 80 years lifetime, including power uprates in some cases. In Sweden there are no defined operating license limits but for an approval of lifetime extension from the governing public authority, the RPV steel status with respect to irradiation induced material embrittlement must be assessed. Such an assessment requires an implemented surveillance program and solid forecasting models. The reason for assessing the robustness of RPVs is to secure their integrity with respect to failure by brittle crack propagation, which would have fatal human, environmental, and economical consequences.

In the nuclear power industry, surveillance specimens made of the same material as the RPV are installed in capsules within the RPV to enable testing of certain mechanical properties during its lifetime. However, due to the limited number of deposited surveillance specimens, these tests are performed with several years interval. It is therefore for reason of assessing the structural integrity of operating RPVs of great interest to understand and model the RPV steel embrittlement process, which obviously is a knowledge of crucial importance in the material optimization when designing new nuclear RPVs.

Until now Swedish nuclear power plants have relied to the embrittlement trend curve (ETC) in the U.S. Regulatory Guide 1.99-revision 2 [1] for predicting the transition temperature shift (TTS) of the RPVs. The Reg. Guide 1.99-rev. 2 has however become obsolete due to research progress in understanding the embrittlement mechanisms and due to an extended data base for model development. These advances make it interesting to evaluate the reliability of the Reg. Guide 1.99-rev. 2 and some recently proposed ETC models on the Swedish RPVs. The present evaluation include eight models, Reg. Guide 1.99-rev. 2 [1,2], FIM and FIS [3], JEAC4201-2004 [4], ASTM E900-02 [5], EONY [6], FIM-rev. 1 [7], and WR-C(5)-rev. 1 [8].

2. Modelling Charpy V-notch impact toughness data

Nuclear power plants must account the effect from irradiation damage in four situations [9], ¹)when assessing the ability of the RPV to resist fracture during postulated accident scenarios, such as pressurized thermal shock, ²)when assessing the ability of the RPV to resist fracture during routine heatup, cooldown, and hydrotest conditions, ³)when determining which material samples need to be included in a surveillance program for the RPV beltline, and ⁴)when assessing the ability of the RPV to continue safe operation in the presence of flaw detected during either pre- or in-service inspection.

For assessing the fracture resistance and the level of degeneration in irradiated RPV materials, surveillance testing of small irradiated Charpy V-notch (CVN) samples is performed on regularly basis as regulated by public authority. Three different measurement of the fracture resistance are thereafter collected, which are ¹)impact energy (KV), ²)lateral expansion (LE), and ³)the fraction ductile fracture surface. In general the ETC models [1,4–6,8] use only KV as measurement and predicts the TTS at 41 J (ΔT_{41J}). The French ETC models use however both

KV and LE as measurements and predicts the TTS at the maximum [3] or mean [7] values of KV at 56 J (ΔT_{56J}) and LE at $8.9 \cdot 10^{-4}$ m ($\Delta T_{0.89mm}$), i.e. $\max[\Delta T_{56J}, \Delta T_{0.89mm}]$ or $\text{mean}[\Delta T_{56J}, \Delta T_{0.89mm}]$.

To enable a systematic way of predicting transition temperatures from CVN impact toughness (CVT) data several curve fit algorithms are developed [6,10–14]. A compressed example of describing all CVT data obtained from one surveillance capsule using different algorithms is shown in Figure 1. Figure 1 includes the symmetric and asymmetric hyperbolic tangent (tanh) KV/LE algorithms [6], the WCM KV/LE algorithm [11], the modified tanh KV/LE algorithm [14], the combined exponential and tanh KV/LE algorithm [14], and the symmetric tanh crystallinity algorithm [14]. Crystallinity is in this respect a measure of the fraction brittle fracture surface, i.e. the remaining fracture surface after the fraction ductile fracture surface is defined.

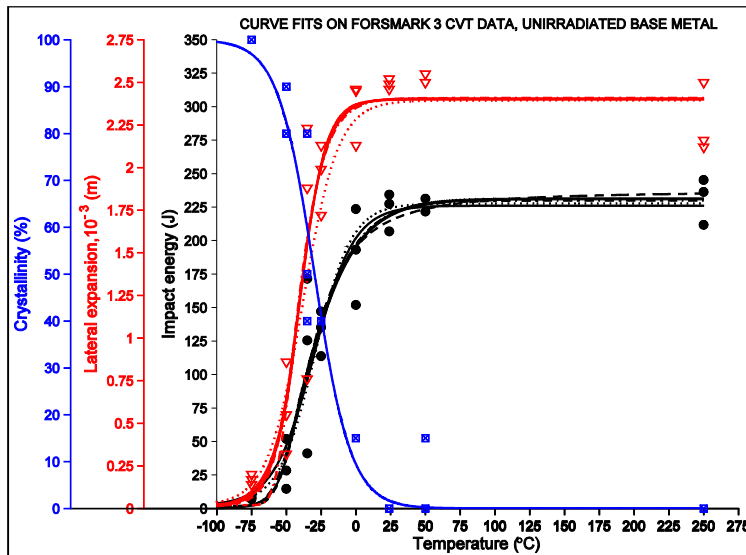


Figure 1. Example of curve fits on CVT data (KV, LE, crystallinity).

For nuclear power plants in Sweden the symmetric tanh algorithm is commonly used for fitting the KV and LE surveillance data. However, as discussed in earlier research reports [6,14], the most suitable curve fit algorithm depends on the characteristic of the data set and the extent of available data. In the present paper two approaches are applied. The first procedure uses only the symmetric tanh algorithm in the computer program for describing the KV and LE data sets. The second approach uses the procedure as outlined by Eason et al. [6], where the best curve fit (i.e. minimum sum of squared residuals) of either the symmetric tanh algorithm or the asymmetric tanh algorithm is automatically chosen. All data sets including the curve fits are thereafter plotted for control of the quality of each individual

curve fit and if necessary, due to obtained local minimum instead of global minimum, changing the guess (or start) data to improve the result. This last procedure is especially important due to the nonlinearity in the asymmetric tanh algorithm. Figure 2 illustrates the gradual embrittlement of a irradiated RPV steel and where the second approach is applied for finding the sought transition temperatures.

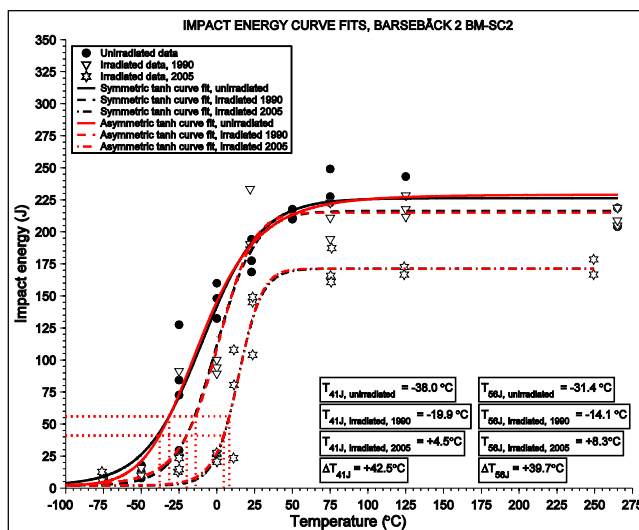


Figure 2. Transition temperature shifts for Barsebäck 2 (shutdown), shell course 2.

The asymmetric tanh algorithm gives in general better fitting when compared with the symmetric tanh algorithm [6]. However, in some cases the symmetric tanh algorithm was preferred before the asymmetric tanh algorithm, although the sum of squared residuals was higher, since it in these cases resulted in a more realistic and conservative description of either the lower or the upper energy level in scarcity of data at these energy levels. Furthermore, in some other cases both these algorithms gave an unrealistic description of the upper shelf energy due to lack of upper energy data at high temperatures. In these cases a bimodal algorithm was used, exponential in the lower part of the curve and hyperbolic tangent in the upper part [14]. Although it is possible to optimize each data set using different fitting algorithms, with respect to the sum of squared residuals and the realism of the whole curve, it can still be concluded that the differences between these algorithms with respect to the sought transition temperatures are not large enough to change the general reliability of a specific ETC model.

As already mentioned, the French ETC models use an approach which includes TTS for both KV and LE and where a linear correlation between T_{56J} and $T_{0.89mm}$ is demonstrated [15]. Figure 3, completed with upper and lower bounds of $\pm 10\text{ }^{\circ}\text{C}$, verifies that this correlation is valid also for Swedish RPVs by showing the correlation between ΔT_{56J} and $\Delta T_{0.89mm}$.

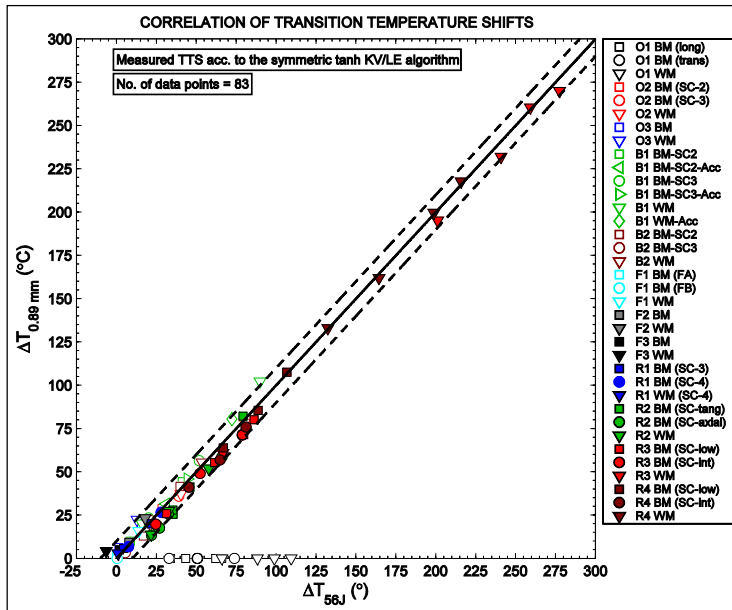


Figure 3. Correlation of transition temperature shifts (some early surveillance data sets lack LE data).

A generalized KV lower shelf is fixed to 2 J after recommendations by Wallin and Nevasmaa of 2 J [13] and by Eason et al. of 1.28 ft-lbs = 1.74 J [6]. Recommendations of a generalized LE lower shelf (LE_{LS}) are harder to find and therefore two approaches have been used to evaluate this matter.

1.1 2.1 Evaluation of LE lower shelf

Sreenivasan [16] developed a model where LE can be estimated by knowing the KV data and the material yield strength for specific temperatures. The Sreenivasan model gives good estimations in the transition area of the LE temperature curve but its usability in the lower shelf area is worse due to a steep gradient (Figure 4).

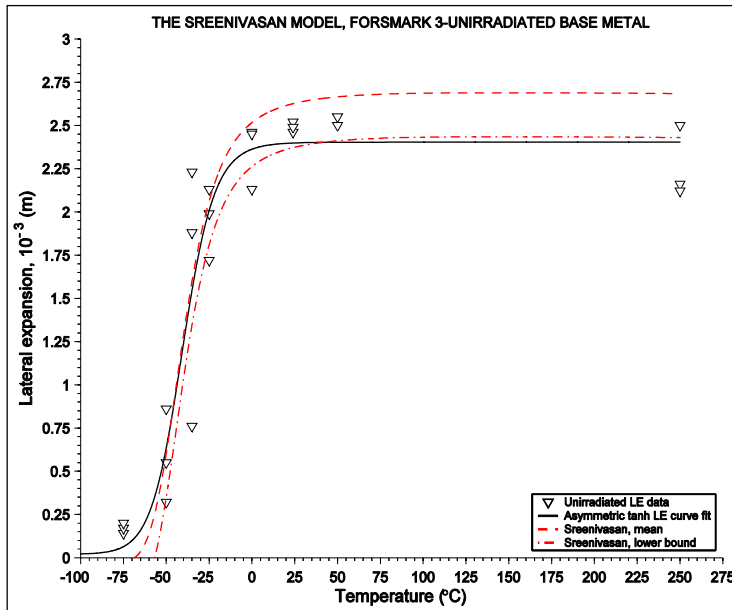


Figure 4. Evaluation of the generalized lateral expansion model according to Sreenivasan.

A way of solving the problem with finding a suitable LE_{LS} is by assuming that the proportions between the lower and upper shelves are equal for the KV and LE data sets. This approach makes it possible to solve for LE_{LS} by performing a least square fit of the KV data as a first stage, which gives the quotient KV_{LS}/KV_{US} . Thereafter a least square fit of the LE data set is performed which is constrained by the equation $LE_{LS}/LE_{US}=KV_{LS}/KV_{US}$ and where LE_{LS} and LE_{US} are variables and where the quotient KV_{LS}/KV_{US} is constant. After evaluating the data sets of Forsmark 3 by using this procedure, it can be concluded that a generalized value within the range $LE_{LS}=1.5 \cdot 10^{-5}$ - $2.5 \cdot 10^{-5}$ m equals $KV_{LS}=2$ J, suggestively $LE_{LS}=2 \cdot 10^{-5}$ m. There are three options here. The first option is to use the above procedure for each KV and LE data sets, which makes the assumption of $LE_{LS}/LE_{US}=KV_{LS}/KV_{US}$ valid but gives a variation of LE_{LS} . The second option is that a generalized value is used for all LE curve fit procedures, which makes the assumption of $LE_{LS}/LE_{US}=KV_{LS}/KV_{US}$ invalid. The third option is that LE_{LS} is constrained between a minimum and a maximum value, e.g. $LE_{LS}=1.5 \cdot 10^{-5}$ - $2.5 \cdot 10^{-5}$ m. In the present paper the second option is chosen such that $LE_{LS}=2 \cdot 10^{-5}$ m.

3. Embrittlement trend curves

3.1 Regulatory Guide 1.99-revision 2

The TTS model in the Regulatory Guide 1.99-rev. 2 [1] is given by

$$TTS = CF \cdot \Phi^{0.28 - 0.10 \cdot \log(\Phi)} \quad (1)$$

The TTS unit is in degrees Fahrenheit (°F) and where division by 1.8 gives degrees Celsius (°C). The chemistry factor (CF) must be interpolated from specific tables [1]. The neutron fluence (Φ) in 10^{19} n/cm² (E>1 MeV) is valid within the range of $\Phi = 1 \cdot 10^{17} - 1 \cdot 10^{20}$ n/cm². The nominal irradiation temperature (T_i) is 288°C (550°F) but a temperature range of $T_i = 274 - 310^\circ\text{C}$ (525-590°F) is applicable. The material data base according to ASME applies to steel grades of SA 302, SA 336, SA 533, SA 508, and their welds and heat-affected zones. The chemical contents in weight percent (wt%) cover Cu=0-0.40 wt% and Ni=0-1.2 wt%, and due to the limitation of only table read-offs there is no possibility for extrapolation.

3.2 FIM

The FIM model is developed both for base and weld metals. It is given as [3]

$$TTS = [17.3 + 1537 \cdot (P - 0.008) + 238 \cdot (Cu - 0.08) + 191 \cdot Cu \cdot Ni^2] \cdot (\Phi / 10^{19})^{0.35} \quad (2)$$

The TTS unit is in °C. The neutron fluence (Φ) varied between $\Phi = 3 \cdot 10^{18} - 8.3 \cdot 10^{19}$ n/cm² (E>1MeV) and $(Cu - 0.08) = 0$ if $Cu < 0.08$ wt% and $(P - 0.008) = 0$ if $P < 0.008$ wt%. The material data base was mainly based on test reactors data and it was oriented towards forgings in Mn-Ni-Mo steel (ASME SA 508 class 3) and associated welds. The chemical composition validity ranges are Cu=0.020-0.185 wt%, Ni=0.08-1.85 wt%, and P=0.005-0.021 wt%.

3.3 FIS

The FIS model is the upper bound of the FIM model. This model is for that reason not comparable with the other ETC models described in this section since these models are designed to yield best (or mean) fits. It is still evaluated in the present paper and is given as [3]

$$TTS = 8 + [24 + 1537 \cdot (P - 0.008) + 238 \cdot (Cu - 0.08) + 191 \cdot Cu \cdot Ni^2] \cdot (\Phi / 10^{19})^{0.35} \quad (3)$$

The prerequisites are described in Section 3.2.

3.4 JEAC4201-2004

The JEAC4201-2004 model is designed to predict the TTS for base and weld metals in the Japanese reactors and is expressed with the following equations [4]

$$TTS_{BM}=[CF]\cdot[FF]_{(f)}=[-16+1210\cdot P+215\cdot Cu+77\cdot(Cu\cdot Ni)^{0.5}]\cdot\Phi^{0.29-0.04\cdot\log(\Phi)} \quad (4)$$

$$TTS_{WM}=[CF]\cdot[FF]_{(f)}=[26-24\cdot Si-61\cdot Ni+301\cdot(Cu\cdot Ni)^{0.5}]\cdot\Phi^{0.25-0.10\cdot\log(\Phi)} \quad (5)$$

The TTS unit is in °C. The neutron fluence (Φ) in 1019 n/cm² (E>1 MeV) is valid within ranges of $\Phi=1\cdot 10^{18}$ - $12.9\cdot 10^{19}$ n/cm² and $\Phi=1\cdot 10^{18}$ - $11.9\cdot 10^{19}$ n/cm² for base metal and weld metal respectively. Ranges of chemical compositions for base metals are Cu=0.03-0.25 wt%, Ni=0.18-0.75 wt%, P=0.003-0.018 wt%, and Si=0.12-0.35 wt%. Ranges of chemical compositions for weld metals are Cu=0.014-0.36 wt%, Ni=0.05-1.08 wt%, P=0.007-0.023 wt%, and Si=0.16-0.68 wt%.

The JEAC4201-2004 model is completed with an adjusted chemistry factor. This factor can be used when more than two surveillance data are available, which in the present paper is interpreted as more than *or* equal to two surveillance data. This procedure divides it from ETC models developed in other countries since it function both as a design and a fitness-for-purpose tool. The adjusted chemistry factor is calculated by the following equation

$$[CF]_{adj}=\frac{\sum(\Delta RT_{NDT.meas})_i\cdot[FF]_{(f_i)}}{\sum[FF]_{(f_i)}\cdot[FF]_{(f_i)}} \quad (6)$$

where $(\Delta RT_{NDT.meas})_i$ is the measured shift in KV transition temperature at the *i*-th surveillance test, $[FF]_{(f_i)}$ is the fluence factor at a fluence of *f_i*, which is the fluence of the *i*-th surveillance capsule.

3.5 ASTM E900-02

The TTS model as standardized in ASTM E900-02 [5] is expressed as follows

$$TTS=SMD+CRP \quad (7)$$

The stable matrix damage (SMD) and copper-rich precipitation (CRP) terms are given by the following expressions

$$SMD=A\cdot e^{\frac{20730}{(T_i+460)}}\cdot\Phi_t^{0.5076} \quad (8)$$

$$CRP=B\cdot(1+2.106\cdot Ni^{1.173})\cdot F(Cu)\cdot[0.5+0.5\cdot\tanh((\log(\Phi_t)-18.24)/1.052)] \quad (9)$$

The irradiation temperature (T_i) and the TTS units are in °F. Factor A equals $6.70\cdot 10^{-18}$ and factor B is related to the product form (i.e. 234 for welds, 128 for forgings, 208 for Combustion Engineering (CE) plates and 156 for other plates). $F(Cu)$ is a copper term and where $F(Cu)=0$ if $Cu\leq 0.072$ wt% and $F(Cu)=(Cu-0.072)^{0.577}$ if $Cu>0.072$ wt%. The neutron fluence and neutron energy spectra are valid within the fluence (Φ_t) and flux (Φ) ranges of $\Phi_t=1\cdot 10^{16}$ - $8\cdot 10^{19}$ n/cm² (E>1MeV) and $\Phi=2\cdot 10^8$ - $1\cdot 10^{12}$ n/cm²/s (E>1MeV) respectively. The irradiation temperature is applicable for a temperature range of $T_i=260$ - 299 °C (500-570°F). The material data base according to ASTM covers the following steel grades: A533 Type B class 1, A302 Grade B, A302 Grade B (modified), A508 class 2-3, and their welds. The variation of the chemical contents are Cu=0-0.50 wt%, Ni=0-1.3 wt%, and P=0-0.025 wt%.

3.6 EONY

The EONY model [6] is an ETC model which includes data from the U.S. surveillance program and is expressed as follows

$$TTS=MF+CRP \quad (10)$$

The matrix feature (MF) and copper-rich precipitation (CRP) terms are given by the following expressions

$$MF=A \cdot (1-0.001718 \cdot T_i) \cdot (1+6.13 \cdot P \cdot Mn^{2.47}) \cdot (\Phi_{te})^{0.5} \quad (11)$$

$$CRP=B \cdot (1+3.77 \cdot Ni^{1.191}) \cdot f(Cu_e, P) \cdot g(Cu_e, Ni, \Phi_{te}) \quad (12)$$

The irradiation temperature (T_i) and the TTS units are in °F. Factor A is related to the product form (i.e. $1.140 \cdot 10^{-7}$ for forgings, $1.561 \cdot 10^{-7}$ for plates, $1.417 \cdot 10^{-7}$ for welds). Factor B is also related to the product form (i.e. 102.3 for forgings, 102.5 for plates in non-Combustion Engineering manufactured vessels, 135.2 for plates in Combustion Engineering manufactured vessels, 155 for welds). The effective neutron fluence (Φ_{te}) is dependent on both neutron fluence (Φ_t) and neutron flux (Φ) and where Φ_{te} and Φ_t are in n/cm^2 ($E>1$ MeV) and $n/cm^2/s$ ($E>1$ MeV). Here $\Phi_{te}=\Phi_t$ if $\Phi \geq 4.39 \cdot 10^{10}$ $n/cm^2/s$ and $\Phi_{te}=\Phi_t \cdot (4.39 \cdot 10^{10}/\Phi)^{0.259}$ if $\Phi < 4.39 \cdot 10^{10}$ $n/cm^2/s$. Cu_e is a copper term and where $Cu_e=0$ if $Cu \leq 0.072$ wt% and $Cu_e=\min[Cu, \text{Max}(Cu_e)]$ if $Cu > 0.072$ wt%. The upper Cu_e limit is fixed to $\text{Max}(Cu_e)=0.243$ for typical Linde 80 welds ($Ni > 0.5$ wt%) and $\text{Max}(Cu_e)=0.301$ for all other materials. Also $f(Cu, P)=0$ if $Cu \leq 0.072$ wt%, and $f(Cu, P)=(Cu_e-0.072)^{0.668}$ if $Cu > 0.072$ wt% and $P \leq 0.008$ wt%, and $f(Cu, P)=(Cu_e-0.072+1.359 \cdot (P-0.008))^{0.668}$ if $Cu > 0.072$ wt% and $P > 0.008$ wt%. The function $g(Cu_e, Ni, \Phi_{te})$ is given by

$$g(Cu_e, Ni, \Phi_{te})=0.5+0.5 \cdot \tanh[(\log_{10}(\Phi_{te})+1.139 \cdot Cu_e-0.448 \cdot Ni-18.12)/0.629] \quad (13)$$

The irradiation temperature is applicable for a temperature range of $T_i=272-299^\circ\text{C}$ ($522-570^\circ\text{F}$). The variation of the chemical contents are $Cu=0.01-0.41$ wt%, $Ni=0.044-1.26$ wt%, $P=0.03-0.031$ wt%, and $Mn=0.58-1.96$ wt%. The neutron fluence and flux cover $\Phi_t=9.26 \cdot 10^{15}-7.13 \cdot 10^{19}$ n/cm^2 and $\Phi=1.81 \cdot 10^8-9.71 \cdot 10^{11}$ $n/cm^2/s$, respectively.

3.7 FIM-revision 1

A discrepancy between the French FIM and FIS models, which were based mainly on test reactors data, and actual surveillance data motivated the development of a revised ETC model. The FIM-rev. 1 model [7] is expressed by the following equation

$$TTS=A \cdot [1+35.7 \cdot (P-0.008)+6.6 \cdot (Cu-0.08)+5.8 \cdot Cu \cdot Ni^2] \cdot (\Phi/10^{19})^{0.59} \quad (14)$$

The TTS unit is in °C. Factor A is related to the product form (i.e. 15.4 for forgings and SRM, 15.8 for welds). The irradiation temperature is valid within the range

$T_i=275-289^\circ\text{C}$. The neutron fluence (Φ) covers ranges up to $8 \cdot 10^{19}$ n/cm² ($E > 1$ MeV), and $(\text{Cu}-0.08)=0$ if $\text{Cu} < 0.08$ wt% and $(\text{P}-0.008)=0$ if $\text{P} < 0.008$ wt%. The material data base according to ASTM covers the steel grade A508 class 3 and its weld. The chemical contents are valid for $\text{Cu}=0.02-0.13$ wt%, $\text{Ni}=0.066-1.43$ wt%, $\text{P}=0.003-0.021$ wt%, $\text{Mn}=1.18-1.88$ wt%, and $\text{Si}=0.03-0.487$ wt%.

3.8 WR-C(5)-revision 1

The WR-C(5)-rev. 1 model [8] is a wide range ETC model which includes data from the U.S. surveillance program, non-U.S. surveillance programs, and test reactor irradiations. The model is expressed as

$$\text{TTS} = \max\{\min[\text{Cu}, 0.31] - 0.052, 0\} \cdot \text{M} + \text{B} \quad (15)$$

$$\begin{aligned} \text{M} = & [\text{M}_W = 1.073, \text{M}_P = 0.989, \text{M}_F = 0.675] \cdot \max\{\min\{\ln(\Phi) - \\ & \ln(1.151 \cdot 10^{17})\} \cdot 138.0, 613.3\}, 0\} \cdot (T_i/550)^{-4.22} \dots \\ & \cdot (0.433 + \text{Ni}^{1.78}/0.63)^{0.58} \cdot (0.1 + \text{P}/0.012)^{-0.105} \end{aligned} \quad (16)$$

$$\begin{aligned} \text{B} = & [\text{B}_W = 1.2, \text{B}_P = 1.315, \text{B}_F = 1.167] \cdot (9.335 \cdot 10^{-10} \cdot \Phi^{0.5503}) \cdot (T_i/550)^{-4.41} \\ & \cdot (0.12 + \text{P}/0.012)^{0.378} \dots \\ & \cdot (0.55 + \text{Ni}^{1.35}/0.63)^{0.42} \cdot (\text{Mn}/1.36)^{0.173} \end{aligned} \quad (17)$$

The irradiation temperature (T_i) and the TTS units are in °F. The neutron fluence (Φ) unit is in n/cm² ($E > 1$ MeV). The chemical contents are in wt%. The indexes W, P, and F stand for weld, plate, and forging, respectively.

4. Experimental data base

There are currently ten nuclear reactors operating in Sweden. The first reactor was of a boiling water reactor (BWR) type and started in 1972 in Oskarshamn (O1), which was followed by altogether eleven reactors separated by four power plants. These eleven reactors are located in Oskarshamn (O2, O3), Barsebäck (B1, B2), Forsmark (F1, F2, F3), and Ringhals (R1, R2, R3, R4). Of these reactors are R2, R3, and R4 pressurized water reactors (PWRs) and the rest BWRs. It should be noted that Barsebäck Units 1 and 2 were permanent shutdown in 1999 respective 2005 due to political issues. The RPV materials are steel of types A302B and A533B class 1 (ASTM), and SA 508 class 2–3 (ASME). Irradiation temperatures of $T_i=280^\circ\text{C}$ and $T_i=300^\circ\text{C}$ are consistently used for BWRs and PWRs respectively.

The reliability evaluation of the ETC models described in section 3 is performed on surveillance results obtained in the surveillance program of base and weld metals from all Swedish nuclear power plants, active or not. The chemical analyzes (copper, nickel, phosphorus, manganese), the number of surveillance results from each material, and the maximum fluence for each material are presented in Table 1.

Table 1. Chemical analyzes (wt%) of Swedish nuclear RPV materials.

Materials	Cu	Ni	P	Mn	No. of surv. results	Max. fluence 10^{18} (n/cm ²)
O1BM (long)	0.153	0.25	0.019	1.51	4	2.67
O1BM (trans)	0.164	0.21	0.009	1.53	4	2.67
O1WM	0.217	0.59	0.01	1.28	4	2.67
O2BM (sc-2)	0.11	0.605	0.011	1.365	2	3.50
O2BM (sc-3)	0.095	0.635	0.009	1.35	2	3.50
O2WM	0.06	1.60	0.008	1.66	2	3.50
O3BM	0.03	0.65	0.006	1.42	1	0.38
O3WM	0.04	1.48	0.016	1.21	1	0.38
B1BM (sc-2)	0.125	0.605	0.013	1.42	3*	0.88, 9.0*
B1BM (sc-3)	0.135	0.63	0.013	1.43	3*	0.88, 9.0*
B1WM	0.11	1.74	0.008	1.54	3*	0.88, 9.0*
B2BM (sc-2)	0.11	0.62	0.009	1.36	2	3.57
B2BM (sc-3)	0.10	0.625	0.012	1.395	2	3.57
B2WM	0.064	1.47	0.011	1.53	2	3.57
F1BM (FA)	0.11	0.65	0.01	1.37	1	0.037
F1BM (FB)	0.125	0.665	0.009	1.33	1	0.037
F1WM	0.05	1.63	0.012	1.61	1	0.037
F2BM	0.12	0.66	0.01	1.48	1	0.098
F2WM	0.03	1.17	0.008	1.24	1	0.098
F3BM	0.06	0.65	0.008	1.40	1	0.427
F3WM	0.05	1.62	0.015	1.38	1	0.427
R1BM (sc-3)	0.11	0.605	0.01	1.325	2	0.77
R1BM (sc-4)	0.12	0.615	0.012	1.36	2	0.77
R1WM (sc-4)	0.052	1.71	0.015	(0.092)	2	0.77
R2BM (sc-tang)	0.10	0.74	0.012	0.66	4	60.1
R2BM (sc-axial)	0.10	0.74	0.012	0.66	4	60.1
R2WM	0.10	0.084	0.017	1.57	4	60.1
R3BM (sc-low)	0.1	0.9	0.006	0.74	4	70.0
R3BM (sc-int)	0.08	0.88	0.006	0.76	4	70.0
R3WM	0.08	1.58	0.009	1.46	5	70.0
R4BM (sc-low)	0.1	0.88	0.006	0.75	3	69.7
R4BM (sc-int)	0.09	0.88	0.006	0.71	3	69.7
R4WM	0.05	1.66	0.015	1.35	4	69.7

* 1 surveillance capsule is accelerated irradiated in test reactor.

5. Results and discussion

In Figures 5–12 the measured TTS, using the symmetric tanh KV/LE algorithm, versus the predicted TTS are plotted for each empirical derived ETC model, completed with upper and lower bounds of $\pm 20^\circ\text{C}$ to facilitate model comparisons. In addition to the adjusted JEAC4201-2004 model (Figure 13) an adjusted ETC model, referred to as ETCadj, is developed as an alternative fitness-for-purpose approach to handle the Swedish surveillance data. In the ETCadj model two approaches with respect to sought TTS is adopted, i.e. $\text{TTS}=\Delta T_{41J}$ and $\text{TTS}=\max[\Delta T_{56J}, \Delta T_{0.89\text{mm}}]$, and where ETCadj-1 refers to the former approach (Figure 14) and ETCadj-2 to the latter (Figure 15). The ETCadj-1/2 models use the adjusted chemistry factor from the JEAC4201-2004 model (eq. 6) but where the fluence factor is changed to the one used in the FIM model, i.e. $[\text{FF}]_{(f)\text{new}}=(\Phi/10^{19})^{\text{exp}}$, and thus

$$\text{TTS}=[\text{CF}]_{\text{adj}} \cdot [\text{FF}]_{(f)\text{new}} = \left\{ \sum (\Delta \text{RT}_{\text{NDT, meas}}) \right\} \cdot [\text{FF}]_{(f)\text{new}} / \sum [\text{FF}]_{(f)\text{new}} \cdot [\text{FF}]_{(f)\text{new}} \cdot [\text{FF}]_{(f)\text{new}} \quad (18)$$

For ETCadj-1 the optimal global fluence exponent is 0.53 and locally, the optimal fluence exponents are 0.47 for base metals and 0.55 for weld metals. For ETCadj-2 the optimal global fluence exponent is 0.57 and locally, the optimal fluence exponents are 0.50 for base metals and 0.60 for weld metals. In Figures 14–15, global fluence exponents are used.

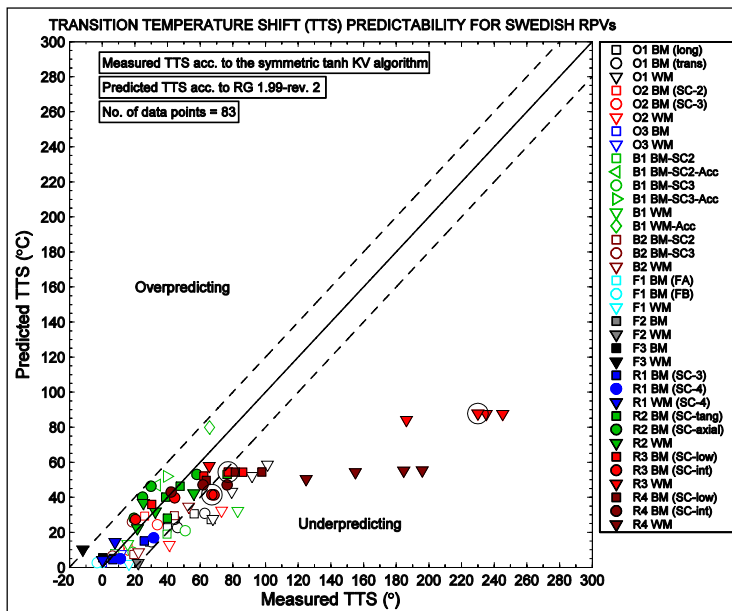


Figure 5. Predictability of TTS, RG 1.99-rev. 2.

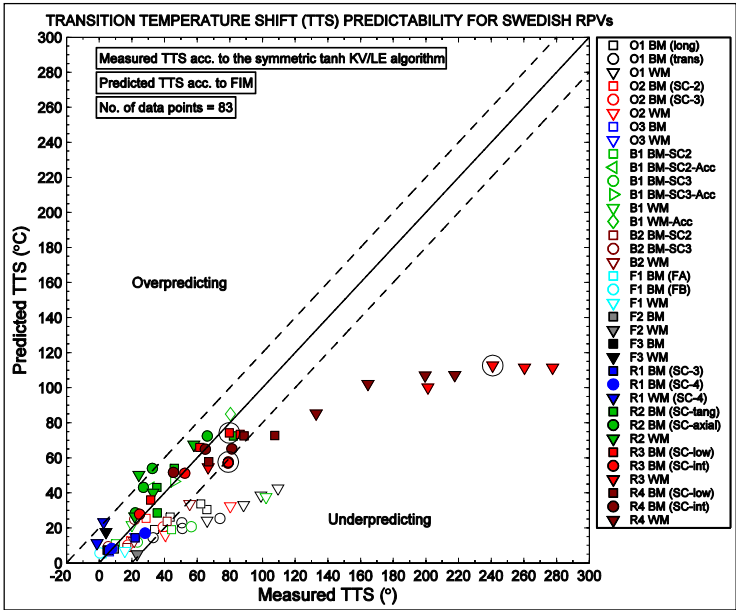


Figure 6. Predictability of TTS, FIM.

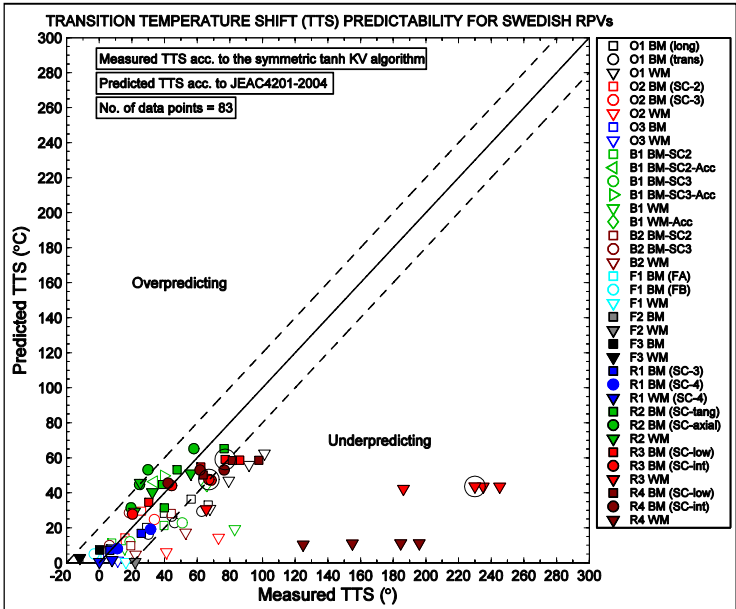


Figure 7. Predictability of TTS, JEAC4201-2004.

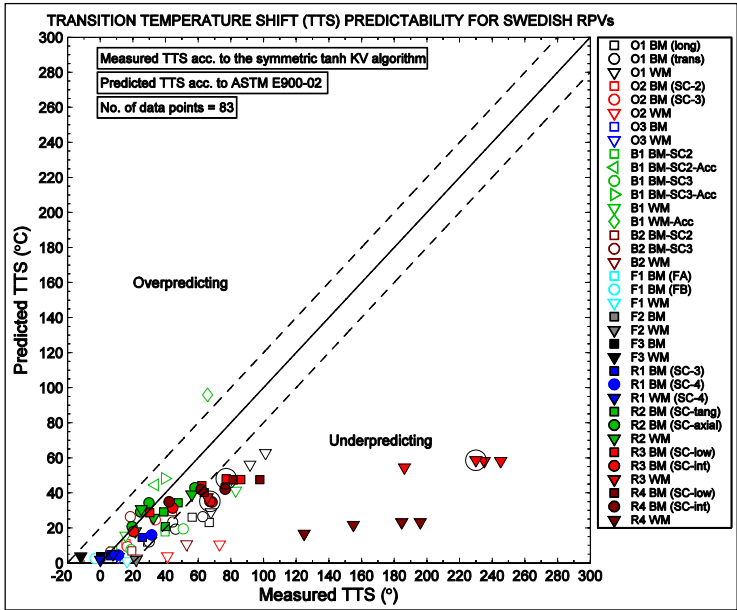


Figure 8. Predictability of TTS, ASTM E900-02.

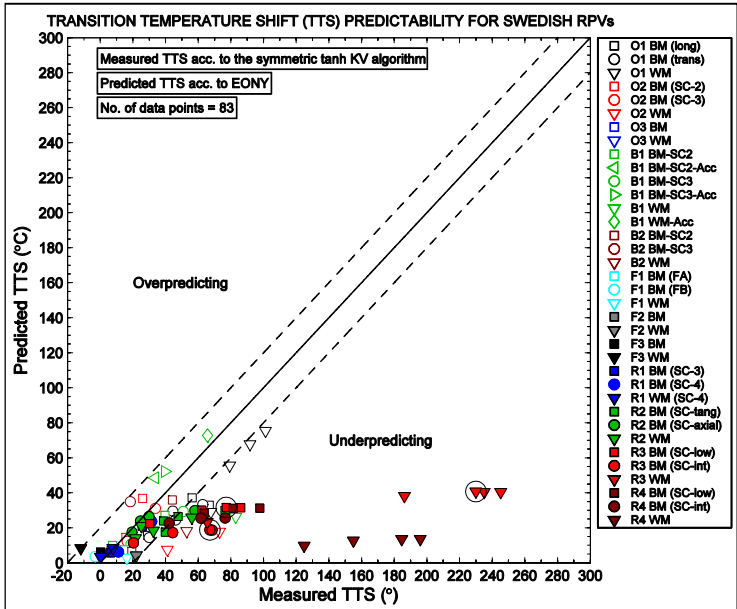


Figure 9. Predictability of TTS, EONY.

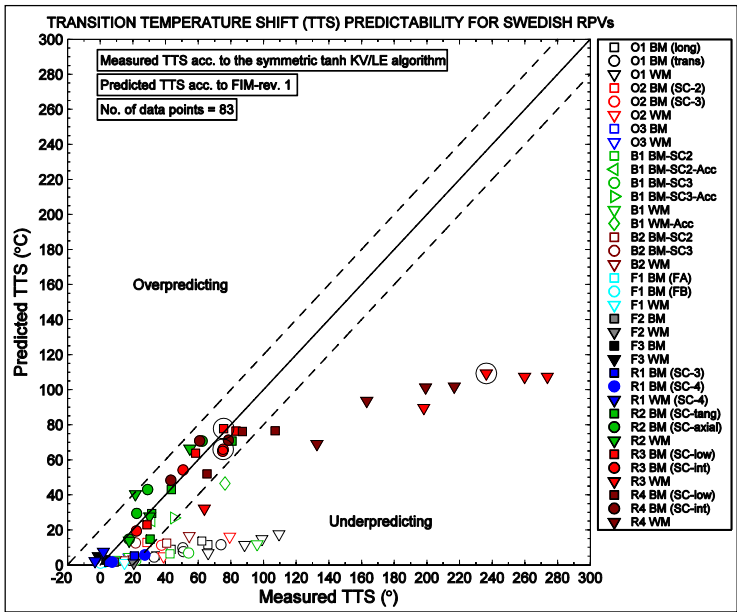


Figure 10. Predictability of TTS, FIM-rev. 1, $TTS_{measured} = \Delta T_{56J}$ for O1 BM/W/M due to lack of early LE data.

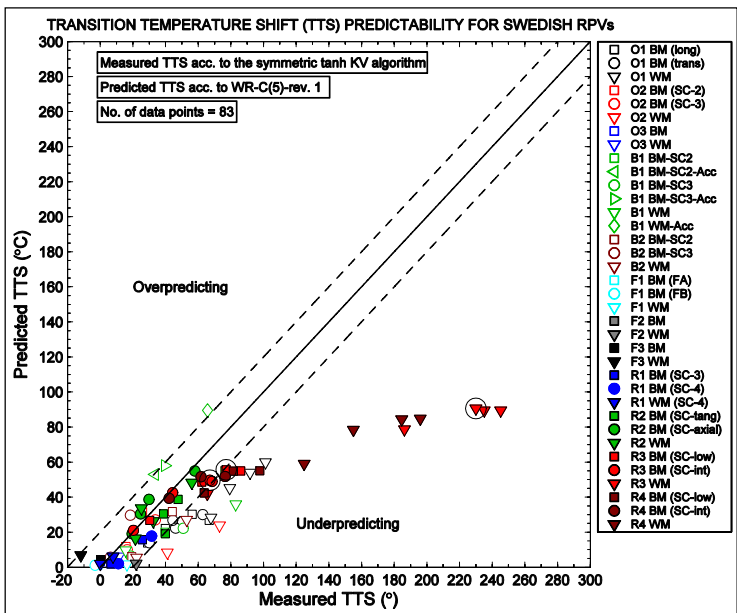


Figure 11. Predictability of TTS, WR-C(5)-rev. 1.

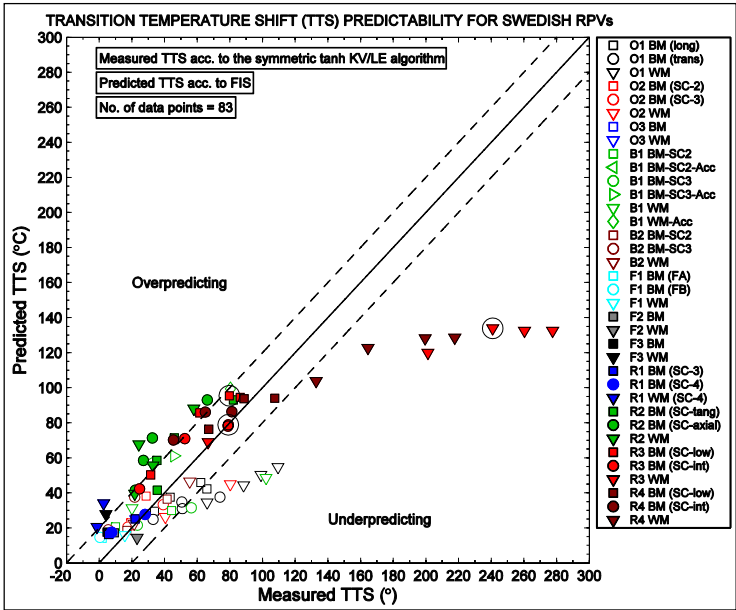


Figure 12. Predictability of TTS, FIS.

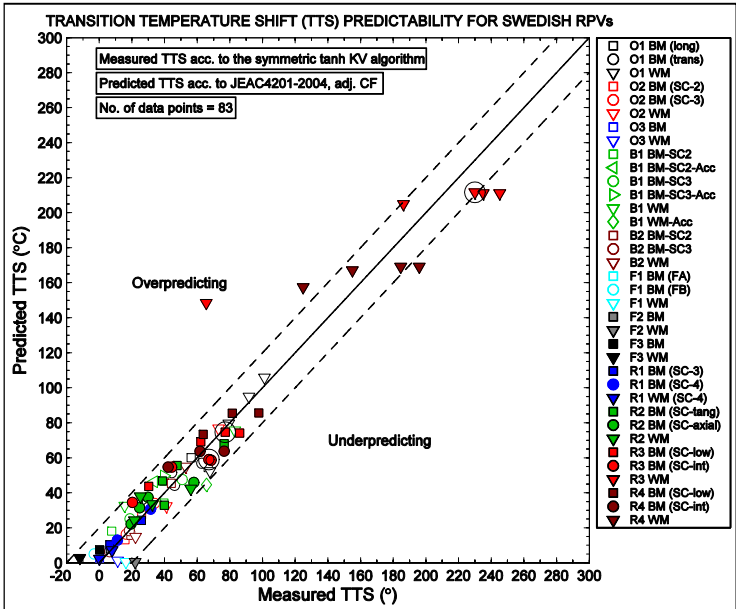


Figure 13. Predictability of TTS, JEAC4201-2004, adjusted CF.

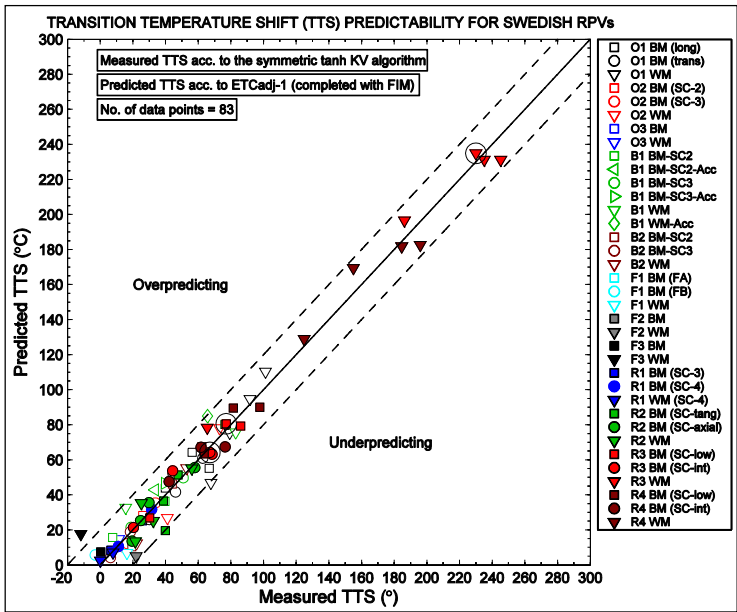


Figure 14. Predictability of TTS, ETCadj-1, adjusted CF, $TTS = \Delta T_{41J}$.

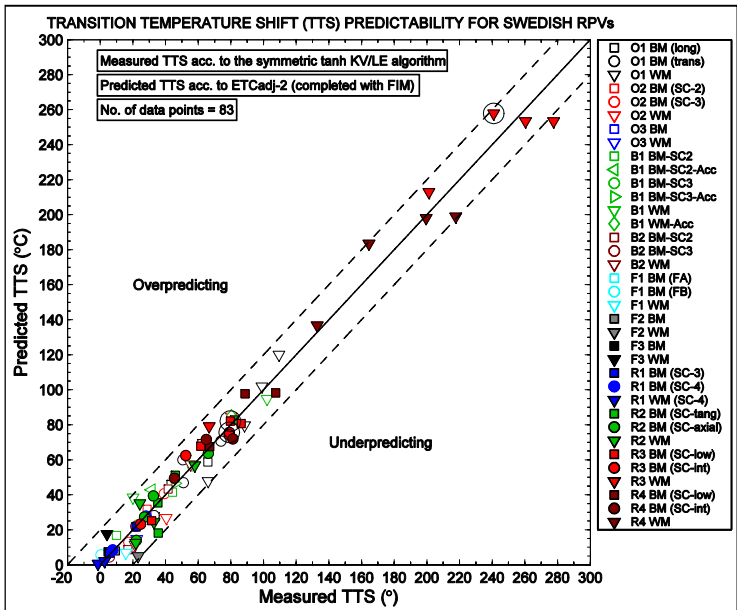


Figure 15. Predictability of TTS, ETCadj-2, adjusted CF, $TTS = \max[\Delta T_{56J}, \Delta T_{0.89mm}]$.

Only materials containing more than or equal to two surveillance data affect the fluence exponent optimization for ETCadj-1/2 (see Table 1). This implies that a part of the TTS data are plotted in Figures 14–15 by using chemistry and fluence factors from the FIM model (Eq. 2). By using the adjusted chemistry factor no information of the mechanisms involved in the irradiation embrittlement process is obtained since this approach simply connects actual surveillance data to a generalized fluence factor. However, an ETC based on actual data can be useful in the decision process for lifetime extension of RPVs and which importance increases the larger the deviations between experimental data and an empirical ETC becomes. Thus, these approaches represent two different angles of views and where both approaches could be relied on when assessing the fitness of an ageing RPV.

When studying the empirical best fit ETC models in Figures 5–11 it becomes clear that all models are globally underpredictive by various degrees but also that this result is largely a contribution from an underprediction of TTS for welds. Additional to a comparison made from simply viewing Figures 5–11, a quantitative comparison is performed by calculating the sum of squared residuals (SSR) for each ETC model evaluation, summarized in Table 2. The summarization shows that the accurateness of the empirical best fit ETC models to globally predict the TTS of Swedish RPVs is as follows in descending order: WR-C(5)-rev. 1, FIM, RG 1.99-rev. 2, FIM-rev. 1, ASTM E900-02, JEAC4201-2004, and EONY. Since the predictability of TTS is dependent on the product form (BM=base metal, WM=weld metal), ranking are also made locally for each product form, as shown in Table 2. For BM the order of precedence is altered and is as follows in descending order: JEAC4201-2004, FIM, WR-C(5)-rev. 1, RG 1.99-rev. 2, ASTM E900-02, FIM-rev. 1, and EONY. For WM the order of precedence is also altered and is as follows in descending order: WR-C(5)-rev. 1, FIM, RG 1.99-rev. 2, FIM-rev. 1, ASTM E900-02, JEAC4201-2004, and EONY.

Table 2. Sum of squared residuals (SSR) for each ETC model evaluation (in 10^5).

ETC model	Total	BM	WM
RG 1.99-rev. 2	1.591	0.159	1.432
FIM	1.407	0.144	1.262
FIS	1.045	0.145	0.900
ASTM E900	2.382	0.221	2.160
EONY	2.839	0.341	2.499
JEAC4201-2004	2.625	0.127	2.498
FIM-rev. 1	1.786	0.256	1.530
WR-C(5)-rev. 1	1.394	0.154	1.240
JEAC4201-2004, adj.	0.151	0.025	0.126
ETCadj-1	0.039	0.015	0.024
ETCadj-2	0.050	0.015	0.035

For RG 1.99-rev. 2 (Figure 5), FIM (Figure 6), JEAC4201-2004 (Figure 7), and WR-C(5)-rev. 1 (Figure 11), the TTS predictions for BM and WM are satisfactory respectively greatly underpredictive. It should be noted that only WMs from Oskarshamn 1, Forsmark 2, and Ringhals 2 have Ni contents within the validity range as specified in tabular form in RG 1.99-rev. 2. This means that WMs from the other RPVs have non-extrapolated chemistry factors based on Ni=1.2 wt%. The high Ni content in some WMs of the Swedish nuclear RPVs seems to be an extraordinary characteristic in a world-wide perspective, which imply that almost all evaluated ETC models are invalid in this regard.

For ASTM E900-02 (Figure 8), EONY (Figure 9), and FIM-rev. 1 (Figure 10), the situation is worse since they give unacceptable underpredictions for both BM and WM, even though their predictability of BM is better than for WM. It is interesting that the FIS upper bound model (Figure 12) gives better global TTS prediction than all evaluated best fit ETC models, with a slight overprediction of BM and a great underprediction of WM. In a global perspective, the results correspond with a similar evaluation performed on the Belgian RPVs [17], where it was shown that the ASTM E900-02 and the EONY models underpredicted the actual shift and that this was even more accentuated at high measured shifts, corresponding to high fluences. In that investigation, RG 1.99-rev. 2 resulted in a very scattered cloud of points and overpredicted to a great extent at low fluences while it underpredicted at higher fluences. It was also concluded that from all evaluated ETC models (FIM, RG 1.99-rev. 2, ASTM E900-02, EONY), the FIM model yielded best global TTS prediction. However, in a local perspective all evaluated ETC models tended, more or less, to overpredict the TTS of WM and underpredict the TTS of BM. This local tendency is however non-correspondent with the present evaluation since an underprediction of the TTS for WM is more apparent here. The SCK•CEN hardening model as presented in the Belgian evaluation [17] is not evaluated in the present paper due to lack of model information.

Finally Figures 13–15 show the applicability of ETC models with adjusted chemistry factors since these models give more accurate TTS predictions. This type of ETC model must therefore be considered as more reliable to predict embrittlement trends for Swedish RPVs, especially for WM. The developed ETCadj-1/2 models (Figures 14–15) yield better TTS predictions in a global and a local perspective than the adjusted JEAC4201-2004 model (Figure 13) and where the differences between ETCadj-1 and ETCadj-2 are very small. It should be observed that these three ETC models with adjusted chemistry factors are not comparable with the empirical ETC models, with respect to the sum of squared residuals in Table 2, since the number of materials included in the calculations is reduced.

Without any further discussion it is noticed that the latest surveillance testing of Ringhals Unit 3 shows an unexplained deviation from the embrittlement trend (highlighted data with circles in Figures 5–15).

In an earlier paper, experts from the Swedish nuclear industry discussed the great discrepancy between the measured and the predicted TTS for the WMs in Ringhals Units 3 and 4, and where corrective measures were proposed in order to regain the safety margin for continued operation [18]. In a following paper the

synergistic effect of high Ni and high Mn was suggested as a possible cause for this discrepancy [19]. In Figure 16, the empirical best fit ETC models and the ETC models with adjusted chemistry factor are demonstrated on the WM in Ringhals Unit 4 (R4 WM) and where it is seen that the empirical ETC models greatly underpredict the TTS from the surveillance data (note that the EONY model is excluded from Figure 16 due to the use of an effective neutron fluence in that model). However, the adjusted JEAC4201—2004 model and the adjusted ETCadj-1/2 models, with optimal global fluence exponents, recalculate the chemistry factors such that these ETC models now give the most correct TTS predictions, although the curve slope in the JEAC4201-2004 model is inaccurate. The non-conservatism of the empirical ETC models in this specific case is an interesting and important issue which at the moment is unexplained. Irradiation hardening is a very complex process and not yet fully modelled and depends on metallurgical and irradiation variables such as alloy composition, heat treatment, product form, irradiation temperature, and neutron flux, fluence and spectra [6]. As noted earlier, all applied empirical ETC models besides the French FIM and FIS models are invalid for such high Ni contents and combined with a high fluence level an embrittlement mechanism could have emerged which is not enough represented in these ETC models. There is however a well-known relationship between Cu and Ni on the embrittlement of irradiated RPVs. For instance, in the EONY model the relationship between Cu and Ni (extrapolated) and their synergistic effect on the TTS is illustrated in Figure 17. Figure 17 shows that the TTS is constant when $Cu \leq 0.072$ wt%, which means that the CRP term (eq. 12) has no contribution to embrittlement in this case, under the assumption that this condition is valid also for an extrapolated Ni content of 1.66 wt%. According to the EONY model the embrittlement of R4 WM is thus solely caused by defect cluster complex MF and fine-scale precipitates (or solute Cu clusters), which act as obstacles to dislocation glide [6]. An explanation regarding the lack of TTS predictability for R4 WM should in other words be found within this type of embrittlement mechanism due to the low copper content in R4 WM. Note the abrupt transition in Figure 17 at high Cu contents and Ni=0.5 wt%, which is explained by the constraints in the $Max(Cu_e)$ term.

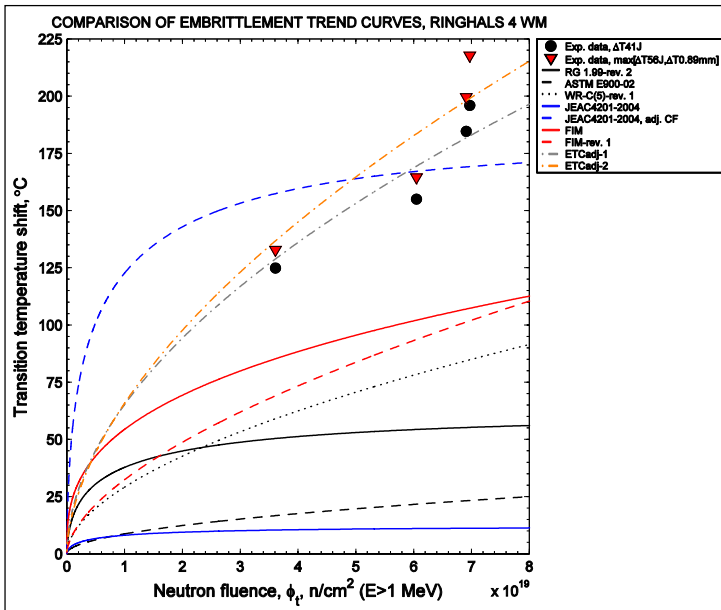


Figure 16. Embrittlement trend curves for Ringhals 4 WM, only measured data using ΔT_{41J} and $\max[\Delta T_{56J}, \Delta T_{0.89mm}]$ are plotted since $\max[\Delta T_{56J}, \Delta T_{0.89mm}] \approx \text{mean}[\Delta T_{56J}, \Delta T_{0.89mm}]$.

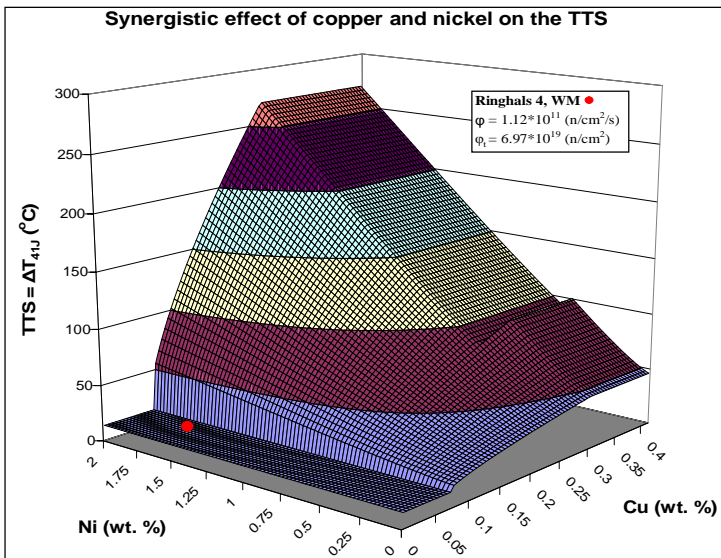


Figure 17. Synergistic effect of Cu and Ni on the TTS for Ringhals 4 WM, EONY (extrapolated Ni content).

6. Conclusions

The forecast reliability of eight empirical ETC models and three ETC models with adjusted chemistry factors has been evaluated on the Swedish nuclear RPV fleet. From this evaluation it can be concluded as follows:

- All empirical best fit ETC models yield global non-conservative TTS prediction for the Swedish nuclear RPV fleet.
- The local TTS predictability with respect to base and weld metals differ greatly for all empirical best fit ETC models. Four best fit ETC models (RG 1.99-rev. 2, FIM, JEAC4201-2004, WR-C(5)-rev. 1) yield satisfactory TTS prediction for base metal. All evaluated best fit ETC models yield non-conservative TTS prediction for weld metal.
- One upper bound ETC model (FIS) yielded best global TTS prediction among all evaluated empirical ETC models, although it locally resulted in overprediction of base metal and underprediction of weld metal.
- One established ETC model with adjusted chemistry factor (JEAC4201-2004) yielded satisfactory TTS prediction for base metal and somewhat less satisfactory TTS prediction for weld metal. Two new ETC models with adjusted chemistry factor (ETCadj-1/2) yielded satisfactory global and local TTS predictions.

References

1. Regulatory Guide 1.99 Revision 2, Radiation embrittlement of reactor vessel materials, U.S. Nuclear Regulatory Commission, Washington D.C., May 1988.
2. P. N. Randall, Basis for revision 2 of the U.S. Nuclear Regulatory Commission's Regulatory Guide 1.99, Radiation Embrittlement of Nuclear Reactor Pressure Vessel Steels: An International Review (Second Volume), ASTM STP 909, L. E. Steele, Ed. American Society for Testing and Materials, Philadelphia, pp. 149–162, 1986.
3. C. Brillaud, F. Hedin, and B. Houssin, A comparison between French surveillance program results and predictions of irradiation embrittlement, Influence of Radiation on Material Properties: 13th International Symposium, ASTM STP 956, F. A. Garner, C. H. Henager, Jr., and N. Igata, Eds., American Society for Testing and Materials, Philadelphia, pp. 420–447, 1987.

4. N. Soneda and A. Nomoto, Characteristics of the new embrittlement correlation method for the Japanese reactor pressure vessels steels, *Jour. of Engineering for Gas Turbines and Power*, pp. 9, Vol. 132, Oct 2010.
5. ASTM E900-02 (2007), Standard guide for predicting radiation-induced transition temperature shift in reactor vessel materials, E706 (IIF), 2007.
6. E. D. Eason, G. R. Odette, R. K. Nanstad, and T. Yamamoto, A physically based correlation of irradiation-induced transition temperature shifts for RPV steels, ORNL/TM-2006/530, 2006.
7. P. Todeschini, Y. Lefebvre, H. Churier-Bossennec, N. Rupa, G. Chas, and C. Benhamou, Revision of the irradiation embrittlement correlation used for the EDF RPV fleet, Fontevraud 7, paper A084-T01, 2010.
8. M. Kirk, A wide-range embrittlement trend curve for Western reactor pressure vessel steels, *Effects of Radiation on Nuclear Materials*, 25th volume, STP 1547, T. Yamamoto, Ed., ASTM International, West Conshohocken, pp. 20–51, 2012.
9. M. EricksonKirk, Technical basis for revision of regulatory guide 1.99: “NRC guidance on methods to estimate the effects of radiation embrittlement on the Charpy-V notch impact toughness of reactor vessel materials”, U.S. Nuclear Regulatory Commission, 2007.
10. G. Hofer and C. C. Hung, Experimental evidence for the use of the gauss function in the functional description of the ductile-brittle transition of ferritic steels, *Nuclear Technology*, Vol. 49, August, pp. 492–497, 1980.
11. P. L. Windle, M. Crowder, and R. Moskovic, A statistical model for the analysis and prediction of the effect of neutron irradiation on Charpy impact energy curves, *Nuclear Engineering and Design*, 165, pp. 43–56, 1996.
12. J. L. Helm, The interpretation of Charpy impact test data using hyper-logistic fitting functions, *Effects of radiation on materials: 17th International Symposium*, ASTM STP 1270, D. S. Gelles, R. K. Nanstad, A. S. Kumar, and E. A. Little, Eds., pp. 363–374, 1996.
13. K. Wallin and P. Nevasmaa, A procedure for extrapolating Charpy transition temperature from the data at other temperature and in the case of incomplete transition curves, *Welding in the World*, Vol 49. No. 11/12, pp. 70–76, 2005.

14. P. Langenberg, W. Bleck, J. Buchholz, A. Voelling, P. Balladon, K. Wallin, and P. Nevasmaa, Development of a fracture toughness quality system tool applicable for steel producers and steel users of heavy plates, profiles and weldments, European Commission-technical steel research, 2007.
15. C. Brillaud and F. Hedin, In-service evaluation of French pressurized water reactor vessel steel, Effects of Radiation on Materials: 15th International Symposium, ASTM STP 1125, R. E. Stoller, A. S. Kumar, and D. S. Gelles, Eds., American Society for Testing and Materials, Philadelphia, pp. 23–49, 1992.
16. P. R. Sreenivasan, Charpy energy-lateral expansion relations for a wide range of steels, International Journal of Pressure Vessels and Piping, 83, pp. 498–504, 2006.
17. A.-S. Bogaert, R. Gérard, and R. Chaouadi, Comparison of embrittlement trend curves to high fluence surveillance results, Fontevraud 7, paper No. A137 T01, 2010.
18. P. Efsing, C. Jansson, T. Mager, and G. Embring, Analysis of the ductile-to-brittle transition temperature shift in a commercial power plant with high nickel containing weld material, Journal of ASTM International, Vol. 4, No. 7, Paper ID JAI100719, 2007.
19. P. Efsing, J. Rouden, and M. Lundgren, Long term irradiation effects on the mechanical properties of reactor pressure vessel steels from from two commercial PWR plants, Effects of Radiation on Nuclear Materials, 25th volume, STP 1547, T. Yamamoto, Ed., ASTM International, West Conshohocken, pp. 52–68, 2012.

Application of Alloy 690 and associated weld metals in PWRs

H. Hänninen

*Aalto University School of Engineering, Department of Engineering Design and Production,
FINLAND*

Abstract

The operating experience of major nuclear power plant pressure boundary components has recently shown that Alloy 600 components and dissimilar metal welds (DMW) can markedly affect the plant availability and safety because of increased incidences of environment-assisted cracking (EAC, PWSCC) of Alloy 600 and corresponding weld metals (Alloys 182/82). Alloy 690 and associated weld metals (Alloys 152/52) are widely used for repair and replacement of the affected thick-section components in old PWRs. In new-built reactors they are the major structural materials in a number of components. Weldability of the nickel-base materials is the key issue in manufacturing. In addition to hot cracking in welding EAC susceptibility is the other major concern of Alloy 690 and associated weld metals of Alloy 152/52 during operation of the PWR plants.

Introduction

Dissimilar metal welds (DMWs) are widely used in high-temperature operating components in nuclear power plants (NPPs) to join the low-alloy steel nozzles of reactor pressure vessels, steam generators and pressurizers to the austenitic stainless steel or nickel-base Alloy 600/690 safe-ends. DMWs have been found susceptible to environment-assisted cracking (EAC) in both boiling and pressurized water reactor (BWR and PWR) conditions where their microstructures and prevailing residual stresses/strains affect the EAC susceptibility [1-5]. The operating experience of major NPP pressure boundary components shows that DMW joints can markedly affect the plant availability and safety because of increased incidences of EAC and primary water stress corrosion cracking (PWSCC) of Alloy 600 and corresponding nickel-based weld metals, such as Alloy 182/82. The selection of Alloy 690 and its associated weld metals of Alloy 152 and 52 relies on good laboratory results on their EAC resistance and up to over 20 years service experience. The long-term behaviour of these materials and their performance in the plant has still to be demonstrated.

Regarding materials, structural design and fabrication welding, there are certain recent development trends that need to be taken into account in view of structural integrity assessment of NPP multi-metal components. New high-chromium (about 30%) nickel-based filler metals such as Alloys 52, 152 and 52M with high PWSCC resistance are extensively used to replace former Alloy 82 and 182 in fabrication of new PWRs, as well as for repair and replacement of the affected thick-section components in existing NPPs [1-4]. Simultaneously, advanced welding processes such as narrow-gap welding methods (NGW) have been introduced as GTAW and GMAW of thick-section components including DMWs for safe-ends, made without any buttering layer. All these changes inevitably require mastery of the mixing (dilution) of the base material, the compositional gradients of alloying elements, the resulting microstructures and damage and failure phenomena in DMWs.

Background

Reactor pressure vessel head penetration cracking was first observed in France in 1991 as a leak during a hydrotest in Bugey 1 PWR plant. After year 2000 several other plants have had primary water leaks to atmosphere as a result of cracking in the upper head penetration region of the reactor pressure vessel (RPV). Three plants have had reactor pressure vessel nozzle cracking (Summer and Ringhals 3/4) including one through wall crack at Summer hot leg.

These defects have resulted in requirements for various inspections for susceptible welds; upper head, bottom head penetrations and dissimilar metal butt welds. The requirements (ASME Code Cases) set new in-service inspection frequencies for surface and volumetric examinations, identify coverage requirements and set standards for demonstration of inspection capabilities. If indications are found, the flaw (length, depth...) has to be characterized. The flaw has to be evaluated for continued service based on new acceptance criteria and flaw evaluation methods. The flaws must be resolved into axial and circumferential components and their location relative to the attachment weld must be determined. Evaluation process includes prediction of the future growth due to PWSCC and fatigue. The future growth is compared with the acceptance criteria with margins to determine next inspection. For crack growth evaluation the residual stress distributions have been determined using finite element models. However, the residual stress distributions can be quite different depending on the stage of the welding process modelled. The final residual stress distributions should not be very different, which, however, may not be true in case of weld repairs.

Repair/replacement of the component may be required. Inlay and onlay concepts with Alloy 52/152 filler metal have been adopted for the mitigation method. Inlay requires excavation into the ID surface, but onlays do not require excavations. Both mitigation methods provide a corrosion resistant barrier to prevent PWSCC crack initiation and growth. Requirements for inlay and onlay including welding, inspection and analysis are in current ASME Code Case N-766. For inlay as-deposited weld metal Cr-content has to be >24% Cr, i.e. material is PWSCC resistant. Then PWSCC crack growth rate analysis is not required, but a fatigue crack growth analysis is required. Postulated initial axial and circumferential flaws are half of the inlay min. thickness. In case of the overlay repair there are several important issues which are related to the depth of the repair, inspectability requirements and ID stress levels.

Alloy 690/52/152 Experience

As the result of the extensive history of stress corrosion cracking of Alloy 600 components in primary water (PWSCC), thin-wall steam generator tubing of PWRs has increasingly been fabricated from high-chromium Alloy 690 for more than 20 years. Service experience with regard to PWSCC in steam generator tubing application has been outstanding, with no cracking reported to date. Recently, thick-section Alloy 690 material with matching high-Cr weld metals Alloy 52/152 has also been widely used. Alloy 690 and Alloy 52/152 weld metals are, thus, the replacement materials for Alloy 600 thick-wall components and Alloy 82/182 weld metals due to their high resistance to primary water stress corrosion cracking. After hundreds of reactor years experience no crack initiation has been observed in primary water PWR environment for Alloy 690 and associated weld metals Alloy 52/152, but based on laboratory experience Alloy 690 is not immune from PWSCC. In the laboratory conditions crack growth has been observed in Alloy 690 and its weld metals Alloy 52/152. Cold work in certain directions has led even to high crack growth rates in Alloy 690. There are large orientation effects on environment-assisted cracking (EAC) susceptibility. Regardless of the product form Alloy 690 is not always homogeneous, and

microstructural banding is often present. Crack growth rate in the plane of the plate (S-L) is the highest. This may, thus, not be a practical problem as it would lead to a lamination. Orientation effects are expected to be similar in Alloy 600 and 690.

Findings to date show that there is significant scatter in the PWSCC results for Alloy 690 and its weld metals Alloy 52/152. This is because a number of variables which contribute: cold work, crack orientation, temperature, hydrogen content of the water, weld vs. base metal, etc.. Sometimes these variables have significantly different effects from those of Alloy 600 and its associated weld metals. For example, the base metal PWSCC rate is faster for Alloy 690 than that of the weld metals, but for Alloy 600 the opposite is true.

For Alloy 690 base metal there is a similar scatter in the PWSCC results as for Alloy 600. There is not enough data to develop a statistical model for Alloy 690 as yet, and thus a factor of improvement has been the best approach. The data support a factor of improvement of 100 over the Alloy 600 data.

For Alloy 52/152 weld metals there is also a similar scatter of PWSCC results as for Alloy 182, but there is otherwise no discernable difference in behaviour. Again, there is not enough data to develop a statistical model as yet, so a factor of improvement seems to be the best approach. The data support a factor of improvement of 100 over the Alloy 182 data. This is a conservative approach since the crack growth rate is much lower than that of the base metal. Also it seems that there is no difference between Alloy 52 and Alloy 152 behaviour.

Issues to be Resolved

The level of cold work is crucial in cracking sensitivity of Alloy 690/52/152. Therefore to understand how cracks may advance in the real structures of a PWR the crack fronts and paths have to be analysed (engagement issue). The amount of residual strain has to be related to the cold work. The level of cold work which exists in typical applications of Alloy 690/52/152 has to be determined. In general, residual plastic strain near Alloy 690 welds varies between 12...28%. For stainless steels residual strains may be even higher, but weld repairs are more likely with nickel-based alloys. As a rule of thumb, residual strain of a weld repair relative to the original weld with nickel-based alloys is: one repair 2,1X, two repairs 2,7X and three repairs 3,0X. More PWSCC data are needed for different as-received materials, with no cold work, and cold-worked materials of typical application.

Weldability of high-chromium nickel-based weld metals requires extensive understanding of the solidification behaviour and solidification cracking as well as ductility-dip cracking. Filler metal development concentrates to development of high-Cr filler metal that is resistant to both solidification and ductility-dip cracking. The work includes development of the database for high-Cr filler metals, elemental effects on solidification behaviour (e.g., solidification temperature range) and cracking susceptibility, including both intentional alloying additions (e.g., Nb, Ti...) and impurity elements and evaluation of the effects of dilution on the solidification behaviour and the metallurgical properties of the weld metals.

For development of Alloy 690/52/152 degradation management considerable PWSCC testing for crack initiation and growth has to be continued in order to be able to characterize their PWSCC resistance and to develop the predictive models for cracking. For this purpose EPRI started in 2007 an expert panel to determine the knowledge gaps related to Alloy 690/52/152 PWSCC behaviour. The aim of the research extending until 2015 is:

- Determine PWSCC initiation/growth improvement factors over Alloys 600/182/82,
- Develop crack growth rate curves for Alloy 690/52/152,
- Develop guidelines for Alloy 690 procurement and fabrication to maximise PWSCC resistance (grain size, allowed carbide distribution, microstructural banding).

Crack growth rate data to inform inspection have still some high-priority gaps such as PWSCC susceptibility of HAZ, effect of weld defects in Alloy 52/152 on PWSCC susceptibility, effects of weld composition (dilution effects) and welding procedure on PWSCC and LTCP (Low-temperature Crack Propagation) as well as welding fabrication and repair effects on defect population, residual stresses, grain boundary carbide structure and PWSCC susceptibility. It is known that all weld HAZ microstructures are very different and can vary markedly within each weld as well as that the residual plastic strains in the weld root regions are the highest. However, the absence of detected PWSCC initiation in these alloys in plants to date, and the difficulties to initiate PWSCC in laboratory tests, indicate that longer inspection intervals may be technically justifiable, e.g., on a risk-informed basis.

Conclusions

Regarding Alloy 600 and associated weld metals crack growth rates for thick-wall (penetration nozzles) vs. thin-wall components (steam generator tubing) are well defined. There are, however, some uncertainties concerning K threshold effects and material processing and welding parameter effects. Flaw analysis uncertainties in these components include weld residual stress uncertainties including repair effects on residual stresses/strains, heat-affected zone microstructures, initial flaw size and shape (inspection sizing criteria).

Regarding Alloy 690 and associated weld metals it has to be considered how to account for the possibility of cracking in these highly resistant materials in problem areas: areas of high stress and residual strain such as HAZ and weld repairs, weld dilution zones with lower Cr-content, weld fabrication defects and poor welding process control. For flaw analysis the low crack growth rates of Alloy 690 base metal and the associated weld metals make the establishment of inspection frequency and mitigation techniques (inlay/onlay, excavation and reweld etc.) challenging both in new and replacement components. The main issue is how much conservatism is necessary to address uncertainties. With Alloy 690 and the associated weld metals in addition to residual strain (cold work) effects dilution properties of the low-alloy steel (buttering, temper-bead welding and narrow-gap welding) sides of the welds, mitigation interfaces (Alloy 82/182, stainless steel), effects of hot cracking and ductility-dip cracking have to be considered.

Improved understanding of PWSCC of Alloy 690 and its associated weld metals Alloy 52/152 results in reduced uncertainty (optimized inspection intervals, increased remaining life of reactor components), greater confidence on cracked component decisions (repair or replace) and improved technical understanding.

References

1. H. Hänninen, P. Aaltonen, A. Brederholm, U. Ehrnstén, H. Gripenberg, A. Toivonen, J. Pitkänen and I. Virkkunen: 'Dissimilar metal weld joints and their performance in nuclear power plant and oil refinery conditions'. *VTT Research Notes 2347*. VTT Technical Research Centre of Finland: Espoo, Finland, 2006. 209 p.

2. H. Hänninen, A. Brederholm, T. Saukkonen, H. Gripenberg, A. Toivonen, U. Ehrnstén and P. Aaltonen: 'Hot cracking and environment-assisted cracking susceptibility of dissimilar metal welds'. *VTT Research Notes 2399*. VTT Technical Research Centre of Finland: Espoo, Finland, 2007. 177 p.
3. H. Hänninen, A. Brederholm, T. Saukkonen, M. Ivanchenko, A. Toivonen, W. Karlsen, U. Ehrnstén and P. Aaltonen: 'Environment-assisted cracking and hot cracking susceptibility of nickel-base alloy weld metal'. *VTT Research Notes 2582*. VTT Technical Research Centre of Finland: Espoo, Finland, 2011. 155 p.
4. R. Mougnot and H. Hänninen: 'Microstructures of nickel-base alloy dissimilar metal welds'. Aalto University publication series SCIENCE + TECHNOLOGY 5/2013. Aalto University: Espoo, Finland, 2013. 178 p.
5. P. Holmström et al., 2013: 'Effect of strength mismatch and microstructure on mechanical properties of BWR dissimilar metal safe-end welds'. To be published in Proc. Conf. "*Environmental Degradation of Nuclear Materials 2013*".

Performance of copper overpack for repository canisters

Juhani Rantala, Pertti Auerkari, Stefan Holmström,
Anssi Laukkanen & Tom Andersson

VTT Technical Research Centre of Finland
Kemistintie 3, Espoo, P.O. Box 1000 FI-02044 VTT, Finland

Abstract

The final disposal of the canisters containing spent nuclear fuel involves long term storage in a deep geological repository. The canisters include a 50 mm overpack (top layer) of oxygen free phosphorus doped (OFP) copper for corrosion protection. In storage the canister is subjected to some heating by the residual activity of the contents, requiring reliable prediction of safe creep life from the available rupture and strain properties of the overpack that includes electron beam (EB) or friction stir welds (FSW) for sealing. Assessments of creep strain and rupture at relevant service conditions are inevitably susceptible to any bias in the applied material models, the underlying material data and predictive tools. FSW appears to generally produce stronger welds, although significant creep weakening has been indicated in case of small scale root defects. In EB welds large grains and characteristic patterns of solidification result in some anisotropic mismatch to reduce creep strength and increase strain localisation of welds. In this paper FSW and EB cross weld test results are assessed and compared for creep response. The models have been converted to comply with the requirements for in-house Finite Element Assessment (FEA) code and used for simulating the FSW behaviour. The simulated strain response is compared with corresponding measurements in long term creep testing. The results of the simulations and material models are discussed in the view of targeted life span of the canister overpack. Observations are presented regarding the expected stress, strain and multi-axial constraint in the welded structure.

1. Introduction

As a structural material, the attractive properties of copper include good corrosion resistance in common atmospheric and soil environments. For example, native copper is one of the few metals that can be found as metallic lumps in soils and rocks, millions of years after the formation of natural copper-containing ores. Aiming to benefit from the corrosion resistance, the Finnish disposal concept for spent nuclear fuel is based on 400 m deep geological (bedrock) storage of cast iron canisters with a 50 mm thick overpack of P-doped (OFP) copper for corrosion

protection. The canister will be surrounded by bentonite clay that forms yet another barrier against unwanted transport of radionuclides. The hydrostatic pressure of groundwater and swelling pressure of bentonite may add up to a total pressure of about 14 MPa. The temperature of the canister surface will first increase by the residual radioactive heating up to about 75–80°C before the first 100 years, and then slowly cool to the temperature of the bedrock, Figure 1. The external pressure will first plastically deform the copper cylinder against the insert and then drive it to creep further in the areas where air gaps remain. It is of interest to predict the long term performance of the overpack and the weld between the cylindrical body and the covering lid.

Although relatively mild in usual engineering terms, the repository conditions imply a technical challenge to life estimation for ensuring the integrity of the overpack. This is because of the discrepancy between the longest conventional laboratory test (decades at most) and the expected time in repository (of the order of a glaciation cycle (about 10^5 years) to allow for radioactive decay close to the background level. This time difference by a factor of 10^4 also exceeds the usual range of extrapolation from laboratory experiments to real service conditions in most (or any) comparable engineering applications.

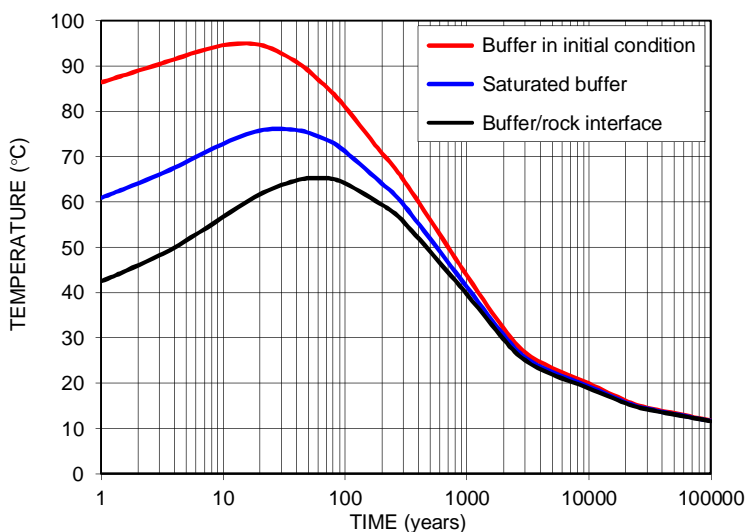


Figure 1. Predicted temperature evolution at the canister surface for EPR fuel [2]; the red curve assumes dry environment with a 10 mm gap around the canister, the blue curve assumes bentonite being wetted by groundwater.

The aim of this work has been to conduct creep experiments to complement the copper creep database and to develop and validate a creep model and finally to apply this model in FE analysis of the copper canister. The experimental testing has included tensile tests, medium and long-term creep testing for uniaxial and CT

specimens. The creep strain model is based on the in-house LCSP creep model [6] with the Wilshire equation for the rupture model.

The project is part of the Finnish national research program on nuclear waste management 2011–2014 (KYT2014). The project also includes specific issues defined by SSM (Sweden).

2. Materials and methods

The oxygen free phosphorus doped OFP copper material for the experiments including friction stir welded (FSW) material from a full scale section provided by SSM/SKI (Sweden) and the Swedish program for canister studies. The sample materials included cylindrical parts (material code T17 and T31) and a cover lid (TX 82) welded together, and a sector of a full FSW joint (L75) and an EB-welded joint XK10. Before selecting OFP copper for use in the repository, oxygen free high conductivity (OFHC) copper was the candidate material and has since been used only as a reference material in research work. The chemical compositions of the OFP and OFHC coppers are shown in Table 1.

Table 1. Chemical composition of OFP and OFHC copper (in ppm).

	OFP	OFHC
Cu	bal.	99.994%
P	30–100	<10
Ag	13	<25
S	<8	<10
O	<5	3
H	<0.6	

The OFP test materials (Figure 2) were subjected to uniaxial and multiaxial (compact tension, CT) creep testing. The diameter of the uniaxial specimens is 10 mm and the initial thickness (B) of each CT specimen is 25 mm. The notch of the OFP copper CT specimens with welds was the natural gap tip of the joint. Metallography using optical, scanning electron and FESEM/EBSD (Aalto University) microscopy has been applied for as-new materials and test specimens after each given testing period. Interrupted testing has been applied for multiaxial testing to inspect for damage evolution. For load setting and interpretation of the results, life modelling with extended parametric and other techniques has been applied. For creep modelling, the combined Wilshire and LCSP models have been applied and further developed [6] to support robust FE analyses under non-homogenous stress and strain fields.

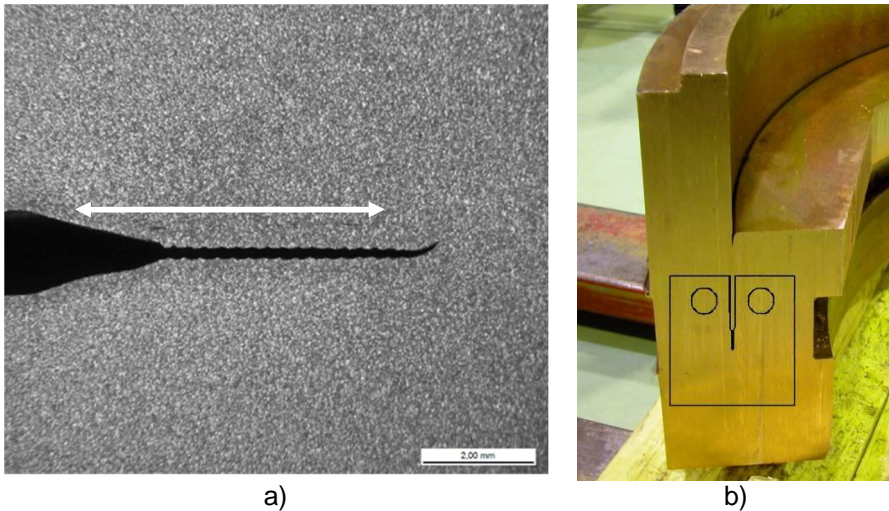


Figure 2. a) EB-welded CT specimen after wire erosion (arrow shows the region of the natural joint gap) and b) extraction of FSW CT specimens for testing.

3. Materials modelling: rupture

Copper is initially soft but strongly strain hardening material, and somewhat challenging to model due to the scatter in observed creep strength at high stresses that are necessary when testing for sensible test durations at temperatures close to the repository conditions. Therefore the Wilshire rupture model that uses normalization by the tensile strength is used here. The selected Wilshire equation [3] has provided a methodology for direct fitting and prediction of minimum strain rate, time to strain and time to rupture. The method needs additional tensile test data at the creep test temperatures for stress normalization. The model avoids the varying stress exponent of conventional models, and the creep activation energy can be defined in a straightforward way. By using the Wilshire model the long term predictions of both rupture and strain have been improved.

The Wilshire equation for time to rupture t_r at stress σ and temperature T is expressed as

$$\ln(\sigma / \sigma_{TS}) = -k[t_r \exp(-Q_c^* / RT)]^u \quad (1)$$

where k and u are constants obtained by fitting to the test data, Q_c^* is the apparent activation energy and σ_{TS} is tensile strength or another reference stress (like yield stress) at the specified temperature. The application of this model obviously requires data from both creep rupture testing and hot tensile testing. The base

material constants, determined as shown in Figure 3 for OFP, are presented in Table 2.

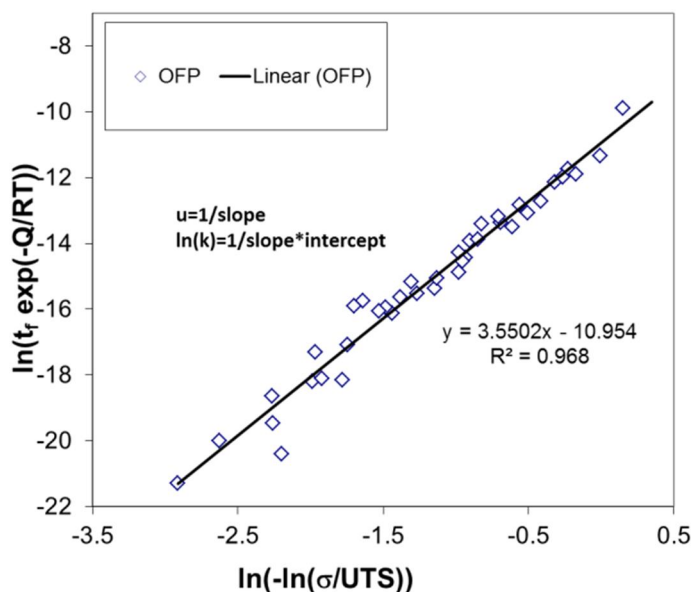


Figure 3. Linear regression to determine the parameters k and u for OFP copper.

It is to be noted that the predictions are sensitive to the optimized apparent activation energy and that the values applied in this work are the ones giving the optimal fit for the available data. For OFP copper somewhat larger Q_c^* have been presented in earlier work [5, 6].

Table 2. Wilshire equation parameters for time to rupture of the base material (OFP copper).

Parameter	Value
$Q_c^*_{-ref}$	95.0 kJ/mole
k_{ref}	21.87
u_{ref}	0.2817

The results of the life predictions are shown in Figure 4. The rupture life models are updated when more data is available. The tensile strength used for the Wilshire model strength normalisation is presented in Figure 5. The Wilshire model for base metal (BM) including FSW data is shown in Figure 6.

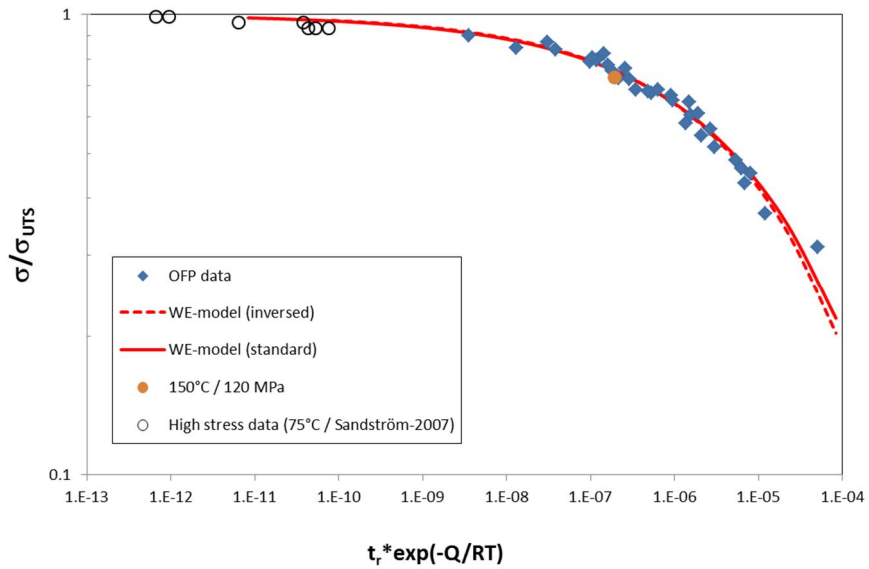


Figure 4. Wilshire model based life prediction for base material (BM) of OFP copper; the large red dot is the running 150°C/120 MPa uniaxial test (running at 10.4 years, predicted life 16.2 years).

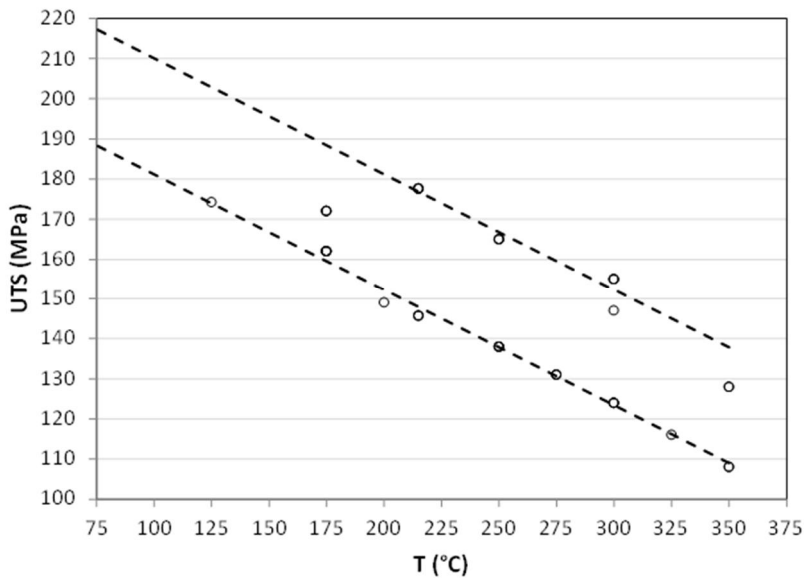


Figure 5. Temperature dependence of tensile strength of OFP copper (lower line: UTS = 210 – 0.289·T (°C)).

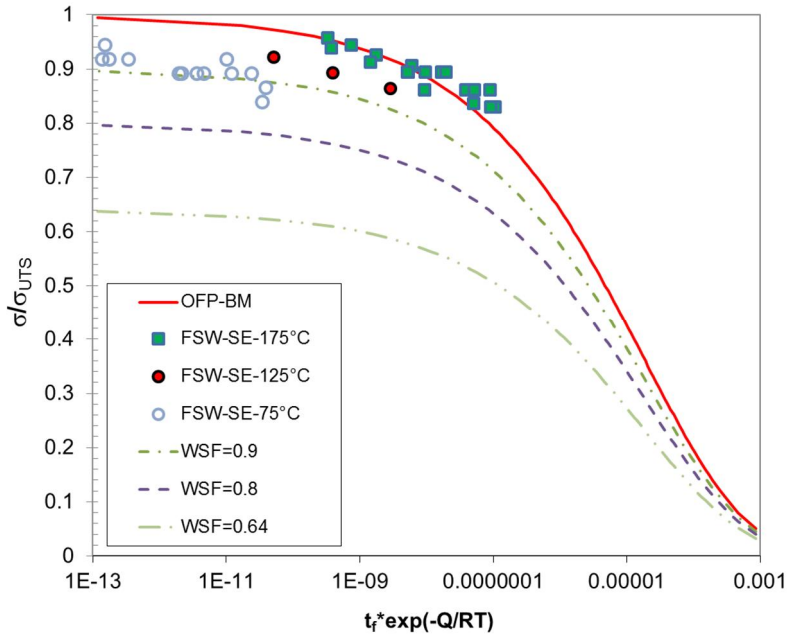


Figure 6. Wilshire model for BM with FSW data; the higher temperatures show similar creep strength as BM, at lower temperatures the weld strength factor is about 0.9.

4. Materials modelling: creep strain

The observed capability of the LCSP model to predict well the strain rates [4] can be taken to suggest inversely a fair ability to predict time to rupture from relatively early strain data of unfailed specimens. The strain and strain rate dependence of stress, temperature and time can be described by the LCSP functions:

$$\log(t_\varepsilon) = \frac{\log(t_r) + C}{1 + \left(\frac{\log(\varepsilon)}{x_0}\right)^p} - C, \quad (2)$$

$$\log(\varepsilon_r) = \left(\frac{\log(t_r) + C}{\log(t_\varepsilon) + C} - 1 \right)^{1/p} \cdot x_0, \quad (3)$$

$$\dot{\varepsilon} = -\varepsilon \cdot k_1 \cdot k_2 \cdot x_0, \quad (4)$$

where t_r is the time to rupture and x_0 , p and C are fitting factors. In its simplest form the last three are constants but in the general case dependent on stress and temperature. The factors k_1 and k_2 are functions of time to strain. The model allows for convenient evaluation of minimum strain rates. The available data seems to be compatible with the Monkman-Grant expression for time to rupture and minimum strain rates, but with fair amount of scatter towards longer creep life (Figure 7).

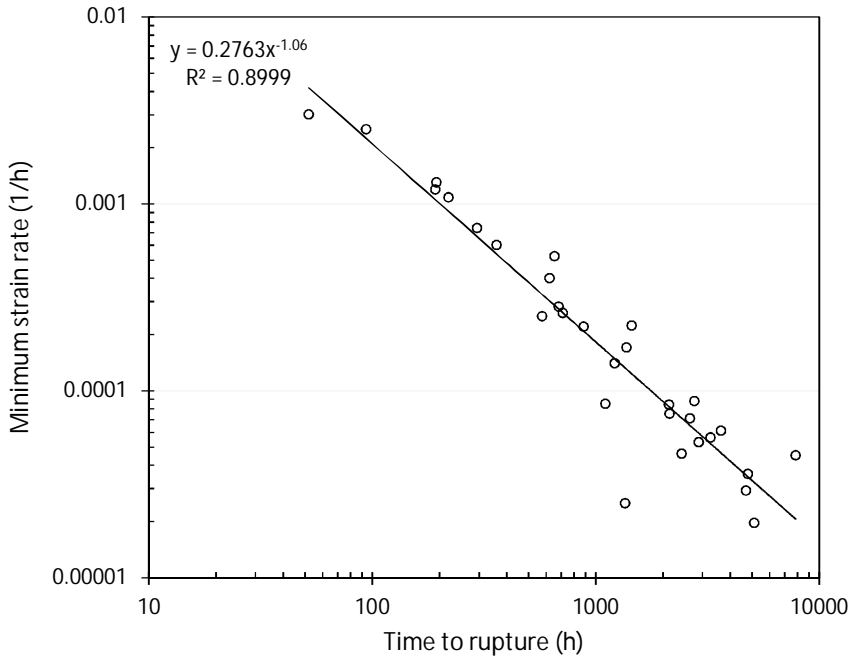


Figure 7. Monkman-Grant plot of the Cu-OFP creep data.

The LCSP model can be considered as an equally suitable but simpler than the classical θ -model [7]. The combination of the Wilshire rupture model and the LCSP strain and strain rate models appear to work well for accurate and robust prediction of long term creep response. It should be noted that the available creep test data appears particularly to lack results from low stress regime with low initial strain levels. This is unfortunate because it is one of the main factors introducing uncertainty to long-term life prediction.

5. Observations on creep ductility and strain localisation

Material ductility is conventionally described by strain to failure (elongation, e_f) and reduction in area (RA), also in creep testing (Figure 8a). Strain localization is bet-

ter revealed by these quantities in combination (Figure 8b). A parameter to describe the extent of localization [8] is $Q = (RA/q) - 1$, where $q = 1 - [1/(1+e)]$.

It is seen from Figure 8a that in creep of OFP copper, RA generally decreases with increasing time to rupture (here temperature-compensated by PLM), and this seems to apply to both base metal and cross-weld specimens. At short term and low temperature end of the testing range, RA is high for both base material and welds, but towards longer time and higher temperature the ductility of welded specimens is reduced on average more than for base metal. There is nevertheless no clear difference in RA of EBW and FSW specimens, although the EBW tests only included relatively short to medium term cases. However, in terms of strain localization (Q), EB welds in Figure 8b show clearly higher mean values than BM or FSW specimens, and more independently on the level on ductility (RA). Note also that the tests with lowest values of RA and Q in Figure 8 were conducted at high testing temperatures far above those in the repository.

The creep test results hence generally indicate lower ductility and more extensive failure localization for cross-weld EB welded specimens than for FSW specimens under comparable creep loading. This is not surprising, given the details of EB welding process and the characteristic pattern of solidification.

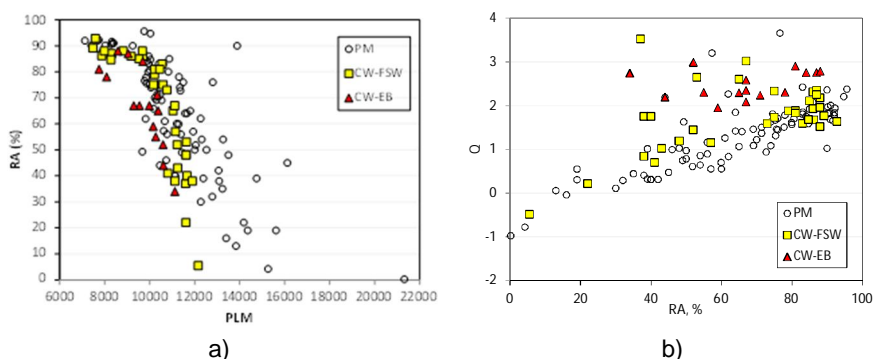


Figure 8. a) RA as a function of temperature-compensated time to rupture (PLM) for welded OFP copper; $C = 20$; b) strain localisation parameter Q as a function of RA.

6. FEA modelling and simulations

The LCSP model is implemented in Abaqus 6.12-1 finite element analysis package via a user subroutine interface. The subroutine contains the implicit and explicit time integration procedures and the multi-axial material model follows a normality preserving constitutive model. The subroutine is called at material points of the FE mesh for a specific increment and as a result it returns the integrated creep strain increments. The LCSP model is always accompanied by a time-independent elastic-plastic material model since an accurate description of the overall plastic response is important for accurate resolution of strain rates. Multi-

linear stress-strain curves are utilized with an isotropic incremental plasticity model. The implementation is applied using a finite strain description for deformation.

Creep weld strength factors are applied to material regions within the subroutine by dividing the applied stress with their specific value, yielding typically an increase in creep strain rate for different weld regions. The derivation of the finite element analysis Fortran code is performed by computing these terms using Mathematica 8.0 and writing the user subroutine via a Python (open source code) module.

The long-term creep analysis is carried out by exposing the canister to an applied external pressure of 14 MPa at a temperature of 80°C the elastic-plastic material model being active. This pressure consists of the hydrostatic pressure at the repository and the bentonite swelling pressure. Pressure by glacial ice is assumed not to appear during the first 1000 years when creep takes place. Then an isothermal simulation is performed the viscoplastic creep model being active with a weld strength factor of 0.95 for the FSW weld. Weld residual stresses are not included in the current analyses.

A 20 degree slice of the copper canister from half-length upwards is constructed containing the FSW weld and its geometry, the weld being a single material region, see Figure 9. Symmetry constraints are enforced in a polar coordinate system and the model is fixed at its bottom in the axial direction of the cylinder. For radial and axial gaps between the insert and the copper shell and the groove between the lid and cylinder of the canister contact constraints are introduced. A finite sliding Lagrangian contact formulation is applied with frictionless sliding. A fairly coarse mesh of quadratic 20 node brick elements with reduced integration is constructed in order to facilitate the lengthy time integration to several tens of thousands of years. Stable incrementation ranges from below an hour to several tens of thousands of hours, and usually a time increment count in the range of several millions is required. Somewhat coarse meshes also introduce a degree of non-localness for the LCSP material model, which especially for the copper in question known to have a high primary creep rate response is a feasible property.

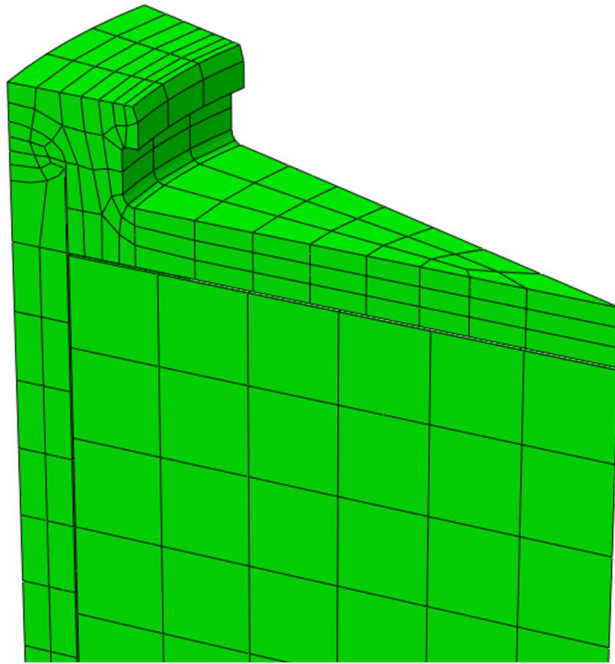


Figure 9. The mesh used in the initial analysis.

The maximum principal stress distribution after 0.3 hours is shown in Figure 10. Compression of the lid against the inner vessel causes tensile stresses in the middle of the upper surface of the lid. Surprisingly the inner corner of the lid is not heavily stressed. Most heavily stressed locations are the FSW joint notch tip region (compressive stress) and the outer surface of the FSW (tensile stress) as shown in Figure 10. The analysis suggests that the cylinder will come into contact with the insert already during loading as the stress caused by the external pressure exceeds the yield stress of copper. However, below the lid an air gap remains between the cylinder and the insert.

The tensile stress on the FSW outer surface after loading is in the order of 80 MPa as shown in Figs. 10 and 12. After 10^8 hours (11 400 years) the predicted stresses have relaxed to a very low level, see Figs. 11 and 12. The maximum stress point inside the FSW in the compressive stress region is an anomaly.

These initial results suggest that the stresses relax very rapidly at the outer perimeter of the lid, where the critical stress areas are located. In Figure 12 the rapid decrease of the maximum principal stress in the middle of the FSW on the outer surface is shown. The initial stress peak relaxes quickly and then the stress level stays practically constant up to 10^5 hours (11 years). During this time the contact point between the cylinder and the insert moves closer to the lid as the cylinder creeps against the insert and this keeps the stress level in the FSW constant. After

10⁵ hours the cylinder is in contact with the insert except close to the lid where the air gap remains. A very similar trend is observed on the lid/cylinder contact point as shown in Figure 13. The lid/cylinder contact point is the lid corner which is compressed against the cylinder. A maximum principal strain of 3.1% is reached after 4.92*10⁸ hours (56 100 years), see Figure 14. This is also very much lower than what was reported in [2]. In the middle of the FSW on the outer surface the strain reaches a value of only 0.42% during loading, and this value does not increase much during the exposure, see Figure 15.

An interesting point is the tip of the notch between the lid and the cylinder. The initial notch width is 0.75 mm and there is a compressive state of stress immediately after loading as shown in Figure 10. The compressive stress remains after creep as shown in Figure 11. The calculated maximum strain is 1.3% according to Figure 14.

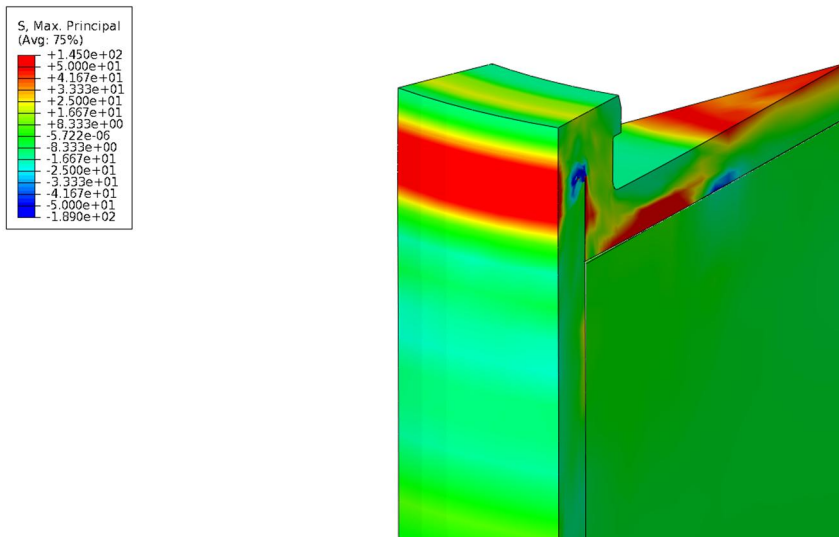


Figure 10. Maximum principal stress distribution after 0.3 h.

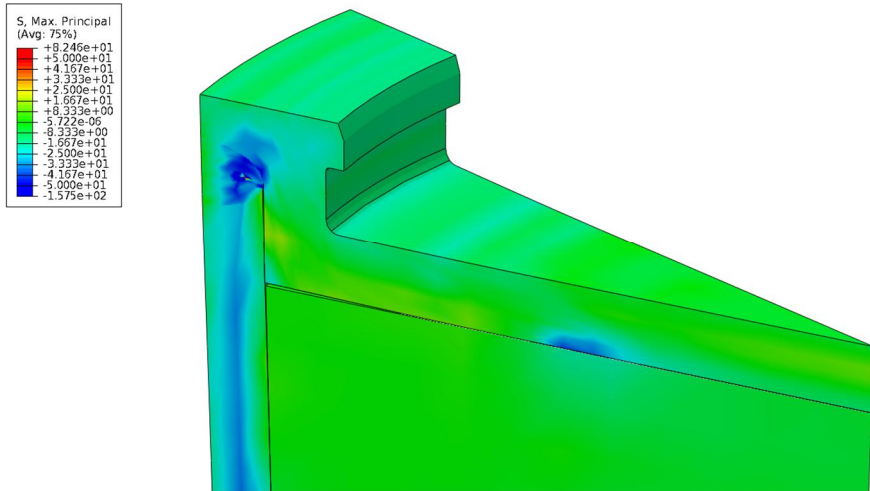


Figure 11. Maximum principal stress distribution after 10^8 hours (11 400 years).

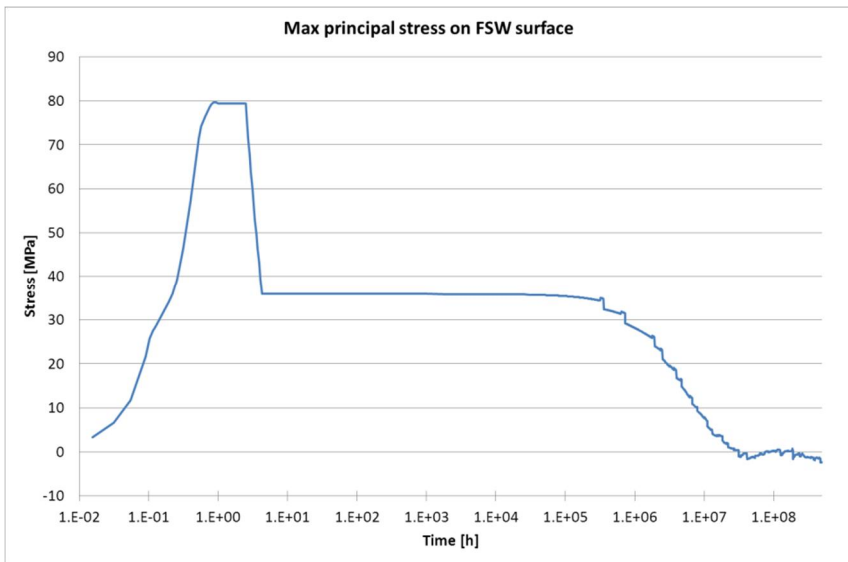


Figure 12. Maximum principal stress as a function of time on the FSW outer surface.

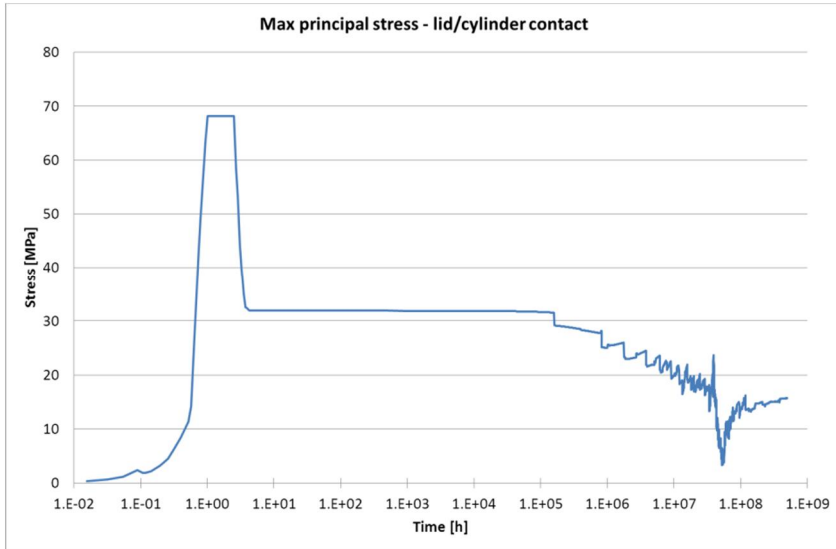


Figure 13. Maximum principal stress as a function of time on the lid/cylinder contact point.

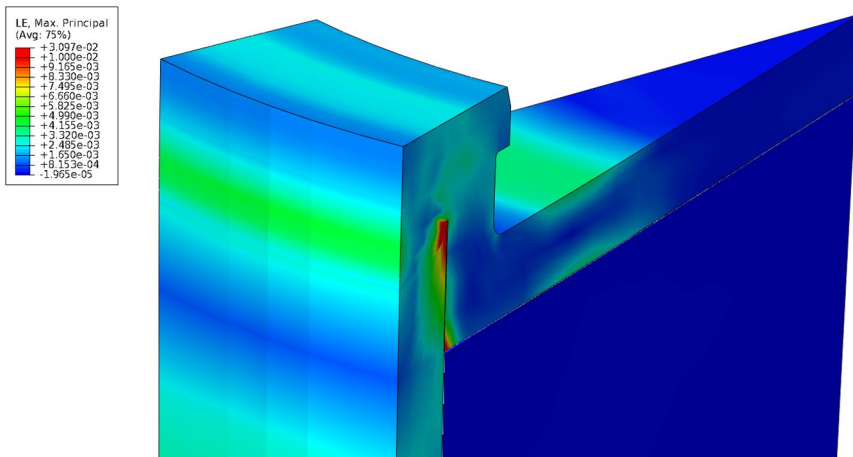


Figure 14. Maximum principal strain distribution after $4.92 \cdot 10^8$ hours (56 100 years).

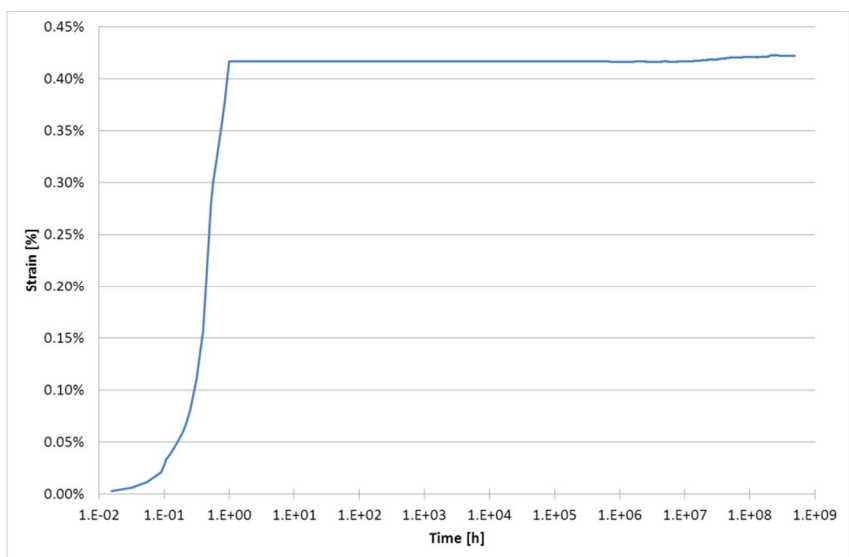


Figure 15. Maximum principal strain (tensile) evolution on the outer surface of FSW.

7. Discussion

The relaxation of the stresses is expected as the loading case of the copper over-pack is forced displacement when the canister is compressed against the insert by the hydrostatic stress. The rapid relaxation is, however, in contradiction with the results shown in [2]. This also raises the question how accurate is the current analysis for predicting relaxation, when using standard creep models developed for “forward creep” where the stresses are normally either approximately retained or increase in time.

An aspect of the materials behaviour that seems to deserve more attention is creep ductility, particularly in welds and other locations of local discontinuity. From this point of view, creep strain localisation at such locations has not been experimentally addressed to the same extent and time of exposure as for intact base material. For example, EB welds seem to show strong tendency towards strain localisation, possibly independently of the level of conventionally measured ductility (reduction in area). This could also carry important implications for the acceptable size and character of weld defects.

The implementation of the LCSP material model will be further developed with respect to non-local behaviour and parallel computational efficiency, enabling improved local resolution of stress-strain fields and mesh refinement. Also the effect of loading rate will be studied in more detail as the loading rate has a large impact on the stress levels that develop in the elastic-plastic calculation. With instantaneous loading high initial stresses and strains will develop before stress relaxation. It has been estimated that due to the slow movement of water in the

bedrock the wetting process of bentonite and the development of full hydrostatic pressure can in reality take up to 6000 years. With a slow loading rate the stress peak is substantially reduced, but creep starts already during loading, affecting the predicted life. One of the important conclusions is that it is essential to be able to model accurately the initial part of the creep curve and the corresponding initial part of other loading configurations like relaxation to successfully and accurately predict the long-term life of the canister overpack.

8. Conclusions and recommendations

The base material and EB and FSW welded OFP copper have been extensively tested for more than a decade using uniaxial and multiaxial specimens. The test data base has been exploited to develop and verifying creep models for assessing the behaviour of the copper overpack of the repository canister.

It is suggested that further experimental attention is paid on creep ductility and strain localisation in welds, weld defects and other positions of material discontinuity. Experimental verification of the creep models is also proposed to cover loading configurations resulting in significant stress relaxation.

The creep strain model (LCSP) was implemented to FEA code. The results of FEA suggest sustained concentration of tensile stress and strain close to the external (FSW) weld surface, with potential for locally concentrating damage. The predicted maximum principal strain was about 3% located near the FSW joint tip after about 56 000 years. Otherwise, the predicted stress distributions differ markedly from those suggested previously elsewhere, and further work is suggested to clarify the discrepancy. In particular, the short and long-term relaxed stress levels are substantially lower than those previously predicted. It is essential to be able to model accurately the initial part of the loading response to successfully predict the safe long-term life of the canister overpack.

References

1. Finnish Research Program on Nuclear Waste Management, KYT 2014. Framework programme for the research period 2010–2014, 16.3.2010. MEE Publications, Energy and Climate 68/2010.
2. Raiko H. Canister Design 2012. Helsinki, Posiva Oy. Report POSIVA 2012-13.
3. Wilshire, B. & Bache, M. B. Cost effective prediction of creep design data for power plant steels. 2nd Intl. ECCC Conference on Creep & Fracture in High Temperature Components – Design & Life Assessment. Dübendorf, Switzerland, 21–23 April 2009.

4. Savolainen, K., Saukkonen, T. & Hänninen, H. Banding in copper friction stir weld. *Science and Technology of Welding and Joining*, 2012, Vol. 17, pp. 111–115.
5. Rantala, J., Salonen, J., Auerkari, P., Holmström, S. & Saukkonen, T. Long-term integrity of copper overpack – Final report 2010. Espoo, VTT, 2011. Research Report VTT-R-01581-11. 28 p.
6. Holmström, S. Engineering tools for robust creep modeling. Dissertation. Espoo, VTT Technical Research Centre of Finland, 2010. VTT Publications 728. 94 + 53 p.
7. Andersson-Östling, H. & Sandström, R. Survey of creep properties of copper intended for nuclear waste disposal. SKB Technical Report TR-09-32, 2009.
8. Kulas, M.-A., Green, W. P., Taleff, E. M., Krajewski, P. E. & McNelly, T. R. Failure mechanisms in superplastic AA5083 materials. *Metallurgical and Materials Transactions A*, 2006, Vol. 37A, pp. 645–655.

The effect of sulphide exposure on the mechanical behaviour of OFP copper

Konsta Sipilä, Esko Arilahti, Taru Lehtikuusi, Timo Saario & Päivi Varis

VTT Technical Research Centre of Finland,
P.O. Box 1000, FI-02044 VTT, Finland

Abstract

A Japanese research group reported in 2008 susceptibility to stress corrosion cracking of oxygen free phosphorous doped copper (CuOFP) in sulphide containing sea water at $T = 80^{\circ}\text{C}$ and under uniaxial slow dynamical loading conditions. More evidence for stress corrosion cracking has not been found under multiaxial constant loading conditions in sulphide containing groundwater at $T = 25^{\circ}\text{C}$. Indications of possible sulphur ingress to CuOFP grain boundaries from sulphide containing groundwater were found, which initiated further studies on the possibility of grain boundary embrittlement through such ingress. Further studies were conducted in order to clarify the effect of sulphide exposure on the mechanical behaviour of CuOFP.

Tensile and creep tests were performed with specimens exposed to sulphide and reference specimens. In the studies presented in this paper only small concentrations or no sulphur at all was found on fracture surfaces, in contradiction with earlier studies with precracked compact tension (CT) specimens under constant load. It is suggested that the high concentrations found earlier may have been caused by the method of opening up the fracture surfaces (i.e. post-exposure fatigue in air) and thus be an artefact.

The tensile tests performed after the exposure to sulphide containing groundwater indicate a degrading influence of the exposure on mechanical properties of CuOFP. The result is based on adequate number of specimens and a standard test practise.

The creep tests performed within the studies presented in this paper seem to indicate a minor degrading influence of the exposure to sulphide containing groundwater. However, when compared with all the publicly available creep data on CuOFP from different heats and laboratories the current finding is still within the scatter band.

1. Introduction

Disposal of spent nuclear fuel in Sweden and Finland is planned to be executed according to the Swedish KBS-3-concept. The concept includes a canister which outer shell is manufactured from CuOFP. The canister is buried in 400 to 500 meters deep bedrock and bentonite clay is used to isolate the canister from the

surrounding bedrock. [1] The canister will last if proper environmental conditions are present throughout the disposal process.

After the closure of the repository air will remain trapped within it. The oxygen contained in the air will be consumed by various reactions such as microbial activity, reactions with rock minerals and copper corrosion. When evaluating copper corrosion the initial oxic period is considered to be most harmful to the copper canister. Various calculations estimate that the oxic period would last 10 to 300 years. During this period oxygen and chlorine are the main constituents which stimulate the corrosion processes. [2] When all entrapped oxygen is consumed by various reactions corrosion will be sustained by sulphide. Sulphide is present at the deep groundwater and corrosion rates will depend on the amount of dissolved sulphide reaching the surface of the copper canister. [3]

The temperature of the repository will be elevated for thousands of years due to the heat radiating from the spent nuclear fuel. After about 10000 years the temperature will approach the natural temperature value. The maximum temperature of the canister at the near field will be reached between 10 and 30 years after the disposal. The calculated maximum temperature at the near field of canister for dry bentonite would be 100°C but when the bentonite is wet the temperature would be 85°C. [3]

In 2008 a Japanese research group reported that sulphide (S^{2-}) can cause intergranular stress corrosion cracking (IGSCC) in pure copper under anoxic seawater conditions [4]. They found with slow strain rate test (SSRT) method that clear stress corrosion cracks formed at sulphide concentration of 320 mg/l, whereas at lower concentrations of 160 mg/l and 32 mg/l slits and crevasses were found, indicative of intergranular attack.

Later in a VTT study [5] CT-specimens with a pre-crack were used instead of SSRT specimens, because the stress-strain state of a CT-specimen more closely simulates that of the thick-walled canister. Constant load was used in contrast with the Japanese study. No clear indication of crack growth caused by exposure to sulphide (up to 200 mg/l S^{2-}) containing groundwater was found in the experiments. However, post-test fractography with scanning electron microscopy indicated high concentrations of sulphur on the crack surfaces. This was taken as an indication of sulphide/sulphur being able to diffuse from Olkiluoto-type groundwater into the CuOFP grain boundaries, which could cause embrittlement, e.g. stress corrosion cracking (SCC) and/or brittle creep failure.

In this paper the effect of sulphide exposure on the mechanical properties of CuOFP and the diffusion of sulphide from groundwater into the copper matrix are examined. This was performed by conducting tensile and creep tests for reference materials and materials exposed to sulphide. The diffusion of sulphide to the copper matrix was evaluated by using SEM/EDS analysis. All the exposures were performed under static loading. Thus, the effect of dynamic loading or loading rate was not studied in this work, in spite the findings of the Japanese research group were exclusively on dynamically loaded specimens.

2. Experiments

Tensile and creep tests were conducted in order to clarify the effect of sulphide exposure on the mechanical properties of CuOFP. The examined test material is the same as is planned to be used in copper canister and was delivered by Posiva Ltd. The composition of the used CuOFP is shown in Table 1. The addition of phosphorous improves the creep properties of copper.

Table 1. The composition of the test material.

Element	Share	Unit
Cu	99,993	%
P	55	ppm
Ag	11,2	ppm
S	3,7	ppm
O	1,5	ppm

2.1 Sulphide exposure

During the sulphide exposure the EDS/SEM, tensile and creep samples were sealed in a vessel containing artificial groundwater composition of which simulates the one present at the repository site. The composition of the artificial groundwater is presented in Table 2. The duration of the exposure was 5 weeks.

Table 2. The composition of the artificial groundwater.

Element	Concentration	
	mg/l	mmol/l
Na ⁺	4800	208,8
K ⁺	21	0,54
Ca ²⁺	4000	100
Mg ²⁺	54,6	2,3
Sr ²⁺	35	0,4
B ³⁺	0,92	0,08
SO ₄ ²⁻	4,2	0,044
Cl ⁻	14500	412,7
F ⁻	1,2	0,063
Br ⁻	104,7	1,31
I ⁻	0,9	0,007
pH	8,2	

2.2 SEM/EDS analysis

In examination of surface properties SEM/EDS analyses and optical microscopy (OM) were used. SEM was used to examine the structure of the sulphide layer of the coupons. The composition of the sulphide layer was determined by performing EDS analyses on the cross sectional area of the sample and at the surface of the sample. The sample used in cross sectional study was made from one of the coupons by cutting it in half and the cross sectional area was polished with micro grit diamond paste. The sulphide film thickness formed on the surfaces of the coupons was then examined with OM.

Fracture surfaces of the exposed creep specimen were analysed with EDS to determine whether sulphide can diffuse into the bulk material. Three areas at about 0.5 mm inwards from the outer edge of the fracture surface, three areas about 0.5 mm further inwards and one area in the centre of the fracture surface were analysed.

2.3 Tensile tests

Tensile tests were conducted according to standard SFS-EN ISO 6892-1. Flat tensile test specimens with 40mm gauge length were used. Prior to the tensile testing flat tensile specimens were exposed to artificial groundwater environment for five weeks. The amount of sulphide in the groundwater varied in different test patches between 1mg/l, 10mg/l and 200mg/l. The obtained test results were compared to the results obtained from reference specimen which had no sulphide exposure.

2.4 Creep tests

The conducted creep tests consisted of in situ and ex situ testing. Samples used in in situ testing were cylindrical notched rods with 10mm gauge length. In in situ testing the sample was under constant load while it was in sulphide containing solution. Tests were conducted in the same artificial groundwater and with same sulphide concentrations as the tensile tests and at room temperature. The load of 20MPa was accomplished by using standardized servohydraulic testing machinery.

In ex situ testing samples were cylindrical shaped with 50mm gauge length and they were first exposed to sulphide solution and then applied to the constant load. A total of six constant load tests were conducted at 215°C where three reference and three exposed samples were compared at three different stress levels of 125MPa, 115MPa and 100MPa.

3. Results

3.1 Surface properties

3.1.1 Surface film thickness

The surface film thickness after exposure to RGW + 200 mg/l S²⁻ for five weeks was measured from cross-sections using optical microscopy. An example of the surface film thickness is shown in Figure 1. The film is seen to have a rather even thickness. The gap between the surface film and the CuOFP base material formed during the curing process of the plastic. The average surface film thickness (from a total of 70 individual measurements while standard deviation was 2.9) was $d = 9.2 \mu\text{m}$.

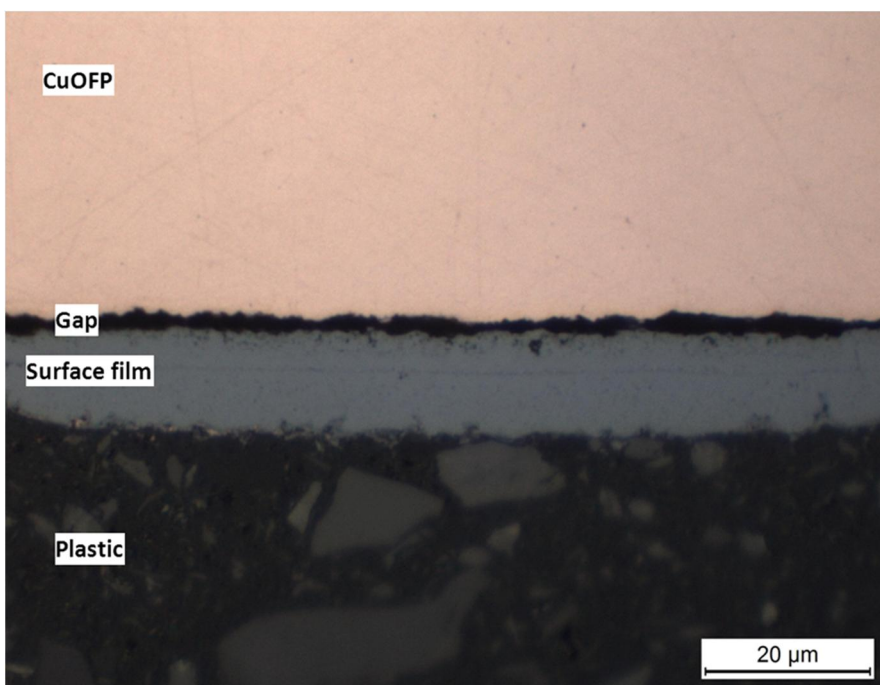


Figure 1. An example of a cross-section of a CuOFP sample after exposure.

3.1.2 Surface film structural and compositional analyses

Figure 2 shows the surface structure of a CuOFP coupon exposed to RGW + 200 mg/l S²⁻ for five weeks. The surface film consists mainly of small crystals in the few micron size scale. The surface film compositional analyses was performed using SEM/EDS and are shown in Table 3. The sulphur concentration (about 8 a-%) is rather low in comparison to the presumed stoichiometric composition of Cu₂S (i.e.

33 a-%). However, in the compositional analyses of a cross-section of a similar sample (Figure 3 and Table 4) a much higher sulphur concentration within the surface film, i.e. 23 a-% was found. Small amounts of elements apparently originating from the groundwater could be detected in the bulk CuOFP metal. However, these could be carry-over from the surface film due to the polishing operation.

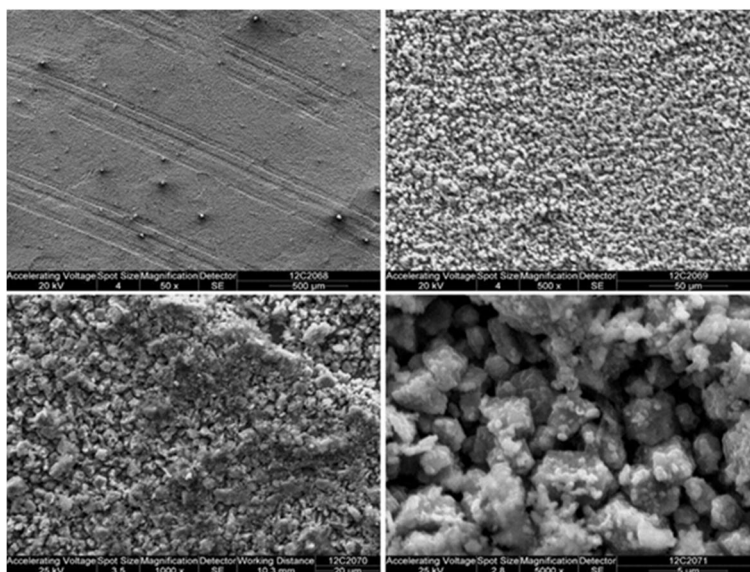


Figure 2. Surface structure of a CuOFP coupon exposed to RGW + 200 mg/l S²⁻ for five weeks (up, left 50x, up, right 500x, down, left 1000x and down, right 5000x).

The up-left picture in Figure 2 shows some corrosion pit like objects, one of which is shown in detail in Figure 4 and compositional analyses of the pit interior in Table 5. It seems that the pits are enriched in Mg, Si and S. The lines in the up-left picture in Figure 2 are remnants from sample manufacturing process.

Table 3. Compositional analyses of the surface shown in Figure 2 (50x).

Element	Weight %	Weight % Error	Atom %	Atom % Error
O	10,98	+/- 0,12	29,75	+/- 0,32
Na	0,85	+/- 0,15	1,60	+/- 0,29
Mg	2,58	+/- 0,09	4,60	+/- 0,17
Al	0,17	+/- 0,04	0,28	+/- 0,06
S	5,61	+/- 0,07	7,58	+/- 0,10
Cl	0,44	+/- 0,03	0,54	+/- 0,04
Ca	3,71	+/- 0,08	4,01	+/- 0,08

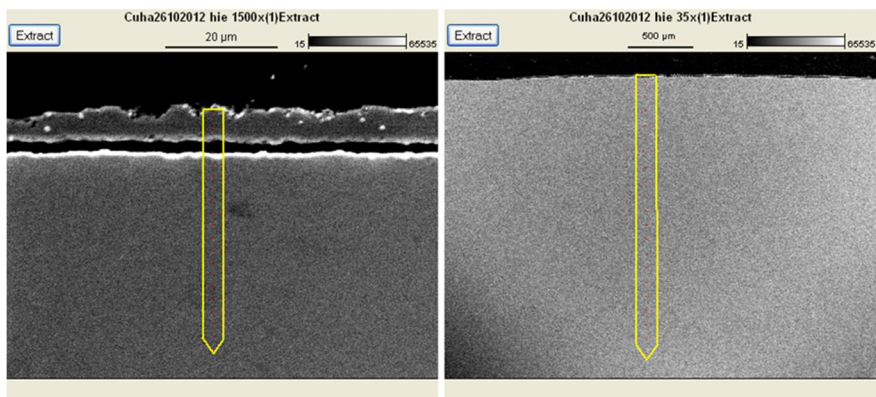


Figure 3. Locations of SEM/EDS compositional line analyses (red dots), the results of which are shown in Table 4.

Table 4. The SEM/EDS line analyses results of the exposed specimen cross-section along the lines shown in Figure 3.

Distance/ µm	O/a-%	Na/a-%	Mg/a-%	S/a-%	Cl/a-%	K/a-%	Ca/a-%	Cu/a-%
Surface	29,04	0	6,31	13,3	0	0,15	0,56	50,65
2,2	18,76	1,2	1,7	22,98	0,14	0	2,56	52,65
4,2	14,99	0,58	0	21,83	0	0	2,78	59,82
6,2	6,9	0,82	0	16,78	0	0,12	0,17	75,21
9,2	6,02	2,02	0,72	6,67	0	0,18	0,15	84,23
11,5	3,58	3,85	0	0	0	0	0,05	92,52
13,7	3	0	0,92	0,07	0,18	0,11	0,23	95,49
16	1,09	0	0	0	0	0,32	0	98,59
18,3	0,33	0	0	0,17	0	0,07	0	99,43
20,6	0,57	0,55	0,24	0	0,47	0	0	98,17
29,8	2,37	1,92	0	0	0,23	0	0,03	95,45
41,2	0,49	0,51	0	0	0	0,05	0	98,95
101	0,23	3,32	0	0,32	0	0	0	96,12
202	0,29	0	0	0	0	0	0,16	99,54
303	0	0	0	0	0,13	0	0,15	99,72
405	1,45	0	0	0	0	0,2	0,11	98,24
506	1,04	0,55	0,72	0,06	0,24	0	0	97,38
1011	1,98	1,56	0	0	0,14	0,14	0	96,19
1517	0,7	0,97	0,48	0	0	0	0,28	97,57
1922	3,3	0	0,2	0,05	0,2	0,1	0,08	96,07

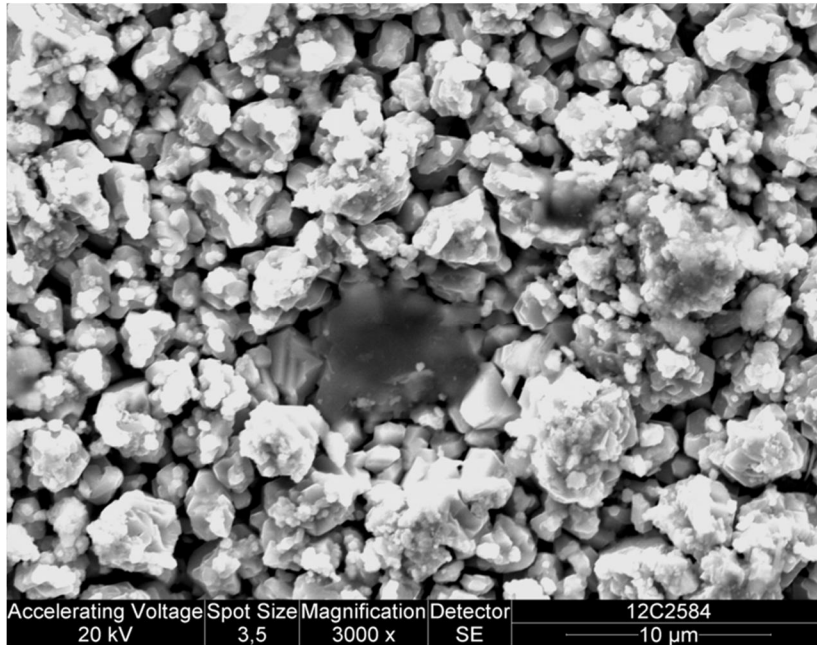


Figure 4. Detail of the structure, showing one of the corrosion pits in Figure 2 (up, left).

Table 5. Compositional analyses of the EDS-spectra in Figure 4.

Element	Weight %	Weight % Error	Atom %	Atom % Error
O	20,31	+/- 0.14	39,19	+/- 0.28
Na	0,25	+/- 0.17	0,34	+/- 0.22
Mg	13,18	+/- 0.12	16,73	+/- 0.15
Al	0,25	+/- 0.04	0,28	+/- 0.04
Si	13,04	+/- 0.09	14,33	+/- 0.09
S	6,98	+/- 0.07	6,72	+/- 0.07
Cl	0,07	+/- 0.02	0,06	+/- 0.02
Ca	0.16	+/- 0.02	0.12	+/- 0.02
Cu	45.78	+/- 0.46	22.24	+/- 0.22

3.2 Tensile tests

The standard flat tensile specimens exposed to the groundwater with sulphide for five weeks were tested according to the tensile testing standard SFS-EN ISO 6892-1:2009 A222. Table 6 shows a compilation of the post exposure test results

of specimens exposed to groundwater with 200 mg/l, 10 mg/l and 1 mg/l sulphide, as well as un-exposed reference specimens along with the tensile test data reported by Posiva Ltd for this particular material lot. Figure 5 shows the data in graphical form. There seems to be a trend towards a higher yield stress and a lower fracture strain with increasing sulphide concentration in the groundwater. Based on the tensile test results reported by Posiva Ltd for the same material lot (with specimens extracted from the same piece of material but at a distance of roughly 100 mm) there is a rather high inherent scatter in tensile properties of the studied material lot. However, it seems reasonable to conclude even taking into account the scatter that there is some detrimental effect of exposure to groundwater with 200 mg/l sulphide for five weeks on the tensile properties of CuOFF.

Table 6. Comparison of the standard flat tensile test specimen data from unexposed specimens (Cuha L4 to L6), and specimens exposed to groundwater with 1, 10 and 200 mg/l sulphide for five weeks (Cuha L1 to L3, Cuha L7 and L8, and Cuha L21 to L23, respectively). Also shown is the data reported by Posiva for this particular material lot.

Specimen	Yield stress / MPa	Ultimate tensile stress / MPa	Fracture strain / %
CUHA L21	55	200	48
CUHA L22	66	205	48
CUHA L23	62	198	48
<i>AVG 200 mg/l</i>	<i>61</i>	<i>201</i>	<i>48</i>
<i>SD 200 mg/l</i>	5.6	3.6	0
CUHA L7	61	200	49
CUHA L8	55	197	53
<i>AVG 10 mg/l</i>	<i>58.0</i>	<i>198.5</i>	<i>51.0</i>
<i>SD 10 mg/l</i>	4.2	2.1	2.8
CUHA L1	53	197	54
CUHA L2	52	198	63
CUHA L3	56	198	54
<i>AVG 1 mg/l</i>	<i>53.7</i>	<i>197.7</i>	<i>57.0</i>
<i>SD 1 mg/l</i>	2.1	0.6	5.2
CUHA L4	56	198	55
CUHA L5	52	197	57
CUHA L6	55	200	51
<i>AVG 0 mg/l</i>	<i>54.3</i>	<i>198.3</i>	<i>54.3</i>
<i>SD 0 mg/l</i>	2.1	1.5	3.1
Posiva reported	39–50 (AVG 44.0)	206–208	51–54

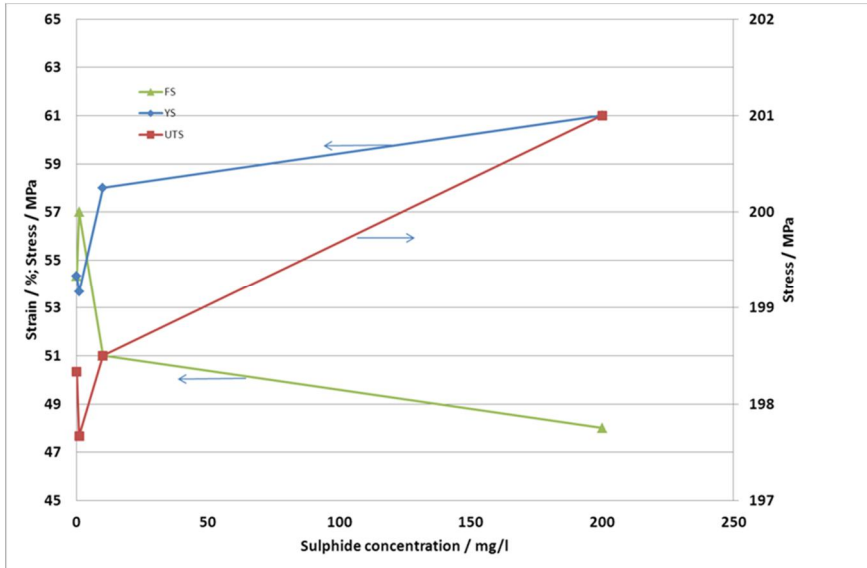


Figure 5. Fracture strain (FS), yield stress (YS) and ultimate tensile stress (UTS) of CuOFP as a function of sulphide concentration after exposure to saline reference groundwater for five weeks at room temperature.

3.3 Creep tests

3.3.1 In situ creep tests

During each 5 week exposure one circumferentially notched specimen was kept under constant load. The increase of displacement during the exposure can be taken as a measure of creep, consisting of a mechanical and an environmental part. Figure 6 shows the comparison of displacement for a specimen exposed to groundwater + 200 mg/l S^{2-} and a specimen exposed to groundwater + 1 mg/l S^{2-} as a function of time. The specimen exposed to the lower sulphide concentration shows a clearly smaller increase in displacement. The step-wise increase in displacement close to the end of exposure of specimen P1 was caused by a small peak in loading (malfunction of the servo-hydraulic loading machine). The increase in displacement (after the first loading increase) during the five week exposures for the three sulphide concentrations studied is shown in Table 8.

In SEM/EDS -studies of specimens P1, P3 and P4 (Table 7) only traces of or no sulphur was found on the fracture surface. This is in contradiction with the earlier findings of high sulphur concentrations on CT-specimen fracture surfaces [5].

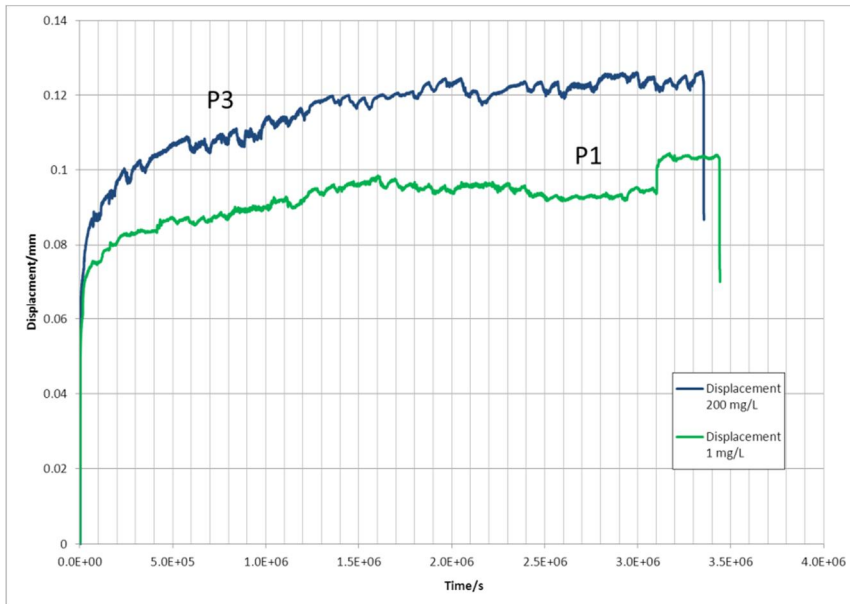


Figure 6. Comparison of displacement (right axis) and displacement rate (left axis) during exposure to RGW + 1 mg/l S^{2-} (green lines) and RGW + 200 mg/l S^{2-} (blue lines).

Table 7. Increase in displacement during the exposure. Stress level = 20 MPa.

Specimen	Sulphide concentration mg/l	Displacement increase μm
P1	1	34
P3	10	56
P4	200	50

3.3.2 Ex situ creep tests

The ex situ creep tests were performed according to the standard SFS-EN ISO 204 at $T = 215^{\circ}\text{C}$ in order to speed up the creep process without changing the creep mechanism, i.e. staying within the power-law creep area. The surface films on exposed specimens were not removed before starting the creep experiments. As of now, tests have been completed at stress levels of 125MPa and 115MPa, and those at 100MPa are expected to end in July 2013. At each stress level, one un-exposed reference specimen and one specimen pre-exposed to RGW+200 mg/l S^{2-} have been tested simultaneously. The test arrangements and results have been described in detail in [6].

Figure 7 shows the creep curves, i.e. strain – log(time) –curves and Table 8 the results in numerical form. For the two stress levels at which the tests have been completed (115 and 125MPa), the reduction of area, time to fracture and fracture strain all are consistently smaller for the specimens that have been pre-exposed to the sulphide containing groundwater.

The fracture surface of specimen y361 tested at stress level 115MPa is shown in Figure 8 (SEM image). The morphology shows a typical dimple structure, where voids have opened at sites of internal particles. In Figure 8 the red squares mark the areas on which a compositional analysis was performed with EDS. The results are shown in Table 9. Sulphur, sodium and chloride supposedly originating from the groundwater were found at the distance 0.5 mm inwards from the outer edge of the fracture surface, but not at the areas more inwards.

In order to determine whether the variations in the obtained rupture times between exposed and reference data are remarkable, the results were compared to publicly available creep data. Due to different testing parameters used in creep tests the creep data must be normalized. One way to normalise creep data is to use the so-called Wilshire model. Figure 9 shows the publicly available data [7] with the data from the creep tests presented above. One may notice that although the present data seems to indicate a degrading effect of sulphide exposure on the creep properties, when normalised and shown with data from various heats and laboratories, the scatter between the different sets of data is of the same magnitude as the difference between the reference and exposed specimens in the present work.

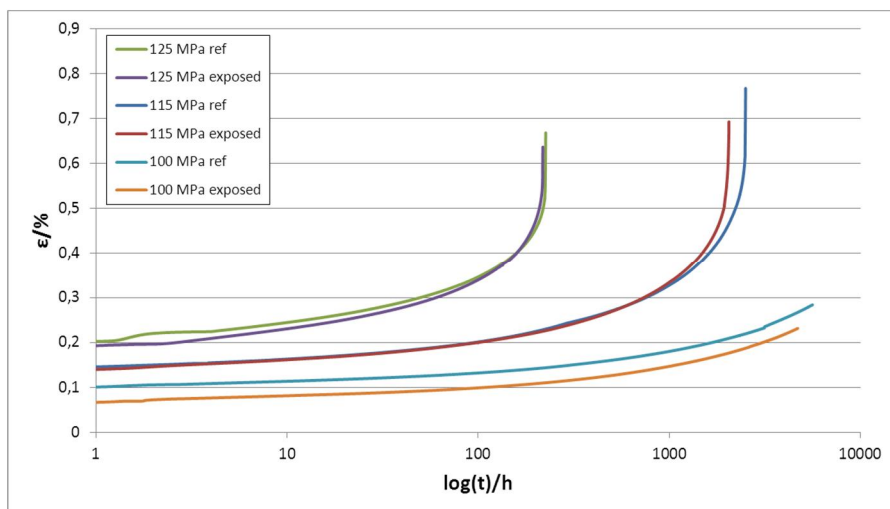


Figure 7. Strain as a function of time for the three levels of stress studied.

Table 8. Effect of sulphide exposure (RGW+200 mg/l S²⁻, five weeks) on reduction of area, time to fracture and fracture strain in creep tests. Tests conducted at 100MPa are still running and are expected to terminate at July 2013.

Specimen	Stress [MPa]	Sulphide exposure	Reduction of area [%]	Time to fracture [h]	Fracture strain [%]
y359	125	no	82	226	66,9
y362	125	yes	67	218	63,7
y358	115	no	78	2508	76,7
y361	115	yes	75	2053	69,3
y360	100	no	running	running	running
y363	100	yes	running	running	running

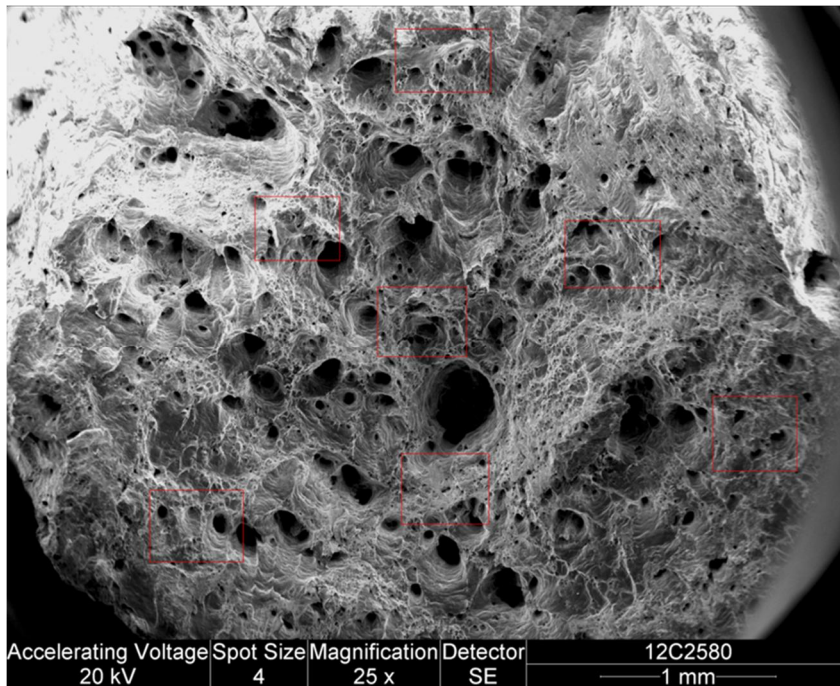


Figure 8. SEM picture of the fracture surface of specimen y361 tested at stress level 115MPa. The red squares mark the areas on which a compositional analysis was performed.

Table 9. Compositional analysis of the different locations (red squares) shown in Figure 8.

Location	Element	Weight %	Weight % error (+/-)	Atom %	Atom % error (+/-)
Edge	Cu	84,75	0,86	60,84	0,62
Edge	N	0,90	0,13	2,96	0,43
Edge	O	11,56	0,18	32,43	0,52
Edge	Al	0,34	0,05	0,57	0,09
Edge	Si	0,42	0,04	0,65	0,06
Edge	S	0,49	0,05	0,67	0,07
Edge	Cl	1,20	0,06	1,52	0,08
Edge	Ca	0,33	0,03	0,36	0,03
Middle	Cu	99,34	0,93	97,89	0,91
Middle	O	0,37	0,07	1,45	0,28
Middle	Al	0,29	0,06	0,67	0,13
Center	Cu	99,36	0,97	98,05	0,96
Center	O	0,29	0,07	1,15	0,28
Center	Al	0,34	0,06	0,80	0,14

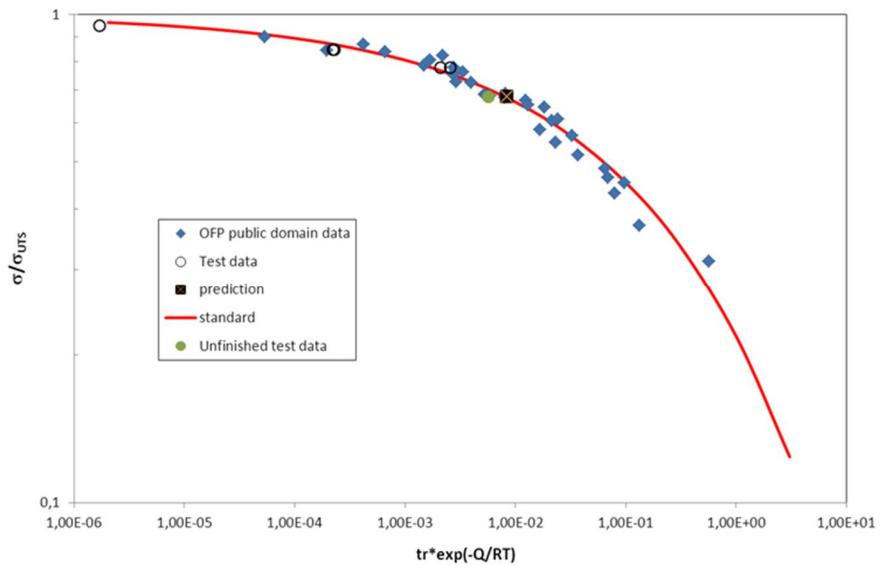


Figure 9. The Wilshire -model presentation for CuOFP. [6]

4. Discussion

One of the targets of this study was to investigate further the possibility of sulphur ingress into CuOFP from sulphide containing groundwater. The SEM/EDS -studies on fracture surfaces and cross-sections of exposed specimens revealed in some cases small concentrations of sulphur on the surfaces. In case of cross-sections of exposed specimens, one may argue that there can be a carry-over from the sulphur containing surface film due to the sample preparation technique (i.e. polishing). In case of the creep specimens, the sulphur may have diffused via surface diffusion from the external sulphur containing surface film e.g. during the cool down of the creep oven after the specimen had been fractured by creep. Thus, based on the results from this work one cannot definitely conclude that sulphur has actually diffused into CuOFP from sulphide containing groundwater during the exposure.

The creep test results at elevated temperature seem to indicate a degradation of the mechanical properties due to the pre-exposure. However, when compared with the publicly available creep data from different batches of CuOFP and different laboratories, the effect is still within the overall scatter.

The tensile test results of pre-exposed specimens, with adequate statistical number of specimens and standard test method do indicate a degradation of the mechanical properties of CuOFP due to the exposure.

5. Conclusions

A Japanese research group reported in 2008 susceptibility to stress corrosion cracking of CuOFP in sulphide containing sea water at $T = 80^{\circ}\text{C}$ and under uniaxial slow dynamical loading conditions. Further evidence for stress corrosion cracking has not been found under multiaxial constant loading conditions in sulphide containing groundwater at $T = 25^{\circ}\text{C}$. Indications of possible sulphur ingress to CuOFP grain boundaries from sulphide containing groundwater were found, which initiated further studies on the possibility of grain boundary embrittlement through such ingress.

In the present project only small concentrations or no sulphur at all was found on fracture surfaces, in contradiction with earlier studies with precracked CT-specimens under constant load. It is suggested that the high concentrations found earlier may have been caused by the method of opening up the fracture surfaces (i.e. post-exposure fatigue in air) and thus be an artefact.

The creep test results presented within this paper seem to indicate a degrading influence of the exposure to sulphide containing groundwater. However, when compared with all the publicly available creep data on CuOFP from different heats and laboratories the current finding is still within the scatter band.

The tensile tests performed after the exposure to sulphide containing groundwater indicate a degrading influence of the exposure on mechanical properties of CuOFP.

References

- [1] Rosborg, B., Werme, L. 2008. The Swedish nuclear waste program and the long-term corrosion behaviour of copper. *Journal of Nuclear Materials* 379(1–3), pp. 142–153.
- [2] Rosborg, B., Kosec, T., Kranjc, A., Pan, J., Legat, A. 2011. Electrochemical impedance spectroscopy of pure copper exposed in bentonite under oxic conditions. *Electrochimica Acta* 56(23), pp. 7862–7870.
- [3] King, F., Lilja C., Pedersen, K., Pitkänen, P. & Vähänen, M. 2011. An Update of the State-of-the-art Report on the Corrosion of Copper Under Expected Conditions in a Deep Geologic Repository. Posiva Report 2011-1, Posiva, Olkiluoto, Finland. 246 pp.
- [4] Taniguchi, N. and Kawasaki, M., 2008. Influence of sulphide concentration on the corrosion behaviour of pure copper in synthetic seawater. *Journal of Nuclear Materials* 379 (2008) 154–161.
- [5] Arlahti, E., Lehtikuusi, T., Olin, M., Saario, T. and Varis, P., Evidence for internal diffusion of sulphide from groundwater into grain boundaries ahead of crack tip in Cu OFP copper. *Corrosion Engineering Science and Technology*. Vol. 46 (2011) No: 2, 134–137.
- [6] Sipilä, K., The Effect of Sulphide-Containing Groundwater on Creep Behaviour of Copper, Master of Science Thesis, December 2012, Tampere University of Technology, 101+11 pages (in Finnish).
- [7] Andersson-Östling, H., Sandström, R. Survey of creep properties of copper intended for nuclear waste disposal. 2009, SKB. Technical Report TR-09-32. 96 s.

NDE of the disposal canisters

Ari Koskinen¹, Tarja Jäppinen¹, Matti Sarkimo¹, Aarne Lipponen¹, Jonne Haapalainen¹, Stefan Sandlin¹, Esa Leskelä¹
& Jorma Pitkänen²

¹ VTT Technical Research Centre of Finland

Espoo, Finland

²Posiva Oy

Eurajoki, Finland

Abstract

The Finnish concept of high activity nuclear waste disposal is based on deep geological storage in copper canisters with cast iron inserts. Disposal canisters will be embedded in Olkiluoto bedrock at the depth of approximately 400 metres. Therefore it is essential to inspect the canisters with non-destructive testing (NDT) methods as well as possible before the final disposal.

The lid of the copper disposal canister for high activity nuclear waste is sealed with a weld. Before accepting the canister to the final disposal the weld will be inspected by four non-destructive testing methods. These methods are ultrasonic testing (UT), radiographic testing (RT), eddy current testing (ET) and remote visual testing (VT) using cameras. The copper overpack and the lid are also inspected with multiple NDT methods; UT, ET and VT. The nodular cast iron insert is inspected with UT and VT.

In this paper the four NDT inspection methods for inspection of different parts of the disposal canister are presented in brief. All information in this paper is collected and summarised from public reports and from the procedures of each method and inspection records. Also experts have been interviewed.

All of the four NDT methods detect defects in slightly different directions and based on different physical principles. The four methods are therefore supplements to each other in inspection of different parts of the disposal canister.

1. Introduction

The Finnish concept of nuclear waste disposal is based on deep geological storage in copper canisters with a cast iron insert. Canisters will be embedded in Olkiluoto bedrock at the depth of approximately 400 metres. Therefore it is essential to have a careful inspection as thorough as possible to the canisters with non-destructive inspection methods before the final disposal.

The final disposal canister for high activity nuclear waste consists of a copper overpack, a copper lid and a nodular cast iron insert. The nodular cast iron insert

gives strength to the structure of the canister to withstand the mechanical stress originating from the bedrock in the underground repository. Oxygen-free copper overpack forms a corrosion resistant shell to the canister. The copper lid of the canister will be sealed with electron beam welding (EBW) or with friction stir welding (FSW) to the copper overpack.

During manufacturing defects may be generated in the components. The welding process may produce different types of welding defects, for instance voids, internal root defects, porosity and cavities [4]. Lifting of the canister at the encapsulation plant is one factor that could cause defects or make small defects to grow. Thus, there is a limited number of lifts that are allowed. Possible handling incidents could cause defects on the outer surface of the copper overpack.

The disposal canister material quality as well as quality of the weld has to be verified according acceptance criteria before the final disposal of the canister. Those criteria for accepting the canister are created to control and ensure the wanted strength and corrosion resistance levels for the canister. Non-destructive testing methods give possibility to reveal defects in the base material and in the weld. The four NDT methods used are: are ultrasonic testing (UT), radiographic testing (RT), eddy current testing (ET) and remote visual testing (VT) using cameras.

Several different inspection methods are used to gain the best possible information on different types of discontinuities. These include visual, ultrasonic, eddy current and radiographic inspection methods. Ultrasonic and radiographic methods are used for volumetric inspections. Visual and eddy current methods are used surface and near surface inspections

Non-destructive testing of the canister weld is carried out in the encapsulation plant before the decision to move the canister to final disposal. The encapsulation plant (Figure 1) is located at the ground level above the actual repository. All NDT methods will be remotely controlled. Non-destructive testing is operated automatically in an isolated area because of the radiation originating from the high active waste filled in disposal canister. The objective of the NDT testing is to acquire and analyse the data to detect possible manufacturing defects in the closure weld of the disposal canister. In NDT there are different phases such as data acquisition and data analysis.

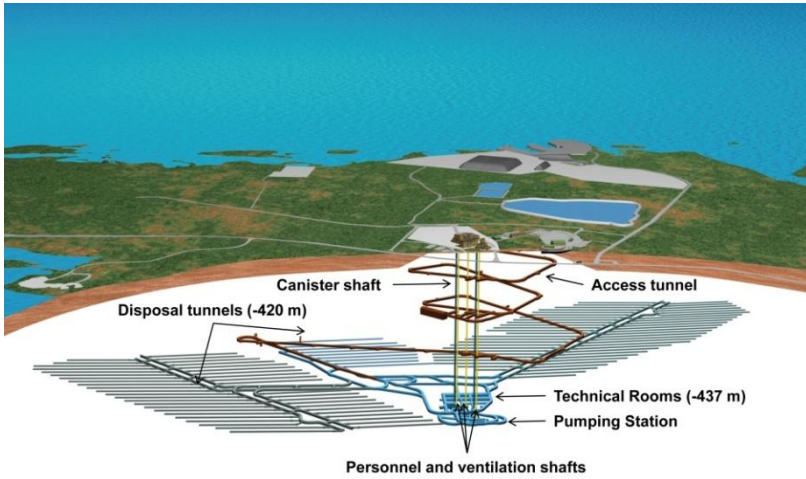


Figure 1. The encapsulation plant is located above the actual repository (Posiva Oy).

2. Disposal canister

The disposal canister consists of nodular cast iron insert, copper overpack and copper lid (Figure 2).



Figure 2. The disposal canister (Posiva Oy).

2.1 Nodular cast iron insert

The main task for the nodular cast iron insert is to give strength to the structure of the canister to withstand the mechanical stress originating from the bedrock in the underground repository. There are three different types of cast iron inserts (Figure 3), one type for Loviisa 1 and Loviisa 2 (VVER 440 type), second one for Olkiluoto 1 and Olkiluoto 2 (BWR type) and third one for Olkiluoto 3 (EPR type).



Figure 3. Different types of nodular cast iron inserts for VVER 440, BWR and EPR (from left to right) [1].

2.2 Oxygen-free copper overpack and lid

Overpack including the bottom and the lid of the canister are made of oxygen-free copper which forms a corrosion resistant shell to the canister. Overpack thickness is 50 mm. The geometry of the lid depends on the chosen welding method due to different weld orientation between electron beam welding and friction stir welding.

3. Non-destructive evaluation of the canisters

Four different methods are used for non-destructive evaluation of a disposal canister. For surface and near surface inspections remote visual testing and eddy cur-

rent testing are used. For volumetric inspections ultrasonic testing and radiographic testing are used. In all inspections Inspectors shall be qualified according to SFS-EN 473 level 2 suitable for used method. Only in radiographic inspections the operator shall have a level 1 certification according SFS-EN 473. Nevertheless the person evaluating the radiographic images shall have a level 2 certification according SFS-EN 473.

3.1 Visual testing

Visual testing is conducted for all the disposal canister components including welds. The visual inspection in the encapsulation plant will be done with cameras.

After the welding the area to be inspected is the surface of the upper part of the lid. Especially 100 % of the weld area and the entire upper end of the lid are inspected. Also the vertical upper outer surface of the lid shell and the vertical inner surface of the lid are inspected. The illuminance degree is required to be high enough (minimum 500 lx). Additional lightning is needed from multiple lightning directions due to the variable reflection of the copper surface because of characteristics of copper and its oxides. The surface to be examined is required to be clean.

The purpose of the visual testing is to verify, document and evaluate the surface area. During this inspection both manufacturing originated surface defects and handling defects can be detected. This information is critical for the integrity of the canister but also for verifying the indications primarily detected in eddy current testing and secondly by ultrasonic and radiographic testing. Especially outer surface defects which can be seen in radiographic images. Indications that exceed reporting values will be reported by location, dimensions and defect type. Indication sizes correspondingly locations are tabled and compared to the relevant acceptance criteria. There are stamped identification marks in the weld, lid and shell that need to be documented and checked.

3.2 Eddy current testing

Eddy current testing is a well-known and widely used surface inspection technique. In disposal canister inspection eddy current testing is a combination of low frequency and high frequency probe measurements. With high frequency technique surface breaking defects and surface extensions can be accurately measured. With low frequency eddy current deeper surface breaking defects and defects having small ligament can be evaluated. Overpack, lid and especially weld are inspected with eddy current technique. In the inspections of the electron beam (EB) weld the surface and near surface areas are inspected up to a depth of about 10 mm. Surface breaking defects up to 10 mm can be detected and sized, and defects with ligament of about 5 mm can also be detected [5].

In the current inspection procedure inspection is done using 4 channel eddy current equipment. In 4 channel electronic board it is possible to use 4 probes or 4 frequencies. At the present maximum scanning speed is 160 mm/s. 5 sam-

ples/mm are recorded. The scan is visualised with in a form of colour coded C-scan (Figure 4).

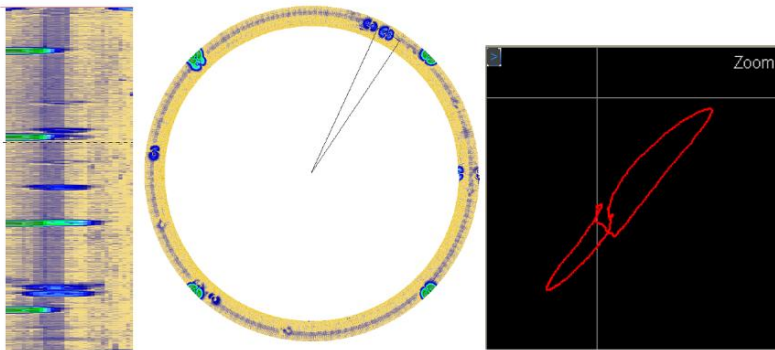


Figure 4. Example of scan visualisation from low frequency coil EB weld inspection [5].

A probe array consisting of pancake coils is held on the surface of the copper lid with a probe holder. The array and holder is moved by a manipulator (Figure 5).

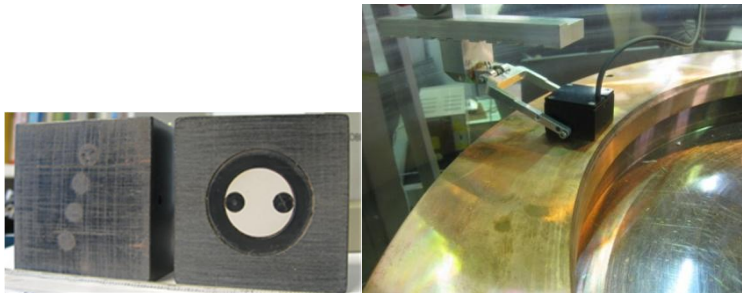


Figure 5. Eddy current probe holder on the left, HF and LF coils on the right.

The upper planar surface of the lid is inspected using a coil probe array in order to detect defects. In inspection surface breaking defects will be detected, sized and classified. The inspection speed depends on the effective width of the probe array and on the frequency of the probe.

3.3 Ultrasonic testing

Ultrasonic testing is a volumetric testing method and in disposal canister inspections it is used for all the components of the canister. Phased array ultrasonic inspection is used for all inspections due to possibility to modify electrically the

sound field during the inspection. This enables the sound field adjustment dynamically for different situations and for detection of different types of flaws. In cast iron insert inspections also other ultrasonic methods are used. Frequency of phased array effects on detectability and sizing and therefore a good compromise 3.5 MHz for both is chosen for copper part inspections. At the moment ultrasonic inspections are performed using the Multi 2000 phased array ultrasonic system of M2M with 128 channels. During the examination of the EB weld an ultrasonic transducer is scanning the outer surface of the lid in circumferential direction. Simultaneously the phased array probe also carries out electronic scanning in axial direction. A-scan data in RF-form of each measurement is stored. There are about 1500 measurement positions in circumference. Two different focus depths will be used which demands own focal laws for both. Also three different techniques using $+20^\circ$, 0° and -20° refraction angles is used.

As can be seen in figure 6 the ultrasonic phase array probe is positioned on the outer vertical surface of the canister at the distance of 0.1 mm from the scan surface.

An electronic scan is performed in the direction of the weld penetration. The longitudinal wave velocity in copper is $v = 4760$ m/s. The attenuation of the sound is dependent on the grain size of copper, bigger the grains more there is attenuation. Large grains extending over 2 mm occur in the weld in circumferential direction. In radial direction the grain size is smaller but large enough to produce higher attenuation compared to base material of the tube and lid. In some cases also in the tube and the lid large variations in grain size can be detected. The grain size is controlled in the manufacturing process of the base material in order to minimise the grain size and its distribution. The ultrasonic testing will be carried out in local immersion at the encapsulation plant.

Before the examination the performance and the stability of the system is verified with a reference block containing different kind of reflectors. The block has the same geometry and material properties as the canister.

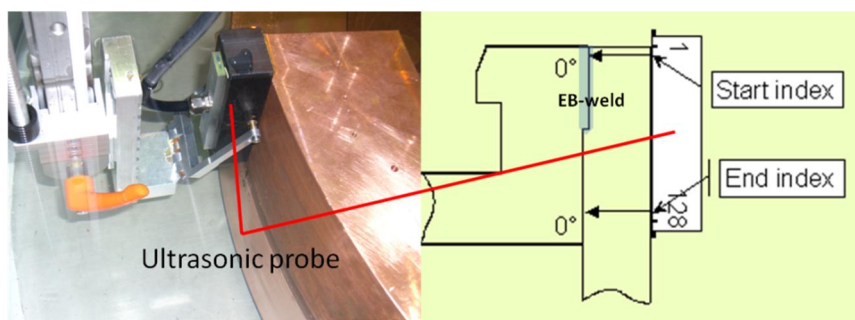


Figure 6. Linear phased array ultrasonic testing of EB weld.

Nodular cast iron insert is also inspected with ultrasonic methods. The longitudinal wave velocity in nodular cast iron is $v = 5600$ m/s. Inspection is performed from

the outer surface of the insert. First inspection is performed with 5 MHz phased array probe to verify the steel channel edge location and the channel distortion in casting (Figures 7 and 8).

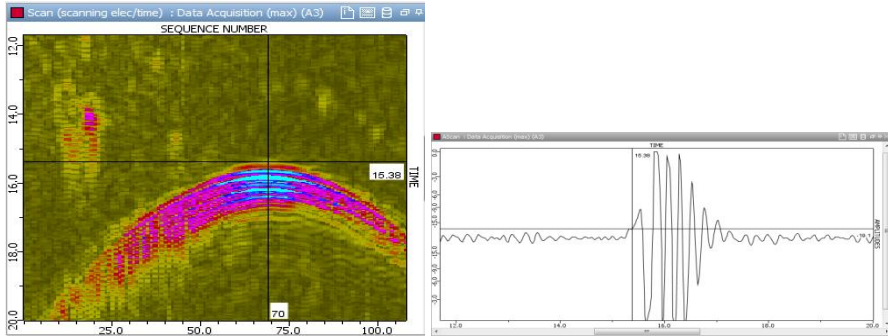


Figure 7. Nearest edge distance point in A-scan is the cross point of the back wall signal and noise where the signal rises up clearly from the noise.

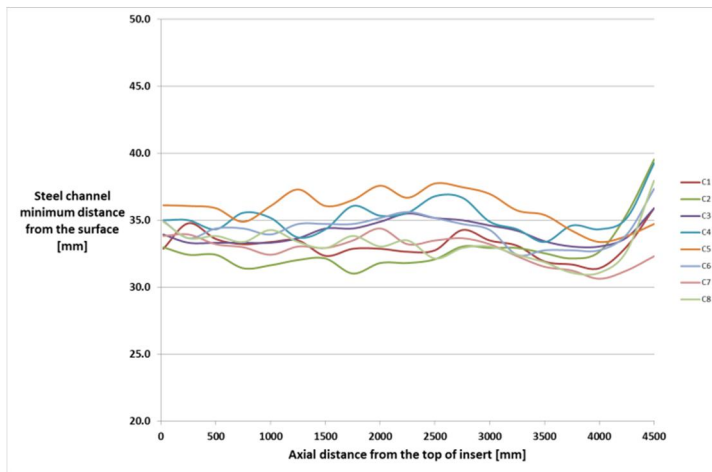


Figure 8. The minimum distance variation of each steel channel from the surface in axial direction measured from the top of the insert in millimetres.

After steel channel inspections 0° longitudinal wave using curved 5 MHz phased array probe using different focus depths is used for certain areas of insert. Near surface area of the insert is inspected with transmitting receiving longitudinal TRL- 70° wave (conventional) probes using four inspection directions (0° , 90° , 180° , 270°). Technique TRL A means that the scanning occurs in axial direction and TRL C corresponding the scanning direction in circumferential direction. The fourth ultrasonic inspection for insert is performed using transmission technique with 2

MHz phased array probes to detect defects between the steel channels. At the same time with the same probes also transmit-receive inspection is performed for the same area. Due to three different types of inserts (BWR, VVER 440 and EPR) inspection is also highly dependent on the insert type.

3.4 Radiographic testing

Another used volumetric method is radiographic inspection. Radiographic inspection is used for the disposal canister welds and due to thickness of the component it is carried out with a 9 MeV linear accelerator. The centreline of accelerator beam is directed at a 10° angle to the lid surface. For radiographic inspection a digital x-ray detector is used. As can be seen in Figure 9 the detector is placed behind the outer surface of the canister.

The high energy X-ray equipment used by SKB in Oskarshamn for pilot examination of the lid to canister weld consists of a 9 MeV linear accelerator (Varian Linatron 3000), a collimated line detector and a manipulator system.



Figure 9. The accelerator and the detector in SKB Oskarshamn site.

The canister will be rotated in a carrier. Rotation speed is controlled by the RT-software that controls the radiation source and the detector. Before placing the canister on the carrier it is important to center it, the distance tolerance is maximum 1.5 mm. 100 % of the weld and the heat affected zone, 10 mm at both sides of the weld is inspected. There is a marked zero-point on the canister surface. In the circumferential direction scanning exceeds the total circumference with suitable overlap. The 0 -point and the rotation direction are marked also on the examination plan.

Before the actual measurement of the canister, calibration test for intensity setting shall be carried out to check the proper intensity in the detector. A separate calibration block made of the same material as the cylinder with known wall thickness is used for calibration. The calibration of the measurement is carried out simultaneously with the weld inspection.

An image quality indicator (IQI) is placed on the detector side surface of the canister so that the calibration hole in IQI is visible on the x-ray picture. Because the quality of the image cannot be controlled during scanning, the quality of the picture is monitored afterwards with IQI sensitivity and intensity value.

For examination the exposure voltage is nominal voltage of the 9 MeV x-ray accelerator. The minimum distance from source to object is defined as a factor of maximum allowed geometric unsharpness (Ug).

A minimum contrast ratio is defined for the display in order to evaluate data properly. The images are analysed partly already during the scan in the encapsulation plant.

4. Welding

Lid of the canister is welded with electron beam or friction stir welding. Both welding methods have been studied and the final choice will be made later on by Posiva Oy.

4.1 Friction stir welding

Friction stir welding is a solid state joining method originally developed by TWI. Basic principle is that the rotating tool is plunged between the pieces to be welded when the friction between the tool and the piece generates heat and plasticises the welded material (Figure 10). Then the tool is moved to the wanted welding direction. There are many advantages in FSW. For example mechanical properties are good in as-welded state, automation is fairly easy and it can be operated in all welding positions [2].

In spite of advantages there are several possible defect types in FSW. These include [3, 4]:

- pores and porosity
- worm hole
- voids
- oxide inclusions and entrapped oxide
- tool trace material
- incomplete penetration
- joint line hooking
- faying surface flaw.

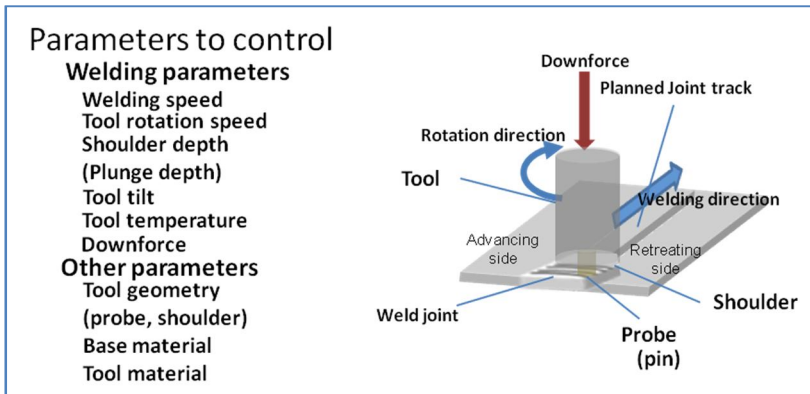


Figure 10. Basic principle of FSW and parameters to control [5].

4.2 Electron beam welding

Electron beam welding is a fusion welding method. In EBW a beam of high-velocity electrons is applied to two materials to be joined. EBW is usually performed under vacuum conditions to prevent dissipation of the electron beam. Due to total heat input being lower than in any arc welding process, the effect on surrounding material is minimal and heat-affected zone (HAZ) is very narrow. The possible defect types in EBW include:

- gun discharge defects
- gas porosity
- cavities
- internal root defects
- incomplete penetration
- excess of penetration
- run out.

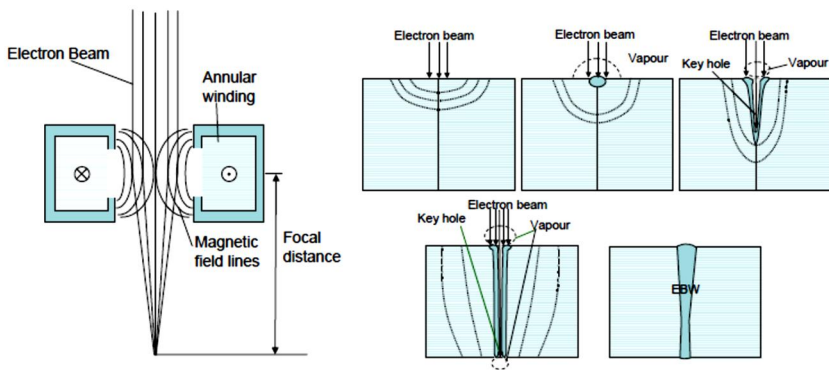


Figure 11. Electron beam welding principle and key hole formation [6].

5. Discussion and comparison to design criteria

Cast iron insert is giving the main mechanical strength to entire disposal canister. Therefore it is essential to identify the criteria to be met. In the shear loading case a semi-elliptical flaw has been identified as the most dangerous flaw. Acceptable dimension of the flaw are 4.5 mm in depth and 27 mm in length [7,8]. As mentioned before for the insert surface area TRL ultrasonic inspection is used. In damage tolerance design $a_{90/95}$ is commonly used as a measure of the minimum size of the reliably detected flaw. With TRL ultrasonic inspection it is shown that in insert inspection this reliably detected flaw is 15.9 mm^2 . Compared to acceptable dimensions the reliably detected flaw could be almost six times larger. Therefore it can be concluded that this system is adequate for this inspection task. [7]

Above mentioned criteria is of course not the only criteria for the cast iron insert. There are many other criteria for example related to location of steel channels and geometry etc which also partly applies to copper parts of the canister. These issues are not in the scope of this paper and are not presented in detail.

Copper overpack, bottom and the lid are the corrosion resistant and gas tight barrier of the disposal canister. One critical part of the copper canister is the weld. It is known that welding can cause different types of flaws in material as mentioned already earlier. Weld, whether it is EBW or FSW, is inspected with all four NDT methods in the encapsulation plant. Studies made for SKB [8] have shown that for the copper part of the canister, no kind of postulated crack, defect or cavity of reasonable size has proven to be critical. The copper shell withstands the design loads with a good margin even with large postulated defects. The large variety of material testing that has been conducted during the studies has shown that the cracks in copper blunt under tension load and no crack growth is detected at applicable temperatures. With copper shell the main design criteria is the corrosion barrier and therefore all the found indications with different NDT methods are added together to verify the needed corrosion barrier thickness all over the disposal canister. In final disposal environment creep of the copper shell has to be an issue and there are several studies regarding creep behaviour of copper shell.

6. Conclusions

The disposal canister is designed to resist corrosion and to have adequate mechanical strength for final disposal environment. To be able to predict and ensure the integrity of the disposal canister certain design criteria has to be set. To ensure that the criteria are met non-destructive methods for inspections are needed. In this paper the four NDT inspection methods (UT, RT, ET, VT) for inspection of different parts of the disposal canister are presented in brief. All of the four NDT methods detect defects in slightly different directions and based on different physical principles. The four methods are therefore supplements to each other in inspection of different parts of the disposal canister.

It is shown in different studies [7,8] that applicable criteria for cast iron insert is found and criteria can be verified with used NDT methods. For the copper parts of the canister as well as welds the most important criteria is the adequate corrosion barrier for the final disposal timeline. Studies have shown that the welds can be categorized according the quality and defects have been found [7]. Nevertheless there are still some techniques that need to be improved. At the moment there are lot of studies going on to improve the inspections in the area of non-destructive testing of disposal canisters. These studies include for example probability of detection, simulation, human factors, combination of inspection results etc.

References

1. Raiko, H. 2005. Disposal Canister for Spent Nuclear Fuel. Posiva Oy. Design Report 2005-02.
2. Nicholas, ED. 1998. Developments in the friction-stir welding of metals. ICAA-6: 6th International Conference on Aluminium Alloys. Toyohashi, Japan.
3. Bird C.R. and Kleiner D., The phased array inspection of friction stir welded aluminium plant, Proceedings of OMAE 2004: 23rd International Conference on Offshore Mechanics and Arctic Engineering, Vancouver, Canada 20–25 June 2004.
4. Pitkänen J., Inspection of Bottom and Lid Welds for Disposal Canisters, Report POSIVA 2010-04, Posiva Oy.
5. Pitkänen J., Lipponen A., Surface and near surface defect detection in thick copper EB-welds using eddy current testing, Baltica VIII Life Management and Maintenance for Power Plants, Vol.1, May 18–20, 2010, Helsinki–Stockholm–Helsinki, Finland–Sweden, pp. 240–255.
6. Schultz H. Electron Beam Welding. Abington Publishing, Great Britain. 1993. 240 p. ISBN 1-85573-034-0.
7. Pavlovic M., Mueller C., Ewert U., Pitkänen J., Safe product design – the role of the NDT reliability analysis. MP Materials Testing 04/2013, pp. 270–275.
8. Raiko H., Sandström R., Rydén H., Johansson M., Design analysis report for the canister, SKB Technical report SKB TR-10-28, ISSN 1404-0344, 2010.

TÜV NORD concept COOP – A powerful tool to meet the challenges of power plant flexibilization

Stefan Goers¹, Detlef Rieck², Axel Schulz³ & Robert Wernicke⁴

¹TÜV NORD Sweden
Große Bahnstraße 31, 22525 Hamburg, Germany

²IGN Ingenieurgesellschaft Nord mbh & Co. KG
An den Wurthen 28, 17489 Greifswald, Germany

³TÜV NORD SysTec GmbH & Co. KG
Große Bahnstraße 31, 22525 Hamburg, Germany

⁴TÜV NORD Systems GmbH & Co. KG
Große Bahnstraße 31, 22525 Hamburg, Germany

Abstract

The energy systems in Europe and the rest of the world are currently undergoing severe changes. Not only due to the growing feeding from fluctuating renewable energies (wind, solar) the energy generation is becoming a highly dynamic system. The number of full-load hours is considerably decreasing and plants are undergoing numerous start-ups and shut-downs with fast load gradients.

The flexible operation regimes probably cause for the components of thermal power units (coal and gas power plants as well as solar power plants and methane production) a paradigm shift in the in-service material degradation mechanism. Particularly for thick-walled components low-cycle fatigue due to faster start-up and shut-down thermal transients gains in relevance versus creep degradation.

To effectively deal with these requirements, the TÜV NORD Group has designed a strategy, COOP (Cycle Optimized Operation), that allows, on the one hand, a reduction of conservative assessments and, on the other hand, the development of new safety standards in the evaluation of the remaining service lifetime.

These conceptual prognosis tools will allow a timely optimization of plant operating modes, a smart NDT inspection concept and finally reduce the life cycle consumption and the maintenance efforts.

1. Introduction

For the future there is expected a rapid expansion of regenerative power generation, not only in Germany. Caused by the fluctuating nature of regenerative forms

of energy, the need for backup capacities in the form of similar-sized thermal power plants is clear. Consequently, components of gas and coal-fired power plants are exposed to fast transients and a high number of cycles.

But conventional coal and gas power plants were not designed to navigate the production peaks and valleys of today's and even tomorrow's energy landscape. Originally built to produce continuous power, they are increasingly being used as backup to supplement sustainable forms of energy.

Due to the fluctuating nature of regenerative forms of energy (wind, solar), energy storage units and backup power plants will be expected to manage fast performance and temperature transients and, at the same time, the drastically increasing number of cycles.

If European design regulations are observed, these operating requirements will lead to high levels of fatigue utilization of the integrated components. As a result, a reduction in the components' life cycle is to be expected and inspection and maintenance efforts will increase.

COOP - Cycle Optimized Operation

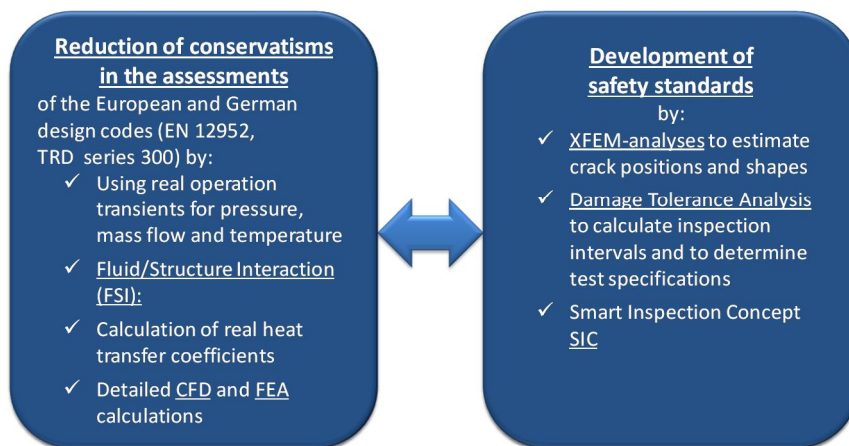


Figure 1. Concept of the strategy COOP.

To effectively deal with significantly higher requirements, calculation methods and tools are connected to a strategy, **COOP (Cycle Optimized Operation)**, that allows, on the one hand, a reduction of conservative assessments (COOP module 1) and, on the other hand, the development of new safety standards (COOP module 2) in the evaluation of the service lifetime. See Figure 1 for the conceptually main aspects of the COOP strategy.

The advanced functions of the commercial finite element analysis (FEA) programs like Abaqus® and ANSYS® play a key role in the COOP strategy for detailed Fluid Structure Interaction (FSI) estimations including Computational Fluid

Dynamics (CDF) and structural FEA (temperature and stress fields) calculations within COOP module 1 as well as XFEM (Extended Finite Element Method) calculations within COOP strategic module 2.

In contrast, the applicable regulatory framework (EN 12952-3 [3], EN 12952-4 [4], TRD 301 [1], TRD 303 [2]) is based on extremely over-simplified assumptions:

- Start-up and shut-down processes are carried out in approximately quasi-stationary operating procedures
- Heat transfer conditions are not taken into consideration.

Due to these simplified assumptions, the components' fatigue utilization might be significantly overestimated following the existing regulatory framework. These conservative assessments can be reduced by the FSI method within COOP strategic module 1. Tests show that a stress reduction on a cold start can be reduced by 40% in comparison to the standard regulatory framework.

Moreover, additional safety standards can be applied in the service lifetime assessment by deploying a series of measures.

Furthermore, the results of the FSI calculation can be used as a basis for optimizing the component design, may be when a component replacement is intended. Herewith the present CFD flow analysis can be used to adapt the component contour to the flow progress. As a result, pressure losses can be reduced, noise emissions lowered and local bending stresses also reduced. Minor changes in detail can deliver significant improvements to the fatigue strength.

By combining XFEM methods and downstream crack propagation analyses within COOP strategic module 2, the entire service lifetime of components comprising both fatigue utilization and subsequent stable crack growth can be determined. With the crack propagation calculation, inspection intervals can be determined and secured. In addition, the crack path and crack geometry analyses conducted with the XFEM method can be used to create qualified in-service inspection specifications.

The crack propagation analysis with the means of fracture mechanics is of significant importance as very high levels of fatigue utilization will be achieved in calculations due to the increase of load variation and considerably faster operating transients. Without a method for assessing a component's service lifetime reserves, significantly shorter inspection intervals have to be defined.

For these reasons, the use of fracture mechanics methods (crack propagation analysis added by XFEM) represents a core element within the framework of the COOP strategy.

The cross-type valve in the main steam line is one of the key components in a coal power plant, see Figure 2. Investigations for this component are presented below as an example for the strategic module 1 "Reduction of conservatism in the assessments" as well as strategic module 2 "Development of safety standards" of the TÜV NORD concept COOP.

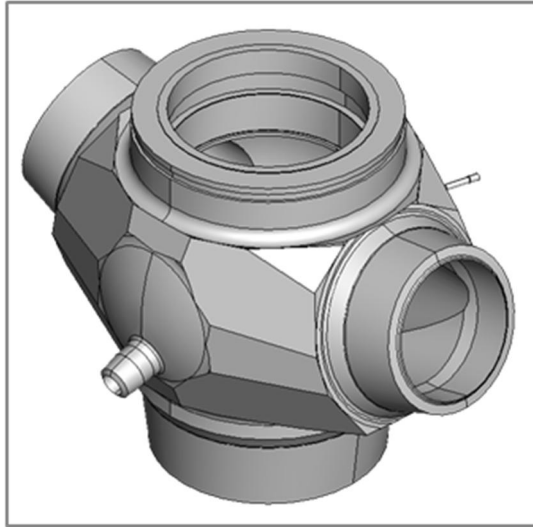


Figure 2. Cross-type valve of a main steam line.

2. COOP strategic module 1: Reduction of conservatism in the assessments

2.1 Derivation of input parameters

In the first module of the COOP's two-part process we use Fluid Structure Interaction (FSI) capabilities to simulate real-world heat transfer conditions within plant components. The results are more realistic assessments of components' thermal stresses and less conservative design codes.

FSI utilizes transient temperature, pressure and mass flow as input parameters. These data are gathered through the evaluation of the operational instrumentation or, if available, on the basis of the measurements of an online monitoring system (Figure 3).

Based on the measurement evaluation, a corresponding "sample transient" is derived for each of the cyclic operation processes (e.g. cold start, see Figure 4). These are based on averaged transients of the monitored previous operations. "Threshold transients" are derived from these "sample transients" using the specified number of cycles. This procedure facilitates a later optimization of the plant operation, because a precise definition of "threshold transients" for the operation or switching processes is provided.

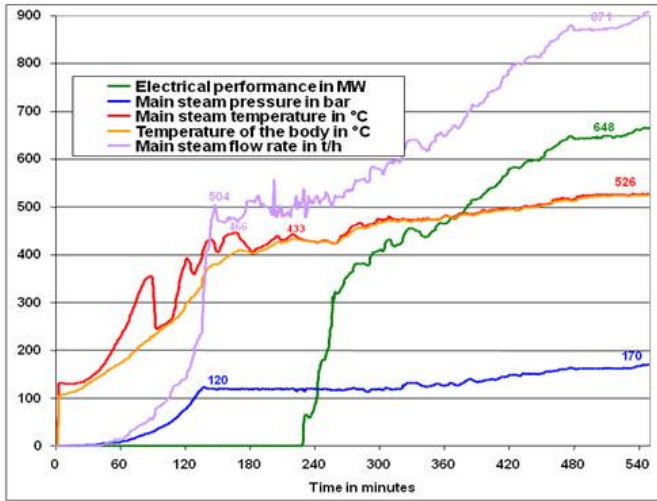


Figure 3. Measured transient developments.

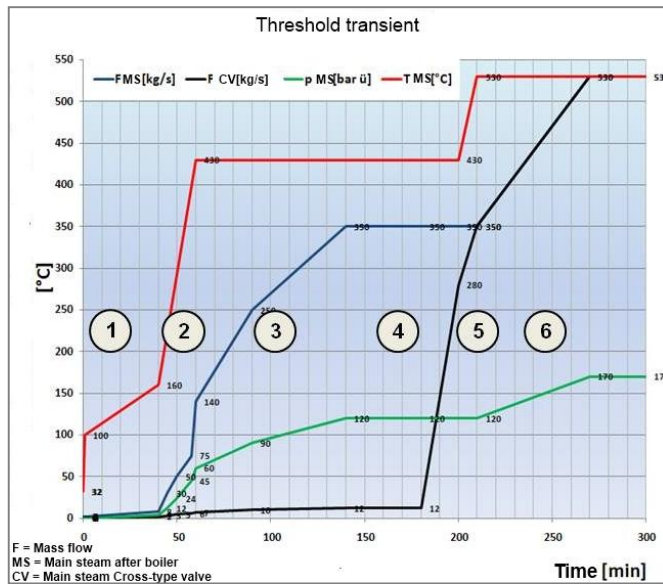


Figure 4. Derived "threshold transients".

In the following we compare the procedure on the basis of the FSI calculation with the German rules TRD 301 [1] and TRD 303 [2] for the cross-type valve shown in Figure 2 for the load case "Cold start phase – increase of the main steam temperature to 530°C".

2.2 Process based on FSI

The heat transfer conditions are determined in the entire component by an upstream, realistic flow calculation (CFD). Based on the flow simulation, the flow velocity and thus the heat transfer cycles and inner wall temperatures at each location of the wall surfaces are determined for each point in time. For this purpose, the complete recording of the real geometry and the exact calculation of the temperature and pressure corresponding material parameters of the medium are required. In Figure 5 the flow velocity determined in the cross-type valve are shown.

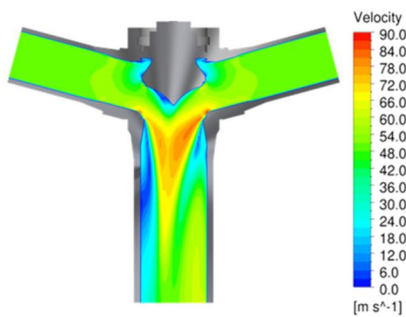


Figure 5. Flow velocity in the component (m/s).

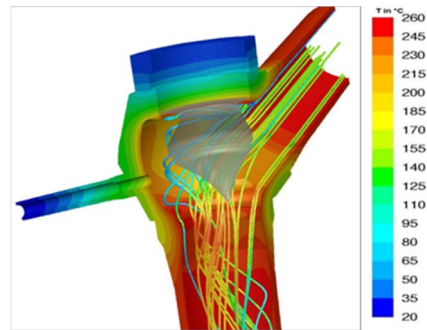


Figure 6. Temperature distribution within the component.

From the flow inside the cross-type valve, shown in Figure 5, areas of flow separation can be recognized. Outgoing from formed areas with low flow velocities, an uneven heat transfer in the valve is resulting.

Based on this flow simulation by CFD, the temperature distribution in the component wall is determined by structural FEA calculation for each point in time of the transient. In Figure 6 the temperature distributions inside the component as well as in the components' wall are shown based on a defined point in time of the "threshold transient".

The thermal stresses in the component are determined using FEA and based on the FEA-calculated temperature distribution. The stress distribution is identified for all component areas at each point in time of the transient. Unlike the calculation processes in accordance with the standards and rules (e.g. TRD 301 [1] and EN 12952-3 [3]), which only take into account temperature differences over the component wall, deformations and stresses from uneven heating of the component are also incorporated within this method. Using this procedure, the real component geometry and the temperature-dependent material parameters are considered. In Figure 7 the thermal + internal pressure stress distribution in the component determined in this manner is shown based on a defined point in time of the "threshold transient".

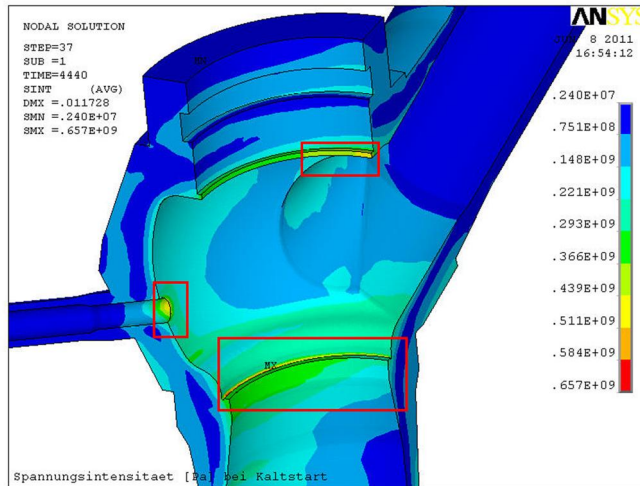


Figure 7. Maximum stress intensity at the valve seat (groove), support edge and housing edge.

The determination of the allowable number of cycles or corresponding start-up velocity takes place on the basis of the assessment procedure of TRD 301 [1] or DIN 12952-3 [3]. These rules and standards specify the design fatigue curves.

In the rules additional requirements for service lifetime-reducing influences such as creep or a crack of the magnetite protective layer of ferrite materials as a consequence of local plastic strains (limitation of the stress range) have to be taken into account.

2.3 Comparing the COOP procedure module 1 with the German rule TRD 303 [2]

In order to be able to calculate a typical cross-type valve in accordance with TRD 303 [2], an idealization of the real geometry as a sphere with a nozzle takes place. TRD 303 [2] is closely linked to TRD 301 [1] in regard to the applied method.

The calculation of the temperature distribution and the resulting stresses in the component are based on the following procedure:

- Consideration of the temperature dependence of the material parameter over definitive temperature of the cycle

$$g^* = 0.75 \cdot \hat{g} + 0.25 \cdot \check{g} \quad (1)$$

- Calculation of the thermal stresses on the basis of the results of R. Pich [5]:

$$\sigma_{i\theta} = \frac{v_{g1}}{W \cdot V} = \beta_{Lg} E_g \cdot \frac{\Phi_K}{1-\nu} \cdot \frac{v_{g1} s_b^2}{a_g} \cdot 1.5 \quad (2)$$

The calculation is based on the assumption of a quasi-stationary temperature behavior. The heat transfer is still not taken into consideration, so the calculation of the inner wall temperature of the component corresponds to the steam temperature of the medium.

In Figure 8, by contrast, the determined heat transfer coefficients are shown on the basis of the FSI analysis. The low heat transfer coefficients of approximately 250 W/(m²K) from the start of the transient until approx. 180 min. are based on the low mass flow. In the further progress of the transient, due to the increase of the mass flow, the heat transfer coefficients in the interior of the housing of the cross-type valve increase to 5,800–11,000 W/(m²K), depending on the location.

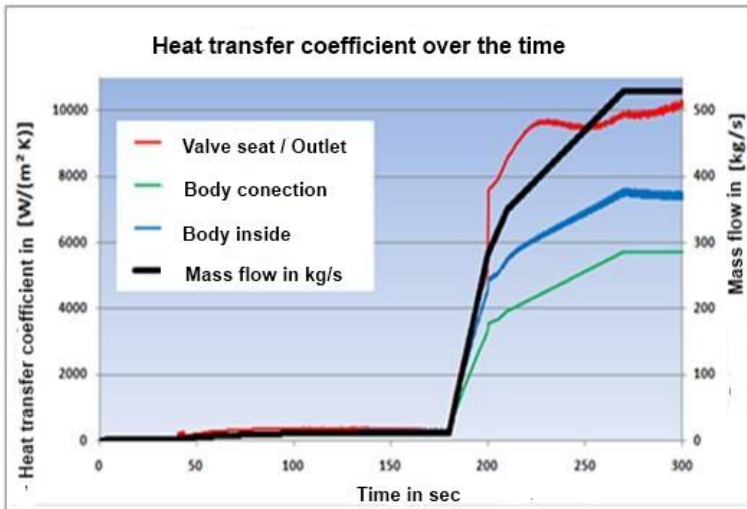


Figure 8. Development of the heat transfer during the transient.

The result of an optimization process on a typical cross-type valve in regard to the maximum allowable start-up velocity represented in [6] shows that reserves can be utilized, allowing a faster start-up of the plant in comparison with the earlier procedure based on TRD 301 [1], TRD 303 [2], due to a more precise calculation based on the FSI method. Based on the previous cold start process of the plant of approx. 200 min. until the service main steam temperature, a possible reduction of the start-up time by approx. 60 min could be shown. Therefore, a significant increase in availability is possible to compensate the fluctuations in future power production.

2. COOP strategic module 2: Fracture mechanics crack propagation analyses – Determining required inspection intervals

As mentioned above, conventional coal and gas power plants were originally built to continuously produce power. Under respect of these service conditions the inspection programs are developed for the safety relevant components. In the German rule TRD 508 [7] there is the requirement of additional inspection measures, if 50% of the fatigue utilization is reached. Based on new fatigue analyses under respect of the new fluctuating service conditions this could demand comparatively much shorter inspection intervals.

For the following described component the result of a fatigue analysis based on a new load case specification yields a utilization $D = 3.36$ for 20 years, i.e. much larger than 1. According to TRD 508 [7] additional inspection measures are required already 3 years after starting operation.

An effective possibility for the assessment of high fatigue utilization factors of components is given by means of the fatigue crack propagation analysis in the scope of linear-elastic fracture mechanics. The fatigue crack propagation analysis enables an incorporation of additional service lifetime reserves of the component – beyond the “classic” fatigue analysis. For this purpose, the in-service inspection intervals can be quantified in accordance with requirements and the inspection instructions can be optimized (damage tolerance analysis).

Based on the example mentioned in the previous section, a cross-type valve of a main steam line made of martensitic steel P91 (X10CrMoVNb9-1, 1.4903), the procedure [8] for the fracture-mechanics assessment of cyclic plant operation loads is presented in the following.

The subsequently shown method is based on the interaction of the calculations by means of FEA (without and with crack modeling), XFEM (Extended Finite Element Method) and an analytic fracture-mechanics process. The fracture-mechanics analyses are based on FSI and FEA stress analyses, taking over the results of COOP – Strategic module 1.

Within the fatigue crack propagation analysis a cooling transient (shut down with leak test) was evaluated as that load case with the largest effect on a possible fatigue crack growth because of the highest local principal stress ranges. In the first phase of the transient the service temperature decreases slowly from 530°C down to 280°C. Subsequently a fast cooling occurs as a result of a cold water feed (water temperature 50°C).

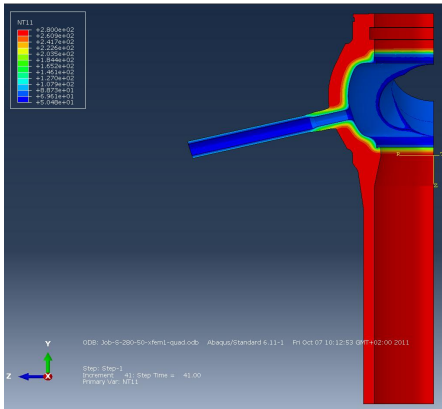


Figure 9. Temperature distribution at $t = 40$ s.

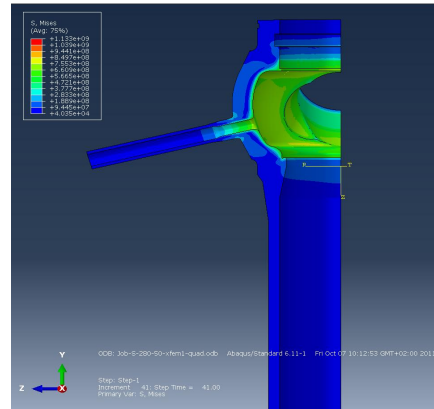


Figure 10. von Mises-equivalent stress at $t = 40$ s.

The stress analysis indicates a stress maximum in the circumferential groove near the valve seat about 40 s after the beginning of the cold water feeding. Figure 9 shows the temperature distribution at this time and Figure 10 shows the von Mises-equivalent stresses which correspond locally to the 1st principal stresses. This stress distribution is the base for the following calculation procedure.

3.1 Fracture-mechanics analyses with XFEM

The XFEM method represents a modern, elegant technique for determining the potential crack location, the crack geometry and the crack propagation to be expected in the component.

In the process, the location and the arrangement of the crack are determined independently of the mechanism of the damage (plastic deformation as a consequence of permanent stress or dislocation creep due to load changes). As a result, reliable input parameters for the subsequent crack growth analyses are provided.

For the load scenario of a cooling transient investigated here, the crack initiation criterion (crack initiation stress) is reduced to the extent that the crack formation is initiated by computer, see Figure 11.

After the crack initiation, the XFEM calculation shows an intensive crack growing on the component surface along its circumference, see Figures 12 and 13. It must be observed that only half of the crack length is represented on the basis of the model symmetry.

In the XFEM-calculation the temperature transient is assumed as a quasi-static, sustained load. Based on the high thermal stresses near the surface and the exponential reduction of the stress level in the middle and outer material layers, only very minor crack depth propagation is recorded by a factor of approx. 1/20 less than the crack length growing, see Figure 13.

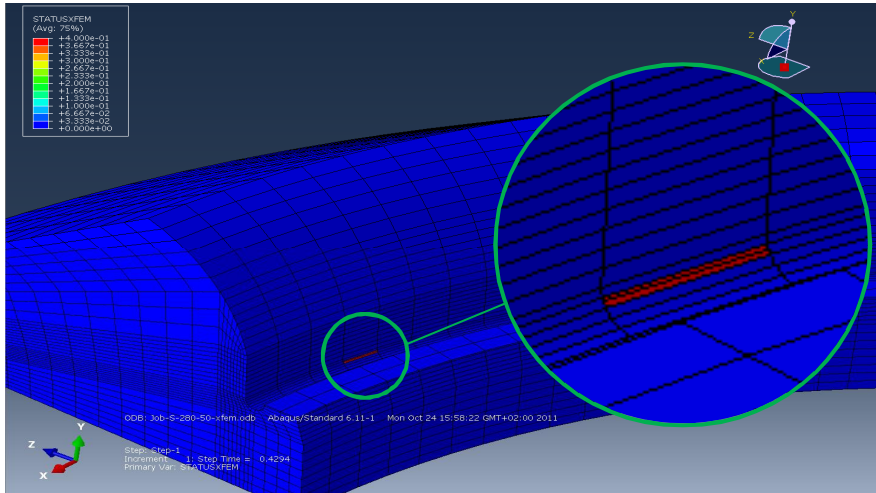


Figure 11. Localization of crack initiation (XFEM calculation).

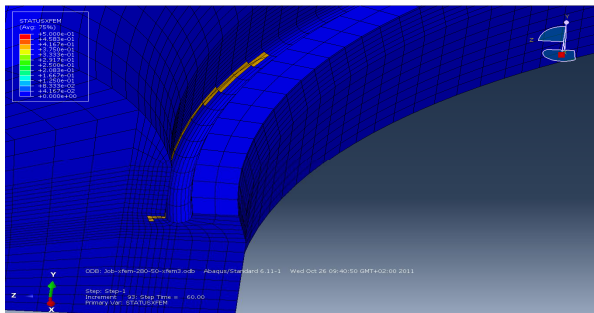


Figure 12. Crack position within the component at the end of XFEM calculation.

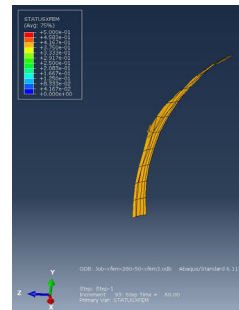


Figure 13. Final crack geometry.

The calculated crack growth very precisely follows load-type “Mode-I” as a result of the dominance of the axial stresses near the interior surface. The XFEM calculation additionally comprises potential changes of the crack growth direction with greater crack lengths.

The location of the crack initiation as well as the resulting shape of the crack proved to be relatively independent of the selected value of the crack initiation stress MAXPS (200–600 MPa) for the present application. This is significant for the applicability of the procedure.

The transfer of the crack shape characteristics determined by means of XFEM as a starting point for the successive crack growth analyses is supported by the

thesis that the quasi-static loads of the XFEM calculation produces at least a comparable, similar crack shape as the cyclic loads of the crack growth analysis.

3.2 Fracture-mechanics analyses using FEA (J Integral Calculation)

In the procedure presented here, XFEM is used to determine the potential crack position, the crack geometry and the expected propagation of the crack, but not for the quantification of the J integral along the arising crack front. For this the contour-integral calculation in Abaqus [9] has been used. This requires the remodeling of the crack geometries determined with XFEM in the scope of the "classic" FEA.

The calculation of the J integral values serves for the adjustment and verification of the subsequent analytical fracture-mechanics calculations by means of IWM-VERB [10] in the application described here.

Figure 16 shows the comparison of the stress intensity factors at the crack tip determined from the contour-integral solutions within Abacus [9] (see Figure 14) with the solutions generated for various crack half-axis ratios by using the analytical fracture mechanics program IWM VERB [10] on the basis of the stress distribution determined on the FEA model without a crack (see Figure 15).

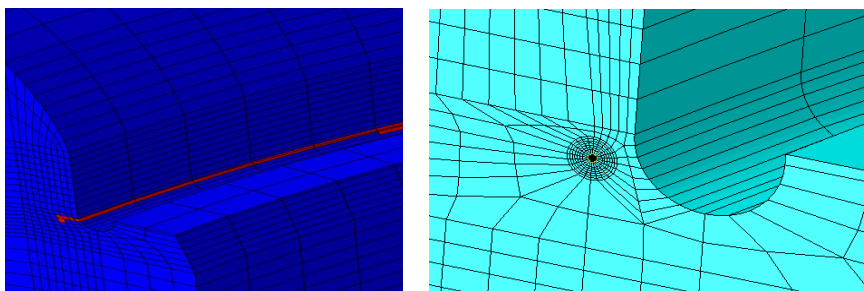


Figure 14. Crack modeling to get contour-integral solutions within Abacus [9].

With the analytical solutions for semi-elliptical surface cracks shown in Figure 16, the crack growth parameters described in the following chapter were already taken as a basis, which leads to a change of the semi-axis ratio a/c with an increasing crack depth a . The stress intensity factors determined correspond to the respective stress range ΔK , because the non-pressurized, cold and stress-free zero state was defined as a stress minimum.

As Figure 16 shows, the analytical crack growth solution, based on a surface crack with depth $a = 0.1$ mm and the semi-axis ratio $a/c = 0.1$, the contour-integral solution comes closest, whereas the additionally investigated analytical solutions with smaller semi-axis ratios are covering the contour-integral solution.

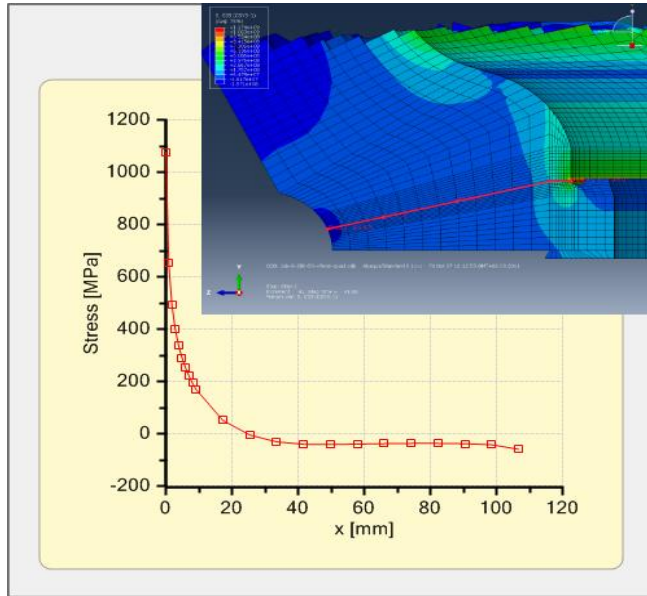


Figure 15. Stress distribution along a (red) path through the component wall, based on the FEA model without a crack.

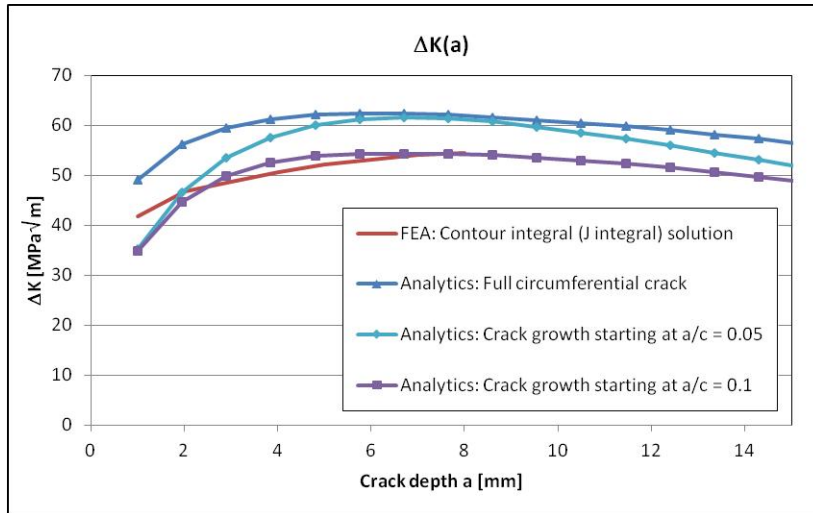


Figure 16. Stress intensity factor (range) depending on crack depth.

3.3 Fracture-mechanics analyses – Fatigue crack propagation

For the implementation of numeric crack growth analyses with justifiable computing time, only analytical user programs are currently available, such as [10]; a direct crack propagation simulation with cyclic loads does not currently appear to be possible with XFEM. This is the deeper-lying motivation for the interplay of FEA, XFEM and analytical fracture-mechanics analysis presented in the current application example. However, this also reveals the obvious motivation for the continuation of work like [11] for the further development and application testing of XFEM.

An additional research and development potential arises from the fact that there is currently only an insufficient fracture-mechanics material data basis under the stress conditions of flexible power plant operation, both in regard to the static crack initiation characteristics and in regard to the fatigue crack propagation characteristics in the relevant temperature range above 100°C, but below the relevant creep and creep fatigue influences.

Only the curves shown in Figure 17 from [12] to [14] are available in the open technical literature for at least covering fatigue crack propagation characteristics under the requirements mentioned above. In our analysis of power plant operation, we used crack propagation rates in accordance with [13] for ferritic steels in water environment.

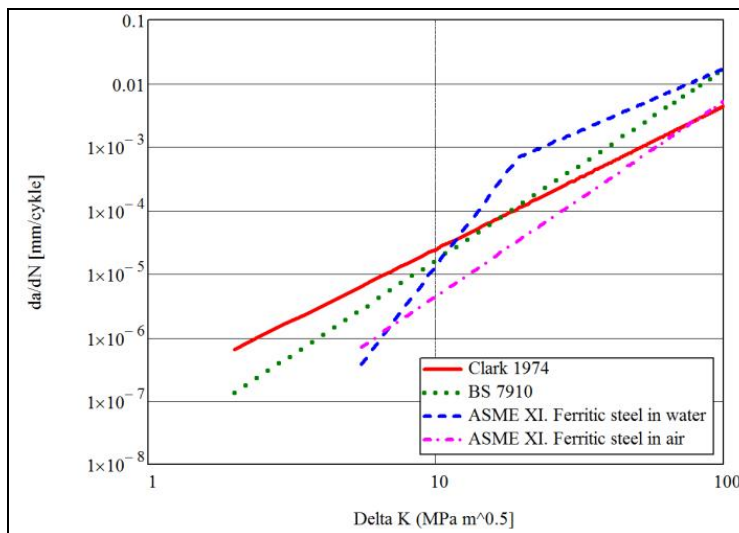


Figure 17. Crack propagation rates of ferritic steels (Stress ratio $R = 0$).

Figure 18 includes the results of the crack propagation calculations for a circumferential crack as well as a semi-elliptical crack with a starting semi-axis ratio $a/c = 0.1$. As an initial crack depth, $a = 1$ mm was specified and the planned operating

time was surpassed several times with the excessive value 10,000 as the number of load cycles.

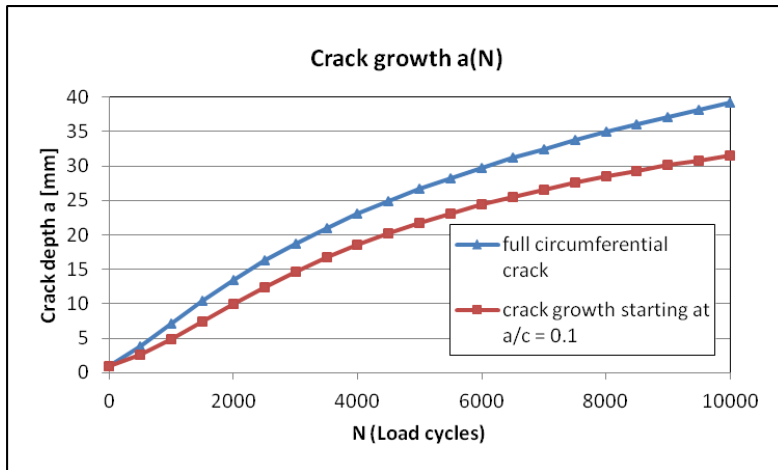


Figure 18. Fatigue crack growth calculations.

Independently of the selected initial crack configuration, decreasing crack growth with an increasing number of stress cycles can be recognized from Figure 18. In addition, the approach of a larger initial crack depth of 3 mm or 5 mm only leads to slightly greater crack depths after 10,000 corresponding stress cycles.

The reason for this tendency is the continued reduction of the range of the stress intensity factor $\Delta K(a)$, already recognizable in Figure 13, for greater crack depths on the basis of the thermal stress peaks only occurring in the inner wall areas, and the rapid drop of thermal stresses to the wall centre towards the exterior surface.

This is a clearly beneficial factor for the applicability of module 2 of the COOP concept, which becomes even more obvious when comparing with other representations of mechanical but not thermal fatigue crack propagation, such as can be found e.g. in aircraft, railways or wind off-shore industry applications. There one finds the tendency of increasing crack propagation rates for larger crack depths.

The inspection intervals have to be defined with a safety margin against the crack instability – i.e. for reaching the critical crack depth size. This safety margin to meet the scatters and insecurities of analysis input parameters is not included in Figure 18. But, as can be seen in Figure 18, in the present case the defined initial crack configurations tend to not reaching the critical crack depth by fatigue crack propagation, which is only insignificantly below the wall thickness and determined by plastic failure.

So, in our case the safety margin between maximum possible grown crack depth after the last in-service inspection and the critical crack depth is not necessary to be defined – it is intrinsic!

Following that, the inspection intervals can be set on the basis of the capability and availability of the NDT-techniques. For the detectable crack depths, the safety against crack instability is guaranteed, also with respect to further fatigue crack propagation. In this case premature replacement of components as well as short inspection intervals, therefore are not necessary.

4. Conclusions

The present example shows the applicability of module 1 and module 2 of the TÜV NORD COOP concept to tap into assessment reserves of power plant components subject to high stress levels and load cycle numbers.

The described procedures offer the possibility to better quantify as well as extend residual service lifetime of the considered plant components. This in consequence leads to a safer and more economic operation because of quantifying necessary inspection intervals and reducing costs of unnecessary maintenance outages as well as component replacements.

With the capabilities of the strategic and integral concept COOP, a sum of methods is given to react to the new requirements of a flexible operation of conventional coal and gas power plants.

References

1. TRD 301 Appendix 1. Calculation of alternating stress fatigue due to fluctuating interior pressure or combined interior pressure and pressure change. Version: 08.98
2. TRD 303 Appendix 1. Calculation of spherical shells with openings against cyclic strain stressing of the internal bearings. Version: 07.97.
3. EN 12952-3. Water-tube boilers and auxiliary installations – Part 3: Design and calculation for pressure parts.
4. EN 12952-4. Water-tube boilers and auxiliary installations – Part 4: In-service boiler life expectancy calculations.
- 5 R. Pich, VGB Booklet 87, Cologne 1963. Die Berechnung der elastischen instationären Wärmespannungen in Platten, Hohlzylindern und Hohlkugeln mit quasistationären Temperaturfeldern.
6. Schulz, Röglin, Schulze, Dr. Wernicke, Linke, Küppers, Hagelkreutz, Dr. Fielenbach. Optimierte Lebensdauerbewertung eines begrenzenden Bauteils als Baustein zur Flexibilisierung eines Braunkohlekraftwerks (Optimised service lifetime assessment of a limiting component as a module for the

flexibilisation of a brown coal power plant). VDI Conference: Optimierung Bestandskraftwerke (Optimisation of Existing Power Plants) 2012.

7. TRD 508. Additional Inspections of components calculated with time depend strength parameter. Version: 10.78
8. Rieck D., Schulz A., Wernicke R. Optimierung von Prüfintervallen in konventionellen Kraftwerken (Optimisation of Inspection Intervals in Conventional Power Plants). 44. Tagung DVM-AK Bruchvorgänge (44th DVM-AK Fracture Processes Conference), Darmstadt, Feb. 2012.
9. Abaqus/CAE 6.11-1, Dassault Systèmes, USA 2011.
10. IWM Fraunhofer-Institut für Werkstoffmechanik Failure Assessment Software IWM VERB. Version 8.0, 2009
11. Mutschler, P., Schulz, A., Rieck, D., Sander, M. Ermittlung des zulässigen Inspektionsintervalls für einen optimierten Twistlock auf der Basis von Rissfortschrittsanalysen mit ABAQUS (XFEM) (Determining the Permissible Inspection Interval for an Optimised Twistlock on the Basis of Fracture Propagation Analyses with ABAQUS (XFEM)). 44. Tagung DVM-AK Bruchvorgänge (44th DVM-AK Fracture Processes Conference), Darmstadt, Feb. 2012.
12. British Standard BS 7910:2005 Guide to methods for assessing the acceptability of flaws in metallic structures British Standards Institution, 2005.
13. ASME Boiler and Pressure Vessel Code, Section XI, 2010 Edition Rules for In-service Inspection of Nuclear Power Plant Components American Society of Mechanical Engineers.
14. Clark, W. G. How fatigue crack initiation and growth properties affect material selection and design criteria, Metals Engng. Quarterly 16, 1974.

Risk assessment of power station production unit

Jana Markova, Milan Holicky & Miroslav Sykora

Klokner Institute, Czech Technical University in Prague
Solinova 7, Prague, Czech Republic

Abstract

Risk assessment of the production unit of a fossil power station are based on probabilistic methods in conjunction with application of Bayesian networks. Expected risks are assessed considering available data for failure rates and economic consequences due to outages of key energetic devices of the production unit, and social consequences due to potential injuries. Proposed procedures make it possible to analyse the significance of individual devices and their components with regard to availability of the production unit and human safety.

1. Introduction

Risk assessment of the production unit of a fossil power station is based on failure rates (determined from available data and expert judgements) and consequences due to malfunctioning of selected devices. Submitted assessment concerns key devices of a power production unit including chimney, cooling tower, flue gas desulphurisation, boiler pressure system, steam piping, steam turbine, generator and transformer. A failure of these devices may lead to outage of the whole production unit. Potential social consequences of failures of the key devices are also taken into account.

Resources of information include databases of a plant operator, standards, manuals for management of the power plant, reports on testing and operational guidelines. The failure rates are based on the previous performance of key devices, on expert judgements and on periods of non-availability of significant devices. Failure probabilities and expected risks under specified hazard situations are assessed using Bayesian networks.

2. Basis of probabilistic risk assessment

When for mutually independent danger situations H_i (hazards) the failure F of the component given a particular situation H_i occurs with the conditional probability $P(F|H_i)$, then the total probability of failure P_F is given by the law of total probability as

$$P_i = \sum_j P(F | H_i) P(H_i) \quad (1)$$

Conditional probabilities $P(F|H_i)$ are determined by analyses of hazard situations H_i which may lead to several events E_{ij} (e.g. excessive deformations, fatigue of materials, vibrations) with adverse consequences C_{ij} expressed e.g. by time of the unit outage. The total risk R relevant to the danger situations H_i may be expressed as

$$R = \sum_j C_j P(E_{ij} | H_i) P(H_i) \quad (2)$$

Consequences of adverse events E_{ij} may consist of several components denoted as $C_{ij,k}$ (e.g. costs of unplanned unavailability of the production unit or harm to human health). Components R_k of the total risk may be assessed from the relationship

$$R_k = \sum_{i,j} C_{ij,k} P(E_{ij}|H_i) P(H_i) \quad (3)$$

When acceptable limits on risk $R_{k,d}$ are determined for components with consequence C_k , the individual energetic devices and the total power-station production unit may be assessed on the basis of the condition of acceptable risk, $R_k < R_{k,d}$, which supplements the basic reliability requirement $P_i < P_{id}$, where P_{id} is the target value of failure probability [1, 2].

When the criterion of acceptable risks is not fulfilled it is necessary to modify the system by appropriate interventions aiming at reduction of probability of occurrence of adverse events or at reduction of their consequences.

3. Risk assessment based on Bayesian networks

The risk assessment of a power station production unit using the Bayesian networks facilitates

- to break down of a complex task into smaller sub-tasks that can be analysed separately by individual experts on particular devices,
- illustrative interpretation of knowledge concerning devices based on results of measurements and expert appraisals,
- consideration of uncertainties with respect to material and geometrical properties, operational conditions, inaccuracy of measurements and possibly also theoretical models applied in analyses of devices,
- updating of results when new information is available,
- to get information for decision-making concerning operational processes and their maintenance.

Seven key devices considered in the following analysis include chimney and cooling tower, flue gas desulphurisation, boiler pressure system, steam piping, steam turbine, generator and transformer. It should be noted that the number of devices can be readily modified if needed.

Assessment of Bayesian network is based on specification of conditional probabilities of some nodes under assumption of information on other nodes (in direction of causal links). The analysis is based on the concept of conditional probabilities and the theory of probability. Detail information on analyses of networks may be found in [3, 4, 5, 6].

For each key device or its component, the utility node of unavailability time and the utility node of societal consequences (if relevant) is illustrated in Figure 1. The nodes describe economic and social risks connected with failures of devices. In such a manner the Bayesian network facilitates to specify risks for the whole production unit, for individual devices and their components. Applied software GeNie enables incorporation of submodels (illustrated as rectangles with round corners in Figure 1) which facilitate to make risk analyses. As an example the submodel of a high-pressure turbine is shown in Figure 2.

The risk assessment reveals that the availability of the whole power station production unit may be estimated to 91%. However, this value represents an upper bound of the availability since outages due to failures of the key devices are considered only and contributions to failures of other energetic devices are not taken into account.

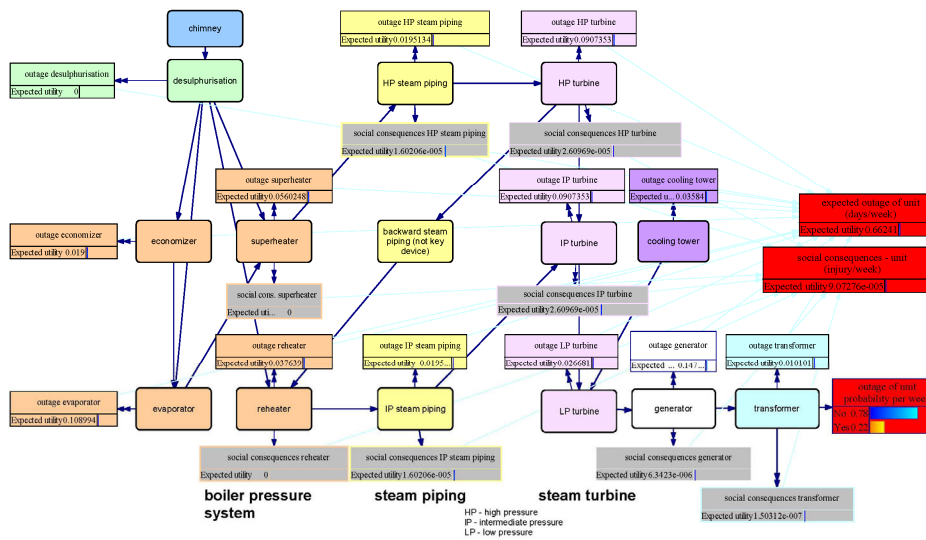


Figure 1. Bayesian network.

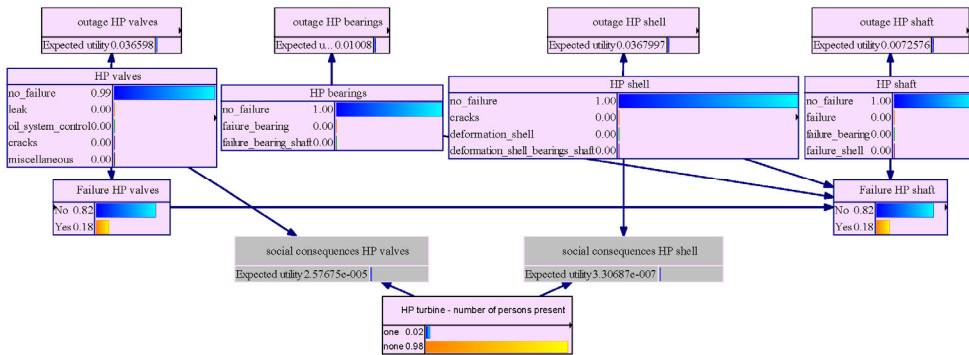


Figure 2. Submodel of a high-pressure turbine.

4. Risk assessment based on Bayesian networks

Economic risks of individual components are determined on the basis of Bayesian network. Contribution $P_{R,i}$ of a component i of a selected device to the total economic risk R of the production unit is given as

$$P_{R,i} = R_i / R = R_i / (\sum_i R_i) \quad (4)$$

where R_i is the economic risk of the component. Summation of risks is made across all considered components of selected devices.

Contributions of the selected devices to the total economic risk for the power station production unit are illustrated in Figure 3.

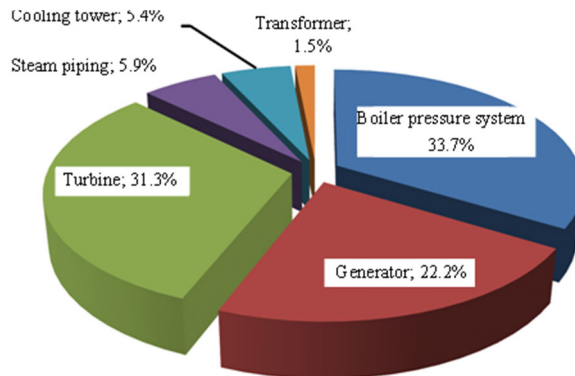


Figure 3. Contributions of selected devices to the total economic risk.

Contribution of individual components of the boiler pressure system to the economic risk is illustrated in Figure 4. Similarly, contributions of other energetic devices may be determined.

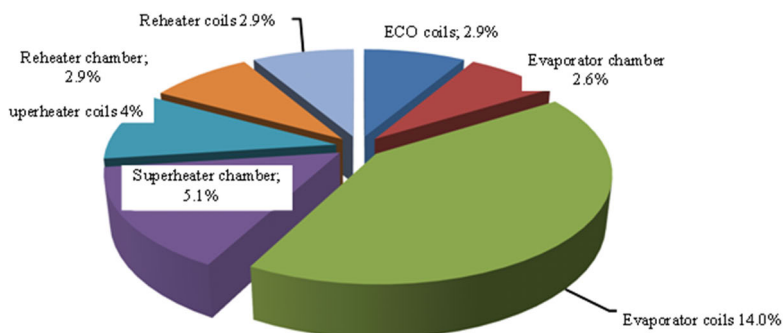


Figure 4. Contributions of components of the boiler pressure system to the total economic risk.

For indicative evaluation of economic losses of a plant operator due to injuries, the statistics of the Center of Transport Research of the Czech Republic are applied. For evaluation of costs of production, the gross domestic product per a habitant is used:

- loss of life: 390.000 EUR
- major injury: 128.000 EUR
- minor injury: 14.400 EUR.

The Bayesian network can be applied for the analysis of expected number of injuries for a considered reference period. The ratio $P_{SR,i}$ of social risk SR_i of a component i in total social risk SR of the production unit is given as

$$P_{SR,i} = SR_i / SR = SR_i / (\sum_i SR_i) \quad (5)$$

Summation is made over all components of considered devices. Contribution of individual components to the social risk is illustrated in Figure 5. Similarly, contributions of other energetic devices may be determined.

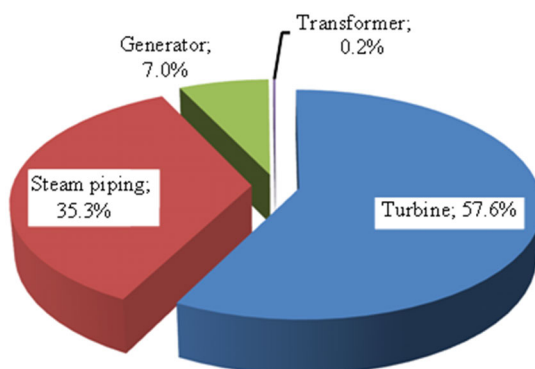


Figure 5. Contributions of components of boiler pressure system in social risk.

Note that the presented results relate to the time of the assessment. The risks can be also determined for future operation of the power plant predicting trends of parameters describing the key devices. Description of this prediction is, however, out of the scope of the present paper.

5. Conclusions

Bayesian networks represent an effective tool for risk analysis of components of power station production units. They provide valuable background information for decision-making concerning priorities of financial resources on maintenance or planning of replacement of technological devices. Bayesian networks can also take into account expected trends of technical parameters describing state of individual components and make assessment of an impact of maintenance on economic and social risks.

Risk assessment is illustrated on selected devices of a power-station production unit. It is shown that the probabilistic approach makes it possible to consider real operational data supplemented by expert judgement. The devices with significant influence on economic risk of the selected production unit include the boiler pressure system, steam turbine and generator. It is shown that the societal risks are primarily affected by the steam turbine and steam piping.

Acknowledgement

This study has been conducted within the research project TE01020068 Centre of research and experimental development of reliable energy production supported by the Technological agency of the Czech Republic.

References

1. ISO 2394 General principles for reliability of structures, 2003.
2. ISO 13824 Bases for design of structures – General principles on risk assessment of systems involving structures, 2009.
3. Holický M., Reliability analysis for structural design, SUN MeDIA Stellenbosh, 2009.
4. Jensen F.V., Introduction to Bayesian networks, Aalborg University, Denmark, 1996.
5. Diamantidis D., Holický M., Risk and robustness of road tunnels, In: Applications of Statistics and Probability in Civil Engineering. Londýn: Taylor & Francis Group, 2011, p. 2140–2148.
6. Stewart M.G., Melchers R. E., Probabilistic Risk Assessment of Engineering Systems, Springer, Berlin, 1997.

Importance of pressure equipment inspection in power plants: Looking to the future

Paolo A. Bragatto & Corrado Delle Site

INAIL Italian Workers' Compensation Authority – Research Certification and Verification Area

Rome, Italy

Abstract

In process industries, equipment failure rates (FR) drive many essential issues in plant management such as inspection programming. Also a few decisions of Competent Authorities, including installation licensing and land use planning (LUP) are driven by FR. A large information entropy, unfortunately, affects Failure rates. FR's currently in use for process equipment derive from systematic studies conducted even in the sixties and seventies. Many new materials and new production method have been introduced and their effects on aging mechanisms on a large scale are almost unknown. Plant Operators and Authorities could make questionable decisions, using poor or generic data. A few European Competent Authorities are trying to face the problem, by stating a set of failure rates, suitable just for LUP. INAIL – Research, Certification and Verification area, as in charge for pressure equipment control throughout Italy, is gathering data for updating general Failure frequencies. This effort is aiming to provide "numbers", on which Authorities and enterprises can count, but above all to pool the knowledge about failure modes in order to better address management of the equipment throughout the process industry. That may improve probabilistic risk assessment and management.

1. Introduction

The power plants have remained for a long time excluded from the scope of the Seveso Directive (Directive 2012/18/EU Seveso III on the control of major-accident hazards involving dangerous substances, amending and repealing the Directive 96/82/EC Seveso II). The Directives are based on the classification of substances, thus, as soon as the fuel oil dense has been reclassified "toxic for the environment", according to the REACH regulation, a number of power plants has fallen within the Seveso Directive. The power industry is already used to carefully manage equipment inspections, as reliability is essential to ensure system availability and production continuity. These controls become even more important with the Seveso Directive, which calls in particular for a more integrated view of all safety related issues. The paper discuss how in Seveso practice equipment inspections are essential in risk assessment and management. The detailed knowledge of the equipment reliability is an essential for a probabilistic safety

assessment, as required by Seveso Directive. On the other hand the periodical audits are essential in order to assure a systematic integration of all control activities, including the mandatory verifications, required by national legislations. Furthermore a more systematic approach could also be useful to implement a risk based program of inspection (and maintenance), aiming to optimize safety costs. In Chapter 2, both risk assessment and risk management are discussed, focusing the importance of the equipment reliability and inspections. In Chapter 3 the recent development in reliability approach across the European Seveso industries. In Chapter 4 a comparison of a few reliability data are presented, focused on pressure equipment. The last chapter discuss the potential of an improved understanding of reliability matter for power plants

2. Probabilistic risk assessment and management in the practice of “Seveso” industries

2.1 Safety report

The practice of risk analysis in the Seveso legislation Article 10 Of Directive 2012/18/EU on the control of major-accident hazards involving dangerous substances, amending and repealing the Directive 96/82/EC requires operators of concerned establishments to provide every five years a revised “safety report”, which will be evaluated by the Competent Authorities. In Italy the Competent Authority is the Technical Committee Regional (CTR), which is participated by environmental local authority ARPA, fire brigade VVF and INAIL, as in charge of occupational accident prevention. From the assessment of the Safety Report descend important decisions, including the prescription of plant modifications. Core of the safety report is a semi-quantitative analysis of risk. This is carried out by the operator, or rather by a few advisers and consultants. Given the importance of the decisions arising from the evaluation of the risk, it is important to analyze in detail the practice followed.

In the common practice of the risk analysis is mainly divided into four phases: i) Identification of units of equipment critical to the method indices MOND / ISPESL or equivalent qualitative methods, based on objective data, however elementary; ii) For each critical units, identification of TOP-EVENT (accidents with major consequences) with the HAZOP method, based on knowledge of the physical and chemical processes that occur in the system; iii) For each TOP-EVENT, calculation of the probability of release of a hazardous substance with the analysis of the 'fault tree (FTA Fault Tree Analysis) based on the probability of non-operation of the individual components of the system (whether mechanical, hydraulic, electrical, electronic, or human). Combination is also used in the event tree (ETA Event tree analysis), which considers the reliability of technical and organizational issues involved after release and can mitigate the consequences, iv) for each event credible (probability 10^{-6}) calculation, depending on the specific type of danger (fire, explosion, toxic) and weather conditions, areas of damage, discriminating areas of

high mortality, early lethality, irreversible damage to people, reversible damage to persons, property damage and possible domino effects. The calculations are based on knowledge of the physical and chemical mechanisms of the phenomena involved (dispersion, diffusion, ignition, combustion, propagation, change of status, etc.). Scenarios with consequences within or outside the establishment's fences are discriminated.

The probabilistic evaluations coupled with consequence modeling and potential impact area computation are essential for Authorities to make vital decisions about new plants approval, emergency planning (including resource allocation) and land use planning LUP. Even the identification of critical system with hazardous plants is driven by the failure rates, which, in such a way, affect also the safety management procedures. In a few countries like France and Italy the compatibility criteria rely more on the severity of the possible "consequences". The probability enters as a filter for the scenarios and related damage areas to be included (typically > 10⁻⁶). In other countries, such as Netherlands or UK, are used the decisions driven by the calculation of the Individual Risk and the Societal Risk, which involve calculating the probability of death of persons at a given exposure (Uijt de Haag & Ale 1997). The Probability is derived from event probability that in turn depend on failure rates. In both cases general failure frequencies drive shared decisions. The scientific weakness of the generic failure frequencies have been discussed by a historical review of Fragola (1996). Authorities must anyway accept a trade-off to make standardized and uniform decisions. An inadequate value of a single failure rate value in the fault tree is able to affect vital decisions. Recent innovations are increasing component reliability but if the authorities accept any arbitrary extrapolations of failure rates, could make imprudent decisions, excluding possible catastrophic events. A conservative approach is highly preferable for the Authorities' decisions. The Buncefield incident has demonstrated the importance of an accurate assessment of the risk of involvement in the area of industrial accidents and the criticality of the general frequency of fault, for which the final report on the "lessons learned" complains a level of trust too low (HSE 2007). Following this report, an initial feasibility study on upgrading accrued fault according to the decision-making process was promoted by the British authorities (Bellamy & al. 2012). It has to be stressed than in consequence based method, as likelihood becomes an absolute filter, the error propagation could be even higher than in FN curves.

2.2 Inspections

Following the implementation of Directive 96/82/EC for the control of major accident hazard (Seveso), since 2000 in Italy has been enforced a system of mandatory inspections or audits at the establishments, according to a prescribed procedure. The Seveso inspection are based on a detailed verification of the safety management system, but of course the issues of equipment reliability and safety is even essential. When the Seveso legislation was introduced, an overlapping with potential conflicts, with the traditional equipment inspections system was envis-

aged. Nothing could be more wrong. The testing and verification activities for pressure equipment were born with process industries and developed over the years to establish itself in a particularly effective and stable system, which is one of the pillars of safety in the process industries (chemicals and energy in particular). In Italy, many pages of this story was written, first by ANCC and then by ISPESL. In the subsequent development of legislation "Seveso" the focus was on human factors and organizational, as the issue of equipment reliability and safety was assumed already managed very well everywhere in Europe. In Seveso plants the operator must just put controls and verifications (voluntary and mandatory) within the system of safety management. Essential elements of the management system are inspection planning, inspection program implementation, inspection results analysis for improvement. These elements must be inspected in the Seveso inspections, whilst for the direct testes measurements, including non destructive controls, are in charge of equipment integrity and functionality inspections (Bragatto & al. 2009).

To address Seveso inspectors and avoid useless overlapping and conflict a procedure has been delivered in 2008 and emended in 2009. According to this procedure, derived by a similar procedure successfully applied by Dutch Competent Authorities (Bellamy 1999), the operator must provide the inspector with a work document where, for each single TOP-EVENT in the safety report, are highlighted the organizational and technical systems for preventing accidents and for mitigating consequences. Mitigation measures include the protection of people, environment and structures and the scenario monitoring. In practice it is required to the operator to derive from the analysis of risk already present in the safety report the so-called "bow-tie", that bring together on the left and right respectively, the fault tree that leads to the event of loss of physical containment and the event tree that leads to the loss of containment accident scenarios. Obviously the center of the "bow-tie" the single top event. In figure 1 an example of bow-tie is shown.

In the document should be listed, analyzed and discussed technical and organizational safeguards to prevent the event and the means of intervention foreseen at the time of the event, according to the accident scenarios find out in the Safety Report. It is expressly required to include scenarios characterized by low frequency of occurrence, because they are usually the result of a combination of many specific prevention measures, for which a failure is anyway conceivable. This document is the instrument for carrying out the review "planned and systematic", as required by the European Directive. The auditors "plan" the activity of control, deciding whether to analyze all systems or a representative sample. Furthermore, the review is "systematic", as it is based on the assumptions of the safety report. Must be verified that the functionality of critical systems is controlled through a plan of preventive maintenance and periodic inspections. Priority is given to the more severe scenarios from the point of view of the consequences. In order to verify the effective functioning of the "critical" components for the prevention / mitigation of accidents, tests are done to sample the critical elements listed by the operator, including visual inspections of mechanical components and sample testing of alarm systems, when you can provoke intervention by varying the set-

point conditions. As the procedure is entirely based on the evaluation of the actual condition of the preventive and protective barriers the probabilistic evaluations present in the safety report may be emended and updated on the basis of actual equipment condition, as well as on the actual adequateness of organizational measures and human resources.

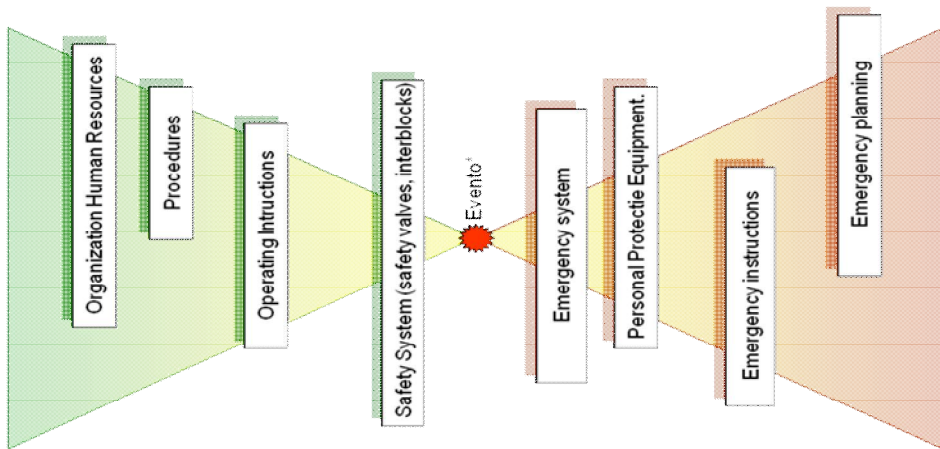


Figure 1. An example of bow-tie.

2.3 Other issues

The potential of RBI Risk Based Inspection for optimizing Inspection planning at Seveso establishments has been widely discussed in many recent papers, including Medina et al. (2011). The basic idea of RBI is the optimization of inspection intervals, instead of fixed frequencies, required by traditional time based approach. In RBI, inspection times and modes are affected by an adequate assessment of failure risk, assumed as the combination of likelihood and consequences, as well as by the tolerable risk level and by the results of previous inspections. At Seveso establishments, RBI is considered acceptable just if the risk level is definitely lower than the risk level resulting by the fixed inspection frequencies. On the other hand, the results of Seveso audits on human and organizational factors may be exploited to improve RBI program. Basically if an establishment receive a higher score for human and organizational factors may be assumed to have also a lower equipment failure probability, as demonstrated by Bragatto & al. (2012).

3. A short history of the information sources for the “Failure Rates”

As discussed in previous chapter, in Seveso Establishments the probabilistic assessment is essential for both risk assessment (safety report) and risk manage-

ment (inspections). At the very basis of the complex architecture there are the equipment failure rates. The present paper focuses just mechanical failures on pressure equipment. For pressure equipment it is less difficult to gather data, because all pressure life-cycle, certification, installation, periodical inspection and disposal, are driven by national regulations. Instrument failures and human errors are equally important but are not subject to strict regulations.

Since the early 70s a huge effort was made to provide the nuclear and chemical engineers with a credible set of reliability data of pressure vessels. In an article by Bush (1988), the historical studies, conducted over 60–70 years in three major industrial countries, USA, UK and Germany, are reviewed and compared in a critical way. In the review eight national studies on pressure vessels are reported in detail. In each study, 10.000 to 100.000 pieces of equipment were observed for ten years and more. Those studies consider as a whole 3 million years-pressure vessels (both fired and unfired) with some thousand faults. Table 1 is a synthetic elaboration of Bush data.

Table 1. “Historical” pressure equipment failure rates.

Weighted average frequency of minor failures	3,89E-04	Weighted average frequency of major failures	2,61E-05
Quadratic deviation	18,44%	Quadratic deviation	88,72%
number of minor events	8.611	Number of major events	155
Number of equipment year	3.119.000	Number of equipment year	1.586.000

In the early 80’s, the first scientific LUP studies were presented for the areas of Canvey Island in UK (Canvey 1981) and Rijmond in NL (Covo 1981). The two studies proposed two sets of failure frequencies, which have been widely used for area risk studies. Both failure rates sets have been derived from large historical datasets, handled by a number of experts, which customized them for process industries. This values are still trusted, due to the lack of alternatives.

Since the 90s, two things occurred that completely changed the industry: quality management, which has been completely revolutionized by ISO 9000, and the management of the certification that has been completely revolutionized by the PED Directive. Furthermore, plants are aging more and more, due to poor investments; the “new” materials, introduced in the 70s and 80s are not well known on a large scale. Also acceptance criteria for in-service inspections are critical for ageing equipment. For all these reason, it’s essential to update the recognized national and international information sources for the failure rates, in particular for the pressure equipment.

3.1 Recent efforts for updating failure rates data

The quality of the data on equipment failures used in Italy must be updated to promote a more effective use in risk management, both for companies and authorities. Since 2012 INAIL is in charge to organize a data base of the verification activities for working equipment, including fired and unfired pressure vessels and pressure piping. This is a good chance indeed to organize the knowledge about pressure equipment life cycles, defects, anomalies and failures. A critical review comparison of data currently used in Europe, in order to identify strengths and weaknesses of the different approaches in the area of pressure equipment Failures Rates. The second step has been the analysis of the knowledge potential of data gathered in the verification activities throughout Italy, which are in charge of INAIL.

3.2 European experiences

As a first step has been considered the recognized sources of the European countries, which are likelihood-oriented in LUP decisions and, consequently, committed to maintain shared failure rates. The main sources are the following:

- a) The “PURPLE BOOK” is a study ordered by the Dutch Competent Authority to the TNO (Uijt de Haag & Ale 1997). The values of frequencies are the result of discussions between representatives of the competent authorities and the government. The frequencies are often based on old data available at that time, in combination with expert judgment (Pasman 2011).
- b) FRED (UK) is managed by HSE, the British Competent Authority (HSE 2012). The method is similar to that of the Purple Book, i.e. processing of consolidated data and expert judgment. The study, however, is more recent and the approach is much more conservative, thus the failure rates are systematically higher.
- c) AMINAL (BE), the study AMINAL from Belgium is recent (Aminal 2009). It is not far from the Purple Book, although data are presented in a different format.
- d) American Petroleum Institute (API) Even though it is a private body, API is highly influencing the Oil & Gas industry. The general failure rates are provided for many types of equipment, in the frame work of the resources to be used to implement a Risk Based Inspection (RBI) program (API 2008).

3.3 Other potential source of data

The HSE study (Bellamy 2012) is trying an innovative path, to consider as a valuable information source the major accident records, which, by the Seveso Directive, must be reported to the Competent Authorities. The difficulty is figuring out

which is the reference population, because there are no data on the total number of pipes and pressure vessels at the Seveso establishments (Manuel 2012). The proposal to exploit Google Earth is applicable just for external pipelines, not for establishments. Furthermore, only the catastrophic failures can be considered. The National Archives of fatalities managed by INAIL could be interesting as the reference “equipment population” is wider, but just faults with fatal consequences may be studied. That is misleading as there major failures without injuries.

3.4 Control bodies

The mandatory periodical inspections of pressure equipment, which is present in many European Countries, including Italy, could provide a valuable source of information. From the data on testing at installation (or first occurs), the periodic checks on the redevelopment after repairs and modifications, as well as notices of demolition or decommissioning essential information may be extracted. Unfortunately most information is scattered throughout the local agencies and the regional authorities. A few years ago, a study has been presented by the Region Emilia-Romagna, where the recorded were analyzed anomalies as verified by the public control body (Frabetti & al. 2002). Featuring 46.000 units pieces of equipment under observation and five years observation period, the study is significant indeed. Furthermore for each failure there is a free text description useful for further deepening. This is a valuable experience, which should be continued and extended to the national level.

4. Results

4.1 Synopsis of “official” data

The synopsis from the data reported in the sources detailed in chapter 2 has some difficulty, because of the size of the heterogeneous data, for smaller events, in some studies, including severe defects detected in a test. In other cases are distinguished various types of faults, according to the leak's. Figure 1 shows a graph comparing accrued fault for pressure equipment reported by the four cited sources Aminal, Fred, TNO and APIs. The values derived from the study of Emilia-Romagna Region (Frabetti & al. 2002) and the values used in the Canvey and Rijmond studies have been added in the fifth and sixth column. The values derived from historical studies, included in the review of Bush (1988) are in the last column. For uniformity of comparison were considered only failures with loss of containment. The small and large classification depends only on the diameter of the loss, greater and less than 10 mm. The full aperture of the bottom or the shell is considered to be rather catastrophic. It has to be stressed that values in the first four columns come directly from the cited references whilst the other ones are original elaborations of the authors. The collection of data from pressure equip-

ment inspections in a few years will provide a sound set of failure rates for the risk assessment very credible and updated, in the meantime, the British generic values (FRED-HSE) can certainly be suggested to the Competent Authorities to make decisions.

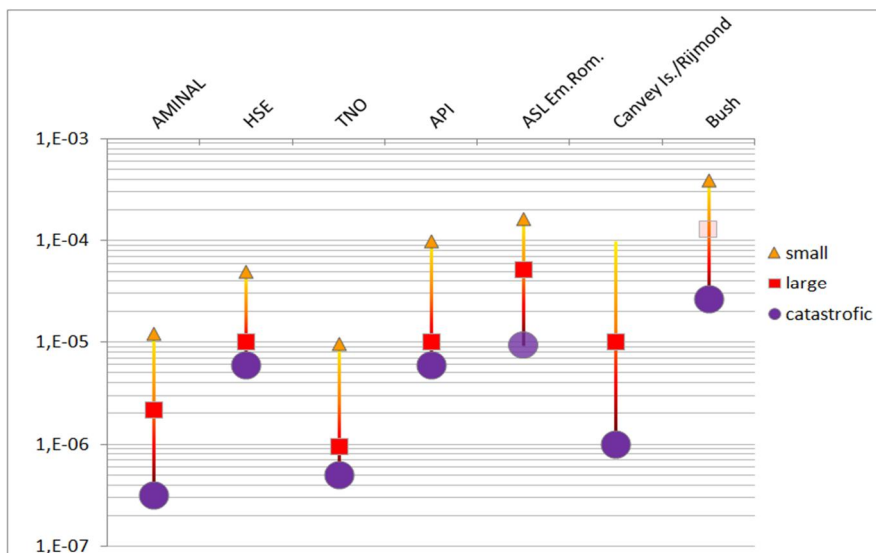


Figure 2. Comparing pressure equipment failure frequencies according to the most reputed sources.

5. Conclusions

Probabilistic assessment has been a pillar of safety since the first Safety directive in the Eighties. The assessments have always a higher uncertainty and must be verified in the actual safety management. Audits, as required by the Seveso legislation, are the moment to compare the actual performances and the theoretical evaluations. By using the bow-tie approach the results of mechanical and function inspections may be linked to the level of efficiency of the barriers, which was adopted to prevent accident and to mitigate consequences. In such a way the probabilistic assessment is less far from the practical management of safety. Operations, including inspection and maintenance, may be driven by probabilistic assessment, but they provide in turn valuable data to tune the probabilistic assessment, take into account the actual equipment condition. Even though the importance of probabilistic assessment is moderated by the results of the equipment inspections, it is anyway essential to have more trustable assessments. The failure rates are an cornerstone of any probabilistic assessment; but unfortunately the “historical” and “official” values are obsolete and could be misleading. The systematic collection of data on pressure vessels subject to mandatory verifica-

tion, and their failures, is a great opportunity to increase knowledge on the matter. An updated set of general failure frequencies for risk assessment and decision making, is urgent, even though the updated values by HSE are, at now, suitable for a conservative approach, as demonstrated by the resulting comparison. The structured grids to collect information from the field is suitable to organize the inspector practical experience, which, otherwise, would be isolated and useless. The structured data that will be collected throughout Italy. The failure rules, extracted by means of the ontology, will be exploited to promote sound risk management procedures throughout the Italian Process Industries. Power industry could exploit the new burdens of the Seveso Legislation, implementing risk based inspections and maintenance programs.

References

- Aminal 2009 Handbook failure frequencies for drawing up a safety report Flemish Government LNE Department BE <http://www.lne.be/en/safety-reporting/downloads>
- API Risk-Based Inspection Base Resource Document RP581, 2008 American Petroleum Institute, Washington, USA.
- Bellamy, Linda J. & Williët GJ Brouwer. "AVRIM2, a Dutch major hazard assessment and inspection tool." *Journal of hazardous materials* 65.1 (1999), pp. 191–210.
- Bragatto, P. A., Pittiglio, P. & Ansaldo, S., 2009. The management of mechanical integrity inspections at small-sized "Seveso" facilities. *Reliability Engineering and System Safety*, 94(2), pp. 412–417.
- Bragatto, P., Delle Site, C. & Faragnoli, A., 2012. Opportunities and threats of risk based inspections: The new Italian legislation on pressure equipment inspection *Chemical Engineering Transactions*, 26, pp. 177–182.
- Bush, S. H., 1988. Statistic of Pressure Vessel and Piping Failures *Journal of Pressure Vessel Technology* 110, pp. 225–233.
- Camossi, E., Giannini, F., Monti, M., Bragatto, P., Pittiglio, P. & Ansaldo, S., 2008. Ontology driven certification of pressure equipments. *Process Safety Progress*, 27(4), pp. 313–322.
- Canvey 1981 Canvey: A Second Report. A Review of the Potential Hazard from Operations in the Canvey Island/Thurrock Area Three Years after Publication of the Canvey Report. HM Stationery Office, London.

- COVO Commission 1981. Risk analysis of six potentially hazardous object in the Rijnmond area, a pilot study. Report to the Rijnmond Public Authority, Central Environmental Control Agency, Schiedam, the Netherlands.
- HSE – Buncefield Standards Task Group 2007 Safety and environmental standards for fuel storage sites <http://www.hse.gov.uk/comah/buncefield/final.htm>.
- HSE 2012 Failure Rate and Event Data for use within Land Use Planning Risk Assessments updated 28-6-2012 <http://www.hse.gov.uk>.
- Fragola, J. R., 1996. Reliability and risk Analysis data base development: an historical perspective. Reliability Engineering & System Safety, 51, pp. 125–136.
- Frabetti, M. Bondi, M., Pallavicini, L., Dellantonio, E., Notari, V., Bazzocchi, G., Grassano, G., Giuliani, M. & Zanotti, M., 2002. Anomalie degli apparecchi a pressione Regione Emilia Romagna – Bologna. (In Italian).
- Bellamy, L., Lisbona, D., Johnson, M., Kooi, E. S., Manuel, H. J., 2012. The major accident failure rates project HSE/RR915 www.hse.gov.uk.
- Manuel, H. J., Kooi, E. S., Bellamy, L. J., Mud, M. L., Oh, J. I. H., 2012. Deriving major accident failure frequencies with a storybuilder analysis of reportable accidents Process Safety Progress Volume 31, Issue 4, pp. 381–389, December.
- Medina, H., Arnaldos, J. & Casal, J., 2011. Risk-based Inspection and Its Application to the Optimization of Chemical Plants, Chemical Engineering Transactions, 25, pp. 201–206.
- Pasman, H. J., 2011. History of Dutch process equipment failure frequencies and the Purple Book. J. of Loss Prevention, 24, pp. 208–213.
- Uijt de Haag, P. A. M. & Ale, B. J. M., 1997. Guideline for quantitative risk assessment Purple book CPR 18E <http://www.publicatiereeksgevaarlijkstoffennl/publicaties/PGS3.html>.

Investigations of superheater materials from Nordjyllandsværket coal-fired plant after 100.000 hours service

L. Korcakova, M. Montgomery & H. T. Jensen

Vattenfall AB
Støberigade 14, Copenhagen, Denmark

Abstract

The Danish coal-fired Ultra Super Critical (USC) plant, Nordjyllandsværket, was commissioned in 1998 with 290 bar and 580°C/580°C steam data. The boiler was designed as an USC once-through Benson tower type boiler with double reheat. The challenging steam conditions required the use of state of the art materials, such as P91 or TP347HFG for the construction of the boiler. The plant has now reached 100.000 hours of operation. Taking advantage of the boiler maintenance programme, tube sections were removed from more than 20 different locations in the boiler during the 2012 summer shutdown to assess the materials conditions of the boiler.

The tubes have been investigated to document wall thickness, fireside corrosion and steamside oxidation rates and morphology and microstructure evolution after 100,000 hours exposure. This data together with the temperature data of the plant will serve to give a lifetime evaluation of the boiler components. The present paper focuses on understanding and modelling corrosion and thermal stability of the austenitic alloy TP347HFG that was used as a construction material for superheaters and re-heaters.

1. Introduction

Very little data exists in the literature which describes long-term exposure of TP347HFG and TP347H although there are many articles on short term laboratory exposures and initial experiences in power plants.

Sigma phase is an intermetallic Fe, Cr phase that forms in austenitic steels during long term exposure at high temperatures. The presence of sigma phase leads to embrittlement of the material at low temperatures. The presence of sigma phase is a problem for steels with a higher Cr content however has not been recognised as being present for TP347HFG. The microstructural evolution of TP347HFG has been discussed for exposures between 1000–50,000 hours, where sigma phase develops within 1000 hours at 700°C and within the first 50,000 hours at 650°C [1]. Such temperatures ranges are not utilised for at Nordjyllandsværket, however sigma phase is observed.

The monitoring of steam oxidation of TP347HFG and TP347H is also relevant as austenitic steels are known to give problems due to spallation of outer oxide layers [2]. The screen tubes at Nordjyllandsværket were initially fabricated in TP347H coarse-grained but due to fast corrosion rates and spallation were replaced with TP347HFG. Such spalled oxide can result in blocking of tubes or erosion of turbine blades. Since the introduction of TP347HFG in Denmark, various investigations have been conducted to follow and try and understand the growth behaviour of this steamside oxide.

2. Investigation methods

Figure 1 shows a schematic drawing of the boiler at Nordjyllandsværket power plant. Table 1 gives an overview of the test samples and conditions to which the samples were exposed. The composition of TP347HFG is given in Table 2. The superheater and re-heater materials had been in service for 100,000 hours, whereas the screen material had been in service for 60,000 hours. As there are no direct measurements of the tube wall temperatures, they were estimated based on flue gas and steam temperatures according to EN standard [3].

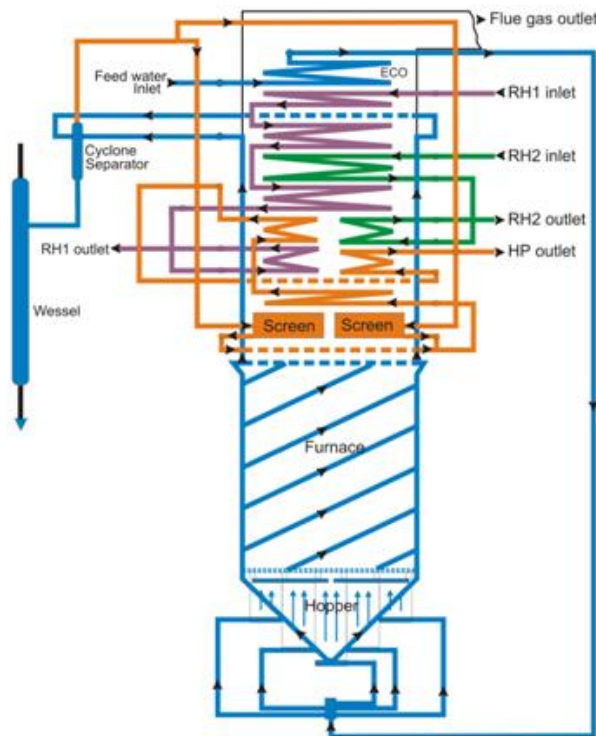


Figure 1. Schematic drawing of Nordjyllandsværket's boiler.

Table 1. Sample overview and operation conditions.

Sample No.	Position	Material	Dimensions [mm]	Steam p [bar]	Flue gas T [°C]	Steam T [°C]	Tube T [°C]
10	Outlet SH1	TP347HFG	ø38.0 x 8.0	290	815	565	585
11	Outlet RH2.2	TP347HFG	ø44.5 x 3.6	20	815	580	600
13	SH1 middle	TP347H	ø38.0 x 7.1	290	980	535 (calc.)	585
14	Outlet RH1.2	TP347HFG	ø42.4 x 3.6	80	980	575	590
15	Outlet SH2	TP347HFG	ø38.0 x 8.0	290	980	580	600
16	Inlet SH2	TP347HFG	ø38.0 x 7.1	290	1120	570	620
17	Inlet RH1.2	TP347HFG	ø42.4 x 3.6	80	1120	535	585 / 570
18	Inlet SH1	TP347H	ø38.0 x 7.1	290	1120	500	535
19	Inlet SH1	TP347H	ø38.0 x 7.1	290	1230	500	550 / 535
20	Outlet Screen	TP347HFG	ø42.4 x 8.0	290	1230	520	570 / 555
21	Outlet Screen	TP347HFG	ø42.4 x 8.0	290	1230	520	570 / 555

Table 2. Nominal chemical composition of TP347HFG in wt%.

	C	Si	Mn	Cr	Ni	Other
TP347HFG	0.06–0.10	Max 0.75	Max 2.0	17.0–20.0	9.0–13.0	8xC<Nb+Ta <1.0

Specimen rings from the exposed tubes were prepared according to standard metallographic preparation techniques. The specimens were then investigated with respect to steamside oxide and tube wall thickness. The residual metal minus internal attack was also measured. Measurements were undertaken at eight locations around the circumference. The orientation of the samples in the boiler has a great influence on the microstructure and corrosion. Therefore all samples were orientated in the same way such that the side facing the furnace was marked as position 0° and the side facing away from the furnace was marked 180°. The specimens were further investigated with Light Optical Microscopy (LOM), Vickers Hardness (HV) and Scanning Electron Microscopy (SEM) equipped with Energy Dispersive X-ray Spectroscopy (EDS). Specimens were etched electrolytically with 10% oxalic acid to reveal microstructure. The investigations methods used in the project are summarized in Table 3.

Four samples were chosen for detailed SEM-EDS investigations, two from coarse grained and two fine grained version of TP347H. The difference between the two samples from each material was in steam and flue gas temperatures. The samples of TP347H had different metal temperatures of approximately 585°C and 535°C for sample 13 and 18, respectively. The samples from TP347HFG had approximately the same metal temperature of about 585°C.

Table 3. Summary of investigation methods.

Sample No.	Placement	LOM	HV	SEM
10	Outlet SH1	x		
11	Outlet RH2.2	x		
13	SH1 middle	x		x
14	Outlet RH1.2	x		x
15	Outlet SH2	x		
16	Inlet SH2	x		
17	Inlet RH1.2	x	x	x
18	Inlet SH1	x		x
19	Inlet SH1	x	x	
20	Outlet Screen	x		
21	Outlet Screen	x		

3. Results

The average worst case metal loss based on initial measurements, inner and total steam-side oxide thickness and ASTM grain size measurements are given in Table 4. The Average Worst Case (AWC) is the average of the worst quartile of measurements and is relevant as the corrosion rate around the tube can vary greatly.

Table 4. Summary of results.

Sample No.	Placement	Material	AWC metal loss [mm]	Inner oxide thickness [μm]	Total oxide thickness [μm]	ASTM grain size
10	Outlet SH1	TP347HFG	0.69	20	35	7–9
11	Outlet RH2.2	TP347HFG	0.15	22	46	6–8
13	SH1 middle	TP347H	0.28	69	75	7–8
14	Outlet RH1.2	TP347HFG	0.19	19	27	7–8
15	Outlet SH2	TP347HFG	0.50	29	51	6–8
16	Inlet SH2	TP347HFG	0.38	10	18	7–9
17	Inlet RH1.2	TP347HFG	0.35	23	56	7–9
18	Inlet SH1	TP347H	0.20	50	56	8
19	Inlet SH1	TP347H	0.41	66	72	8–9
20	Outlet Screen	TP347HFG	0.22 ³	16	25	5–8
21	Outlet Screen	TP347HFG	0.36 ¹	10	19	5–8

³ Screen was in service for 60,000 h.

3.1 Sigma phase formation

Sigma phase was observed in the majority of the samples investigated, see Table 5. Sigma phase was found in greater amounts in position 0°, which is facing directly to the furnace and thereby meets the hottest flue gas. A sigma phase free band of about 300–400 µm at the surface on the flue gas side was observed. The greatest concentration of sigma phase was in the middle of the tubes and its content was decreasing towards the steam side of the tubes. Small amounts of sigma phase were observed also in position 180° that is facing away from the furnace and is partially shielded from the hot flue gas by surrounding tubes. Figure 2 shows the difference in sigma phase content in position 0° and 180° for sample 17, the SEM-EDS measurements were then used to confirm the composition of sigma phase in the large precipitates, see Table 6. In addition to the large sigma phase precipitates, fine needle type precipitates were also present which could not be analysed. Sigma phase was not observed on the replaced screen tubes exposed for 60,000 hours or in the outlet of SH1 and RH2.2.

The sigma phase is known to influence the mechanical properties, especially toughness, of materials at lower temperatures. The results of hardness tests show a slight increase in hardness for the exposed materials compared to the material in as delivered conditions. Other material tests as tensile test, fracture toughness or fracture toughness test are still in progress.

Table 5. Sigma phase in TP347H and TP347HFG.

Sample No.	Placement	Material	Sigma phase		Tube T [°C]
			0°	180°	
10	Outlet SH1	TP347HFG	-	-	585
11	Outlet RH2.2	TP347HFG	-	-	600
13	SH1 middle	TP347H	+	(+)	585
14	Outlet RH1.2	TP347HFG	+	(+)	590
15	Outlet SH2	TP347HFG	+	(+)	600
16	Inlet SH2	TP347HFG	++	(+)	620
17	Inlet RH1.2	TP347HFG	+++	(+)	585 / 570
18	Inlet SH1	TP347H	+	-	535
19	Inlet SH1	TP347H	++	(+)	550 / 535
20	Outlet Screen	TP347HFG	(+)	-	570 / 555
21	Outlet Screen	TP347HFG	-	-	570 / 555

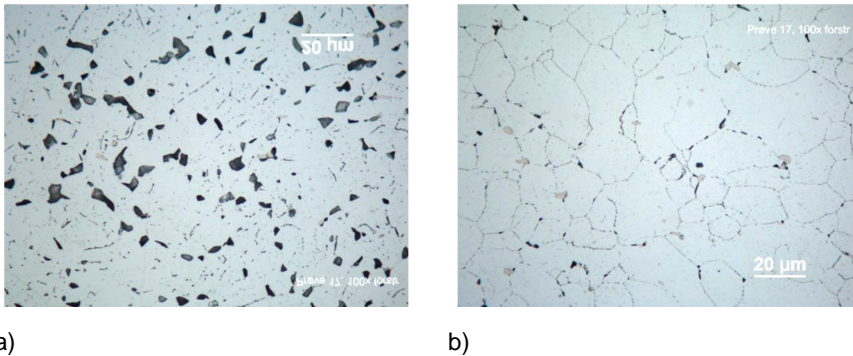


Figure 2. LOM image of sample 17. a) position 0° – large amount of sigma phase, b) position 180° – small amount of sigma phase.

Table 6. Sigma phase composition measured with SEM-EDS (wt %).

Sample No.	Si	Cr	Mn	Fe	Ni	Nb	Mo
13	1.0	38.4	2.0	53.5	4.4	-	0.7
	1.2	38.4	1.6	54.1	4.1	-	0.8
17	1.0	36.3	1.5	54.2	6.1	-	0.8
	1.5	40.1	1.4	51.0	4.7	0.4	1.0
18	2.0	37.2	2.5	52.6	3.4	1.0	1.3

3.2 Steamside oxidation

3.2.1 TP347H

Relatively thick oxide had developed on both samples of TP347H during service. The oxide consisted of two layers, the inner and the outer oxide layer, respectively (Figure 3 a1), b1)). The interface between the outer and inner oxide layers was assumed to be the original metal surface. The outer oxide layer was approximately 5 times thinner than the inner layer and it was partially spalled. Pores were visible at the inner oxide-outer oxide interface where spallation was not observed suggesting poor adhesion between the two oxides. The SEM-EDS measurements of the composition of the outer layer showed that it consisted of Fe-oxide, see Figure 3 b2) analysis 6. The results of the SEM-EDS analyses are given in Table 7.

The inner oxide layer was of uniform thickness and its morphology was similar for both samples. The only exceptions were the presence of a homogeneous layer of Cr-Fe rich oxide on the metal oxide interface, Figure 3 b1) analysis 5, and a layer of Cr-Fe-Ni rich oxide on the interface between the inner and outer oxide

layers (analysis 1) in the sample exposed to higher metal temperature. These layers were missing in the sample exposed to lower metal temperature, Figure 3 b2). The inner oxide layer of both samples consisted of oxidized austenitic grains with a mixture of Cr-Fe-Ni oxides (analyses 3, 7, 8), where the darker oxide is most probably rich in Cr and the brighter oxide is rich in Ni. The oxide on the former grain boundaries was Fe-Cr rich (analysis 4, 9) with embedded metallic Nb and Fe-Ni particles (analysis 1, 10).

Chromium depletion on the steam side was observed close to the metal – oxide interface at higher metal T ~ 585°C. The Cr depleted zone was approximately 5–10 µm wide. No Cr depletion was observed in the coarse grained sample at the lower metal T ~ 535°C.

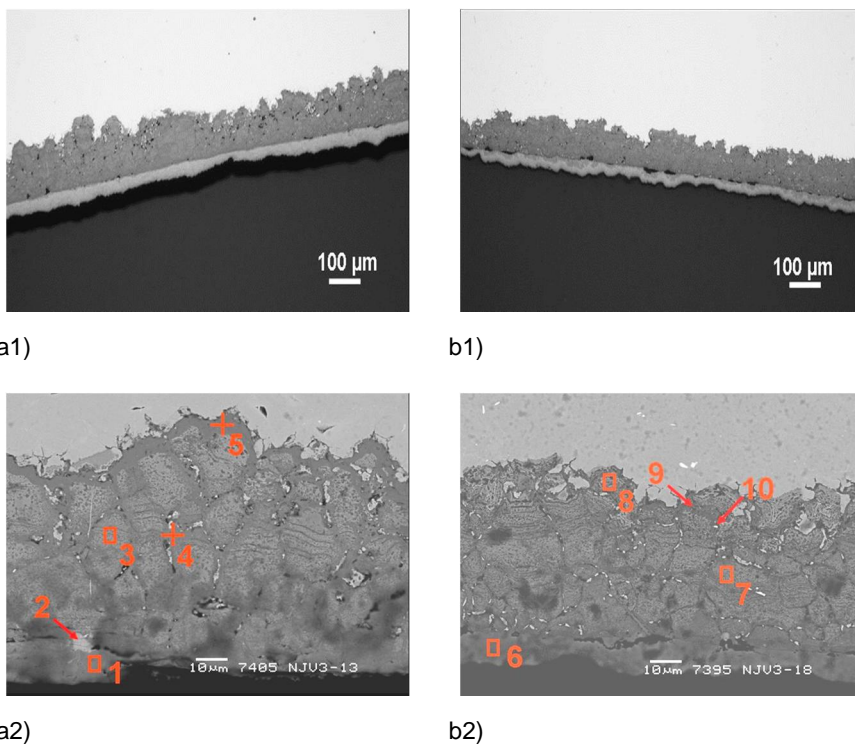


Figure 3. LOM (1) and SEM (2) images of steamside corrosion of TP347H in position 0° at a) higher metal T ~ 585°C; b) lower metal T ~ 535°C. The results of the SEM-EDS analyses are given in Table 7.

Table 7. Results of SEM-EDS analysis of steamside oxides. The analysed areas are marked in Figure 3 a2) and b2). All analyses are in wt%.

Figure	An.	O	Si	Cr	Mn	Fe	Ni	Others
3 a2)	1	9.7	0.9	38.9	2.2	29.9	17.9	Nb
	2	13.5	-	1.9	3.2	16.2	3.8	Nb
	3	9.3	1.0	30.2	3.2	33.2	22.5	Nb
	4	11.6	0.7	22.2	2.9	60.2	2.1	Mo
	5	13.7	0.8	56.2	3.7	23.9	0.8	Nb
3 b2)	6	14.6	2.0	1.3	0.8	80.7	0.80	-
	7	10.9	1.2	27.8	3.5	29.6	26.0	Nb
	8	11.9	1.8	34.6	3.7	33.1	13.8	Nb
	9	6.5	5.3	20.5	1.9	52.8	12.1	Nb, Mo
	10	7.0	0.6	11.2	1.0	18.8	61.4	-

3.2.2 TP347HFG

The oxide on the fine-grained samples was thinner than the coarse-grained samples and it consisted of two layers, the inner and the outer oxide layer, respectively (Figure 4 a1), b1)). As mentioned above, the interface between the outer and inner oxide layers was assumed to be the original metal surface. The outer oxide layer was much thinner than the inner layer and it was partially spalled. The SEM-EDS measurements of the composition of the outer layer showed that it consisted of Fe-oxide, see Figure 4 b2) analysis 3. The results of the SEM-EDS analyses are given in Table 8.

As it seen from Figure 4 the inner oxide layer appeared to be very irregular. It consisted of Ni rich Fe oxide at the interface between the inner and outer layer (analysis 1, 4). Cr rich oxide with a small amount of Fe and Ni was observed beneath the Ni rich layer (analysis 2, 5).

The chromium depleted zone close to the metal – oxide interface was approximately 15 μm wide.

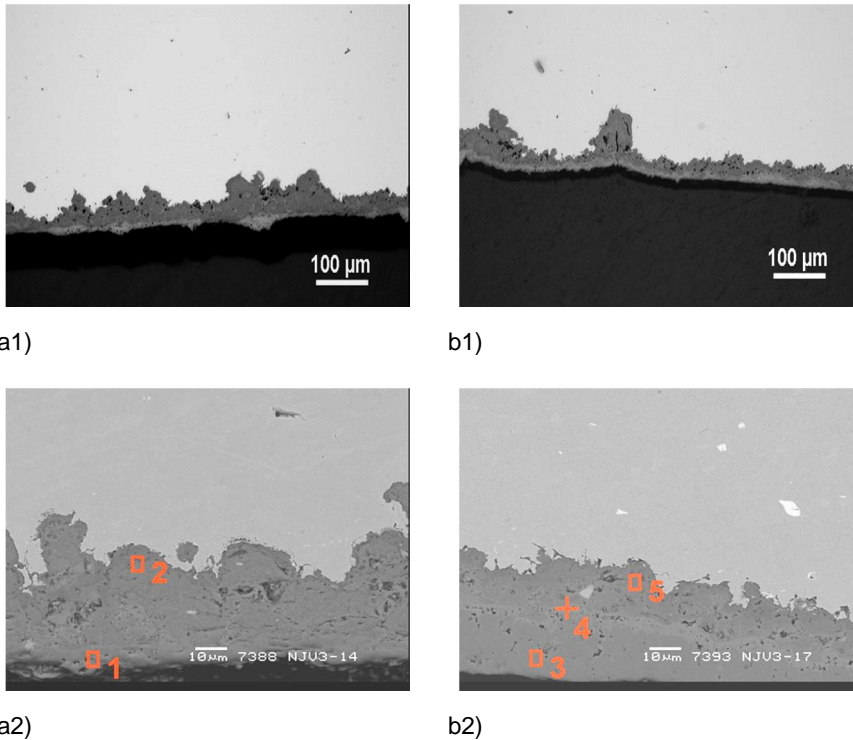


Figure 4. LOM (1) and SEM (2) images of steamside corrosion of TP347HFG in position 0° at higher metal T ~ 585°. The results of the SEM-EDS analyses are given in Table 8.

Table 8. Results of SEM-EDS analysis of steamside oxides. The analysed areas are marked in Figure 4. a2) and b2). All analyses are in wt%.

Figure	An.	O	Si	Cr	Mn	Fe	Ni	Others
4 a2)	1	8.8	0.5	9.7	4.1	55.5	20.6	Nb
	2	14.3	1.2	69.0	2.6	8.3	3.0	Nb
4 b2)	3	12.1	-	-	-	87.9	-	-
	4	10.6	-	2.8	0.1	57.6	28.6	-
	5	11.2	1.2	52.6	7.4	15.7	9.9	Nb

3.3 Fireside corrosion

3.3.1 TP347H

The oxide on the coarse grained samples consisted of several layers; outer layer, inner layer and grain boundary attack (Figure 5). Thicker total oxide was observed on the sample with a higher metal temperature. Sulphur from the flue gas was present in all oxides. The outer oxide layer consisted of iron oxide and flyash particles (Figure 5 a2)) and on many places it was partially spalled. The SEM-EDS measurements of the composition of the oxide show the presence of Si in the Fe-rich oxide as well as small amounts of Al, K or Ca (analysis 1, 4). The results of the SEM-EDS analyses are given in Table 9.

Some differences in composition of the inner oxide layer of the two samples were observed. The inner oxide on the sample with higher metal temperature consisted only of Cr rich oxide (analysis 2, 3). Whereas, the inner oxide on the sample with lower metal temperature was Cr-Fe-Ni rich close to the inner – outer oxide interface and became more Cr rich close to the oxide – metal interface (analysis 5, 6).

Analyses of precipitates causing the grain boundary corrosion showed that the precipitates are Mn, Cr or Fe/Mn rich sulphides. Example of sulphide composition is given in Table 10, Figure 6, analysis 1.

Line scans near the metal – oxide interface were performed in order to investigate Cr depletion. The Cr depleted zone was approximately 5–10 μm wide, an example of line profile shows the changes in Cr, Fe and Ni content in Figure 6. Again, no Cr depletion at metal – oxide interface was observed in the coarse grained sample at lower metal T ~ 535°C. Moreover, the performed line scans show that all samples suffer from 5–10 μm Cr depletion related to the grain boundary corrosion at distance of approximately 25–40 μm from the surface, where the grain boundary corrosion ends; this is also visible on the line scans in Figure 6.

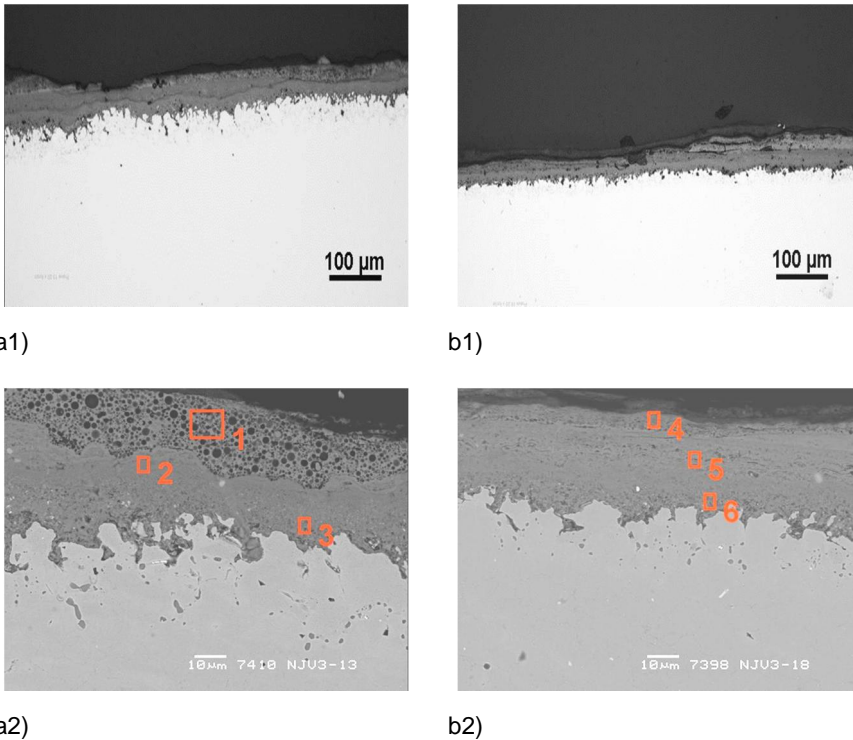


Figure 5. LOM (1) and SEM (2) images of fireside corrosion of TP347H in position 0° at a) higher metal T ~ 585°C; b) lower metal T ~ 535°C. The results of the SEM-EDS analyses are given in Table 9.

Table 9. Results of SEM-EDS analysis of steamside oxides. The analysed areas are marked in Figure 5. a2) and b2). All analyses are in wt%.

Figure	An.	O	Si	S	Cr	Mn	Fe	Ni	Others
5 a2)	1	19.1	11.9	1.6	1.0	0.6	55.9	-	Al, K, Ca, V
	2	14.2	1.1	1.0	74.1	0.9	8.5	0.2	
	3	11.3	1.0	7.1	72.5	1.8	6.1	0.2	
5 b2)	4	22.1	5.5	2.7	1.3	0.8	59.6	1.9	Al, P, Ca
	5	15.9	1.6	3.3	43.5	1.6	23.7	9.4	Nb
	6	13.8	1.6	6.9	60.4	1.3	15.5	0.4	

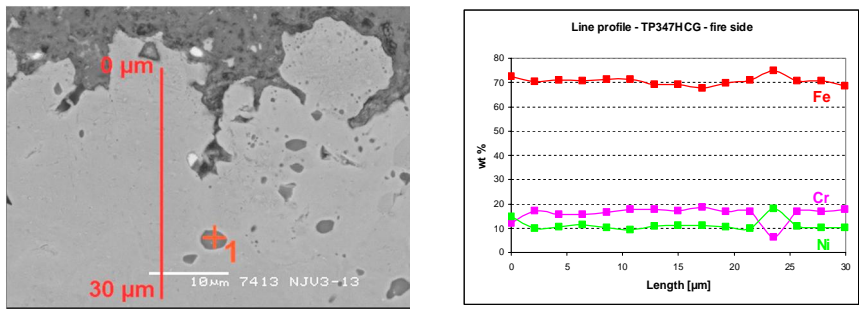


Figure 6. Cr, Fe, Ni line profile at fire side in TP347H in position 0° at higher metal T ~ 585°C.

Table 10. Results of SEM-EDS analysis of steamside oxides. The analysed areas are marked in Figure 6. Analysis is in wt%.

An.	Si	S	Cr	Mn	Fe	Ni
1	-	30.5	13.0	43.7	11.0	1.8

3.3.2 TP347HFG

The oxide on the fine-grained samples consisted of several layers; outer layer, inner layer and grain boundary attack (Figure 7 a1) and b1)). Sulphur from the flue gas was present in all oxides. The outer oxide layer was porous (Figure 7 a1)) and on many places it was partially spalled. The SEM-EDS measurements of the composition of the oxide reveal the presence of Si in the Fe-rich oxide, small amounts of Na, Mg, Al, P, K or Ca were also present in the oxide (analysis 4), i.e flyash constituents.

As it can be seen from Figure 7 a2) and b2), the thickness of the inner oxide as well as the grain boundary oxidation in the samples varied greatly. The inner oxide on both samples consisted from Cr-Fe rich oxides (analyses 1, 2, 5, 6), where the concentration of Fe was decreasing toward the metal – oxide surface.

Grain boundary corrosion was also observed in the samples. The grain boundaries contained Cr rich oxides (analysis 3) and particles of sulphides. Similar to the coarse grained samples Mn, Cr and Fe/Mn rich sulphides were observed.

Line scans near the metal – oxide interface show, that the Cr depleted zone in fine grained samples was approximately 15–25 µm wide. Also fine grained samples were found to suffer from 5–10 µm Cr depletion related to the grain boundary corrosion at distance of approximately 25–40 µm from the surface.

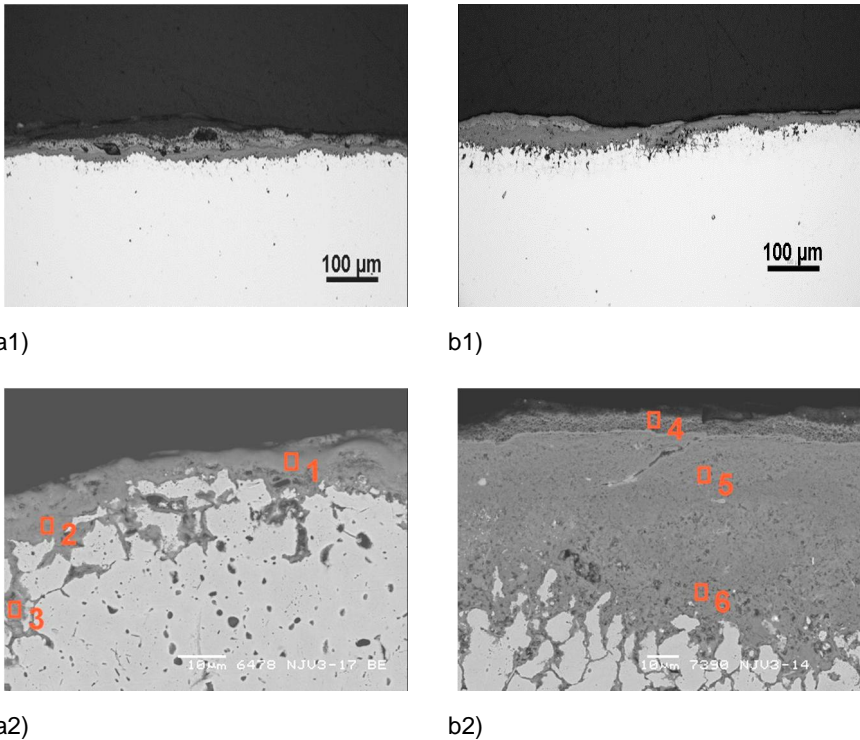


Figure 7. LOM (1) and SEM (2) images of fire side corrosion of TP347HFG in position 0° at higher metal T ~ 585°C. The results of the SEM-EDS analyses are given in Table 11.

Table 11. Results of SEM-EDS analysis of steamside oxides. The analysed areas are marked in Figure 7 a2) and b2). All analyses are in wt%.

Figure	An.	O	Si	S	Cr	Mn	Fe	Ni	Others
7 a2)	1	12.6	2.0	2.2	68.5	3.1	6.5	1.5	Al, K, V, Nb
	2	14.9	1.7	0.8	63.2	-	15.2	2.9	K, Nb
	3	9.8	1.6	2.2	62.4	8.9	12.8	1.3	V
7 b2)	4	34.6	20.9	3.0	1.0	0.7	18.3	-	Na, Mg, Al, P, K, Ca
	5	14.5	1.0	0.8	57.4	2.2	23.4	-	Nb
	6	13.7	1.5	6.8	69.5	1.0	6.9	-	Nb

4. Discussion

4.2 Sigma phase formation

The microstructure of TP347H is austenitic strengthened with primary Nb-rich precipitates of MX type. Precipitation of secondary MX, $M_{23}C_6$ and sigma phase takes place during service at elevated temperatures. In the present work only NbC and sigma phase were detected after 100,000h of service. Minami's [1] long term aging experiments of austenitic steels also show presence of NbC and sigma phase at temperatures below 650°C. These observations are in a good agreement with MatCalc calculations that predicts MX and sigma phase as the equilibrium phases in TP347H (Figure 8). The formation of sigma phase is dependent on C, Nb and Cr content in the material [4]. Thermodynamic calculations of the effect on C on formation of sigma phase, show the rapid decrease of the content of sigma phase when C content increases to 0.1 wt% [5]. According to [4] Sigma phase will form when C content is below a critical level and Cr equivalent is greater than 18 wt%. The critical C content can be reached by precipitation of Nb carbides, thus the Nb/C ratio is an important factor for sigma phase formation.

The presence of a sigma phase free area on the fireside could be due to either a higher temperature where sigma phase is no longer stable, or a slightly higher C presence in this area which was not easily detectable.

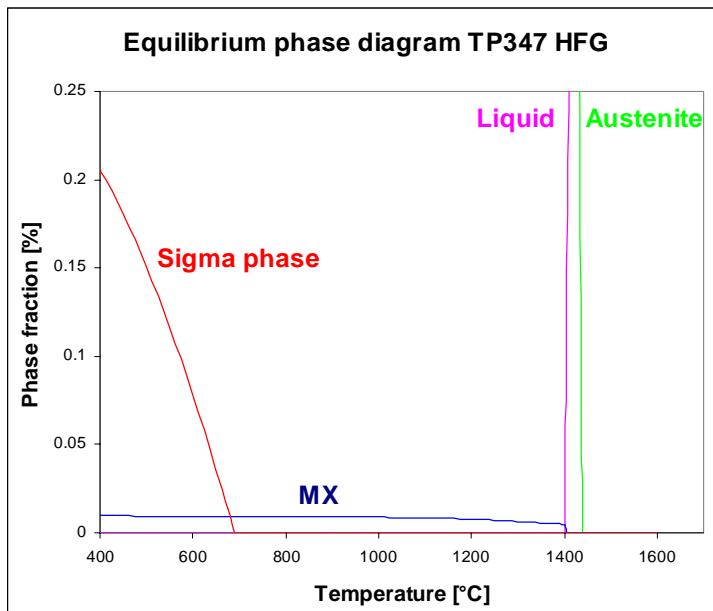


Figure 8. Equilibrium phase diagram for TP347HFG calculated with MatCalc software [6].

4.2 Steamside oxidation

4.2.1 TP347H

Figure 9 is the Arrhenius plot showing parabolic rate constant for the inner steamside oxidation of TP347H and compare the present data with data from literature and from other Danish power plants. The results are depicted with respect to the calculated or estimated surface metal temperature. It is the surface metal temperature that is relevant for the reaction, although this cannot be measured in the plant. The surface metal temperature will depend on the heat flux, which varies for different locations in the plant. The results for steamside inner oxide measurements on TP347H fit reasonably well with data from other sources. When the inner oxide in TP347H reaches a critical thickness of 60–70 μm , there is a risk of outer oxide spallation [7]. The spalled oxides can block the steam tubes by accumulated magnetite as observed in other plants in Denmark [2]. The inner oxide thickness in the present work is 55–65 μm , thus it is important to be aware of this problem.

The exposure temperature seems to influence the morphology of the inner oxide. The exposure of the material to higher temperatures has led to formation a homogeneous layer of Cr-Fe rich oxide on the metal oxide interface and a layer of Cr-Fe-Ni rich oxide on the interface between the inner and outer oxide layers. This can be explained by faster Cr diffusion at higher temperatures.

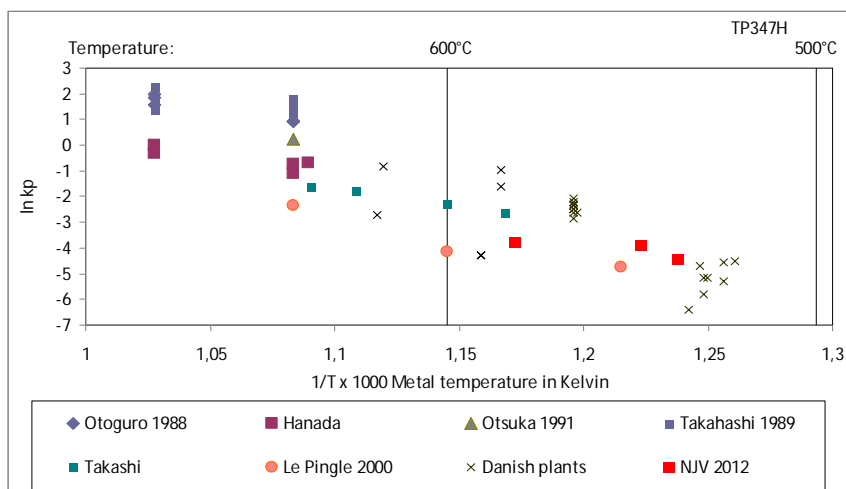


Figure 9. Arrhenius plots depicting parabolic rate constant for the inner steamside oxidation of TP347H. Since the plot is in metal temperature, where steam temperature has only been given, 20°C has been added to give an estimated metal temperature, not only for data from the Danish plants but also for some of the references [8, 9, 10, 11, 12, 13].

4.2.2 TP347HFG

Figure 10 shows the Arrhenius plot depicting parabolic rate constant for the inner steamside oxidation of TP347HFG, and compare present data with data from literature and from other Danish power plants. Again a estimation or calculation of the surface metal temperature is used. The oxide growth in fine grained samples does not follow the parabolic law, therefore it is difficult to predict the oxidation behavior of the fine grained materials. In fact there is a immense spread in the oxidation rates measured, however they do generally lie below TP347H. The reasons, why the fine grained material does not follow the parabolic law are still being discussed. It is most probably combination of several factors, such as applied pressure, composition, grain size, the amount of cold work.

Hansson et al. [14] and Jianmin et al. [15,16] proposed that the higher pressure in the tubes facilitates faster Cr diffusion promote formation of protective Cr-rich oxide. This was not confirmed in present work, the superheater samples, exposed to high pressures, do not show difference in oxidation behavior from re-heater materials, exposed to lower pressures.

The grain size has been found to have influence on steamside oxide thickness [17]. As smaller grains create more paths for chromium diffusion and thus formation of a chromium rich layer, which gives a thinner steamside oxide. The grain size of the coarse-grained samples was measured to be similar ASTM No to fine-grained samples, yet difference in morphology and thickness of the inner oxide scale was observed. The inner oxide on the fine grained samples did contain more Cr than the inner oxide observed on the coarse grained samples, and the mobility of cations is evident as the original grain structure is not apparent, and nickel has diffused to form a Fe-Ni oxide within the outer oxide.

Hansson et al. [14] also proposed the influence of compositional changes on oxidation behaviour of TP347HFG. aspect deserves further investigations. The variations in oxide morphology and oxidation rates for TP347H FG may be due to different temperature ranges in the first few thousand hours when the oxide is formed and the surface treatment of the tube.

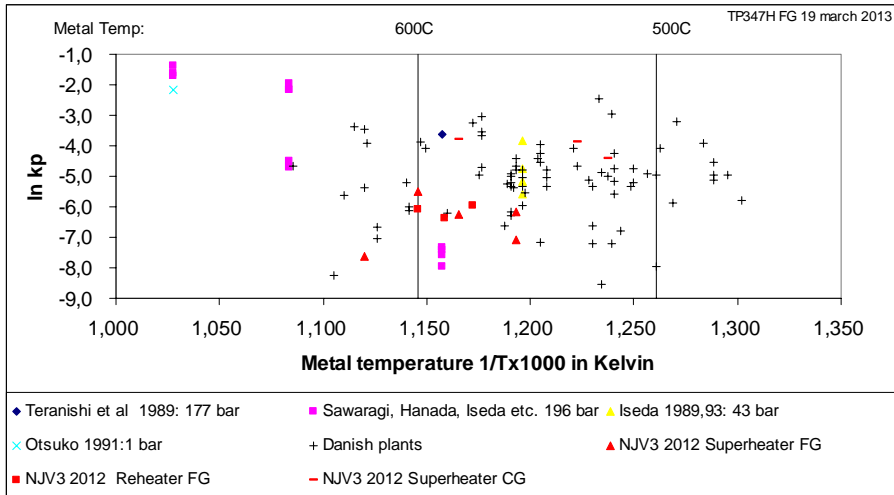


Figure 10. Arrhenius plots depicting parabolic rate constant for the inner steamside oxidation of TP347HFG. Since the plot is in metal temperature, where steam temperature has only been given, 20°C has been added to give an estimated metal temperature, not only for data from the Danish plants but also for some of the references [12,18,19,20].

4.3 Fireside corrosion

Fireside corrosion in coal fired power plants, contrary to biomass fired power plants, is usually not a problem. The present investigations show that the corrosion rate for all samples investigated is below the acceptable limit of 1 mm / 100,000 hours.

An interesting observation regarding chromium depletion has been made. Two Cr depleted zones have been observed close to the metal – oxide interface. The first was related to the formation of the inner oxide and was present only in samples exposed to higher metal temperatures. The second Cr depleted zone was in the metal and was connected to the formation of sulphides at grain boundaries (see Figure 6). No Cr depletion was then observed within the grains. The sulphur from the flue gas uses grain boundaries as easy diffusion paths and depending on the partial pressure it forms different kinds of sulphides, such as Cr, Mn or Mn/Fe.

5. Conclusions

The microstructure of TP347H is austenitic strengthened with primary Nb-rich precipitates of MX type. The presence of Sigma phase has been observed in the samples facing the hot flue gas.

The steamside oxidation in TP347H follows the parabolic law. The morphology of the inner oxide is temperature dependent. Faster Cr diffusion at higher temperatures leads to formation of Cr rich oxide at the interfaces between the metal – inner oxide and inner – outer oxide.

The steamside oxidation in TP347HFG does not follow the parabolic law. Most probably due to a combination of several factors, such as applied pressure, composition, grain size, the amount of cold work. The present work did not confirm the influence of the applied pressure or grain size on the oxidation behavior of TP347HFG.

The fireside corrosion rate for all samples investigated was found to be below the acceptable limit of 1 mm / 100,000 hours. Two Cr depleted zones have been observed close to the metal – oxide interface. The first was related to the formation of the inner oxide and the second Cr depleted zone was in the metal and was connected to the formation of sulphides at grain boundaries.

References

1. Y. Minami, H. Kimura and Y. Ihara: *Materials Science and Technology*, Vol. 2, 1986, pp. 795–806.
2. O. H. Larsen, R. B. Frandsen, R. Blum: *VGB PowerTech*, 7, 2004, pp. 89–94.
3. EN 12952-3:2001 (Paragraph 6, Table 6.1-1).
4. T. Sourmail: *Materials Science and Technology*, 17, 2001, pp. 1–14.
5. Ch. Chi, H. Yu and X. Xie: *Advanced Austenitic Heat-Resistant Steels for Ultra-Super-Critical (USC) Fossil Power Plants, Alloy Steel – Properties and Use*, Dr. Eduardo Valencia Morales (Ed.), 2011.
6. <http://matcalc.tuwien.ac.at/>.
7. M. Montgomery, S. A. Jensen, A. N. Hansson, O. Biede, T. Vilhelmsen: 9th Liege Conference : *Materials for Advanced Power Engineering 2010*, pp. 1096–1105.
8. Y. Otugoro et al: *Trans ISIJ* Vol. 28, 1988, pp. 761–768.
9. Personal communication from Takashi to Elkraft.
10. T. Hanada, M. Takahashi, M. Sotooka: 2nd International Conference on Improved Coal-fired Power Plants. EPRI, Nov 1988, pp. 3-3 to 3-61.
11. V. Le Pingle et al: *Proceedings Eurocorr 2000*, Queens Marys College, London.

12. N. Otsuka, H. Fujikawa: *Corrosion* 47, April, 2005, pp. 240–48
13. T. Takahashi et al: *Tetsu to Hagane* 76 (7), 1990, pp. 1131–1138.
14. A. N. Hansson and M. Montgomery: 9th Liege Conference: Materials for Advanced Power Engineering 2010.
15. J. Jianmin, M. Montgomery, O. H. Larsen and S. A. Jensen: *Materials and Corrosion* 56 (7), 2005, pp. 459–467.
16. J. Jianmin, M. Montgomery, O. H. Larsen and S. A. Jensen: *Materials and Corrosion* 56 (8), 2005, pp. 542–548.
17. H. Matsuo, Y. Nishiyama and Y. Yamadera: 4th International Conference on Advances in Materials Technology for Fossil Power Plants, 2004, pp. 441–484.
18. H. Teranishi et al: *The Sumitomo Search* 38: May 1989, pp. 63–74.
19. Y. Sawaragi et al: *The Sumitomo Search* 48: January 1992.
20. A. Iseda et al: *The Sumitomo Search* 40: November 1989, pp. 41–56.

Assessment of remaining lifetime of the boiler tube and microstructure analysis

Zbynek Bunda, Josef Volak & Eva Chvostova

Research and Testing Institute Plzeň
Tylova 1581/46, Pilsen 301 00, Czech Republic

Abstract

Assessment of remaining lifetime represents a very complicated problem, which needs the knowledge of degradation processes in the material of a component, and also the service conditions of the components, e.g. way of loading and the influence of the surrounding environment. There is a common interest to operate the produced components as effectively as possible and thus as long as possible without reducing their safety and reliability, what could cause economic and human losses. This is a problem of safe operation and its prolongation in justifiable cases.

As a result of new modern and more resistant materials development, the general interest is to be able to evaluate the extent and rate of degradation processes at various service conditions, mainly to prevent the components from brittle fracture. The goal even in the stage of a component design is to guarantee their long-time operation. At present, the assessment of component material microstructure is one of the methods that makes it possible to evaluate its remaining lifetime.

It is thus important to be able to evaluate the extent of material mechanical properties degradation as a result of various service factors and the elaboration of methods for its assessment.

Nowadays, the evaluation of component material microstructure represents one of the possible methods for remaining lifetime assessment.

1. Introduction

The article deals with the evaluation of the remaining lifetime on the basis of microstructure evaluation of selected materials in the power producing industry. At first, the microstructure investigation of selected component, where the customer's demand was to assess the remaining lifetime by means of traditional creep tests. On the basis of performed creep tests the remaining lifetime was determined by usual procedure. After finishing the creep tests the microstructure was investigated again. The evaluation of the creep tests and comparison of the microstructure before and after the tests is in detail summarized in this article.

2. Creep tests

The main principle of a creep test is heating of a testing pole to the pre-defined temperature and loading of the testing pole by tension force in a direction of the longitudinal axis of the pole. The following standards are valid for creep tests at higher temperatures: ČSN EN 10 291- 6/2001, DIN 50 118 and ASTM E 139. The tests are performed on special testing devices that are called “stands”.

Evaluation of creep test results – especially stress rupture strength R_{mT} and creep strength R_T – are based on a large number of tests. It can be determined for the following periods of time: 103 h, 5 x 103 h or 105 h (it means that the time duration of a test is more than 10 years). While verifying properties of a new kind of steel up to 30 testing poles need to be evaluated. Total time duration of those tests is approximately (1-3) x 105 h, however, time duration of some testing poles must be more than 104 h.

2.1 Time extrapolation of creep test results

Time extrapolation of results is performed during creep tests. One of the most frequently used methods of interpolation is a method that makes use of Larson-Miller parameter. This extrapolation is based on Arrhenian relation, therefore it is possible to mutually substitute influence of temperature and time during the process. The following relation is valid for the Larson-Miller parameter P:

$$P = T_1 \cdot (C + \log t_1) = T_2 \cdot (C + \log t_2) \quad (1)$$

It means that effect of temperature T_1 during test time t_1 is equivalent to the effect of temperature T_2 during test time t_2 . Process at a temperature T_1 and a very long time t_1 can be substituted by a process much shorter but at a higher temperature [1]. Another possibility is a combination of increase or decrease of stress at the same temperature. The following table and graph summarize results of creep tests that were performed on the material SA 213 – T22 [2].

Table 1. Results of creep tests – steel SA 213 – T22.

Locality	Temperature T [°C]	Stress [MPa]	Time to rupture [h]	Parameter Larson – Miller [P _{LM}]
Superheater 1	580	75	1965	19873
		80	890	19579
		100	185	18997
		120	50	18512
		140	7	17784
Superheater 2	580	75	1841	19849
		80	681	19480
		100	148	18915
		120	51	18520
		140	9	17877
Superheater 3	580	75	1507	19774
		80	792	19536
		100	206.5	19038
		120	50	18512
		140	15	18066

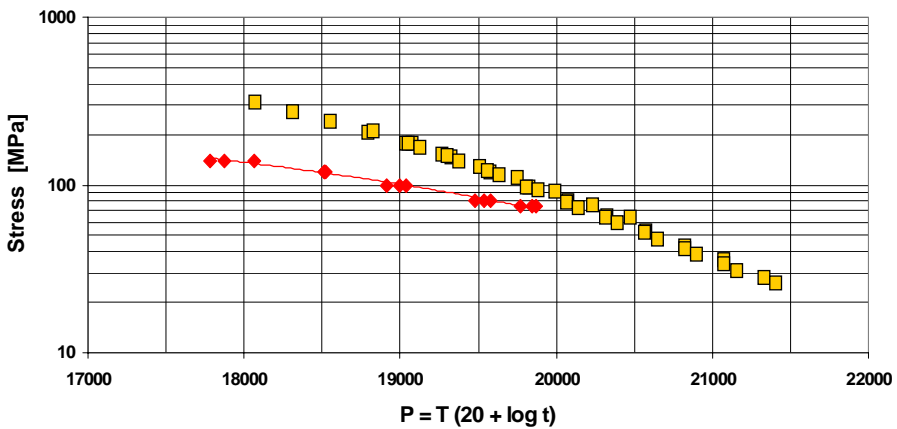


Figure 1. Results of creep tests, steel SA 213 – T22.

Superheater:

$$P_{LM} = 19990 \quad (2)$$

$$P_{LM} = T \cdot (20 + \log \tau_{rboiler}) \quad (3)$$

Residual lifetime of the boiler steam piping for temperature 539°C is:

$$\tau_{rboiler} = 10^{\left(\frac{P}{T} - 20\right)} = 10^{\left(\frac{19990}{539 + 273,15} - 20\right)} \cong 41085 [h] \quad (4)$$

3. Microstructure analysis

There are several methods to examine the quality and condition of materials and joints at the stage of new pressure equipment manufacturing as well as during the operational lifetime of any industrial pressure equipment [3].

Reliability of power plant components depends also on preventing material defects which is closely linked to the estimation of the residual lifetime of power equipment. Verification of microstructural status can significantly contribute to this purpose. This verification can be done in two ways – using nondestructive investigation of microstructure or traditionally by sampling. The aim is to find out real status of power plant parts and essentially contribute to the estimation of residual lifetime in power plant parts.

The goal was to evaluate the microstructure of the inspected power plant components and to classify the material status according to the microstructure degradation standard scales, which were set up using real micrographs.

The samples before and after the creep tests were chosen for the evaluation. The samples were etched in the etching agent Nital. Microstructure analysis was carried out by an optical microscope Nikon Epiphot 300. Pictures of the fracture areas were taken by an electron microscope but because of the heavy oxidation of the crack surfaces it was impossible to get any qualitative characteristics.

The analysis was primarily focused on type, shape and size of structure formations, volume and distribution of the phases present and character of imperfections. The purpose of the metallographic analysis and evaluation was to determine grade of the material degradation.

Instead of cutting off a part of power plants components, it is also possible to use nondestructive Replica – technique [4, 5, 6] which is used especially directly in power plants.

The microstructures of the investigated samples were evaluated according to two scales. The first one was the scale of the microstructure changes due to the long-term effect of high temperature which contains five (1–5) grades of damage and the second one was the scale for evaluation of the material degradation due to the cavitation damage which includes six (I–VI) grades [7].

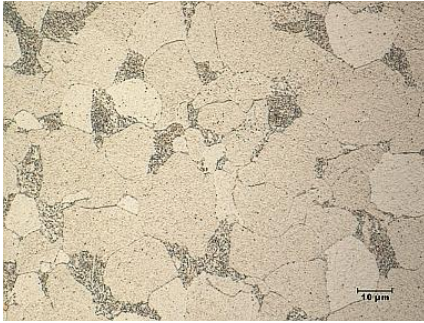


Figure 2. Microstructure before creep tests, mag. 1000x.



Figure 3. Structure lines, mag. 50x.



Figure 4. Ferrite – pearlite structure, inner surface, mag. 200x.



Figure 5. Outer affected surface, mag. 200x.

The microstructure of the samples before the creep testing consisted of ferrite–pearlite with uniformly distributed carbides which were spheroidized (Figure 2). The structural elements were aligned in bands as a result of cold working (Figure 3, Figure 4) and there were also noticeable thin decarburised layers (cca 30 μm) in areas which were close to the inner and outer surfaces of the pipes (Figure 5). Classification of the microstructure before the creep testing is 3/IV according to the scales POS-AZL/15-52/013.

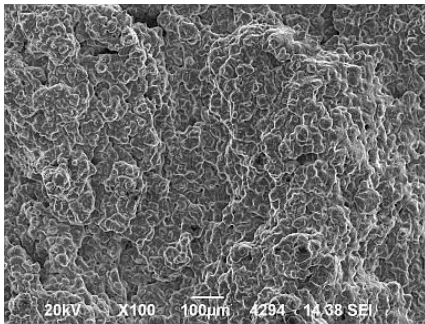


Figure 6. Fracture area, electron microscope, mag. 100x.



Figure 7. Cavities, mag. 1000x.



Figure 8. Cavities close to the fracture, mag 50x.

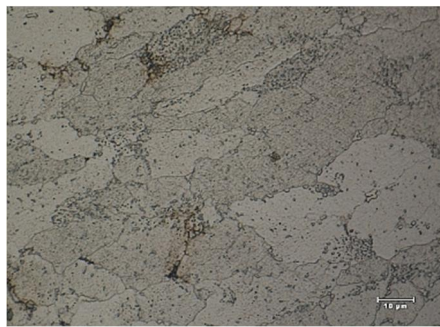


Figure 9. Cavities and grains, mag. 1000x.

The creep tests were carried out at the temperature of 580°C and the strains from 75 MPa to 140 MPa. It is possible to observe a large number of cavities especially close to the intergranular fracture; these cavities coagulate and form macrocavities. The carbide particles are much coarser and are precipitated on the grain boundaries. Classification of the microstructure before the creep testing is 5/VI according to the scales POS-AZL/15-52/013.

4. Conclusions

From the comparison of the results obtained by the traditional creep tests and by the microstructure examination of the steel SA 213 – T22 it implies that it is also possible to evaluate the residual lifetime of the power plant components on the basis of the microstructure investigation. However, it is necessary to set up a database of correlations between micrographs of the materials concerned and the

results obtained by the creep tests of these materials. These results can be also correlated with the hardness measurements.

The results of the creep tests of the material tested presented in this paper indicate that the residual lifetime is approximately 5 years which is in an agreement with the microstructure status classified according to two microstructure degradation standard scales. This problem deserves a comprehensive approach because of a major economic benefits can be expected due to the possibility of non-destructive replica testing.

References

1. SKÁLOVÁ, J., KOVÁŘÍK, R. & BENEDIKT, V. Základní zkoušky kovových materiálů, ZČU Plzeň, 2000.
2. CHVOSTOVÁ, E. Zkoušky tečení z materiálu trubek šotového přehříváku páry PPII. Research report No. VYZ 1226/09. Škoda Research GmbH, Pilsen 2009.
3. ORFANOUDAKIS, N. G. & KRALLIS, K. Selection of the optimum NDT methods for determination of steam boiler remaining life. The 8th International Conference of the Slovenian Society for Non-Destructive Testing, Portorož, Slovenia, 2005, pp. 59–67.
4. ASTM E 1351 Standard Practice for Production and Evaluation of Field Metallographic Replicas, 2001.
5. DIN 54150 Non-destructive testing, impression methods for surface examination (Replica – technique, 1977).
6. ISO 3057 Non-destructive testing – Metallographic replica techniques of surface examination, 1998.

Long term and pilot study of HAZ creep behaviour of weld repaired low alloyed heat resistant steels

Rui Wu¹ & Jan Storesund²

¹Swerea KIMAB
Box 7074, SE-164 07 Kista, Sweden

²Inspecta Technology
Box 30100, SE-104 25, Stockholm, Sweden

Abstract

In a Värmeforsk project, a plate and waisted HAZ specimen has been developed to examine the creep properties of heat affected zone (HAZ). Comparing to the bar cross weld (CW) specimens taken from weld repairs, the plate and waisted HAZ specimen gives longer rupture time and higher creep ductility. This agrees with the results that all the bar CW specimens fail in the ex-serviced parent metal, meaning that the parent metal is weaker. The creep testing results show also that matched weld repair prolongs creep lifetime for components made of low alloyed steels such as 10 CrMo 9 10, which is frequently used in the power generation industry. Thus, matched weld repair is strongly recommended.

1. Introduction

In order to ensure safe operation, to extend economic life of existing power plants, and to reduce cost for service maintenance, experiments and simulations of creep behaviour on weld repaired low alloy heat resistant CrMo and Mo steels were previously carried out [1], [2] and [3]. Some results and recommendations can be briefly recalled:

- 1) The current weld repair procedure is able to prolong lifetime of ex-serviced components, because rupture occurred always in the ex-serviced parent metal of cross weld (CW) specimens far from the weld joints at short term tests.
- 2) The simulations at a stress much lower than tested stresses indicate, however, most creep damage development and rupture in the heat affected zone (HAZ).
- 3) A full matched weld repair, where creep properties in both parent and weld metals are similar, is recommended.

Although long term creep tests more than 30,000 hours are available for the weld metals, such tests are unfortunately absent for the cross welds (CWs), where the heat affected zone (HAZ) is included. The HAZ has been considered as a key part of a weld.

In addition to the need of long term creep data on the cross weld repairs, creep behavior of the HAZ itself is essential for the weld repairs because failure takes place frequently in the HAZ. This has been demonstrated by laboratory creep tests, service experiences, and computer simulations. Laboratory based uniaxial cross weld testing has been widely used to study high temperature creep performance and to assess remaining lifetime of repair welds [4], [5] and [6]. However, there are no available data just for the HAZ, simply because there are no standard specimen, established method and measuring technique suitable for HAZ creep testing. The lack of HAZ creep data may make the related simulations less accurate and correct and, in many cases, uncertain assumptions have to be adopted.

The purposes of this project are to

- 1) initiate a pilot trial to develop a creep specimen, a test method and a measuring technique being capable of generating creep data just for a real HAZ.
- 2) conduct long term creep tests for CW repairs.
- 3) investigate creep damage initiation and evolution in terms of various micro-structures across the cross weld repairs during long term creep exposure.
- 4) implement obtained creep data for reliable and accurate simulation to fully understand the creep behavior of the weld repairs as a whole.

2. Materials and experiment

2.1 Materials

An ex-serviced pipe made of 10 CrMo 9 10 was used. The accumulated service time was 212.000 hours with an internal pressure of 138 bar at 540°C. More information about material and chemical composition, can be found in [1] and [2].

2.2 Weld repair

The ex-serviced pipe of 10 CrMo 9 10 was divided into four 400 mm long samples. Three of the samples were prepared for matched weld repairs using three different fillers, namely 10 CrMo 9 10, 13 CrMo 4 4, and 15 Mo 3. The fourth sample contained an old butt weld 10 CrMo 9 10 to itself.

Some weld repairing parameters and post weld heat treatment (PWHT) are briefly summarised as below:

Preheat temperature: 200–250°C.

Interpass temperature:	Approximately 250°C, occasionally as high as 300°C.
First two layers:	Buttering using a Ø3,25 mm electrode with 50% overlap.
Filling:	Ø4 mm electrode, 350 mm long.
Weld line energy Q:	1,6 kJ/mm in mean
Weaving:	± 2 mm
PWHT:	650°C/1 hour for weld made with 15 Mo 3 filler. Heating and cooling rate 100°C/hour.
PWHT:	670–680°C/2 hours for welds made with 10 CrMo 9 10 and 13 CrMo 4 4 type filler metal, Heating and cooling rate 100°C/hour.

The PWHT procedure is commonly used in production and installation.

2.3 Pre-test metallography

Cross sections of the weld repairs are shown in Figure 1(a). Weld metals consist of bainite and ferrite. In the HAZ, coarse grains are seldom seen as a result of refinement by subsequent welding operation. The ex-serviced 10 CrMo 9 10 consists also of bainite and ferrite. Carbides have coarsened and precipitated in the ferrite.

The highest hardness values appear in the vicinity of the fusion boundary, independent of weld metals, see Figure 1(b). For different weld metals, 13 CrMo 4 4 shows the lowest hardness 3–4 mm below the outer surface. In the middle of the weld metals, 10 CrMo 9 10 shows the highest hardness values in comparison to 13 CrMo 4 4 and 15 Mo 3, in which the hardness are nearly the same.

2.4 Extraction of cross weld (CW) creep specimens

Three series of plain bar cross weld (CW) creep specimens were extracted from the weld repaired joints, namely, 10CW (ex-serviced 10 CrMo 9 10 parent metal and virgin 10 CrMo 9 10 weld metal), 13CW (ex-serviced 10 CrMo 9 10 parent metal and virgin 13 CrMo 4 4 weld metal), and 15CW joint (ex-serviced 10 CrMo 9 10 parent metal and virgin 15 Mo 3 weld metal). In addition, one series plain bar CW specimens, 10EXCW, were taken from ex-serviced 10 CrMo 9 10 thick walled pipe for comparison. The dimension of the plain bar creep specimens is Ø5 mm and 50 mm in gauge length.

The cross weld specimens were taken near the outer surface of pipe. Each cross weld specimen contains weld metal (WM), HAZ, as well as ex-serviced 10 CrMo 9 10 parent metal (PM).

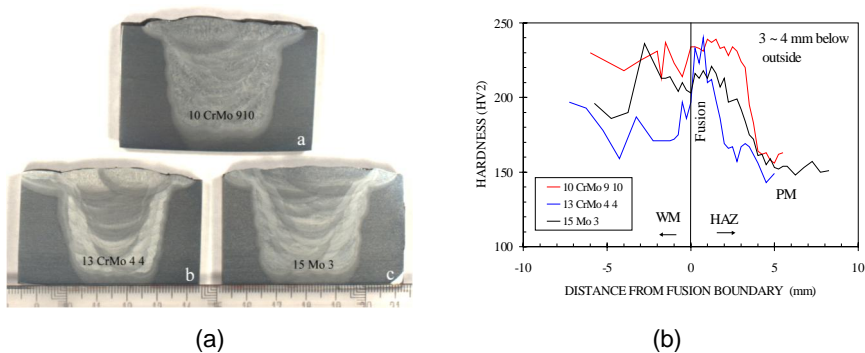


Figure 1. (a) Cross section of weld repaired joints having ex-serviced parent metal of 10 CrMo 9 10, but different weld metals. (b) Hardness measurements.

2.5 Extraction of plate and waisted HAZ creep specimens

One series of plate and waisted HAZ creep specimens has been extracted from the service-exposed 10 CrMo 9 10 weld joint for study of HAZ creep behaviour, see Figure 2. The plates for manufacturing HAZ specimens have been firstly cut off, ground, polished and finally etched to expose the HAZ and the fusion boundary. Generally, the width of the HAZ was found to be about 2~3 mm.

Great care must be paid to include only the HAZ in the gauge length. To do this, the following procedures were applied:

- 1) Fusion boundary is vertically placed to the stress orientation.
- 2) The gauge length of the plate and waisted HAZ creep specimen should be the same as the width of the HAZ. To do this, a 2.5 mm plate mill having 0.2 mm radius is used to machine the gauge length. Afterwards, the radius is re-machined to 0.5 mm to minimise the stress concentration, see Figure 3(a). The dimension of the plate and waisted specimen is given in Figure 3(b). It is seen *i*) the gauge length is fortunately located within the HAZ, *ii*) the gauge length is approximately the same as the width of the HAZ, and *iii*) the gauge length starts at fusion boundary and ends at intercritical HAZ.
- 3) All the specimens are Ni-coated prior to creep testing to minimise the material loss by oxidation. The thickness of Ni-coating is about 40 μm .
- 4) Hardness measurement (HV2, 2kg load) across the HAZ has been carried out, see Figure 4. The distance between the two nearest indentations is 0.5 mm. Series number and corresponding hardness value are also shown in Figure 4. The weld metal has higher hardness than the parent metal. Hence, the weld metal is on the right hand side. The fusion boundary should be located between nr 1 and 7, and between nr 28 and 29.

- 5) Hopefully, the hardness indentations will exist after creep test. By measuring the distance between indentations, the local deformation can be obtained. The local deformation is highly desired to understand and estimate weldment integrity. The value of the local deformation is an important input for numerical simulations as well.

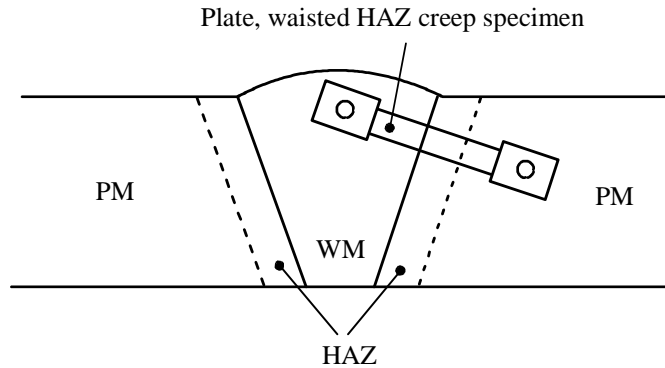


Figure 2. Schematic illustration of position for extraction of plate and waisted HAZ creep specimen.

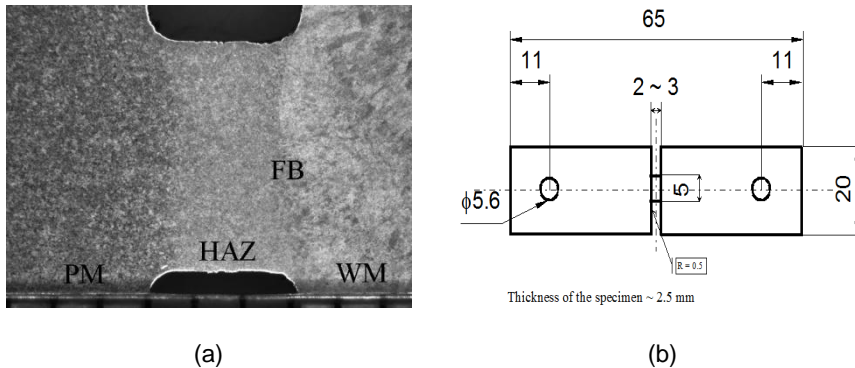


Figure 3. (a) An example of plate and waisted HAZ creep specimens. (b) Dimension of plate and waisted HAZ creep specimens. Thickness of the specimen is about 2.5 mm.

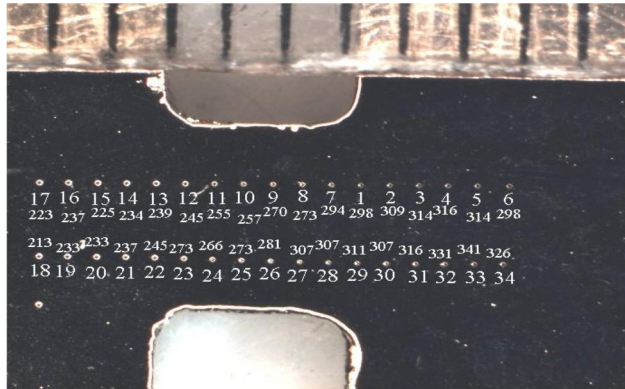


Figure 4. Plate and waisted HAZ creep specimen after Ni-coating. Micro-hardness (HV2, 2kg load) measurements are made across the HAZ.

2.6 Creep test

The stress for HAZ creep tests is determined by measuring the cross-section of the waisted part, for instance, $5 \times 2.5 \text{ mm}^2$, see Figure 3(b).

By using single specimen, constant load creep testing machines the plain bar and the plate and waisted HAZ creep specimens were iso-thermally tested at 540°C in air. All the tests were allowed to progress to final rupture. Creep strain and temperature were periodically recorded by a logger. The maximum temperature variations with time were controlled within $540 \pm 2^\circ\text{C}$.

2.7 Post-test metallography

Selected creep specimens were metallographically examined after failure using LOM. The selected specimens were sectioned at mid-thickness which is perpendicular to the fracture, ground and polished to $0.1 \mu\text{m}$ before etching in 4% nital.

3. Results

3.1 Creep testing results of plain bar cross weld (CW) specimens

Creep curves, where creep strain ϵ is plotted against time t , are shown in Figure 5. Creep rupture time t_R as a function of stress σ is given in Figure 6, in which the results from [2] are included. The creep rupture times for the series 10CW and 15CW are clearly longer than those for the series 10EXCW and 13CW at given stresses. The longest time is found in the series 15CW. The series 10EXCW and 13CW have nearly the same lifetime. Linear relation between creep rupture time t_R and stress σ in the double logarithmic scales can be described in Eq. (1) as

$$t_R = C \cdot \sigma^{-v} \quad (1)$$

where c and stress index v are empirically determined constants. The v -values for all the series are about 8–9.

Minimum creep strain ϵ_{\min} is plotted as a function of stress σ in for all series, see Figure 7. The results from [2] are also included. It is seen that ϵ_{\min} for the series 13CW and for the both series 10CW and 15CW takes the highest and the lowest value at lower stresses, respectively. The ϵ_{\min} for the series 13CW is even higher than that for the series EXCW10. The relation between the minimum creep strain rate $\dot{\epsilon}_{\min}$ and stress σ follows the Norton's law, see Eq. (2)

$$\dot{\epsilon}_{\min} = B \cdot \sigma^n \quad (2)$$

where B is the constant and n the stress exponent. n is 6.9 for the series 13CW. The n -values for the other series are about 9 to 9.5.

Elongation at rupture as a function of rupture time is exhibited in Figure 8, in which the results from [2] are included. It seems that there is a trend that the elongation at rupture decreases at longer rupture times for all the series. This must be, however, verified as all the tests are complete.

3.2 Creep testing results of plate and waisted HAZ specimens

Creep curves based on the total displacement measurement are exhibited in Figure 9, in which creep curve for a bar CW specimen taken from the same pipe is included for comparison. The rupture time as a function stress, the Norton's law and the elongation at rupture as a function of the rupture time are shown in Figure 6, Figure 7 and Figure 8, respectively, in comparison to the corresponding results for the CW specimens. It is clear that the HAZ specimens display both longer rupture time and larger creep strain at rupture, by approximately a factor of three, in comparison to the CW ones. The minimum creep strain rates for the HAZ specimens are, however, analogue to those for the CW ones. It seems that the elongation at rupture for the HAZ specimens decreases with increasing rupture time, see Figure 8.

To be able to observe, record and measure local deformation just within the HAZ, a purpose-built microscope SDA-1 has been installed. Many images have been regularly taken during the tests. Some images are shown in Figure 10 for the test at 140 MPa. Due to gradually increased and strong deformation, the hardness indentations are starting to disappear close to rupture.

Local deformation (strain) has been measured and compared with overall strain for the test at 140 MPa, see Figure 11. Assuming that the points 1 to 2 as well as 11 to 12 represent the coarse grained HAZ (CGHAZ) and the points 5 to 7 as well as 16 to 17 represent the intercritical HAZ (ICHAZ), see Figure 10(a), the local deformation (strain) relating to microstructures can be measured. The local strain, together with the overall strain measured by extensometer, is displayed in Figure 11. Noting that strain between points 2 and 5 (or between points 12 and 15) is

excluded in Figure 11. It is seen that the strain in the ICHAZ is much larger, *i.e.* by a factor of 4–6, than that in the CGHAZ, especially at later stage of the creep test. This is in agreement with the hardness in the CGHAZ and in the ICHAZ.

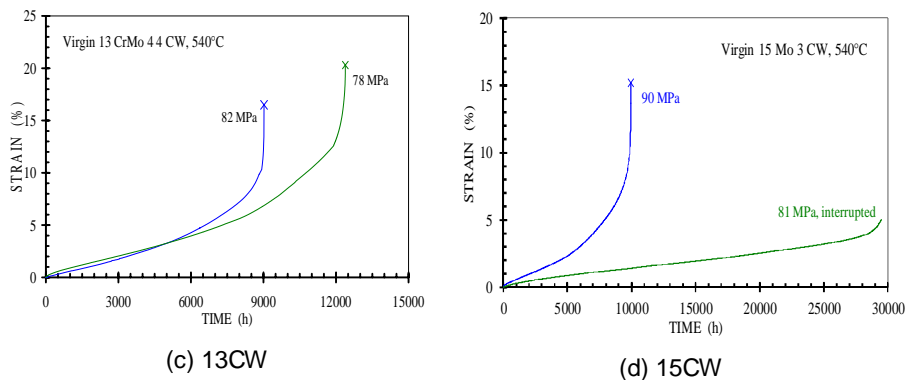


Figure 5. Creep curves for plain bar CW tests.

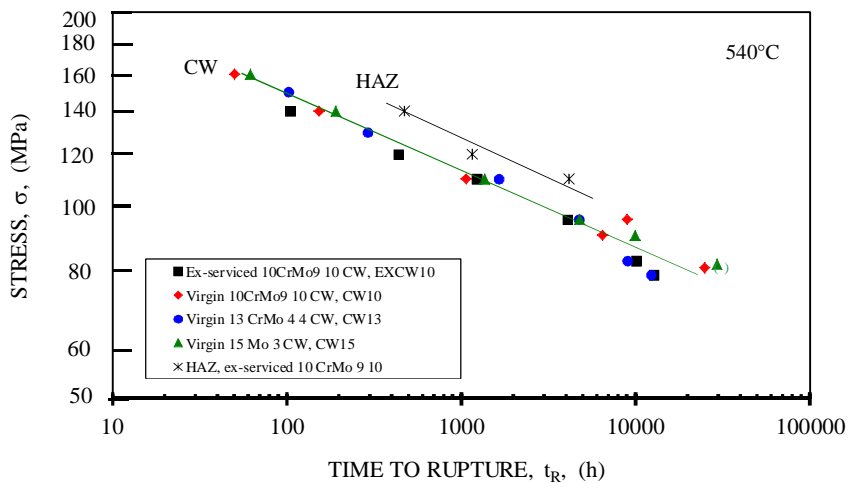


Figure 6. Creep rupture time versus stress for both CW and HAZ tests. Bracket indicates interrupted test. Results from [2] are included for comparison

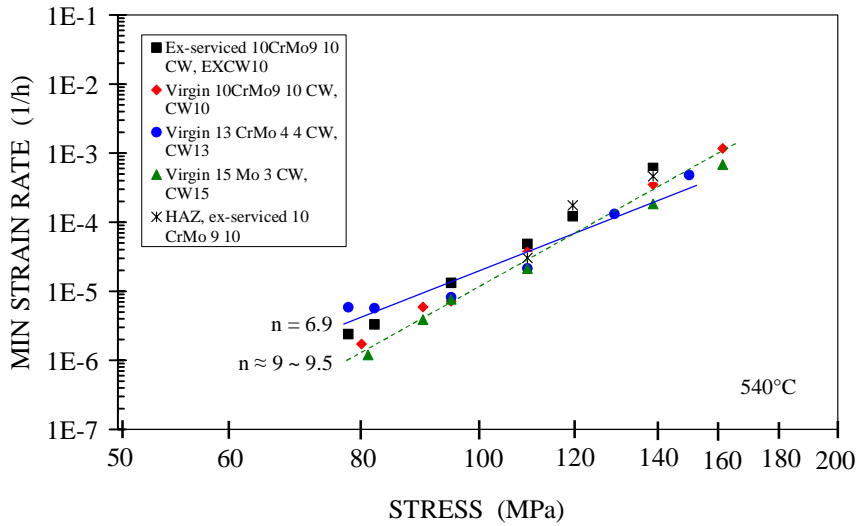


Figure 7. Minimum creep strain rate versus stress, Norton's law, for both CW and HAZ tests. Results from [2] are included.

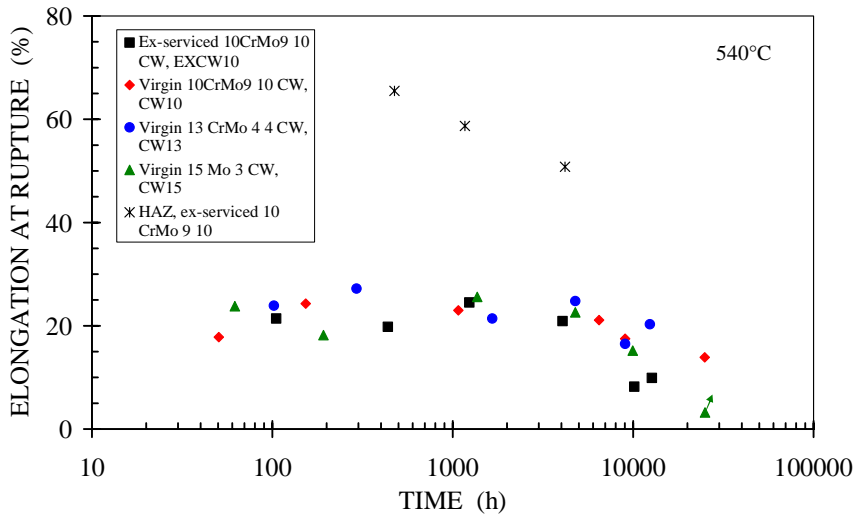


Figure 8. Elongation at rupture versus rupture time for both CW and HAZ tests. Results from [2] are included.

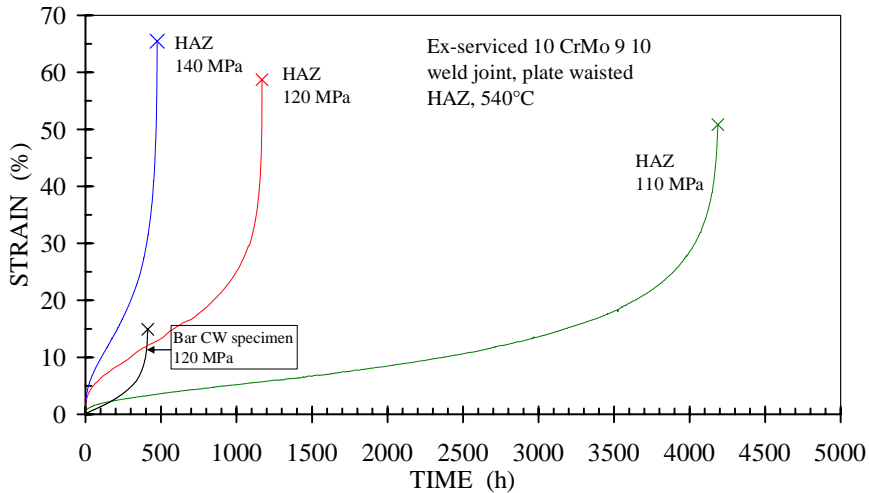
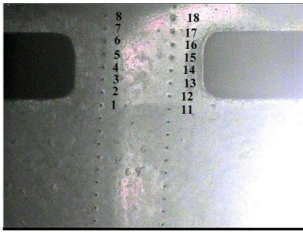


Figure 9. Creep curves based on the total displacement measurement for HAZ specimens. The creep curve for a bar CW specimen is included for comparison.

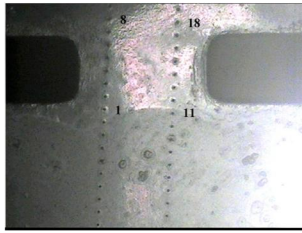
3.3 Post test metallography

Failure takes place in the parent metal for the bar CW specimens, independent of time and weld repairs. Separate cavities are often observed close to fracture. The weld metal and the HAZ are in most cases damage free, except that separate cavities to a large extent are observed in the ICHAZ for series 10CW and 15CW, see Figure 12. This indicates that the ICHAZ may be a weak link. Extensive strings of cavities are visible in the CGHAZ and in the WM close to fusion boundary in the specimen from series 13CW at 78 MPa, see Figure 13. It is clear that part of the fusion boundary is parallel to gauge length (also parallel to stress direction). It is very likely that extraction of the specimen is too close to the outer surface, where the fusion boundary is partially parallel to the outer surface, *c.f.* Figure 1.

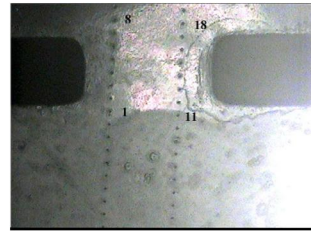
All the plate and waisted HAZ specimens fail in the ICHAZ and large extent cavities are observed adjacent to the fracture, see Figure 14. The CGHAZ is damage free. Due to heavy deformation, the Ni-coating cracks.



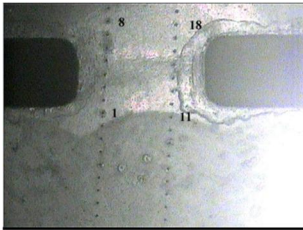
(a) Full load. Start of test.



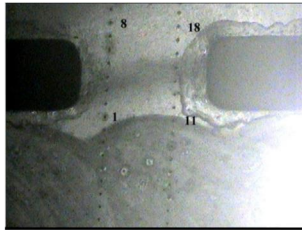
(b) At 49 hours and 7.055% elongation.



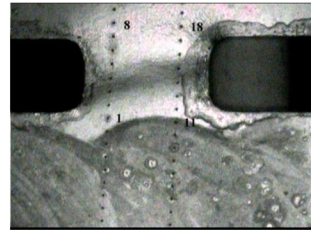
(c) At 97 hours and 9.628% elongation.



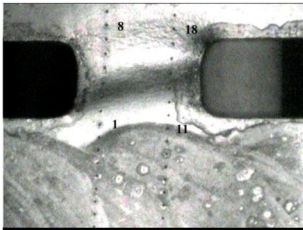
(d) At 143 hours and 11.75% elongation.



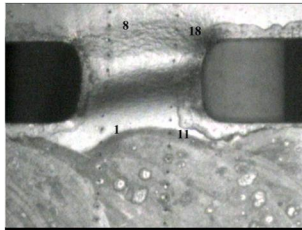
(e) At 247 hours and 16.88% elongation.



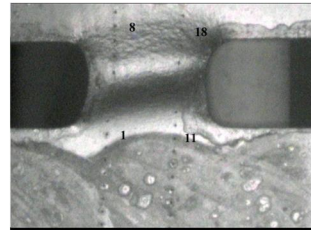
(f) At 310 hours and 20.68% elongation.



(g) At 389 hours and 27.75% elongation.



(h) At 433 hours and 35.17% elongation.



(i) At 457 hours and 43.11% elongation.

Figure 10. Images taken on the specimen HAZ-D at 540°C/140 MPa.

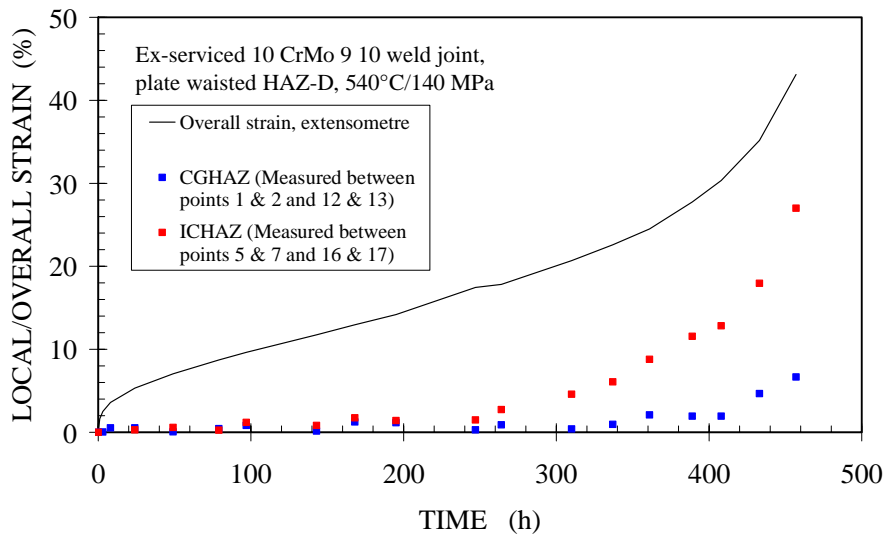


Figure 11. Local strain in given microstructures and overall strain for the HAZ test at 540°C/140 MPa.

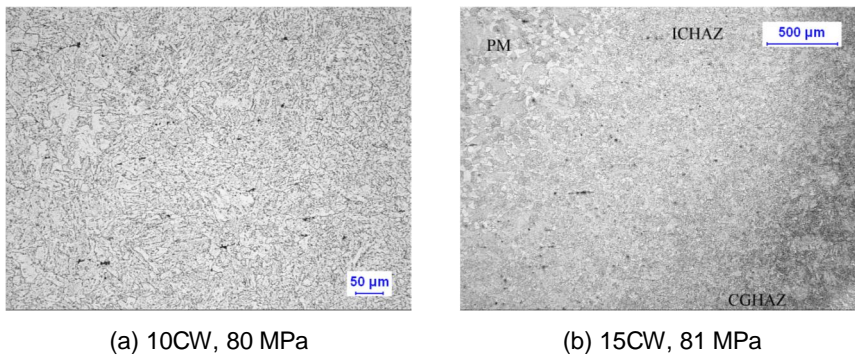


Figure 12. Light optical microscope images showing separate cavities in ICHAZ.

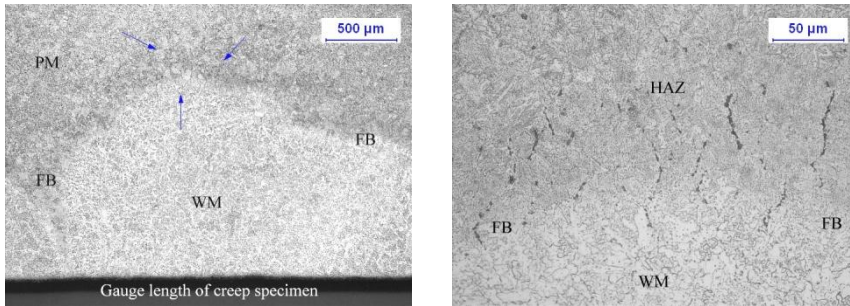


Figure 13. Light optical microscope images showing strings of cavities in CGHAZ and in WM for the specimen from CW13 at 78 MPa.

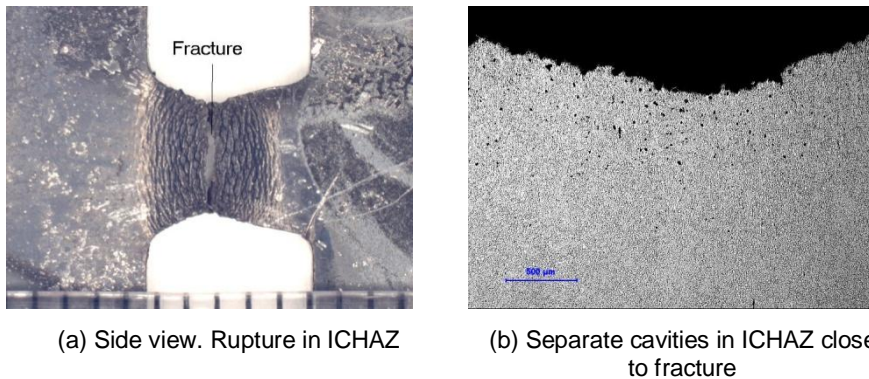


Figure 14. Light optical microscope images from ruptured specimen HAZ at 120 MPa.

4. Discussion

The present results show that the longest creep life is obtained in a 15 Mo 3 weld repair where the weld and parent metal creep properties are quite equal, see Figure 6. Weld metals with much higher creep strengths than the parent metal cause damage development concentrated to local areas in the weld metal and relatively short creep lives [1, 2]. With the present repair geometry the damage development also occurred deep inside the wall [1].

A slight overmatch may, however, still keep the damage at the surface area [7]. Therefore, surface testing with respect to re-occurrence of creep damage after an operation period may be a general problem for many repair welds since filler materials with significantly higher creep strengths than the substrate often are used. Earlier stages of creep damage such as creep cavitations can hardly be detected under such circumstances. Consequently, damage can be detected (e.g. by ultra-

sonic testing) only at relatively late stages of the creep life and there will be a shorter period for planning any re-repair or replacement.

Weld repair with under matched filler metals with respect to chemical composition may imply a lower maximum service temperature (or maximum pressure, or both) than for the parent metal. This can be a difficulty when also the service temperature is higher than the maximum allowed for the repair filler. Such cases can possibly be permitted if it can be shown that the creep strength of the repair is sufficient for the purpose of the repair.

To determine if a matching or an under-matching filler metal would be preferable to prolong creep lifetime of ex-serviced parent metal, a relatively quick and simple action, from inspection and maintenance point of view, may be hardness measurement and calculation of the Larson-Miller parameter of the parent metal. This may indicate the preferable type of filler metal (for instance, under matching filler metal is preferable at relatively high Larson Miller parameter and low hardness).

Alternatively, impression creep testing [8], [9], [10] can also be applied. The impression creep testing is a localised creep testing technique using a cylindrical indenter with a flat end and giving a steady state penetration velocity at constant load. Impression creep tests may take up to several hundreds of hours and give more accurate assessment.

The plate and waisted HAZ specimen shows better creep properties in comparison to the bar CW specimen. However, influence of type of specimen, constraint and multiaxiality should be taken into account and simulated.

5. Conclusions

An ex-serviced 10 CrMo 9 10 pipe is used for weld repairs with three different fillers; namely 10 CrMo 9 10, 13 CrMo 4 4 and 15 Mo 3. Three series of plain bar cross weld (CW) creep specimens are extracted from the weld repaired joints. They are 10CW, 13CW and 15CW. One series plain bar CW specimens, namely 10EXCW, is also taken from the ex-serviced 10 CrMo 9 10 thick walled pipe for comparison. In addition, one series of plate and waisted heat affected zone (HAZ) creep specimens is extracted from the ex-serviced 10 CrMo 9 10 pipe to definitively study the creep properties just in the HAZ. The creep specimens are isothermally tested at 540°C in air. The following conclusions can be drawn:

- 1) The fact that all bar CW specimens fail in the ex-serviced parent metal indicates a successful weld repair.
- 2) Comparing to the bar CW specimen, the plate and waisted HAZ specimen gives longer rupture time by a factor of four and higher creep ductility. This agrees with the results obtained in 1), meaning that the parent metal is weaker.
- 3) For the HAZ specimen, rupture takes place in the ICHAZ. Other microstructures over the HAZ are damage free.

- 4) For the bar CW series, the longest and the shortest creep life is found for series 15CW and for the series 13CW, respectively. The latter has nearly similar creep life to that for the series 10EXCW.
- 5) Although extensive creep cavitations are in many cases only found close to fracture for the bar CW specimens, extensive creep cavitations are observed in intercritical HAZ and in coarse grained HAZ. This may indicate that failure may also occur in the HAZ.
- 6) The developed plate and waisted HAZ specimen is applicable to study the creep behaviour of the HAZ, provided that a routine to extract and to produce HAZ specimen is followed. This routine includes clear exposure and correct identification of HAZ, exact placement of notch (waist), careful specimen machining, and coating. To be able to measure local deformation, hardness indentation is recommended.
- 7) By imaging and measuring the distance between the indentations, the local strain in relation to microstructure can be quantitatively assessed. Larger local deformation is found in the ICHAZ, *i.e.* by a factor of 4–6, than that in the CGHAZ at later stage of the creep test.

Acknowledgement

The financial support from Värmeforsk is gratefully acknowledged. The members of reference committee, Søren Aakjær Jensen, DONG Energy Power, Erik Zakrisson, Siemens Industrial Turbomachinery and Stig-Björn Westberg, Vattenfall, are thanked for their interests, comments and careful reading of manuscript. Facredin Seitisleam, Swerea KIMAB, is thanked for performing creep tests.

References

1. Wu, R., Storesund, J., Borggreen, K. & Zang, W-L. Creep properties and simulation of weld repaired low alloy heat resistant CrMo and Mo steels at 540°C – ex-serviced parent metal and virgin weld metals. Värmeforsk Report 980, 2006.
2. Wu, R., Storesund, J., Borggreen, K. & von Feilitzen, C. Creep properties and simulation of weld repaired low alloy heat resistant CrMo and Mo steels at 540°C – ex-serviced 2.25Cr1Mo weld metal and cross weld repairs. Värmeforsk Report 1027, 2007.
3. Wu, R., Storesund, J. & Borggreen, K. Creep properties of weld repaired low alloy heat resistant CrMo and Mo steels at 540°C', OMMI, April 2009, Vol. 6, Issue 1, www.ommi.co.uk .

4. Hyde, T. H. & Tang, A. Creep analysis and life assessment using cross-weld specimens, *J of International Materials reviews*, 1998, Vol. 43, No 6, pp. 221–242.
5. Law, M., Croker, A. & Payten, W. Cross weld creep testing in the assessment of repair welds, *OMMI*, August 2003, Vol. 2, Issue 2.
6. Hyde, T. H., Williams, J. A., Becker, A. A. & Sun, W. A review of the finite element analysis of repaired welds under creep conditions, *OMMI*, August 2003, Vol. 2, Issue 2.
7. Hyde, T. H., Sun, W. & Becker, A. A. Creep crack growth in welds; a damage mechanics approach to prediction initiation and growth of circumferential cracks, *Second Int. "HIDA" Conf. Advances in defect assessment in high temperature plant*, MPA Stuttgart, Germany, 4–6 October 2000.
8. Li, J. C. M. Impression creep and other localised tests, *Mat. Sci. & Eng.*, 2002, A322, pp. 23–42.
9. Hyde, T. H. & Sun, W. A novel, high-sensitivity, small specimen creep test. *J. Strain Analysis*, 2009, Vol. 44, pp. 171–185.
10. Sun, W., Hyde, T. H. & Brett, S. J. Application of impression creep data in life assessment of power plant materials at high temperatures, *J. Materials Design and Applications*, 2008, Vol. 222, No. 3, pp. 175–182.

Corrosion resistance of Kanthal A-1 and Fe-12Cr-2Si alloy coatings in Cl-containing environment

Teemu Sarikka¹, Risto Ilola¹, Rami Pohja² & Hannu Hänninen¹

¹Aalto University School of Engineering, Department of Engineering Design and Production

Puumiehenkuja 3, 02150 Espoo, Finland

²VTT Technical Research Centre of Finland

Kemistintie 3, 02150 Espoo, Finland

Abstract

Boiler and tubing materials used in biomass-fired energy production are susceptible to corrosion in severe corrosive environments caused by inorganic constituent such as chlorine at the operating temperatures. In conventional stainless steels, which rely on the formation of a chromia scale for protection against corrosion, the Cl present in the environment reacts with the Cr in the alloy to form volatile CrCl_2 and CrCl_3 compounds and, thus, reduces the formation of an external, stable chromia scale. The volatile CrCl_2 and CrCl_3 compounds formed on the surface of the alloy are not able to provide protection against further corrosion and due to the formation of these compounds the conventional stainless steels may lose their resistance to the Cl-containing environment. Alumina and silica forming alloys have been considered as possible solutions against corrosion in these types of applications.

In this study, overlay weld coatings with FeCrAl and FeCrSi type consumables were manufactured on 10CrMo9-10 steel by gas-tungsten arc welding method. Kanthal A-1 with a nominal composition of 5.8 wt. % Al was chosen as an alumina-forming alloy and a silica-forming alloy was Fe-12Cr-2Si alloy with a nominal composition of 2.0 wt. % Si. Performance of the overlay coatings was tested in 168 h potassium chloride (KCl) exposure tests at 600°C in as-welded condition and after 24 h pre-oxidation at 950°C. Composition distributions of the coatings and the formed oxide layers in the KCl exposure were characterized with FEGSEM and EDS.

1. Introduction

Conventional heat-resistant stainless steels used in the critical components of biomass-fired power plants rely on chromia (chromium oxide, Cr_2O_3) scales for protection against high-temperature oxidation and corrosion attack. Typical biomass-fired power plant environment contains significant amounts of inorganic constituent such as Cl and the operating temperatures are usually quite high.

Many metals react easily with halogen gases, such as Cl, at elevated temperatures to form volatile metal halides. Many of these metal halides exhibit low melting points, and some even sublime at relatively low temperatures. As a result, the metal-halogen reactions can proceed at a rapid rate at elevated temperatures and therefore alloys containing elements that form volatile or low melting-point halides may suffer severe high-temperature corrosion¹. Therefore, the Cl present in the operation environment of a biomass-fired power plant reacts with Cr in the stainless steel to form volatile CrCl_2 and CrCl_3 compounds, thus, eliminating the formation of an external, stable Cr_2O_3 scale. The volatile CrCl_2 and CrCl_3 formed on the surface of the alloy are not able to provide protection against further corrosion and due to the formation of these compounds the stainless steel loses its resistance to the environment. Cl containing environment usually contains also oxygen, which causes FeCr-spinel oxide layer to form on the surface of the alloy. The spinel oxide layer allows faster Fe-ion diffusion through the oxide scale to the oxide-atmosphere interface than chromia layer leading to a formation of a top layer of Fe oxides¹. Thus, the chromia scales may no longer provide sufficient protection against high-temperature corrosion attack and new approaches are needed to replace the chromia as the provider of the high-temperature corrosion resistance of the construction materials. Possible replacement solutions to chromia in iron-based high-temperature alloys are alumina (aluminum oxide, Al_2O_3) and silica (silicon oxide, SiO_2).

Aluminum is a very effective alloying element in improving the alloy's resistance to oxidation and other types of high-temperature corrosion attack¹. As an alloying element, the purpose of Al is to form a layer of alumina on the surface of the oxide layer at the gas-scale interface to protect the structural material against high-temperature corrosion attack. The alumina scale protects the material against high-temperature oxidation by acting as a diffusion barrier to metal and oxygen ions trying to penetrate the oxide scale². Growth rate of an alumina scale is 1 to 2 orders of magnitude lower than that of Cr_2O_3 . Alumina is also significantly more thermodynamically stable than chromia. Alumina scales have been proven to be specifically beneficial in the presence of aggressive carbon- or sulphur-species encountered in combustion and chemical process industry applications³. The most critical factors in the formation of the protecting alumina scale on Fe-Cr-Al alloys are the temperature in which the scale forms and the aluminum content which has to be high enough to develop and maintain an alumina scale and prevent the following breakaway oxidation of the alloy².

There are several different types of alumina scales formed on the surface of Fe-Cr-Al alloy and the type of the scale depends on its formation temperature. When the oxide scale formation occurs in temperatures higher than 1000°C , the forming oxide scale will be thermodynamically stable $\alpha\text{-Al}_2\text{O}_3$ scale and it is continuous, has very low defect concentration, and will provide the material with outstanding oxidation resistance⁴. $\alpha\text{-Al}_2\text{O}_3$ is a stable high temperature form of alumina, which has a slow growth rate and a large band gap which makes the electronic conduction difficult². The Al_2O_3 scale formed in temperatures higher than 1000°C consists mainly of $\alpha\text{-Al}_2\text{O}_3$. The $\alpha\text{-Al}_2\text{O}_3$ scale provides effective protection against

high-temperature corrosion because it is chemically inert and grows relatively slowly. The oxidation rate of the material slows down rapidly after a continuous layer of $\alpha\text{-Al}_2\text{O}_3$ has formed⁵. The aluminum oxide scales, which are formed in temperatures $< 1000^\circ\text{C}$, are so called transition aluminas, e.g. $\gamma\text{-}$ and $\theta\text{-Al}_2\text{O}_3$. They have different crystal structures compared to the stable $\alpha\text{-Al}_2\text{O}_3$. When oxidation takes place in temperatures above 1000°C , the transient aluminas can be observed during the initial stages of oxidation². These transient aluminas are metastable and they will convert into the thermodynamically stable $\alpha\text{-Al}_2\text{O}_3$ over time, however, the transformation is temperature dependent and it is relatively slow at temperatures below 1000°C . Transition aluminas are not desired due to their larger defect concentration and higher growth rate⁴.

Silicon additions in iron-based alloys have a beneficial effect on oxidation resistance of the alloy because of the formation of silicon oxide layer at the metal-oxide interface. Furthermore, the formation of protective chromia scales on the surface of the alloy is promoted by this silicon oxide layer due to the fact that the silicon oxide layer acts as a diffusion barrier to Fe and Cr ions penetrating the oxide layer. The outward diffusion of chromium through either the silicon oxide or the chromium oxide layers controls the rate of oxidation⁶. Upon oxidation, Si containing iron-based alloys form a layer of Fe_2SiO_4 below the other oxides in the oxide scale. At Si contents above 2 wt. %, an outer protective layer of Fe_2SiO_4 or SiO_2 grows on the surface of the oxide scale and provides the material with very good protection against high-temperature corrosion attack⁷.

During the transient stages of oxidation of Fe-Cr-Si alloys, a Cr_2O_3 scale is developed following nucleation of oxides of all the alloying elements. However, silicon is much less effective than aluminum in developing rapidly a layer of its oxide; SiO_2 tends to form more slowly than Al_2O_3 and develop less effectively in the early stages. Thus, considerably more transient oxidation, including Cr_2O_3 formation and growth, occurs before the steady-state layer is produced by lateral coalescence of the developing internal oxide precipitates⁸. The promoting effect of silicon on the formation of protective Cr_2O_3 scales has been found in a number of studies, in which mainly two possible mechanisms are discussed. The first is the formation of a thin silica layer under the chromia scale, acting as a diffusion barrier and slowing down the rate of alloy oxidation. The other mechanism discussed is that the addition of silicon increases the diffusion of chromium in the alloy⁹.

2. Experimental methods

The coating materials chosen for the study were a commercial ferritic aluminum containing Kanthal A-1 alloy and a Fe-12Cr-2Si silica-forming alloy. Standard 10CrMo9-10 steel was chosen as a base material for the coatings. Nominal chemical compositions of the chosen materials are presented in Table 1. The coatings were welded on the structural material using a GTAW (gas-tungsten arc welding) method as two-pass layers in the case of Kanthal A-1 and three-pass layers in the case of Fe-12Cr-2Si. Multiple-pass layers were welded in order to minimize the

amount of subsequent Al, Si, and Cr dilution of the coatings by the base material and, thus, to ensure that the coatings have sufficient Al, Si, and Cr compositions.

Table 1. Nominal chemical compositions of the studied materials.

Sample	Fe (%)	Cr (%)	Si (%)	Mo (%)	Ni (%)	Mn (%)	S (%)	P (%)	Al (%)	C (%)
Kanthal A1	Balance	22.0	0.7	-	-	0.4	-	-	5.8	0.08
Fe-12Cr-2Si	Balance	13.1	2.0	-	0.01	0.02	-	-	0.04	-
10CrMo9-10	Balance	2.17	0.21	0.96	-	0.54	0.01	0.02	0.04	0.12

KCl-tests were performed in order to study the material behavior in high Cl-environments. Two 20x20x12 mm samples of each coating material were cut from the overlay welds. The cutting surfaces of the samples were polished using 320 grit paper, one sample of each type was preoxidized in air atmosphere at 950°C for 24 h, and all the samples were exposed to a KCl-containing environment for 168 h at 600°C. The exposed samples were examined using FEGSEM and EDS in order to determine the effects KCl environment had on the oxide scales of the samples.

3. Results

Table 2 shows the measured chemical compositions of the studied coatings. The measurements were done using a standard SEM-EDS point analysis method with multiple analysis points from each sample and the presented compositions are averages calculated from the measured values. The Al and Cr compositions of the Kanthal A-1 coating were around 4.7 wt. % and 18.0 wt. %, respectively, and the Si and Cr compositions of the Fe-12Cr-2Si coating were around 1.6 wt. % and 9.0 wt %, respectively. In both coatings, the alloying elements were quite evenly distributed throughout the coatings and fluctuation in the composition measurements was quite small. Kanthal A-1 oxidized sample and KCl-exposed Kanthal A1 sample of as-welded state had slightly lower Al and Cr compositions than those of the as-welded reference sample. However, the deviation is well within the standard deviation and, thus, no evident breakaway oxidation has occurred during the oxidation or KCl testing.

Approximations of the oxide layer thickness of the samples are presented in Table 3. As can be seen, the oxidized Kanthal A1 samples had an oxide layer thickness of about one tenth of those of the as-welded sample. Oxide layer on the oxidized Fe-12Cr-2Si sample was also quite thin, around 1 μm thick, however, the preoxidation did not have the same effect on the Fe-12Cr-2Si coating as it did on the Kanthal A-1 coating. The oxide layer on the Fe-12Cr-2Si coating was significantly thicker after the KCl exposure on both samples and the oxide scale formed

during the preoxidation did not seem to provide the sample as good corrosion resistance in Cl-containing environment as the corresponding Kanthal A-1 sample.

Table 2. Measured chemical compositions of the studied coatings.

Acquisition	Fe (wt. %)	Cr (wt. %)	Al (wt. %)	Si (wt. %)
Kanthal A-1	76.4	18.4	4.7	-
Standard deviation	0.87	0.66	0.22	-
Kanthal A-1 oxidized at 950°C	77.0	17.7	4.6	-
Standard deviation	1.13	0.91	0.24	-
Kanthal A-1 KCl-tested (as-welded)	76.9	17.9	4.5	-
Standard deviation	0.08	0.15	0.10	-
Kanthal A-1 KCl-tested (preoxidized)	76.4	18.3	4.6	-
Standard deviation	0.98	0.95	0.25	-
Fe-12Cr-2Si	89.3	9.0	-	1.6
Standard deviation	0.30	0.28	-	0.08
Fe-12Cr-2Si oxidized at 950°C	89.2	9.1	-	1.6
Standard deviation	0.24	0.13	-	0.08
Fe-12Cr-2Si KCl-tested (as-welded)	88.8	9.1	-	1.7
Standard deviation	0.27	0.18	-	0.06
Fe-12Cr-2Si KCl-tested (preoxidized)	89.0	9.0	-	1.6
Standard deviation	0.16	0.06	-	0.08

Table 3. Approximations of oxide layer thicknesses.

Sample	Oxide layer thickness (µm)
Kanthal A-1 oxidized at 950°C	1–2
Kanthal A-1 KCl-tested (as-welded)	10–20
Kanthal A-1 KCl-tested (preoxidized)	1–2
Fe-12Cr-2Si oxidized at 950°C	1–2
Fe-12Cr-2Si KCl-tested (as-welded)	40–80
Fe-12Cr-2Si KCl-tested(preoxidized)	40–80

Figure 1 shows SEM (scanning electron microscope) images and EDS (energy-dispersive X-ray spectroscopy) maps of the oxide scales on the surface of Kanthal A-1 coating oxidized at 950°C for 24 h. As can be seen, the oxidation at the particular temperature has caused around 1 μm thick, external oxide scale to form on the surface of the coating and as the EDS maps show, the oxide scale consists of aluminum oxides, presumably α -Al₂O₃. EDS line scan across the oxide scale of the oxidized Kanthal A-1 sample is presented in Figure 2 and it verifies the oxide scale to consist of an external layer of aluminum oxides.

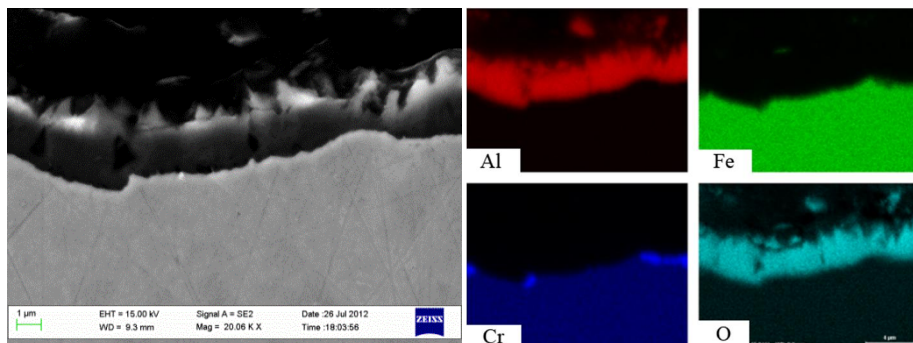


Figure 1. SEM images and EDS maps of oxide scales on the surface of the Kanthal A-1 coating oxidized at 950°C for 24 h.

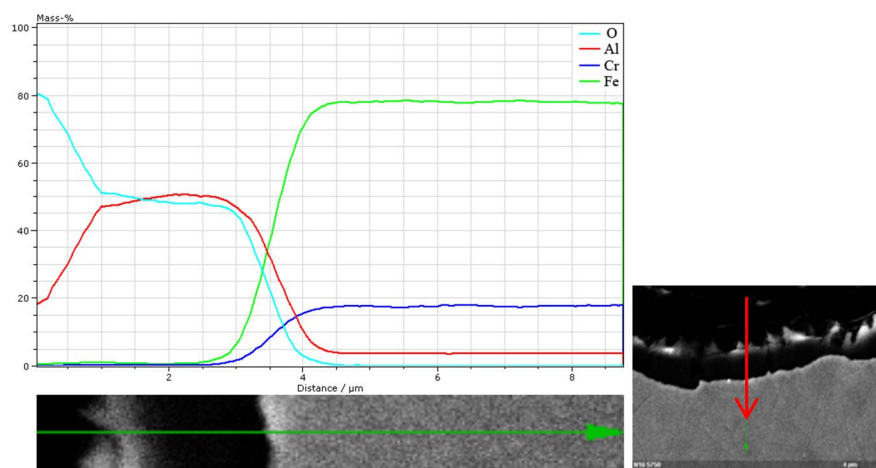


Figure 2. EDS line scan across the oxide scale on the surface of Kanthal A-1 coating oxidized at 950°C for 24 h.

SEM images and EDS maps of the oxide scales on the surface of the KCl-tested Kanthal A-1 coating of as-welded (upper images) and preoxidized (lower images)

states are presented in Figure 3. The oxide scale covered the surfaces of the coatings thoroughly and was similar all over the surface. The oxide scale on the coating of the as-welded sample consists of several individual oxide layers and the scale is clearly thicker on as-welded sample than on the preoxidized sample. As can be seen, the oxide scale on the surface of the as-welded sample consists of the top layer of iron oxides, the middle layer of chromium and aluminum oxides, and beneath the chromium oxide layer is a very thin internal layer of aluminum oxide. The oxide scale on the surface of the as-welded state sample has formed mainly in a KCl-testing temperature, which was 600°C. Due to low oxidizing temperature and the observation that the alumina layer is located beneath the other oxide layers, it is likely that the alumina formed in these conditions is not the stable α -Al₂O₃ but instead some form of transient alumina.

The oxide scale on the surface of the preoxidized sample, on the other hand, consists only of an external layer of aluminum oxide, similarly to the oxidized sample. Thus, the external aluminum oxide scale formed on the sample during the preoxidation has resisted the KCl present in the environment throughout this test and provided the coating with good resistance against corrosion in this particular environment. Based on these experiments, it is hard to assume how long does the preoxidized alumina scale resist the KCl-containing environment before it breaks down. However, the external aluminum oxide scale resisted the KCl environment at least for the duration of this exposure.

To compare the compositions of the oxide scales further, EDS line scans across the oxide scales of KCl-tested Kanthal A-1 samples of as-welded and preoxidized states are shown in Figure 3. Figure 4 clearly verifies that the scale on the as-welded sample consists of top layer of Fe oxides, middle layer of Fe and Cr oxides, and bottom layer of mainly Cr oxides. As for the preoxidized sample, the scale clearly consists of an external layer of alumina.

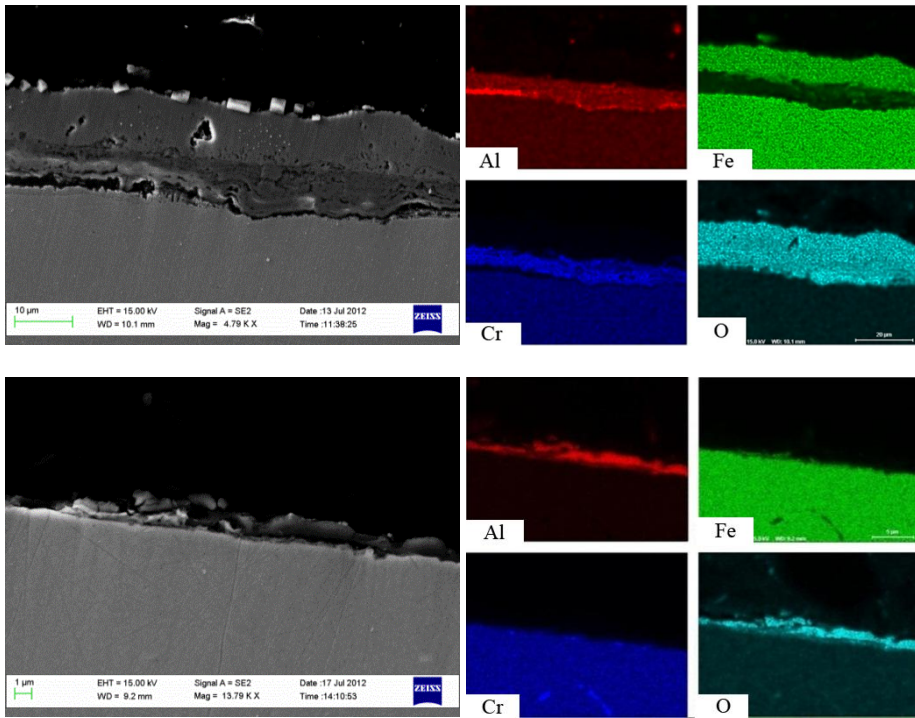


Figure 3. SEM images and EDS maps of the oxide scales on the surface of the KCl-tested Kanthal A-1 sample of as-welded (upper images) and preoxidized (lower images) states.

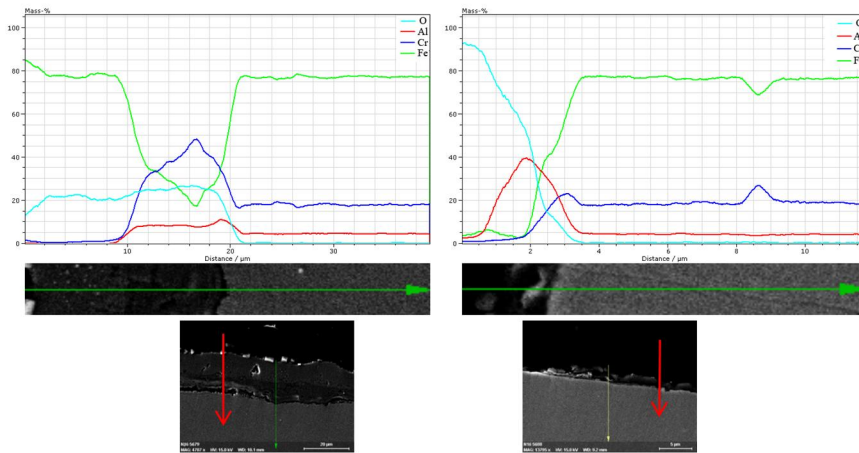


Figure 4. EDS line scans across the oxide scales on the surface of the KCl-tested Kanthal A-1 coating of as-welded (left image) and preoxidized (right image) states.

SEM images and EDS maps of the oxide scales on the surface of the Fe-12Cr-2Si coating oxidized at 950°C are shown in Figure 5 and EDS line scan across the oxide scale is shown in Figure 6. The oxide scale is overall thin, around 1–2 μm . There were a few thicker oxide nodules on the surface of the sample which consisted of a top layer of Fe oxides but otherwise the oxide scale consisted of a top layer of Cr oxides. As can be seen, a fully continuous layer of silica could not be found from the surface of the coating, but instead, there is a clear sequence of Si containing oxide precipitates below the chromia layer and it is possible that the oxidation time just was not long enough for the actual silica layer to form below the main chromia scale since, as mentioned earlier, Si is much less effective than Al in developing rapidly a layer of its oxide. SiO_2 tends to form more slowly than Al_2O_3 and develop less effectively in the early stages of oxidation and, thus, considerably more transient oxidation, including Cr_2O_3 formation and growth, occurs before the steady-state layer is produced by coalescence of the developing internal oxide precipitates. Also, since the cladding had a Si composition of less than 2 wt. %, the Si containing oxides developing below the chromia scale could be Fe_2SiO_4 precipitates as well as SiO_2 precipitates.

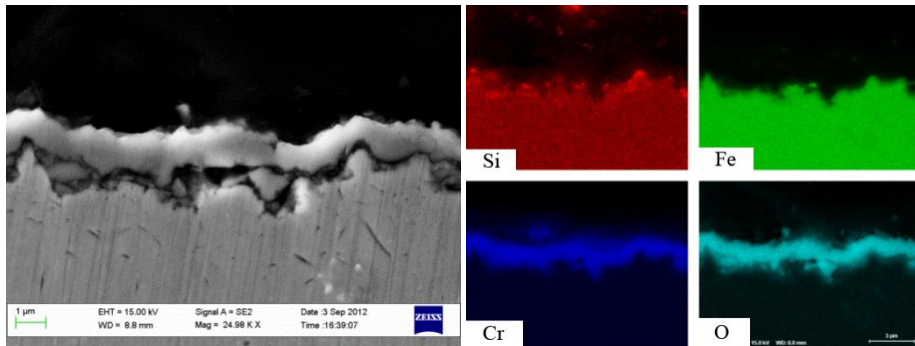


Figure 5. SEM images and EDS maps of the oxide scales on the surface of the Fe-12Cr-2Si coating oxidized at 950°C for 24 h.

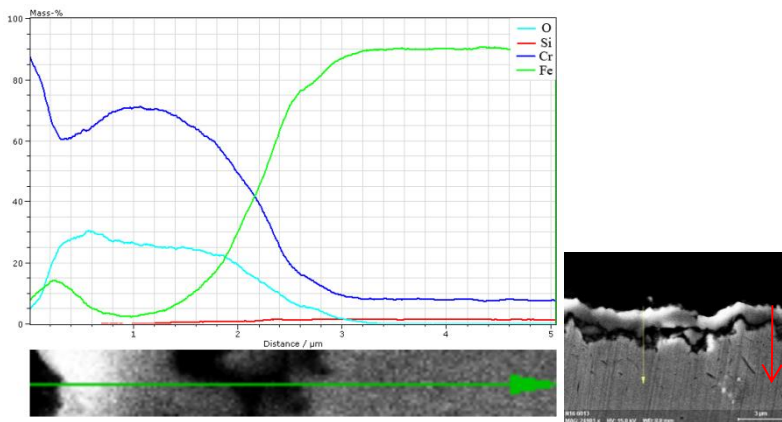


Figure 6. EDS line scan across the oxide scale on the surface of the Fe-12Cr-2Si coating oxidized at 950°C for 24 h.

SEM images and EDS maps of the oxide scale on the surface of the Fe-12Cr-2Si coating of as-welded and preoxidized states are shown in Figure 7. As can be seen, the oxide scale thickness of both coatings is tens of micrometers and the scale consists of multiple oxide layers. The composition of the oxide scale is quite similar to that of the as-welded Kanthal A-1 sample with the exception that instead of any alumina particles, there seems to be a few silicon-containing oxide particles in the bottom of the scale. Otherwise the scale consists of a top layer of Fe oxides and a bottom layer of FeCr-spinel oxides. The thickness and composition of the scale on the surface of the preoxidized sample are quite similar to those of the as-welded sample. The oxide scale of the preoxidized sample was a little thinner than the oxide scale of the as-welded sample; however, the difference in the thickness was quite small.

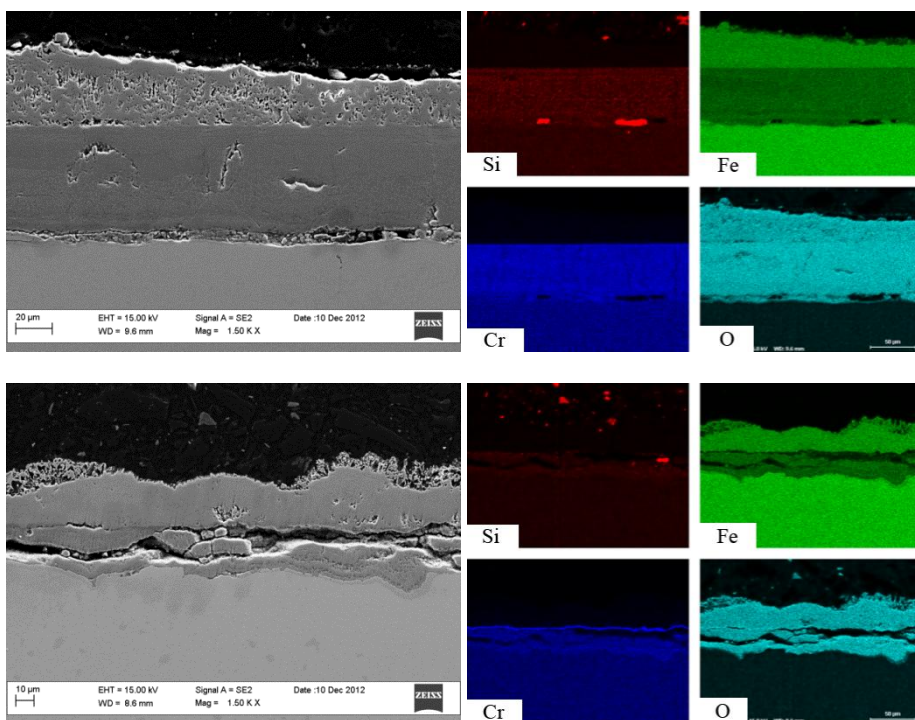


Figure 7. SEM images and EDS maps of the oxide scales on the surface of the KCl-tested Fe-12Cr-2Si sample of as-welded (upper images) and preoxidized (lower images) states.

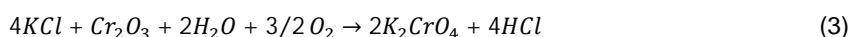
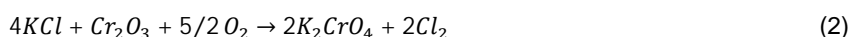
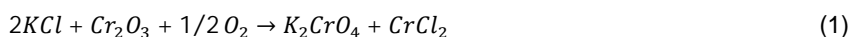
4. Conclusions and discussion

Both welding wires, Kanthal A-1 and Fe-12Cr-2Si, were successfully used in manufacturing of the coatings on T22 steel (10CrMo9-10) by GTAW method and Al, Cr, and Si were evenly distributed throughout the coatings. The compositions of Al and Cr in Kanthal A-1 coating were sufficient to provide the material with the ability to form an external Al oxide scale during oxidation at 950°C. In the case of Fe-12Cr-2Si, the compositions of Si and, especially, Cr were slightly lower than desired. However, the coating did form a thin Cr-oxide layer with a network of Si-containing oxide precipitates underneath during oxidation at 950°C.

The Kanthal A1 coating did not form an external Al-oxide layer in the KCl environment; instead it formed an oxide scale with multiple different types of oxide layers and discontinuous internal Al-oxide layer. That was expected, since the temperature needed for α -Al₂O₃ to form is close to 1000°C and, thus, the formed internal Al-oxide was likely some form of transient alumina. The preoxidation of Kanthal A1 coating formed a thin, continuous, external Al-oxide layer on the sur-

face of the coating with resistance to the KCl environment and, thus, provided the material with good resistance against Cl-containing environment.

The Fe-12Cr-2Si coating of both states formed an oxide scale with multiple oxide layer on their surface during the KCl exposure. The oxide scale on the surface of the preoxidized sample was a little thinner than the oxide scale on the surface of the as-welded sample. However, the difference was quite slight. The oxide scales consisted of a top layer of Fe oxides and a lower layer of FeCr-spinel oxides. Unlike with the Kanthal A-1 coating, the Fe-12Cr-2Si coating did not benefit from the preoxidation treatment, even though the preoxidation did form a very thin oxide scale on the surface of the coating. Since the preoxidized oxide scale consisted mainly of Cr-oxide, the KCl present in the testing environment has likely reacted with the Cr-oxides in the scale to form Cr-chlorides and/or chromites via the following reactions [10–12]



and, thus, the oxide scale behaviour was similar to the Cr-oxide scale formed on the surface of conventional stainless steel relying on Cr-oxides for protection against corrosion.

Acknowledgements

This study was made within the FIMECC DEMAPP research program funded by Tekes and Finnish industry and it was a part of a collaborative project, called Matexon, between Aalto University and VTT (Technical Research Centre of Finland). The authors wish to express their gratitude for all the participants in the project.

References

1. Lai, G. High Temperature Corrosion and Materials Application. ASM International, USA, 2007. 461 p. ISBN-10 0-87170-853-1.
2. Prescott, R. & Graham, M. The Formation of Aluminum Oxide Scales on High-Temperature Alloys. *Oxidation of Metals*, 1992A, Vol. 38, No. 3, pp. 233–254.
3. Brady, M.P., Yamamoto, Y., Santella, M.L., Maziasz, P.J., Pint, B.A., Liu, C.T., Lu, Z.P. & Bei, H. The Development of Alumina-Forming Austenitic Stainless Steels for High-Temperature Structural Use. *JOM Journal of the Minerals, Metals & Materials Society*, 2008, Vol. 60, No. 7, pp. 12–18.

4. Liu, F., Götlind, H., Svensson, J.-E., Johansson, L.-G. & Halvarsson, M. Early Stages of the Oxidation of a FeCrAlRE Alloy (Kanthal AF) at 900°C: A Detailed Microstructural Investigation. *Corrosion Science*, 2008, Vol. 50, No. 8, pp. 2272–2281.
5. Engkvist, J., Canovic, S., Hellström, K., Järtnäs, A., Svensson, J.-E., Johansson, L.-G., Olsson, M., & Halvarsson, M. Alumina Scale Formation on a Powder Metallurgical FeCrAl Alloy (Kanthal APMT) at 900-1,100°C in Dry O₂ and in O₂ + H₂O. *Oxidation of Metals*, 2010, Vol. 73, No. 2, pp. 233–253.
6. Dunning, J. S., Alman, D. E. & Rawers, J. C. Influence of Silicon and Aluminum Additions on the Oxidation Resistance of a Lean-Chromium Stainless Steel. *Oxidation of Metals*, 2002, Vol. 57, Nos. 5/6, pp. 409–425.
7. Engell, H.-J. & Grabke, H. J. *Steel, a Handbook for Materials Research and Engineering, Volume 1: Fundamentals*, ed.: Verein Deutscher Eisenhüttenleute. Verlag Stahleisen, Düsseldorf, Germany, 1992. 737 p. ISBN: 3-514-00377-7.
8. Stott, F.H., Wood, G.G. & Stringer, J. The Influence of Alloying Elements on the Development and Maintenance of Protective Scales. *Oxidation of Metals*, 1995, Vol. 44, Nos. 1/2, pp. 113–145.
9. Zehs, A., Spiegel, M. & Grabke, H.J. The Influence of Alloying Elements on the Chlorine-Induced High Temperature Corrosion of Fe-Cr Alloys in Oxidizing Atmospheres. *Materials and Corrosion*, 1999, Vol. 50, pp. 561–578.
10. Li, Y.S. & Spiegel, M. High temperature interaction of Cr and KCl, 6th International Symposium on High Temperature Corrosion and Protection of Materials, Les Embiez, France, 2004.
11. Li, Y.S., Spiegel, M. & Shimada, S. Effect of Al/Si addition on KCl induced corrosion of 9% Cr steel. *Materials Letters*, 2004, Vol. 58, pp. 3787–3791.
12. Karlsson, S, Pettersson, J., Johansson, L.-G. & Svensson, J.-E. Alkali Inducted High Temperature Corrosion of Stainless Steel: The Influence of NaCl, KCl, and CaCl₂. 2012.

A material solution against fireside chloride corrosion

S. Yli-Olli, T. Suhonen, J. Virta, S. Holmström, T. Varis,
S. Tuurna & T. Kinnunen

VTT Technical Research Centre of Finland
P.O. Box 1000 FI-02044 VTT, Finland

Abstract

The paper describes the development of a new material solution to protect fireside surfaces against high temperature (500–700°C) chlorine corrosion in severe combustion environments of the energy and process industry. The proposed solution is based on introducing an innovative coating as a surface layer to prevent chlorine and oxygen diffusion into the substrate to be protected.

For experimental verification of the concept, new coatings and hot isostatic pressed materials against chlorine corrosion (Cl-trap coatings) have been exposed to an aggressive chlorine environment at 600°C. The new Cl-trap materials with Ni barriers strongly retarded chlorine corrosion by preventing Cl penetration through lamellar boundaries into the substrate material. The required nearly pure Ni layers were not retained in the HIPed alloys that therefore did not perform equally well.

1. Introduction

For competitive low carbon or carbon neutral combustion, future boilers will need to utilize an increasing amount of biomass. The resulting combustion environment is a challenge for the boiler since the biomass-derived fuels contain large amounts of severely corrosive constituents that attack existing materials and might drastically limit their durability and lifetime. To avoid undue loss of thermal efficiency or facing an increasing number of unscheduled outages new solutions in protecting the existing material (by coatings and overlay welds) need to be developed.

High temperature corrosion in the convection surfaces of boilers is usually through oxidation, sulphidation, chlorine induced corrosion or melt deposition attack, or a combination of the phenomena [1, 2]. Oxidation requires oxidizing and sulphidation reducing surrounding. Aggressive melt depositions, like sodium and potassium chlorides, can exist both in oxidizing and reducing conditions. The role of chlorine and sulphur in complex oxidizing environments are detrimental. In chlorine induced corrosion chlorine reacts with metal forming volatile metal chlorides. Chlorine diffuses through cracks and pores of the oxide scale towards the metal/scale interface and metal chlorides are formed at low $p(\text{O}_2)$, at this interface. At temperatures of 400°C and higher, evaporation of metal chlorides takes place and subsequent outward diffusion of the volatile metal chlorides towards the gas

phase occurs. By reaching regions with a higher $p(O_2)$, the metal chlorides are transformed to oxides, growing in cracks and pores of the scale and leading to subsequent cracking and spallation. [3, 4, 5, 6, 7]

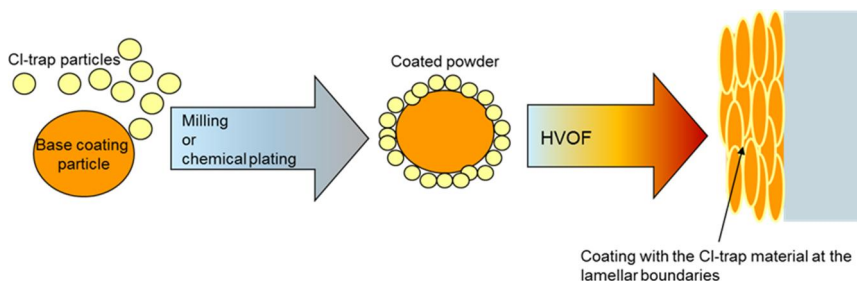


Figure 1. Principles of a Cl-trap coating [8].

2. Materials and methods

Different NiCr-materials were tested against high temperature chlorine corrosion at 600°C in a controlled high temperature corrosion testing oven [9] for 168h in moist synthetic air (+20% H₂O) with a KCl deposit sprayed on the surface. The test materials are presented in Table 1.

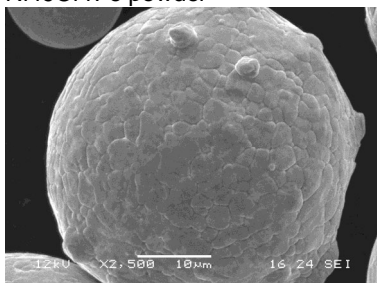
Table 1. Test materials.

Material	Method	
Ni49Cr1Fe – Ni – Ni49Cr1Fe	HVOF -DJ Hybrid	Layered structure
Ni49Cr1Fe – Ni	HVOF -DJ Hybrid	Layered structure
Ni – Ni49Cr1Fe	HVOF -DJ Hybrid	Layered structure
Ni	Chemically plated	
Ni49Cr1Fe	HVOF -DJ Hybrid	Reference
Ni49Cr1Fe	HVOF -DJ Hybrid	15wt-% Ni by chemical plating
Ni49Cr1Fe	HVOF -DJ Hybrid	10wt-% nano-Ni milled
Ni49Cr1Fe	HIP	Reference
Ni49Cr1Fe	HIP	+ 15 wt-% Ni by chemical plating
Ni49Cr1Fe	HIP	+ 10 wt-%milled nano-Ni

Materials include layered coatings, Cl-trap coatings and hot isostatic pressed (HIP) materials. NiCr-coatings were produced by high velocity oxy-fuel (HVOF) spraying with the DJ Hybrid, described in more detail in previous publications [e.g. 10]. In the layered coatings the nickel layers were chemically plated, with a Ni-P solution. Materials were also HIPed at 1150°C, 1000 bar for 3h, to model ideal

coating structure without inhomogeneities like lamellar boundaries. For the Cl-trap coatings Ni49Cr1Fe powder was coated by either milling with nano-nickel particles (Figure 2) or by chemical nickel plating.

Ni49Cr1Fe powder



Milling with nano-nickel (Ni = 60 nm) and chemical plating with Ni(P)

⇒ Cl-trap powder

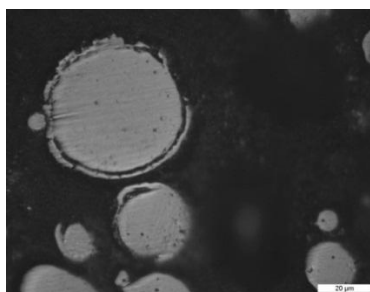
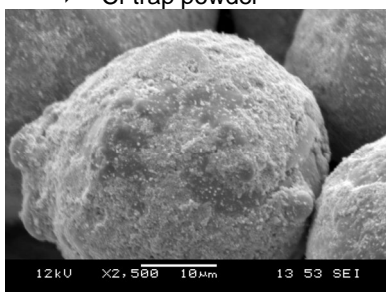


Figure 2. 50Ni50Cr powder before and after nano-nickel and chemical plating Ni(P) coating.

After corrosion testing the materials were weighed and sectioned for metallography. The cross-sections were analysed optically with a light optical microscope (LOM) and with a scanning electron microscope (SEM), and the formed surface layers were analysed with energy dispersive x-ray spectroscopy (EDS).

3. Results

SEM images of the cross-sections of the layered coatings and the reference Ni49Cr1Fe -coating after exposure are shown in Figures 3-6. Corrosion is observed in all samples. In the reference material Ni50Cr, corrosion penetrates the coating clearly through the lamellar boundaries (Figure 3). The plated Ni coating has retarded corrosion for a while, since corrosion has not penetrated the substrate more aggressively, but after penetration through the Ni layer corrosion has begun at the substrate (Figure 4). Same can be observed in the coating where a Ni layer has been chemically plated on a HVOF coated Ni49Cr1Fe layer (Figure

5). When a Ni layer was chemically plated between HVOF sprayed Ni49Cr1Fe coatings, the outer layer of the coating was corroded, but the Ni-layer stopped the corrosion front (Figure 6).

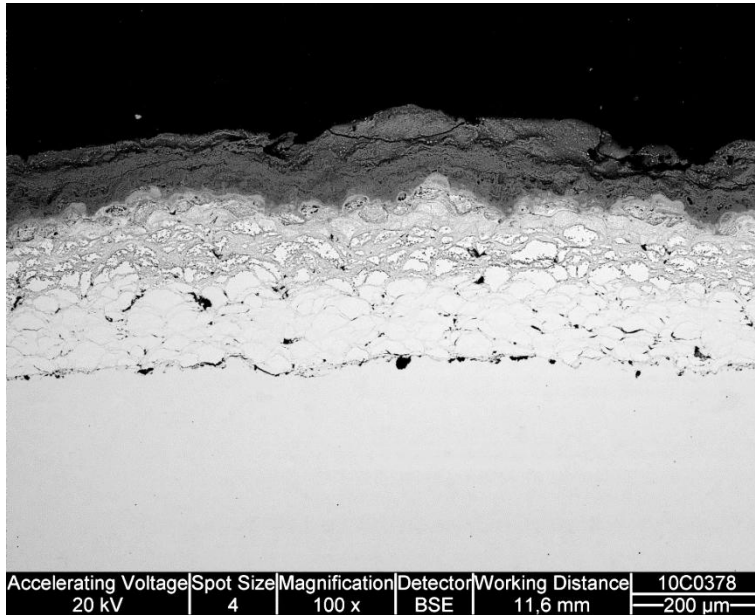


Figure 3. Reference Ni49Cr1Fe coating after exposure.

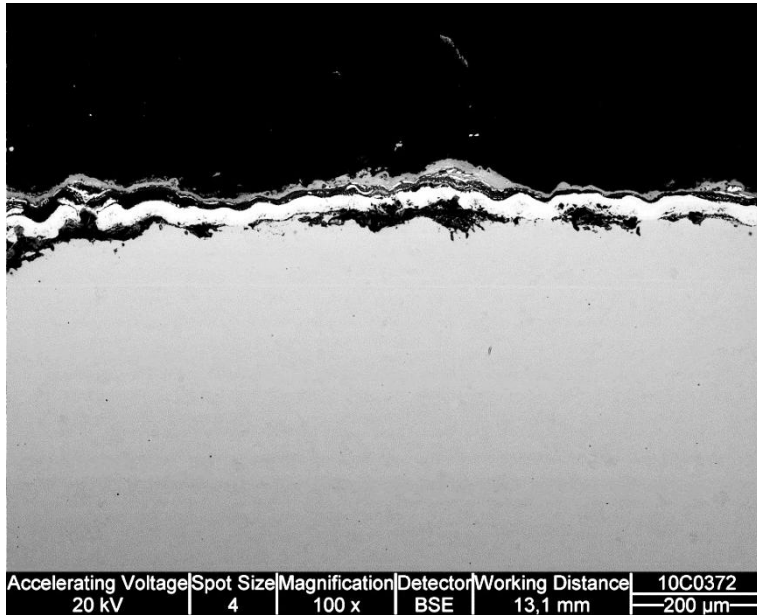


Figure 4. The chemically plated Ni coating after exposure.

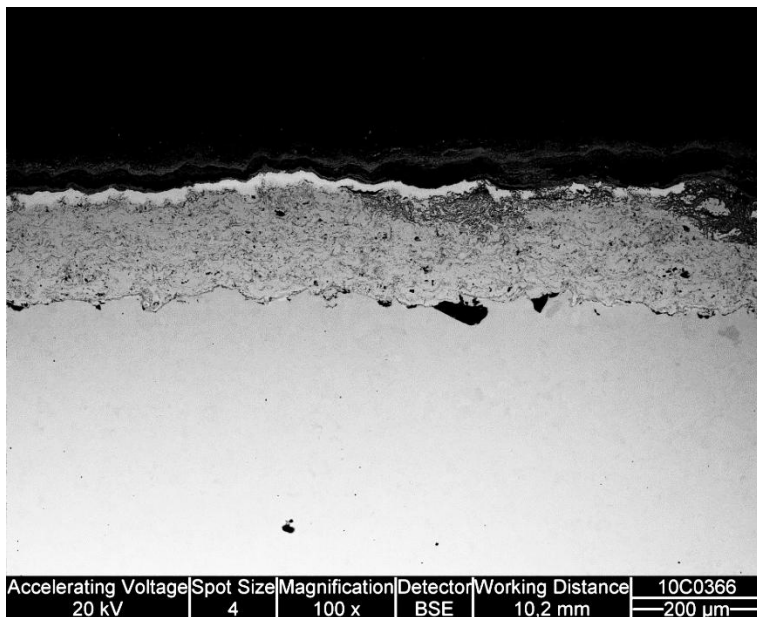


Figure 5. Ni₄₉Cr₁Fe-Ni(P) layered coating after exposure.

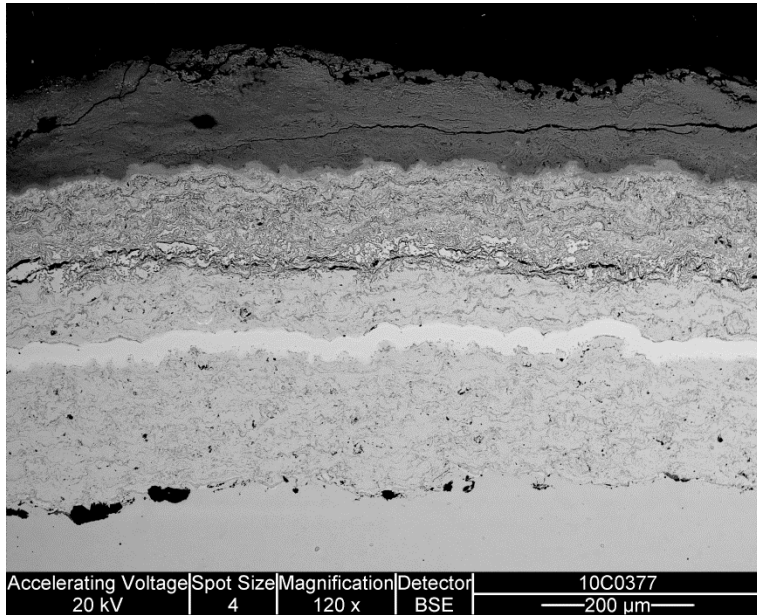


Figure 6. Ni₄₉Cr₁Fe-Ni(P)- Ni₄₉Cr₁Fe layered coating after exposure.

Figure 7 shows the reference Ni₄₉Cr₁Fe and the Ni₄₉Cr₁Fe with 15w-% chemically plated Ni coatings before exposure. The coatings are dense, but the Ni coating has not formed uniformly on the lamellar boundaries as intended. Ni₄₉Cr₁Fe reference coating (Figure 8) after exposure suffered from some corrosion, which proceeds through the lamellar boundaries. Corrosion was also observed in the Cl-trap materials (Figures 9 and 10), but not to the same extent.

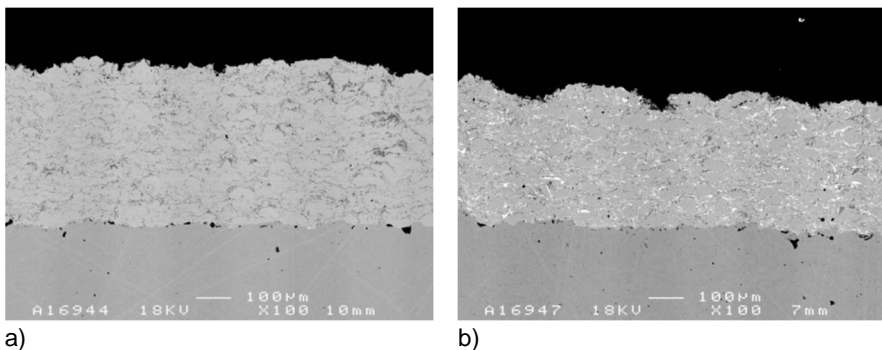


Figure 7. Coatings before exposure a) reference Ni₄₉Cr₁Fe coating and b) Ni₄₉Cr₁Fe + 15wt-% chemically plated Ni.

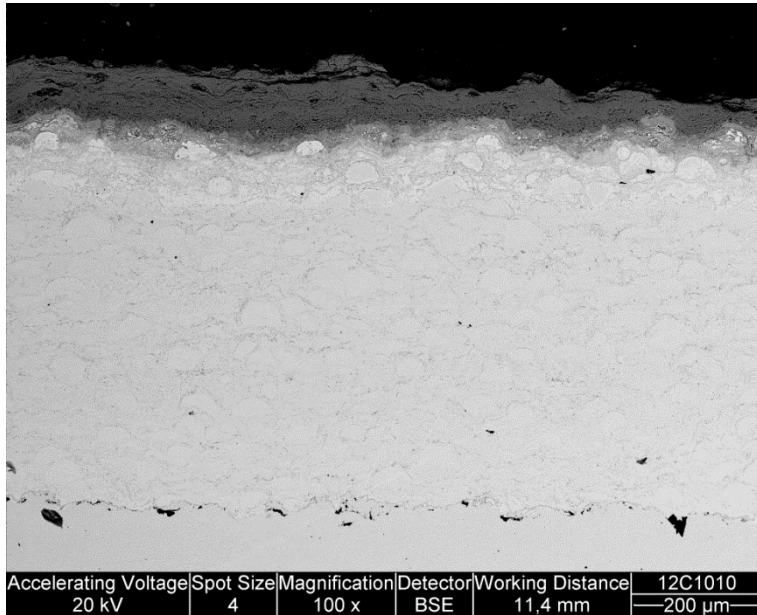


Figure 8. Ni₄₉Cr₁Fe reference coating after exposure.

The surface of Ni₄₉Cr₁Fe with 10wt-% milled nano-Ni after exposure was analysed with EDS and the element mapping is shown in Figure 11. Here is shown that the chromium from the upper part of the coating has diffused to the reaction surface, and left a chromium depleted zone beneath. Also in this coating the milled Ni has not formed a uniform web on the lamellar boundaries.

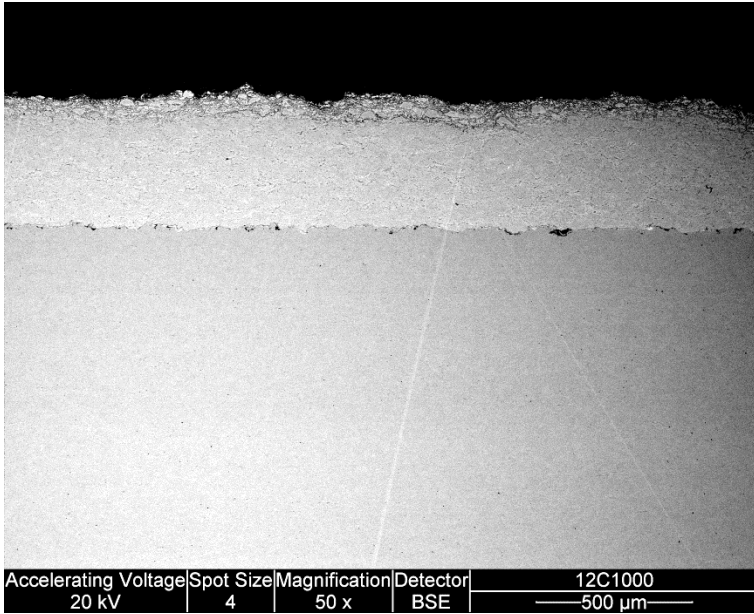


Figure 9. Ni₄₉Cr₁Fe + chemically plated 15wt% Ni(P) after exposure.

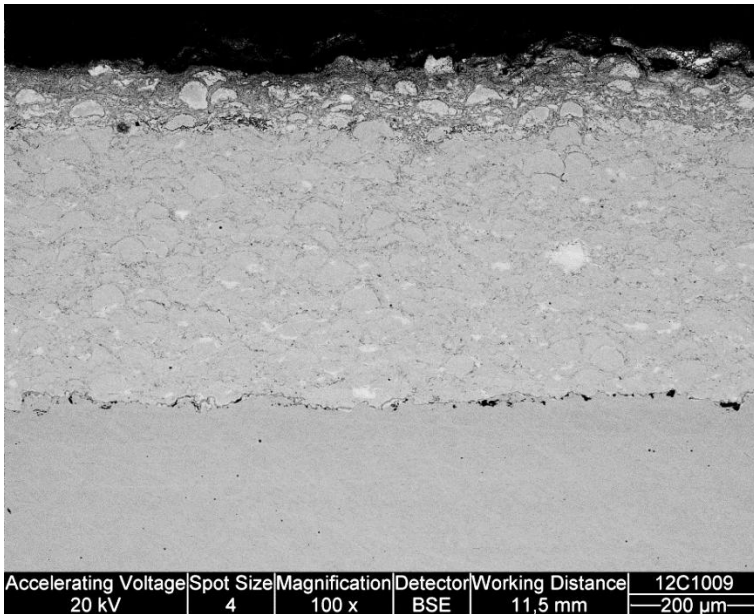


Figure 10. Ni₄₉Cr₁Fe + milled 10wt-% nano-Ni after exposure.

The microstructures before exposure and the cross-sections of the HIPed materials are shown in Figures 12–14). All the HIPed materials were dense, and corrosion could be observed in all materials. Table 2 shows the composition of the corrosion product formed on the surface of the HIPed Ni49Cr1Fe with milled nano-Ni in Figure 13. Figure 15 shows the EDS mapping of the layers formed on Ni49Cr1Fe with the chemically plated Ni(P).

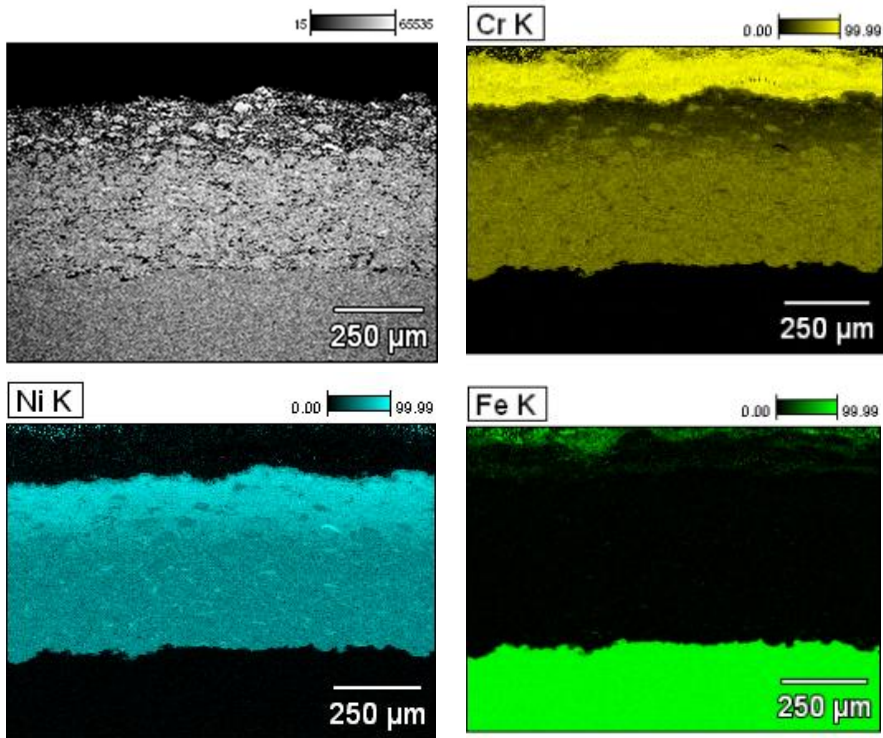


Figure 11. EDS element maps of Ni49Cr1Fe with 10wt-% milled nano-Ni after exposure.

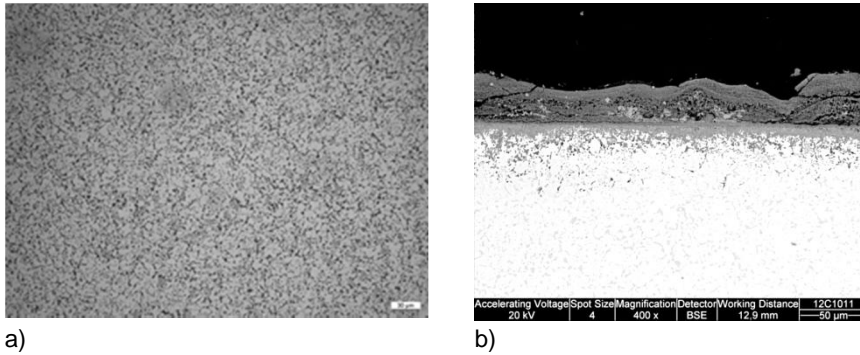


Figure 12. HIPed Ni49Cr1Fe reference a) microstructure before testing and b) after exposure.

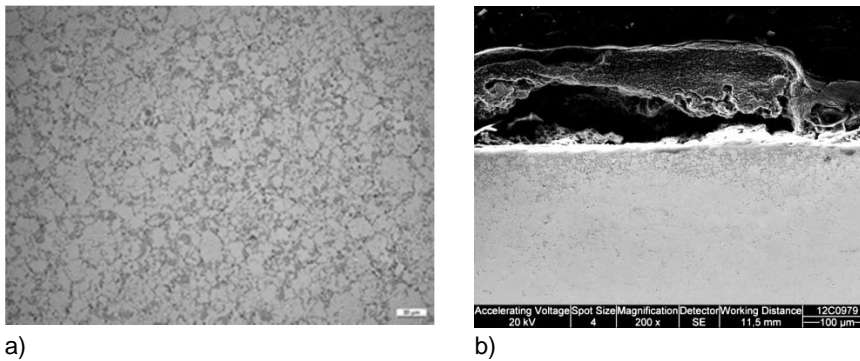
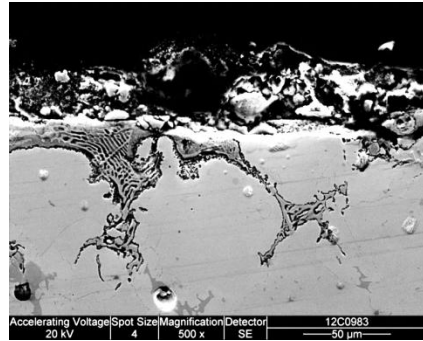
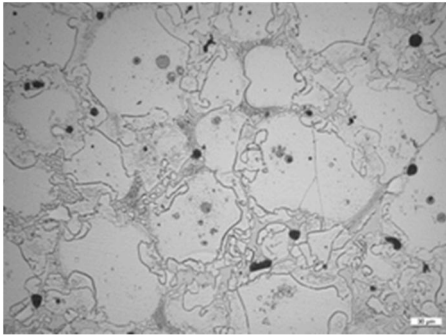


Figure 13. HIPed 50Ni50Cr with milled nano-Ni a) microstructure before testing and b) after exposure.

Table 2. Composition (EDS) of the corrosion product on HIPed 50Ni50Cr with milled nano-Ni (Figure 13).

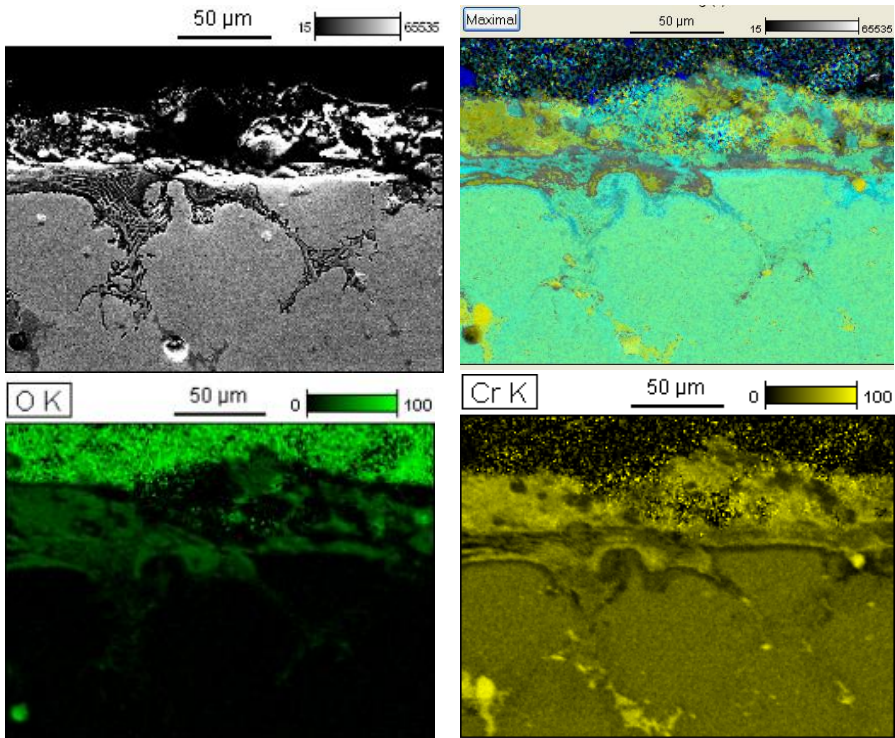
Element	Weight %	Atom %
O	21.2	39.4
Al	0.1	0.2
Si	0.3	0.3
Cl	0.1	0.1
K	2.8	2.1
Cr	65.1	37.2
Fe	0.2	0.1
Ni	2.2	1.1



a)

b)

Figure 14. HIPed Ni50Cr (chemically plated Ni) a) microstructure before testing and b) after exposure.



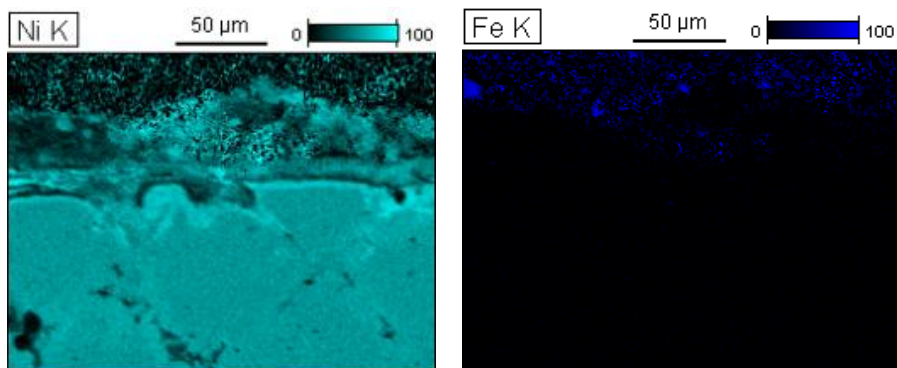


Figure 15. EDS element maps from HIPed Ni₄₉Cr₁Fe (chemically plated) after exposure.

4. Discussion

The exposed layered coatings show that corrosion penetrates through the lamellar boundaries (Figure 3) and the coated reference Ni₄₉Cr₁Fe was not sufficient to protect against chlorine corrosion for long in the test environment. It was also seen that only a thin Ni-layer will retard chlorine corrosion if the layer is dense and adherent. Destructive corrosion is however resumed if chlorine penetrates the Ni-coating as seen in Figure 4. Promising results were obtained by using layered structures (Figure 6, Figure 5) with an added Ni layer to retard chlorine corrosion. In this case, the outer layer of Ni₄₉Cr₁Fe acts as a sacrificial layer and the Ni-layer as a barrier blocking the corrosion front from penetrating to the rest of the coating. When only the Ni-barrier is coated on the surface of Ni₄₉Cr₁Fe coating, the risk of barrier failure is higher, as seen from Figure 5.

The Cl-trap coatings performed in satisfactory manner, although they were not optimised to fully cover the lamellar boundaries with Ni (Figure 7). Both types of Cl-trap materials resisted corrosion better than the reference Ni₄₉Cr₁Fe coating. The EDS results showed that chromium had diffused to the surface leaving a nickel rich zone in the layer beneath the corrosion product, and this layer may also protect from additional chlorine corrosion.

Dense HIPed materials were produced to represent an ideal coating. The microstructure of the reference material and the samples made of the milled powder appeared as typical dense Ni₅₀Cr material. The microstructure of the material produced from chemically plated powder shows Ni₅₀Cr grains surrounded by a relatively thick layer of a phase mixture with higher Ni content. After corrosion testing, chromium had diffused to the surface corrosion product, where only minor quantities of nickel were found (Table 2, Figure 15). All HIPed materials suffered from chlorine corrosion, including the material made of chemically Ni plated Ni₅₀Cr, where the corrosion particularly penetrated along the particle boundaries that were clearly no more protected by Ni.

5. Conclusions

Promising results were obtained with the new Cl-trap materials. Layered Ni-barriers between Ni₄₉Cr₁Fe-coatings retard high temperature chlorine corrosion by preventing chlorine from penetrating through lamellar boundaries to the substrate material. An attempt to produce a corresponding idealised structure by a HIPed alloy failed to provide similarly protective results, presumably due to lost layers of sufficiently high Ni content. In contrast, the HVOF produced Cl-trap coatings successfully retarded chlorine corrosion even when the nickel web was not uniform at the lamellar boundaries. Further optimisation is on-going for the Cl-trap material and its production process. Coatings based on similar principles are also being developed for sulphur containing environments.

Acknowledgements

The work was conducted in the Matexon - Materials for extreme conditions of sustainable processes – project within the FIMECC DEMAPP research program. The research was made in collaboration with various research groups within VTT and Aalto University. The authors wish to acknowledge all project partners as well as Tekes, Andritz, Telatek, Fortum and Outotec for funding the project.

References

1. Kawahara, Yuuzou, Application of High Temperature Corrosion-Resistant Materials and Coatings Under Severe Corrosive Environment in Waste-to-Energy Boilers, *Journal of Thermal Spray Technology* 16(2007)2, pp. 202–213.
2. P.S., Mohanty, A.D. Roche, R.K. Guduru, V. Varadaraajan, Ultrafine Particulate Dispersed High-Temperature Coatings by Hybrid Spray Process, *Journal of Thermal Spray Technology* , 19(2010)1–2, pp. 484–494.
3. Y. Y. Lee, M.J. McNallan, *Metallurg. Trans.* 18A, (1987), 1099.
4. H.P. Nielsen, F.J. Frandsen, K. Dam-Johansen, L.L. Baxter, The implications of chlorine-associated corrosion on the operation of biomass-fired boilers, *Progress in Energy and Combustion Science* 26(2000)3, pp. 283–298.
5. N. Hiramatsu, Y. Uematsu, T. Tanaka, M. Kinugasa, *Materials Science and Engineering, A* 120(1989) 319.
6. J. Klöwer, F.E. White, High temperature corrosion of commercial heat-resistant alloys under deposits of alkali salts: recent laboratory data, in: *Proceed-*

ings of the 8th International Symposium on Corrosion in the Pulp & Paper industry, Tappi Press, Atlanta, USA, 1995, pp. 179–188.

7. A. Zahs, M. Spiegel, H.J. Grabke, Fundamental aspects of chlorine induced corrosion in power plants, *Materials at high temperatures*, 20(2003), pp. 153–159.
8. T. Suhonen, T. Varis, PCT/FI2012/050304.
9. S. Tuurna, L. Heikinheimo, M. Arponen, M. Hämäläinen, Oxidation kinetics of low alloyed ferritic steels in a moist atmosphere, Eurocorr 2003, Budapest 28.9.-2.10.03.
10. M. Oksa, E. Turunen, T. Suhonen, T. Varis, S.-P. Hannula, Optimization and Characterization of High Velocity Oxy-fuel Sprayed Coatings: Techniques, Materials, and Applications, *Coatings*, MDPI AG, vol. 1, 1, pp. 17–52, 2011.

Corrosion and carburization of superheater materials in oxyfuel combustion

Satu Tuurna, Sanni Yli-Olli & Pekka Pohjanne

VTT Technical Research Centre of Finland

P.O. Box 1000, FI-02044 VTT, Finland

Abstract

The energy sector is globally the largest CO₂ emitter. Carbon capture and storage (CCS) is a concept to reduce greenhouse gas emissions resulting from the use of fossil fuels in power generation, and integrated oxyfuel combustion concepts, combustion in oxygen-enriched environment to make post-combustion extraction easier, is studied one of the options for CCS. Oxyfuel combustion can be expected to differ from combustion in air by e.g. modified distribution of fireside temperatures, much reduced NO_x but increased levels of fireside CO₂, SO₂ and water levels due to extensive flue gas recirculation. Increased flue gas recirculation may increase the concentration of a number of contaminants in the deposited ash and promote fouling and corrosion. In addition to development of low CO₂ emitting energy generation technologies, improved energy efficiency is essential in order to reach emission reduction targets. Increasing process efficiency requires high in-service temperatures for superheaters and reheaters.

In this paper the corrosion performance of two superheater austenitic steels (TP347HFG and Sanicro 25) has been studied in laboratory tests under simulated oxyfuel conditions with and without a synthetic deposits (85 CaCO₃ - 15 wt% CaSO₄, CaSO₄-0.55 wt% KCl) at 650 and 720°C up to 1000 hours.

1. Introduction

CO₂ emissions are gaining a significant attention in the policy reducing air pollutant emissions. The most cost effective and readily available option is to mitigate CO₂ emissions by increasing the plant efficiency. At the same time new technologies to CO₂ emissions reduction such as carbon capture and sequestration (CCS) processes have been developed. In these processes, CO₂ is captured from the cleaned products of combustion or gasification. It has been estimated that CCS for base load power generation is likely to become commercially available at around 2025. Oxyfuel combustion is one of the CCS technologies under research focus to CO₂ capture from flue gases. Compared to conventional air-fired combustion, the oxyfuel process will use a combination of oxygen, with a purity of more than 95 vol %, and recycled flue gas to combust the fuel producing a gas consisting of mainly CO₂ and water vapour, which is after purification and compression ready for storage [1, 2]. The risk of enrichment of corrosive species, such as SO₂ and Cl,

in the flue gas environment increases due to recycling of flue gas in oxy-fired combustion compared to air firing. The changes in the combustion gas chemistry will also affect the chemistry and formation of deposits, with potentially increasing corrosion and internal attack of the boiler components that are in contact with the combustion and flue gas environment [3–5].

The corrosion mechanisms and limiting factors in air-fired combustion have been extensively studied over the past years. However, there is still relatively little experimental information available about the effects of oxyfuel combustion on the boiler material performance. The first demonstrations of the oxy-fuel concept are carried out currently used high temperature materials. Typically the presence of sulphur strongly increases the corrosion rate, but the influence of sulphur on corrosion can be complicated, as in the form of SO_2 it can also slow down corrosion. The phenomenon is dependent on time, fireside environment, gas partial pressures and alloying elements [6–11]. In oxyfuel combustion the likelihood of the presence of sticky deposits is increased [12–13]. Sulphation and carbonation of ash particles under oxyfuel combustion is higher due to high SO_2 and CO_2 potential. There are indications that oxide scales developing in $\text{O}_2/\text{CO}_2/\text{H}_2\text{O}$ atmospheres are not that protective and internal carburisation may occur [8, 14–15]. Limestone (CaCO_3) can be used in oxyfuel circulating fluidized bed (CFB) boilers as absorbent for capture of SO_2 . In oxyfuel combustion the CaO-CaCO_3 equilibrium comes close to the normal operating temperature and the capture mechanisms may change from normal sulphation ($\text{CaCO}_3\text{-CaO-CaSO}_4$) to direct sulphation path ($\text{CaCO}_3\text{-CaSO}_4$) due to high CO_2 concentration. Hard deposits may occur during the simultaneous occurrence of calcination, sulphation and recarbonation. Such a deposit may cause operational problems like plugging of gas channels and/or corrosion of superheaters [16].

2. Experimental

Two superheater austenitic steels (TP347HFG and Sanicro 25) have been studied in laboratory tests under simulated oxyfuel conditions ($2\%\text{O}_2\text{-}29\%\text{H}_2\text{O}\text{-}44\%\text{CO}_2\text{-}0.6\%\text{SO}_2\text{-}0.2\%\text{HCl-N}_2$) with and without synthetic deposits (85 wt% CaCO_3 – 15 CaSO_4 , $\text{CaSO}_4\text{-}0.55$ wt% KCl) at 650 and 720°C up to 1000 hours. Table 1 shows the chemical composition of used materials. Rectangle shape specimens with dimensions of 15 x 15 x 3 mm were machined from thick walled tubes. The samples were bright polished with SiC paper (P1200), washed with deionized water and ultrasonically degreased in ethanol. Exposure testing was carried out in horizontal Al_2O_3 tube furnace. The test environments were prepared from premixed and/or pure gases that were mixed based on flow rates and controlled using calibrated mass-flow controllers. The flow rate of gases was 10 l/h. The carrier gas was passed through a humidifying unit containing deionized water before the furnace, to add moisture to the gas mixture. In tests with synthetic deposit, deposit covered the half of sample, Figure 1.

After testing the samples were moulded in plastic after which the prepared and polished sample crosssections were studied with optical and scanning electron microscope (SEM). The composition of oxide layers was determined with energy dispersive X-ray spectroscope (EDX).

Corrosion behaviour of the materials was based on the estimation of the oxide layer thickness and depth of material degradation. The oxide thickness was determined by optical microscopy. There was some spallation of the oxide layers and thus the measurement results are taken as indicative only. In addition to oxide thickness measurement, weight change measurements were carried out for the specimens exposed without deposit.

Table 1. Chemical composition of test materials [wt%].

Alloy	Cr	Ni	Mo	Nb	Fe	Other
TP347HFG	18.3	11.7	0.23	0.92	bal.	1.64 Mn, 0.33 Cu, 0.4 Si, 0.07 C
Sanicro 25	22.3	24.9		0.5	bal.	3.4 W, 1.5 Co, 2.9 Cu, 0.2 Si, 0.3 Mn, 0.24 N, 0.06C



Figure 1. Sample set-up during exposure with deposit, the half of sample covered with deposit.

3. Results

Table 2 summarises the observed oxide thickness values and depth of possible internal degradation after 1000 h of exposure at 650 and 720°C under 2%O₂-29%H₂O-44%CO₂-0.6%SO₂-0.2HCl-N₂ gas.. After 1000 h exposure without deposit at 650°C TP347HFG showed more extensive oxidation than Sanicro 25. Uneven oxides with a two-layer nodule structure formed on the TP347HFG surface although locally a continuous scale was found in some parts of the sample. With short exposure times (168 and 500 h), only very thin or no oxide scale formed on alloy TP347HFG. EDX analyses showed an iron rich outer oxide layer

and a mixed oxide inner layer mainly containing iron, chromium and nickel. At 720°C only a very thin oxide (~1 µm) formed on the TP347HFG surface and the weight change was negative. The oxidation rate of Sanicro 25 was almost negligible at 650°C. A negative weight change was observed at 720°C and a very thin Cr rich oxide scale was found on the surfaces. Figure 2 shows the weight change results of the exposure without deposit at 650 and 720°C.

Table 2. Summary of the observed oxide thickness and depth of internal degradation on the tested materials after 1000 h of exposure at 650 and 720°C. *outer layer detached.

Material	Environment	650°C		720°C		Notes
		Oxide	Internal	Oxide	Internal	
TP347HFG	Gas exposure	~ 20 µm		~1 µm		2-layer structure (Fe + Fe-Cr oxide layers) at 650°C Cr rich oxide at 720°C
	with CaCO ₃ – 15 wt% CaSO ₄	~80 µm	~50 µm	~150 µm*	~80 µm	Internal carburization, S at GB's at 720°C
	with CaSO ₄ – 0.55 wt% KCl	~100 µm	~30 µm	~100 µm*	~100 µm	S penetration through GB's
San 25	Gas exposure	0.5...1 µm		~1 µm		Cr-rich oxide
	with CaCO ₃ – 15 wt% CaSO ₄	~10 µm	~20 µm	very badly corroded		S at GB's at 720°C
	with CaSO ₄ – 0.55 wt% KCl	200–500 µm	~20–50 µm	<300 µm*	300–500 µm	S, Cl traces at GB's at 720°C

Corrosion was observed under deposits on both test materials. The oxide scale on TP347HFG was continuous around the sample both under deposit layer and above it (deposit covered only the half of the sample). Under the deposit layer the formed oxide was thicker. At 650°C a two layer oxide scale was observed, and at 720°C the outer layer of the oxide was detached, Figure 3. Sulphur was detected inside the oxide scale, and also at grain boundaries under the oxide. No chlorine was observed in the corrosion products. In addition to oxidation, carburisation of TP347HFG was observed at both exposure temperatures with the CaCO₃-CaSO₄ deposit, Figure 4. Carburisation occurred both in the gaseous environment (in the part of sample above the deposit) and under the deposit.

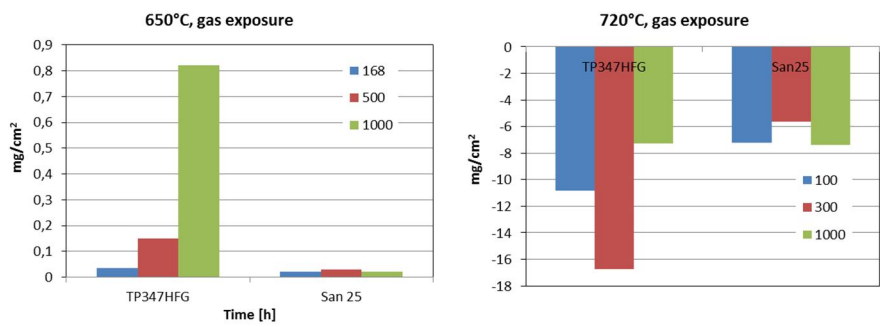


Figure 2. Weight change results at 650 and 720°C under 2%O₂-29%H₂O-44%CO₂-0.6%SO₂-0.2HCl-N₂ gas without deposit.

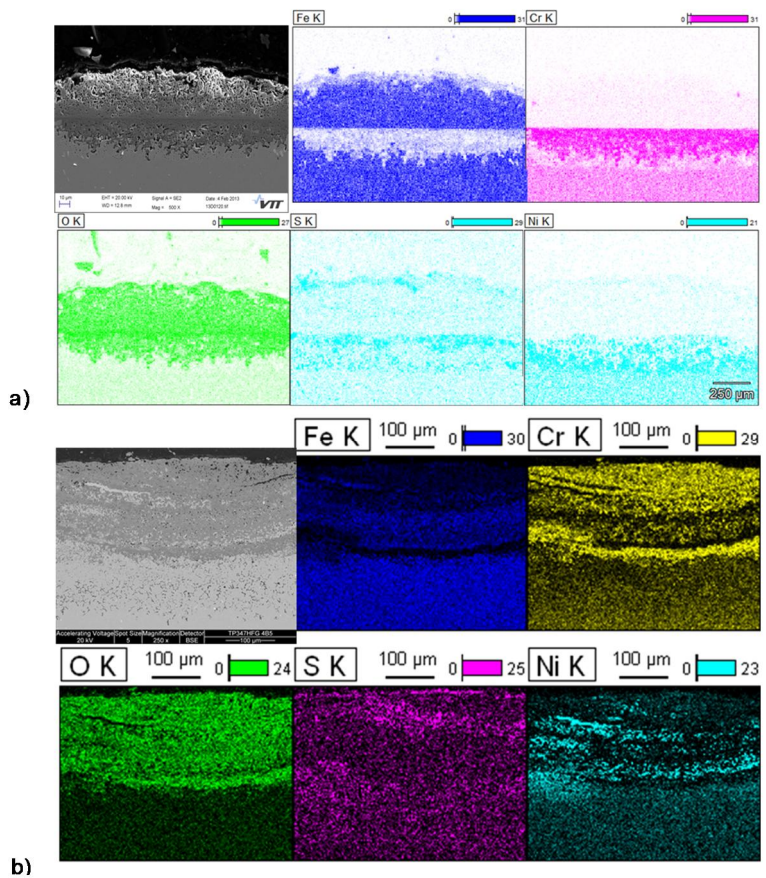


Figure 3. EDX analyses of oxides formed on TP347HFG steel after 1000 h exposure, a) at 650°C with CaSO₄-0.55 wt% KCl and b) at 720°C with CaCO₃ - 15 wt% CaSO₄. Note scales.

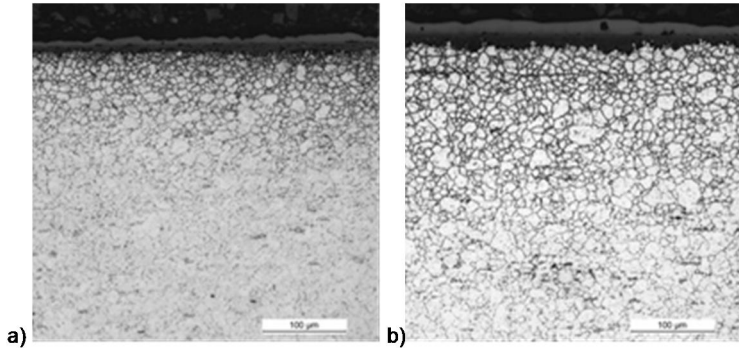


Figure 4. Carburisation of TP347HFG after a) 500 h and b) 1000 h under CaCO_3 - CaSO_4 deposit with simulated oxyfuel conditions at 650°C .

The deposits accelerated corrosion of Sanicro 25 samples under the deposit. A thin oxide layer and some deeper pits through grain boundaries were detected in the gaseous environment (above the deposit), Figure 5. The deposit containing KCl accelerated corrosion of Sanicro 25 at 650°C . With the CaCO_3 -15 wt% CaSO_4 deposit a relatively thin oxide formed on the Sanicro 25 surface and composed mostly of Cr_2O_3 . With the CaSO_4 -0.55 wt% KCl deposit a thick layered oxide was formed structure with an outer Fe rich oxide and an inner Cr rich scale, Figure 6. When the exposure temperature was increased to 720°C , corrosion was accelerated remarkably, especially with CaCO_3 -15 wt% CaSO_4 deposit and the part of specimen covered with deposit was almost completely destroyed, Figure 7. Sulphur was detected in the oxide structures, and traces of Cl were found in the oxide and at the grain boundaries under the oxide scale with the CaSO_4 -0.55 wt% KCl deposit.

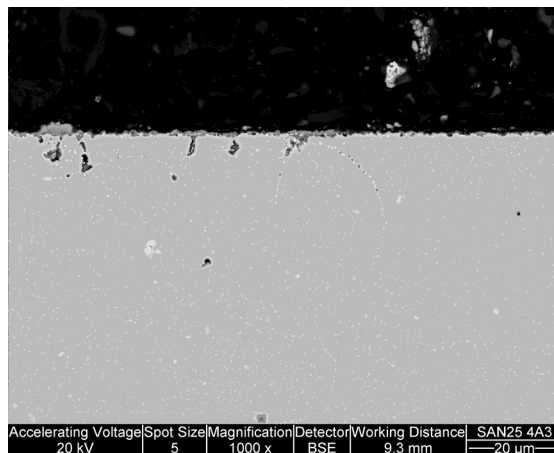


Figure 5. Micrograph of Sanicro 25 exposed at 720°C , the part of the sample above CaCO_3 – 15 wt% CaSO_4 deposit.

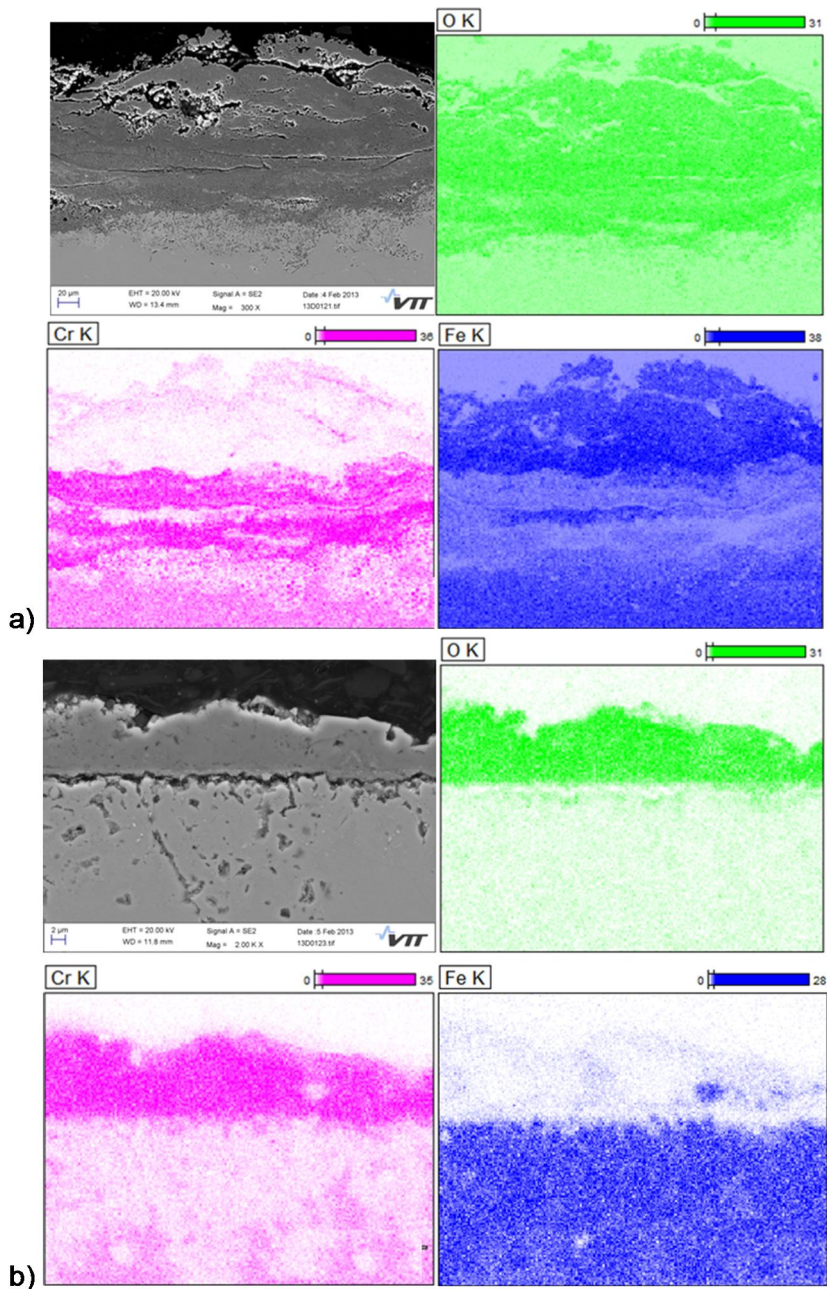


Figure 6. Main components of the oxides formed on Sanicro 25 after 1000 h exposure at 650°C a) with CaSO₄-0.55 wt% KCl and b) CaCO₃ – 15 wt% CaSO₄. Note different scales.

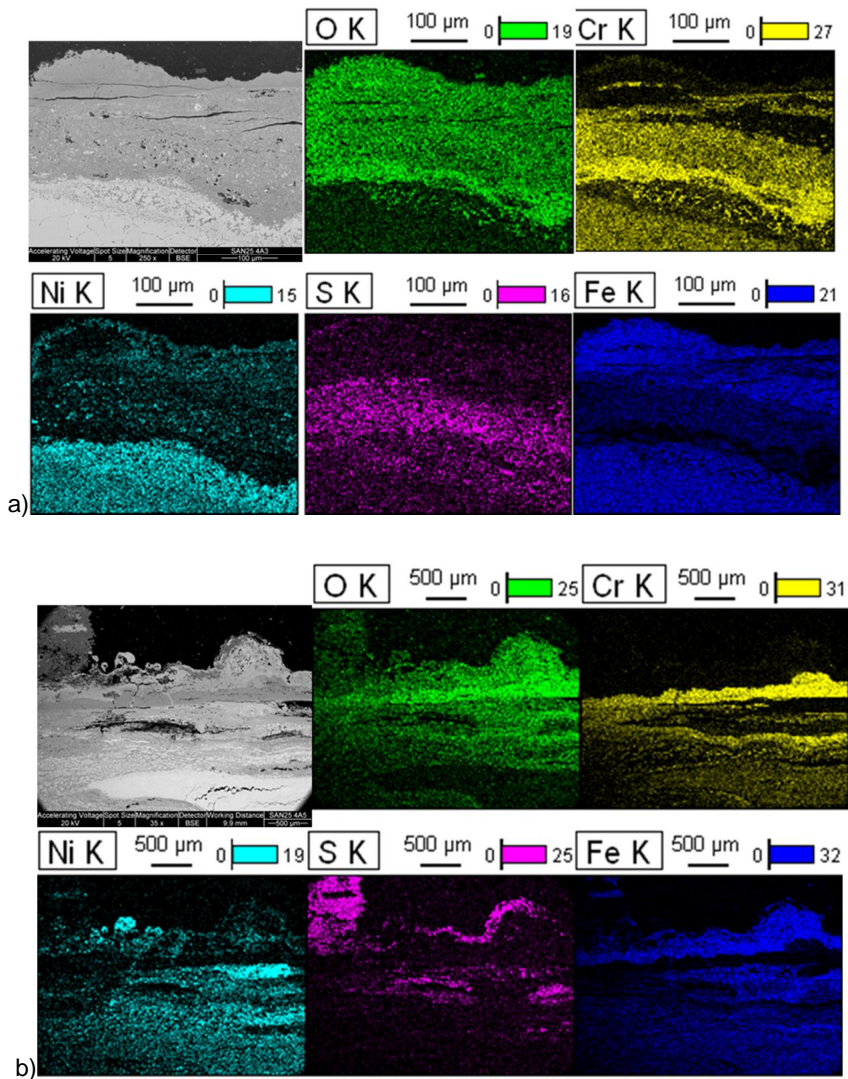


Figure 7. EDX analyses of the oxides on Sanicro 25 after exposure at 720°C a) with CaSO₄-0.55 wt% KCl and b) CaCO₃ - 15 wt% CaSO₄. Note different scales.

4. Discussion

The results imply that without deposit, the oxidation rate under simulated oxyfuel conditions (2%O₂-29%H₂O-44%CO₂-0.6%SO₂-0.2HCl-N₂) is very reasonable at 650°C after 1000 h for both tested materials. At 720°C the oxidation rate was also quite low, however negative weight change was observed due to chromium evapo-

ration, no spallation of formed scales was seen. There is a general agreement that water vapour tends to accelerate the oxidation of chromia formers, especially at temperatures above 700°C [e.g. 17]. The scatter in results (no linear weight loss) was probably due to the depletion of surface chromium causing at least temporary diminishing of evaporation until new chromium is diffused to the surface area.

Corrosion of both test materials was found to occur under deposits. Some sulphur penetration was observed through grain boundaries in chromium depletion area under the oxide scale. At the 650°C exposure with deposits the oxide formed on TP347HFG had a two-layer structure, which had started by nodule formation at weak points such as grain boundaries. This nodular growth would have continued until the nodules grow together to form a continuous oxide covering the whole surface. At 720°C the oxidation rate was higher and the part of the oxide scale, probably outer Fe-rich layer, had peeled off. In particular, exposure with the carbonate deposit resulted in corrosion and carburisation by formation of grain boundary carbides in TP347HFG steel. Earlier results [16] suggest that the critical limits of Cr and Ni content for carburisation are around 20% under the applied gas and deposit environments. The limits may be affected by the Cr/Ni ratio, extended time of exposure, and changes in the chemical and thermodynamic equilibria of the surfaces due to gradual modification in alloys, its oxides and deposits.

At 650°C the KCl containing deposit accelerated the corrosion of Sanicro 25 compared to exposure with CaCO₃ – CaSO₄ deposit. At 720°C this carbonate base deposit was more aggressive and the part of the specimen covered with deposit was almost completely destroyed.

5. Summary

Two boiler tube steels (TP347HFG and Sanicro 25) have been subjected to oxidation/corrosion testing at 650 and 720°C under simulated oxyfuel conditions with and without CaSO₄ based deposits.

A protective chromia was formed on Sanicro 25 during gas exposure without deposits at 650°C. On the surface of TP347HFG a two layer oxide structure with iron based oxides was formed. At 720°C both materials suffered from chromium evaporation. The materials exposed with deposits retained an oxide without notable spalling at 650°C, but at 720°C the spallation of outer oxide layer occurred. Also internal material degradation was observed and some sulphur penetration at grain boundaries below oxide scale was detected. The increase of test temperature to 720°C was detrimental and corrosion rate accelerated remarkably, especially in the case of Sanicro 25 under the CaCO₃ – CaSO₄ deposit.

Acknowledgements

The authors would like to acknowledge the financial support from VTT Technical Research Centre of Finland, Tekes and EU-MacPlus project. The authors would

also like to acknowledge the skilful assistance of T. Kinnunen, J. Veivo, T. Lehtikuusi, J. Metsäjoki and A. Kukkonen.

References

1. Oxy-fuel combustion for power generation and carbon dioxide capture, Ed. Ligang Zheng, Woodhead Publishing Series in Energy 2011, 374 p.
2. Scheffknecht, G., Al-Makhadmeh, L., Schnell, U., Maier, J. Oxy-fuel coal combustion—A review of the current state-of-the-art. *International Journal of Greenhouse Gas Control* 5S (2011) S16–S35.
3. Hjörnhede, A., Montgomery, M., Bjurman, M., Henderson, P., Gerhardt, A. Preliminary experiences with materials testing at the oxyfuel pilot plant at Schwarzepumpe, *Materials for Advanced Power Engineering 2010*, e by J. Lecomte-Beckers, Q. Contrepois, T. Beck, and B. Kuhn 2010.
4. Wigley, F., Goh, B. Characterisation of Rig Deposits from Oxy-coal Combustion, 1st Oxyfuel Combustion Conference, 2009, Cottbus, Germany.
5. Stein-Brzozowska, G., Babat, S., Maier, J., Scheffknecht, G. Influence of oxy-coal on fly ash transformations and corrosion behavior of heat-exchangers, *Proceedings of Oxyfuel Combustion Conference 2*, 2011, Queensland, Australia.
6. Tuurna, S. Sroda, S. Heikinheimo, L. Corrosion kinetics and mechanism of boiler steels under combustion conditions. *Baltica VI: Life Management and Maintenance for Power Plants*, Vol. 1, Helsinki–Stockholm–Helsinki, 8–10 June, 2004.
7. Covino, B., Matthes, S., Bullard, S. Effect of oxyfuel combustion on superheater corrosion, *NACE Corrosion 2008*, Paper No. 8456, Houston, Texas, 2008.
8. Natesan, K., Rink, D.L. Corrosion performance of structural alloys for oxy-fuel combustion systems, 21st Fossil Energy Materials Conference, Knoxville, TN (2007).
9. Fry, A. Adams, B. Davis, K. Swensen, D., Munson, S. Fire-side corrosion rates of heat transfer surface materials for air- and oxy-coal combustion. *IEAGHG Special Workshop on SO₂/SO₃/Hg/Corrosion Issue under Oxy-fuel Combustion Conditions*, January 2011, London.

10. Kiga, T. Experimental study results on corrosion issues in oxyfuel combustion process. IEAGHG Special Workshop on SO₂/SO₃/Hg/Corrosion Issue under Oxyfuel Combustion Conditions, January 2011, London.
11. Fryda, L. Sobrino, C., Cieplik, M., van de Kamp, W.L. Study on ash deposition under oxyfuel combustion of coal/biomass blends. *Fuel* (2010), Vol. 89, pp. 1889–1902.
12. Stein-Brzozowska, G., Maier, J., Scheffnecht, G. Deposition behaviour and superheater corrosion under coal fired oxyfuel conditions. IEAGHG Special Workshop on SO₂/SO₃/Hg/ Corrosion Issue under Oxyfuel Combustion Conditions, January 2011, London.
13. Hünert, D., Schulz, W., Kranzmann, A. Corrosion of steels in H₂O-CO₂ atmospheres at temperatures between 500°C and 700°C, ICPWS XV Berlin, September 8–11, 2008.
14. Piron Abellan, J., Olszewski, T., Penkalla, H.J., Meier, G.H., Singheiser, L., Quadackers, W.J. Scale formation mechanisms of martensitic steels in high CO₂/H₂O-containing gases simulating oxyfuel environments. *Materials at high temperatures* (26) 2009, pp. 63–72.
15. Sellakumar, K.M., Conn R., Bland, A. A Comparison study of ACFB and PCFB ash characteristics. 6th International Conference on Circulating Fluidized Beds, Wurzburg, Germany August 22–27, 1999.
16. Pohjanne, P., Tuurna, S., Auerkari, P. Fireside corrosion and carburization of superheater materials in oxyfuel combustion, Corrosion 2012, Salt Lake City, UT, 11–15 March 2012, International Corrosion Conference Series, NACE International. 2012, pp. 4969–4980.
17. Astemann, H., Svensson, J.-E., Johansson, L.-G. Evidence for chromium evaporation influencing the oxidation of 304L: The effect of temperature and flow rate. *Oxidation of Metals*, Vol. 57, Nos. 3/4, April 2002, pp. 193–214.

A renaissance in Small Punch testing at Swansea University

R. C. Hurst, R. Lancaster, G. Norton, R. Banik & M. R. Bache

Institute of Structural Materials, College of Engineering, Swansea University
Singleton Park, Swansea, SA2 8PP Kingdom

Abstract

For the present work, two specific applications of the Small Punch (SP) test assessment technology were selected, completely different from earlier work in this laboratory. It is shown that the first of these applications takes on board the unique potential of the SP test for testing small quantities of novel or even exotic materials which are candidates for aero engine applications but which cannot easily be produced in quantities which would allow conventional mechanical testing. This has additionally required the development and procurement of new SP test facilities capable of operation up to 1000°C and above. The examples given in this paper are TiAl intermetallic alloys and niobium silicide alloys studied utilising the Code of Practice for SP Creep Testing (Part A). The second application described in this paper illustrates the use of SP testing to assess the tensile and creep properties of repair welded Inconel 718 alloys. The tensile testing was carried out in a specially designed SP test jig but using the SP Tensile and Fracture Testing (Part B) of the Code of Practice. In all applications, the ranking capabilities of SP testing are proven.

1. Introduction

Already, in the early 1990's, Swansea University was devoting significant effort in exploiting the promise of the small punch test in assessing creep and fracture behaviour of steel power plant components [1, 2]. This work tailed off before 2000 principally due to the limited acceptance of the methodology by plant operators but a round robin test programme [3] kick started the formulation of the two part CEN European Code of Practice for SP Testing [4] covering Small Punch Tensile (SPT) and Small Punch Creep (SPC) testing. This rigid foundation for the methodology encouraged a major engagement by many laboratories, particularly in Europe, to exploit the technique further. The authors' laboratory continued for a while in parallel with the development of the Code of Practice, concentrating on power and petrochemical plant components [5, 6] but, as reported in the present paper, has more recently extended its efforts towards new fields.

This extension particularly recognises firstly the unique potential of the SP creep test for testing small quantities of novel or even exotic materials which are

candidates for aero engine applications but which cannot easily be produced in quantities which would allow conventional mechanical testing. Here the continuous evolution of the jet engine has led to the need to develop new alloys to withstand the increasing temperatures experienced in service, providing a major challenge to materials scientists and engineers. Recent advances have led designers to re-evaluate the suitability of traditional alloy systems for high temperature components as operating temperatures approach the limitation of many currently employed Ni-based single crystal blade alloys. Although advanced cooling procedures and thermal barrier coatings continue to ameliorate this issue, development of the so-called "Vision 20 alloys", materials which are envisaged to replace the established nickel-based superalloys for elevated temperature turbine disc and blade applications, within a twenty year horizon, now constitutes a major research activity. The promising mechanical properties at service temperatures in excess of 1000°C make refractory metals and alloys, such as niobium silicides, potential choice candidates for ultra-high temperature applications. For assessment of these candidate materials, the small punch (SP) test technique immediately becomes a front-runner amongst presently available miniaturised assessment techniques and offers a cost effective method of supporting future alloy design. Notwithstanding this application for new materials, as mentioned above, the evolution to higher turbine entry temperatures requires high integrity and reliability of the protective coatings applied even to current turbine alloys which, in principle, could also be studied using the unique advantage of SP testing for small zones in components but is not the subject of the present work. To date, the vast majority of interest in the SP technique has focussed on relatively ductile alloys. Prior to the application of SP tests to potential Vision 20 alloys, some of which may be brittle in nature at least at ambient temperature, a thorough assessment of the technique for an archetypal brittle alloy must be considered. Therefore, the present paper provides evidence to support the use of SP testing to define creep characteristics for a titanium aluminide intermetallic alloy, including correlations to conventional creep data. Finally, the laboratory reports on the use of the SP test as a methodology to rank fracture behaviour in a variety of solutions related to repair technologies and associated post-weld heat treatments applied to Inconel 718 components.

2. Experimental procedures

Three pieces of test equipment have been developed for the range of testing foreseen in this work: a traditional, but modified, SP creep tester for tests up to 750°C, an advanced creep tester for higher temperatures up to 1100°C and a test jig for tensile and fracture testing up to 850°C as described in Section 3.3. The traditional SP test rig (as displayed in Figure 1) consists of a top loading system that applies a constant load via a 2mm diameter, high strength Nimonic punch to the centre of the sample located in a recess on a stainless steel die and clamped around the edges by a stainless steel upper die.

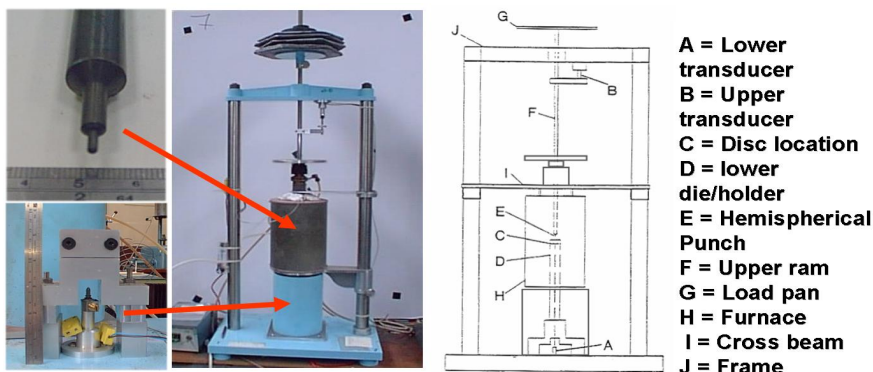


Figure 1. Traditional SP test rig facility.

Displacement is measured by upper and lower linear variable displacement transducers (LVDT), one positioned to monitor the deflection underneath the sample and the other to measure the penetration depth of the punch into the top surface of the disc. A single zone radiant furnace applies heat and argon, which is contained within a metallic tube, is introduced from the bottom of the chamber to protect the sample from oxidation. This experimental set up has successfully been utilised for many years for the characterisation of a range of materials, notably copper based alloys, steels and their weldments and aluminium. After the publication of the CEN Code of Practice, some modifications were introduced in order to accurately reflect the Code approved design. The Code of Practice also describes the required test procedure covering disc specimen preparation, installation, heating, loading and environmental control, which were in any case based on the procedures practised in this laboratory.

For advanced high temperature testing a completely new design has been introduced which facilitates test temperatures up to 1100⁰C with a specially designed furnace and protective environment control along with new construction materials. An illustration of the new test set up to accommodate higher temperatures is displayed in Figure 2. In the traditional SP test set-ups, a stainless steel tube is commonly used to contain the flow of argon around the disc but this had to be replaced by an alumina tube at such high temperatures. To avoid argon leakage, cooling jackets were fitted to the ends with PTFE seals to aid in the retention of frictional contact between the jacket and the tube, and to ensure a hermetic seal for the argon. On the traditional test set-up, the majority of the internal components including the rods and die, were made from stainless steel. However, due to the temperature limitations of the material, these components have now been remanufactured from a Nimonic alloy.

Perhaps the most crucial change concerns the puncher itself. The majority of previous SP testing has been performed using a high strength Nimonic alloy punch, whereas some other laboratories also use ceramic spheres retained in an alloy punch. This alloy, however, has its own limitations and was found not to be

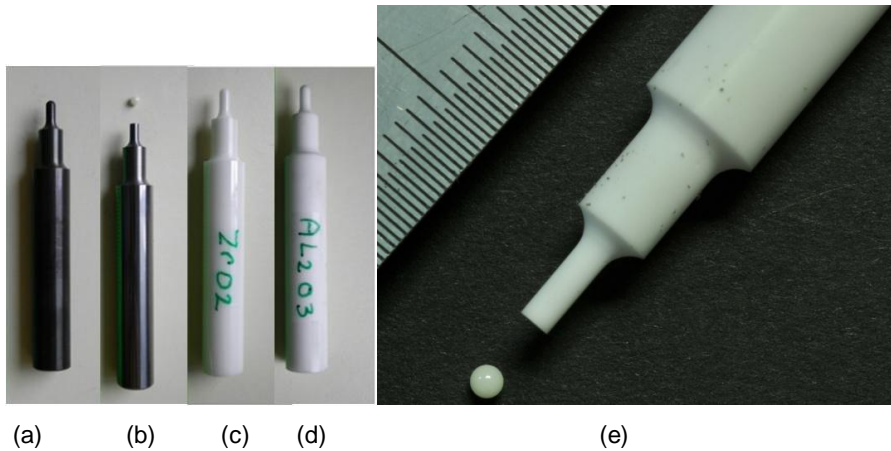


Figure 3. Alternative punch designs and materials (a) tungsten carbide punch (b) tungsten carbide punch with concave end and ceramic ball (c) zirconium oxide punch (d) aluminium oxide punch (e) aluminium oxide punch with concave end and ceramic ball.

An initial feasibility study using a tungsten carbide punch in the traditional design (3a) showed reasonable promise as the indenter exhibited minimal oxidation or deterioration to the radius tip over a short term period. However, in longer-term tests the tip of the punch appeared to deform and oxidation was evident on the surface of the tip radius. A similar result occurred with a tungsten carbide indenter in the form of 3b, as the end of the indenter deformed under long term loading leading to non-uniform contact with the ball.

A series of ceramic indenters in the two designs were then manufactured from aluminium oxide and zirconium oxide. Tests using the 3e design indenters were performed but difficulties were found during loading due to the intricate machining required for the concave end of the punch to match the spherical profile of the ball. Contact between ball and punch was unstable, leading to the tip of the punch breaking under a bending motion. The fully integral alumina and zirconia punches have proven to be an effective choice of material and design as post-test studies have revealed no oxidation effects due to the nature of the material and little or no damage of the punch tip.

In all the experiments reported in this paper, the miniature SP disc samples were sectioned from 9.5mm diameter rods to an approximate thickness of 0.8mm then ground and polished to the final thickness of 0.5mm ($\pm 5\mu\text{m}$) in preparation for testing.

3. Results and discussion

3.1 Small Punch Creep testing applied to a γ TiAl intermetallic alloy

Small Punch (SP) Creep testing has been applied to the gamma titanium aluminide Ti-45-2-2 with the data obtained being utilised as a benchmark for the relatively quick and inexpensive assessment and ranking in terms of creep performance. Such γ TiAl intermetallics have been the subject of much development over the past twenty or so years and are beginning to see service in both the automotive and aerospace industries [11]. Despite this development these materials still remain 'inherently brittle' at room temperature, although ductility is much improved at elevated temperatures.

The traditional SP creep testing equipment and apparatus has been employed for this research with the procedure following that proposed in the European Code of Practice. A 2mm diameter Nimonic alloy punch with a 1mm die clearance was used on 9.5 mm diameter specimens with a thickness of 0.5 mm ($\pm 5 \mu\text{m}$). In the first instance it was important to demonstrate that the technique was capable of obtaining reproducible results for such materials, especially when considering the initial high stress plate bend loading nature of an SP specimen. Figure 4 shows examples of SP creep curves obtained at the same load but at three different temperatures and figure 5 shows how the failure develops directly above the punch tip and not around the periphery for this material.

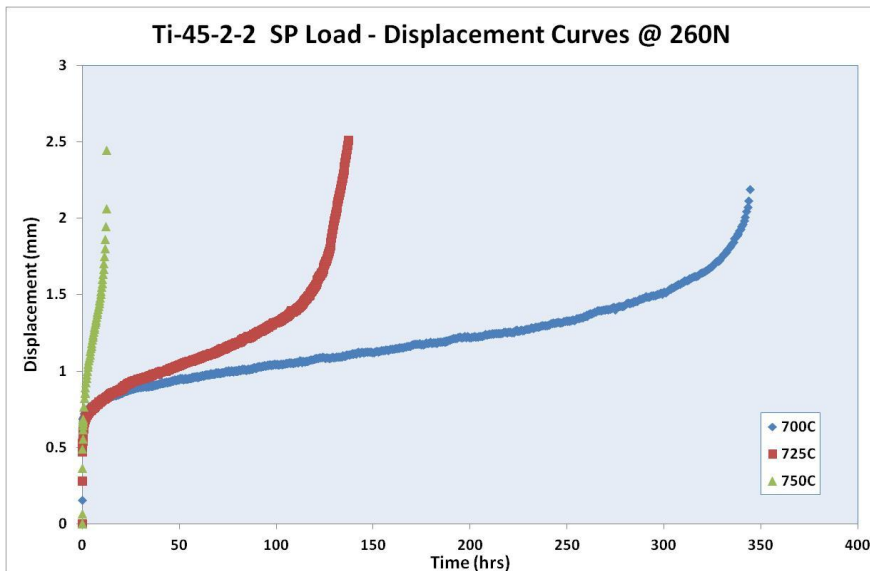


Figure 4. Temperature dependence of SP creep curves for Ti-45Al-2Mn-2Nb.

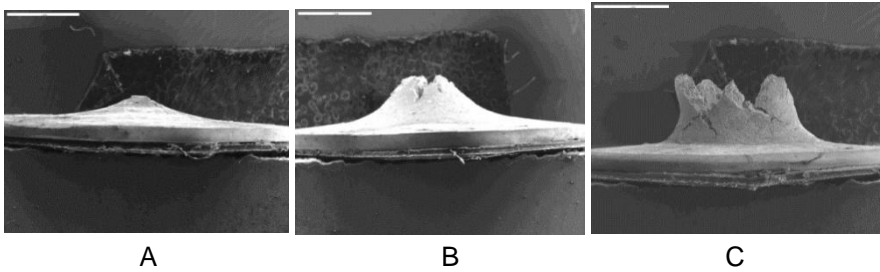


Figure 5A–C. illustrate the through disc deformation at life fractions of 0.25, 0.5 and 1 respectively, for a test conducted at 750°C and 235N.

The load-failure life results obtained at 700 and 750°C shown in Figure 6 show the consistency of the SP results to be as good if not better than many uniaxial creep results, which augurs well for the ranking capabilities of SP creep testing should newly developed intermetallics will be compared with one another. Furthermore, SEM fractography revealed that all SP tests exhibit an inter-lamellar failure mode in the same manner as equivalent uniaxial tests.

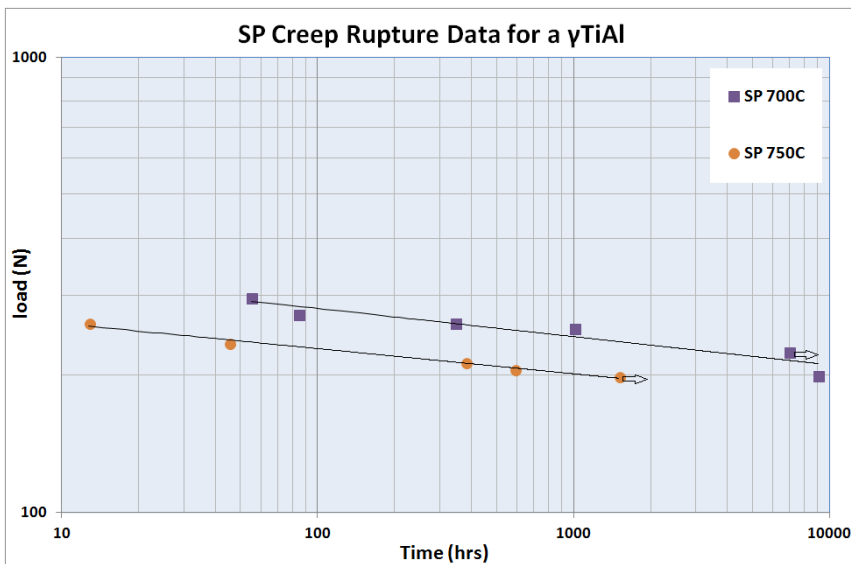


Figure 6. Rupture life dependency on applied SP load.

The data presented in Figure 6 were compared to equivalent uniaxial data obtained at the same temperatures. However, this uniaxial data was obtained under constant stress conditions as opposed to constant load, which did not lend itself to defining a clear cut k_{SP} value to satisfy the SP load-uniaxial stress correlation

equation, $F_{SP}/\sigma = 3.33 k_{SP} R^{-0.2} r^{1.2} h_0$, as proposed in the Code of Practice. However in the absence of constant load creep data, it was shown that SP minimum displacement rate (Δ_{min}^{\bullet}) could be simply correlated with uniaxial minimum creep (ϵ_{min}^{\bullet}) rate according to $\Delta_{min}^{\bullet} = \epsilon_{min}^{\bullet} / 0.15$ providing a Monkman-Grant [12] type relationship as shown in Figure 7. One advantage of such a correlation when ranking different materials is the reduction in test duration to reach the minimum creep rate rather than awaiting rupture.

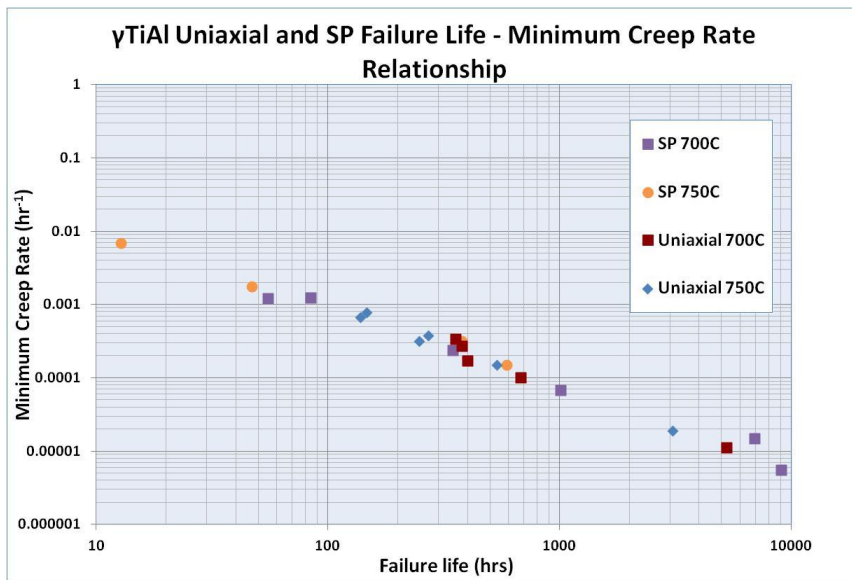


Figure 7. Monkman-Grant relationships for SP and uniaxial data.

3.2 Small Punch Creep testing applied to Niobium Silicide alloys

Refractory metal-based silicide alloys are under consideration to replace more traditional nickel base superalloy material systems for high temperature turbine operations. A particular class of these materials include the niobium silicide (NbSi) alloys, which offer an increased temperature capability (melting temperature >1700°C) and reduced density. This family of alloys typically consist of a high strength Nb₅Si₃ phase held within a niobium solid solution and previous studies have revealed that the creep rupture properties of NbSi materials compare favourably to second and third generation single crystal superalloys. However, as previously mentioned, for the purpose of determining the creep properties of a range of novel experimental alloys, conventional uniaxial creep can be an expensive procedure due to the relatively large volumes of stock material required to cover a full stress-

temperature matrix. Small punch creep testing on the other hand offers a far more pragmatic solution where material availability is limited.

A series of small punch creep experiments is ongoing for a range of NbSi material variants alongside an established single crystal superalloy CMSX-4. The compositions of these alloys are considered proprietary at this stage; therefore the three variants currently reported are simply designated A to C. One other variant had failed during loading. The same test conditions were used throughout, including an applied load of 150N, temperature of 1050°C and an argon atmosphere to limit oxidation effects. Figure 8 illustrates the small punch creep behaviour of the three NbSi variants compared to CMSX-4. The results show that variant A has a comparable performance to CMSX-4, with the other two alloys exhibiting less favourable creep properties. However, post test inspection revealed that variant A had indeed failed, with brittle radial cracking around the periphery of the punched hole, (also found in variants B and C), whilst at the same exposure time the single crystal material was still intact as shown in Figure 9. From Figure 8, it is also possible to rank the materials in relation to the time period taken to endure 500 µm of displacement, with variant A performing the best and variant C the worst. This ranking method is an efficient tool but rather arbitrary in the choice of a suitable displacement for making the comparison. An alternative is to compare the minimum displacement rates of the different materials and these results are given in Table 1. The table shows that the minimum displacement rate for variant A is similar to the single crystal alloy whereas variants B and C show higher rates.

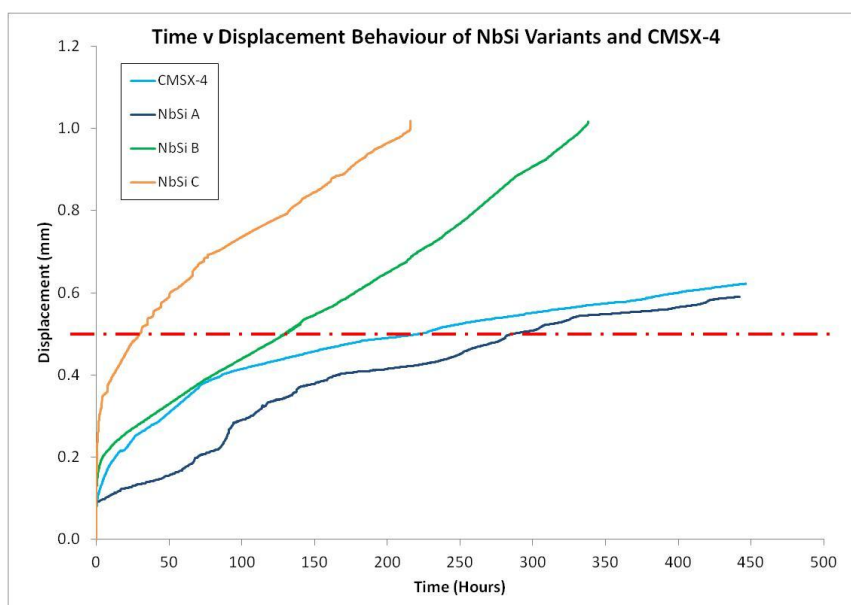


Figure 8. Displacement v time behaviour for NbSi variants in comparison to CMSX-4.

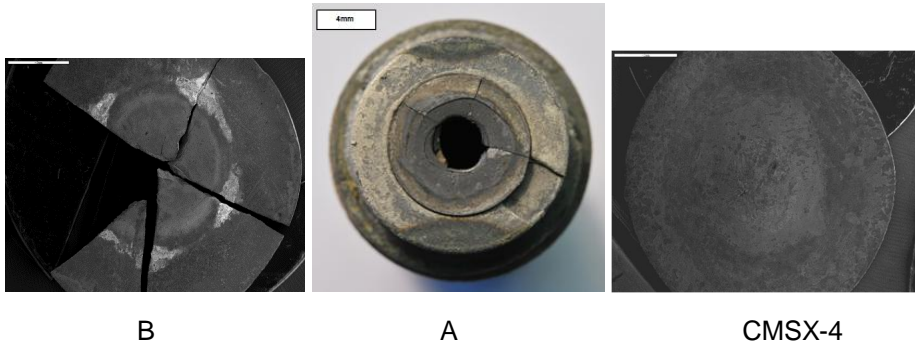


Figure 9. Fracture surface image of NbSi variant B and A (still in test jig) compared to CMSX-4 alloy.

Table 1. NbSi variants ranking positions for minimum displacement rate and time to fixed displacement.

Alloy	Minimum Displacement Rate (MDR) (mm/hour)	MDR Ranking	Time to Fixed Displacement (TFD) – 500 μm (h)	TFD Ranking
NbSi A	6.9E-08	1	286	1
CMSX-4	1.1E-07	2	222	2
NbSi B	5.5E-07	3	129	3
NbSi C	7.3E-07	4	30	4

3.3 Small Punch Creep testing applied to repair welded IN718 alloys

Both the SPT and SPC test allow meaningful mechanical property data to be obtained from welded regions and low volume additive structures created from the use of novel repair processes. For the nickel based superalloy IN718, the SP test techniques are being applied to both laser based additive structures (ALM) and substrate material subjected to multiple or localised heat treatments. Three heat treatment conditions of wrought IN718 and three orientations of the ALM material are under assessment. The SPT tests have been conducted in a special test jig constructed completely from Nimonic 90, capable of operating up to 850°C, inserted into the load train of a universal testing machine. The 9.5 mm diameter SP discs, were either extracted from heat treated wrought IN718 or from ALM IN718 deposition “fingers” using wire electrical discharge machining. The orthogonal orientations for the ALM discs were designated axial, transverse and longitudinal, Figure 10.

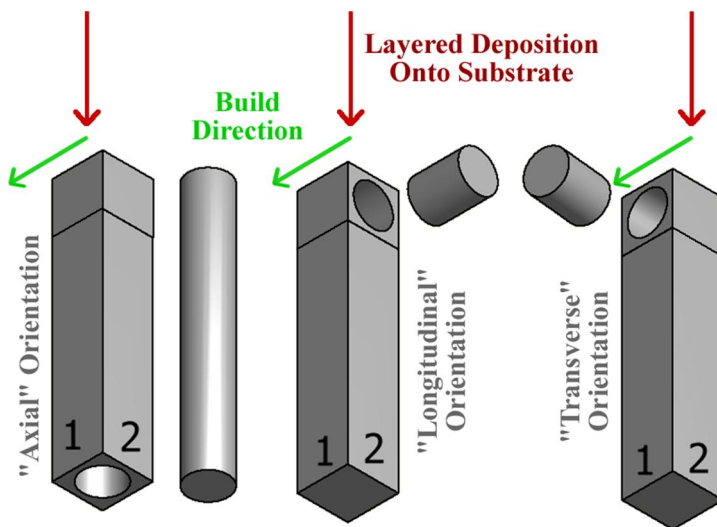


Figure 10. Orientations of extracted cylinders for ALM SP disc preparation.

Due to the extremely high strength of this material at the test temperatures, leading to early failure of punchers, a deviation from the Code of Practice had to be made by using a 4mm diameter punch and a receiving die of 6.4mm. The first series of results obtained at a temperature of 630°C, are shown in Figure 11.

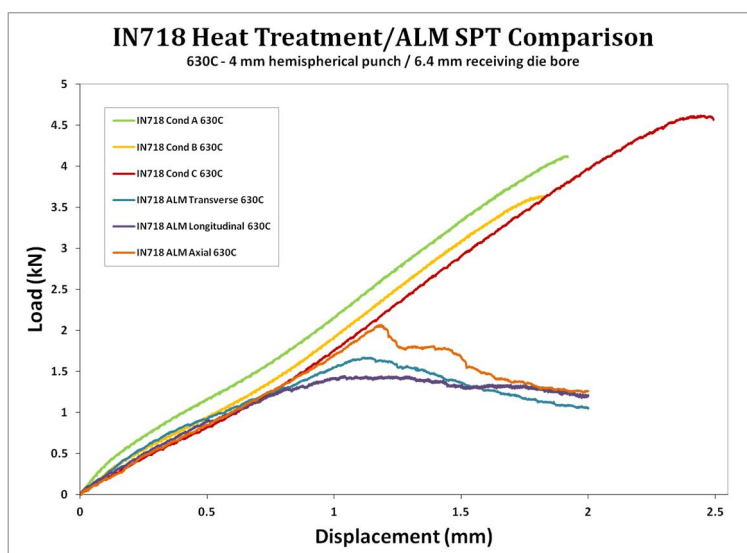


Figure 11. SPT load-displacement curves of IN718 ALM from different orientations compared to heat treated conditions A, B & C at 630°

The series of heat treatments pertain to increasing levels of post weld heat treatment with A being the least and C being the most extensive. The tensile curves reflect the effect of decreasing performance with increasing heat treatments in terms of the slopes of the curves even though the condition C specimen exhibited a higher failure load. Tests on conventional tensile specimens from heat treatments A and B give average UTS values of 1207 and 1125 MPa and average yield stress values of 994 and 915 MPa respectively, indicative of the same trend. The ALM SP specimens, on the other hand, exhibit quite different tensile curves with an inability to withstand increasing load after less than 1mm displacement. The fact that there appears to be some dependence on the test piece orientation is not strictly surprising in view of a directionality that evolves within the microstructure resulting from the additive process but the SP test involves a biaxial load and interpretation is not a formality. Distinct differences in fracture behaviour were shown by the wrought and ALM materials, as shown in Figure 12, where a ductile cup failure is typical of the heat treated IN718 whilst relatively brittle multiple cracking was noted in the ALM discs.

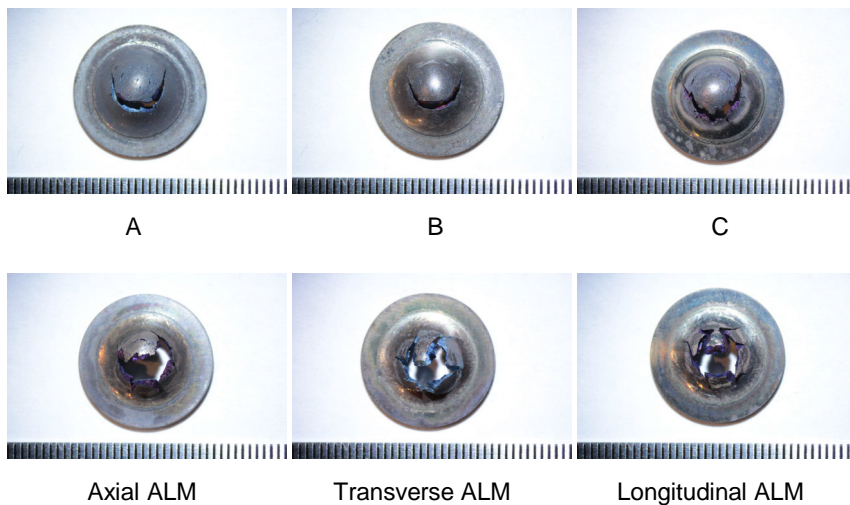


Figure 12. Images of failed heat treated (A,B and C) and ALM discs.

The SP creep tests are also being conducted at 630°C employing the improved traditional SP creep equipment. As the main purpose of the SP creep testing is to quickly rank any effect of multiple post weld heat treatments, it is proposed to only take the SPC tests so far as to identify the minimum displacement rates. Unfortunately only a single test result, on heat treatment C, is available at the present time but demonstrates the potential of the SP creep test in enabling the determination of minimum displacement rates, in this case 0.0006 mm/hr. In Figure 13 the first 100 hours of the SP creep curve is shown for comparison with a conventional uniaxial creep curve for heat treatment A under a similar test loading. The main

difference between the curves appears to lie in the enhanced primary region commonly observed in SP creep tests. It is recognised that SP displacement and uniaxial strain are by no means equivalent even if the loads are comparable and without the challenging conversion of displacement to strain no absolute comparison of minimum creep rates can be made at present.

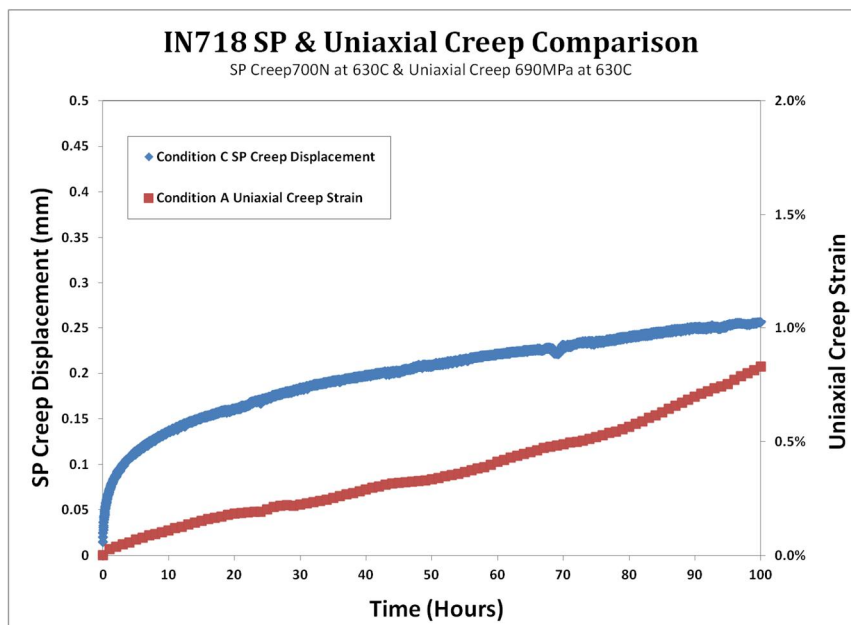


Figure 13. SP creep curve for condition C compared to uniaxial creep curve for condition A.

4. Conclusions

SP creep and SP tensile testing equipment has been successfully modified in order to facilitate high temperature testing and ranking of novel alloys and repair welded components for future aerospace engine applications.

γ TiAl intermetallic alloys have been evaluated in the temperature range 700–750°C both for minimum creep rate and stress rupture behaviour yielding consistent results which will provide a satisfactory baseline for ranking against alternative alloys.

Three new niobium silicide alloys have been SP creep tested for comparison with a CMSX-4 single crystal alloy under a single load at 1050°C. The SPC test was perfectly capable of ranking the three NbSi alloys. One variant was found to compare favourably with the creep displacement response for the single crystal but not in terms of creep fracture resistance. This variant warrants further investigation whereas research on the other two variants could now be terminated.

A comparison between the tensile properties of heat treated and laser prepared (ALM) IN718 alloys at 630°C using the SP tensile test revealed the potential for the test to differentiate between the effects of multiple post weld heat treatments. A SP creep series has been started at the same temperature and the first test shows promise for eventual creep rate determination. The application of SP tensile tests to ALM material is able to detect the anisotropic material behaviour related to microstructure and micro-texture

Acknowledgements

The current research is funded by the EPSRC Rolls-Royce Strategic Partnership in Structural Metallic Systems for Gas Turbines (Grants EP/H500383/1(Research) and EP/H022309/1(Training)).

References

1. Parker, J. D. & James, J. D. Pressure Vessels and Piping, ASME, 1994, Vol. 279, pp 167–172.
2. Norris, S. D. & Parker, J. D. Deformation Processes During Disc Bend Loading. Mater. Sci. Technol., 1996, Vol. 12, pp 163–170.
3. Bicego, V., Rantala, J. H., Klaput, J., Stratford, G. C., Di Persio, F. & Hurst, R.C. The Small Punch test method: Results from a European creep testing Round Robin. Proceedings of the 4th International Conference on Advances in Materials Technology for Fossil Power Plants, 2005, pp. 692–702.
4. CEN Workshop Agreement, Small Punch test method for metallic materials. Brussels: CEN; 2006. CWA 15627:2006 E.
5. Di Persio, F., Stratford G. C. & Hurst R. C. Validation of the Small Punch Test as a method for assessing ageing of a V modified low alloy steel. Baltica VI, Life Management and Maintenance for Power Plants. Helsinki, June 2004. VTT Symposium 234, Vol. 2, pp. 523–535.
6. Stratford, G. C., Kobayashi, K. & Klaput, J. The Small Punch (SP) Creep Testing of Low Alloy Steels. Proc. of Int. Conf. Materials Science and Technology 2005 (MS&T'05), Pittsburgh, 2005.
7. Roberts, P. R., Borradaile, B. J. & Mitchell, R. J. Material Sampling from Components within the Nuclear Industry and the Extraction of Useful Materials Information. Derby : 2010.

8. Blagoeva, D. T. & Hurst, R. C. Proc. 3rd Int Conf. on Integrity of High Temperature Welds. IOM Communications Ltd., London, April 24–26, 2007, pp. 463–472.
9. Gülçimen, B., Durmu, A., Ülkü, S., Hurst, R., Turba, K. & Haehner, P. Determination of low temperature mechanical behaviour of the heat affected zone of a P91 steel weld using the small punch test technique, Determination of Mechanical Properties of Materials by Small Punch and other Miniature Testing Techniques, SSTT-2. Ostrava, 2012
10. Wallin, K. The scatter in K_{Ic} results. Engineering Fracture Mechanics, 1984, Vol. 19, pp. 1085–1093.
11. Norris, G. Power House. <http://www.flightglobal.com/news/articles/power-house-207148/>, 13/06/2006.
12. Monkman, F. C. & Grant N. J. Proc. ASTM, 1956, 56: p. 593–602.

Practical application of impression creep data to power plant

S.J. Brett ¹, J.H. Rantala ² & S. Holmström ²

¹Nottingham University
Nottingham, UK

²VTT Technical Research Centre of Finland
Espoo, Finland

Abstract

The measured “minimum” creep rate in the impression creep (IC) test is currently obtained from a “stabilized” deflection rate, and the time to “stabilization” is somewhat arbitrarily chosen at durations up to 500 h, regardless of the applied load. Nevertheless, IC tests have been successfully utilized for aged ½CrMoV and P91 steam line components by conducting tests at the same load so that the deflection rates can directly be compared and used for ranking. By this experience, the IC test is an excellent tool for material ranking and lifing of service exposed material.

However, further development in the IC data assessment procedures and the translation between IC and uniaxial test is still needed for determination of the lower stress range material creep properties from the IC test. It is suggested that the deflection rate should be correlated to a Monkman-Grant type relation with the calculated deflection rate at specified “strain/deflection” against the corresponding uniaxial strain rate at the same specified strain. The modified MG relationship should correct the increasing error expected at IC test conducted at decreasing loads. To be able to do this the strain rate as a function of time (or strain) should be available for primary creep of the uniaxial test. The corrective impact of the modified MG has to be verified by further analysis and testing.

1. Introduction

The impression creep (IC) test is well established and the validity of the technique has been supported by test data for a number of metallic materials at different temperatures and stresses. Over recent years, the test method has attracted increasing attention in power plant material and component assessment. The small sample size means that the method is often practically non-destructive. The method is also useful in nuclear materials research projects where the amount of test material is often limited. This paper describes the test techniques and shows some examples of practical applications of the method on power plants.

2. Impression creep test techniques

The impression creep test involves the application of a constant load by a flat 10*1 mm indenter on a 10*10*2.5 mm material sample in the creep regime. The loading arrangement developed by Nottingham University is shown in Figure 1. The displacement is recorded and displacement rate as a function of time is calculated from the data. The test duration is typically only 500 hours and the displacement rate at the end of the test can be correlated with uniaxial creep rate of the material at the same stress. The reference stress approach based on FE analysis of the test has been used to convert the mean pressure, p , under the indenter to the corresponding uniaxial stress, σ , i.e.

$$\sigma = \eta p \quad (1)$$

and to convert the creep displacement, Δ^c , to the corresponding uniaxial creep strain, ε^c , i.e.

$$\varepsilon^c = \frac{\Delta^c}{\beta d} \quad (2)$$

where η and β are the conversion factors and d is the width of the rectangular indenter, normally 1 mm. The method of determining the η and β values has been described in [1–3]. Figure 2 shows typical specimen dimensions used for the tests using a rectangular indenter. When the indentation displacement is small, it is assumed that the η and β values are only dependent on the dimension ratios, w/d and h/d , of the specimen. For the 10*10*2.5mm square specimen with an indenter width $d = 1$ mm, the conversion factors obtained from 3D analyses [3] are $\eta = 0.430$ and $\beta = 2.180$. Up to 5 different load levels or temperatures can be applied on a single test specimen in a stepped test, which is useful in cases when test material is scarce.

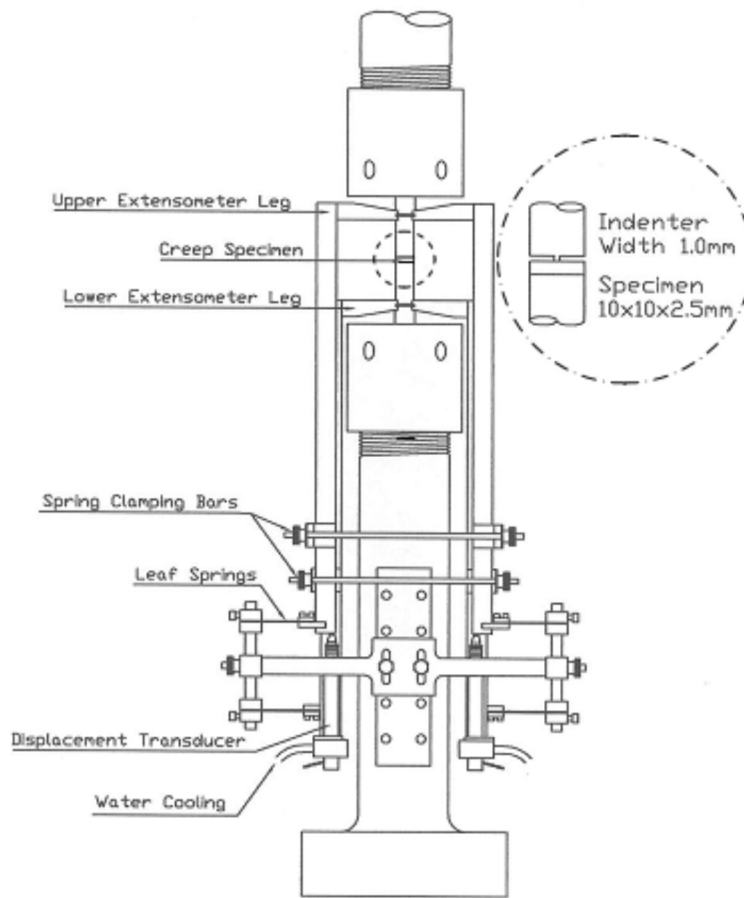
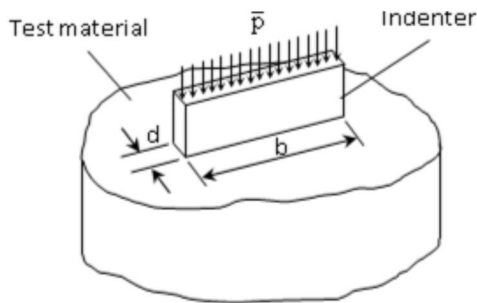
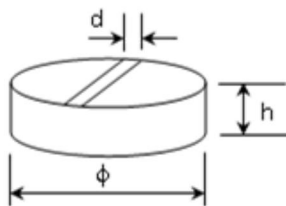


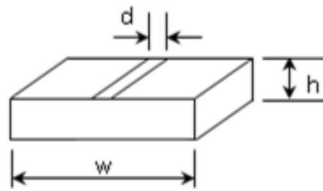
Figure 1. Loading arrangement and extensometry for the impression creep test.



(a) Schematic diagram of impression creep testing with a rectangular indenter



(b) Cylindrical specimen



(c) Square specimen

Figure 2. Loading Impression creep principle and test specimens.

3. Examples of application of impression creep data.

Impression creep data has so far mainly been applied practically to power plant in the case of two materials, aged $\frac{1}{2}$ CrMoV and grade 91 steels.

The steel $\frac{1}{2}$ CrMoV was widely adopted for the high temperature steam pipe-work systems on coal and oil fired plant built in the UK in the 1960s and early 1970s and many of these units remain in operation today. In the case of the coal fired plant, the units have now operated well beyond their original design life (typically 100kHrs) and possible failure of parent material has to be addressed as a structural integrity issue. The role of small scale sampling and impression creep testing is to rank the component parts of steam lines, ie. the individual pipe lengths, in terms of current creep strength, allowing the weakest to be targeted for inspection during future plant outages. The aim is to inspect those components most vulnerable to creep failure in service sufficiently frequently to detect damage development at as early a stage as possible. The components can then be replaced before failure as part of a managed long term strategy.

More recently, grade 91 steel has been used throughout the world as a high temperature material for headers and steam pipework. In the UK the first applications started in the late 1980s, with the oldest plant now approaching 100kHrs operation against a typical design life of 150kHrs. Most structural integrity issues to date have been associated with welds and it might be argued that parent material failure is a less urgent issue. While this may be true of grade 91 steel pro-

duced in the correct martensitic microstructural condition, it is not necessarily true of this steel in an incorrectly microstructural condition. Unfortunately numerous examples have been encountered of grade 91 steel entering service with an aberrant non martensitic or mixed martensitic/ferritic microstructure. Material in this condition may have a creep strength below the expected lower bound of the material scatter band. The role of small scale sampling and impression creep testing here is to provide an estimate of the strength of suspect components relative to the normal scatter band and to aid decisions about whether to replace them immediately or to leave them in service.

The proposed assessment methodologies are slightly different for the two steel types, reflecting the different types of data that have so far been accumulated.

3.1 Aged $\frac{1}{2}$ CrMoV

To date in the UK approximately 180 individual main steam and hot reheat pipe sections have been sampled and impression creep tested using a standard test condition of 2.248kN (96.7MPa) at 600°C [4]. All samples were taken on coal-fired units producing steam nominally at 568°C. This constitutes a substantial background database against which to compare any new data generated, constituting an estimated 6–7% of the component population of the units involved and an estimated 1–2% of the total UK population.

The data generated are shown in Figure 3 in terms of values of Log impression creep rate (Log ICR) along the vertical axis as a histogram converted into a line plot. This represents the as-measured creep strength in a typical bell shaped curve with strength increasing from left to right, allowing individual results to be placed within the observed scatter band. The vertical broken line passes through the impression creep result of material which a parallel programme of conventional creep testing has shown to have a conventional uniaxial creep life corresponding to the lower bound ISO value. In principle all specimens to the right of this line represent material having current creep strength sufficient to have met the original design life requirement when the plants were built. Unless these plants are required to operate for longer than a further design life therefore, these components represent a low structural integrity risk. Approximately 43% of the population lie to the right of (ie are stronger than) the ISO LB value.

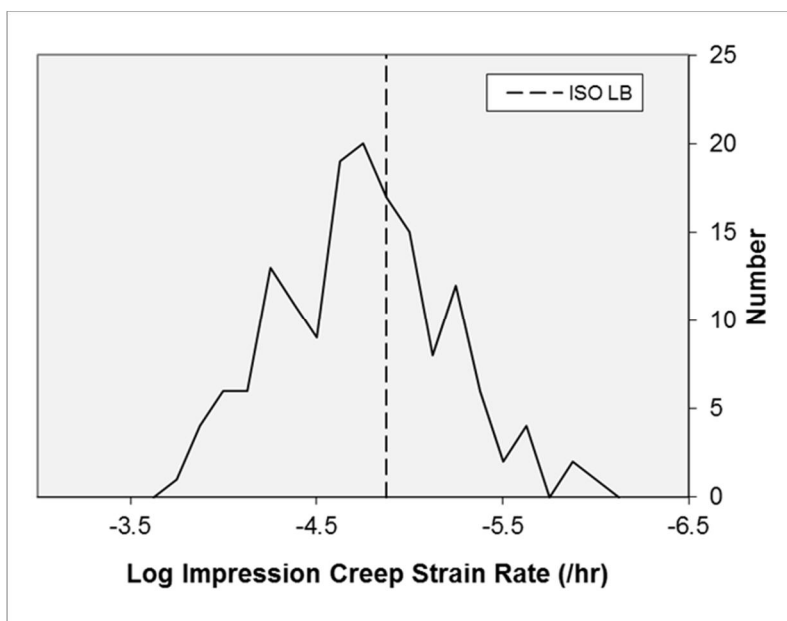


Figure 3. Distribution of impression creep strength of sampled ½CrMoV specimens tested (measured as-sampled values).

The relative simplicity of the test makes the result highly reproducible. As an example, four tests carried out on the same ex-service ½CrMoV material (identified as JFA2676) using four different impression creep rigs at two laboratories have produced creep strain rates with a mean and standard deviation of $1.3705\text{E-}05 \pm 2.16661\text{E-}06$ /hr. This corresponds to -4.8675 ± 0.0720 on a log scale. This level of experimental scatter is much smaller than the overall range of creep strength encountered (see Figure 4), making the test technique a viable discriminator of strength level.

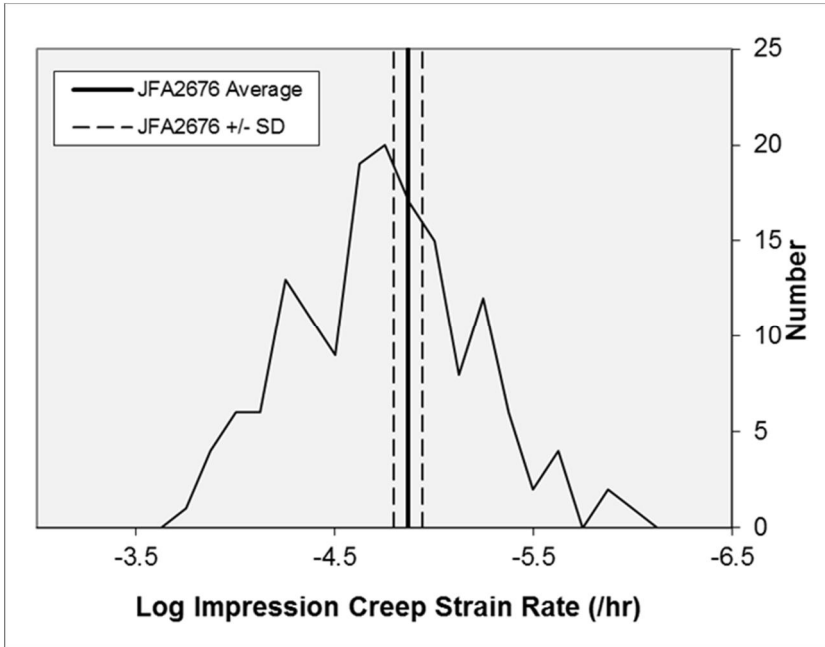


Figure 4. The mean value (four tests) \pm 1 standard deviation for one chosen $\frac{1}{2}$ CrMoV material compared to the background distribution of impression creep strength of all specimens tested.

The strength of each individual item in the distribution reflects the period of operation after which it was sampled. For the first 171 samples tested the operating hours were $\sim 194\text{kHrs} \pm 31\text{kHrs}$. Provided the operating hours of any further steam pipe sections sampled from coal-fired plant are broadly comparable, and they are tested under the same conditions, their strength can be immediately placed within the existing as-measured distribution.

Where the further items sampled have been in service for a period significantly different from the range of operating hours of the samples tested to date, a correction for operating hours may be required to provide a more appropriate comparison.

This can be carried out in the following way. Figure 5 shows the variation with operating hours of impression creep strain rate obtained from main steam samples taken from a range of stations and units. As might be expected, there is a tendency for the strain rate to increase with the operating hours at the time of sampling, as creep strength degradation increases with time.

The line drawn through the data has the simple form:

$$\text{LOG ICR}_{\text{as-sampled}} = C \times [\text{Operating Hours}] - D \quad (3)$$

where $\text{ICR}_{\text{as-sampled}}$ is the impression creep rate in the as-sampled condition and C and D are constants.

This can be used to correct the impression creep rate measured on a specimen sampled after one period of operation to the expected value after any other period of operation. In particular it can be used to move points up or down parallel to the line to a common point of comparison. This allows the strength of specimens to be compared after eliminating the effect of operating hours.

In principle any common period of operating hours could be chosen, but one of particular interest is the start of life. In this case, in terms of the ratio of log impression creep strengths for each specimen:

$$\text{LOG ICR}_0 / \text{LOG ICR}_{\text{as-sampled}} = -D / C \times \text{Operating Hours} - D \quad (4)$$

$$\text{LOG ICR}_0 = -D \times \text{LOG ICR}_{\text{as-sampled}} / C \times \text{Operating Hours} - D \quad (5)$$

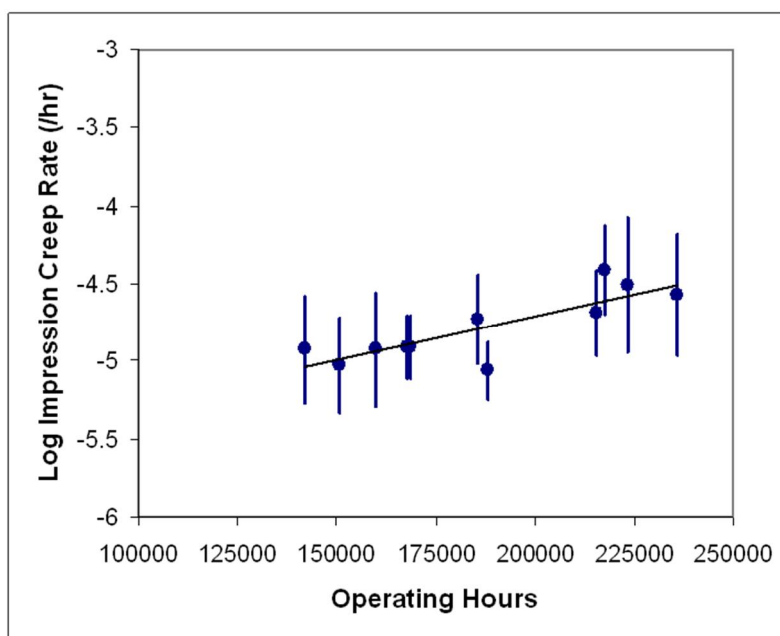


Figure 5. Relationship between impression creep strength and operating hours at the time of sampling for main steam line specimens.

The modified distribution is shown in Fig.6. In principle, this represents the distribution of impression creep strength values which would have been obtained if all the materials concerned had been tested before they entered service.

In fact, because the correction preserves the relative position above or below the line of each point in Fig.5, and also the scatter associated with it, the spread of the distribution is likely to be somewhat wider than the actual distribution which would have been obtained at the start of life. The measured relative strength and scatter is a result both of the original strength on entering service and subsequent degradation in service. Material which has experienced less arduous operating

conditions will appear stronger while material which has experienced more arduous operating conditions will appear weaker. These effects can be expected to cancel each other out in the middle of the distribution so the mean value will be more accurate.

With this caveat, Fig.6 represents a best estimate of the original creep strength distribution for the material investigated. It should also be noted that it has been derived from tests on real plant materials and can therefore be described as representing the “true” scatter band.

Further samples tested, with their as-measured creep strength corrected for operating hours in the same way, can be placed within this distribution. This effectively places their creep strength at the start of life within the material scatter band.

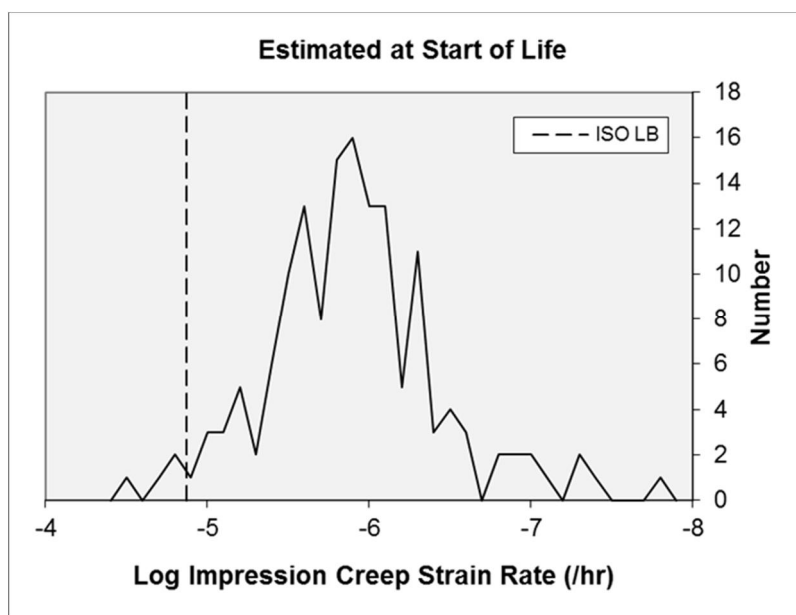


Figure 6. Distribution of impression creep strength of specimens tested corrected to the start of life, using a conversion factor derived from Figure 5.

3.2 Grade 91

For grade 91 the situation is a little different. Firstly fewer samples have been taken from plant and secondly, although grade 91 is used widely, the plant operating conditions vary. The earliest UK applications, retrofit headers, have tended to operate at ~580°C, pipework and headers on early CCGTs typically at 540°C, and pipework and headers on current CCGT plant operating at 565°C. However significant amounts of data have been produced on a limited number of casts, including one (identified as Bar 257) which has been demonstrated to have a creep strength

at the lower end of the scatter band for the normal martensitic microstructural condition. This material can be used to illustrate an alternative strategy for estimating creep strength relative to the normal scatter band.

The starting point is the Monkman Grant relationship for grade 91 quoted by Parker [5] from data produced by Spigarelli, Kimura and Ellis:

$$\text{MCR} = 0.1 t_f^{-1.16} \quad (6)$$

where MCR is the minimum creep strain rate (1/hr) and t_f the failure time (hrs) in conventional uniaxial creep tests.

The relationship was found to fit data generated independently by RWE npower well, providing confidence in its more general applicability. Accepting this relationship, the Cipolla creep life equation for grade 91 [6] can be used to derive lines of MCR corresponding to mean and lower bound strength levels, as shown in Figure 7 for 600°C.

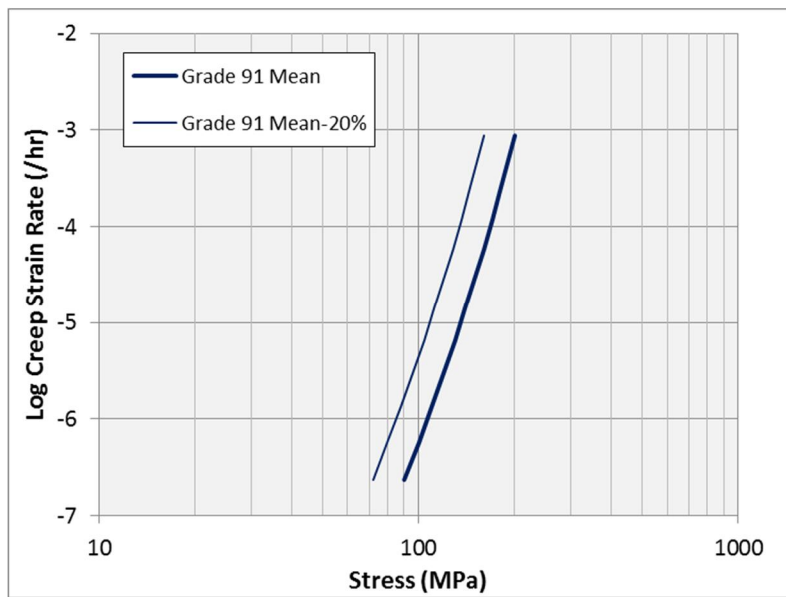


Figure 7. MCR corresponding to mean and lower bound [6] strength levels at 600°C.

The next step is to compare these lines with the creep strain rates obtained on Bar 257, known to represent lower bound material as shown in Figure 8 [7]. The data show both good agreement between uniaxial and impression results and also good agreement for both types of test with the lower bound line, particularly at stresses >100MPa. It should be noted that, for testing normal strength grade 91 at 600°C, 100MPa is the lowest stress that can be used if usable impression creep strain rates are to be obtained within an acceptably short test duration.

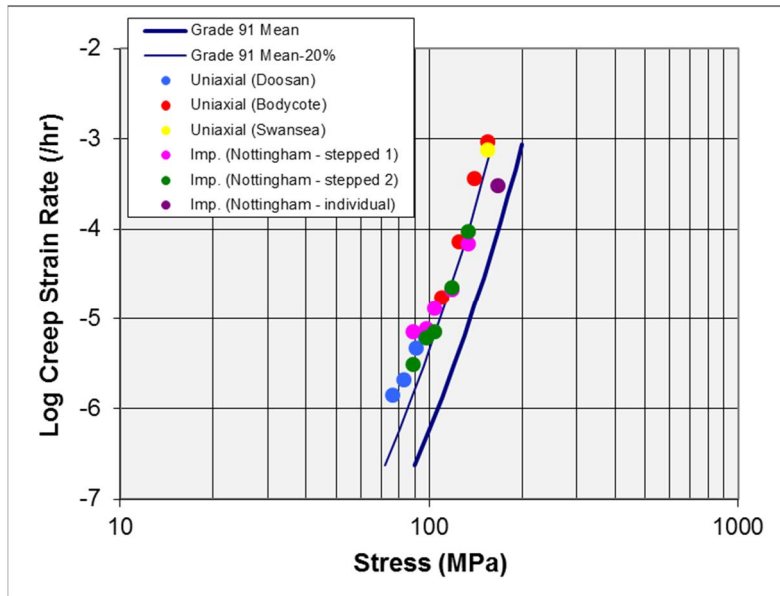


Figure 8. Uniaxial (MCR) and impression creep strain rate data for material Bar 257 compared to the Monkman Grant derived MCR lines for mean and lower bound [6] material at 600°C.

In principle the creep strength of any other material can be estimated in a similar way by plotting its impression creep strain rate on this graph. As examples the Bar 257 results from stepped stress impression test are shown with results from two other grade 91 materials in Figure 9. One (2328) is a typical P91 pipe which has been demonstrated by conventional uniaxial creep testing to be stronger than Bar 257. The other (RWE Sim) is a P91 pipe deliberately mis-heat treated to produce an aberrant non martensitic microstructure. The test results in Figure 9 are sufficient to successfully identify Bar 257 as lower bound, material 2328 as stronger, and the aberrant RWE Sim material as weaker.

The results from all three materials can also be converted into estimates of rupture life using the Monkman Grant relationship. In Figure 10 the rupture lives derived in this way are shown with actual creep lives measured for these materials. The correct relative creep strength is reproduced.

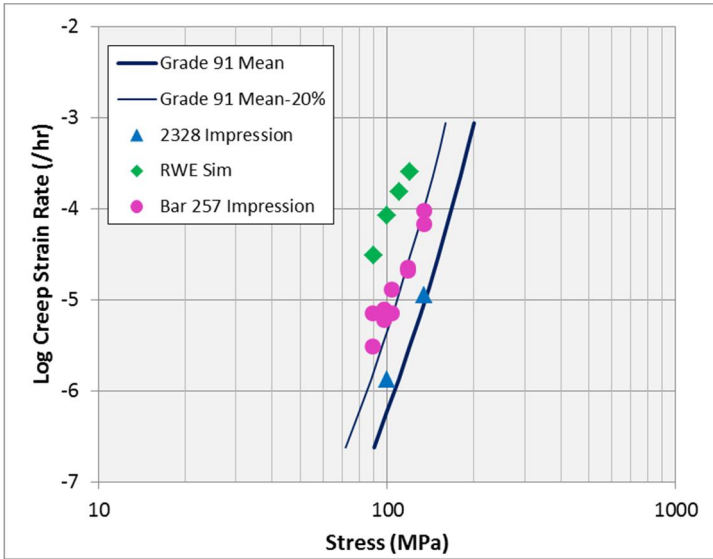


Figure 9. Impression stepped stress tests on three grade 91 materials of differing creep strength compared to the Monkman Grant derived MCR lines for mean and lower bound [6] material at 600°C.

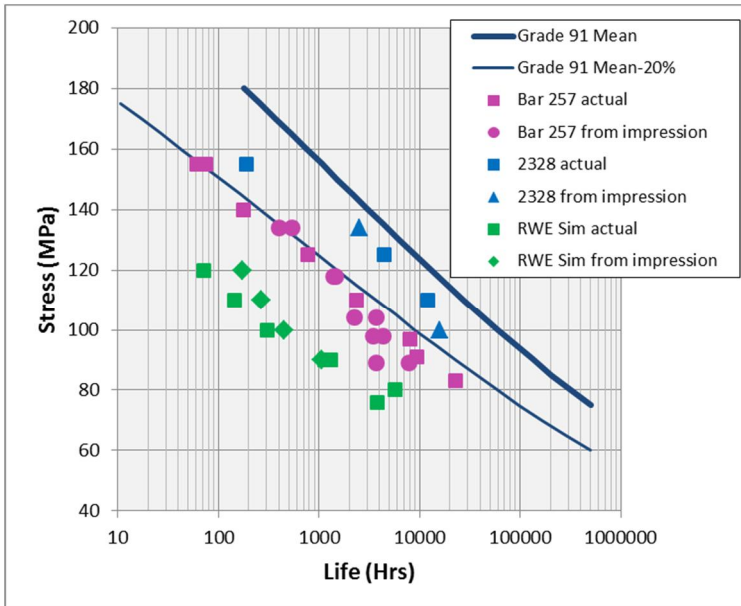


Figure 10. Creep lives estimated from impression creep tests and the Monkman Grant relationship for the three materials shown in Figure 9 compared to actual lives obtained in uniaxial tests at 600°C.

Discussion

As shown earlier in this paper the measured (momentary) IC creep rate can be correlated by the Monkman-Grant relation, i.e. minimum strain rate vs. uniaxial rupture time. The IC "minimum creep rate" is calculated from a "stabilized" deflection rate (time derivative of Eq.2). The IC strain rate is directly proportional to the measured deflection rate. The time to "stabilization", i.e. at what instant in time (or deflection) should the deflection rate be measured, and what should the time step be, are questions yet not entirely defined for the IC methodology. To date the deflection rate used in the strain rate calculation derive from deflection rate measured at durations of up to 500 h, regardless of the applied load.

As shown for P91 the measured IC strain rates at lower stresses (<100 MPa) are consequently "too high" in comparison to the minimum strain rates from uniaxial test (see Figs 8, 9). The higher IC strain rates lead to decreasing calculated creep lives (in comparison to corresponding uniaxial test rupture lives) as can be seen in Fig.10. The reason for the deviation is most likely that at 600°C the "saturation time" of around 500h in the IC test in comparison to the time to minimum strain rate for uniaxial test do not translate into the same "location" on the creep curve, the IC test most likely still being in primary creep regime.

It is suggested that the deflection rate should be correlated to a Monkman-Grant type relation with the calculated deflection rate at specified "strain/deflection" against the corresponding uniaxial strain rate at the same specified strain. The modified MG relationship should correct the increasing error expected at IC test conducted at decreasing loads. To be able to do this the strain rate as a function of time (or strain) should be available for primary creep of the uniaxial test. This is though not usually supported by the standard way of reporting creep results. In most cases only time to rupture and minimum strain rate are reported. The corrective impact of the modified MG has to be verified by further analysis and testing.

The above mentioned potential discrepancy does not affect the utilization of the IC test as has been done for the ½CrMoV material since all the test have been conducted at the same load and the different deflection rates can directly be compared and used for ranking.

The IC test is an excellent tool for material ranking and lifing of service exposed material. Further development in the IC data assessment procedures and the translation between IC and uniaxial test is still needed for determination of the lower stress range material creep properties from the IC test.

Acknowledgements

The impression creep tests for all materials shown in this report were carried out at Nottingham University for RWE npower. One of the authors (SJB) would also like to thank RWE npower for their agreement to include some previously unpublished uniaxial and impression creep data for this subproject collaboration.

References

1. Hyde, T.H., Yehia, K.A. and Becker, A.A. (1993) Interpretation of impression creep data using a reference stress approach, *Int. J. Mech. Sci.*, 35, 6, pp. 451–462.
2. Hyde, T. H., Sun, W. and Becker, A. A. (1996) Analysis of the impression creep test method using a rectangular indenter for determining the creep properties in welds, *Int. J. Mech. Sci.*, 38, 10, pp. 1089–1102.
3. Hyde, T.H. and Sun, W. (2009) Evaluation of the conversion relationship for impression creep testing *Int. J. of Pres. Ves. & Piping* 86 (11), pp. 757–763.
4. Brett S J. Small Scale Sampling and Impression Creep Testing Applied to Aged $\frac{1}{2}$ CrMoV Steam Pipework Systems, EPRI International Conference on Advances in Condition and Remaining Life Assessment for Fossil Power Plants – Coal, Gas and HRSG, Hilton Head Island, South Carolina, October 17–19, 2012.
5. Parker J. Private communication
6. Cipolla L & Gabrel J. New Creep Rupture Assessment of Grade 91, ETD Conference: Industry and Research Experience in the Use of P/T91 in HRSGs/Boilers, IOM3, London, December 7–8, 2005.
7. Brett S J. Application of Impression Creep Testing, Presentation at “Practitioners Meeting” held at Nottingham University, March 8, 2011.

“On site” X-Ray Diffraction method to observe the creep phenomenon and its propagation at the nano-scale

Giovanni Berti^{1,2}, Francesco De Marco² & Maria Eva Del Seppia²

¹University of Pisa, Earth Science Department, Lab. R&D on XRD
Via S.Maria 24, 56126 Pisa, Italy

²XRD-Tools s.r.l.
Via Cosimo Ridolfi 14, 56124 Pisa, Italy

Abstract

This paper introduces some elementary concepts to recognise creep occurring in metals and welds, using X-Ray diffraction as a non-destructive method. Understanding creep is complicated by the intrinsic difficulty to observe the on-going process. We introduce here new achievements of X-Ray Diffraction (XRD) as a non-destructive test in its strictest sense, and examples are reported on measurements carried out on a P22 grade steel collector and welded T92 grade steel component.

Progressive dynamic deformation results in plastic effects which affect the crystal rheology, or more generally the lattice rheology; this rheology depends on the associated micro-nano scale structural properties. Moreover, time, temperature and specific loads (pressure) play the conditioning role of grain boundaries size and shape, thus affecting the microstructure, mechanical properties and component integrity. Methods and related technology capable to investigate nano-scale for in-service inspections are currently needed as claimed by several industrial circumstances. In this context, when using XRD, the lattice d-spacing becomes observable with true metrological impact. When welds are considered, d-spacing and microhardness show significant similarities which testify how the dynamic deformation is translated on average from nano to micro scales.

1. Introduction

When heating a material to extended and repeated cycles, it tends to be affected from progressive and dynamic deformations. This phenomenon is denominated “creep”; it is connected to typical plastic and viscous behavior of materials. Such deformations affect the crystalline lattice arrangement and are related to the conformational properties, time and temperature of thermal exposure, along with the applied load intensity.

The phenomenology of creep is described by a “power law” [1], where tensile and nano-structural properties play a fundamental role. From a practical point of view, the nowadays technology achievements enables observations, analyses and measures from exhausted systems after their life cycles consumption. In general said components are for heat exchanging coils in thermo-electric plants and, in particular, on ultra-supercritical coal boilers, and on a steam collector and a boiler bottom plate. The present work shows the state of the art and the results obtained from

- a large exhausted P22 steel component from a steam collector used in large scale electric power generation industries;
- a new small T92 steel component as manufactured and welded, never used on plant.

With no claim to offer exhaustive solutions to this complex problem, the present paper aims to illustrate the following salient points based on preliminary investigations on the XRD sensitivity to evaluate

- 1) changes of the structural integrity on critical points of components
- 2) micro/nano structural set up in relation to the changes
- 3) procedures to detect deformations, degradation and creep related effects when using DifRob® type diffractometer that has been intended to be used for in service inspection.

Aiming at this goal we here will present component analyses carried out in laboratory, as a preliminary step to on site investigation of creep on plants in service.

The technology requirements to observe dynamic deformations with the appropriate resolution are the capability to distinguish among the various crystal lattice arrangements, the different atom aggregations and the deviation from the lattice arrangement taken as a reference. The scale of observation of said technology should be at least on the order of nanometers or tenths of nanometers. XRD meets these requirements although it is traditionally confined to observations on either exhausted or removed or cut components; moreover the investigated specimens are usually adapted to the diffractometers, in order to achieve the best result from diffraction analyses. In other words traditional XRD provides static observations on specimens which may be poorly representative of the investigated creep phenomenon as dynamical deformation.

2. Experiments and methods

Several tests have been carried out on said components of industrial interest, taken from plants and investigated by using the non-destructive XRD method.

DifRob®4 is a prototype which has been used to perform the X-ray measurements. DifRob®2 is a new instrument with advanced performances which is intended to improve the results presented here. It suffices here to give reasonable evidence of the sensitivity to investigate creep related factors and detectability of the phenomenon.

2.1 “On site” X-Ray Diffraction and related technology

The measures presented here are carried out in lab, though we would use the term “On site X-ray Diffraction” because they are prelude to actual on site measurement. It is of interest here to state that “On site X-ray Diffraction” is the concept intended to perform measurements directly from the specimen under investigation. Differently from the traditional in lab XRD, such method shall invert the concept of adaptability. It is in fact up to the instruments to adapt themselves as much as possible to the manufactures under investigation. This new inverted concept allows for the following:

Table 1. Data of the main devices from the first and the second generation of DifRob®, in comparison.

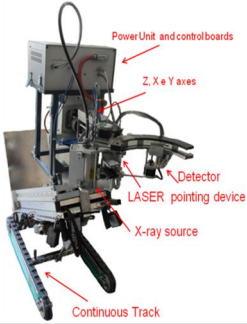
a: DifRob®1		DifRob®1	DifRob®2	b:DifRob®2
	Size (cm)	220x100x100	100x50x100	
	Weight(Kg)	250	100	
	X-ray tube Power (nominal) (W)	2200	50	
	X-ray tube Power (effective) (W)	450	50	
	Cooling	Liquid	Air	
	Detector	Geiger	Micro Detector	
	Interface	RS232	USB	
	Moving	wheels	Continuous track	

Figure 1. DifRob®1 (a) and DifRob®2 (b). and related technical specifications for comparison. [2]

- 1) it extends the applicability of X-ray diffraction to specimens, independently of their size, weight and shape;
- 2) it merges the consolidated knowledge on X- ray diffraction with the new technological aspects (e.g. robotics, communication technology).

⁴ Trademark owned by XRD-Tools s.r.l.

Figure 1 shows the first prototype DifRob[®]1 (a) and the second one DifRob[®]2 (b). The related technical specifications are reported in Table 1. The instrument can be considered an industrial robot where the main arm is equipped with a double Euler cradle and it can turn around a joint rotation axis and around an axis which is orthogonal to the investigation plane. The robot is placed on a mobile device which allows for a number of degrees of freedom which are necessary to perform in service inspections [2],[3].

DifRob[®]2 is equipped with a forced-air cooling on the X-ray tube; the reduced X-Ray power consistently reduces the exposure risk of the operators and the working area delimitation. The detector is provided with a Si pin diode. The prototype DifRob[®]2 has been recently developed, with improvements related to the adaptability for industrial components and usability on site.

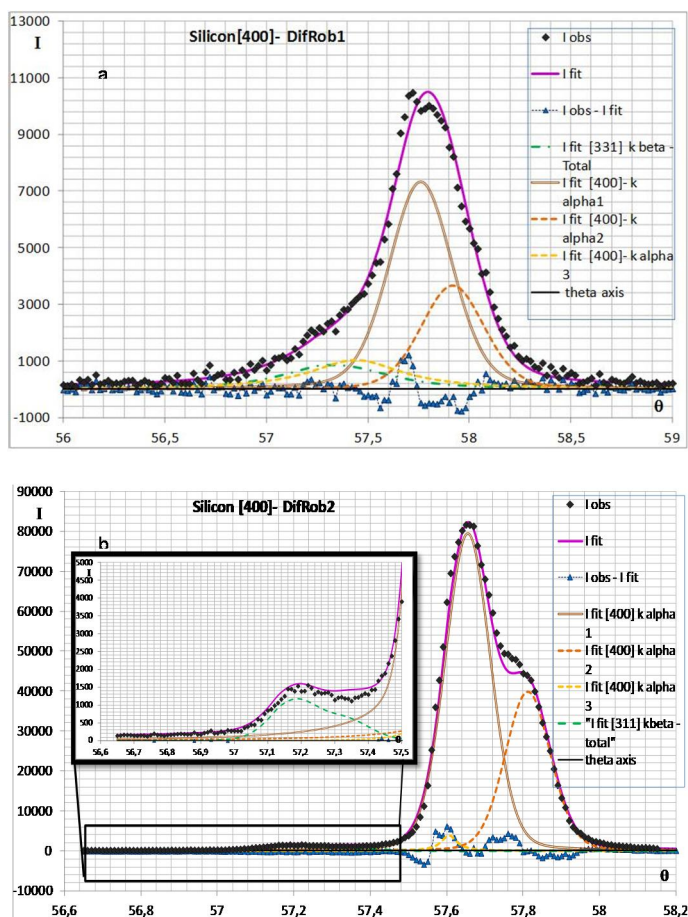


Figure 2. Patterns from a [400] oriented Silicon specimen and related decomposition of the XRD signals in α_1 , α_2 and α_3 radiation. Data have been collected by DifRob[®]1 (a) and DifRob[®]2 (b). The interpolation system is DISVAR 96 [4].

Figure 2 reports on the data collected from the same [400] oriented Silicon sample when using both DifRob[®]1 (a) and DifRob[®]2 (b). The numerical interpolations of data proves the significant reduction in the Full Width Half Maximum (FWHM) parameter of the main diffraction line. This enhanced resolution enables the emerging background modulation, from which the residual trace of the $K\beta$ radiation from the [331] silicon plane reflection becomes recognisable.

Figure 2a and 2b report on the diffraction line decomposition in their radiation elementary components (i.e. $K\alpha_1$ and $K\alpha_2$) of the silicon plane [400]. The blue line straddling around the background indicates the difference between the collected data and the interpolation. There is an additional contribution (yellow dashed line) that is traditionally labelled as the $K\alpha_3$ component which has an instrumental origin. This contribution is significantly reduced in Figure 2b, thus enabling the clear separation between the green lines ([311] plane) and the yellow line (instrument) which have distinct origin. This improved resolution of DifRob[®]2 is in fact relevant to in-service detection of creep.

Table 2 reports on the parameters values used for the interpolation process and related decomposition of the diffraction line profile. The representation function is the pseudo-Voigt [4] with the following parameters:

- θ is the diffraction line position of the α_1 component
- I is the maximum intensity distribution of the α_1 component
- FWHM is the full width at half maximum of the α_1 component
- P is the mixing parameter of the α_1 component; this parameter is typical of the pseudo-Voigt function which merges among Lorentian and Gaussian shape factors.
- SH_{31} is the relative spectroscopic shift on the diffraction pattern of the α_1 and α_2 components.
- Sl_3 is the line broadening of the instrument origin component α_3 .
- I_3/I_1 is the ratio between the maximum of intensity distribution of α_3 and α_1 components.
- The h,k,l are the indices of the reflecting planes of $K\beta$ radiation [331] and $K\alpha$ [400] respectively.

Table 2. Comparison between the interpolated profile parameters, related to the patterns collected by DifRob[®]1 (the first prototype) and DifRob[®]2 (the latest prototype) on the same oriented Silicon specimen.

h	k	l	θ	l	FWHM	p	SH ₃	Sl ₃	l ₃ /l ₁
DifRob[®]1									
3	3	1	57,29	612	0,5608	0,295	0,05	0,05	0,05
4	0	0	57,761	7325	0,3677	0,78	0,32	0,555	0,141
DifRob[®]2									
3	3	1	57,182	1109	0,1673	0,883	0,049	0,049	0,049
4	0	0	57,655	79496	0,14	0,861	0,049	0,049	0,049

3. Preliminary tests on industrial components

3.1 P22 steel component

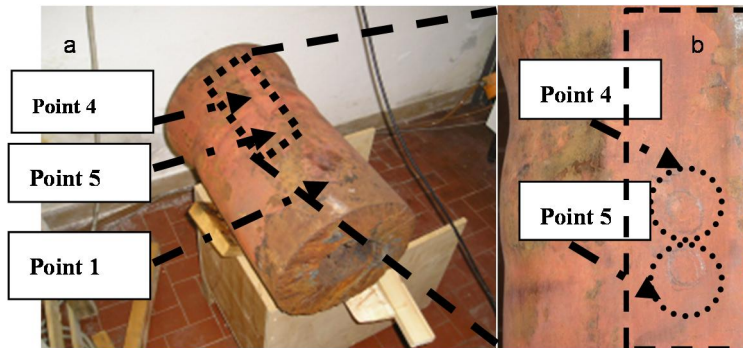


Figure 3. Exhausted steam collector in massive P22 steel extracted after its life-cycle (a). Rectangular square shows the area from where the metallographic replica has been extracted after polishing.

Several distinct points have been selected on the surface of a voluminous and massive steam collector extracted after its life cycle in a large scale power plant (Figure 3a). The material is a P22 steel. Data have been collected by using DifRob[®]1 from point 1 that is taken as a reference and located in an area far from both the edge of the component and from points 4 and 5 which were located in a critical area (Figure 3b) [5].

3.2 T92 steel tube

XRD tests have been carried out on a T92 steel tube. The component shows a large welded butt joint. In the proximity of the weld zone, two alignments have been selected (Figure 4) and data have been collected along the weld joint and 1mm, 2mm, 5mm and 15 mm from the weld border. The external diameter of the tube is 44.5 mm and the minimum thickness is 7.1 mm (the average or “actual” thickness is 8 mm). The specimen is composed by ASME SA 213 T92, a martensitic chromium steel (9% Cr) for data collections performed by DifRob®1. [5]

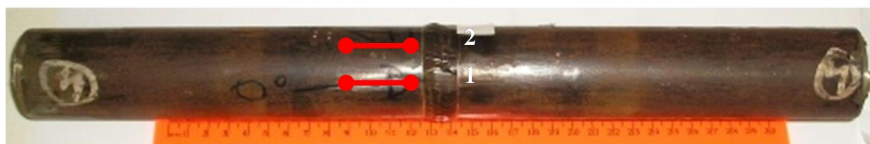


Figure 4. Welded joints on T92 steel tube. Points 1 and 2 indicate the red lines selected on the weld joint defining two distinct longitudinal alignments.

4. Results

4.1 P22 steel component

The analyses on the steam collector in massive P22 aim to reveal the sensitivity of the technology to the different local conditions around the selected areas of interest. The sensitivity results in the variation of intensity, position and shape of the diffraction line. Optical micrographs were obtained from the metallographic replicas [6] collected from the points 4 and 5 of Figure 3b. These micrographs in Figure 5a are showing microstructural arrangement with microcavitation, ranked in the class 1 on a scale of 5, according to the Italian guidelines ISPESL section 6 LG v.1 [7].



Figure 5. Optical micrographs at magnification of 500X from the metallographic replica of points 4 and 5 of Figure 3 b (a); $\Delta FWHM$ vs. $\Delta\theta$ (b).

The graph of Figure 5b was obtained by plotting $\Delta FWHM$ vs. $\Delta\theta$, where the parameters refer to the diffraction line collected from the points 1, 4, 5 of Figure 3.

These parameters have been reported in Table 3. The point 1 has been chosen as a reference and then translated in the origin of the plot ΔFWHM vs. $\Delta\theta$. It seems worthwhile to state that the sensitivity of X-ray diffraction measures to the relative deformation effects of Figure 5b is quite promising.

Table 3. Calculation of the relative deformation effect, determined as the ratio between the variation of FWHM and the variation of the position of the diffraction line. Point 1 is taken as a reference.

Table 3	POINT1(ref)	POINT 4	POINT 5
Line position (θ_{obs})	65,78	64,38	65,48
$\Delta\theta_{\text{obs}} = (\theta_{\text{ref}} - \theta_{\text{obs}})$	0	1,4	0,3
FWHM_{obs}	1,16	1,18	1,32
$\Delta\text{FWHM}_{\text{obs}}$	0	0,02	0,16
$\Delta\text{FWHM}_{\text{obs}} / \Delta\theta_{\text{obs}}$		0,014	0,533

In Table 3 the ratio $\Delta\text{FWHM}/\Delta\theta$ gives significant differences when calculated for point 4 and point 5. Such values indicate the ratio between the microstructural elastic effects (FWHM) and the tensile plastic deformation ($\Delta\theta$). These values can be in principle related to the local relative deformation or, equivalently becomes an empirical estimate of the dynamic deformation (i.e. creep), according the power law [1]. We cannot neglect anyway the combined effects of hot oxidation and creep that may introduce local variations in the lattice rheology, whose decomposition into the basic effects shall be further investigated in detail.

4.2 T92 steel tube

Data have been collected on distinct longitudinal alignments of the welded joint of T92 steel tube. Data collection has been repeated on about the same alignments after a long time interval of several months and using a smaller X-ray spot size (Figure 6). At the present stage of preliminary and qualitative investigation, the uncertainty on the graphical reporting of points can be approximately equivalent to the indicator dimensions. It is of interest here to demonstrate a certain relative reproducibility of the variation of the d-spacing values against the distance from the weld centre. A more detailed discussion is reported elsewhere [6].

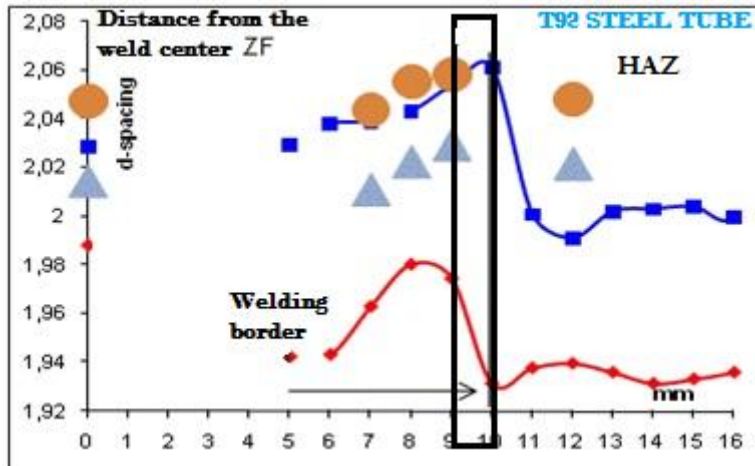


Figure 6. Values of the lattice parameter (d-spacing) vs. the distance from the weld center, expressed in mm. Data have been collected along two main alignments, which are parallel to the longitudinal axis.

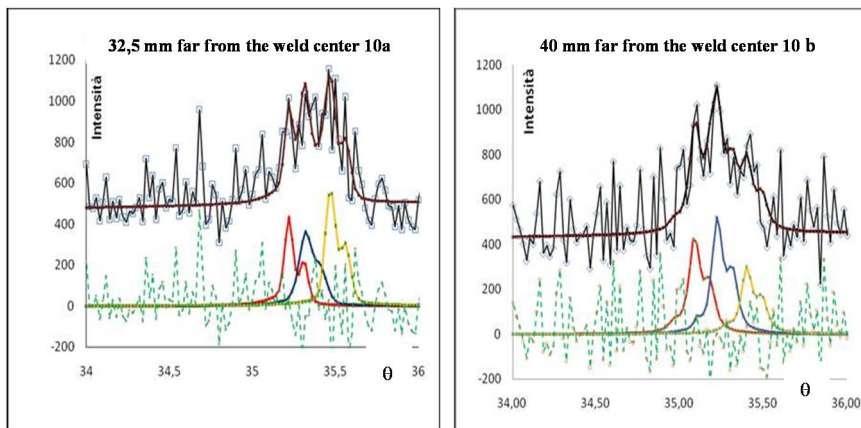


Figure 7. Peaks clusters observed at two distinct distances from the weld center: at 32.5 mm (a); at 40 mm (b). The interpolation profile (i.e. mean equivalent profile) is used to define the diffraction lines produced from the carbides and deduced from the signal decomposition.

In Figure 6 the circle and triangle indicators stand for the data collected with using respectively the rectangular, 0.5 x 3 mm fine focus sized spot and a round diaphragm 0.75 mm wide. Moreover a tolerance of ± 1 mm in the spot position has been introduced to point out the similarities between the various data collection and the d-spacing mapping on the weld border, thus determining the size of the weld borders at 1 mm [6].

The diffraction line position has been used to determine the mean value of the lattice d-spacing, then this value has been plotted versus the distances from the weld center (Figure 6).

The values of the diffraction lines used for the determination of the d-spacing in Figure 8 have been obtained from the profiles interpolation, as the ones shown in figures 9a and 9b. Each profile is actually a cluster made up of many diffraction lines; each diffraction line can be decomposed in the $K\alpha_1$ e $K\alpha_2$ components. The black lines indicates the observed data, the brown line is the distribution of the interpolated data, obtained from the best square fitting, according to χ^2 method; the dashed green line represents the difference between the observed data and the best fitting line [4].

The three profiles in red, blue and yellow are found to be in compliance with the theoretical data of " M_xC_y, M_wC_z " carbides, where x,y,w, z are compositional indexes of multiple phase – carbides; C stands for Carbon and M is a general indicator for the elements most frequently found in T92 steels (as reported in procedural guidelines and normative documents [8], [6], [9]). The analysis on the interpolated data obtained from the carbide peaks, leads to the conclusion that a compatibility exists with carbides with a general formula M_xC_y, M_wC_z where $x=23$, $y=6$ and $w=7, z=3$.

5. Discussion and conclusions: The state of the art of “On Site X-Ray Diffraction” for the observation of creep and steel degradation phenomena

Dynamic deformation relates the lattice microstructural and tensional asset of materials with the alloy compositions and the working conditions of industrial plants in service. These microstructural and tensional set up are translated into either elastic or plastic effects and/or the combination of the two; this lattice asset influences the intensity distribution of each X-Rayz diffraction line and the background modulation of the XRD pattern. So the parameters of the diffraction signal becomes representative of the lattice set up at the first approximation. In this sense the ratio $\Delta FWHM/\Delta\theta$ of Table 3 and Figure 2 gives the approximation or the relative deformation in more quantitative term than the optical magnification of metallographic replica. This special combination of elastic and plastic effects becomes an effective and simple way to picture the punctual state of creep on the points 4 and 5 with reference to the distant point 1 in Section 3.1.

On this same direction the lattice d-spacing can be calculated from the solution of the Bragg equation $2d \sin \theta = \lambda$, where λ is the irradiation wavelength and θ is the angular position of detected X-ray diffraction line. When plotting the d-spacing against the distance from the weld centre, the d-spacing shows in Figure 6 a significant reduction of value when crossing the weld border (soft zone). It seems interesting to note the trend the hardness (HV) values shows when passing from the weld metal to the soft zone of Figure 8.

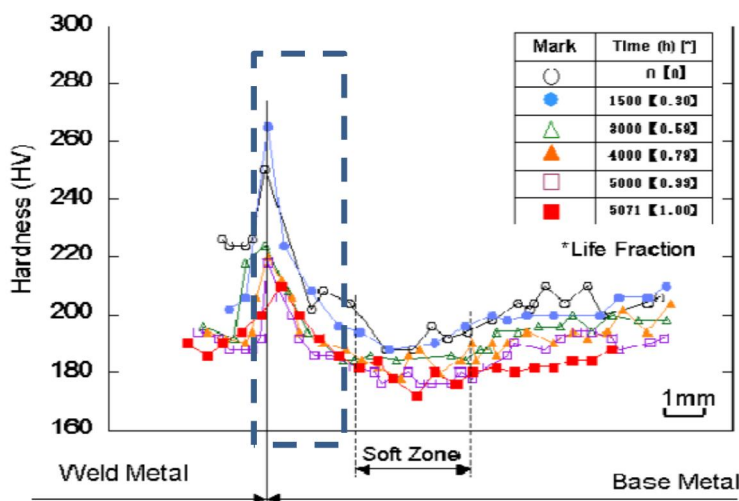


Figure 8. Variation of the hardness profile depending on the exposure time and the distance from the weld border of a 9% Cr steel [10].

The similarities of the trend to reduce the values of hardness and d-spacing revealed by comparing Figure 6 and Fig 8 in the closeness of the weld border stimulate further investigations of the relations between the nanoscale behavior (d-spacing) and the microscale (hardness). Systematic examinations of components are out of the scope of the present paper and should be encouraged.

Figure 6 demonstrates the reproducibility and repeatability of the XRD observation with the coherence of the relative variations of the d-spacing valued vs. the distance from the weld centre. This coherence is obtained by considering the diffraction signal as the whole envelop of clusters and not the individual cluster composition. It interests in Figure 6 the relative position of the d-spacing not its absolute values. The decomposition of the cluster analysis gives some further interesting information. The analysis of the fine structure of the diffraction line profiles can be applied to increase the signal resolution and to identify the complementary microstructural effects of Figure 7. The signal decomposition in its elementary components allows for the identification of carbides, and their different composition in relation to the distance from the weld centre. Figure 7 is the picture of the microstructural asset achieved at that distances from the weld centre. Said distance is far enough to consider negligible the welding process effects on the alloy matrix material. One observes in Figure 7 one peak on the left which is more or less invariant from the distance from the weld centre and two peaks (the central one and the right one) which are mutually variable. Table 4 reports on the parameters related to said diffraction line profiles. By considering the reference on the distance at 40 mm from the weld centre and reporting the differences in θ and FWHM as in Figure 5b, Figure 9 shows the circular indicator falls close to zero

thus indicating the already claimed invariance of the alloy matrix at said distance from the weld. The consequence is that there is space to a better understanding of the relative microstructural arrangement; in particular it interests here how the welding process thermal shocks can influence the material lattice to make X-ray diffraction sensitive to lattice properties variations. Figure 7 illustrates two peaks which are changing one at the expenses of the other; moreover the diffraction pattern in this area has a lattice arrangement which is compatible with the carbides composition. All the aforesaid indicated that the carbide formation can be related to the microstructural modulation and may be generated even far from the welding location (or even at the very early stage of the welding process or even the creep nucleation). It indicates diffusive creep behavior. In Figure 6 the significant variation of the d-spacing across the border, where the thermal shock has reached its final target the creep has typical dislocation behavior.

Table 4. Parameters of the diffraction line profile of the invariant peak on the left of Figures 7a and 7b.

Distance from the weld centre	32.5 mm	40.0 mm
Intensity (c/sec)	398	411
Line position (θ)	35.22	35.09
FWHM (θ)	0.06	0.08
$\Delta\theta$ (fit)	0.133	-
Δ FWHM (θ)	-0.0174	-
Δ FWHM (θ)/ $\Delta\theta$	-0.131	-

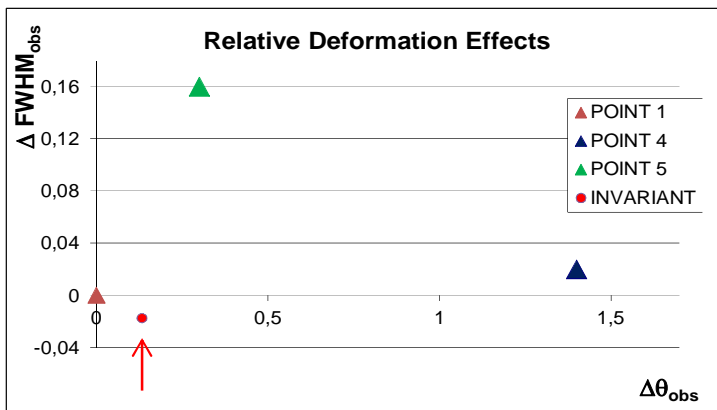


Figure 9. Addition of the point indicated with the arrow in the diagram of the relative deformation confirms the invariant effect of the welding process on the tube of Figure 4 when data have been collected far from the weld location.

The X-ray diffraction method and related technology for “on site” application seems very promising. Systematic investigation should be encouraged in order to provide a thorough knowledge base to be translated into effective qualification of structural integrity of materials for in service inspections.

Finally it is worthwhile to recognize the limited penetration of X-ray diffraction into the materials and components of industrial interest. This limitation implies that only surface damage and degradation can be investigated. There are anyway new technological developments which have high potential to investigate the deep integrity of materials. A patent can be here mentioned for this specific purpose [11].

Acknowledgements

Authors thank Dr. Ing. Andrea Tonti (INAIL), Prof. Elisabetta Gariboldi (Politecnico di Milano), Dr. Ing Donato Pincioli (SOFINTER) for the positive discussions on the paper related matters and for their supplying of specimens and scientific documentation.

References

1. G. Berti & F. De Marco. X- Ray diffraction for diagnosis at the nano-scale. Proc. of 17th International Colloquium Tribology 2010: Solving Friction and Wear Problems, 19–21 January 2010, Technische Akademie Esslingen (TAE), Ostfildern, Germany.
2. G. Berti. Diffractometer and method for diffraction analysis. Patent US 7,260,178, 2003.
3. G. Berti. Variable Center Diffractometer. Patent US 7,483,512B2, 2009.
4. G. Berti. A method for routine comparison of XRPD measurements, Powder Diffraction, 2001, Vol. 16, 1–5.
5. G. Berti, A. Nicoletta, F. De Marco, A. Tonti, G. Augugliaro & D. Pincioli. Il metodo XRD per l'osservazione di fenomeni alla scala nanometrica: comportamento a creep e sua propagazione, negli Atti della Conferenza Nazionale Sicurezza ed Affidabilità delle attrezzature a pressione SAFAP2008, Cagliari, 2008. Vol. 1, pp. 629–639.
6. G. Berti, F. De Marco & D. Pincioli. Efficacia ispettiva e solidità della metodica “XRD in loco” per il rilevamento dei potenziali fenomeni a creep. SAFAP, 2010. Pp. 146–153.
7. ISPESL Linee guida per il prelievo di repliche morfologiche –cavitazionali su componenti eserciti in condizioni di scorrimento viscoso.

8. UNI EN 10216-2:2008. Condizioni tecniche di fornitura – Parte 2: Tubi di acciaio non legato e legato per impieghi a temperatura elevata. UNI Gennaio, 2008. Pp. 1–45.
9. D. Richardot, J. C. Vaillant, A. Arbab & W. Bendick. The T92/P92 Book. Valloirec & MannesmannTubes 2000.
10. F. Masuyama. Integrity and life assessment of P91 components. In Proc. of Int. Seminar Industry & Research experience in the use of P/T91 in HRSGs/boilers. London, UK, European Technology Development, 2005.
11. G. Berti. Mobile device for irradiation and detection of radiation. EP 1896837, 9 January, 2013.

Differences in defect indications of three artificially produced defects in ultrasonic inspection

Ari Koskinen & Esa Leskelä

VTT Technical Research Centre of Finland
Espoo, Finland

Abstract

Different types of artificial defects are used for qualification of ultrasonic inspection procedures, equipment and personnel for in-service inspections of nuclear components. To reliably evaluate the performance of an inspection, the defects have to be representative enough compared to the real service-induced defects.

Fatigue cracks can nowadays be produced artificially as thermal fatigue or mechanical fatigue cracks. Thermal fatigue crack production is very well controlled in matter of size and opening and those cracks are very realistic option compared to the real service-induced defects. Mechanical fatigue crack production is a well-known and widely used method and can be used to produce very realistic cracks as well.

Ultrasonic indications are highly dependent on defect characteristics like roughness, crack opening, tilt and branching. This work studies the influence of different reflector properties on defect indications. Two different types of artificial defects from different manufactures are inspected with conventional ultrasonic (UT), phased array (PA) and scanning acoustic microscope (SAM) techniques. The aim of the study is to get a wider perspective on the differences in similar type of defects from different manufacturers.

1. Introduction

This study was conducted to compare two different types of artificial defects to test and study the influence of different reflector properties on ultrasonic indications. Another objective was to produce new data on artificial reflectors for the needs of qualification as well as inspection.

There are many ways to produce artificial defects in different materials. Different defects have different responses when they are inspected and it is crucial for the reliability to know how well artificial defects correspond to service-induced cracks. Fatigue cracks can nowadays be produced using thermal fatigue or mechanical fatigue. In this study thermal fatigue and mechanical fatigue cracks of similar size were produced in two test samples. These artificial defects were examined using mechanized ultrasonic techniques, first conventional ultrasonic

transducers and after that with more sophisticated ultrasonic methods. Besides image-based analysis also some fast Fourier transformation (FFT) analysis was applied to get more information about the defects.

2. Experiments

2.1 Fatigue crack samples

Two different fatigue samples were studied. Both samples were made of austenitic stainless steel 316L (ASTM) plate with a thickness of 25 mm. Samples were butt welded of two pieces and both weld face and root sides were ground. The cracks were produced on the root side along the fusion line (Figure 1). The dimensions of the cracks in both samples were targeted to be 15 mm in length and 5 mm in depth. These dimensions will be confirmed after the final destructive investigation in 2013 as a part of the Finnish Research Programme on Nuclear Power Plant Safety 2011–2014 SAFIR2014 MAKOMON project. One of the samples contained one thermal fatigue crack and the other contained two mechanical fatigue cracks.

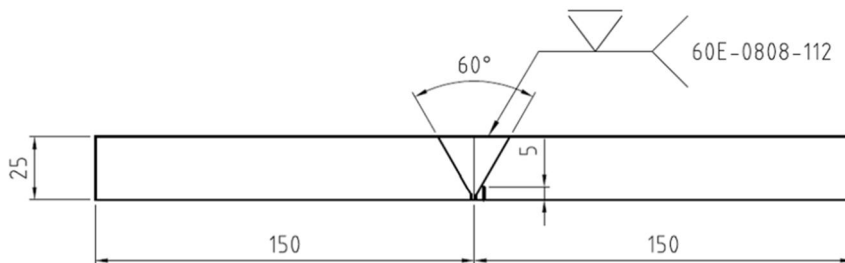


Figure 1. Schematic picture of the sample.

2.2 Conventional ultrasonic inspection

Inspections using conventional ultrasonic technique were carried out using OmniScan ultrasonic device with motorized scanner (SPIDER) with software control by UltraVision. Probes, angles and wave forms used can be seen in Table 1. Scanning was performed from both sides of the weld on weld face side using water as couplant.

Table 1. Conventional ultrasonic inspection details.

Probe	Wavemode	Angle	Frequency (MHz)	Focus (mm)	Transducer size (mm)
MWB45-2	Transverse	45°	2	-	8x9
MWB55-2	Transverse	55°	2	-	8x9
MWB70-2	Transverse	70°	2	-	8x9
MWK45-2	Transverse	45°	2	-	8x9
MWK55-2	Transverse	55°	2	-	8x9
MWK70-2	Transverse	70°	2	-	8x9
MWK45-4	Transverse	45°	4	-	8x9
MWK55-4	Transverse	55°	4	-	8x9
MWK70-4	Transverse	70°	4	-	8x9
TRL45-2	Longitudinal	45°	2	~30	2(8x14)
TRL60-2	Longitudinal	60°	2	~25	2(8x14)
TRL70-2	Longitudinal	70°	2	~25	2(8x14)

2.3 Phased array ultrasonic inspection

Phased array inspection with techniques PA-1 and PA-4 was performed using OmniScan 16/128PR with software control by UltraVision. PA testing with techniques PA-2 and PA-3 was performed using Dynaray Lite 64/64PR. Scanning in techniques PA-1, PA-2 and PA-3 was carried out using Zetec's Manual Pipe Scanner and in techniques PA-4 using motorized scanner (SPIDER). More detailed information on inspection parameters can be seen in Table 2 and more detailed probe parameters in Table 3.

Table 2. Phased array inspection details.

Technique	Description
PA-1	Scanning from weld face side using dual matrix phased array probes with sectorial scan. Scanning was performed from both sides of the weld using manual encoded scanner with several scan lines along the weld. Technique is qualified to be used in in-service inspections of piping welds in nuclear power plants in the USA. Procedure: Zetec OmniScanPA01 rev. C.
PA-2	Scanning from weld face side using single linear phased array probes with sectorial scan. Scanning with a resolution of 1 mm was performed from both sides of the weld using manual encoded scanner with several scan lines with an index resolution of 5 mm.
PA-3	Scanning from weld face side using single linear phased array probe with linear electronic scan. Scanning with resolution of 1 mm was performed from both sides of the weld using manual encoded scanner with several scan lines with an index resolution of 10 mm.
PA-4	Scanning from weld face side using single linear phased array probe with sectorial scan. The aim was to generate inner surface creeping wave. Scanning was performed from both sides of the weld using automated scanner with several scan lines with an index resolution of 5 mm.

Table 3. Phased array probe parameters.

Technique	Probe	Wedge	Wavemode	Angles	Frequency (MHz)	Focus (mm)	Aperture (mm)
PA-1	1.5M5x3E17.5-9	ADUX576A	Transverse	40°–70°	1.5	25 TD	2x(9x17.5)
	1.5M5x3E17.5-9	ADUX582A	Longitudinal	40°–70°	1.5	25 TD	2x(9x17.5)
PA-2	2L16A10	SA10-N55S	Transverse	40°–70°	2.25	25 TD	9.6x10
	5L32A11	SA11-N55S	Transverse	40°–70°	5	25 TD	11.4x10
PA-3	5L32A11	SA11-N55S	Transverse	45°, 55°, 70°	5	25 TD	11.4x10
PA-4	5L16A10	SA10-N60L	Longitudinal	60°–89°	5	-	9.6x10

2.4 Scanning acoustic microscope

The probe used in inspection with scanning acoustic microscope (SAM) was a commercial 5 MHz probe manufactured by Panametrics. The focal distance of the probe was 3 inches (76.2 mm) and the probe diameter 0.5 inches (12.7 mm). To detect the discontinuities in the test samples, a 45 degree transverse wave was chosen for inspection. To produce a 45 degree transverse wave in steel the probe was tilted 19 degrees in water according to Snell's law.

$$v_1/v_2 = \sin(\alpha_1)/\sin(\alpha_2) \quad (1)$$

where v_1 is the velocity of longitudinal wave in water, v_2 is the velocity of transverse wave in steel, α_1 is the transverse wave angle in steel and α_2 is the longitudinal wave probe angle in water (i.e. probe angle) [1].

2.5 Data analysis

Data analysis was performed for volumetrically merged data. Signal to noise ratio was defined as a ratio between average noise level and the highest amplitude of reflector. Additional image analysis for B-scan images was performed by raising the soft gain on the level where the maximum amplitude of each crack was nearly 100 % FSH.

2.6 Fast Fourier transformation (FFT) analysis

The FFT mode of UltraVision was used for online measurements of centre frequency and pulse duration for defect indications with different techniques. There was also an EDM reference notch available which was made in thermal fatigue sample. The values are taken from the maximum amplitude of the defect signal. With phased array techniques, the best performing angle of sectorial scan was used. Typically that angle varied between 45–50 degrees.

3. Results

3.1 Signal to noise ratio in conventional ultrasonic inspection

In Figure 2 signal to noise ratios (SNR) for transverse wave conventional ultrasonic inspection with all 12 probes are shown for mechanical fatigue cracks (MF15X5A and MF15X5B) and thermal fatigue crack (TF15X5). As can be seen, there are significant differences in SNR of defects depending on which side of the weld the scanning has been performed. When scanning is performed from the crack MF15X5A side of the weld (90), that crack has usually better SNR than other cracks. When scanning is performed from the opposite side of the weld (270), thermal fatigue crack TF15X5 and mechanical fatigue crack MF15X5B have significantly better signal to noise ratio compared to that of crack MF15X5A. Only in four cases SNR is higher for the crack inspected through the weld (MWB55-2 90, MWB70-2 90, MWB70-2 270 and MWK70-2 270). MWK type probe seems to be more efficient when inspecting from the defect side.

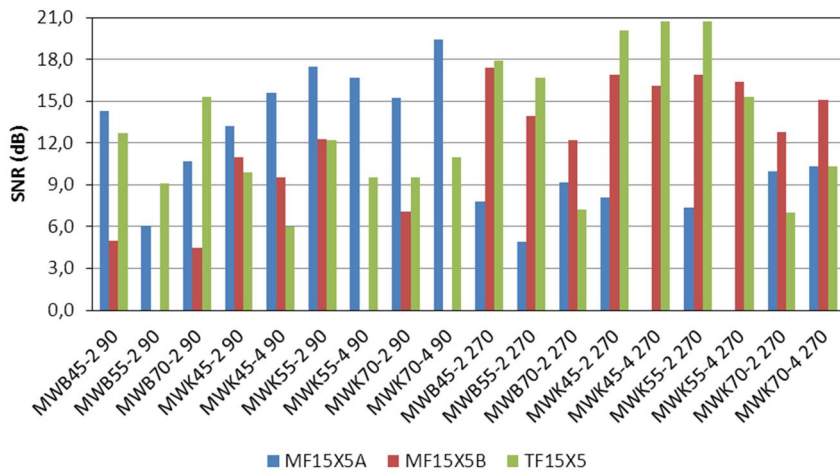


Figure 2. Conventional ultrasonic inspection results for transverse wave.

In Figure 3 longitudinal wave inspection results for conventional ultrasonic testing shows that a 45 degree probe is the most efficient for both, inspection from the crack side and from the opposite side of the weld. It is clearly seen that when probe angle increases the SNR decreases significantly in all cases.

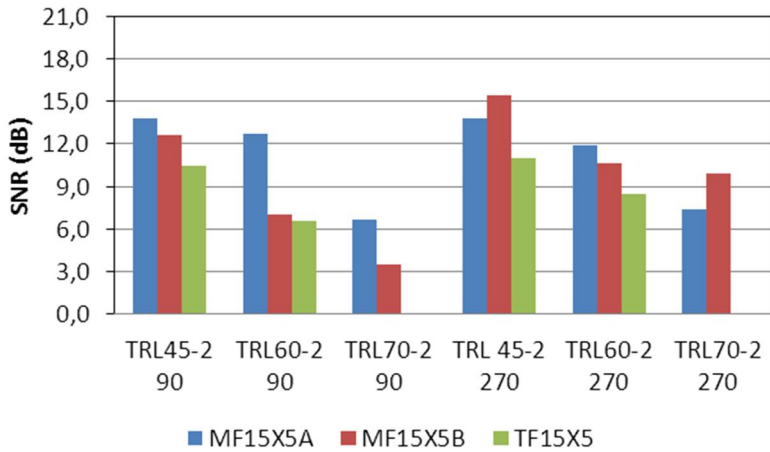


Figure 3. Conventional ultrasonic inspection results for longitudinal wave.

3.2 Signal to noise ratio in phased array ultrasonic inspection

As can be seen in Figure 4, for crack MF15X5A the highest SNR values were measured when scanning was performed from the crack side (90). For crack MF15X5B the highest SNR values were also measured when scanning was performed from the crack side (270). The difference between these two cracks was that MF15X5A received the highest SNR value with longitudinal wave PA probe whereas MF15X5B received its highest SNR value with shear wave PA probe. With crack TF15X5 the two highest SNR values were measured with shear wave PA probe and surprisingly the highest SNR value for crack TF15X5 was measured when inspection was performed from the opposite side of the weld (90).

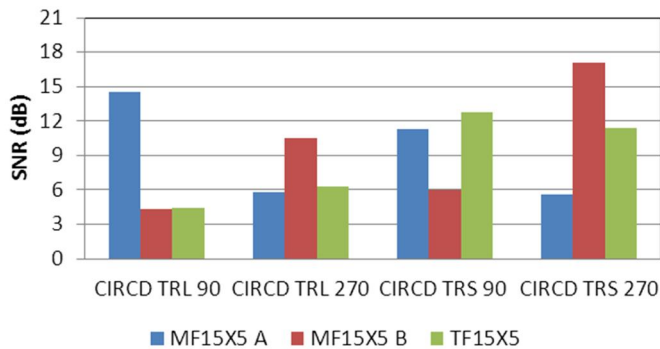


Figure 4. Phased array inspection (PA-1) using dual matrix phased array probes with sectorial scan.

With PA-2 technique only shear wave mode PA probes were used with two different frequencies 2.25 MHz and 5 MHz. Cracks MF15X5A and MF15X5B were detected only from the crack side (90 for MF15X5A and 270 for MF15X5B) as can be seen in Figure 5. Crack TF15X5 was detected both from the crack side (270) and through the weld (90). It seems that there is no significant difference in SNR between lower and higher frequencies when inspection was performed from the crack side.

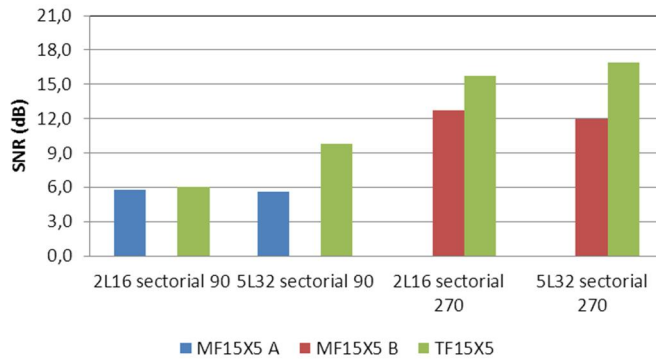


Figure 5. Phased array inspection (PA-2) using single linear phased array probes with sectorial scan.

In PA-3 technique tests almost similar results were obtained as in PA-2 tests as can be seen in Figure 6. Both mechanical fatigue cracks MF15X5A and MF15X5B were detected only from the crack side. Thermal fatigue crack TF15X5 was detected both from the crack side and from the opposite side with one exception. With inspection through the weld using a 70 degree angle, TF15X5 defect was not detected. With PA-4 technique the SNR of mechanical fatigue cracks were similar when measured from crack side and vice versa. The highest SNR was measured for thermal fatigue crack when measured from crack B side (270).

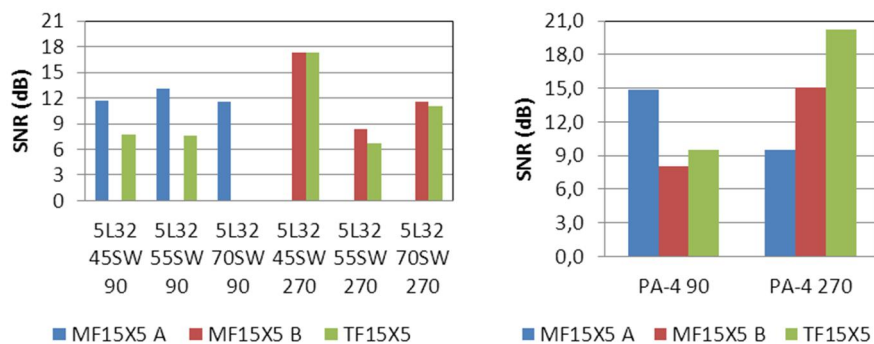
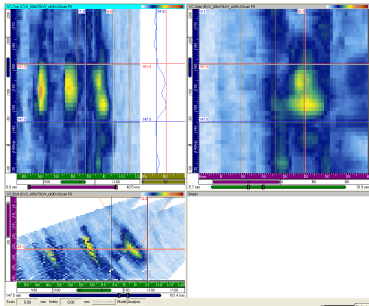
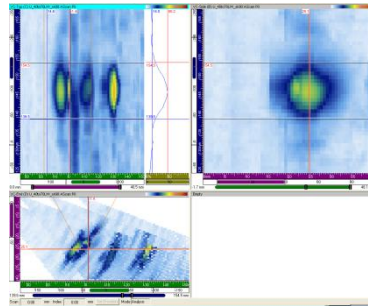


Figure 6. Phased array inspection on the right (PA-4) using single linear phased array probe with linear scan and on the left (PA-3) with creeping wave.

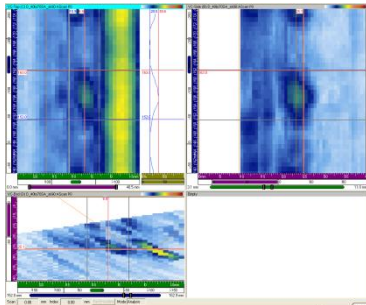
Figures 7 (MF15X5B) and 8 (TF15X5) show inspection results of PA-1 technique with similar gain settings. It is clearly visible that there is a significant difference between longitudinal and shear wave inspections. In these two cases the shear wave inspection produced the best indication when inspection was performed from the crack side. On the other hand when inspection was performed from the opposite side of the weld, in Figure 7 longitudinal wave produced clearer indication and in Figure 8 shear wave is the one that produced the more clearly visible indication.



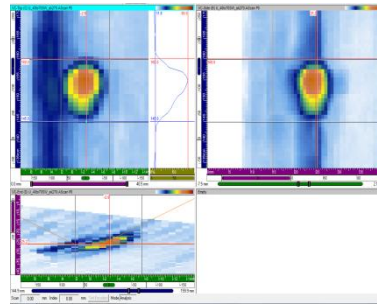
CIRCD TRL 90 – PA longitudinal wave – far side



CIRCU TRL 270 – PA longitudinal wave – near side

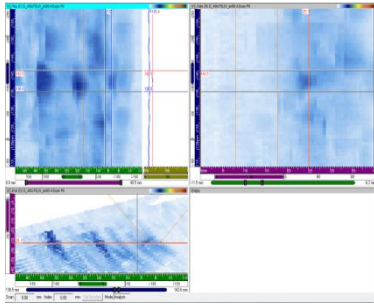


CIRCD TRS 90 – PA shear wave – far side

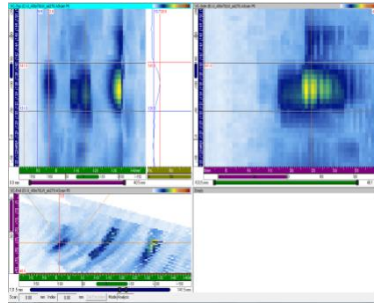


CIRCU TRS 270 – PA shear wave – near side

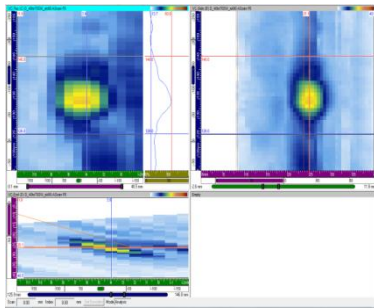
Figure 7. Phased array ultrasonic inspection sample with C-, B- and D-scans of crack MF15X5B.



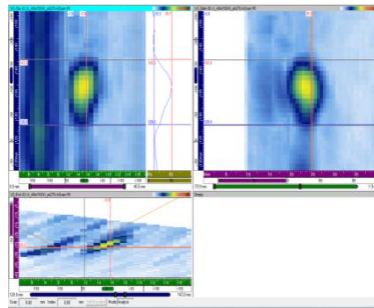
CIRCD TRL 90 – PA longitudinal wave – near side



CIRCU TRL 270 – PA longitudinal wave – far side



CIRCD TRS 90 – PA shear wave – near side

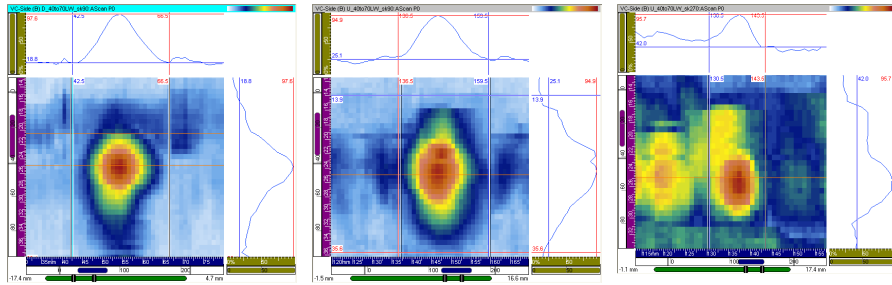


CIRCU TRS 270 – PA shear wave – far side

Figure 8. Phased array ultrasonic inspection sample with C-, B- and D-scans of crack TF15X5.

3.3 Crack image comparison with phased array testing

Figures 10–13 show B-scans of two mechanical and one thermal fatigue crack with PA-1 technique, Figures 14–17 with PA-2 technique, Figure 18 with PA-3 technique and Figure 19 with PA-4 technique.

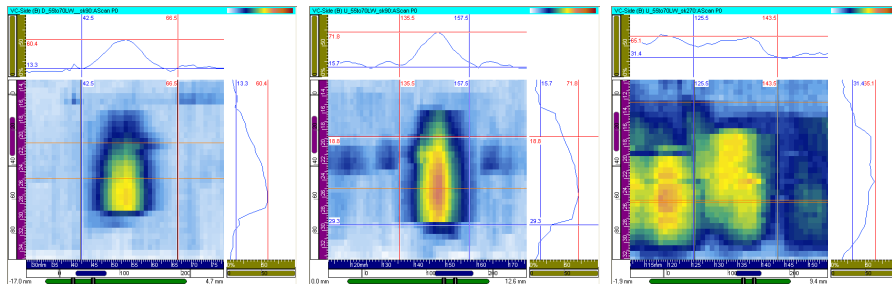


MF15X5A 40°-70°

MF15X5B 40°-70°

TF15X5 40°-70°

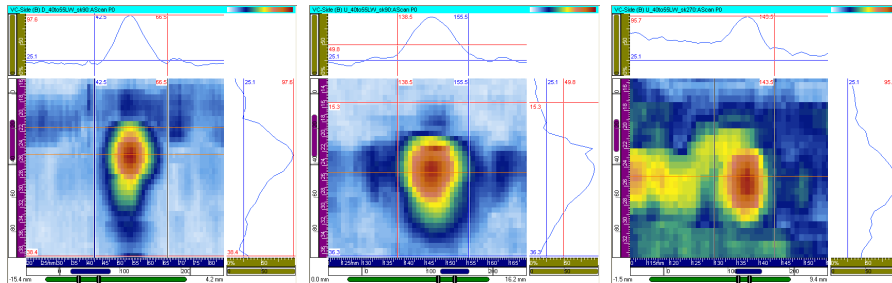
Figure 9. B-scans of crack indications with PA-1 technique, longitudinal wave.



MF15X5A 55°-70°

MF15X5B 55°-70°

TF15X5 55°-70°

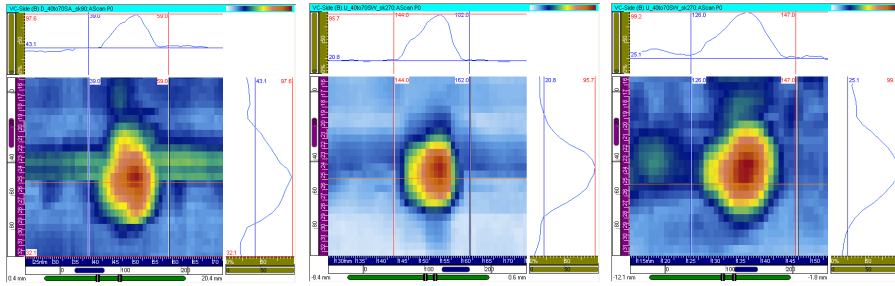


MF15X5A 40°-55°

MF15X5B 40°-55°

TF15X5 40°-55°

Figure 10. B-scans of crack indications with PA-1 technique, longitudinal wave. Comparison between higher and lower beam angles.

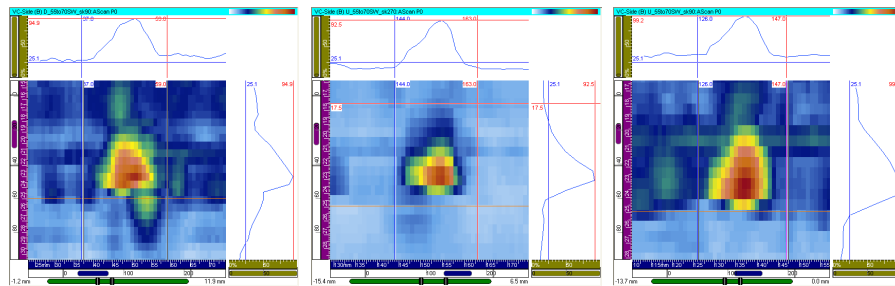


MF15X5A 40°–70°

MF15X5B 40°–70°

TF15X5 40°–70°

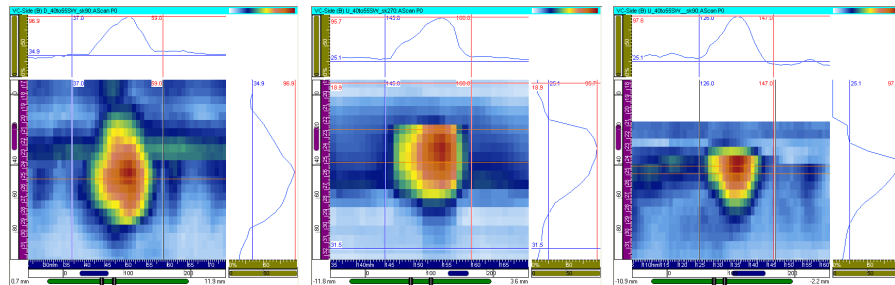
Figure 11. B-scans of crack indications with PA-1 technique, transverse wave.



MF15X5A 55°–70°

MF15X5B 55°–70°

TF15X5 55°–70°



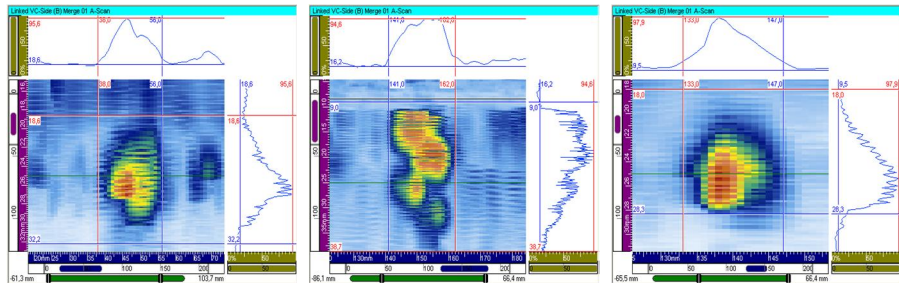
MF15X5A 40°–55°

MF15X5B 40°–55°

TF15X5 40°–55°

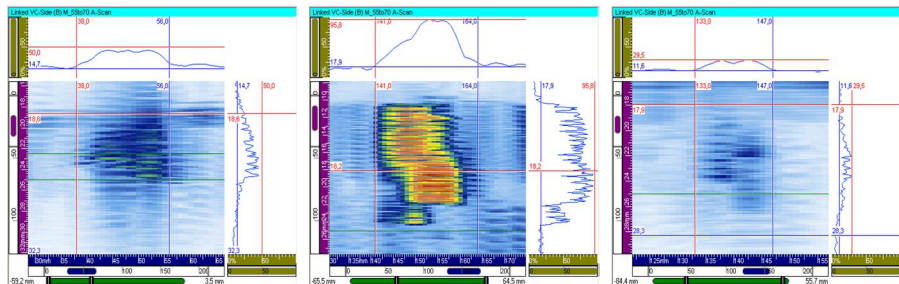
Figure 12. B-scans of crack indications with PA-1 technique, transverse wave. Comparison between higher and lower beam angles.

3.3.1 PA-2: 2.25 and 5 MHz transverse wave sectorial scan

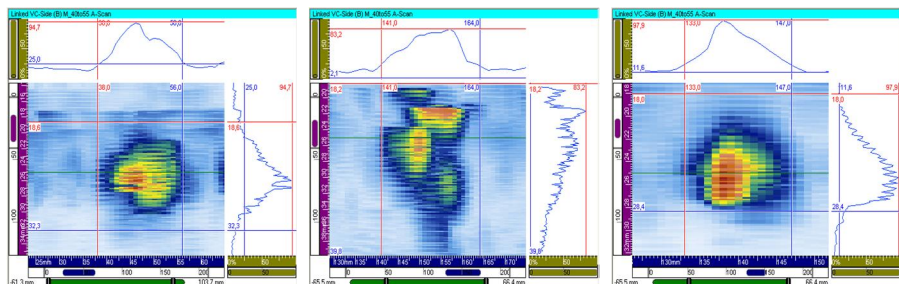


MF15X5B 2.25 MHz 40°-70° MF15X5B 2.25 MHz 40°-70° TF15X5 2.25 MHz 40°-70°

Figure 13. B-scans of crack indications with PA-2 technique, 2.25 MHz transverse wave sectorial scan with angles from 40° to 70°. There is some misalignment between the scan lines in the data of MF15X5B causing the diffuse shape of the indication.

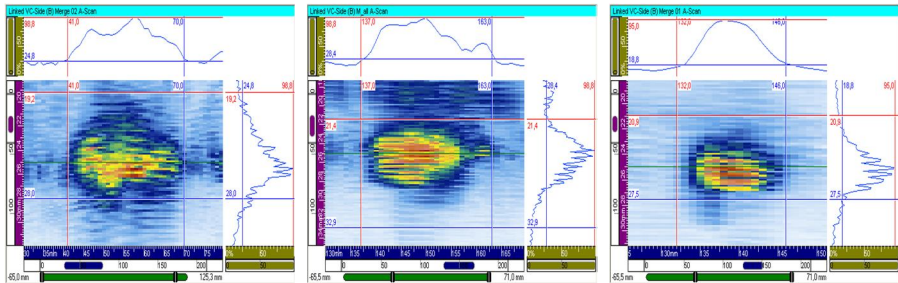


MF15X5A 55°-70° MF15X5B 55°-70° TF15X5 55°-70°



MF15X5A 40°-55° MF15X5B 40°-55° TF15X5 40°-55°

Figure 14. B-scans of crack indications with PA-2 technique, 2.25 MHz transverse wave sectorial scan. Comparison between higher and lower beam angles.

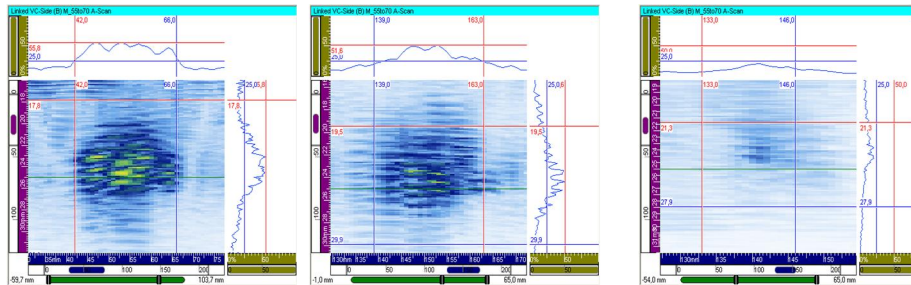


MF15X5A 5 MHz 40°–70°

MF15X5B 5 MHz 40°–70°

TF15X5 5 MHz 40°–70°

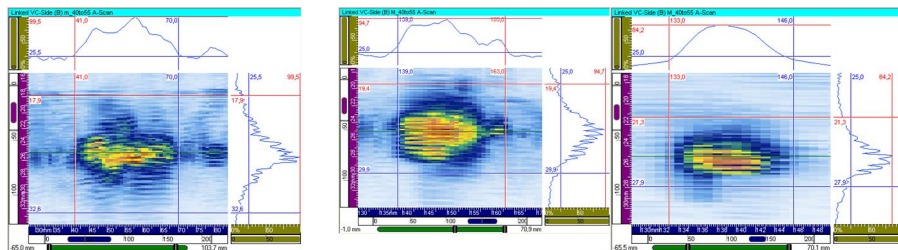
Figure 15. B-scans of crack indications with PA-2 technique, 5 MHz transverse wave sectorial scan with angles from 40° to 70°.



MF15X5A 55°–70°

MF15X5B 55°–70°

TF15X5 55°–70°



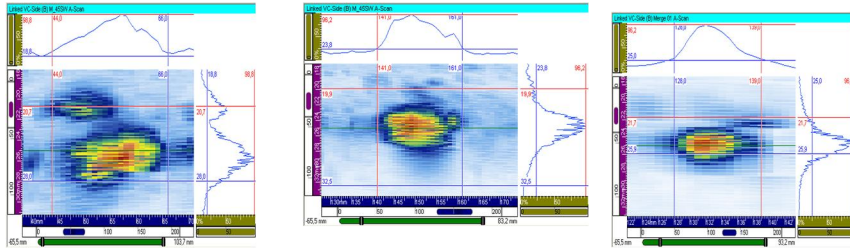
MF15X5A 40°–55°

MF15X5B 40°–55°

TF15X5 40°–55°

Figure 16. B-scans of crack indications with PA-2 technique, 5 MHz transverse wave sectorial scan. Comparison between higher and lower beam angles.

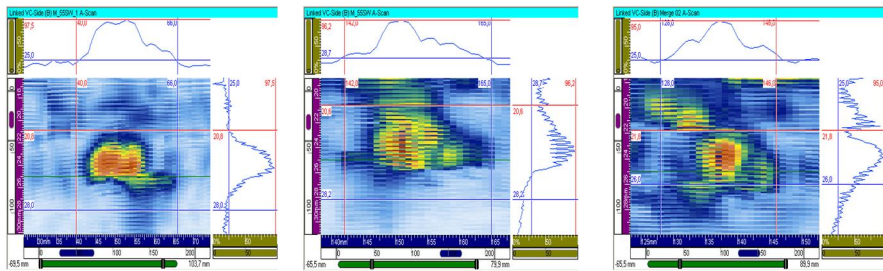
3.3.2 PA-3: 5 MHz transverse wave linear scan



MF15X5A 45°

MF15X5B 45°

TF15X5 45°



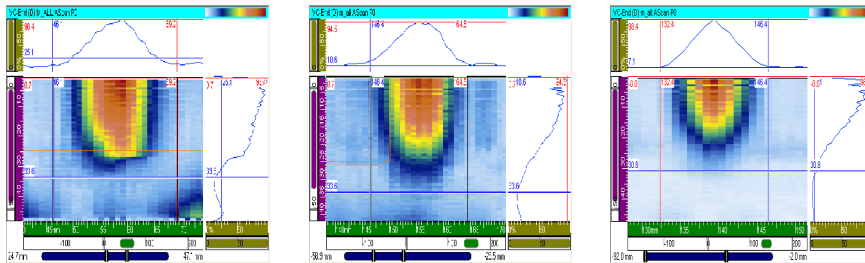
MF15X5A 55°

MF15X5B 55°

TF15X5 55°

Figure 17. B-scans of crack indications with PA-3 technique, 5 MHz transverse wave linear scan with angles 45° and 55°.

3.3.3 PA-4 technique: ID creeping wave



MF15X5A

MF15X5B

TF15X5

Figure 18. B-scans of crack indications with PA-4 technique, 5 MHz longitudinal wave sectorial scan with angles from 60° to 89°, ID creeping wave.

3.3.4 Amplitudes

Amplitude responses from each crack with phased array techniques are shown in Figure 19.

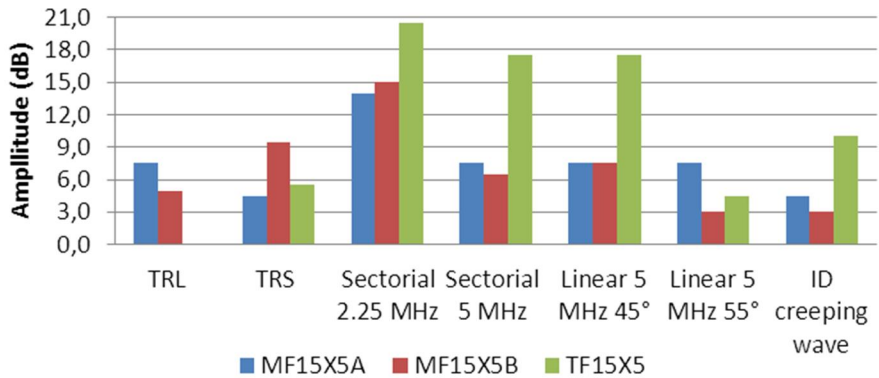


Figure 19. Amplitude responses from each crack with phased array.

3.4 Scanning acoustic microscope (SAM) 45° transverse wave

B-scan images of inspection with scanning acoustic microscope (SAM) are shown in Figure 20.

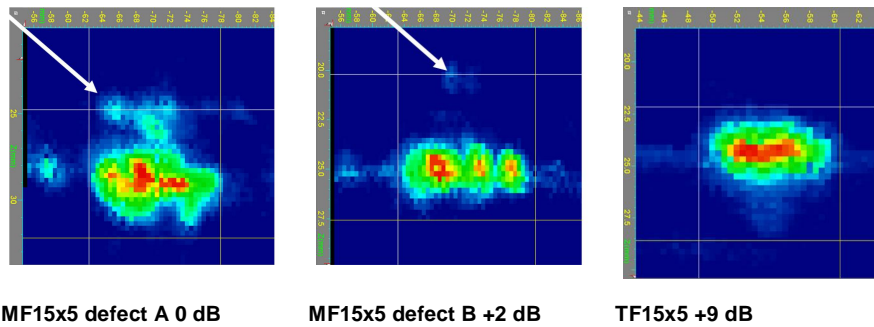


Figure 20. B-scans of crack indications with SAM, 5 MHz 45° transverse wave. Crack tip signals are pointed with arrows.

3.5 FFT measurements with conventional ultrasonic testing

3.5.1 Centre frequency

The centre frequencies of all three defects and EDM notch with conventional transverse 2 MHz probes are presented in Figure 21, with 4 MHz probes and by longitudinal 2 MHz TR probes in Figure 22.

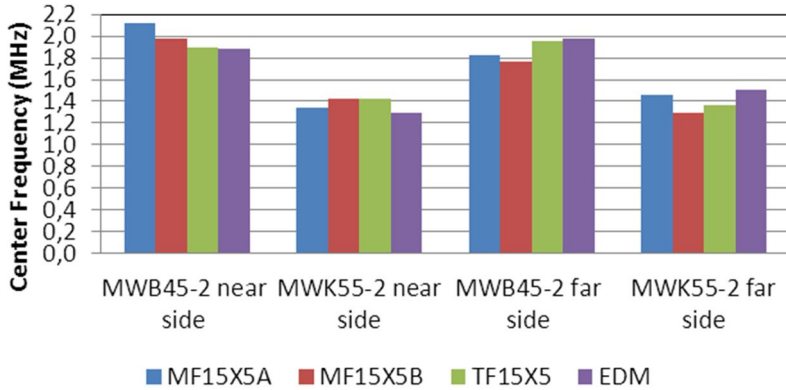


Figure 20. Centre frequency of all cracks and EDM notch with 2 MHz transverse wave probes measured from near and far side of the defects.

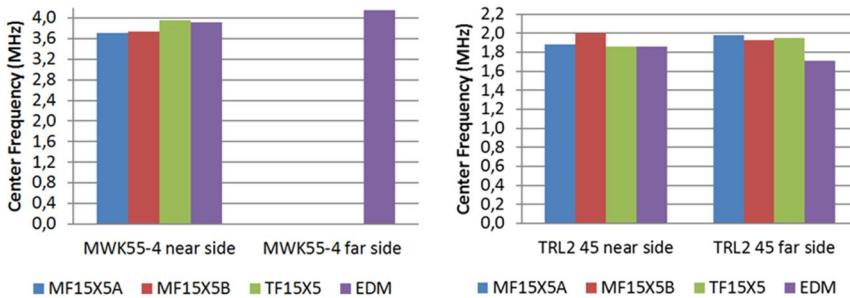


Figure 21. On the left the centre frequency of all cracks and EDM notch with 4 MHz transverse wave probes measured from near and far side of the defects. Only EDM notch gives a proper response from far side. On the right the centre frequency of all cracks and EDM notch with 2 MHz longitudinal TR probes measured from near and far side of the defects.

3.5.2 Pulse duration

The pulse duration of all three cracks and EDM notch with conventional transverse 2 MHz probes are presented in Figure 23, with 4 MHz transverse probes and longitudinal 2 MHz TRL probes in Figure 24.

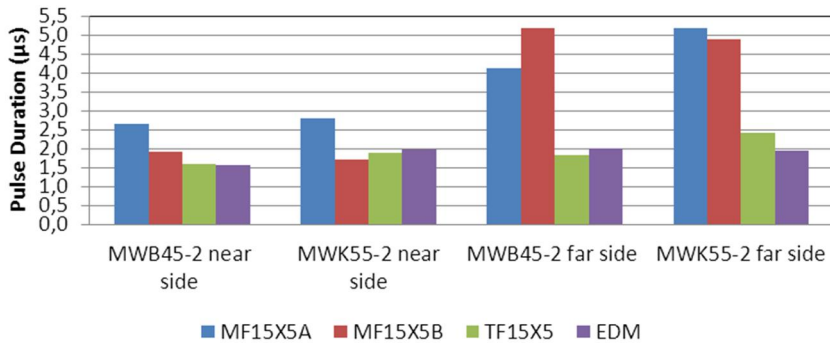


Figure 22. Pulse duration of all cracks and EDM notch with 2 MHz transverse wave probes measured from near and far side of the defects.

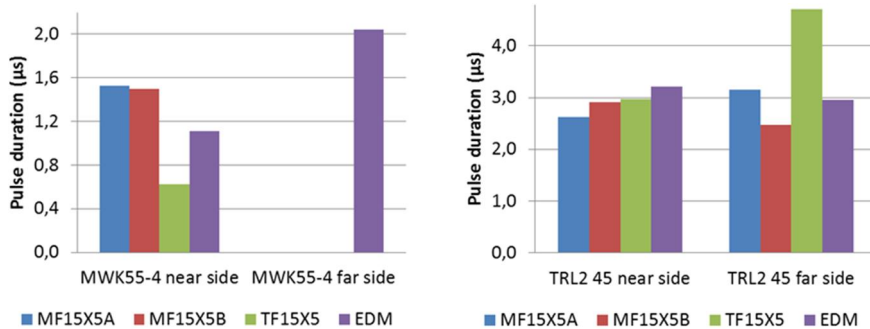


Figure 23. On the left the pulse duration of all cracks and EDM notch with 4 MHz transverse wave probes measured from near and far side of the defects. Only EDM notch gives a proper response from far side. On the right the pulse duration of all cracks and EDM notch with 2 MHz longitudinal TR probes measured from near and far side of the defects.

3.6 FFT measurements with phased array techniques

3.6.1 Centre frequency

The centre frequencies of all three cracks and EDM notch with phased array 1.5 MHz TR longitudinal and transverse techniques are presented in Figure 26 and with 2.25 MHz and 5 MHz sectorial scan techniques in Figure 27.

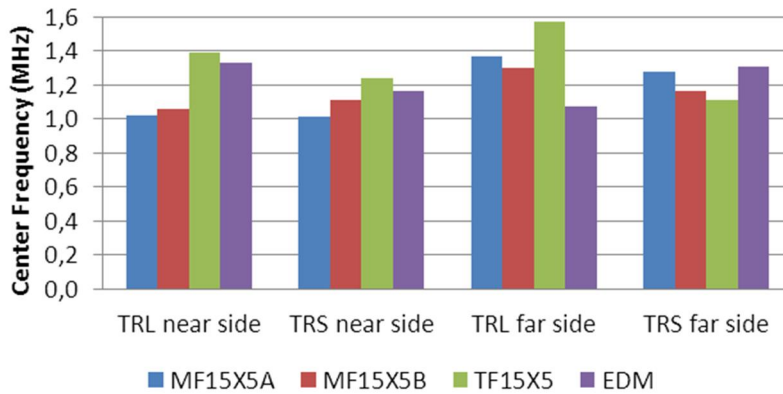


Figure 24. Centre frequency of all cracks and EDM notch with 1.5 MHz TR techniques measured from near and far side of the defects.

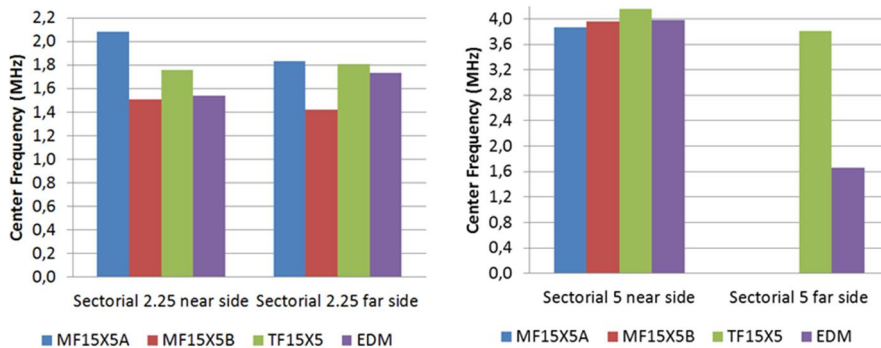


Figure 25. On the left the centre frequency of all cracks and EDM notch with 2.25 MHz transverse sectorial scan technique from near and far side of the defects. On the right the centre frequency of all cracks and EDM notch with 5 MHz transverse sectorial scan technique from near and far side of the defects. Only thermal fatigue crack and EDM notch produced a proper response from far side.

3.6.2 Pulse duration

Pulse durations of all three cracks and EDM notch with phased array 1.5 MHz TR longitudinal and transverse techniques are presented in Figure 28 and with 2.25 MHz and 5 MHz sectorial scan techniques in Figure 29.

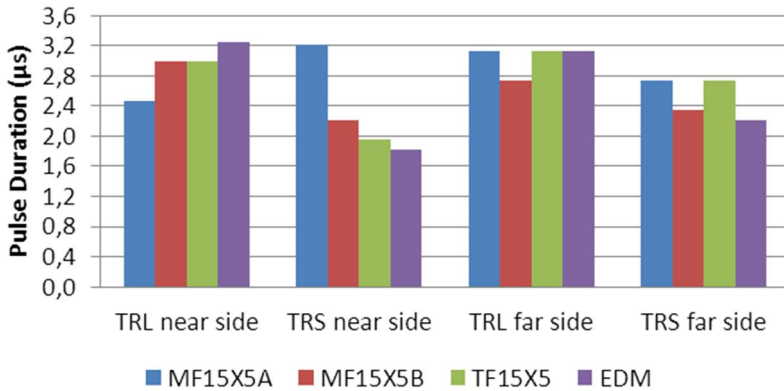


Figure 26. Pulse duration of all cracks and EDM notch with 1.5 MHz TR techniques from near and far side of the defects.

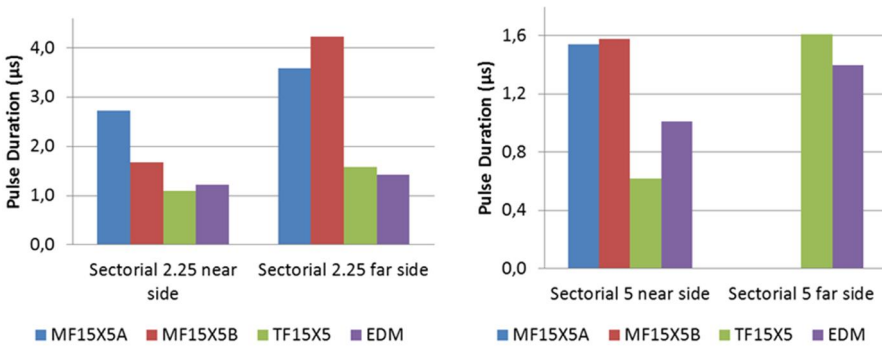


Figure 27. On the left the pulse duration of all cracks and EDM notch with 2.25 MHz transverse sectorial scan technique from near and far side of the defects. On the right the pulse duration of all cracks and EDM notch with 5 MHz transverse sectorial scan technique from near and far side of the defects. Only thermal fatigue crack and EDM notch produced a proper response from far side.

4. Discussion

In this paper only some results of the differences in NDE reflectors study were briefly presented. Even in these results it is clearly seen that defect characteristics have a significant impact on ultrasonic indications. Not only between different

types of fatigue cracks but also between two mechanical fatigue cracks. These results presented in this paper encourage studying this subject more. Cracks examined in this study are rather low and short so the crack images do not show much variation caused by crack morphology.

Crack image analysis of phased array inspections shows that with PA-1 technique (Figures 9–12) using longitudinal wave the amplitudes are higher with smaller angles whereas using transverse wave there is no difference in the amplitudes between smaller and higher angles. Dynamic range in depth direction is wide so indications are easily characterized as surface opening service-induced defects. With such a low frequency there is no interaction with crack morphology distinguished. With PA-2 technique using 2.25 MHz probe (Figures 13 and 14) larger angles give a strong indication of mechanical fatigue crack B while with other cracks the result is the opposite to that. The result deviates from the results with other phased array techniques. With PA-2 technique using 5 MHz probe (Figure 17) there is some interaction with crack morphology seen in images of mechanical fatigue cracks. The image of thermal fatigue crack is more uniform and crack is hardly detected with larger angles. With cracks used in this study, it seems that phased array sectorial scan does not give much benefit compared to linear scan with fixed angle of 45 degrees. Actually, linear scan with 45 degrees is the only technique where crack tips are detected. With inner surface creeping wave (Figure 18), the images of mechanical fatigue cracks are identical to each other. The dynamic range of thermal fatigue crack in depth direction is smaller than that of aforementioned.

A clear difference between cracks is seen in the B-scans from inspection by scanning acoustic microscope with 5 MHz 45° transverse wave (Figure 20). There is much more interaction with crack morphology in the B-scans of mechanical fatigue cracks while the image of thermal fatigue crack is rather smooth. Also the images of two mechanical fatigue cracks differ from each other. Like in phased array inspection with 5 MHz 45° linear scan (Figure 17) the tip signal of mechanical fatigue crack A is clearly stronger than the tip signal of mechanical fatigue crack B. There is no tip signal from thermal fatigue crack. There is 2 dB difference between the two mechanical fatigue cracks in maximum amplitude but the maximum amplitude of thermal fatigue crack is 9 dB higher than the maximum amplitude of mechanical fatigue crack A. The highest amplitude responses with phased array testing were received with 2.25 MHz probe. The response from thermal fatigue crack was clearly higher with single probe inspections than that of mechanical fatigue cracks except with 55 degrees linear scan. There is more variation in the amplitude of thermal fatigue crack between techniques compared to mechanical fatigue cracks (Figure 19).

In conventional ultrasonic testing the centre frequency with MWB45-2 probe is clearly higher than with MWK55-2. There is only minor difference between the cracks and no significant difference whether the centre frequency is measured from near or far side. With 4 MHz MWK probe there is no significant difference in the centre frequency between the cracks. Only EDM notch produced a proper response from far side with that probe. With 2 MHz TRL probe there is no signifi-

cant difference whether the centre frequency is measured from near or far side or between the cracks.

With 2 MHz transverse wave probes pulse duration of mechanical fatigue crack A measured from near side is clearly longer than that of the other cracks. When measured from far side, the pulse durations of mechanical fatigue cracks are significantly longer than that of thermal fatigue crack. The pulse duration of thermal fatigue crack and EDM notch signals are near to each other and when measured from near side, also the pulse duration of mechanical fatigue crack B is quite similar with those two reflectors.

Thermal fatigue crack produces a very short pulse with 4 MHz probe. There is no big difference between the two mechanical fatigue cracks. Only EDM notch produced a proper response from far side and the pulse duration is much longer in that case. With 2 MHz TRL probe there is no significant difference whether the pulse duration is measured from near or far side or between the flaws Thermal fatigue crack is an exception in that case producing a significantly longer pulse measured from the far side of defect.

In phased array testing the centre frequencies of mechanical fatigue crack signals are lower when scanned from near side with 1.5 MHz TR techniques. The centre frequency of thermal fatigue crack is the highest except with TRS technique when measured from far side. Mechanical fatigue crack B gives the lowest centre frequency with 2.25 MHz linear probe and there is difference between that and the centre frequency of mechanical fatigue crack A. There is no significant difference between centre frequencies of different defects when measured from near side with 5 MHz transverse sectorial scan. When measured from far side, thermal fatigue crack produces a high and EDM notch produces a low frequency response. Mechanical fatigue cracks are not detected from far side with 5 MHz probe.

The pulse duration of mechanical fatigue crack B with 1.5 MHz TRS technique is longer when measured from near side. Pulse durations of other defects are somewhat longer with 1.5 MHz TRL technique. There is no significant difference in pulse duration with 2.25 MHz transverse wave sectorial scan whether the measurement is done from near or far side. The pulse durations of mechanical fatigue cracks are longer and the difference is significant when measured from far side. With 5 MHz transverse wave sectorial scan the pulse durations of mechanical fatigue cracks are longer than the pulse durations of thermal fatigue crack and EDM notch when measured from near side. When measured from far side the pulse durations of thermal fatigue crack and EDM notch are on the same level as the pulse durations of mechanical fatigue cracks while those are not detected from far side.

5. Conclusions

- There is more interaction with crack morphology in mechanical fatigue cracks compared to thermal fatigue cracks studied here.
- Higher frequency gives more information of crack morphology and can also enable height sizing of some of the studied cracks (MF).
- The small changes in the coupling and in the shape of the scanning surface or in probe position can cause variation in the results of FFT measurements and diminish the repeatability of measurements.
- Flaw morphology causes variation to FFT measurements. Signal response depends on angle and spatial position of data point. Therefore more measurements would be needed for reliable conclusions whether FFT measurements are applicable for crack characterization.
- When there is an access from both sides of the weld and especially if the weld cap is ground a 5 MHz transverse ultrasonic technique is applicable for crack detection in austenitic welds with thicknesses of at least up to 25 mm.
- Especially smaller angles (~40–55 degrees) produce strong indications for both mechanical and thermal fatigue cracks studied here.
- 5 MHz linear phased array probe and probe MWK55-4 are not applicable for far side inspection.
- Mode conversion technique is well applicable to verify crack detection.

References

1. Koskinen, A., Haapalainen, J., Virkkunen, I. & Kemppainen, M. Differences in Ultrasonic Indications – Thermal Fatigue Cracks and EDM Notches. 18th World Conference on Nondestructive Testing, 16–20 April 2012, Durban, South Africa.
2. Jäppinen T., Koskinen, A., Leskelä, E., Tuhti, A., Haapalainen, J., Sandlin, S. Monitoring of the Structural Integrity of Materials and Components in Reactor Circuit (MAKOMON), SAFIR2014 The Finnish Research Programme on Nuclear Safety 2011–2014, Interim Report, Kaisa Simola (Ed.), Espoo 2013, Pp.292–301.

Detection of magnetite piles on steam generator tubing with eddy current method

Tarja Jäppinen & Kari Lahdenperä

VTT Technical Research Centre of Finland
P.O. Box 1000, 02044 VTT, Espoo, Finland

Abstract

The magnetite deposits and deposit piles on the secondary circuit of the steam generator tubing are detected with eddy current method in in-service inspections. The volume of the detected deposit pile is not evaluated. In many cases the growing defects are located at the same area as the magnetite deposit piles. For this reason it is important to locate and to size the piles of magnetite on the steam generator tubing.

In this study experiments were conducted by using eddy current method using bobbin probe techniques and small mock-up simulating the horizontal steam generator tubing. The goal of the experiment was to size the thickness of magnetite piles under and around the test tubes. The results of low frequency tests showed that the thickness of magnetite layer under the steam generator tube can be measured up to 11 mm. The results of the tests showed also that in more general case, where the tube is embedded into unsymmetrical pile, the pile thickness cannot be measured using ordinary single probe technique.

1. Introduction

During operation of the VVER-440 pressurized water reactor (PWR) deposits precipitate on the outer surface of the steam generator (SG) tubing. Material of the deposits is magnetic and it is composed mainly of magnetite. After deposits have grown thick enough, the deposits peel as flakes from the surface of the tubes. These magnetite flakes can form piles between the tubes, on the tube supporting plates or on the bottom of the horizontal steam generator. The deposits and magnetite piles can be detected in standard eddy current in-service inspections (ISI) by using absolute technique and low inspection frequency (e.g. 25 kHz). So far, the eddy current indications are not generally used to quantify the thickness of the magnetite deposits or piles.

This study is a part of the MAKOMON project in the Finnish Research Programme on Nuclear Power Plant Safety SAFIR 2014. The goal of the study is to develop a method applicable to quantify the amount of the magnetite in piles on the tubing of a steam generator.

In this study the results of the laboratory measurements of the thickness of magnetite piles are given. The measurements were conducted using eddy current

method and standard bobbin probes. The results of two different low frequency eddy current techniques in sizing the thickness of magnetite piles on the outer surface of the SG tube are given.

2. Magnetite on steam generator tubing

Walls of the steam generator tubing are part of the pressure boundary of the primary water circuit of the PWR. Deterioration of SG tubing can restrict the lifetime of the reactor. The integrity of the SG tubes is important and it is imperative to conduct careful, regular well-planned inspections. The main inspection method of steam generator tubes is eddy current method. The method has high inspection speed and it is sensitive to both inner surface (ID) and outer surface (OD) defects.

One of the concerns in the field of steam generator tubing is magnetite deposits accumulating on the secondary side of the tube. Material of the deposits or sludge is ferromagnetic material and is mainly composed of magnetite. The iron oxide in the secondary water forms magnetite layers on the SG tubes. When deposit is thick enough, magnetite layers i.e. deposits peel from the surfaces of the tubes and fall on the tubes, tube supporting plates or on the bottom of the horizontal steam generator and build up magnetite piles.

In many cases the corrosion induced defects are nucleating and growing under the magnetite deposit and deposit piles. Although the deposits and deposit piles promote degradation of the tubes, the deposits indications detected in in-service inspections are usually not analysed or reported in details. It is important to develop an eddy current analysis to be able to detect and to size the magnetite piles on the SG tubing to get more information of the crack initiation and growth.

If the absolute eddy current technique has been applied, the inspection data of steam generator tubing includes also the information of tube wall thickness changes. It is possible to study the the growth of magnetite deposits and piles on SG tubing by comparing the data of the low frequency inspections over the years.

3. Eddy current inspection of the steam generator tubing

The purpose of in-service eddy current inspections is to detect and to characterize the possible degradation of the steam generator tubes. Bobbing probes have been a standard tool for eddy current inspection of the steam generator tubes for decades. Bobbing probes are sufficiently reliable and give repeatable results in detecting and sizing volumetric defects and axial cracks at straight free tube sections. The drawback of the bobbing probes is the inability to detect the circumferential cracks. Tube sections with more complex geometries generate large geometric indications. This reduces the probability to detect defects in these sections with bobbin probes.

4. Detection of magnetite piles

Magnetite piles can build up a complex geometry that generates high amplitude indications. In laboratory scale, several mock-up structures have been used for detection of magnetite piles [1–4].

There have been successful set-ups to measure the thickness of the magnetite deposit on the surface of the tube [3, 4]. In these set-ups the circumferentially symmetric magnetite layer extended around the tube. The thickness of the magnetite was constant at each cross-section. The thickness of the magnetite was changing in axial direction. The amplitude of the eddy current signal correlated well with the thickness of the magnetite deposit. The graph of the amplitude deposit thickness of this data can be used as a reference curve when analysing actual inspection results. However, this applies only when the thickness of the magnetite deposit is constant on the whole circumference, because the eddy current signal is sensitive to all changes of the geometry of the deposit. If the deposit is not circumferentially symmetric i.e. the deposit thickness is not constant in each cross-section, the maximum or minimum thickness of the deposit cannot be judged from the data of a single bobbing coil.

5. Experimental methods

The purpose of the conducted experiments was to study the effect of the outer surface magnetite piles on the eddy current signal of the bobbing probe. To be able to detect the magnetite piles, the eddy current frequency has to be low enough to penetrate the tube wall. To be able to measure the thickness of magnetite piles outside the tube, the magnetic field generated by eddy currents has to extend to magnetite pile on the outer surface of the tube.

The experiments were conducted using two different bobbin probes. The applied eddy current frequencies were 10 and 25 kHz. These frequencies are optimal for the magnetite detection (Table 1.) Diameters of the applied probes were 11.5 mm and 12 mm. The fill factors of the probes were 0.78 and 0.85 respectively. The eddy current equipment Zetec MS5800 and Magnify 2.0R3 software were used. The applied parameters are shown in Table 1. Absolute and differential techniques were used simultaneously. Only the results of absolute technique will be presented.

A simple mock-up of the horizontal steam generator tubing was used in the experiments. The horizontal free span between tubes in VVER-440 type horizontal steam generator and in the mock up is 14 mm. The mock-up consists of the stainless steel tubes and magnetite flakes. Steel tubes were Ti-stabilized stainless steel AISI 316 Ti, outer diameter 16 mm and wall thickness 1.5 mm.

Table 1. The applied parameters in eddy current tests.

Test	Description	Probe dia	Frequency	Gain	Comments
A	Magnetite pile thickness sizing, pile under the tube (abs. channel)	11.5 mm	10 kHz 25 kHz	48 dB	The thickness of magnetite pile under the test tube: few flakes, 1, 2, 5, 6, 8, 11, 15, 20, 25, 30, 35 and 40 mm
B	Magnetite detection with a large magnetite pile (abs. channel)	12 mm	10 kHz 25 kHz	32 dB	Tube surrounded with magnetite, only the amount of magnetite on one side of the tube is varied 5.5, 8.5, 11.3 and 14 (full) mm
C	Magnetite detection from adjacent tube (abs. channel)	12 mm	10 kHz 25 kHz	32 dB	Probe is in clean tube and it is detecting the varying magnetite pile in the adjacent tube 5.5, 8.5, 11.3 and 14 (full) mm

The magnetite, applied in the test serie A, located under the tube and in contact with the tube as shown in Figure 1. The thickness of magnetite layer varied from few flakes up to 40 mm as presented in Table 1.



Figure 1. Test series A: Test tube on the magnetite pile.

In the test series B and C two parallel tubes were used. The thickness of the magnetite pile in horizontal direction between the tubes was controlled by a plastic plate (Fig 2.). Another tube was embedded in the magnetite pile. In the test series B, the indication due to magnetite pile seen from the embedded tube was studied. In the test series C the indication due to magnetite pile seen from the free tube outside the pile was studied. The extension of the pile was restricted with acrylic plastic plates. Thickness of the plates and at the same time, the distance between

the pile and the outer surface of the free tube, were 8.5, 5.5, 2.7 mm. One measurement was conducted without plastic plate. In that case the thickness of the magnetic pile between the tubes is 14 mm i.e. the distance between the tubes.

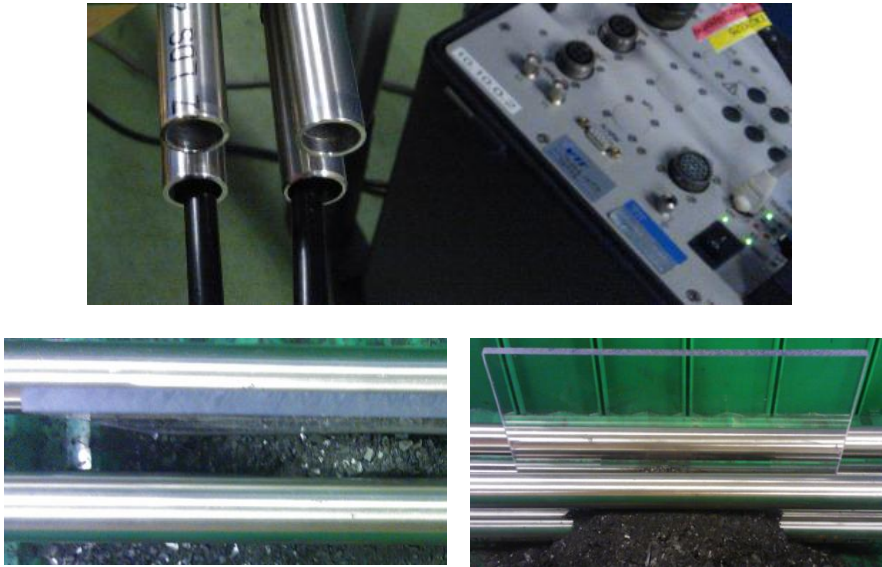


Figure 2. Test series B and C: The mock-up simulating horizontal VVER-440 steam generator tubing. The bottom tubes attached to the acrylic plastic plate were free of magnetite piles and deposits. The other tube was embedded into the pile. The free space between two bottom tubes was filled by acrylic plastic plate and magnetite flakes. The thickness of the pile in horizontal direction between the tubes was controlled by the plate.

6. Results

The results of the conducted tests show that the sensitivity in magnetite detection is greater when the lower 10 kHz inspection frequency was used. The amplitude of the magnetite indication is increasing when the thickness of the magnetite pile is increasing under the test tube.

The amplitude of the eddy current indication, in test A, is presented in Figure 3 as a function of magnetite pile thickness. When the eddy current frequency was 10 kHz, the amplitude of the magnetite indication was increasing, when the thickness of the magnetite layer under the test tube was increasing up to 10 mm. After that the signal saturated and the increase in the amplitude was not significant. When the 25 kHz eddy current frequency was used, the eddy current signal started to saturate when the thickness of the magnetite layer exceeded 8 mm.

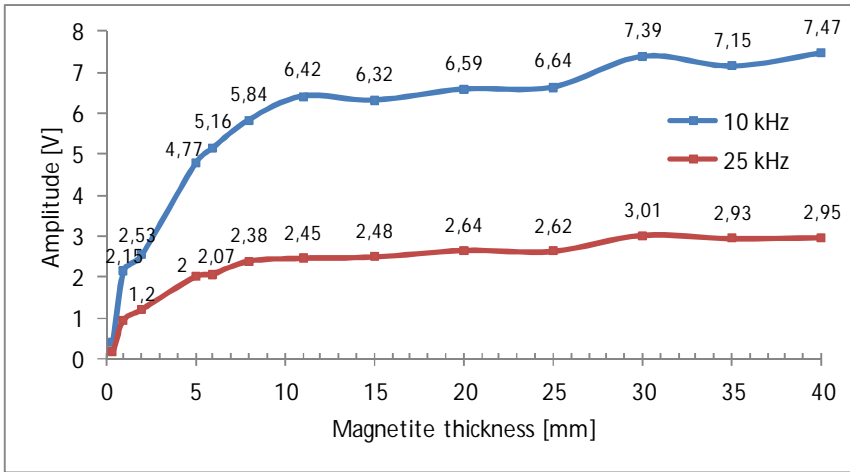


Figure 3. The amplitude of the magnetite indication as a function of the thickness of magnetite pile under the test tube. The increase in the amplitude was greater with inspection frequency 10 kHz. The amplitudes of the indication (10 kHz) due to a 1.3 mm through wall hole and the 10% OD groove were 0,9 V and 2.15 V.

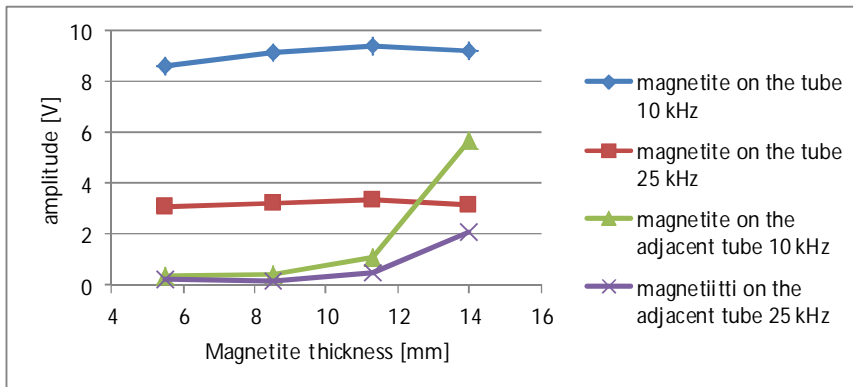


Figure 4. The amplitude of the magnetite indication as a function of the thickness of magnetite pile between the tubes. One of the studied tube was completely in magnetite pile. The amplitudes of the indication (10 kHz) due to a 1.3 mm through wall hole and the 10% OD groove were 0,4 V and 1.22 V.

The tests with tube embedded in the magnetite pile show, that the pile can be detected but the thickness variations of the pile on only one side of the tube cannot be detected with a single bobbin probe technique. The magnetite around the tube gives rise to a saturated indication and the changes of the thickness on one

side of the magnetite pile is not detected. The small amplitude variation seen in the upper curves of Figure 4 cannot be used to size the thickness of magnetite.

Tests, where the probe was in the tube outside the pile showed that the amplitude of the magnetite indication started to increase when the thickness of the magnetic pile between the tubes exceeded 11.3 mm, see the two lowest graphs in Figure 4. When the pile thickness between the tubes was 11.3 mm the distance between the pile and the outer surface of the probed tube was 2.7 mm. When the pile thickness was 14 mm the pile filled the space between the tubes.

6.1 Discussion

The results of the study showed that the thickness of the magnetite pile under the tube can be measured up to 10 mm if the eddy current frequency is 10 kHz and if the material of the pile is known.

In the case the tube was completely embedded in the unsymmetrical magnetite pile, the measurement the thickness of the pile was not possible with a single probe technique.

Development of the technique to measure the thickness of the magnetite pile will be continued. In the next phase two probes will be applied simultaneously. With this new technique it could be possible to map the areas where magnetic piles fill the volume between the steam generator tubes.

7. Conclusion

In this work the aim was to measure the thickness of the magnetite pile on the SG tubing. The results of the tests showed that the thickness of the magnetite pile can be measured, if the range of pile thickness is from 1 mm to 10 mm and the pile is located only on one side of the tube. A pile thicker than 10 mm saturates the magnetite indication.

The study will continue. The goal of the further studies is to develop a technique where two probes are used for measuring the thickness of the magnetite piles between two tubes.

References

1. Kupperman, D.S., Muscara, J., Bakhtiari, S., Park, J.Y. & Shack, W.J. Eddy current analysis round robin using the NRC steam generator mockup. Proceedings of the 4th International Steam Generator Conference. Toronto, Canada, May 5–8. 2002.
2. Son, D., Jung, W., Park, D.G. & Ryu, K.S. Magnetic Sensor for the Defect Detection of Steam Generator Tube With Outside Ferrite Sludge. IEEE Transactions on Magnetics, 2009, Vol. 45, No. 6, pp. 2724–2726.

3. Piriou, M. & Glass, S.W. Steam Generator Secondary Side Deposit – NDE Method for Support Plate Clogging. 7th International Conference on NDE in Relation to Structural Integrity for Nuclear and Pressurized Components. Yokohama, Japan, 12–15 May 2009.
4. Kim, M., Yim, C., Um, K., Kim, J., Kim, C. & Lee, S., Development of Scaled Deposit Measurement Technologies for Steam Generator Tubing. Singapore International NDT Conference & Exhibition. 4th April 2011.

Model assisted calculations for NDE reliability

Jonne Haapalainen & Esa Leskelä

VTT Technical Research Centre of Finland
Kemistintie 3, P.O. Box 1000, 02044 VTT, Finland

Abstract

There are multiple techniques to assess the reliability of non-destructive evaluation (NDE). Probability of detection (POD) curves can be used to find out the smallest flaw that will be detected with a certain probability and receiver operating characteristic (ROC) curves can be used to determine the performance of the amplitude-based classification systems. However, the problem with these techniques is that they require a large number of measurements for good results.

In this study, ultrasound simulations were used to generate data for POD and ROC analysis. In total 463 cracks with height from 0.5 mm to 10 mm were simulated. Skew and tilt angles of the cracks were normally distributed random variables with deviation of 5°. From height vs. amplitude data, POD and ROC curves were extracted.

Results indicate that due to varying tilt and skew angles, both detectability and classification accuracy decreases due to high variation of the amplitude signal. Moreover, the results show also the capabilities of model assisted probability calculations as a tool to improve NDE methods.

1. Introduction

There are many analytic methods to evaluate the reliability of NDE measurements. However, usually these require a large amount of empirical data which is expensive and time consuming to acquire. For instance typical probability of detection (POD) analysis requires at least 40 to 60 measurements for different size of flaws. Simulation of NDE gives many opportunities that are not possible with traditional measurement techniques. Simulation time for typical flaw response is ca. 10 minutes, which means that over hundred simulations can be done in 24 h.

1.1 POD

POD curves give the probability that a flaw with certain size (or larger) will be detected. For example if probability of detection for a flaw with height of 5 mm is 76%, it means that 76% of flaws higher than or equal to 5 mm will be detected and 24% of the flaws will be missed. In real situation flaws can have tilt, skew, roughness or some other properties which make the detection harder and those proper-

ties has to be taken into account when calculating POD curves. Therefore, some knowledge of true flaws is needed.

When generating a POD curve, the first step is to create multiple flaws. Size and other properties of the flaws, as well as properties of the base material, have to be as close to the real parameters as possible. Also, the measurement equipment and procedures used, need to be the same as those used in actual measurement. After this, samples are measured so that either ultrasound amplitude from flaw is recorded (a vs. \hat{a} model), or the measurement is performed as a blind test and flaws detected are reported (hit/miss model) [1]. The calculation of the final POD curve depends on the recorded data. Typically after calculation, a_{50} or a_{90} values are extracted from POD curve. These values are the flaw sizes where 50% or 90% of the flaws are detected.

Due to limited number of data points, 95% confidence limits of the POD curve are also calculated and $a_{90/95}$ is extracted. $a_{90/95}$ is the maximum size of the flaw which is detected nine times out of ten with 95% confidence. In other words, if POD curve generation is repeated 40 times with similar flaws the a_{90} value is over initial $a_{90/95}$ size once (and once under $a_{90/95}$ -size). The $a_{90/95}$ size increases a lot when number of flaws is small (Figure 1).

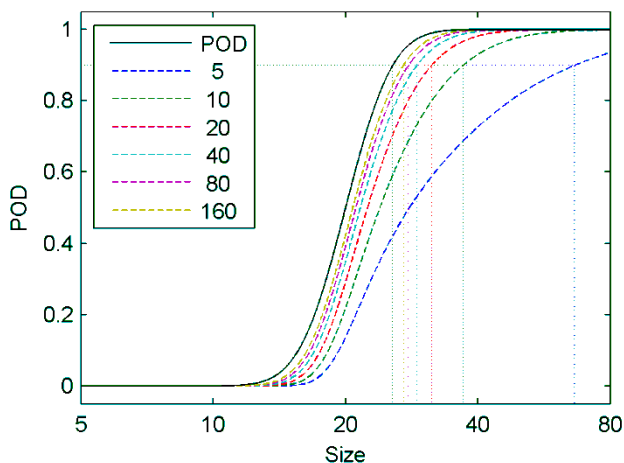


Figure 1. Example of POD curve (black solid line) and 95% confidence limits calculated with 5 to 160 measurements. a_{50} and a_{90} sizes from the POD measurement are 20 and 25.6 mm, whereas $a_{90/95}$ sizes for 5, 10, 20, 40, 80 and 160 measurements are 66.7, 37.1, 31.5, 29.1, 27.9 and 27.1 mm.

1.2 ROC

If classification of flaws is done by the amplitude, some limit is needed to classify the flaw signals as real and false flaw signals. In the classification, true flaw signals are signals from a defect that should be classified as defect, and false flaw

signals are signals from small defects or noise signals. The discrimination value can be determined with ROC curve. In ROC analysis, true class of each flaw is known, and by varying the discrimination value and comparing the classification results to actual classes, best classification accuracy can be found. As a result of ROC analysis, so called "confusion matrix" is usually presented to demonstrate the classification accuracy (Table 1).

Table 1. Confusion matrix for ultrasonic testing. Four different classes based on actual and predicted class exist.

		Actual class	
		Positive	Negative
Predicted class	Positive	<u>True positive (TP)</u> Large flaw is classified correctly and repaired	<u>False positive (FP)</u> Small flaw is repaired even though there is no actual need for repair. <i>Extra costs.</i>
	Negative	<u>False negative (FN)</u> Large flaw is missed. <i>Possible leak.</i>	<u>True negative (TN)</u> Small flaw is classified correctly. No action required.

If the classification was perfect, there were no FN and FP results, and the predicted classes were always the same as actual classes. However, with real data this is not the case and the best compromise has to be solved. Typically this is done with ROC curve, where true positive rate (TPR, true positives divided by all actual positives) and false positive rate (FPR, false positives divided by all actual negatives) are calculated as a function of threshold value and plotted against each other (Figure 2). In perfect classification, FPR should equal to 0 and TPR to 100% (upper left corner on ROC curve).

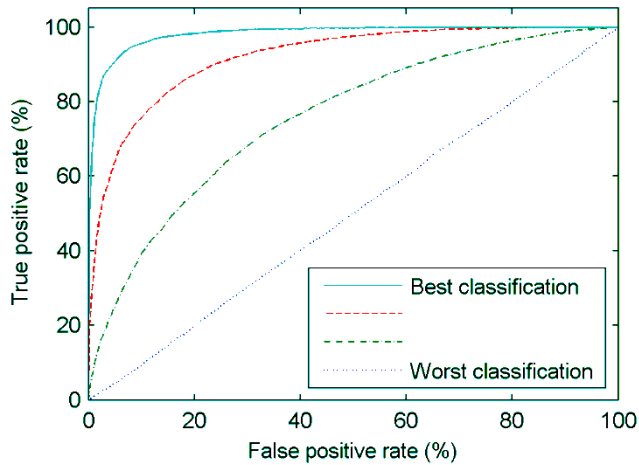


Figure 2. Four different ROC curves. Straight line with TPR=FPR represents a case where classifying is random, and there are as many true as false positives. In the best case, the data set has FPR of 7% and TPR of 93%.

2. Methods

The following measurement was simulated: 45° angle probe with 2 MHz transducer (MWB45-2), the flaw is surface breaking and has a semi-elliptical shape (length/height = 4). The probe is linearly scanned over the centre point of the flaw. The probe is located on a steel plate with thickness of 25 mm and transverse sound velocity of 3230 m/s (i.e. steel). The flaw and probe are on the opposite sides of the plate.

The defects were made by generating a random surface. Typical crack parameters (roughness, correlation length) were calculated from the random surface and the values were matched to literature values. Surfaces were then meshed to triangular pieces and every piece was individually placed into model so that they constructed a solid plane with realistic roughness (Figure 3). Meshing, parameter extraction and the generation of defects were automatized with MATLAB 2010b.

Surface roughness of $R_a = 100 \mu\text{m}$ was used, and tilt and skew of the flaws were randomly varied with a variance of 5°. These values are in the range of the measured parameters in actual in-service flaws [2]. In total, 463 flaws with height from 0.5 mm to 10 mm were generated. After simulations, the maximum amplitude was extracted from the data, and POD and ROC curves were calculated from data with MATLAB R2010b.

For POD calculation, detection limit (i.e. smallest detected signal) was equal to signal from smooth and perfectly perpendicular semi-elliptical crack of $1 \times 4 \text{ mm}^2$. Moreover, the assumptions for ROC calculation were that flaws smaller than 3 mm should be rejected, and flaws larger than 3 mm should be detected.

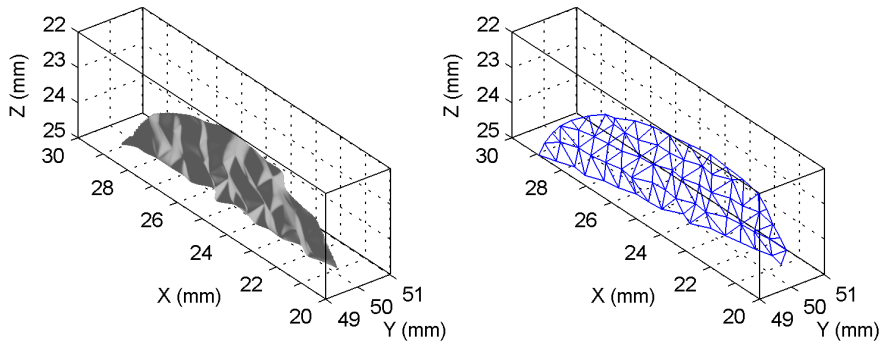


Figure 3. Random surface representing a semi-elliptical crack with size of $2 \times 8 \text{ mm}^2$ (left). Same surface with tilt and skew, and meshed to 108 triangular surfaces which are exported to CIVA 10.1.

3. Results

Maximum amplitude as a function of flaw height is presented in Figure 4.

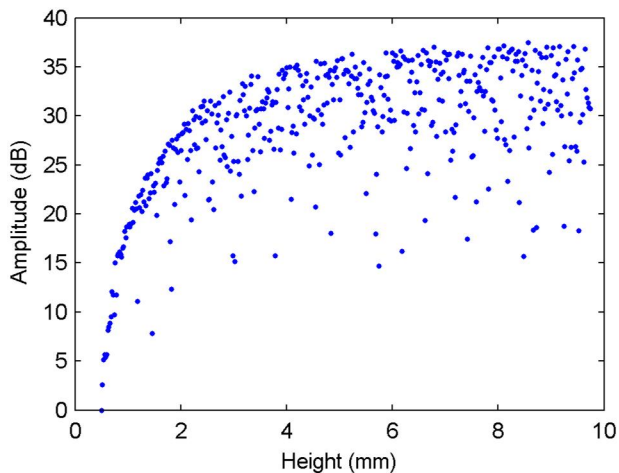


Figure 4. Signal amplitude as a function of flaw height. Amplitude increases as a function of flaw height until ca. 3 mm, where the increase slows. A deviation of $\pm 5^\circ$ in tilt and skew angles causes up to 20 dB amplitude variation.

3.1 POD

Data and calculated POD curve from simulations are presented in Figure 5. POD curve was generated in a log log scale meaning that the amplitude and size of a defect are presented in logarithmic scale.

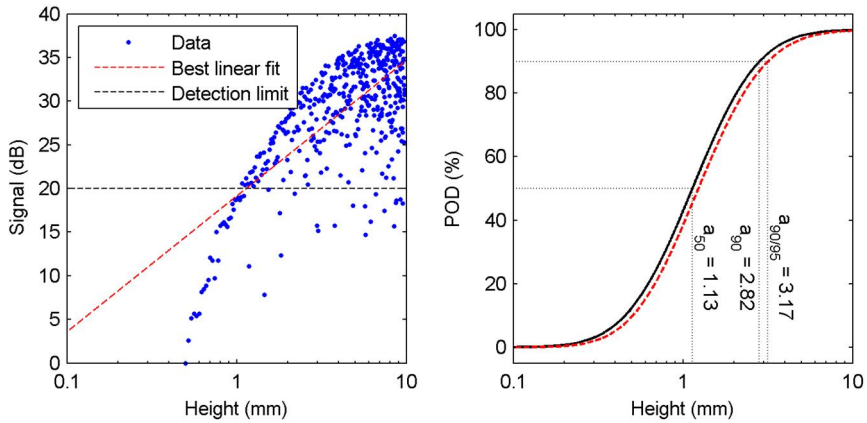


Figure 5. Data (a vs. \hat{a}), best fit and detection limits for simulations (left) and a POD curve calculated from a vs. \hat{a} data.

3.2 ROC

The accuracy of classification (the percentage of correct classifications) and ROC curve are presented in Figure 6. The highest accuracy (82%) is achieved when the limit is set to 25.8 dB. This point is indicated in Figure 6 with a red circle. With the highest accuracy, the TPR and FPR are 90% and 37%. The results of the classification are presented in Figure 7. Classification was also tested with 1 mm and 5 mm limits. The results are presented in Table 2. The effect of noise was not simulated in ROC curves. Because of this, the small defects are detected with a probability of 100% and the accuracy of classification is not affected by missed flaws which would not be the case in true classification.

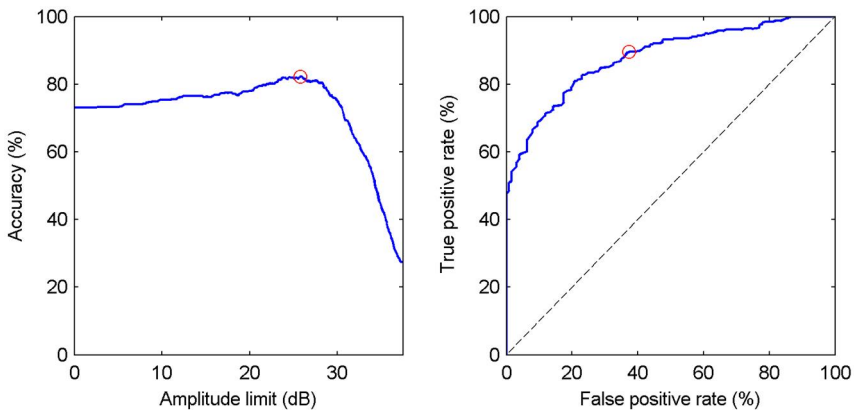


Figure 6. Accuracy (left) and ROC curve (right) of the classification. The best accuracy (82%) point is marked with a red circle in both plots.

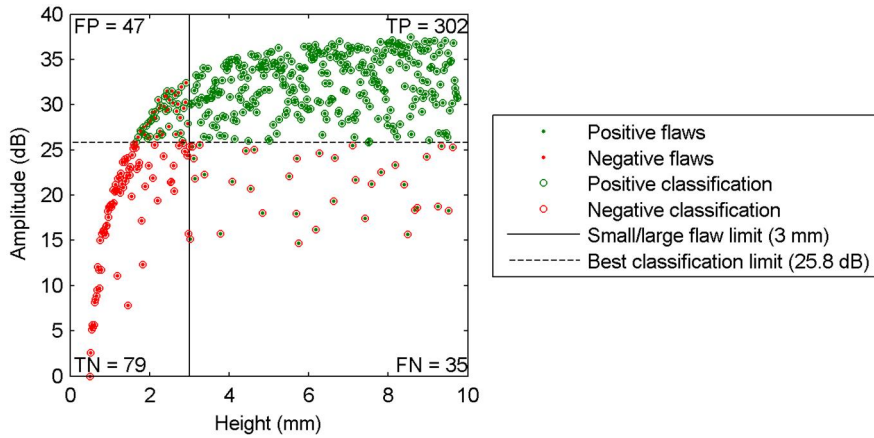


Figure 7. Classified data points. Small flaws under 3 mm are “negative” and large over 3 mm are “positive”. 381 of the 462 flaws were classified correctly when the classification threshold was 25.8 dB.

Table 2. Confusion matrices for ultrasonic testing classification with different limits between actual classes. The classification accuracy decreases as a function of flaw class limit.

1 mm		3 mm		5 mm	
TP = 428	FP = 4	TP = 302	FP = 47	TP = 146	FP = 50
FN = 9	TN = 22	FN = 35	TN = 79	FN = 91	TN = 176
Limit	Accuracy	Limit	Accuracy	Limit	Accuracy
16.7 dB	97%	25.8 dB	82%	31.4 dB	70%

4. Discussion

The generation of POD curves benefits a lot from modelling. Due to fast generation of data, confidence limits can be decreased compared to measurement results with only a few measurement points. The generated POD curve reveals that when compared to smooth and perfectly perpendicular crack (=detection limit), the flaws that are actually detected are much larger. Because of the skew and tilt angle variation and roughness, the $a_{90/95}$ -size of the inspection is 3.17 mm. This value is only 0.35 mm higher than a_{90} -size due to large number of points in dataset.

With ROC curves it can be seen that amplitude is not a sufficient parameter to classify the size of a defect. Tilt and skew angles of the flaws cause amplitude variation which is much higher than the difference between amplitudes from difference size of defects. If smaller deviation of the tilt and skew is assumed, better classification accuracy will be achieved. Also, better classification is achieved when class limit is decreased. This is due to smaller amplitude variation in small

flaws. If the classification presented in Figures 6 and 7 would be adjusted in a way that 95% of the large flaws (true positive rate) should be detected, the false positive rate increases to 61%, meaning that more than half of the actual negative (=small) flaws would be unnecessarily repaired. But if for example each false negative (missed large flaw) is 5 or 10 times more expensive than false positive (extra repair), this adjustment is cost-effective.

5. Conclusions

Model-assisted reliability studies (POD and ROC) of NDE methods give great advantage compared to empirical studies [3]:

- Allows detectability analysis even if actual component and flaws are not available
- Provides data to support the decisions in classification problems
- Allows parametric study for better detectability or higher classification accuracy.

However, there are also some challenges. Possible problems with simulation arise from the reliability of the simulation results compared to measurements. According to initial comparison to measurements of thermal fatigue crack, the effect of tilt to amplitude is not as high as it is according to simulations. This will be confirmed with measurements in the next phase of the project. Also the effect of noise should be analysed on classification and detection of flaws. Moreover, the effect of missed flaws from POD curves should be included to ROC analysis.

References

1. MIL-HDBK-1823A. Department of Defence Handbook: Nondestructive Evaluation System Reliability Assessment, 2009.
2. Wåle, J. Crack Characterisation for In-service Inspection Planning: An Update. Statens kärnkraftinspektion, 2006.
3. Wall, M., Burch, S. & Lilley, J. Review of models and simulators for NDT reliability (POD). Insight-Non-Destructive Testing and Condition Monitoring, 2009, Vol. 51, No. 11, pp. 612–619.

Experience in integrity assessment of steam turbine casings operated beyond the design lifetime

Andrei Dedov, Ivan Klevtsov & Toomas Lausmaa

Tallinn University of Technology (TUT) /
Thermal Engineering Department (TED)
Ehitajate tee 5, Tallinn, Estonia

Abstract

The basic components of power plants are operated under high temperature and high pressure. Long-term exposure in such conditions causes inevitable degradation of the structure and properties of materials. This paper presents the results of mechanical properties measurements of perlitic steel 15Ch1M1FL exposed at high temperature for different service time. Tensile properties have been measured by testing of miniature specimens fabricated from samples extracted from in-service steam turbine casings. All the tests have been performed at room temperature with metal structure investigation.

1. Introduction

More than 90% of electrical power consumed in Estonia is produced in Narva power plants where 200 MW condensing steam turbines K-200-130 are operated. Turbines are manufactured in 1960–70 at LMZ in Russia. Today the service time of turbines is up to 290 kh that exceeds the design lifetime approximately three times. Ensuring of reliable and safe operation of such ageing units is impossible without continuous monitoring of metal conditions. It is necessary to increase continuously the amount of inspection and to involve all possible methods. The experience in assessment of steam turbine casings integrity is presented in this paper.

K-200-130 steam turbines were designed for the steam with temperature of 565°C. However the actual steam temperature at Narva power plants is 510–515°C and the pressure of live steam and reheat steam is 13 MPa and 2.4 MPa respectively. The casings of steam turbines are made from cast steel 15Ch1M1FL. The chemical composition of the steel 15Ch1M1FL is presented in Table 1.

Table 1. Chemical composition of steel 15Ch1M1FL in wt.%.

Steel	C	Si	Mn	Cr	Ni	V	Mo	Cu	S	P
15Ch1M1FL	0.14–0.2	0.2–0.4	0.6–0.9	1.2–1.7	0.3	0.25–0.4	0.9–1.2	0.3	0.025	0.025

2. Investigation methods

It is known that long-term operation of steam turbine causes inevitable degradation of casings metal due to such factors like creep, accumulation of fatigue damages and thermal ageing including influence of corrosive medium. In general metal degradation can lead to decrease of metal mechanical properties (tensile strength, yield strength, relative elongation, hardness), increase of FATT, structure damage by creep cavities. Change in FATT can result in decrease of impact toughness and increase of yield to tensile ratio ($R_{p0.2}/R_m$) measured at room temperature that in turn can cause cracks initiation at the most loaded areas of turbine casings.

In accordance with requirements [1] in order to estimate the extended lifetime of the safe operation of the basic turbine components the following procedures should be carried out:

- metal structure investigation and measuring of metal mechanical properties of basic components for assessment of accumulated damage;
- stress analysis of the components;
- non-destructive inspection for defects detection;
- final analysis with making decisions of possibility, conditions and lifetime of turbine further operation.

3. Mechanical properties measuring

One of the possibilities to estimate the conditions of turbine casing is monitoring of short-term mechanical properties, tensile strength R_m and yield strength $R_{p0.2}$ measured at room temperature. Such monitoring could be performed by means of direct measurements of R_m and $R_{p0.2}$ by testing of specimens sampled from the turbine casings or by means of indirect determination on the basis of measured in-situ metal hardness by portable hardness tester.

According to requirements [1] the basic criteria for turbine casing metal condition assessment is metal yield strength $R_{p0.2}$. The minimal allowable $R_{p0.2}$ for this steel grade is specified to be 255 MPa. Metal hardness can be also as independent criteria of metal condition so Brinell metal hardness number HB for post-exposed steel 15H1M1FL should be not less than 145 [1].

In the past tensile strength and yield strength were measured by tensile testing of standard cylindrical proportional specimens. Specimens were fabricated from the big samples extracted from the internal surface of the turbine casings in the area of steam inlet of high pressure (HP) and intermediate pressure (IP) sections

of turbine (Figure 1, areas H and I.). These areas were specially intended by turbine manufacture (LMZ) for metal sampling. Tensile strength and yield strength were measured at room temperature and at operation temperature. Impact strength and FATT were also measured. Since 1998 the special sampling machine MASM-1 was used for extraction of miniature samples from internal and external surfaces of the turbine casings [2]. Areas of sampling see Figure 1.

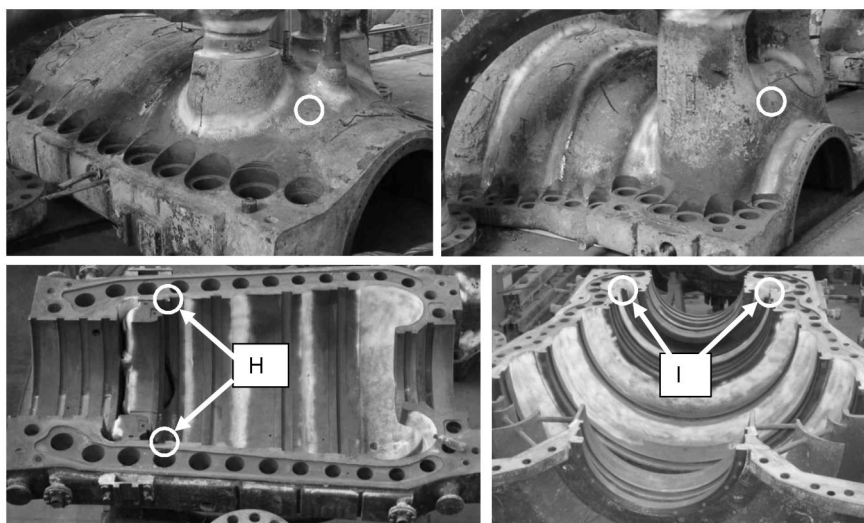


Figure 1. Metal sampling areas of HP and IP turbine casings.

On the basis of the samples the metal structure was analysed and tensile properties were measured by small punch testing [3] or mini-tensile testing [4]. Miniature samples were also extracted from turbine rotors, steam drums, headers, bends of live and hot reheat steam pipes. As a result quite large database was obtained. This allows monitoring, in particular, decreasing of R_m and $R_{p0.2}$ depending on service time. An example of change in R_m and $R_{p0.2}$ measured at room temperature for metal of turbine casing is presented in Figure 2. It is seen that the values of R_m and $R_{p0.2}$ have a quite large scatter, which is typical for cast metal, characterized by a significant heterogeneity of the properties even for new material. It is quite difficult to perform the data analysis in this way.

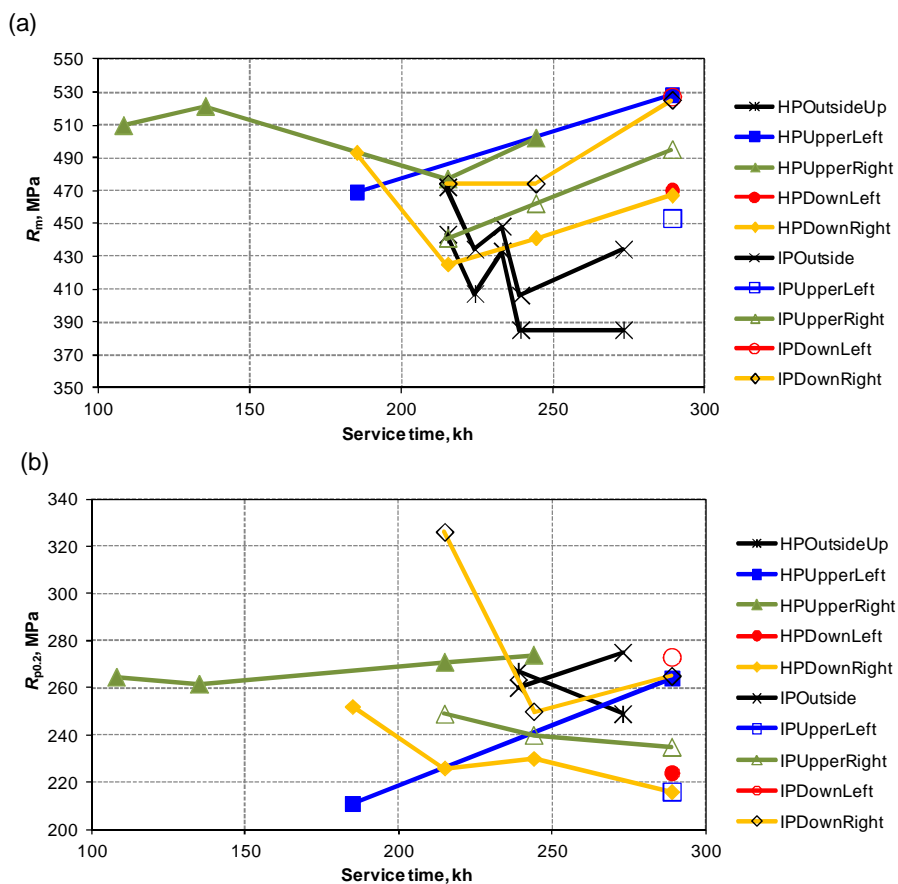


Figure 2. Trend of R_m and $R_{p0.2}$ measured at room temperature depending on service time for unit No. 1.

According to [5] the relationship between R_m and $R_{p0.2}$ measured at room temperature for cast steel 15Ch1M1FL and service time could be presented by the following empirical equations:

$$R_m = 780 \cdot \tau^{-0.04}, \text{ MPa} \quad \text{and} \quad R_{p0.2} = 569 \cdot \tau^{-0.0627}, \text{ MPa}, \quad (1)$$

that give a linear relationships in logarithmic scale:

$$\lg(R_m) = \lg(780) - 0,04 \cdot \lg(\tau); \quad \text{and} \quad \lg(R_{p0.2}) = \lg(569) - 0,0627 \cdot \lg(\tau). \quad (2)$$

Equations (1) are based on the statistical analysis of the large databases concerning R_m and $R_{p0.2}$ measurements by testing of samples extracted from steam turbines operated at thermal power plants in Russian Federation. Figure 3 presents

the results of $R_{p0.2}$ measurements at room temperature for steam turbine unit No.1 of Narva power plants and their correlation by equation (2), see fit line. It is seen that fit line crosses the line of minimal allowable value of $R_{p0.2} = 255$ MPa at about 187 kh of operation. However, $R_{p0.2}$ measured on some specimens still fulfill requirements.

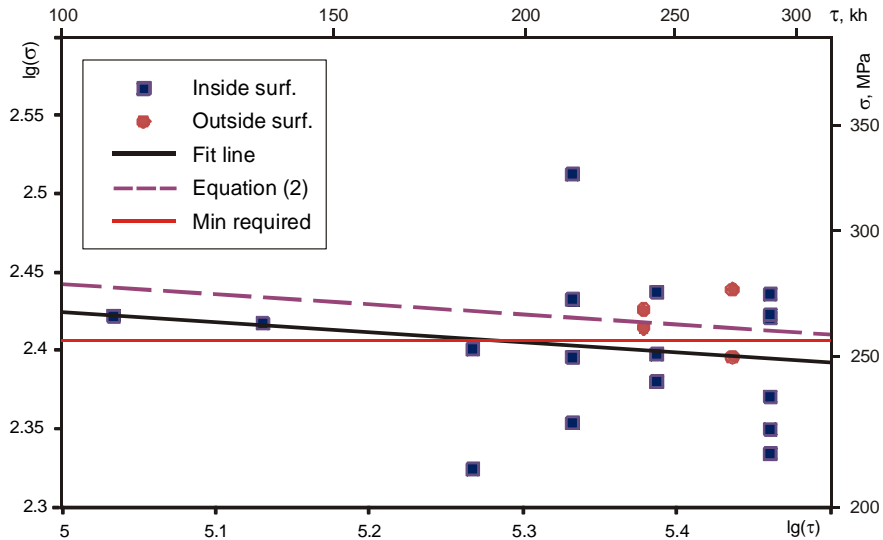


Figure 3. Yield strength of steel 15Ch1M1FL measured at room temperature on specimens extracted from turbine casings of Narva power plants unit No.1 depending on service time.

4. Cracking

Monitoring of cracks initiation in metal of steam turbine elements has been carried out starting with the first outages of units for overhaul. In order to identify the most loaded areas of turbine casing of the HP and IP sections the stress analysis has been performed in TED of TUT. Analysis has been carried out on 3D model (Figure 4) by method of finite elements in COSMOS/M. Steady-state and transient conditions have been analysed taking into account influence of internal pressure and thermal stresses.

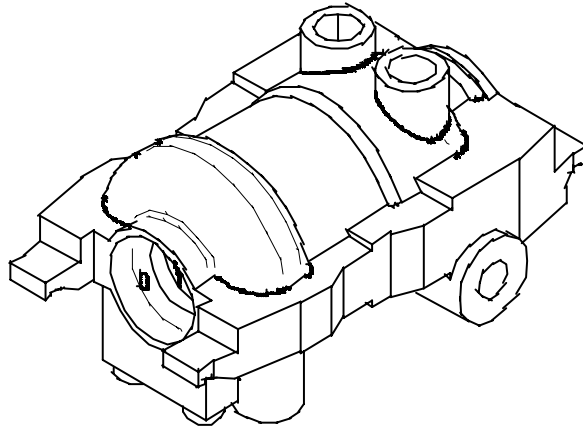


Figure 4. 3D model of K-200–130 turbine casing.

The need for a three-dimensional model is grounded by the fact that the two-dimensional modelling is not accurate enough, since 2D calculation cannot take into account the influence of massive flanges and large fittings, and the difference of upper and lower casings (as it could be seen in Figure 4).

Stress distribution on the internal surface of the turbine HP casing in steady-state and transient (the rate of temperature rise 2°C/min) conditions is presented in Table 2. Location of specific zones is presented in Figure 5. The results of stress analysis of turbine IP casing are presented in Table 3 and Figure 6.

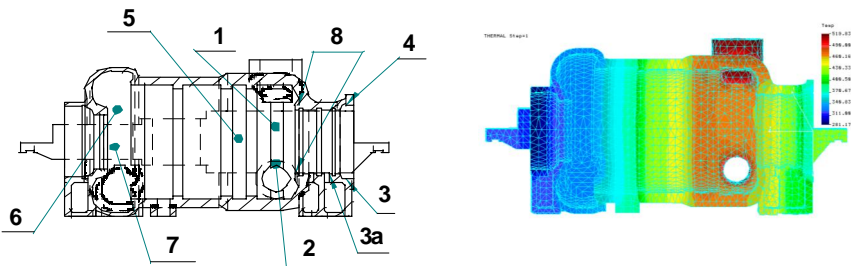


Figure 5. Specific zones and temperature distribution on the internal surface of steam turbine K-200-130 HP casing in steady-state conditions.

Table 2. Temperatures and stresses in the specific zones of steam turbine K-200-130 HP casing.

Steady-state regime			Transient regime		
Zone	Temperature, °C	Stress, N/mm ²	Zone	Temperature, °C	Stress, N/mm ²
1	465	94,4	1	410	203
2	500	82	2	430	206,2
3a	400	157,3	3	340	315,4
-	-	-	4	340	455,9
5	470	75	5	437	158
6	320	112,2	6	297	120
7	320	112,2	7	297	120
8	465	111,7	8	429	211

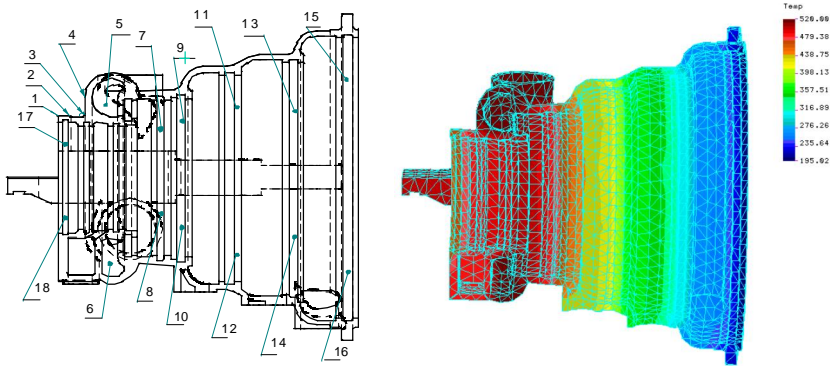


Figure 6. Specific zones and temperature distribution on the internal surface of steam turbine K-200-130 IP casing in steady-state conditions.

Table 3. Temperatures and stresses in the specific zones of steam turbine K-200-130 IP casing.

Steady-state regime			Transient regime		
Zone	Temperature, °C	Stress, N/mm ²	Zone	Temperature, °C	Stress, N/mm ²
1	450	64	1	440	87
2	480	84	2	490	96
3a	510	62,5	3	500	73
-	510	46,4	4	510	55,5
5	515	44,4	5	425	75
6	515	68	6	510	86
7	492	65	7	425	95
8	492	65	8	405	118
9	458	50	9	405	217
10	458	50	10	405	118
11	360	66	11	350	122
12	360	60	12	350	106
13	300	70	13	290	131
14	300	70	14	240	111
15	240	57	15	170	109
16	240	57	16	187	103
17	472	101	17	480	173
18	472	115	18	460	181

Stress distribution in HP and IP casings of turbine K-200-130 is generally similar. The maximum stresses occur in the area of seals (Figure 5, zones 3, 4, 8 and Figure 6, zones 17, 18) in transient conditions. This is due to high thermal stresses in this area, caused by a significant temperature gradient. In the area of steam inlet (Figure 5, zones 1, 2 and Figure 6, zones 4–6), where is the highest temperature, the stress level is rather moderate. So in steady-state regime the stresses in the steam inlet area of HP turbine casing are 80–100 N/mm², for IP casing 45–70 N/mm². High stresses in zone 9 of IP casing in transient conditions are explained by high thermal stresses (vicinity of steam inlet) and stress concentration due to geometry of model.

Visual, ultrasonic and magnet particles inspection of turbine casings is used for cracks detection [1]. If the defect is detected the decision of defect removing is made on the basis of crack dimensions and wall thickness of casing. The location of the crack is also taken into account. Possible decisions could be as following: leaving crack without repair; holes drilling at the tips of the cracks; crack removing without welding and crack removing with post-welding [6]. Limit state for the turbine casing is the appearance of cracks of a certain depth, limiting their reliable operation till the next outage [1].

A detailed location of the detected cracks is not presented in this paper, however it should be mentioned that crack location corresponds to the areas with increased stresses in steady-state and transient conditions. So quite often cracking occurs in zones 7–10 (Figure 6) of IP turbine casings. Cracking of HP casings metal is usually detected in the steam inlet area (zones 1, 2 in Figure 5) and very seldom in zones 3, 4, 8 (Figure 5), where the stresses are higher. The last could be explained by lower temperature in the areas with higher stresses and higher temperature in the steam inlet area that decreases mechanical properties of metal.

Service time influence on the total number of turbine components with detected cracking is presented in Figure 7. The shape of the plot meets the classical curve of failures depending on service time. At the initial stage of operation slightly higher number of detected defects is caused by manufacture defects, residual stresses, etc. More frequent detection of cracks in metal after long-term operation is caused by accumulation of fatigue damage, creep damage, deterioration of mechanical properties, etc. The marked increase in detection of cracks indicates an increase in the risk of further operation of turbine casing. The general analysis of the appearance and growth of cracks in the turbines casings of Narva power plants allows concluding that the catastrophic development of cracks is not observed.

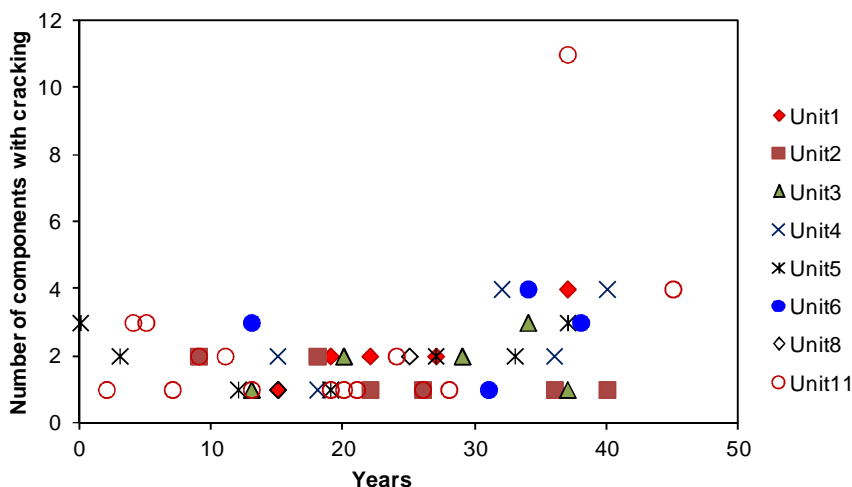


Figure 7. Number of turbine components with detected cracks.

5. Metal structure investigation

Metal structure investigation is performed on metallographic samples extracted from the steam inlet area of turbines, in zone with the highest temperature of metal, Figure 1. Metal structure damage of turbine casings depending on operation time is shown in Figure 8.

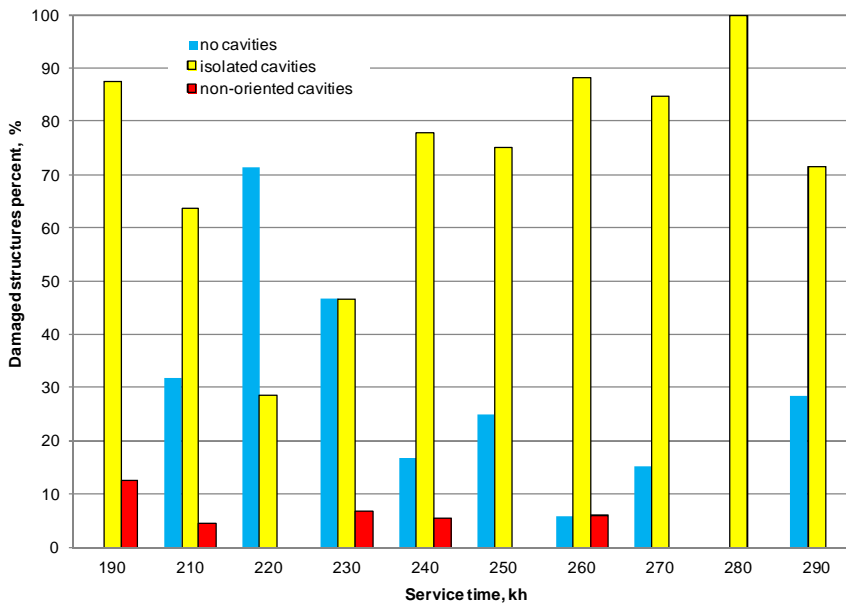


Figure 8. Percent of structures, damaged by creep cavities depending on service time.

To date, mainly the second class (isolated cavities) of metal structure creep damage observed. So low class of structure damage after quite long operation could be explained by the low steam operating temperature (510–515°C). Structure creep damage in this case does not impose significant restrictions on the continued operation of the turbine casing but it is clearly visible increase of number of samples damaged by creep cavities and decrease of undamaged ones.

6. Conclusions

On the basis of conducted investigations 3R (replace, repair, renovation) decision shall be made. If no catastrophic deterioration of material properties and cracks propagation observed, the commission of technical expertise shall appoint the time till the next mandatory inspection.

In the case of unit No 1 turbine casings taking into account above presented results of metal testing the commission of technical expertise decided to allow turbine further operation till the next mandatory inspection that shall be carried out not later than after 25 kh.

References

1. CTO 17230282.27.100.005-2008. Basic components of boilers, turbines and piping of thermal power plants. Metal inspection. Standards and requirements. (in Russian).
2. Dedov, A., Klevtsov, I., Lausmaa, T. & Neshumayev, D. Method of small samples for assessment of properties of power plant components: sampling devices and stress concentration in dimples. Proceedings of International Conference Baltica VII on Life Management and Maintenance for Power Plants, Helsinki – Stockholm – Helsinki, 12–14 June, 2007, Vol. 2, pp. 180–192.
3. Klevtsov, I., Dedov, A. & Molodtsov, A. Using of small punch test for determination of tensile properties of power plant steels. Proceedings of the 6th International Conference of DAAAM Baltic Industrial Engineering – Adding Innovation Capacity of Labour Force and Entrepreneur, 24–26 April 2008, Tallinn, Estonia.
4. Klevtsov, I. & Dedov, A. Condition assessment of power plant components operating under creep by testing of miniature specimens. Proceedings of 2nd ECCC Creep Conference Creep & Fracture in High Temperature Components – Design & Life Assessment Issues, April 21–23, 2009, Zurich, Switzerland, pp. 1126–1137.
5. Report on “Life assessment of turbine K-200-130 unit No.7 of Eesti power plant”, NPO CKTI, 2007.
6. CO 153-34.17.440-2003 Code of practice for steam turbines life extension beyond base life. (in Russian).

Evaluation of mechanical properties and microstructure of dissimilar weld joint of COST F and FB2 steels after long term creep test

Josef Kasl¹, Dagmar Jandová¹, Eva Chvostová¹ & Eva Folková²

¹Research and Testing Institute Plzeň,
Tylova 1589/46, 301 00 Plzeň, the Czech Republic

²Doosan Škoda Power s.r.o.
Tylova 1/57, 301 28 Plzeň, the Czech Republic

Abstract

Trial dissimilar weld joint was prepared from COST F and COST FB2 type steels using TIG HOT-WIRE method in conditions used in industrial praxis for production welded steam turbine rotor. Long-term creep tests to the rupture of smooth cross-weld samples have been carried out at temperatures ranging from 550 to 650°C and at stresses from 70 to 220 MPa. Fractographic analysis, hardness profile measurement and study of submicrostructure using light, scanning and transmission electron microscopy have been performed. Creep strength of weld joint falls into $\pm 20\%$ scatter band of the creep strength of the base material COST F up to 600°C. Different types of cracking were observed in dependency on conditions of creep test: fractures were located in the base material of steel COST F at lower temperatures and higher stresses and in the fine prior austenite grained or intercritically reheated part of heat affected zone of steel COST F where cavitation failure was evident.

1. Introduction

The continuous trend towards more economic electricity production together with reduced environmental pollution can be sustained by improving the thermal efficiency of power generation plants. One way how to increase the efficiency of fossil power plants is increase in temperature and pressure of the steam which finally results in the need for improved materials for the boiler and turbine design.

Rotor is one of the most important components of the steam turbines. Large rotors for turbines of high power can be produced in form of a solid forging or a component welded of several parts. The welded rotors have the following advantages in comparison with solid-forged ones: application of different materials with optimal properties for different parts of rotor at given operating conditions,

reduction in weight of welded parts, which can be forged more precisely than large ones, higher metallurgical accuracy, reduced heat load and faster start-up.

Doosan Škoda Power has recently established a new station for vertical welding of turbine rotors supplied by Polysude enables automated welding of rotors for single-casing turbines intended for high-temperature steam input (600°C) as well as for low-pressure components of the highest output rating turbines with rotors up to 135 tonnes in weight, rotor discs of a maximum diameter of 2.2 m, and a maximum length of 12 m. The maximum permissible weld thickness is 135 mm for diameters ranging from 400 mm to 1,200 mm.

Turbine and generator rotors undergo high stresses and, from a safety aspect, they belong to the most significant components of a turbine generator system. Depending on the appropriate operating temperatures, the shafts can be made of low/high alloy heat resistance material or of low alloyed, highly toughened materials primarily used for low pressure application. Several material combinations for welded rotors production have been or are being still tested in Doosan Škoda Power s.r.o. One of them is a rotor made of steels grades COST F and FB2.

Those higher alloyed steels of the 9–12% Cr class have been developed in the frame of the European COST research programme in which VZU Plzeň was participating since 1992. The standard material in manufacturing turbine rotors is the meanwhile well-established tungsten alloyed 10% Cr-steel COST E (10%CrMoWVNbN). It was originally developed within COST Action 501 (1983–1997) for steam turbine applications as a rotor material, same as steels F and B2 [1]. Recently grade F (10%CrMoVNbN) has become common in production. Both materials are qualified and allow the new generation of fossil fired ultra super critical thermal power station to operate at live steam and reheat steam temperatures of 600°C and supercritical live steam pressures up to approximately 300 bar [2].

The trend to even higher steam conditions was the subject of the COST 522 programme (1998–2003) where the very promising properties of FB2 test material, based on B2 with addition of Co, led to an upscale to industrial heat to manufacture three trial rotor forgings [3]. While short test of trial rotors is already finished, long term creep tests are still running. The results gained so far show that all data lie in one narrow scatter band confirming the trial melt behaviour of FB2. The very good creep behaviour of steel FB2 can be attributed to characteristic microstructural features and their stability under the influence of temperature and stress [4].

This paper deals with the study of rupture properties and microstructure evaluation in the samples of trial dissimilar weld joint of rings made of steels COST F and COST FB2. This weldment was prepared in the same conditions used for the welded rotor production.

Welded joints are the most critical parts of high temperature operating plants and are commonly susceptible to fracture. Rupture is usually initiated in a specific region as a result of structural heterogeneity of the weldment formed either during fabrication or during service. Since cyclic thermal and stress loading after each

weld pass effect on the steel structure, great attention has to be paid to welding technologies and selection of convenient filler materials.

2. Experiments

2.1 Materials and welding process

Dissimilar weld joints were prepared from forgings of two rings (external diameter of 600 mm and thickness of 200 mm) made of steels type COST FB 2 ((X13CrMoCoVNbN9-1-1) – the base material 1 and COST F (X14CrMoVNbN10-1) – the base material 2. Producer of both the forgings was SAARSCHMIEDE GmbH Freiformschmiede according the specification of Doosan Skoda Power s.r.o. The quality heat treatment of forgings was 1070°C/6,5h + 570°C/12,5h + 710°C/24h and 1050°C/6h + 1100°C/6h + 570/12,5h + 720/24h for the base material 1 and the base material 2 respectively. Two filler materials were tested, namely Thermanit MTS 3 (W-CrMo91) and PSM Thermanit MTS 616 (W-ZCrMoVWNb).

Welds were carried out using automat welding method 141+111 (TIG HOT WIRE) into narrow gap in internal protection by argon. The thickness of welded walls was 120 mm. Three post-weld heat treatments processes were applied on the weldments. On the base of evaluation of mechanical properties, hardness and microstructure observation the weld joint with the weld metal of THERMATIT MTS 616 and the PWHT of 710°C/15 hours were chosen as the most promising variant for a rotor production. For inspections of welded zones after post-heating treatments, the ultrasonic testing TOFD method was used as well as standard NDT surface inspection.

The chemical compositions of the base materials COST F and COST FB2 and the filler metal used are given in Table 1.

Table 1. Chemical composition in weight %.

Part	Element																	
	C	Mn	Si	P	S	Cr	Ni	Mo	V	Co	W	Nb	N	B	Al	Sn	As	Sb
Base material FB2	0.13	0.34	0.08	0.005	0.001	9.6	0.17	1.48	0.2	1.32		0.059	0.016	0.0079	0.007	0.002	0.008	< 0.001
Weld metal MTS 616	0.11	0.42	0.3	0.005	0.003	8.87	0.57	0.56	0.18	0.15	1.49	0.051	0.018	0.0036	0.009	0.003	0.022	< 0.001
Base material 2 F	0.11	0.56	0.06	0.008	0.002	10.36	0.64	1.46	0.2			0.059	0.016	0.0079	0.009			

2.2 Sample preparation and used methods

Smooth cross-weld specimens with a length of 92 mm and a diameter of 8 mm were fabricated from the weld joint. Creep tests to the rupture of these specimens were carried as well as of specimens machined from both the base materials. Fracture surfaces of ruptured samples were observed using scanning electron microscope (SEM).

Then specimens were cut along their longitudinal axis. Macrostructure was revealed using Villela-Bain's reagent and location of fracture in the weldment was specified. Hardness measurement along the specimen axis was performed.

Microstructure on longitudinal sections was observed using light microscopy (LM) and scanning electron microscopy (SEM). The substructure was evaluated in transmission electron microscope (TEM). The foils were thinned to the electron transparency by a jet polishing in 6% solution of perchloric acid in methanol at -40°C. Energy dispersive X-ray microanalysis (EDX) and electron diffraction were used for the identification of secondary phases.

3. Results

3.1 Mechanical properties

Integrity and mechanical properties of weld joint have been evaluated according to the welding standards EN 288-2,3. All results were satisfactory.

Mechanical properties of the segment which was used for creep test sample preparation are summarised in Tables 2a,b,c.

Table 2a. Mechanical properties of the weld joint.

Mechanical properties	R _{p0,2} [MPa]	R _m [MPa]	A [%]	Z [%]	Fracture location	Notice
BM1	677	817	16,6	62		
BM2	608	755	18,4	70		
WM	717	821	17,4	65		
Weld joint	637	796	15,0	52.6	BM1	Average value

Table 2b. Mechanical properties of the weld joint. Results of impact tests.

Impact test	KV [J]			
	1	2	3	Average
BM1	68	96	76	80
HAZ BM1 - face of weld	166	174	178	173
HAZ BM2 - weld root	166	170	175	170
BM2	100	163	150	138
HAZ BM2 - face of weld	97	144	86	109
HAZ BM2 - weld root	96	99	100	98
WM - face of weld	52	40	26	39
WM - root of weld	22	31	23	25

Table 2c. Mechanical properties of the weld joint. Hardness measurements.

Hardness HV10	1	2	3	Average
BM1 - face of weld	235	232	233	233
HAZ BM1 - face of weld	224	224	216	221
WM - face of weld	260	258	262	260
HAZ BM2 - face of weld	228	218	218	221
BM2 - face of weld	228	228	232	229
BM1 - weld root	230	233	232	232
HAZ BM1 - weld root	207	224	227	219
WM - weld root	258	260	258	259
HAZ BM2 - weld root	232	221	228	227
BM2 - weld root	225	236	228	230

3.2 Creep tests

The creep rupture testing was carried out in the air at temperatures ranging from 550°C to 650°C and stresses from 70 MPa to 220 MPa. The longest time to the rupture of samples broken up this time is about 7,000 hours. List of specimens investigated is given in Table 3.

Table 3. Creep testing results: time to rupture in h, fracture position (in brackets when in progress).

Temperature [°C]	Stress [MPa]											
	70	80	90	100	120	130	140	150	160	180	200	220
550										(5134)	(5134)	
575						(5134)		(5134)			1345 F	653 F
600			(5134)	(6648)	(7649)		3656 IC/FG HAZ F		2712 F	577 F		
625		7137 FG/CG HAZ F	4736 FG HAZ	1939 FG HAZ	896 FG HAZ		815 IC/FG HAZ F					
650	3552 FG/CG HAZ F	2741 IC/FG HAZ F		343 FG HAZ								

Obtained creep data were evaluated using Larson-Miller parametric equation:

$$P = T * [C + \log \tau], \quad (1)$$

where T represents temperature given in Kelvin degree, C is a specific constant for a given material (36) and τ means time to rupture in hours.

Results of creep tests compared with the creep rupture strength data of COST F steel [5] are graphically represented in Figure 1. Creep rupture strength of original trial COST F steel was used as reference data because of no samples prepared of the base materials used in this experiment have not broken yet. Open symbols in Figure 1 indicate creep tests, which are still running.

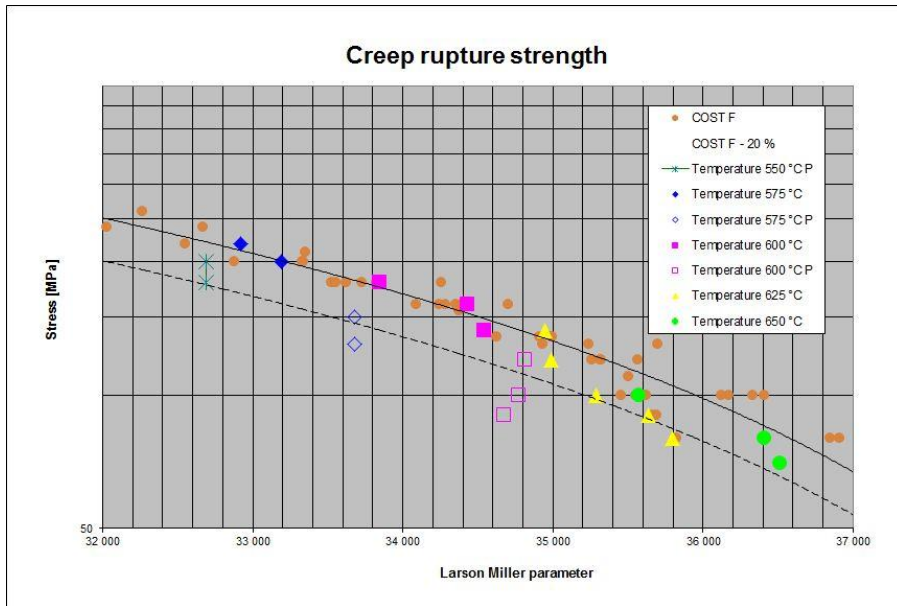


Figure 1. Creep rupture strength vs. LMP.

Samples tested at 550°C are still in progress. Their current creep data are in the permitted scatter band $\pm 20\%$ of the creep strength of the base material. Creep strengths of all ruptured samples tested at 575°C (two samples are still in progress) are comparable with creep strength of the base material. The creep strengths of (ruptured) samples tested at 600°C are on the level of the base material. However three samples are still in progress. The creep strengths of the samples tested 625 °C (all tested samples broken) fall into the scatter band $\pm 20\%$ of the creep strength of the base material COST F with exception of the sample tested at the lowest stress, which is below this scatter band. The creep strengths of samples tested at the highest temperature 650°C are inside of the scatter band.

3.3 Fractography analysis

Fractographic analysis of broken samples was performed. Firstly, it should eliminate an influence of possible defects formed during the welding process on creep results and secondly, it should find the growth mechanisms of cracks.

This analysis and observation of longitudinal sections of the ruptured crept samples showed that locations of fractures depended on the creep conditions. These positions are summarised in Table 3. The samples tested at lower temperatures and higher stresses failed in the base material (BM) of steel COST F unaffected by welding while those tested at higher temperatures and lower stresses ruptured in the grain refined part (FG) or in the intercritically reheated part

(IC) of the heat-affected zone (HAZ) of the base material of steel COST F. Ductile fracture in the BM occurred after short durations of creep tests (up to 2,700 hours). The fractures are transcrystalline ductile with considerable macroplastic deformation (elongation about 18%) and with the dimple morphology of the fracture surface. Its appearance is similar to ductile rupture at tensile tests at the same temperature. Others samples ruptured by transgranular creep fracture in the HAZ of the base steel COST F. Elongations of these specimens were usually a few percent. Individual small cracks formed of growing cavities joined and spread step by step across the sample. Exact positions of fracture change from IC part of the HAZ to boundary between fine grained and coarse grained part of the HAZ with increasing temperature and decreasing stress (Table 3).

3.4 Hardness profiles

Hardness HV10 profiles across the weld joints were determined for the weld joint before and after creep testing. Before creep testing average hardness of both the base materials was about 240 and hardness of the WM about 280. Local minima in the fine grained or in the overheated part of the HAZs were found – 212 in the COST FB2 and 213 in the steel COST F (Figure 2a).

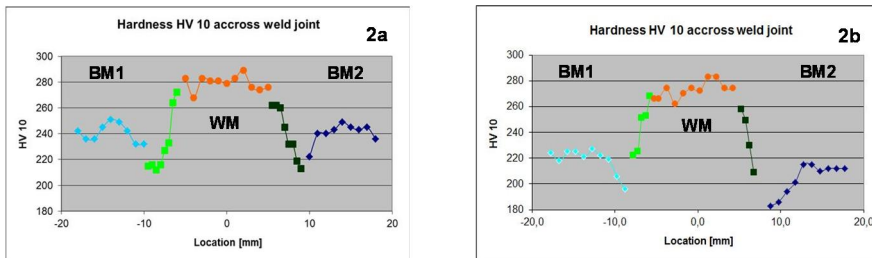


Figure 2a. HV10 profile of the weld joint before creep testing.

Figure 2b. HV10 profile of the sample tested at 625°C and 120 MPa.

During creep test (up to duration about 7,000 hours) the most significant decrease of hardness occurred in the IC part of HAZ of steel COST F. After the creep test at 625°C and 120 MPa the hardness fall on the level of about 180. A larger decrease of hardness of the base material COST F was also found. On the other hand the hardness drop of both the base material COST FB2 and its HAZ was not so considerable. The hardness of the weld metal only slightly decreased (Figure 2).

3.5 Microstructure

Macrostructure of cross-section of the weld joint is shown in Figure 3. Structure of the base material of steel COST F is relatively coarse grained in comparison to

steel COST FB2. A width of heat affected zones ranges from 2.5 to 3.0 mm on both sides of weldment.

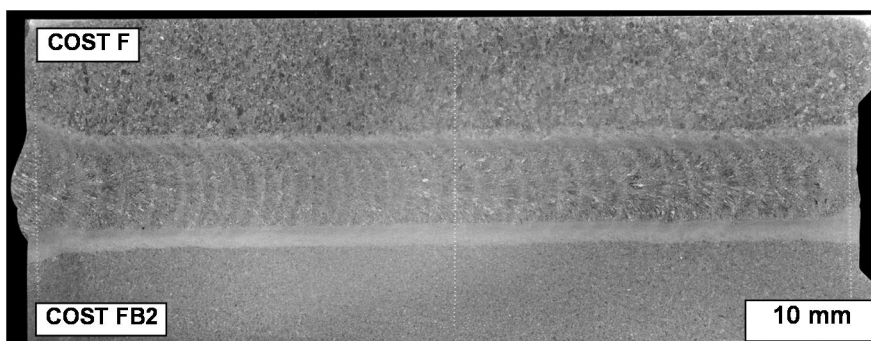


Figure 3. Macrostructure of the cross-section of the weld joint.

Microstructure of the weld joint consists of tempered martensite with a high dislocation density and a large number of particles of secondary phases. Plate-like or lath-like ferritic structure subdivided into subgrains was observed in the base materials (Figure 4), the heat affected zones and the weld metal (Figure 5a). All structures have the same features, nevertheless some differences were found out in individual zones. Particles of δ -ferrite sporadically occurred in steel COST FB2, while no any were not found in steel COST F. Small islands of δ -ferrite were present in the weld metal especially in the root. The base material of steel COST FB2 is coarse grained in comparison with the base material of steel COST F. Coarse particles of primary boron nitrides were not observed in steel COST FB2. Boron is probably dissolved in solid solution and in chromium carbide particles [6]. Fine precipitates and substructure were observed in carbon extraction replicas and thin foils using TEM. Relatively coarse chromium rich $M_{23}C_6$ carbides precipitated at prior austenite grain boundaries, ferrite plate boundaries and subgrain boundaries in all weld zones. Fine vanadium/niobium MX carbonitrides were spread within ferrite laths more often in steel COST F and the weld metal than in steel COST FB2. Density of chromium carbides was higher in steel COST FB2 than in other parts of the weldment. Relatively coarse $M_{23}C_6$ carbides pin grain and subgrain boundaries, while fine carbonitrides act as obstacles for dislocation slip. All these precipitates increase the steel strengthening and retard recovery of dislocation substructure. Dislocation density is slightly higher in steel COST F ($5.9 \cdot 10^{14} m^{-2}$) then in the weld metal ($4.9 \cdot 10^{14} m^{-2}$) and in steel COST FB2 ($4.1 \cdot 10^{14} m^{-2}$). In the weld metal which is alloyed with tungsten, in addition, some Laves phase particles were observed (Figure 5b). The changes of microstructure after creep are not marked due relatively short duration of test.

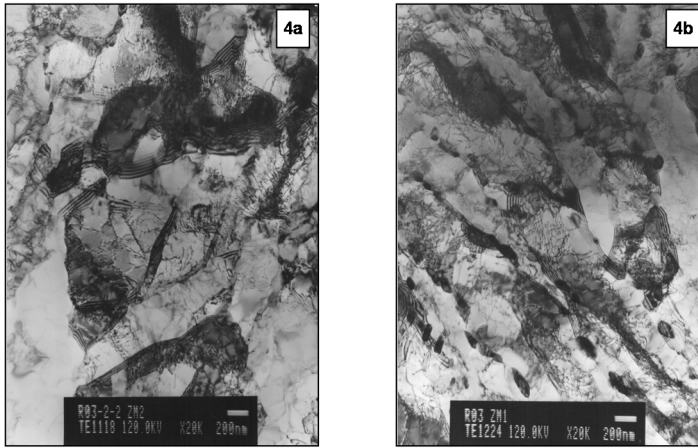


Figure 4. Substructure of the base materials: a) COST F and b) COST FB2. TEM micrographs.

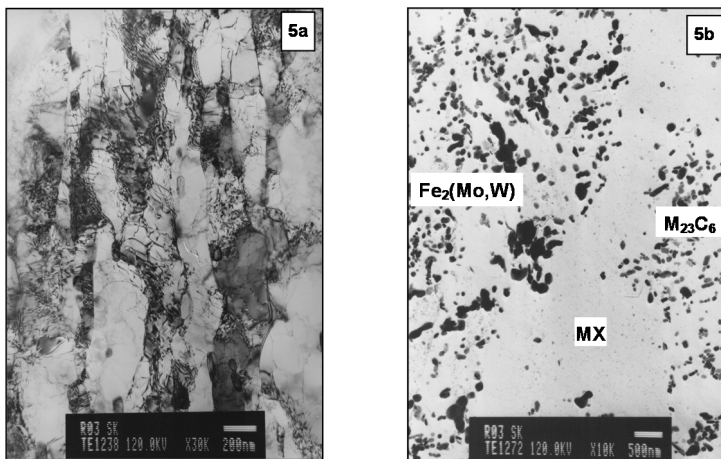


Figure 5. Substructure of the base materials: COST FB2 and COST F: a) thin foil and b) extraction carbon replica. TEM micrographs.

4. Conclusions

Doosan Škoda Power s.r.o. has successfully completed welded-structure turbine rotors of steel type COST FB2 and COST F to meet recent demands from users.

From results gained up this time the following conclusions could be done: Creep strength of weld joint examined falls into $\pm 20\%$ scatter band of the creep strength of a corresponding base material COST F up to 600°C. For testing temperature 625°C the creep strength of the weld joint decreases below the scatter

band for sample tested at low stresses. However for testing temperature it is inside the scatter band.

The samples tested at lower temperatures and higher stresses failed in the base material of steel COST F while those tested at higher temperatures and lower stresses ruptured in the grain refined part or in the intercritically reheated part of the heat-affected zone of the base material of steel COST F.

After post-weld heat treatment the hardness of the weld metal is 280 HV10; local minima are in the fine-grained parts of the heat affected zones in both the base materials on comparable level. During creep test the highest decrease of the hardness occurred in the intercritically reheated part where samples failed.

Creep test of several samples is still in progress. More detailed evaluation of microstructure will be done when sample broken after longer time will be available.

Acknowledgements

This work was supported by Grant project TIP FR-TI2/080 from the Ministry of Industry and Trade of the Czech Republic.

References

1. Berger, C., Scarlin, R. B., Mayer, K. H., Thornton, D.V. & Beech, S. M. Steam turbine materials: High Temperature Forgings. In: Proc. COST Conference on High Temperature Materials for Power Engineering. Liege, Belgium, 3–6 October 1994.
2. Mayer, K. H., Blum, R., Hillenbrand, P., Kern, T. U. & Staubli, M. Development Steps of New Steels for Power Plants. In: Proc. 7th Liege COST Conference. Liege, Belgium, 29 September – 2 October 2002.
3. Kern, T. U., Staubli, M., Mayer, K. H., Escher, K. & Zeiler, G. The European Effort in Development of new High Temperature Rotor Materials up to 650°C – COST 522. In: Proc. 7th Liege COST Conference. Liege, Belgium, 29 September – 2 October 2002.
4. Kern, T. U., Staubli, M., Mayer, K. H., Donth, B. & Zeiler, G. The European Effort in Development of new High Temperature Rotor Materials – COST 536. In: Proc. 8th Liege COST Conference. Liege, Belgium, 19–20 September 2006.
5. Results of creep test COST 522 programme.
6. Hald, J. Development Status and Future Possibilities for Martensitic Creep resistant Steels. In: Proc. 9th Liege COST Conference. Liege, Belgium, 27–29 September 2010.

Determination and solution of power plant furnace problems with pilot-scale studies

Heidi Nevalainen & Martti Aho

VTT Technical Research Centre of Finland
Jyväskylä, Finland

Abstract

VTT has three pilot-scale combustors in Jyväskylä: a 20 kW reactor to simulate bubbling bed combustion, a 50 kW reactor to simulate circulating fluidised bed combustion and a 100 kW reactor to simulate grate combustion. Good scaling up of results to power plant level is based on realistic temperature vs. residence time history in the furnace, realistic ways to bring combustion air in at several stages and inert wall materials (due to high wall area to inner volume ratio compared to power plant furnaces). However, reactors alone would be insufficient to research. In addition, versatile sampling and analysis systems are necessary. VTT has unique probes to gas analysers and to devised for aerosolic fly ash and condensed vapour. These are important to find out and solve corrosion relative problems in power plants. VTT has participated to product development and combustion problem solution work with numerous companies, in EU funded and domestic network projects with these reactors.

1. Introduction

Environmental and political pressure forces to increase the portion of renewable fuels in energy production. Bioenergy has and will have high importance to this field. However, biomass resources are restricted and the need to increase the use of biomass requires utilisation of demanding biomass and waste also. Among biomass heart wood is the best in view of combustion due to even quality and very low ash and Cl contents. Wood pellets are made of this material. Among cultivated biomass, energy willow and reed canary grass are examples of the easily combustible biomass, whereas manures with high ash, chlorine, phosphorous etc. content and waste-based biomass with high concentration of toxic and problematic elements in health and emission viewpoint are other extremes.

Operational problems pertaining power plant furnaces and appearing with biomass and waste are ash melting, slagging, fouling and corrosion. Their severity is often difficult to known accurately beforehand. Risky tests in power plants can become very expensive to power producing companies in form of extensive material damages and shut downs in energy production. Pilot-scale problem determination and solution can become 1–2 magnitudes cheaper than repairing and paying

the power plant damages. There are numerous examples. VTT has determined and solved problems for example in the following cases:

- a) Finding reasons to ash melting and finding means to reduce those problems in grate combustion by flue gas circulation, by grate cooling and by optimising the fuel composition
- b) Finding reasons to bed sand agglomeration in fluidised bed combustion and finding means to solve those problems by temperature and staging optimisation, by material and fuel quality optimisation
- c) Determination of safe upper limit to risky fuel in its blend with protective fuel to prevent corrosive compounds deposition on superheaters
- d) Testing the power of different additives and optimising their use to prevent superheater corrosion
- e) Minimising formation of harmful compounds in view of emissions and end use of combustion residues.

In addition, well-defined combustion environment in these reactors allow testing and comparison of different analysing and sampling technologies for power plant furnace research and operational risk minimisation.

2. Illustration of VTT's pilot plant reactors

2.1 100 kW grate reactor

Figure 1 shows schematic diagram of the 100 kW grate combustor with inner furnace diameter of 0.40 m. The reactor design enables temperature vs. residence times similar to furnaces of electricity producing grate boilers. This feature gives a good prediction ability for example to formation of corrosive alkali chlorides and emissions. Grate power plants can have variable grate constructions. The reactor is equipped with a rotating grate with narrow primary air inlets. A rotation speed of 3 revolutions per minute has typically been used. This construction enabled a cylindrical furnace and effective gas mixing producing as low CO concentrations to the flue gas as a good grate power plant. Other grate constructions would have been less suitable to this reactor size. Suction pyrometers have been used to temperature measurements in order to avoid errors due to radiation.

Bottom ash can be collected on the grate and below the grate. Fly ash can be collected by a cyclone (Figure 1), with a cut diameter of about 30 μ m. Mass distribution and the portion of cake forming ash can be measured by weighing.

The deposit probes inserted at desired metal temperatures simulate the zones where the superheaters can be located in a GC power plant furnace and the metal conditions of the superheaters.

Furnace height of the reactor is 3.72 m. The furnace temperature distribution versus gas residence time and versus relative furnace height (as % of maximum),

can be adjusted to be similar between this reactor and a full scale grate combustion power plant furnace.

The combustor is equipped with a FTIR-spectrometer and conventional on-line analysers for main flue gas compound measurements. Gas samples can be taken with the FTIR-spectrometers from different levels of the reactor.

The combustor is controlled with automation system on which all measurement data is stored.

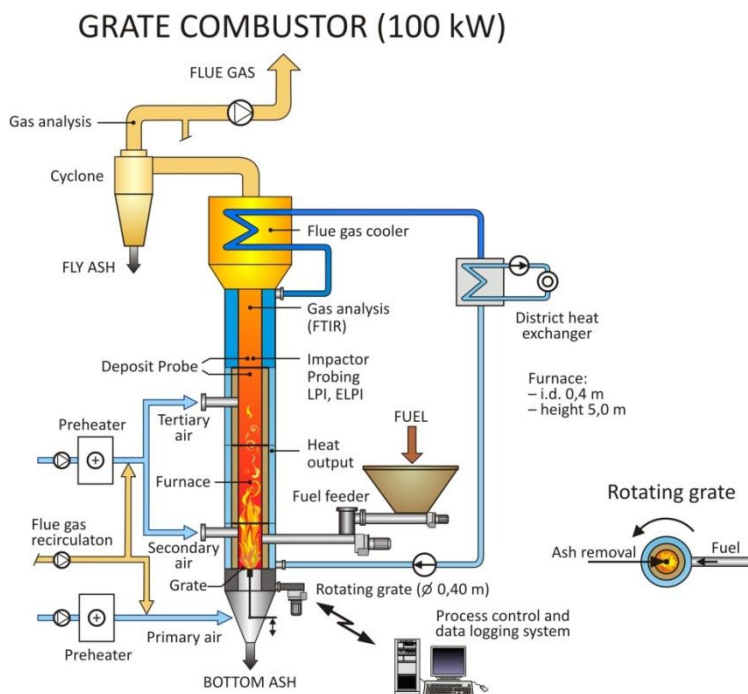


Figure 1. Schematic diagram of VTT's grate combustion reactor.

2.2 50 kW circulating fluidised bed reactor

A scheme of VTT's circulating fluidized bed combustor (CFB) is shown in Figure 2. The test rig can be operated with fuel thermal input ranging between 20–100 kW. The height of the riser is 8.3 m and the inner diameter 167 mm. The combustor is equipped with several separately controlled electrically heated and water/air-cooled zones in order to control the process conditions (for example oxygen level, temperature and load) almost independently. Several ports for gas and solid material sampling are located in the riser area. Bed material (bottom ash) can be sampled above the grid via sampling tube and circulation material sample can be taken below the primary cyclone and from the loop seal. Fly ash samples can be taken from the secondary cyclone, gas cooler, extra gas cooler and bag house

filter. The combustor is controlled with automation system on which all measurement data is stored.

Fuel can be fed into the combustor through two separate feeding lines and additives can be fed through a third line equipped with a high-precision feeder. Fuel and additive containers are mounted on the top of scales which enables the determination of mass flow rates for solid materials as a weight loss against time.

The combustion air can be divided into primary, secondary and tertiary airs. Primary air is fed through an air grid. Oxygen concentration of the primary and secondary airs can be controlled by mixing nitrogen, oxygen or recycled flue gas into the gas flows.

The secondary and tertiary airs can be fed into three different levels of the combustor. The lowest feeding point (1.3 m above the air grid) for the secondary air is mainly used in the test runs and tertiary airs (at two levels) are mainly used in air staging tests.

The combustor is equipped with a FTIR-spectrometer and conventional on-line analysers for main flue gas compound measurements. Gas samples can be taken with the FTIR-spectrometers from different levels of the riser, between the primary and secondary cyclones and after the bag house filter. Normal continuous measurement location of FTIR-spectrometer is between the primary and secondary cyclones. The conventional on-line analysers are connected to the flue gas duct between the gas cooler and bag house filter.

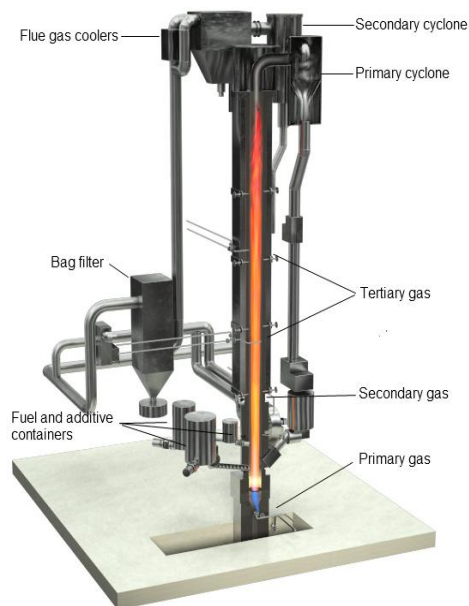


Figure 2. Illustration of VTT's 50 kW circulating fluidised bed reactor.

2.3 20 kW bubbling bed reactor

The schematic diagram of the BFB is given in Figure 3. Bed diameter is 160 mm and freeboard diameter 230 mm. Bed area has been covered with quartz wall as also the lower parts of the freeboard. The walls of the upper parts of the freeboard are made of high temperature and corrosion resistant steel. Natural sand is usually used with particle size range of 0.1–0.6mm (with mean particle size of about 0.33mm). Removal of bed sand is possible during the steady-state period. Electric heaters were placed to fluidising air heater, to bed area, to freeboard walls (three different), to flue gas line between cyclone and freeboard and to cyclone area to produce (together with fuel energy) desired temperature distribution to the reactor.

Fuel can be fed into the combustor through two separate fuel feeding lines and additives can be fed through a third line equipped with a high-precision feeder. Fuel and additive containers are mounted on the top of scales which enables the determination of mass flow rates for solid materials as a weight loss against time.

The combustion air can be divided into primary, secondary and tertiary airs. Primary air is fed through an air grid.

The combustor is equipped with a FTIR-spectrometer and conventional on-line analysers for main flue gas compound measurements. Gas samples can be taken with the FTIR-spectrometers from different locations in the flue gas line. The combustor has large number of sampling ports at different locations.

The combustor is controlled with automation system on which all measurement data is stored.

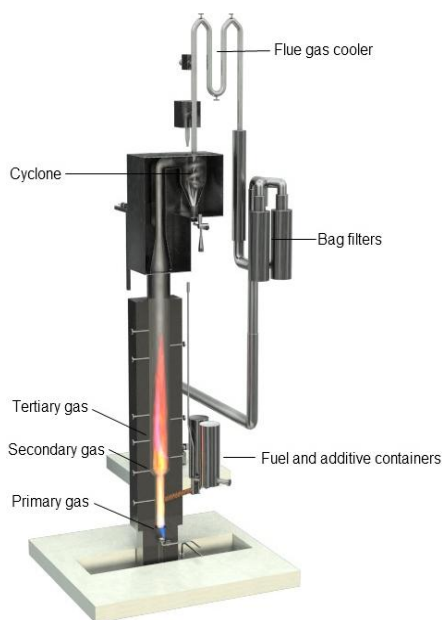


Figure 3. Illustration of the 20 kW bubbling bed reactor.

2.4 Examples of research and obtained results

Optimisation of fuel composition to prevent ash melting, superheater fouling and corrosion has been carried out with all these pilot plants. For example mixtures of different coals with risky biomass were optimised by circulating fluidised bed [1–4] and bubbling bed [5,6]. Mixtures of wood and agro biomass were optimised with grate combustor [7]. Additives to prevent corrosive attack against superheaters were developed with bubbling bed reactor [8–11] and with grate combustor [12].

Problem solutions concepts have been developed to all these ways of combustion to prevent superheater corrosion, slagging and fouling and bed agglomeration.

When determining the severity of superheater fouling and corrosivity of the deposits, sampling probes (which can also be called a superheater simulators) have been used, where the metal temperature can be adjusted to a desired value. Deposits have been collected between 2–4 hours depending to the case. In biomass combustion, concentration of alkali chlorides at the superheater area is usually the key issue. In problem determination stage deposition of Cl on different locations of the probe is measured where after different problem solution concepts can be tested, as additives or protective fuel to destroy alkali chlorides before entering to the superheater area. These methodology can be used in all the reactors described earlier.

When determining the risk of ash melting in grate combustion or bed agglomeration in fluidised bed combustion problem solution concepts such as decrease in fuel bed temperature and air staging can be studied in all these reactors. In grate reactor fuel bed temperate can be decreased with flue gas recirculation, using a water cooled cylinder, changing air staging and decreasing the fuel power. In both fluidised bed reactors bed temperature can be decreased by air staging, cooling the bed area and continuous bed sand removal. In addition, flue gas recirculation is possible in the circulating fluidised bed reactor. In bubbling bed reactor flue gas recirculation can be simulated by decreasing O₂ concentration in the fluidising air for example by nitrogen.

References

1. Aho, M. and Ferrer, E. Importance of coal ash composition in protecting boiler against chlorine deposition during combustion of Cl-rich biomass. *Fuel* 84 (2005), pp. 201–212.
2. Ferrer, E., Aho, M., and Filipczyk, D., Solution of superheater-related problems in CFB during co-firing of demanding biomass residue by coal quality optimisation. VBG workshop Berlin, September 22-24, 2004. 17p.
3. Ferrer, E., Aho, M., Silvennoinen, J., and Nurminen, R.-V., Fluidised bed combustion of refuse-derived fuel in presence of protective coal ash. *Fuel Processing technology* 87 (2005) , pp. 33–44.

4. Nevalainen, H., Leino, T., Tourunen, A., Hiltunen, M., Coda Zabetta, E., Deposits and emissions during the co-combustion of biodiesel residue with coal and biomass in a CFB pilot. CFB9 Hamburg, 13–16 May 2008. *Circulating Fluidized Bed Technology IX* (2008). Pp. 863–868.
5. Aho, M., Gil, A., Taipale, R., Vainikka, P., and Vesala H., A pilot-scale fireside study of co-firing cynara with two coals in a fluidised bed. *Fuel* 87 (2008), pp. 58–69.
6. Aho, M., Vainikka, P., Taipale, R., and Vesala, H., Alkali chloride deposition problem solution with protecting fuel. In proceedings of the 14th European Biomass Conference and Exhibition 17–21 October 2005, Paris, France. 5p.
7. Aho, M., Paakkinen, K., and Taipale, R., Quality of deposits during grate combustion of corn stover and wood chip blends. *Fuel* 104 (2013), pp. 476–487.
8. Aho, M., Reduction of chlorine deposition in FB boilers with aluminium-containing additives. *Fuel* 80 (2001), pp. 1943–1951.
9. Aho, M., and Silvennoinen, J., Preventing chlorine deposition on heat transfer surfaces with aluminium-silicon rich biomass. *Fuel* 83 (2004), pp. 1299–1305.
10. Aho, M., Vainikka, P., Taipale, R., and Yrjas, P., Effective new chemicals to prevent Cl-originated superheater corrosion in power plants. *Fuel* 87 (2008), pp. 647–654.
11. Aho, M., Yrjas, P., Taipale, R., Hupa, M., and Silvennoinen, J., Reduction of superheater corrosion by co-firing risky biomass with sewage sludge. *Fuel* 89 (2010), pp. 2376–2386.
12. Aho, M., Paakkinen, K., and Taipale, R., Destruction of alkali chlorides using sulphur and ferric sulphate during grate combustion of corn stover and wood chip blends. *Fuel* 103 (2013), pp. 562–569.

New model for steam oxidation of power plant steels

Sanni Yli-Olli, Stefan Holmström, Pertti Auerkari & Sami Penttilä

VTT Technical Research Centre of Finland
Espoo, Finland

Abstract

At high temperatures the water/steam side oxidation resistance is an important issue for boiler components like superheaters, where the growing internal oxide decreases heat transfer and increases surface temperature. This is increasingly critical for modern plants that aim for high efficiency from elevated levels of operating temperature and pressure. In this paper, a new simple model is presented to describe the steam/water side oxidation rate of common alloys for the high temperature end of the boiler plant. The model is based on the chemical composition of the alloys, applying equivalence expressions for collapsing the multi-variable problem to a more easily manageable setting with a combined parametric oxidation (POX) model. For verification, a range of experimental water/steam oxidation data from numerous tested alloys has been compared with the model predicted oxide growth. The results suggest a surprisingly good agreement with the model and test data. Although the optimised model parameters differ between e.g. steels and nickel alloys, as expected due to difference in the oxides, they remain very similar within a given material class, e.g. for all tested steels.

1. Introduction

Generally the evolution of high temperature materials for pressure equipment is relatively slow because of the requirement for validation of long term properties. However, the recent decades have seen unusually fast change in the development of the process conditions and other features in thermal power production. The highest temperatures in such facilities occur in the final stages of superheaters and reheaters that suffer from multiple life-limiting processes of damage, such as creep, erosion, fireside corrosion and steam side oxidation. The steam side oxidation has grown in relative importance with the increasing steam values aiming for improved plant efficiency. In this paper, a new model is presented to characterise the steam side oxidation rates as a function of the chemical composition and operating temperature. This model is by formulation fundamentally simpler than those relying on classical approaches based on thermodynamics and diffusion kinetics [1,3–5].

The oxidation rates of metals can be often taken to be linear, parabolic or logarithmic, for example for many low alloyed steels [1, 2]. However, more complex

oxidation behaviour can be expected with higher alloying, for example in the case of new austenitic boiler steels. The current thermodynamic modelling tools like Thermo-Calc or FactSage have sufficient databases for calculating thermodynamic stabilities from the steel composition for simple corrosive atmospheres, providing useful tools for analysing experimental results.

Models that combine kinetics and thermodynamics are based on diffusion of oxygen and oxidising elements to the reaction surface. Major improvements have been made with etc. the DICTRA, ASTRID, InCorr, and CorrApp software [3,4,5]. Diffusion in the bulk material is strongly influenced by e.g. grain boundaries, dislocations and surface defects, and the long term modelling of the diffusion process is complicated by multiple and mixed oxide scales. This increases the uncertainties of the calculations in the current combining models, and many of the variables have to be based on expert judgement. There is a need for a robust but flexible model that can predict the long-term influence of high temperature oxidation and corrosion on the material lifetime, provide guidelines for alloy selection.

The presented model approaches the problem from a combined materials and application design point of view. The model quantifies the impact of the alloying elements on steam side oxidation to facilitate prediction of material lifetime. For this purpose the model will be validated using a wide range of oxidation data and alloy compositions. By only modelling the correlated outcome instead of the details of the oxidation process, no diffusion coefficients are needed for the model.

2. Materials and methods

It is here assumed that the oxidation rate for a constant water environment (conductivity, oxygen concentration, flow rate, temperature) is largely dependent on the chemical composition of the alloy, at least when the surface treatment is similar. It is further postulated that the typical alloying elements of steel can be more or less beneficial for providing protective oxide at the surface and/or microstructural defects to help such elements to diffuse to the surface. On the other hand, another set of alloying elements can be beneficial in retarding diffusion of unwanted elements from the environment into the metal. It is suggested that the first part of the combined protective function can be described by a combination of alloying elements, called “chromium equivalent”, promoting the bcc structure (ferrite), and the latter part by a “nickel equivalent”, promoting fcc structure (austenite). For this purpose, the classical Schaeffler expressions are adopted [2, 6] as

$$Cr(eq) = Cr + 2Si + 1.5Mo + 5V + 5.5Al + 1.75Nb + 1.5Ti + 0.75W \quad (1)$$

$$Ni(eq) = Ni + Co + 30C + 25N + 0.5Mn + 0.3Cu \quad (2)$$

These expressions are combined as an oxidation propensity parameter (POX) as

$$POX = a \cdot Cr(eq) + b \cdot Ni(eq) + c \cdot Cr(eq) \cdot Ni(eq) \quad (3)$$

where a, b and c are constants that may depend on the environment but are suggested to be insensitive to the steel composition.

For model development, a range of steam oxidation test results (as weight gain) on a number of alloys were collected (Table 1). At this initial stage no external data was included, to minimise experimental scatter. The test materials were common boiler steels with values of chromium and nickel equivalents as shown in in Figure 1 and Table 1. Table 1 also shows the amount of weight gain data from each material used for the model. To predict the extent of oxidation as weight gain (per unit area)

$$\Delta m = kt^{\beta} G(C) \quad (4)$$

where k is the rate constant, and t is time, β a constant for the given environment and G(C) a function of alloy concentration, respectively. Taking $\log(k) = \alpha$ and $\log[G(C)] = POX$,

$$\log(\Delta m) = \alpha + \beta \log(t) + POX \quad (5)$$

where α is constant for a given environment.

Table 1. Materials and steam oxidation data used for model development.

Material designation	Material number	Cr(eq)	Ni(eq)	Steam oxidation data (at 650°C)
T22	1	4.07	1.74	5
T23	2	5.12	2.64	5
T91	3	11.97	3.22	5
T92/P92	4	12.30/12.90	2.90/4.45	6
CT3	5	13.96	7.00	1
T122	6	15.39	3.69	5
CT7	7	15.46	7.00	1
VM12	8	15.49	6.04	1
TP347H	9	19.84	12.35	5
316NG	10	20.47	13.92	3
316LN	11	21.22	17.36	1
NF 709	12	23.75	30.00	3
Tempaloy A-3	13	24.02	21.00	3
Sanicro 25	14	25.18	33.55	3
BGA4	15	27.82	26.38	1
310 N	16	28.55	35.75	3

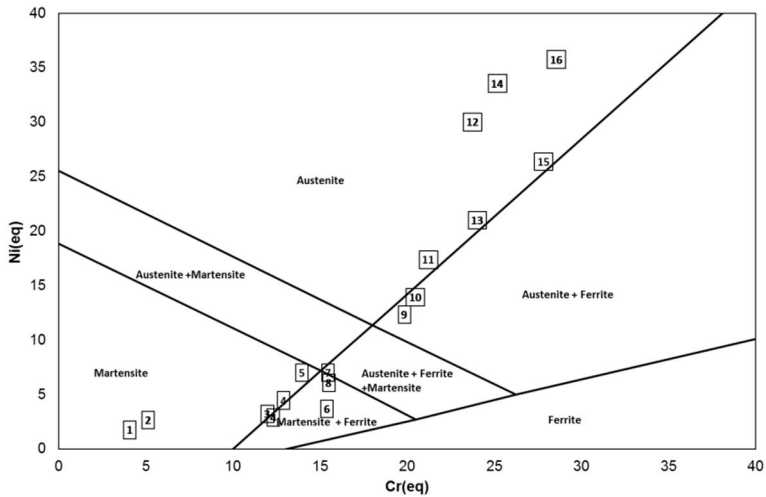


Figure 1. Test materials (material numbers from Table 1) plotted in the Schaeffler diagram.

The materials were used in the experiments as coupons with milled and degreased (ethanol/acetone) surfaces. The specimens were exposed up to 6000 h in supercritical water at 625°C or 650°C / 25 MPa in an autoclave connected to a recirculation loop, Figure 2. The controlled and monitored test conditions include temperature, pressure, inlet and outlet water conductivity, dissolved oxygen content and flow rate. The target water chemistry was nominally pure water with the inlet conductivity less than 0.1 $\mu\text{S}/\text{cm}$ and the dissolved oxygen content in the range of 125–150 ppb. The specimens were weighed before and after each test period, using Mettler AT261 scale with an uncertainty of $\pm 0.002\%$. The mass change per unit area was calculated using coupon dimensions measured before testing.

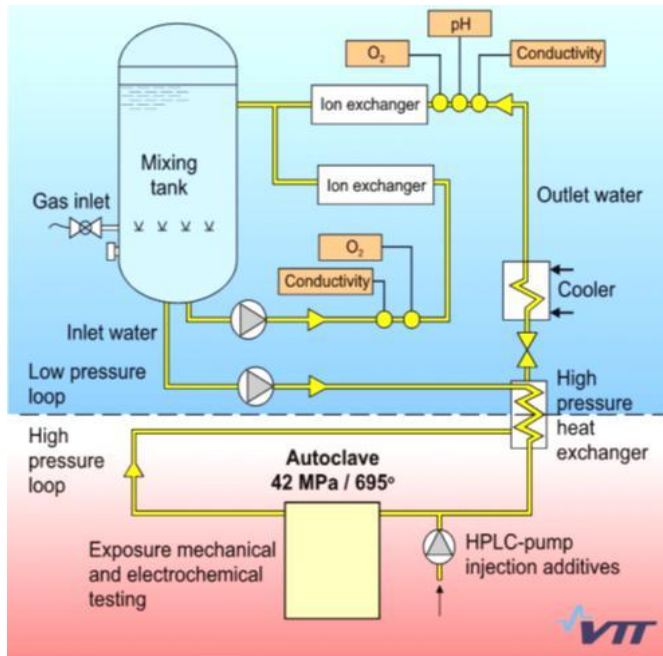


Figure 2. The supercritical autoclave system with water recirculating loop.

3. Results

Fitting the POX model to the test data suggests that for the present set of materials and test conditions the constants of Eq (3) are $a = -0.07914$, $b = -0.09313$ and $c = 0.00192$, and the constants of Eq. (5) are $\alpha = 0.61$ and $\beta = 0.72$. The fitting performance is shown in Figures 3 and 4.

The binomial confidence interval (Z) for 95% of the data is 3.4 and for 99% of the data 4.8, as shown in Figure 4. For verification, a range of experimental water/steam oxidation data from numerous tested alloys has been compared with the model predicted oxide growth.

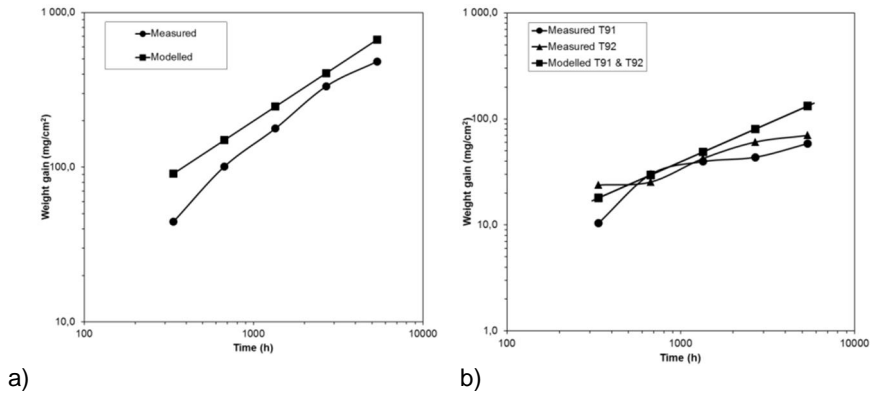


Figure 5 Figure 6) suggest a surprisingly good agreement with the model and test data, in spite of the simplicity of the model.

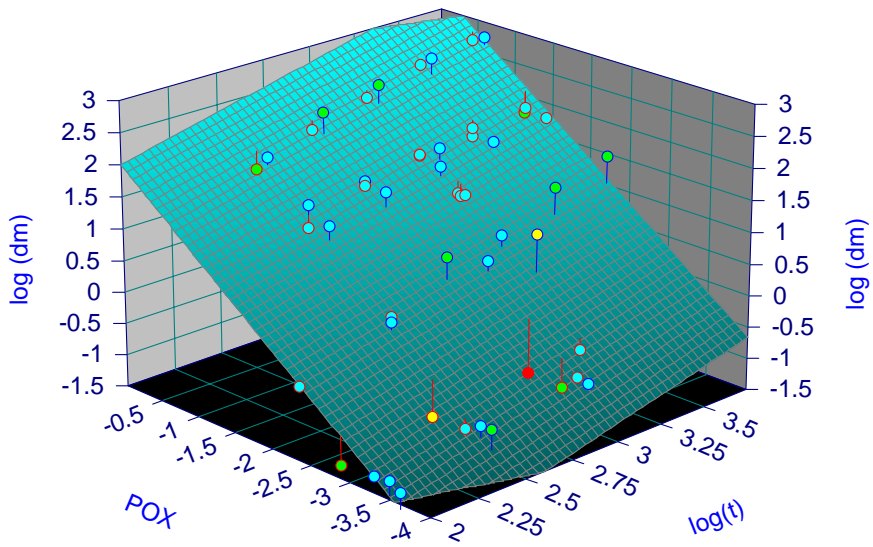


Figure 3. The POX model surface fitted to the steam oxidation data.

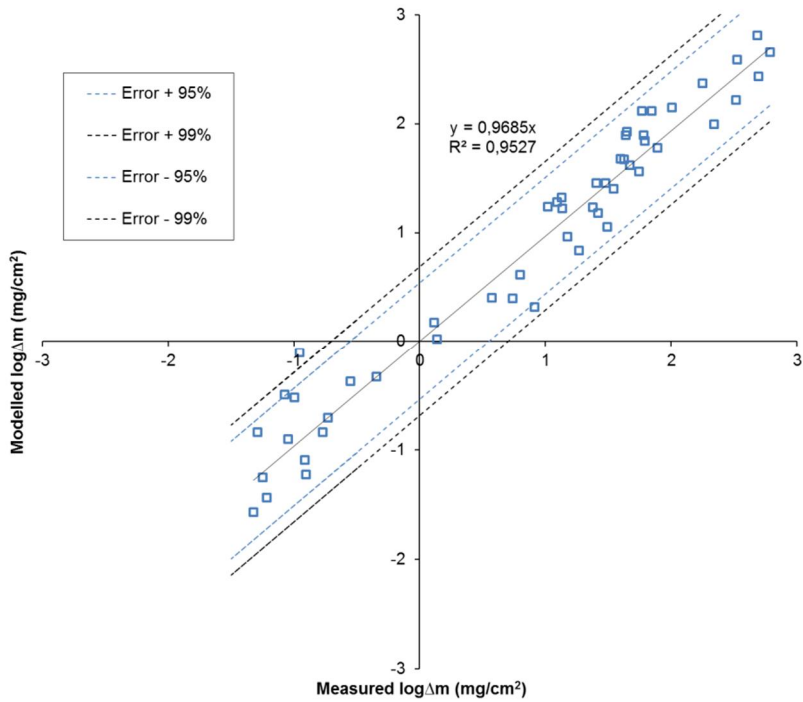
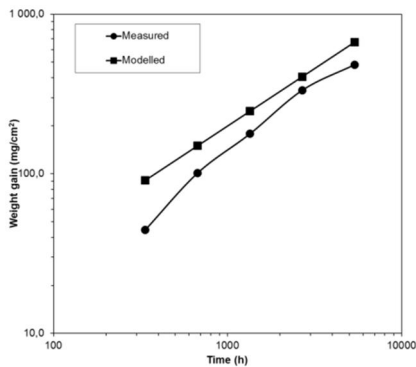
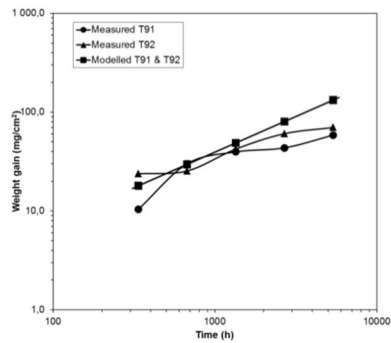


Figure 4. Measured vs. modelled logarithmic weight gain with 95 and 99% binomial confidence intervals for all materials/test data.



a)



b)

Figure 5. Comparison of the measured weight gain and the POX-modelled data for a) T22 and b) P91 and P92 at 650°C as a function of time.

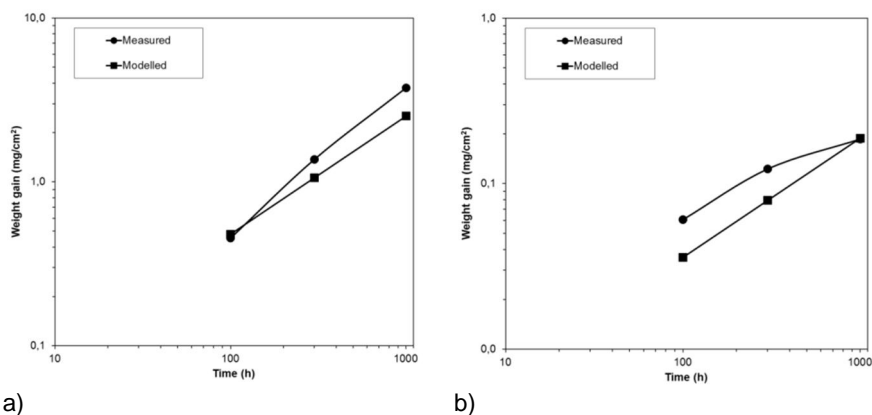


Figure 6. Comparison of the measured weight gain to the POX-modelled data for a) 316NG and b) Sanicro 25 at 650°C as a function of time.

4. Discussion

The model predictions appear to agree surprisingly well with the experimental data considering the variable range of the data including low and high alloy ferritic steels up to austenitic materials. For the chosen 16 steel grades at 650°C the correlation of predicted and measured mass gain was considered to be quite good ($R^2=0.95$). Largest relative uncertainty was observed with the high alloyed materials tested for short times, possibly simply because the formed oxide scale is very thin. On the other hand, the predicted and observed mass gain levels of T22 are very close (Figure 5a) in spite of the alloying that would not normally be considered in terms of the Schaeffler diagram, or taken to be comparable to austenitic steels.

Fair correspondence was also obtained for predicted and measured values of more alloyed ferritic steels P91 and P92 (Figure 5b); for these steels the model predictions were nearly identical. For austenitic steels 316NG (Figure 6a) and Sanicro 25 (Figure 6b) the agreement between predicted and observed mass change was also fair, although not similarly conservative as for the above ferritic steels in the example cases.

Some future improvements are suggested:

- Implementation of additional materials and oxidation data with longer test times
- Extension of the model and the verification data to temperature dependence
- Implementation of the effect of cold work, surface finish and grain size
- Optimisation of the Cr- and Ni-equivalence expressions for high temperature oxidation
- Extension of the model and verification to fireside corrosion.

5. Conclusions

A new simple model was developed and presented to describe the steam/water side oxidation of boiler alloys for the high temperature end of the plant. The parametric oxidation (POX) model applies equivalence expressions for collapsing the multi-variable problem of chemical composition and time of exposure to a more easily manageable setting. For verification, independent oxidation data from a range of tested alloys have been compared with the model predicted oxide growth. The results suggest a surprisingly good agreement considering the simplicity of the model that appears to provide great potential for further optimisation of the concept.

Acknowledgement

The test data have been compiled from in-house results within the European projects COST 536, Opticorr and MacPlus that are gratefully acknowledged for material provision.

References

1. C.A.C. Sequeira, High-Temperature Oxidation, Uhlig's Corrosion Handbook, edit. R. Winston Revie, 3rd edition, ISBN 978-0-470-08032-0, John Wiley & Sons, Inc. 2011.
2. A. J. Sedriks, Corrosion of Stainless Steels, ISBN 0-471-05011-3, John Wiley & Sons, Inc. 1979.
3. M. Auinger, R. Naraparaju, H.-J., Christ & M. Rohwerder, Modelling High Temperature Oxidation in Iron-Chromium Systems: Combined Kinetic and Thermodynamic Calculation of Long-Term Behaviour and Experimental Verification, Oxidation of Metals, vol. 76 pp.247–258, 2011.
4. J.-O. Andersson, T. Helander, L. Höglund, P. Shi & B. Sundman, THERMO-CALC & DICTRA, Computational Tools For Materials Science, Calphad, vol 26, No. 2, pp. 273–312, 2002.
5. D. Baxter & L. Heikinheimo, OPTICORR Guide Book, VTT Research notes 2309, Espoo, pp. 148, 2005.
6. J. Lippold & D. Kotecki, Weld Metallurgy and Weldability of Stainless Steels, ISBN 0-471-47379, John Wiley & Sons, Inc., 2005.

Coating solutions against high temperature corrosion – performance validation and feasibility at biomass fired boilers

M. Oksa¹, J. Kärki² & J. Metsäjoki¹

¹VTT Technical Research Centre of Finland
Metallimiehenkuja 8, Espoo, Finland

² VTT Technical Research Centre of Finland
Koivurannantie 1, Jyväskylä, Finland

Abstract

To overcome severe corrosion problems of heat exchanger surfaces, especially superheaters, in biomass fired boilers protective thermal spray coatings can be applied. Fouling and corrosion in biomass boilers originate from used fuels, which contain alkali metals, chlorine and other corrosive elements, and can lead to tube failure and leakage in the worst case. Different HVOF (high velocity oxy-fuel) and arc sprayed coatings were exposed to biomass co-combustion conditions in a CFB boiler using peat, coal, SRF and biomass as fuel.

VTT is conducting a programme of material exposure trials at the Alholmens Kraft power plant in the city of Pietarsaari. The exposure campaign involves the deployment of one corrosion probe in a 550 MW_{th} circulating fluidised bed boiler. Duration of the measurement campaign was about 1300 hours. The corrosion probe measurement was performed for samples with five coatings: NiCr, IN625, Diamalloy 4006, SHS9172 and NiCrTi. Samples were exposed at two metal temperature ranges of 550 and 750°C, which correspond to both today's and future steam temperatures of a high-efficiency boiler. Used reference tube materials were ferritic steel T92 and nickel super alloy A263.

Performance validation of the coatings was performed as well as an indicative analysis of the effects of fuels, deposit properties and boiler process parameters on corrosion phenomena. Preliminary economic feasibility of the use of coatings to extend lifetime of a superheater was included. Overall at 550°C the coatings had negligible corrosion and at the higher temperature clear differences emerged: NiCr and NiCrTi being the top performers.

1. Introduction

The goal of CO₂ reduction in energy production has lead power plant boiler operators to use alternative fuels instead of fossil fuels. Maintenance of power plant boilers experience great challenges due to use of difficult biomass and recycled

fuels, which can cause e.g. severe corrosion damage to different boiler components. The attempt to increase the efficiency by higher process parameters has led to a decrease in lifetime of metallic components of power plant boilers, because the corrosion damage may be even several millimetres per year. Investigation on suitable materials to encounter the corrosion problems in even higher process temperatures is needed.

As steam temperatures and pressures are increased, both the fireside and the steam-side aspects of the superheater and reheater tubes and the internal surfaces of the steam pipework will be progressively subjected to more aggressive conditions, which may lead to significantly increased wastage rates and other materials-related problems. At VTT research work is going on targeting to assist in the identification of appropriate solutions to these problems mitigating the risks to the performance and integrity of the high temperature boiler components, through either materials and coating development or surface engineering.

Severe fireside corrosion of heat exchanger surfaces e.g. superheaters, encountered in boilers using biomass and recycled fuel can be caused by gaseous or molten attack induced especially by compounds like chlorine, alkali metals (K, Na), sulphur, bromine, and heavy metals (Zn, Pb, Cu, etc.) [Ref 1–3]. Besides using higher alloyed steel and nickel super alloy tubes, thermal spray coatings can be applied to low alloyed tubes with economical cost and high thermo-mechanical properties. In thermal spraying, the coating is formed from molten or semi-melted droplets producing a lamellar structure. High velocity spray methods generate coatings with good adhesion and low porosity. Several high temperature corrosion lab tests have been performed for bulk materials and coatings, e.g. [Ref 4–9], and material testing in both in biomass and recycled fuel boilers has been reported [Ref 10–13], but high temperature exposures up to 750°C in real biomass boiler conditions has not been reported.

2. Experiments

High temperature corrosion performance of five thermal spray coatings and two tube materials were tested in a biomass co-fired circulating fluidised bed boiler for about 1300 hours with a controlled probe measurement.

2.1 Coatings

Five thermal spray coatings were manufactured for high temperature corrosion exposure in a real biomass boiler. Four of the coatings were manufactured by HVOF (high velocity oxy-fuel) method, and one with a wire arc. The deposition was performed on two substrate materials. The coating materials were nickel based NiCr, IN625, Diam4006 and NiCrTi, and an iron based partly amorphous SHS9172. The detailed information of the coating materials are presented in Table 1. The substrate materials were a ferritic steel T92 (ASTM A213 T92) and a nickel

super alloy 263. Chemical composition of the coating and substrate materials are presented in Table 2 and Table 3.

Table 1. Coating powders and a wire used for coating manufacturing.

Material	Powder code	Manufacturer	Particle size	Manufactured	Morphology
NiCr	Ni-980-1/1260F	Praxair	-53 +20 μm	Gas atomized	Spheroidal
IN625	Diamalloy 1005	Sulzer Metco	-45 +11 μm	Gas atomized	Spheroidal
Diam4006	Diamalloy 4006	Sulzer Metco	-53 - 11 μm	Water Atomized	Irregular
SHS9172	SHS 9172HV1	Nanosteel	-53 +15 μm	Gas atomized	Spheroidal

Material	Wire code	Wire size	Manufacturer
NiCrTi	TAFANickel Chromel 45 CT	1.6 mm	Praxair

Table 2. Chemical composition of the coating materials according to manufacturer [wt. %].

Material	Ni	Fe	Cr	Mo	Nb	W	C	B	Mn	Si	Cu	Ti
NiCr	Bal.	1.1	> 45	2.1
IN625	Bal.	2.5	21.5	9.0	3.7	0.1	0.2
Diam	Bal.	<1.0	20.5	9.0	...	10.0	0.75	0.75	4.0	...
SHS9172	...	Bal.	< 25.0	< 6.0	<12.0	< 15.0	< 4.0	< 5.0	< 3.0	< 2.0
NiCrTi	Bal.	...	42–46	0.3–1

Table 3. Chemical composition of the substrate materials [wt. %].

	Fe	Ni	Cr	Mo	Co	W	Ti	V	Mn	Si	Al
T92	Bal.	≤ 0.4	8–9.5	0.3–0.6	...	1.5–2	...	0.15–0.25	0.3–0.6	≤ 0.5	≤ 0.04
A263	<0.7	Bal.	19–21	5.6–6.1	19–21	...	1.9–2.4	...	< 0.6	<0.4	<0.6

The spraying was performed on the perimeter of tube rings with size of $\varnothing 48$ mm x 12.5 mm for exposure at 550°C, and $\varnothing 34$ mm x 15 mm for 750°C. HVOF process with CJS (Carbide Jet Spray by Thermico) spray gun was used for spraying the powders. Depending on process parameters, CJS produces high velocity and low

thermal input on the sprayed powders, generating thick coatings with low oxidation rate and good adhesion to the substrate material. However, small particle size would be optimal for CJS to enhance the melting of the powder particles and hence sufficient cohesion between the lamellas. In this study, the applied powders were designed for previous generation spray gun (e.g. Diamond Jet Hybrid from Sulzer Metco), and therefore slightly too coarse to the used method. Arc spraying was performed with Smart Arc (by Sulzer Metco). The process parameters of the spraying are presented in Table 4.

Table 4. Process parameters for HVOF spraying [l/min]. Spraying distance: 250 mm, and powder feed rate 50 g/min for CJS. Below: process parameters for arc spraying.

Coating	Spray method	H ₂	Keros.	O ₂	N ₂	Sweeps	Thickness [μm]
NiCr	CJS, 140 mm	100	16	1000	6+6	14	345
IN625	CJS, 100 mm	100	16	1000	6+6	10	265
Diam	CJS, 100 mm	100	16	1000	6+6	20	400
SHS9172	CJS, 140 mm	100	16	850	6+6	21	350

Coating	Spray method	Voltage	Current	Distance	Air	Thickness [μm]
NiCrTi	Arc spray	30 V	220 A	150 mm	3.5 / 2.5 bar	300

2.2 Coating characterization

After the exposure the ring specimens were removed from the probe and embedded in cold setting resin on site. The embedded specimens were cross-sectioned by grinding with ethanol followed by polishing. The cross-sections were studied by an optical microscope and a scanning electron microscope (SEM) equipped with energy-dispersive X-ray spectroscope (EDX) for elemental analysis and mapping.

2.3 Measurement methods

VTT has extensive experience in the application of special probes for corrosion monitoring and deposit analysis in high temperature combustion plants. The latest development is an advanced water/air cooled probe which is approximately two meters in length and can accommodate two sections with six test rings in each. One section is water and air cooled and is exposed at metal temperatures of approximately 550°C and the second is air-cooled at metal temperatures around 750°C. A photograph of the probe with the two separate sample regions is presented in Figure 1.



Temperature set point 550 °C (windward)

Temperature set point 750 °C (windward)

Figure 1. VTT's high temperature probe can be applied in analysing both short- and long-term deposition build-up and corrosion risks. During the tests the two metre casing remains cool by water cooling whereas the temperature of the sample exposure heads are adjusted as desired by additional air cooling.

There are several temperature measurements in different sides of the probe for both temperature areas. The primary head consists of stationary part in which there are four thermo-couples and area for detachable material rings. The length of a detachable material ring in the primary head is 12.5 mm/each. In the secondary head the detachable material rings are connected to the system through a separate extension ring. The length of a detachable material ring in the secondary head is 15 mm/each. There are two thermo-couples in the extension ring and material temperatures of the detachable material rings are measured at three rings. The flue gas temperature is measured in the tip of the probe with one covered thermo-couple. The thermal expansion in primary and secondary heads as well as in the casing is eliminated with a special spring system consisting of four separate springs.

The probe is air- and water-cooled with separate controllable cooling unit. During the tests the two metre casing remains cool by water cooling whereas the temperatures of the sample exposure heads are adjusted as desired by additional air cooling. The surface temperatures of the probes vary depending on the direction of the flue gas flow. During the insertion of the probe into the boiler the direction is chosen so that the windward temperature in the sample ring area is maintained constant by adjusting the air cooling rate. The temperatures on other sides of the probe vary depending on the deposit formation and cleaning stages.

2.4 Test facility

VTT is conducting a programme of probe exposure trials at the Alholmens Kraft power plant located in the western coast region of Finland, in the town of Pietarsaari. This facility is one of the largest biomass fuelled power plants in the world producing electricity, district heating and process steam and heat for the UPM-Kymmene plant. The exposure campaign involves the deployment of one corrosion probe in a 550 MW_{th} circulating fluidised bed boiler which has live steam parameters of 194kg/s, 165bar, 545°C, Figure 2. During the measurements the

boiler was fired on average with 30% peat, 10% coal, 50% of biomass (forest residues, industrial wood and bark etc.) and 10% SRF (solid recovered fuel). Daily fluctuations in the fuel shares in comparison to those averages can be wide as well as the fluctuations in the whole process parameters.

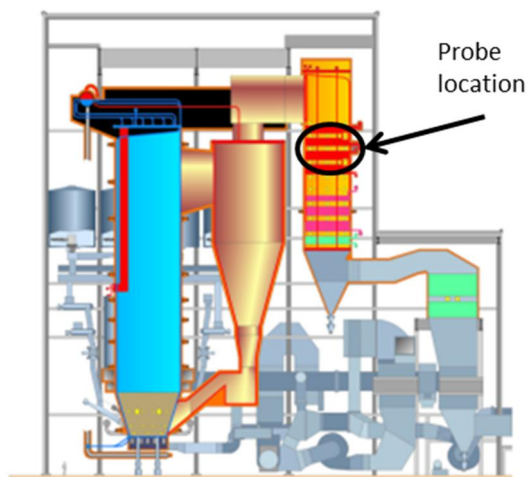


Figure 2. Alholmens Kraft CFB boiler with installed probe location identified.

The overall VTT corrosion probe test programme includes three exposure tests, with a total of 36 test specimens exposed for periods between 1,000 and 7,000 hours. The duration of the first exposure was about 1300 hours. The probe was inserted into superheater area after the cyclones, as shown in Figure 2.

3. Results

3.1 Probe measurement and process data

In the following figures some process and probe measurement data are presented. Plant electricity output varies a lot in short intervals, Figure 3. This has an effect on the flue gas temperatures inside the boiler, Figure 3, and further on the temperatures at the probe surfaces, Figure 4. Some fluctuations are also present in the flue gas emissions, e.g. HCl and SO₂ emissions presented in Figure 5. The probe after the exposure is presented in Figure 6.

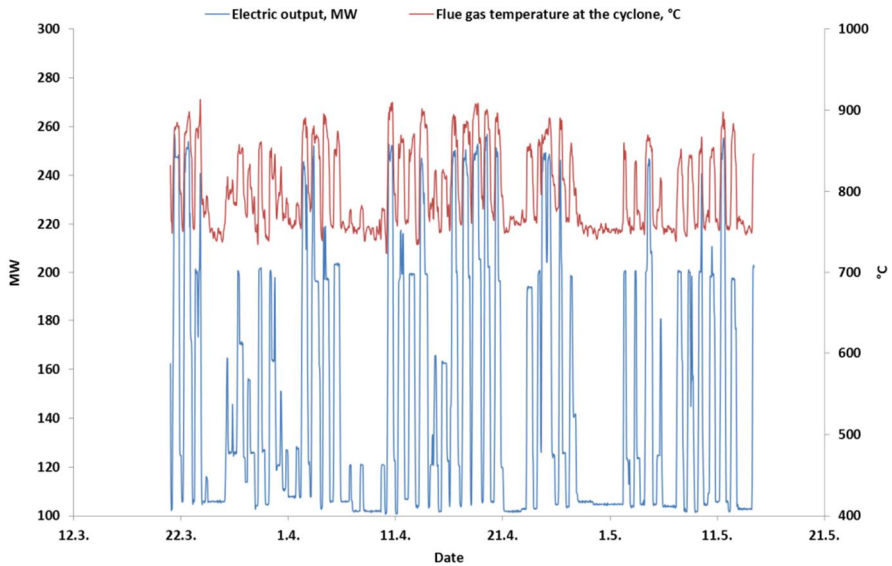


Figure 3. Plant electricity output and flue gas temperature at the cyclone during the measurements.

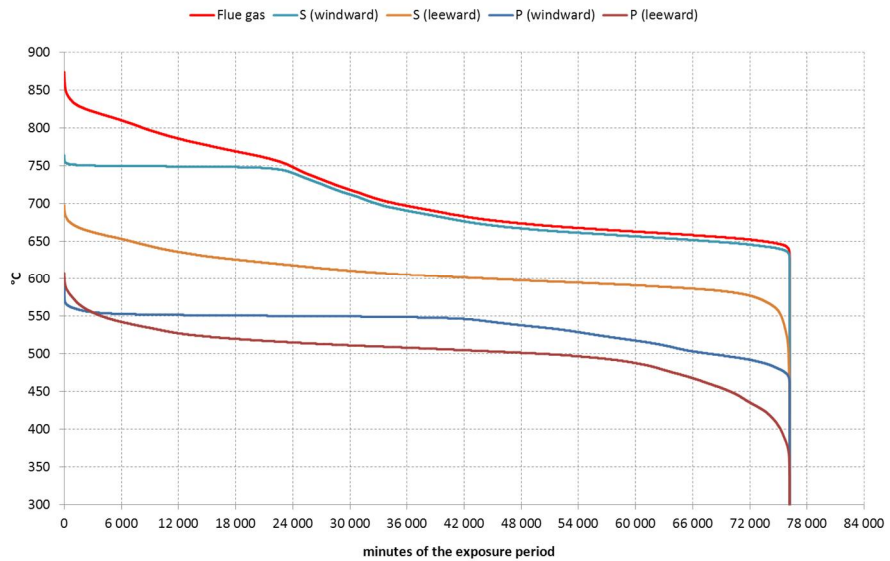


Figure 4. Probe measurement data presented in the form of stability curve for flue gas, windward and leeward temperatures (S=secondary head, P=primary head). Due to high variations in the plant load and process temperatures the probe temperature profiles are also fluctuating.

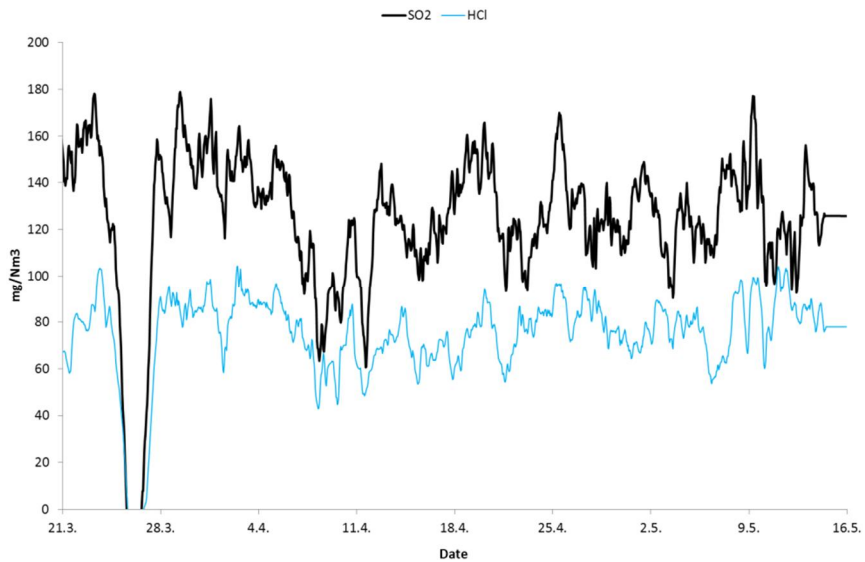
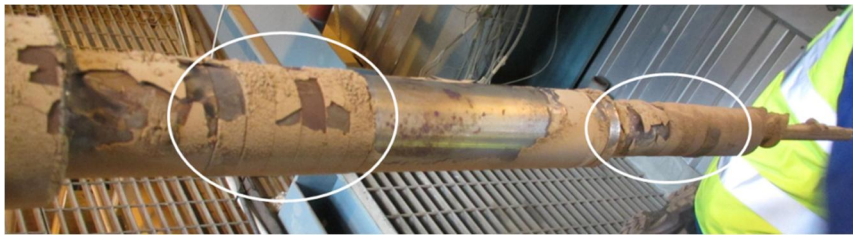


Figure 5. SO₂ and HCl content in the flue gas during the measurements (24 h averages).



Temperature set point 550 °C (windward)

Temperature set point 750 °C (windward)



Figure 6. VTT's high temperature probe after 1300 h exposure. On the left material samples at metal temperatures of approximately 550°C and on the right samples around 750°C.

3.2 Corrosion performance at 550°C

All coated specimens endured the exposure at 550°C without significant changes. Inconel 625 had minor corrosion within the top 20 µm of the coating at flue gas side. The uncoated base material (T92) was in far worse condition after the exposure than the coated specimens. It had up to 200 µm thick porous corrosion product layer both at flue gas and leeward side, Figure 7. The multilayer iron-chromium oxide was porous and detached from the metal surface. The corrosion-deposit layer above consisted mainly of oxygen, iron, sulphur, calcium, potassium, aluminium and silicon. SHS9172 was found to be corroded from the side and peaking at the leeward side, Figure 8, with a 30 µm thick corrosion product layer and internal coating degradation up to 20–40 µm depth. Chlorine was detected at the outer surface of the coating. Diamalloy 4006, Inconel 625, NiCr and TAFE 45CT had developed a 1–2 µm thin Cr rich oxide layer.

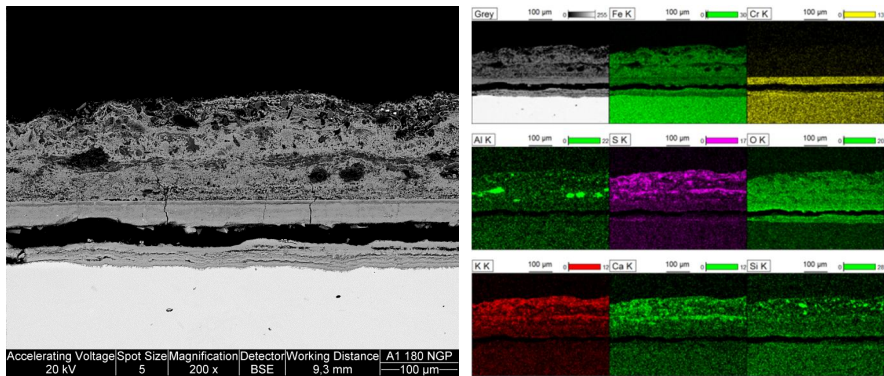


Figure 7. SEM (BSE – back scattered electron) image of the T92 uncoated tube material together with EDX from the leeward side.

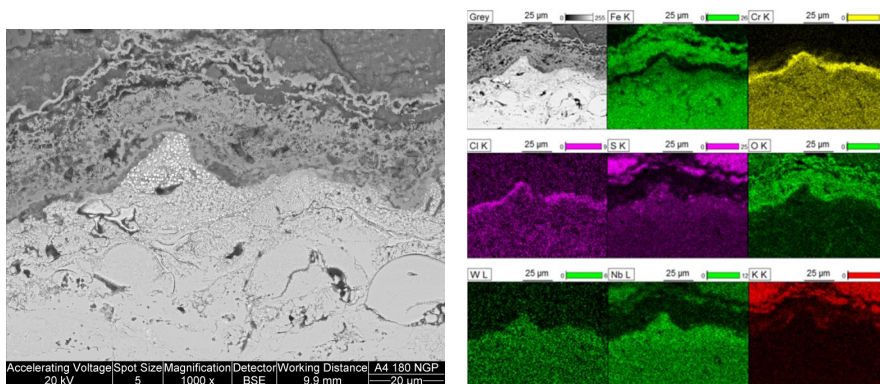


Figure 8. SEM (BSE) image of the outer surface of the SHS9172 coating and EDX map analysis from the leeward side.

3.3 Corrosion performance at 750°C

The coatings exposed at 750° C showed clear differences between the coatings and also between locations within the specimens. Generally the flue gas direction had the most severe corrosion and the leeward direction the least.

Uncoated base material A263 formed a 1–10 μm thin Cr-rich oxide scale, where 10 μm represents slight pitting. On average the scale was around 3 μm thin. The scale was observed to be thickest at the leeward orientation. S, Ti and Al were also found in the Cr-rich oxide scale. However near the flue gas side the scale was lost during removal of the specimen from the probe and therefore the thickness in that region could not be measured. Deepest penetration into the material through grain boundaries was 10 μm.

Inconel 625 (CJS) exhibited pit corrosion not only at flue gas direction but also at side areas of the test ring. In many cases the corrosion had already reached the substrate and continued deeper into it and also widened the pit. One such location was at flue gas side where the coating had been completely lost at a wide area and pits could be seen where there was still coating left. Figure 9 shows the remaining coating at flue gas orientation.

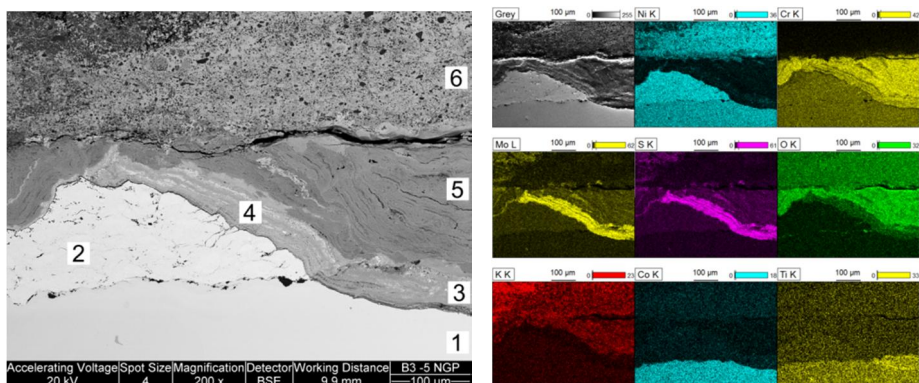


Figure 9. SEM (BSE) image of the remains of the IN625 coating and EDX map analysis from the flue gas side.

SHS9172 (CJS) was corroded rather uniformly. The highest corrosion rate was at flue gas side with a 25–55 µm thick corrosion product that consisted of two irregular layers: topmost being porous Fe and O rich layer which was partially mixed with the deposit. Under the topmost layer was a porous Cr and Nb rich layer. The thickest parts of the corrosion product had the least dense Cr-layer. At leeward and side orientations, the thickness of the corrosion product layer was around 20 µm.

NiCr (CJS) formed a thin, 2 µm thick layer on the coating. EDX analysis revealed that the thin layer contained high amounts of Cr and O. EDX mapping confirmed that the thin layer had protected the coating against the environment: the coating forming elements Ni and Cr were not found on the deposits, which contained mainly K, Ca and Na along with S and O.

Diamalloy 4006 (CJS) was completely consumed on the flue gas orientation, but the corrosion products and deposits were unfortunately lost during removal of the specimen from the probe. Prior the removal it was observed that the deposits around the specimen were massively bulging unlike on the other specimens. At side area some corrosion products were found. EDX analyses revealed that they were related to the corrosion of the substrate, which indicates that the coating had been completely lost even before the unfortunate spallation during specimen removal. At leeward direction a short piece of coating was found. The thickness of the remaining coating was 80 µm of which 30 µm was badly degraded. EDX analyses showed that oxygen had penetrated the coating and formed a layer with chromium next to the substrate. On the other hand sulphur had not been able to penetrate the coating and was found only in the severely degraded topmost 30 µm.

The only arc sprayed coating, NiCrTi, had uniform corrosion throughout the coating surface. EDX analyses revealed that the coating forming elements were protected by a Cr-rich layer on top of the coating. The thickness of the Cr and O-rich layer was at times up to 20 µm, but generally around 2–4 µm. It is worth noting that due to the arc spraying method the coating was sort of pre-oxidized: oxi-

dation at the lamella boundaries is clearly visible in the elemental maps of Figure 10. Sulphur was unable to penetrate the coating.

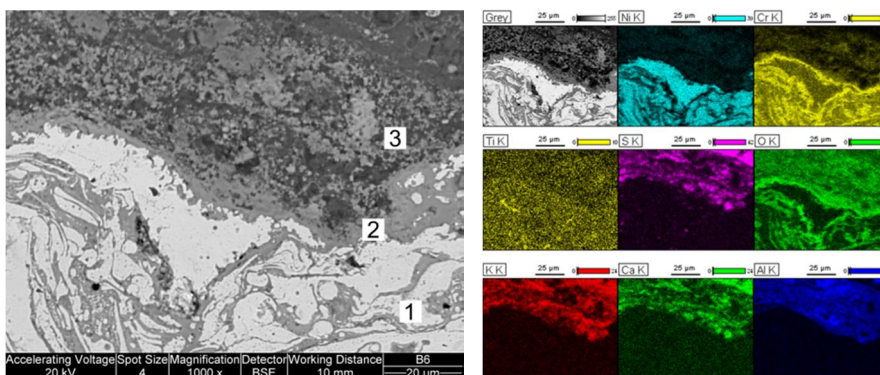


Figure 10. SEM (BSE) image of the outer surface of the arc sprayed NiCrTi coating and EDX map analysis from the leeward side.

3.4 Preliminary economic feasibility of the coating solution

To use coatings as a solution to extend the lifetime of superheaters also the economics must match. Not much information on the economics can be found in public domain thus a very preliminary analysis for the economic feasibility conducted at VTT. In this an investment of 2.5 M€ to a new superheater in a 300 MW biomass fired boiler was considered. Estimations were conducted using a 10% general interest rate for the investment in two base lifetime approaches, 5 and 10 years. With different assumptions on extended lifetime the plant can save money by postponing the next superheater renewal investment. To avoid estimating the needed capital and operation costs from the coating instalment we can define how much the plant would be able to invest on this coating approach with different lifetime extensions. This is presented in Figure 11 as the marginal cost of the coating instalment (in €/MWh_{fuel}). Overall the capital and operation costs can be from tens of thousands to hundreds of thousands euros annually depending on the assumptions.

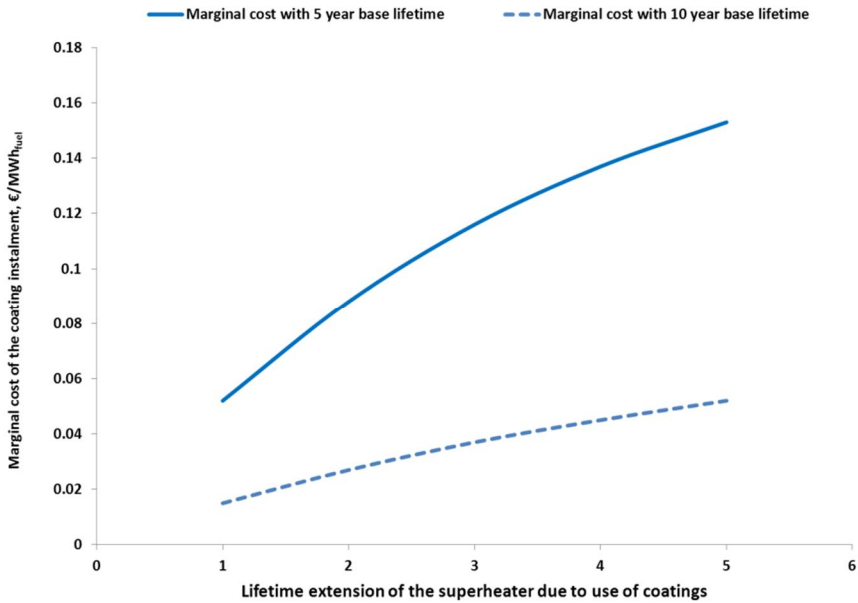


Figure 11. The marginal cost of the coating instalment (in €/MWh_{fuel}) for base lifetime approaches of 5 and 10 years due to postponing the next needed superheater renewal investment in a 300 MW biomass fired boiler with an assumed investment of 2.5 M€ to a new superheater.

4. Conclusions

An exposure campaign with corrosion probe was conducted in a 550 MW_{th} circulating fluidised bed boiler at Alholmens Kraft power plant. During this ~1300 h measurement the samples with five coatings: NiCr, IN625, Diamalloy 4006, SHS9172 and NiCrTi were exposed at two metal temperature ranges of 550 and 750°C together with reference tube materials ferritic steel T92 and nickel super alloy A263.

Due to high variations in the plant load and process temperatures the probe temperature profiles were fluctuating and also fluctuations in the fuel shares were wide. In this context the effects of fuels and boiler process parameters on corrosion phenomena were not straight-forward. However, the relatively high peak and average temperatures in the probe surface and the high shares of biomass and SRF fuels used in the boiler sustained the risks for corrosion phenomena, which were shown also in the analysed samples.

The coating performance at 550°C was excellent compared to the ferritic tube material T92. The corrosion layer thicknesses of the coatings were about 1/7 or negligible compared to the corrosion layer thickness of the T92. At the higher

temperature clear differences between the coatings emerged: tube material A263 together with NiCr and NiCrTi coatings being the top performers.

Acknowledgements

This work was performed in the FP7 EU project NextGenPower – Efficiency increases in existing and new build pulverised coal power plants with a view to CCS. The authors would like to thank Alholmens Kraft Ab for the opportunity to use the power plant for the experiments.

References

1. H. J. Grabke, E. Reese and M. Spiegel, The effects of chlorides, hydrogen chloride, and sulfur dioxide in the oxidation of steels below deposits. *Corrosion Science*, 1995, 37, pp. 1023–1043.
2. M. Spiegel, Salt melt induced corrosion of metallic materials in waste incineration plants. *Materials and Corrosion*, 1999, 50, pp. 373–393.
3. D. Bankiewicz, P. Vainikka, D. Lindberg, A. Frantsi, J. Silvennoinen, P. Yrjas, and M. Hupa, High temperature corrosion of boiler waterwalls induced by chlorides and bromides – Part 2: Lab-scale corrosion tests and thermodynamic equilibrium modeling of ash and gaseous species. *Fuel*, 2012, 94, pp. 240–250.
4. T.S Sidhu, R.D. Agrawal and S. Prakash, Hot corrosion of some superalloys and role of high-velocity oxy-fuel spray coatings—a review. *Surface & Coatings Technology*, 2005, 198, pp. 441–446.
5. Y. S. Li and M. Spiegel, S. Shimada, Corrosion behaviour of various model alloys with NaCl–KCl coating. *Materials Chemistry and Physics*, 2005, 93, pp. 217–223.
6. H.T. Ma, C.H. Zhou and L. Wang, High temperature corrosion of pure Fe, Cr and Fe–Cr binary alloys in O₂ containing trace KCl vapour at 750°C. *Corrosion Science*, 2009, 51, pp. 1861–1867.
7. S.C. van Lith, Flemming J. Frandsen, M. Montgomery, T. Vilhelmsen and S.A. Jensen, Lab-scale Investigation of Deposit-induced Chlorine Corrosion of Superheater Materials under Simulated Biomass-firing Conditions. Part 1: Exposure at 560°C. *Energy & Fuels*, 2009, 23, pp. 3457–3468.
8. N. Bala, H. Singh and S. Prakash, Accelerated hot corrosion studies of cold spray Ni–50Cr coating on boiler steels. *Materials and Design*, 2010, 31, pp. 244–253.

9. T. Hussain, T. Dudziak, N.J. Simms and J.R. Nicholls, Fireside Corrosion Behavior of HVOF and Plasma-Sprayed Coatings in Advanced Coal/Biomass Co-Fired Power Plants. *Journal of Thermal Spray Technology*, published online 30 January 2013, 11 pages.
10. H.P. Michelsen, F. Frandsen, K. Dam-Johansen, O.H. Larsen, Deposition and high temperature corrosion in a 10 MW straw fired boiler. *Fuel Processing Technology*, 1998, 54, pp. 95–108.
11. Y. Kawahara, Application of High Temperature Corrosion-Resistant Materials and Coatings Under Severe Corrosive Environment in Waste-to-Energy Boilers. *Journal of Thermal Spray Technology*, 2007, 16, pp. 202–213.
12. M. Montgomery, T. Vilhelmsen and S. A. Jensen, Potential high temperature corrosion problems due to co-firing of biomass and fossil fuels. *Materials and Corrosion*, 2008, 59, pp. 783–793.
13. A. Phongphiphat, C. Ryu, Y.B. Yang, K.N. Finney, A. Leyland, V.N. Sharifi, J. Swithenbank, Investigation into high-temperature corrosion in a large-scale municipal waste-to-energy plant. *Corrosion Science*, 2010, 52, pp. 3861–3874.

Life in plant – challenges and solutions

Pertti Auerkari¹, Jorma Salonen¹, Stefan Holmström¹,
Juha Viuhko² & Anu Lokkiluoto²

¹ VTT Technical Research Centre of Finland
Espoo, Finland

² Helsingin Energia
Helsinki, Finland

Abstract

Power plant structures operating at high temperatures are designed for a lengthy explicit or implied minimum life, dictated by the expected life-consuming damage mechanisms like corrosion, creep, fatigue and other forms of wear and tear. The actually realised damage shows highest rates at locations of the most adverse combination of material properties (weakness e.g. in welds), loads (mechanical, environmental, thermal) and other features like geometry and deviations from the intended condition. In case of no additional surprises, the technically justified life is likely to nevertheless differ from the assumptions in design. The explicit or implied “safety factors” will offer on average some extended life and service potential to components even after operation up to and beyond the nominal design life. To avoid surprises, it remains wise to be well informed of the evolving material and component condition of an ageing plant. The common questions are when and how should one measure to achieve the required confidence for decisions to run, repair or replace.

In this paper we contemplate the challenges for managing the life of critical components of current and future power plants. Radical changes may happen in the merit order of plants by e.g. shifting fuel prices or public policies, and this could naturally affect the need, available budget and planning to maintain a given plant. Less impact is expected in the established principles of the technical operations like monitoring, inspections and interpretation of the results. However, changes are likely in selected areas related to materials and component lifing.

1. Expected and other changes in design and operational conditions

The issues of affordability (or cost competitiveness), environmental compatibility and social acceptability are generally addressed when considering any means to produce (or convert) and distribute power. Relatively step-like or “revolutionary” development would usually imply a change of the process, like e.g. shifting from coal fired condensing plants to gas fired combined cycle and CHP plants since 1970’s, to halve the specific carbon emissions per MWh, although this change has been a

bumpy road depending on relative fuel prices. Even more radical reduction of emissions would require further shift to renewables or nuclear power. There are considerable differences in this respect between nations [1,2], and the goals for sustainability or globally significant decrease in CO₂ release appear to remain distant (Figure 1). Towards the same goals there is also parallel, more evolutionary development [3] to improve the performance of a given process and its efficiency (Figure 2). The performance of the overall system is also much affected by the characteristics of the production mix, network (grid) connectivity and market positions in the system. For example, increasing share of wind and solar power will enhance the fluctuation of supply, with the consequence that other power sources will have to compensate by operating in a more demanding cyclic or ramping mode [4,5]. With sufficiently increasing share of fluctuating part, it can become challenging to cover the resulting ramps, peaks and valleys of supply and demand by spinning reserve, hydropower, pumping stations and other short-term capacity. Together with diminishing opportunity for base load operation, this will increase the total generation cost, and calls for new solutions.

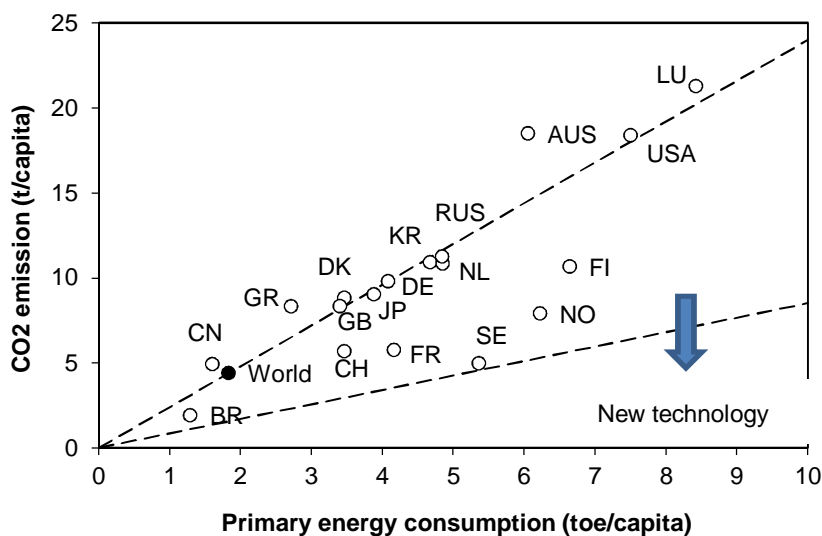


Figure 1. CO₂ emissions vs. primary energy consumption for selected countries (data from [1]).

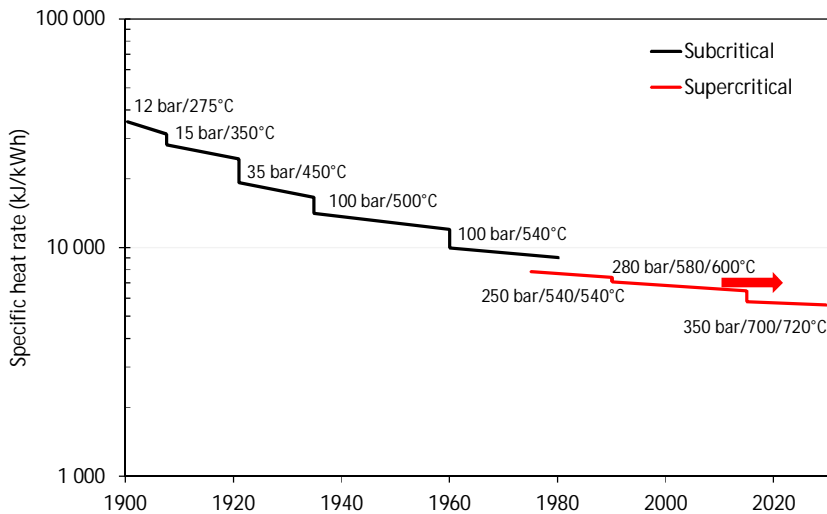


Figure 2. Development of the heat rate of European coal fired power plants, adapted from [3].

For existing thermal power plants this means a shift beyond the type of operation assumed in design, and possibly changes in the order of merit, shortened life and/or increased cost of asset care and production. For new plants the challenges extend to design for coping with e.g. new fuels and modes of operation. Unfortunately a design that aims for higher efficiency to reduce specific emissions with high operating temperatures and pressures is not particularly amenable for new fuels or flexible service with fast ramping or cycling. Adjustments can and have been made in design for improvement, for example in case of gas and steam turbines, but it remains a challenge to provide hundreds or thousands of megawatts in a time frame of seconds to minutes (Table 1). Nevertheless, some flexible/cyclic operation is allowed for such plants, and the technical development including materials improvements can allow for higher efficiency and reduced emissions. This paper aims to address selected materials related issues that limit the performance and life of critical components of thermal power plants.

Table 1. Challenges and materials issues in power technologies; CCS = carbon capture and storage.

Technology	Advantages	Current limitations	Materials issues in
Fossil: coal, gas, oil	Max ~ 1 GWe, also for heating, some cycling and ramping ¹⁾	CO ₂ emissions without CCS, variable/increasing cost	High temperature end, surfaces in contact with flue gas & process media
Nuclear	Nearly CO ₂ -free Max > 1 GWe Modest fuel cost	Limited cyclic duty High investment cost Long term waste	Some issues in most subsystems, surfaces in contact with process media
Biomass, waste, geothermal	Near zero to low CO ₂ Max ~0.1–0.4 GWe Also for heating	Fuel/geography limits Low to modest efficiency	High temperature end, surfaces in contact with flue gas & process media
Solar, wind	Nearly CO ₂ -free No fuel cost Widely available	No load following Cost, geography limits Low efficiency (solar)	Cells, surfaces (solar) Blades, gears, support structures (wind)
Hydro	Max > 1 GWe Nearly CO ₂ -free No fuel cost, good in cycling/ramping	Geographical/seasonal limits, not ideal for heating, cost & other impact of dams	Dams, turbine blades, water conduits/pipes

1) easier cycling/ramping with gas turbines than with steam plant

Fossil plants can be made in large blocks, are suitable also for combined heat and power (CHP), and can be designed for better cycling and ramping characteristics than what is generally allowed for nuclear units, albeit not for as quick response as hydropower [4,5]. Partly for this reason some fraction of fossil plants will be retained in future service, with or without CCS (Figure 3). Fossil fuels also offer other attractive features like high heating value, relatively trouble-free availability and ease of transport, handling and combustion, and advantages in co-firing biomass and waste that are more difficult to burn alone. Nevertheless, without CCS both coal and natural gas will produce high carbon emissions. To reduce the emissions and also to limit the efficiency losses from introducing CCS, there is incentive to improve the baseline efficiency of new plants. This approach is limited by the performance of structural materials, and therefore improved materials are needed to support the development of more efficient power plants [2].

To properly manage the technical condition and life of an existing asset, one normally aims to find the areas of maximum extent and growth rate of damage, ideally in comparison with design and observed state in the beginning or at a time of an earlier in-service assessment. In the less ideal reality, the changes in the operational profiles are not really helpful. Not only is life shortened by increasingly severe or cyclic service, it may also move the critical spots of interest away from the locations of the previous inspection experience. Life prediction for timing of inspections and next assessment is hence complicated by the impact of shifting towards more severe service modes.

The experience from plant has largely provided the established, partly materials dependent, views on the expected locations and timing for inspections and other action at the high temperature end of the power plant. Although inconvenient, the plant experience will have to be re-evaluated after adopting new materials and modes of service. In this sense it is fortunate that the introduction of new materials for high temperature pressure equipment and turbines remains relatively infrequent, to allow for the accumulation of experience on long term damage before retiring a typical plant.

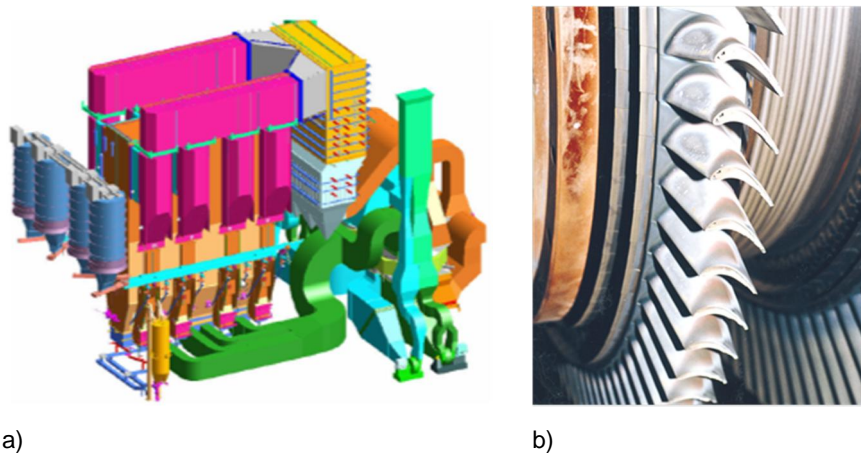


Figure 3. a) Fluidised bed boilers can provide fuel flexibility with increasing unit size; b) costly nickel alloys are applied in minimised volumes e.g. in the hot section of gas turbines of combined cycle plants.

2. Material performance in high temperature components

In terms of operational conditions as well as likelihood and consequences of failure, typical power plants include a wide range of components. For example, in one extreme an in-service failure of a steam turbine rotor is dramatic, dangerous and costly but very rare, and perhaps in the other extreme corrosion-related failures of biomass or waste boiler tubes are not very dramatic or unusual (Figure 3). The resulting risk (probability x consequence) of unavailability can be more comparable, although even then not ideally equal for reasons such as personnel safety. Again, an good idea of the probability (frequency) and consequences of a given type of failure we typically obtain from incidents statistics that is necessarily better for conventional than new designs, materials, and operating conditions.

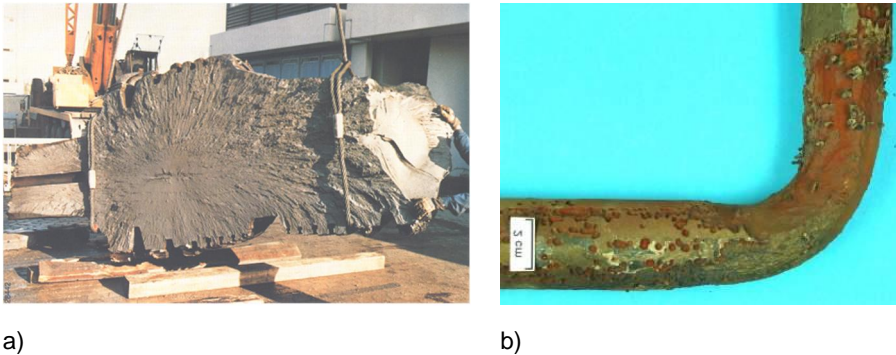


Figure 4. a) Rare type of failure: in-service fracture of a steam turbine rotor; b) not uncommon life-limiting damage: tube wall loss by fireside corrosion in a biomass boiler.

A recent example on materials in this sense can be seen in the attempts to use the newer high strength martensitic-bainitic low alloy steels T24 and T23 in water walls without post-weld heat treatment (PWHT), not with entirely satisfactory success [6–8]. Challenges from elevated hardness, low ductility (also in creep), weld defects, embrittlement, and SCC/hydrogen cracking have been reported already before or during early service. Low ductility of weld metal and the coarse-grained heat affected zone (CGHAZ) can result in high sensitivity to e.g. fatigue, hydrogen or stress corrosion damage. The compounding effects related to or indicated by low ductility may be further aggravated by the effects of ageing. Measures like PWHT to decrease the peak hardness and to improve ductility can help but reduce the advantages of material selection over conventional solutions. The issue has been a subject of considerable research effort, and these materials, particularly when welded, can be characterised as relatively unforgiving to quality deviations, structural constraint and local stresses at defects from welding or environmental impact. Due to reduced creep ductility and weld strength factors, the modified 2% Cr steels like P24 (Figure 5) also do not challenge the use of higher chromium steels like P91 in steam lines and headers [8,9].

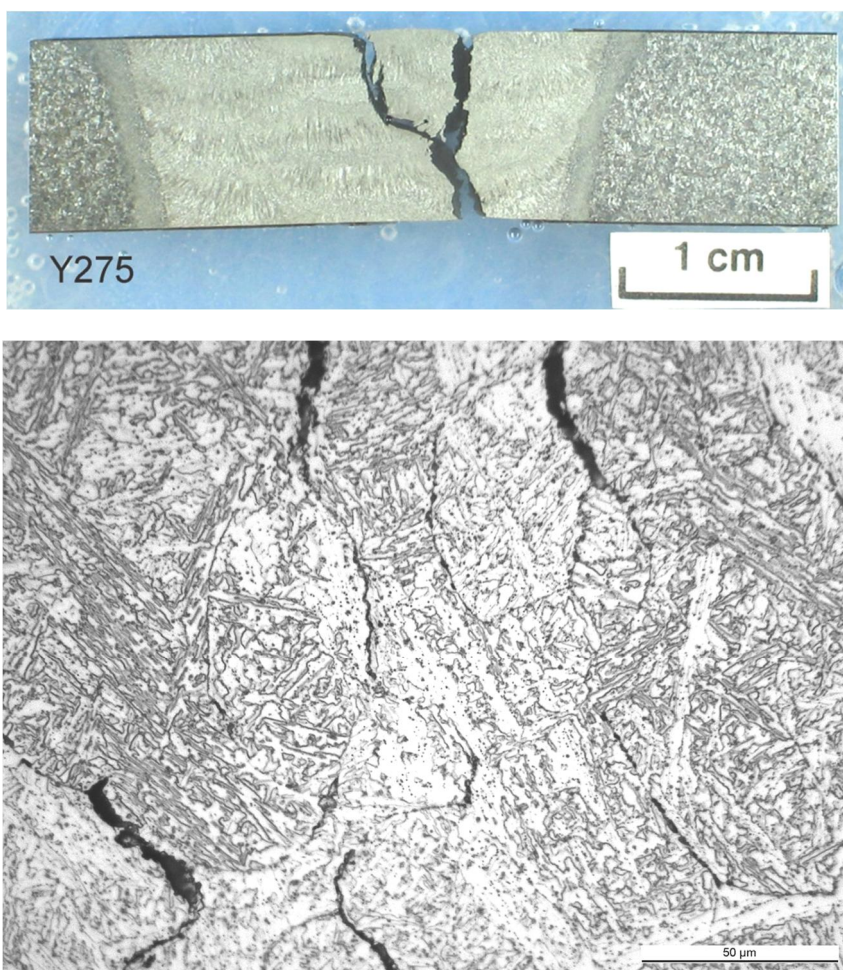


Figure 5. Top: cross-weld creep test of P24 with failure in weld metal; below: creep damage and cracking at grain boundaries in weld metal [9].

Albeit more satisfactory in superheaters, the experience with the modified 2% Cr steels demonstrates a common phenomenon in developing new materials: the initially observed very promising properties may be later balanced by some backlash in other, unforeseen characteristics. This is often seen in creep strength: the first published values for long term rupture strength are nearly invariably higher than those confirmed some 10–20 years later. It is also not a new observation that increasing material strength tends to reduce its ability to deform and yield without damage like cracking or fracture. This certainly applies to low-alloy Cr-Mo steels, and one of the early lessons was with the steel 0.5CMV (14MoV63) that like P/T23 and P/T24 contains vanadium for precipitate (MX) strengthening. In spite of show-

ing better creep strength than P22, this steel has fallen into disuse in new plants, partly because of its propensity to creep cavitation and cracking at welded joints. The difference to P22 appears as lower elongation (strain to fracture) and reduction of area under nearly any testing conditions including those in standard qualification tests [10].

The newer precipitate-strengthened steels such as P91 and P92 can also exhibit much higher potential loss of strength than simpler conventional steels that rely more on solid solution strengthening. Therefore, relatively small deviations from the intended steel chemistry or heat treatment may have much more profound impact on strength and structural performance (Figure 6).

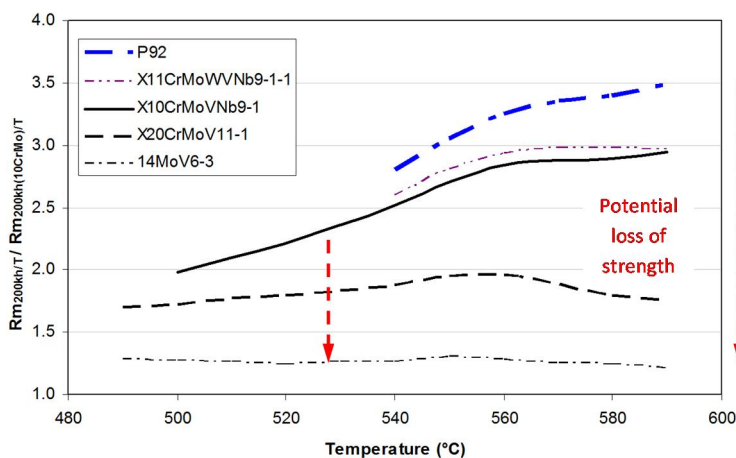


Figure 6. Creep strength (EN 10216) of selected steels normalized to that of 10CrMo9-10.

This is likely to apply to the future generations of improved steels that are slowly being introduced, while the existing materials reveal their characteristics in long term testing and service (Figures 7 and 8). In ferritic 9%Cr steels, creep strength has been improved with modest alloying cost, compared to austenitic steels with higher targets in oxidation/corrosion resistance [2].

In addition to CCS, also biomass, waste and other low grade fuels can limit the plant efficiency through the achievable maximum material temperatures. With the EU emphasis of 20% renewable energy target for 2020, multiple processes can be used to convert biomass into heat, power and fuels, but the availability of biomass and logistics tend to limit the maximum unit size to about 50–100 MW, except perhaps at large harbours or with co-firing/co-gasification of coal. The EU Waste Management Directive requires, in priority order, waste avoidance, recycling, incineration and land-fill for the disposal of waste. In addition to using technology to minimise the risk to health and environment, there is an increasing incentive to improve the efficiency of WtE plant [11,12]. Increasing the operating temperatures

remains a challenge: for example, the current incinerators already routinely use Ni alloys like Alloy 625, so that without e.g. a topping cycle with a cleaner fuel it is difficult to extract much more power from fuels like municipal waste.

Aiming for combined fuel flexibility and high efficiency in biomass combustion has resulted in incidences of severe fouling and fireside corrosion of superheaters and water walls [13,14]. Even the best fossil plant materials do not tolerate these conditions without significant reduction of steam conditions and/or shortened component lifetime.

The process development, e.g. for CCS, will involve materials issues but the initial systems mostly operate with current materials and close to reasonably well known working conditions. Longer term development may require combined process and material optimisation, but change is generally slower for materials than processes. Plants with CCS will also face the cycling/ramping challenge from renewable power, with reduced minimum base load. Accommodation is easier for gas fired and combined cycle plants than for coal fired steam plants, while CCS is more important for the latter.

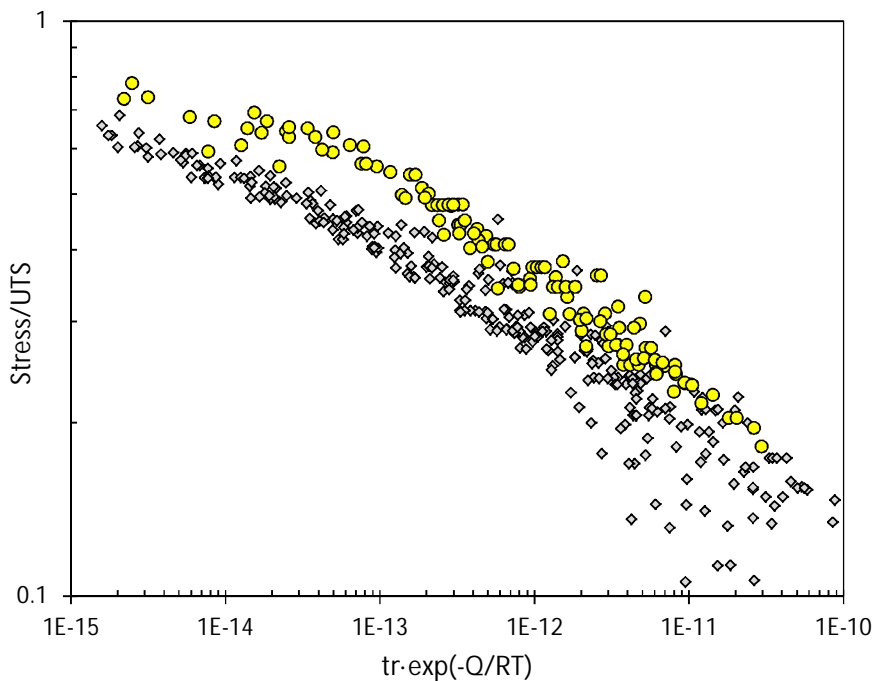


Figure 7. Creep strength (normalised with tensile strength) of austenitic steel 316H, showing loss of long term strength in heats sensitive to sigma phase precipitation (NIMS data).

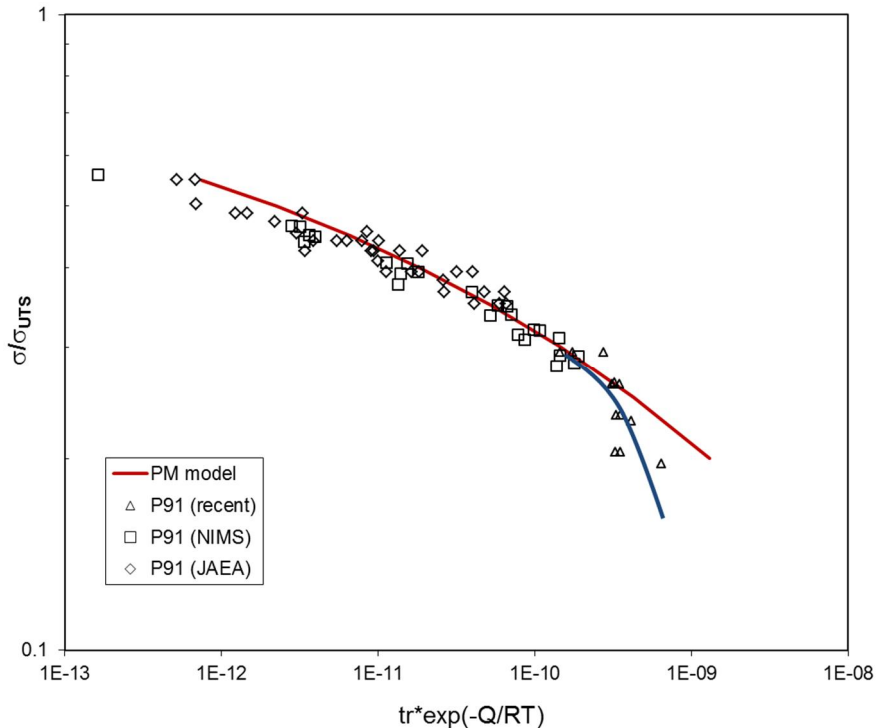


Figure 8. Creep strength of X10CrMoVNb9-1 (P91), suggesting long-term weakness towards the high end of standard Ni content at 600–650°C [K. Kimura, NIMS].

3. Discussion

Some of the above examples of challenges, as well as others not shown, may appear formidable but at least two conclusions can be made:

First, with relatively few exceptions, development of new material that will find widespread use in the high temperature sections of thermal power plants tends to be mainly evolutionary, and gradual both in time and deviation (e.g. in the range of composition) from the tradition. Partly this is a natural consequence of the requirement to verify (test) for long term service performance, and partly due to a conservative approach in committing large scale investment. Yet another reason could be the gradual nature of process development that is co-optimised with the available materials, so that any new step in the process development tends to start with the existing palette of materials. The exceptions could include materials like coatings that are to lesser extent subjected to mechanical loading (structurally critical) or limited to specific ranges of standard compositions.

Secondly, the evidence from the past suggests that not only negative news like lower than expected long term creep strength need to be feared in using new materials. Although a trend of decreasing creep strength seems to exist, there are

compensating features also to protect component life. The features include the realised “safety factors” of design, fabrication and service, which in combination tend to more than balance for possible deficiencies. In addition, also better than expected behaviour is possible, as has been noted from the inspection statistics of X20CrMoV11-1 steam line components (Figure 9). The balancing features would not guarantee good news every time but do make them much more likely. Another good point is that with slow evolution of damage, even faster than expected damage rates can be observed and intervened if there is a guiding indication of locating it from somewhere, and that with large fleets of plants in the globalised world, such indications can be expected to arise in time for most plants and users. There may be exceptions like users of some unique plants under special circumstances, but in general the main challenges should remain tractable.

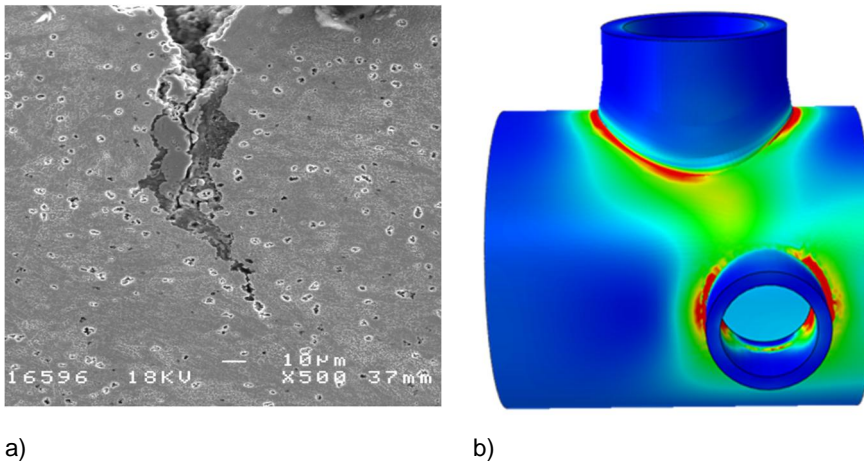


Figure 9. Steam line header (X20CrMoV12-1): a) saddle-point creep cracking at a nozzle weld after 135000 h of service; b) simulated in-service damage.

5. Summary

Power plant components are designed to withstand the expected range of mechanical and environmental challenge, but over the long plant life the initial assumptions are unlikely to be entirely accurate. In particular, the future market may demand even more cycling and ramping than anticipated, and the introduced features such as new technology and new materials may not perform quite as expected. However, long plant life also offers opportunities to demonstrate the learning curve due to the (on average) gradual evolution of in-service damage even when the damage grows at a faster rate than expected. For a competitive plant it is generally imperative that the changes are providing an economical advantage rather than enforced by unavailability. Practical assessments aim to find

and characterise the areas of maximum damage and damage growth rates, for designed inspections and other action to maintain the asset.

Capital-intensive systems for energy conversion and transmission, with lengthy periods for return of investment, promote conservative views on change, while a change is necessary if the greenhouse emissions are to be reduced. Regardless of the mix of the power generation technologies, certain bottlenecks that limit the performance and efficiency of production are due to materials. The material improvements tend to be evolutionary in character so that new variants are only gradually accepted to service. Contradictions can be seen in the development of the mix of generation technology. Despite the expressed good intentions in Europe to reduce greenhouse gas emissions, global action towards this end remains marginal. The challenges to even retard the trend, including the needs related to materials, loom higher than ever.

References

1. IEA Key world energy statistics 2010. International Energy Agency, Paris 2010. 78 p.
2. Blum R. Development of future power plants – demand and challenges. Key-note presentation, Baltica IX Conference, Helsinki–Stockholm 2013.
3. Mayer K.-H, Masuyama F. The development of creep-resistant steels. In F. Abe, T-U Kern & R. Viswanathan (Eds.): Creep-resistant steels. Woodhead Publishing, 2008, p.16.
4. Ludwig H, Salnikova T, Stockman A, Waas U. Load cycling capabilities of German nuclear power plants. VGB PowerTech 91 (2011): 38–44.
5. Hartung M. New power plants in Europe – a challenge for project and quality management. VGB PowerTech 91 (2011): 30–33.
6. Nowack R, Götte R, Heckmann S. Quality management at RWE using T24 boiler material as an example. VGB Powertech 91 (2011) 5 p.
7. Bendick W, Gabrel J, Hahn B, Vandenberghe B. New low alloy heat resistant ferritic steels T/p23 and T/P24 for power plant application. International Journal of Pressure Vessels and Piping 84 (2007) 13–20.
8. Abe F. Bainitic and martensitic creep-resistant steels. Current Opinion in Solid State and Materials Science 8 (2004) 305–311.

9. Auerkari P, Holmström S, Rantala J, Nevasmaa P, Salonen J. Assessment of the performance of welded P24 (7CrMoVTiB10-10). Final Report, Welding Group (FI-1), COST 536. VTT, Espoo, 2008. 12 p.
10. EN 10216-2:2002+A2:2007. Seamless steel tubes for pressure purposes. Technical delivery conditions. Part 2: Non-alloy and alloy steels steel tubes with specified elevated temperature properties. 1+78 p.
11. Co-gasification of Coal/Biomass and Coal/Waste Mixtures. Final Report EC APAS Contract COAL-CT92-0001, University of Stuttgart, Germany (1995).
12. Directive 2009/28/EC of the European Parliament and of the Council of 23 April 2009 on the promotion of the use of energy from renewable sources and amending and subsequently repealing Directives 2001/77/EC and 2003/30/EC.
13. Spliethoff H. Power generation from solid fuels. Springer Verlag: Berlin-Heidelberg, 2009.
14. Montgomery M, Vilhelmsen T, Jensen S.-A. Potential high temperature corrosion problems due to co-firing of biomass and fossil fuels. Mater. Corros. 59 (2008) 783–793.

Title	Baltica IX International Conference on Life Management and Maintenance for Power Plants
Author(s)	Pertti Auerkari & Juha Veivo (eds.)
Abstract	<p>BALTICA IX, International Conference on Life Management and Maintenance for Power Plants, Helsinki–Stockholm–Helsinki, June 11–13th, 2013.</p> <p>The Conference provides an updated review on the current and emerging methods and tools for condition and life management of thermal power plants. Baltica IX focuses on new issues and recent experience in evaluating and maintaining the safe and economic condition of major plant components including materials issues for new and existing plants. The themes also offer an insight into improvements in the methods to evaluate major components and systems, with practical examples on cases and in-plant experience.</p>
ISBN, ISSN	ISBN 978-951-38-8025-5 (USB flash drive) ISBN 978-951-38-8026-2 (URL: http://www.vtt.fi/publications/index.jsp) ISSN-L 2242-1211 ISSN 2242-122X (Online)
Date	June 2013
Language	English
Pages	683 p.
Name of the project	BALTICA IX 2013
Keywords	Thermal power plant, nuclear plant, boiler, turbine, condition, life, fuel, maintenance, inspection, monitoring, risk, reliability, material, damage, corrosion, fatigue, creep, degradation
Publisher	VTT Technical Research Centre of Finland P.O. Box 1000, FI-02044 VTT, Finland, Tel. 020 722 111

ISBN 978-951-38-8025-5 (USB flash drive)

ISBN 978-951-38-8026-2 (URL: <http://www.vtt.fi/publications/index.jsp>) ISSN-L 2242-1211

ISSN L 2242-1211

ISSN 2242-122X (Online)

